Conjugated Polymers for Biological and Biomedical Applications

Conjugated Polymers for Biological and Biomedical Applications

Edited by Bin Liu

WILEY-VCH

Editor

Prof. Bin Liu
National University of Singapore
Chemical and Biomolecular Engineering
21 Lower Kent Ridge Road
Singapore 119077

Cover: © Kotkoa/Gettyimages

Library of Congress Card No.: applied for

British Library Cataloguing-in-Publication Data
A catalogue record for this book is available from the British Library.

Bibliographic information published by the Deutsche Nationalbibliothek
The Deutsche Nationalbibliothek lists this publication in the Deutsche Nationalbibliografie; detailed bibliographic data are available on the Internet at <http://dnb.d-nb.de>.

Print ISBN: 978-3-527-34273-0
ePDF ISBN: 978-3-527-34278-5
ePub ISBN: 978-3-527-34275-4
Mobi ISBN: 978-3-527-34277-8
oBook ISBN: 978-3-527-34274-7

Typesetting SPi Global Private Limited, Chennai, India
Printing and Binding

Printed on acid-free paper

Contents

Preface

Since the conferring of the Nobel Prize in Chemistry to conducting polymers in 2000, this versatile class of polymeric materials has generated tremendous interest from academia and industry. Conjugated polymers are organic macromolecules with π-conjugated backbone, which could be designed to display high electrical conductivity, outstanding photophysical properties, and excellent biocompatibility. They have been actively explored for a wide range of applications, spanning electronics, and energy harvesting to nanobiotechnology and nanomedicine. While the last 15 years have witnessed their rapid development in optoelectronic devices, the emerging field of conjugated polymers for biomedical applications has simultaneously attracted increasing attention recently. Specifically, they have found innovative applications in a variety of biotechnologies, ranging from biosensing that takes advantage of optical amplification, to cell imaging and image-guided therapy that fully utilizes the light-harvesting properties of conjugated polymers and their structure-dependent radiative and nonradiative pathways as well as their self-assembly properties with amphiphilic molecules. In fact, with their unique biophysicochemical attributes, conjugated polymer nanoparticles have been demonstrated to be even superior to other classes of nanomaterials, such as small organic dye-based nanoparticles, semiconducting quantum dots, and inorganic nanoparticles, in many biomedical applications. Remarkably, with the continual advancement in polymer design, synthesis, and processing strategies in the last few years, conjugated polymers have been increasingly reported to be highly promising for bioimaging, sensing, and for applications in disease therapy.

This book focuses on the fundamentals and biomedical applications of conjugated polymers and their nanoparticles for bioimaging, sensing, and disease therapy. It is organized into 13 chapters and has been written by well-recognized experts in the field. The first two chapters introduce the synthesis and optical properties of various conjugated polymers, with highlights on how to make organic soluble polymers compatible with the aqueous environment. Specifically, Chapter 1 provides an overview of the various strategies commonly employed to bring conjugated polymers into aqueous media for biological applications. Chapter 2 describes the different post-polymerization and direct-polymerization methods for the generation of conjugated polymer nanoparticles. The biological imaging and sensing applications of conjugated polymers

and their nanoparticles are covered from Chapters 3–7. Chapter 3 highlights the recent progress in the development of conjugated polymer nanoparticles for molecular sensing *in vitro*. The developments in the areas of conjugated-polymer-based fluorescent probes for *in vivo* fluorescence imaging of tumors, stimuli-responsive fluorescence imaging, *in vivo* fluorescence cell tracking, two-photon excited brain vascular imaging, and dual-modality *in vivo* imaging of tumors are summarized in Chapter 4. In Chapter 5, the mechanism of photoacoustic imaging as well as the preparation and applications of semiconducting polymer nanoparticles for *in vivo* photoacoustic imaging are discussed. Chapter 6 describes the application of conjugated polymer nanoparticles as contrast agents for two-photon live cell imaging. The imaging and sensing applications of water-soluble conjugated polymers are further demonstrated in Chapter 7.

In addition to imaging and sensing applications, conjugated polymers have also been widely explored for numerous therapeutic and functional biointerface applications. Some examples are highlighted in Chapters 8–12. Chapter 8 shows the fundamental properties of conjugated polymers as gene delivery vehicles and recent demonstrations of the utilizations of multifunctional conjugated polymers for the effective delivery of genetic materials, particularly pDNA and siRNA. A broad overview on the synthesis, functionalization, and applications of conductive-polymer-based functional structures for neural therapeutic applications, particularly for electro-stimulated drug delivery, neural cell and tissue scaffolds, and implantable biosensors and neural prostheses, is provided in Chapter 9. In Chapter 10, the design strategies as well as the applications of conjugated polymers for effective photodynamic therapy are discussed using anticancer and antimicrobial treatment as examples. Chapter 11 deals with the promising utilizations of conjugated polymers as near-infrared photothermal agents for image-guided cancer therapy and combination therapy. The potential applications of conjugated polymers and conjugated polymer nanoparticles for the detection of pathogens, cancer biomarker, miRNA, as well as for cancer and neurodegenerative disorder theranostics are discussed in Chapter 12. Finally, Chapter 13 focuses on the emerging field of polymer-grafted conjugated polymers for functional biointerface applications.

This is the first book that specifically focuses on conjugated polymers for biological and biomedical applications. This book has offered a comprehensive and balanced overview on the design, synthesis, and applications of conjugated polymers and their nanoparticles for biomedical imaging, sensing, and therapy. We believe that it is suitable for readers with diverse academic backgrounds and with different knowledge levels on conjugated polymers. It will guide new readers with minimum background to get started on conjugated polymers and also, offer experienced academics and researchers new outlooks and perspectives on this exciting field. Ultimately, we hope that our readers will find this book a pleasure to read and at the same time gain invaluable insights and ideas which will be beneficial to them. We believe that this is an excellent opportunity to highlight the remarkable basic science and technological potential of conjugated polymers, and to use the book to provide readers with a unique single source to understand the emerging applications in the exciting biomedical field.

To end this, we would like to extend our sincere gratitude to all parties who have contributed significantly to bring this book to fruition. Specifically, we thank all the authors for their precious contributions as well as the editorial team at Wiley-VCH for the dedicated and unceasing support.

Singapore 2017 *Bin Liu*

1

Strategies to Bring Conjugated Polymers into Aqueous Media

Jie Liu and Bin Liu

National University of Singapore, Department of Chemical and Biomolecular Engineering, 4 Engineering Drive 4, Singapore 117585, Singapore

1.1 Introduction

Conjugated polymers (CPs) are organic macromolecules with extended π-conjugation along the molecular backbone [1, 2]. Their unique optoelectronic properties that result from the highly delocalized π-electrons can be easily manipulated through modification of the conjugated backbones. As a result, CPs have been widely used in various research fields related to organic optoelectronic devices [3–5], chemo/biosensors [6, 7], and medical diagnosis and therapy [7–9]. For biology-related applications, the main obstacle is to render CPs water soluble or water dispersible. So far, mainly three strategies have been used to bring CPs into aqueous media, which include the design and synthesis of conjugated polyelectrolytes (CPEs) and neutral water-soluble conjugated polymers (WSCPs), as well as the fabrication of water-dispersible conjugated polymer nanoparticles (CPNPs) (Scheme 1.1).

CPEs are a kind of macromolecules characterized by π-conjugated backbones and ionic side chains [10]. Their solubility in aqueous media can be fine-tuned by modification of the ionic side chains. Although neutral WSCPs do not possess any charge, they have amphiphilic segments, for example, oligo(ethylene glycol) [11], that compensate for the hydrophobic nature of the conjugated backbones. These two strategies require the chemical modification of each polymer to bring them into water. A more general and straightforward method is to prepare for the CPNPs, which can in principle bring any organic soluble polymers into aqueous media [12]. To simplify our discussion, in this chapter, we only discuss CPNPs that are prepared from neutral CPs. The water solubility of CPNPs is largely determined by the polymer matrix used and the nanoparticle size, while their optical properties are associated with the neutral CP.

This chapter aims to provide readers with an overview of the strategies that can be used to bring CPs into aqueous media for potential biological applications. In this chapter, we will discuss the synthetic approaches for CPEs first, which is followed by the neutral WSCPs and CPNPs. The section on CPEs is organized

Conjugated Polymers for Biological and Biomedical Applications, First Edition. Edited by Bin Liu

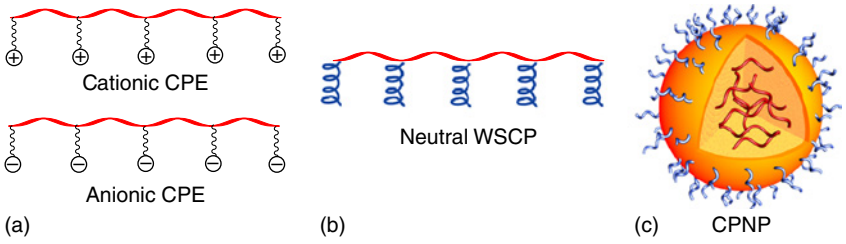

Scheme 1.1 Illustration of typical structures of CPE (a), neutral WSCP (b), and CPNP (c). The red color represents the CP backbone.

according to the charge sign. For each type of charge, we mainly select three types of CPEs (polythiophenes, poly(phenylene)s, and polyfluorenes) as examples to describe how the conjugated backbones can be synthesized and how the charged chains can be incorporated. Similar strategies will be discussed on neutral WSCPs. For the section on CPNPs, we will mainly introduce three strategies for CPNP preparation (e.g., reprecipitation, miniemulsion, and nanoprecipitation) with specific examples. Owing to the limited space, we apologize that we cannot cover every example, and only the most representative ones are selected for discussion.

1.2 Synthesis of CPEs

In the past decades, a large number of CPEs have been successfully developed. According to their chemical structures, the synthesis of CPEs involves two aspects: construction of the conjugated backbones and incorporation of charged side chains. Many well-established polymerization methods have been employed to build the conjugated backbones (Scheme 1.2), which were typically catalyzed with organometallic complexes or bases, including Suzuki, Yamamoto, Stille coupling reaction and $FeCl_3$-catalyzed oxidative reaction for single bond formation; Heck, Witting, Knoevenagel, and Gilch coupling reactions for double bond formation; and Sonogashira coupling reaction for triple bond formation. In addition, $CpCo(CO)_2$-catalyzed homopolycyclotrimerization has also been used to synthesize hyperbranched CPEs [13]. Rational design of the conjugated backbones allows facile manipulation of their optical properties, such as absorption, emission, and quantum yield. The charges can be incorporated via direct polymerization of charged monomers or postfunctionalization of neutral CPs into CPEs (Scheme 1.3). According to the charge sign of the ionic side chains, CPEs can be categorized into three groups: anionic CPEs, cationic CPEs, and zwitterionic CPEs. The anionic groups generally include sulfonate [14], carboxylate [15], and phosphonate [16], while the cationic groups include quaternary ammonium [17], pyridinum [18], and phosphonium [19]. In the following section, we will use specific examples to show the synthetic approaches of CPEs with different charges. We start each section with polythiophenes, as they are commonly synthesized via electropolymerization and $FeCl_3$-catalyzed oxidative polymerization methods. The other CPEs are generally introduced following the sequence of single, double, and triple-bonded CPEs.

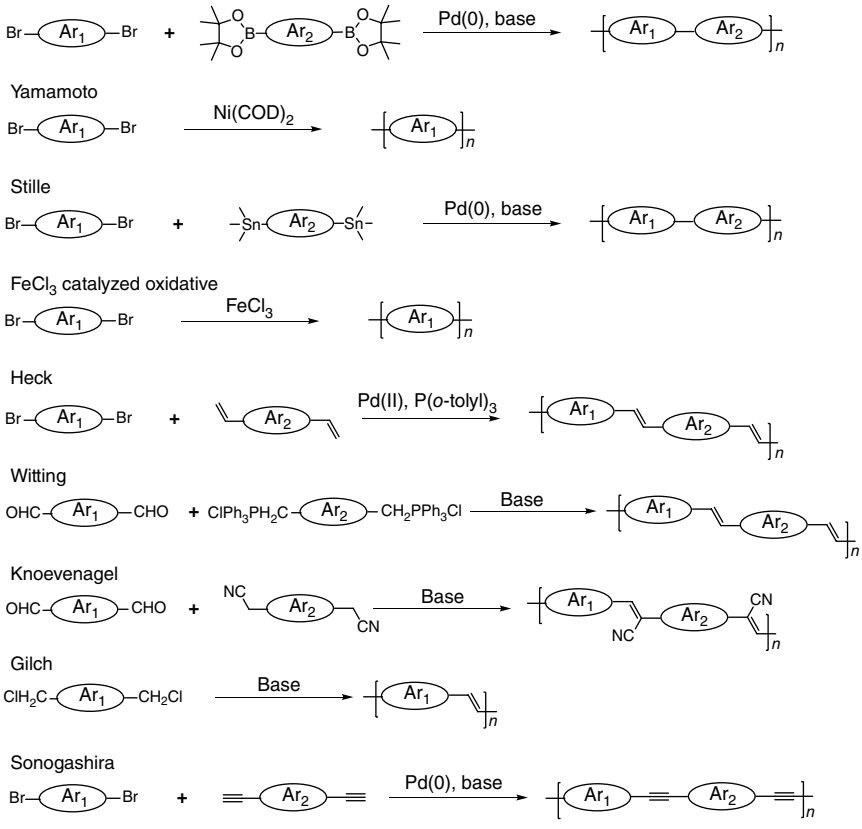

Scheme 1.2 Polymerization methods most widely employed to construct conjugated backbones. Ar_1 and Ar_2 represent aromatic units.

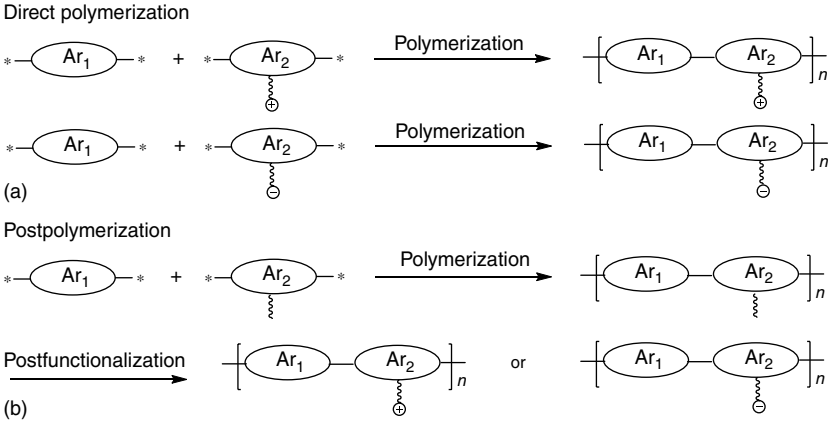

Scheme 1.3 Representative strategies for synthesis of CPEs through incorporation of charges via direct polymerization (a) and postpolymerization (b) method.

1.2.1 Anionic CPEs

1.2.1.1 Sulfonated CPEs

Sulfonated polythiophenes are generally synthesized through electropolymerization or $FeCl_3$-catalyzed oxidative polymerization methods. As shown in Scheme1.4a, the first sulfonated polythiophene **P2** was reported by Wudl's group in 1987 [14]. 2-(Thiophen-3-yl)ethanol **1** reacting with methanesulfonyl chloride yielded methyl 2-(thiophene-3-yl)ethanesulfonate **2**. Electropolymerization of **2** led to a neutral polythiophene **P1**, which was subsequently treated with NaI in acetone to give sulfonated **P2**. Using the same electropolymerization method, another sulfonated polythiophene **P3** was developed by Zotti's group (Scheme 1.4b) [20]. The key sulfonated monomer **4** was synthesized by alkylation of 4*H*-cyclopenta[2,1-*b*:3,4-*b*′] dithiophene **3** in the presence of 1,4-butanesultone and *n*-BuLi. The direct electropolymerization of **4** afforded **P3**. Unlike **P2** prepared via postpolymerization strategy, the sulfonated groups of **P3** are inherited from the key monomer **4**. In addition, Leclerc's group reported a sulfonated polythiophene **P4** by oxidative polymerization method (Scheme 1.4c) [21]. Briefly, the alkoxylation of 3-bromo-4-methylthiophene **5** was performed in *N*-methyl-2-pyrrolidone in the presence of sodium methoxide and copper bromide, leading to 3-methoxy-4-methylthiophene **6**, which reacted with 2-bromoethanol and sodium sulfite in toluene to yield 3-(2-bromoethoxy)-4-methylthiophene **7**. Subsequent treatment of **7** with sodium

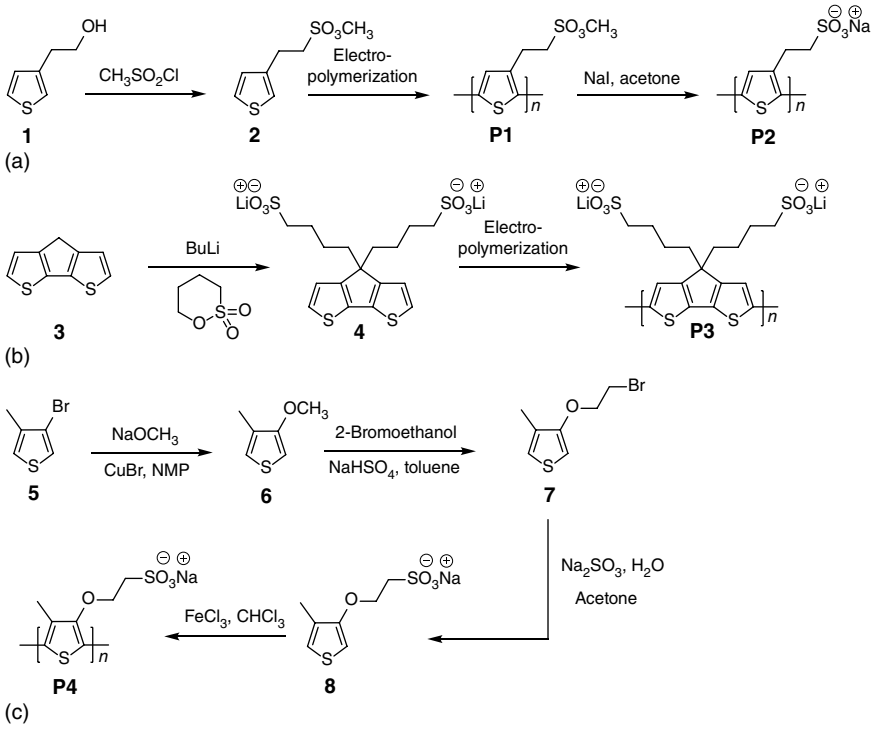

Scheme 1.4 Synthesis of sulfonated polythiophenes **P2–P4**.

sulfite in a mixture of water/acetone led to sodium 2-(4-methyl-3-thiophenyl-1-oxy) ethanesulfonate **8**, which underwent $FeCl_3$-catalyzed oxidative polymerization to afford **P4**.

To synthesize CPEs with single bonded backbones, Suzuki polymerization was often used due to its high reaction yield and good selectivity toward various functional groups [22]. As shown in Scheme 1.5a, the first sulfonated poly(*p*-phenylene) **P6** was synthesized by Wegner's group via the Suzuki polymerization method [23]. The key monomer **10** was prepared via the chlorosulfonation of 1,4-dibromobenzene **9** with chlorosulfonic acid in dichloromethane, followed by treatment with *p*-cresol in the presence of pyridine. Then, Pd-catalyzed Suzuki polymerization between **10** and 2,2′-(2-dodecyl-5-methyl-1,4-phenylene)bis(1,3,2-dioxaborinane) **11** in the presence of sodium carbonate yielded a neutral poly(*p*-phenylene) **P5**. Subsequent solvolysis of **P5** in a mixture of sodium butanolate/1-butanol followed by the addition of water, gave the sulfonated poly(*p*-phenylene) **P6** in quantitative yield. Only one of the two possible positional isomeric structures of the repeated unit is shown in **P5** and **P6** for the sake of simplicity in illustration.

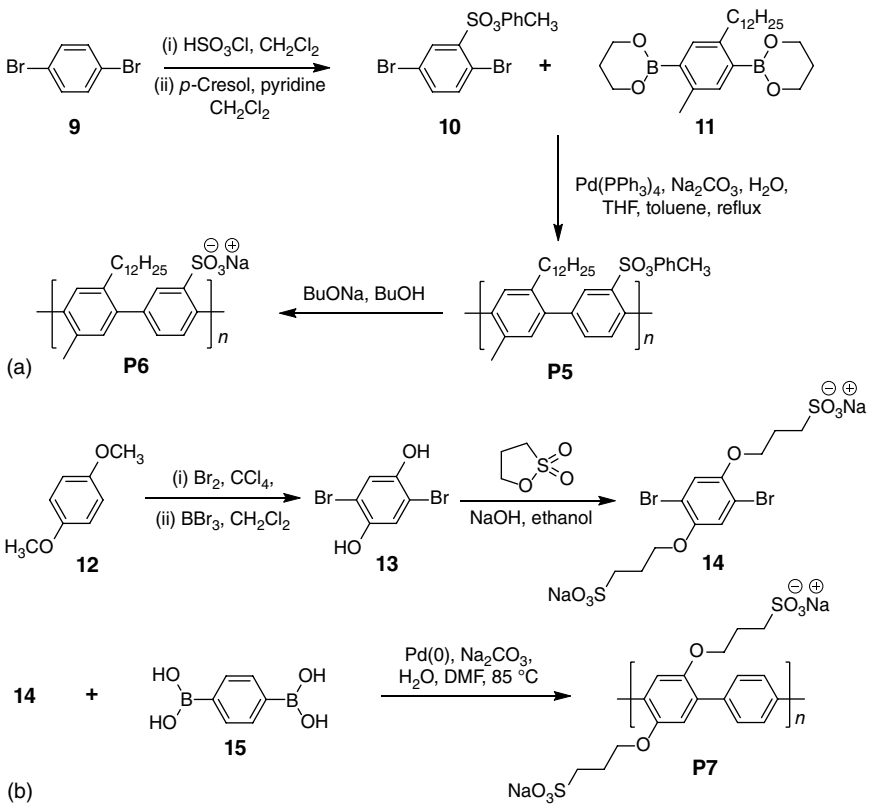

Scheme 1.5 Synthesis of sulfonated CPEs **P6** and **P7** with single-bonded backbones through Suzuki polymerization method.

A direct polymerization method for synthesizing sulfonated poly(*p*-phenylene) **P7** through Suzuki polymerization was reported by Reynolds's group via three steps (Scheme 1.5b) [24]. 2,5-Dibromohydroquinone **13** was synthesized via bromination of 1,4-dimethoxybenzene **12** using bromine in tetrachloromethane, followed by the treatment with boron tribromide in anhydrous dichloromethane. Subsequent sulfonation of **13** with 1,3-propanesultone and sodium hydroxide in absolute ethanol led to the key sulfonated monomer **14**, which directly reacted with 1,4-phenylenediboronic acid **15** through Suzuki polymerization to yield **P7**. Unlike **P5** and **P6**, there is no isomeric structure for **P7** due to its symmetric chemical structure.

To synthesize sulfonated CPEs with double-bonded backbones, various polymerization methods have been employed. Herein, we choose the widely studied poly(*p*-phenylenevinylene)s as the examples. The first sulfonated poly(*p*-phenylenevinylene) **P10** was synthesized by Wudl's group in 1990 [25], starting from the key monomer **16** (Scheme 1.6a). **16** was self-polymerized either in methanol or in water with the help of sodium methoxide or sodium hydroxide, respectively, yielding a reactive *p*-xylylene intermediate **P8**. Further hydrolysis followed by base-assisted elimination led to the sulfonated poly(phenylene vinylene) **P10**. The purity of **16** is very crucial to ensure that **P10** can be obtained with narrow polydispersity and high molecular weight.

Another approach to synthesize **P10** was reported by Gu *et al.* [26] As shown in Scheme 1.6b, potassium 3-(4-methoxyphenoxy)propanesulfonate **18** was prepared through the esterification of 4-methoxyphenol **17** with 1,3-propanesultone in anhydrous ethanol under basic conditions. Further chloromethylation of **18** with paraformaldehyde in acidic aqueous at 40 °C led to the key monomer **19**. Gilch dehydrohalogenation polymerization of **19** was performed using *t*-BuOK as catalyst to give **P10**.

The same group also employed Witting polymerization to synthesize poly(*p*-phenylenevinylene) derivatives (Scheme 1.6c) [27]. A mixture of **19** and triphenylphosphine in anhydrous toluene was kept at reflux conditions leading to the monomer **20**, which was copolymerized with terephthalaldehyde in *tert*-butyl alcohol through Witting condensation with potassium *tert*-butoxide as catalyst to yield alternating sulfonated poly(*p*-phenylenevinylene) **P11**.

Heck polymerization is also an important approach to synthesize sulfonated poly(*p*-phenylenevinylene) derivatives. As shown in Scheme 1.6d, the sulfonated diiodo-substituted monomer **22**, which was synthesized with a similar approach as for **18**, copolymerized with 1,4-dimethoxy-2,5-divinylbenzene **21** using palladium acetate and tri(*o*-tolyl)phosphine as cocatalysts in dimethyl sulfoxide under basic conditions affording the alternating sulfonated poly(*p*-phenylenevinylene) **P12** [28].

In addition to the abovementioned approaches for synthesizing poly(*p*-phenylenevinylene)s, Knoevenagel polymerization has also been used to prepare cyano-substituted poly(*p*-phenylenevinylene) derivatives [29]. As shown in Scheme 1.6e, 4-methoxyphenol **17** subsequently underwent alkylation, chloromethylation, and cyanide exchange reactions to yield **23**. Subsequently, the hydroxyl groups of **23** underwent sequential methanesulfonylation, iodination, and sulfonation, affording the key monomer **24**. Knoevenagel condensation reaction between **24** and the neutral dialdehyde monomer **25** using *t*-BuONa as catalyst in a mixture of *t*-BuOH/DMF led to the sulfonated **P13**.

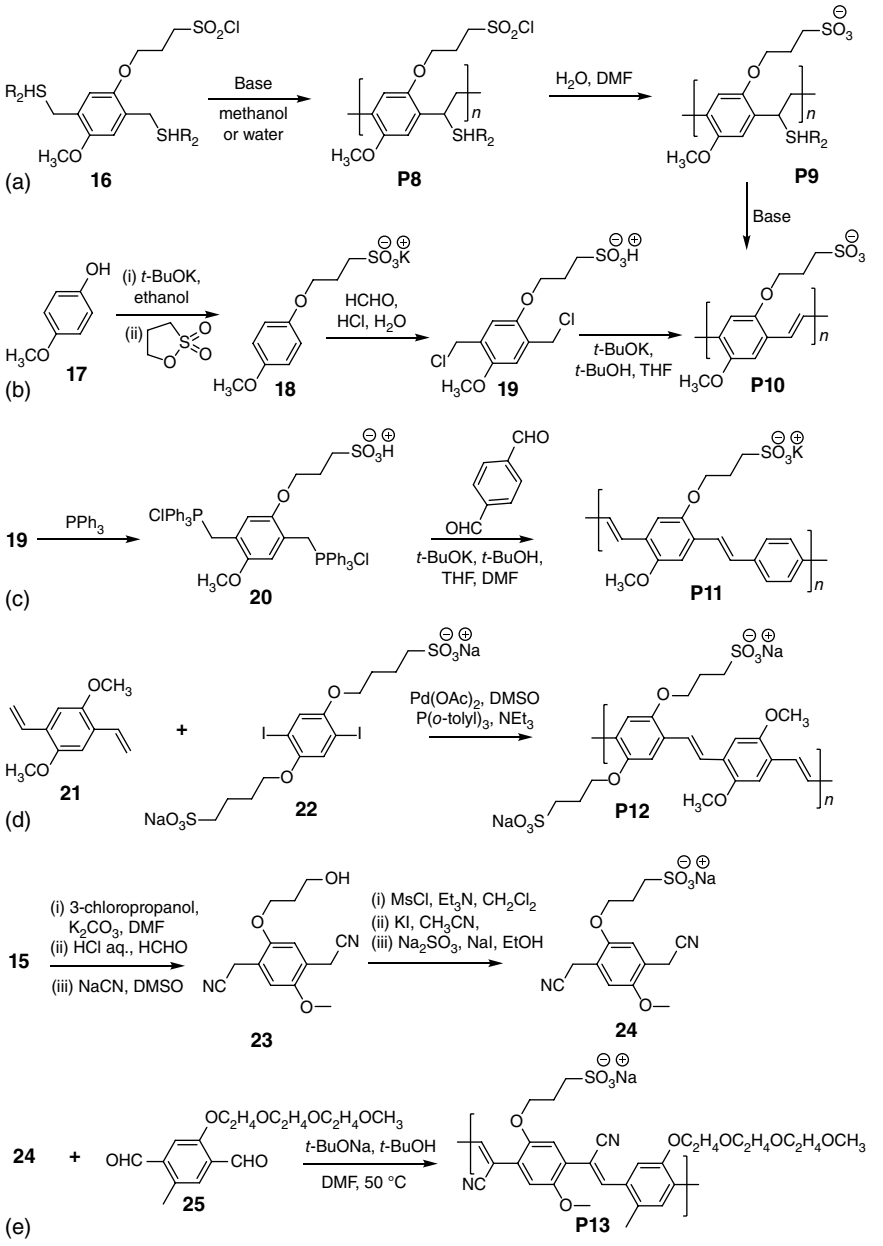

Scheme 1.6 Synthesis of sulfonated CPEs **P10–P13** with double-bonded backbones.

To synthesize CPEs with triple-bonded backbones, Sonogashira coupling reaction is commonly employed. This reaction involves a palladium-catalyzed sp^2–sp coupling reaction between aryl or alkenyl halides or triflates and terminal alkynes, with or without a copper(I) cocatalyst [30]. It can be performed under mild conditions, such as room temperature, in aqueous media. Several

monomers could also be synthesized with sulfonate functional groups. A direct polymerization approach to synthesize sulfonated polyfluorene **P14** was reported by Liu's group (Scheme 1.7a). It only requires one step to synthesize the key monomer 2,7-dibromo-9,9-bis(4-sulfonatobutyl)fluorene **27** via direct alkylation of 2,7-dibromofluorene **26** with 1,4-butane sultone and NaOH in DMSO [31]. The copolymerization of **27** and 4,7-diethynyl-2,1,3-benzothiadiazone **28** under Sonogashira coupling reaction conditions led to the sulfonated poly(fluorene vinylene) **P14** [32]. In addition, as shown in Scheme 1.7b, the key sulfonated monomer **30** can be prepared using procedures similar to **18** and **22**. Sonogashira reaction between 1,4-diethynylbenzene **29** and **30** in basic aqueous/DMF solution using tetrakis(triphenylphosphine)palladium and copper iodide as co-catalysts led to **P15**. In 2006, by utilizing the above mentioned strategy, Schanze's group developed a series of sulfonated poly(phenylene ethynylene)s with variable band gaps based on the monomer **30** [33].

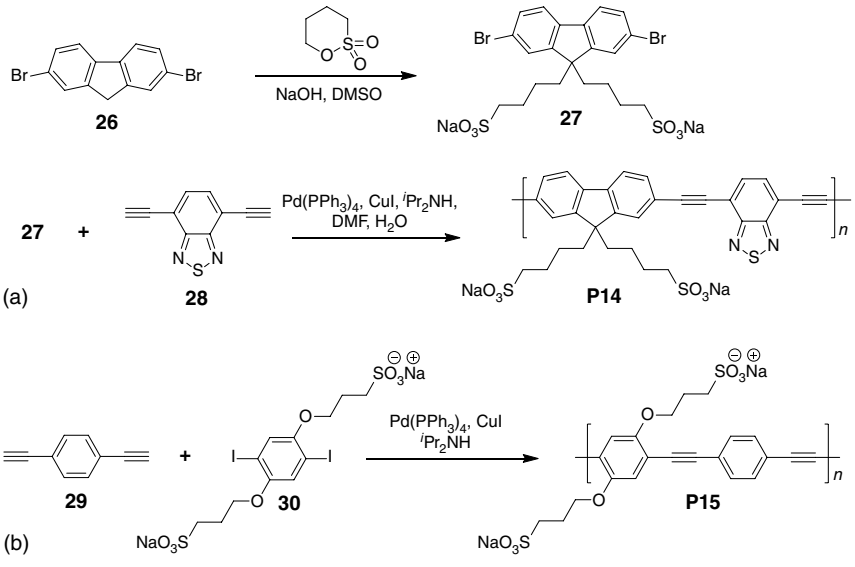

Scheme 1.7 Synthesis of sulfonated CPEs **P14** and **P15** with triple-bonded backbones through Sonogashira reaction.

1.2.1.2 Carboxylated CPEs

Carboxylated polythiophenes have been prepared through Yamamoto coupling polymerization, Stille coupling polymerization, and $FeCl_3$-catalyzed oxidative polymerization. As shown in Scheme 1.8a, the neutral poly(methyl thiophene-3-carboxylate) **P16** was synthesized via the Yamamoto polymerization of methyl 2-(2,5-dichlorothiophen-3-yl)acetate **31** [15]. Subsequently, the hydrolysis of **P16** in 2.0 M NaOH aqueous led to poly(sodium thiophene-3-carboxylate) **P17**. During the purification process, filtration was needed to remove the insoluble fraction. In addition, a CuO-mediated Stille coupling polymerization of **32** was carried out to give poly(4,5-dihydro-4,4-dimethyl-2-(2-(thiophen-3-yl)ethyl)

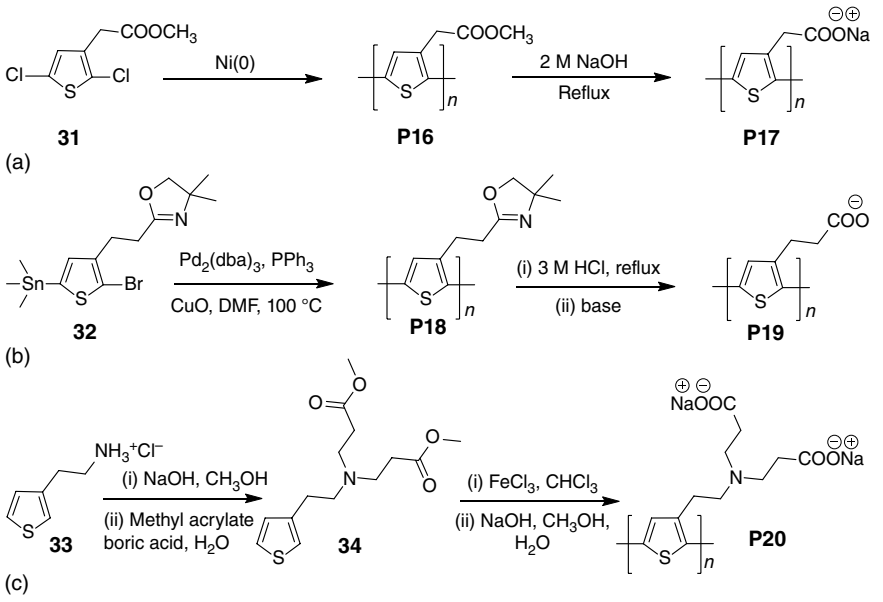

Scheme 1.8 Synthesis of carboxylated polythiophenes **P17**, **P19**, and **P20**.

oxazole) **P18** (Scheme 1.8b) [34], which was converted to **P19** after acid-assisted hydrolysis and base treatment. Compared to **P17** and **P19**, which only have one carboxylate group on each repeat unit, **P20** reported by Wang's group possesses two carboxylate groups on each repeat unit (Scheme 1.8c) [35]. The monomer **34** was synthesized by reacting 2-(3-thienyl)ethylamine hydrochloride **33** with methyl acrylate under basic conditions in the presence of boric acid. Oxidative polymerization of **34** in chloroform using $FeCl_3$ as oxidizing agent followed by hydrolysis in NaOH aqueous solution yielded **P20**.

Suzuki polymerization is generally used to synthesize carboxylated CPEs with single-bonded backbones. The first carboxylated poly(*p*-phenylene) **P21** was reported by Wallow and Novak in 1991 [36]. As shown in Scheme 1.9a, Pd(0)-catalyzed Suzuki coupling reaction between 4,4′-dibromo-[1,1′-biphenyl]-2,2′-dicarboxylic acid **35** and 4,4′-di(1,3,2-dioxaborolan-2-yl)-1,1′-biphenyl followed by treatment with dilute hydrochloric acid yield **P21** with free acid. **P21** was completely insoluble in all common organic solvents, but was soluble in dilute aqueous base as its sodium, potassium, or triethylammonium salt.

A postfunctionalization approach to synthesize carboxylated poly(*p*-phenylene)s was later reported by Rehahn's group starting from the precursor polymer **P22** (Scheme 1.9b) [37]. Owing to the high reactivity of bromide methylene group on **P22**, etherification of **P22** with ethyl *p*-hydroxyl benzoate in a mixture of toluene/DMF in the presence of *t*-BuONa produced **P23** in nearly quantitative yield. During the reaction process, the ester groups were kept intact. Almost all the ester groups of **P23** was cleaved in a homogeneous solution of toluene in the presence of 10 equiv. of *t*-BuOK and only 2 equiv. of water, followed

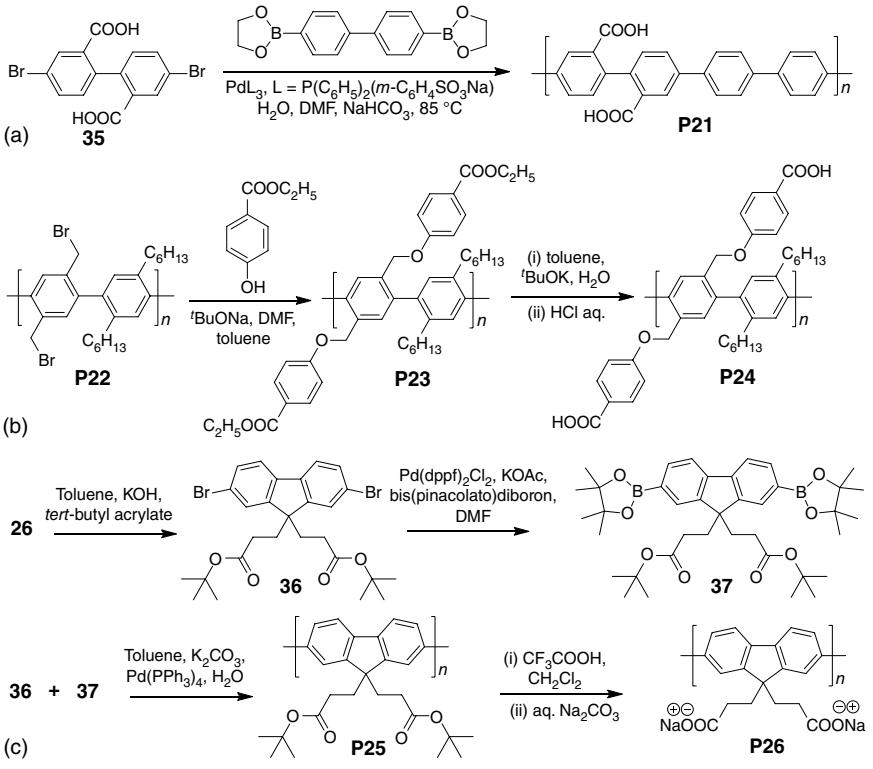

Scheme 1.9 Synthesis of carboxylated CPEs **P21**, **P24**, and **P26** with single-bonded backbones.

by acidification with hydrochloric acid to yield **P24**. However, unexpectedly, no hydrolysis of **P23** was observed in a two-phase system of water/toluene in the presence of NaOH.

Another postpolymerization approach to synthesize carboxylated polyfluorene was reported by Liu's group (Scheme 1.9c) [38]. Direct alkylation of **26** via Michael addition of the 9-position carbon with *tert*-butylacrylate afforded fluorene ester **36**, which was converted to the corresponding diboronate ester **37** under Suzuki–Miyaura reaction conditions in the presence of bis(pinacolato) diborane, $Pd(dppf)_2Cl_2$, and KOAc with anhydrous DMF as the solvent. In the next step, Suzuki polymerization between **36** and **37** led to the neutral precursor polymer **P25**. Contrary to the preparation of **P24** where the hydrolysis was performed under basic condition, **P26** was obtained by the hydrolysis of **P25** in acid condition followed by the neutralization with aqueous Na_2CO_3.

Carboxylated CPEs with double-bonded backbones have been synthesized through Heck and Gilch polymerization methods. As shown in Scheme 1.10a, Heck coupling polymerization between **38** and the diiodo-substituted monomer **39** in DMF using $Pd(OAc)_2$ and P(*o*-Tolyl)$_3$ as cocatalysts yielded the precursor polymer **P27**, which was hydrolyzed into carboxylated **P28** in THF with *t*-BuOK

as the base [39]. **P28** is only soluble in DMSO and dilute aqueous bases such as NaOH and NH_4OH but is insoluble in $CHCl_3$. Similarly, Gilch dehydrochlorination polymerization was also used to synthesize carboxylated poly(phenylene vinylene) **P29** (Scheme 1.10b) [40]. The key monomer **40** was prepared by etherification of 4-methoxyphenol **17** with 1-bromohexanoic acid ethyl ester and MeONa, followed by chloromethylation with formaldehyde and hydrochloric acid. In the next step, Gilch dehydrochlorination polymerization of **40** in the presence of *t*-BuOK yielded the carboxylated **P29**.

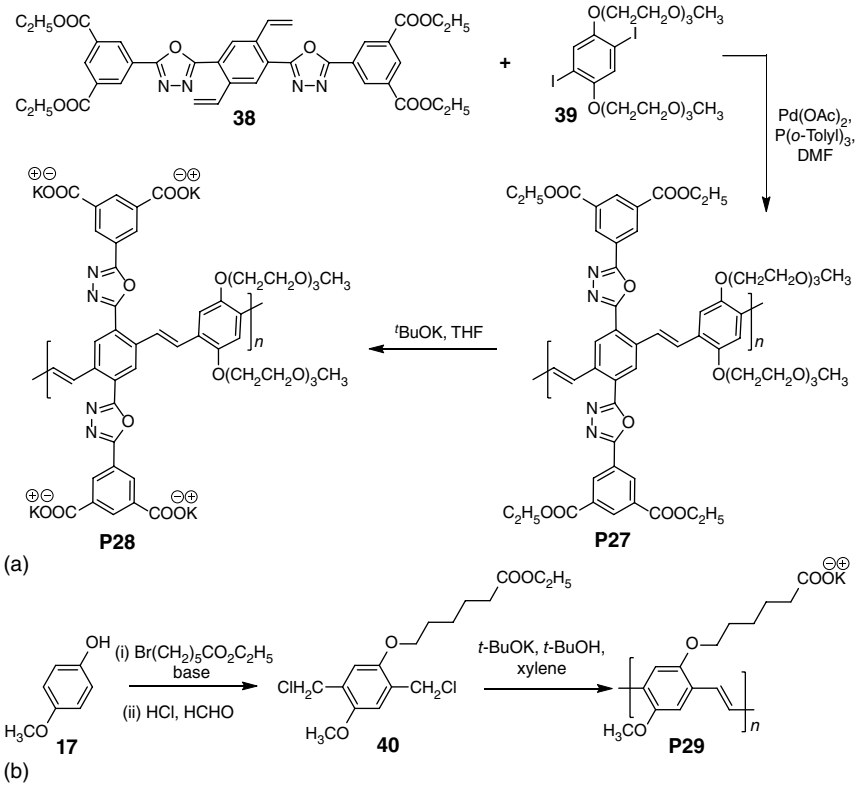

Scheme 1.10 Synthesis of carboxylated CPEs **P28** and **P29** with double-bonded backbones.

Sonogashira coupling reaction is the most commonly used method to synthesize carboxylated CPEs with triple-bonded backbones. As shown in Scheme 1.11a, **P30** was directly obtained by polymerization of 3,5-diiodo benzoic acid **41** with acetylene gas in water in the presence of a water-soluble Pd(0) catalyst, CuI co-catalyst, 1 equiv. of NaOH and 3 equiv. of Et_3N [41].

Bunz's group synthesized **P32** by a postpolymerization method (Scheme 1.11b) [42]. Starting from 2,5-diiodohydroquinone **42**, reaction with 2-bromoethyl acetate in butanone in the presence of K_2CO_3 yielded the ester-protected diiodo-monomer **43**. Subsequent alkylation utilizing trimethylsilylacetylene and the catalysts of $Pd(PPh_3)_2Cl_2$/CuI with trimethylamine as the solvent

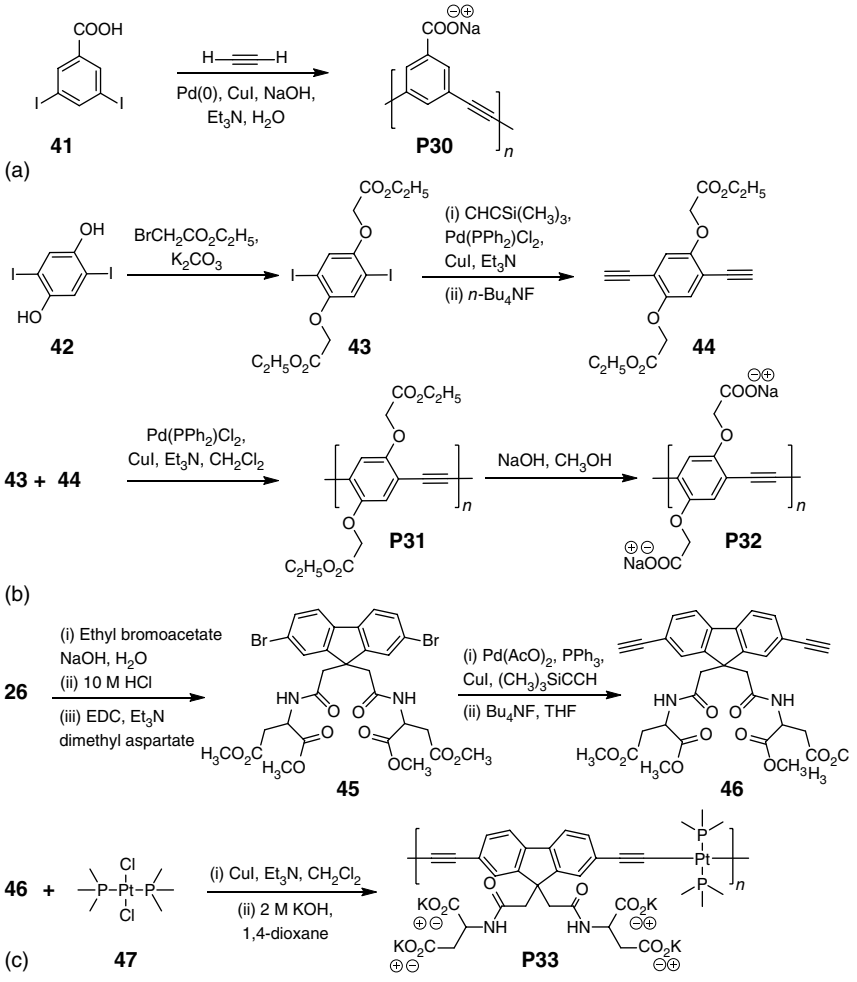

Scheme 1.11 Synthesis of carboxylated CPEs **P30**, **P32**, and **P33** with triple-bonded backbones.

furnished **44** after desilylation with tetrabutylammonium fluoride in THF. It is important to note that the ester groups were not cleaved under such basic conditions. Copolymerization between **43** and **44** under Sonogashira reaction conditions yielded the neutral **P31**, which was converted to **P32** through hydrolysis with NaOH in methanol [42].

To increase the number of carboxylate groups on each repeat unit, Wang's group reported **P33** from the key monomer **46** (Scheme 1.11c). Starting from the alkylation of 2,7-dibromofluorene **26** with ethyl bromoacetate under basic conditions followed by treatment with HCl solution, the obtained intermediate further reacted with L-aspartic acid dimethyl ester hydrochloride via *N*-(3-dimethylaminopropyl)-*N*′-ethylcarbodiimide (EDC) hydrochloride-catalyzed coupling reaction at room temperature to yield **45** [43]. The key monomer **46** can be easily obtained by reaction between **45** and trimethylsilylacetylene using $Pd(PPh_3)_2Cl_2$/CuI as catalyst

followed by desilylation with tetrabutylammonium fluoride in THF. Subsequently, Sonogashira coupling reaction between **46** and $Pt(PMe_3)_2Cl_2$ **47** followed by hydrolysis of the ester groups using 2 M KOH solution as the base yielded the desired carboxylated **P33** with four carboxylate groups on each repeat unit [44].

1.2.1.3 Phosphonated CPEs

As compared to sulfonated and carboxylated CPEs, the studies concerning phosphonated CPEs are less reported [16, 45, 46]. As shown in Scheme 1.12a, 3-(3-bromopropoxy)thiophene **49** was synthesized from 3-methoxythiophen **48**

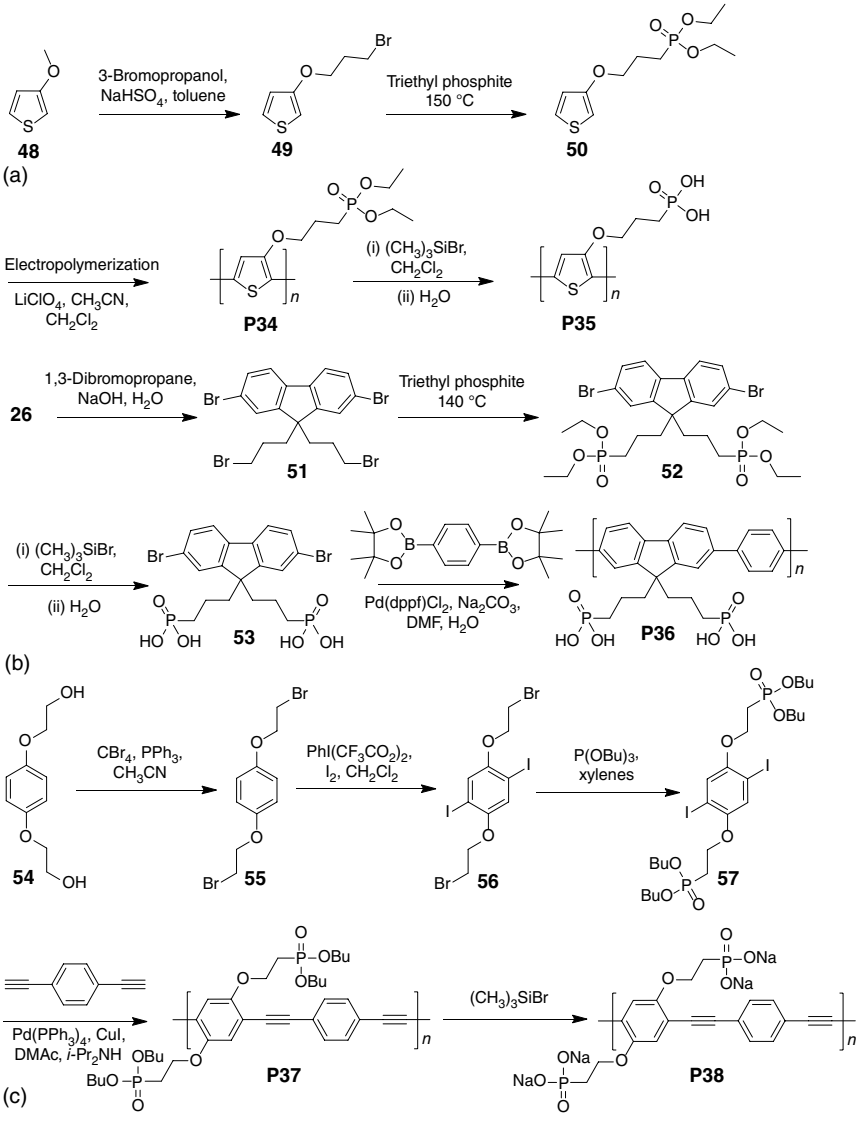

Scheme 1.12 Synthesis of phosphonated CPEs **P35**, **P36**, and **P38**.

and 3-bromopropanol in toluene in the presence of $NaHSO_4$. Treatment of **49** with triethyl phosphite yielded the phosphonic acid diethyl ester **50**. Direct electropolymerization of **50** led to the precursor polymer **P34**, which was hydrolyzed into phosphonated **P35** using bromotrimethylsilane [16].

A phosphonated polyfluorene **P36** was also synthesized by Wang's group via direct Suzuki polymerization method (Scheme 1.12b) [46]. Starting from 2,7-dibromofluorene **26**, reaction with 1,3-dibromopropane in aqueous NaOH yielded 2,7-dibromo-9,9-bis(3-bromopropyl)fluorene **51**, which reacted with triethylphosphite to afford **52** in a quantitative yield. Treatment of **52** with trimethylsilyl bromide and subsequently water yielded 2,7-dibromo-9,9-bis(3-diethoxylphosphorylpropyl)fluorene **53**. Direct Suzuki polymerization between **53** and 1,4-bis(4,4,5,5-tetramethyl-1,3,2-dioxaborolan-2-yl)benzene using $Pd(dppf)Cl_2$ as catalyst in DMF and Na_2CO_3 aqueous solution gave **P36** with molecular weight higher than 15 kDa.

Phosphonated CPE **P38** with triple-bonded backbones was also synthesized. As shown in Scheme 1.12c, bromination of **54** in acetonitrile using carbon tetrabromide and triphenylphosphine yielded **55**, which underwent iodination to give the compound **56**. The key monomer **57** was synthesized from **56** using a similar procedure to **50** and **52**. **P38** was then prepared via Sonogashira reaction between **57** and 1,4-diethynybenzene to yield **P37**, which was followed by trimethylsilyl bromide treatment to promote the hydrolysis of the butylphosphonate ester groups (Scheme 1.12c) [45]. However, Sonogashira reaction between the hydrolysis product of **57** and 1,4-diethynybenzene could not afford high molecular weight for **P38**, presumably because the ionic phosphonate groups can coordinate with and deactivate the catalysts during the polymerization.

1.2.2 Cationic CPEs

1.2.2.1 Ammonium CPEs

Ammonium polythiophene **P39** was reported by Leclerc's group through direct oxidation of cationic thiophene monomer **59** (Scheme 1.13a) [47]. The key monomer **59** was prepared from the Williamson reaction between 3-bromo-4-methylthiophene **5** and 3-(diethylamino)propanol to yield **58**, which was followed by quaternization with bromoethane. Oxidative polymerization of **59** in chloroform using $FeCl_3$ as the oxidizing agent yielded **P39**. Alternatively, a postpolymerization method to synthesize ammonium polythiophene was also reported by McCullough's group [48]. As shown in Scheme 1.13b, a neutral polythiophene **P40** was synthesized from 2-bromo-3-hexylbromothiophene **60** via $Ni(dppp)Cl_2$ catalyzed coupling reaction. Quaternization of **P40** with methylamine in a mixture of THF/methanol yielded the cationic **P41**. It should be pointed out that the chemical structure of **P40** should be written as **P42** with a bromide on the conjugated backbone terminal, according to the reaction. Using **P42** as a macromonomer and 2-bromo-(9,9-dioctylfluorene)-7-pinacolato boronate **61** as AB-type monomer under Suzuki cross-coupling conditions, Scherf's group has successfully synthesized all-conjugated cationic diblock copolythiophenes **P44** through a "grafting from" approach (Scheme 1.13c) [49].

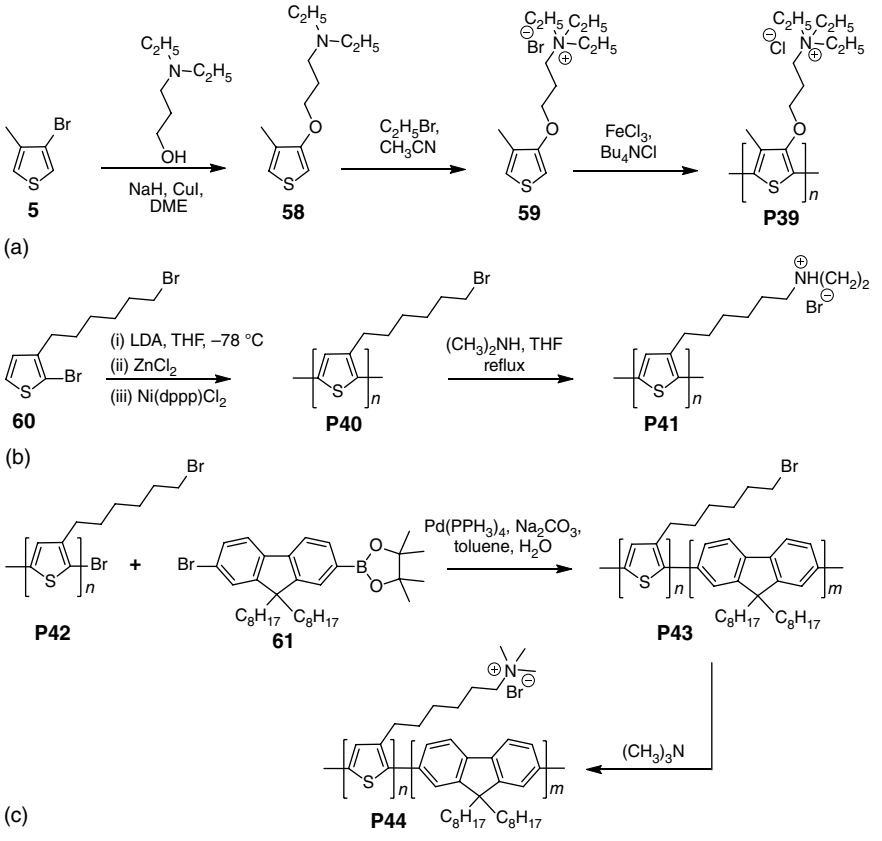

Scheme 1.13 Synthesis of ammonium polythiophenes **P39**, **P41**, and **P44**.

To synthesize single-bonded ammonium CPEs, a direct polymerization strategy was used to synthesize **P45** using Suzuki polymerization (Scheme 1.14a) [50]. Compound **62** was synthesized through Williamson etherification of **13** by refluxing in acetone with 2-chloroethyldiethylamine and K_2CO_3. The key monomer **63** was obtained by quaternization of **62** with bromoethane. Subsequent Suzuki polymerization between **63** and 1,4-bis(5,5-dimethyl-1,3,2-dioxaborinan-2-yl)benzene **64** afforded the ammonium **P45**.

The same group also employed Stille coupling reaction to synthesize thiophene-containing poly(*p*-phenylene) **P47** [51]. As shown in Scheme 1.14b, the key monomer **65** was synthesized using a similar procedure to **62**. It is noted that the diiodo-substituted monomer was chosen over a dibromo-substituted monomer due to its higher reactivity in Pd-catalyzed coupling reaction. Stille coupling reaction between **65** and 2,5-bis(trimethylstannyl)thiophene **66** led to the neutral polymer **P46**, which was treated with bromoethane to afford ammonium poly(*p*-phenylene) **P47**.

In 2002, Bazan's group reported an ammonium polyfluorene via postpolymerization method. **P49** was obtained by the sequence of reactions shown in Scheme 1.14c [52]. Deprotonation of 2,7-dibromofluorene **26** with NaOH in a

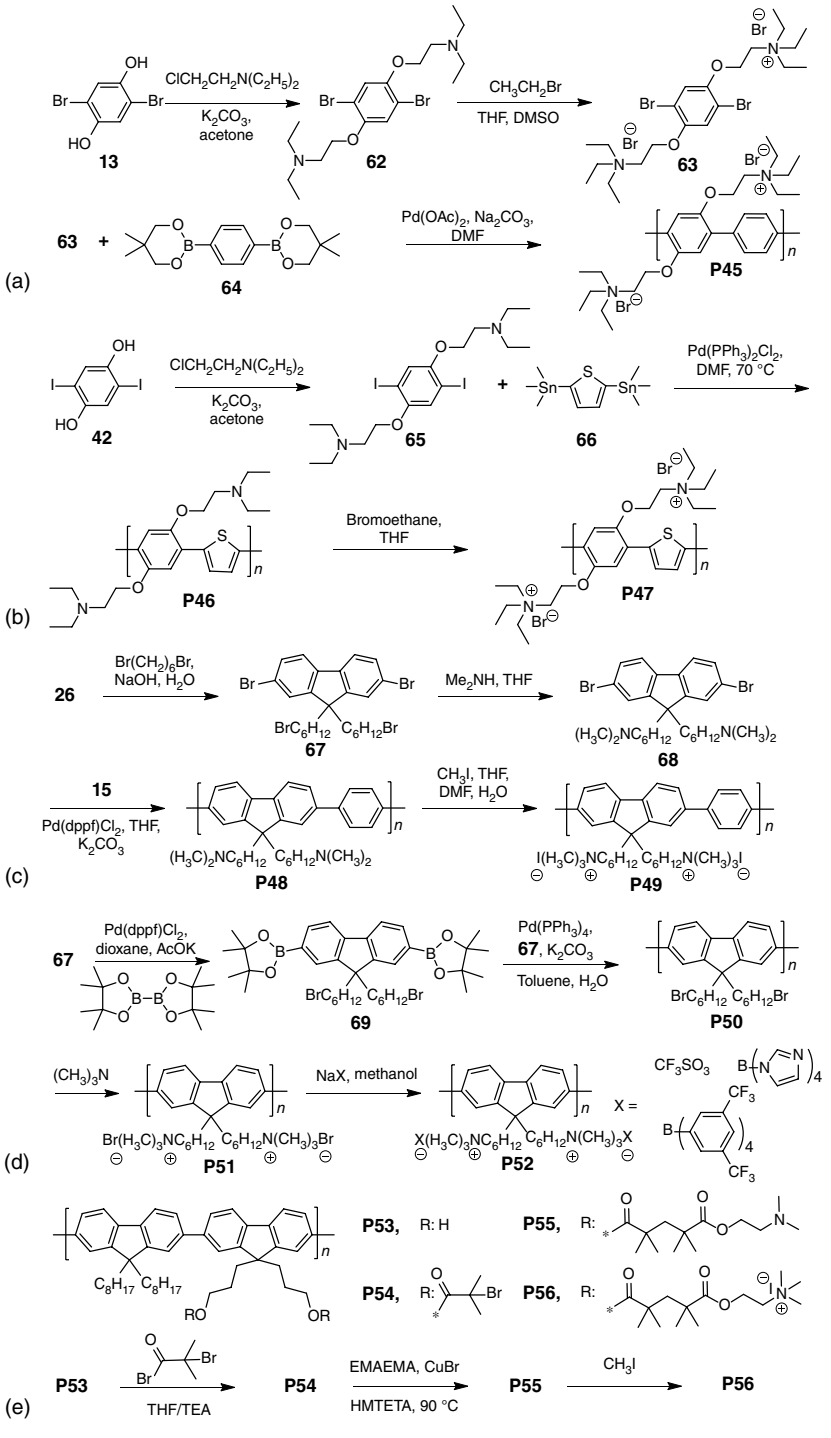

Scheme 1.14 Synthesis of ammonium CPEs **P45**, **P47**, **P49**, **P51**, **P52**, and **P56** with single-bonded backbones.

two-phase mixture of water and 1,6-dibromohexane provided 2,7-dibromo-9, 9-bis(6′-bromohexyl)fluorene **67**, which was treated with dimethylamine to give 2,7-dibromo-9,9-bis(6′-(*N*,*N*-dimethylamino)hexyl)fluorene **68**. Direct Suzuki polymerization between **68** and 1,4-phenyldiboronic acid **15** at a stoichiometric ratio yielded the neutral precursor polymer **P48**. Quaternization of **P48** with iodomethane in a mixture of THF/DMF/water led to the alternating ammonium **P49** in a moderate yield.

The same group also used another postpolymerization method to synthesize homopolyfluorene with different counterions [53]. As shown in Scheme 1.14d, Suzuki–Miyauri reaction between **67** and bis(pinacolato)diboron in the presence of AcOK and $Pd(dppf)_2Cl_2$ in anhydrous dioxane afforded the fluorene boronate ester **69**. The Suzuki polymerization between **67** and **69** using $Pd(PPh_3)_4$ as catalyst and Na_2CO_3 as base in a two-phase mixture of toluene/water yielded the neutral precursor polymer **P50**. Owing to the highly efficient reaction between alkyl bromide and the trimethylamine, subsequent reaction between **P50** and trimethylamine resulted in **P51** with more than 95% degree of quaternization. Upon treatment of **P51** with an excess of different salts, **P52** was obtained with different counter ions.

In 2010, Huang's group successfully synthesized a water-soluble grafted CPE **P56** via atom transfer radical polymerization (ATRP) for the first time (Scheme 1.14e) [54]. Starting from **P53,** which was synthesized by Suzuki polymerization, reaction with 2-bromoisobutyryl bromide afforded the macroinitiator **P54**, which was used to prepare **P55** via the ATRP approach. Subsequent reaction with methyl iodide gave **P56**. The brush-like side-chain architecture of polyfluorenes **P56** endows it with an extremely high ammonium ion density, consequently giving rise to high water solubility ($28\,mg\,ml^{-1}$) and high quantum efficiency (52%).

To synthesize ammonium CPEs with double-bonded backbones, Heck coupling reaction was used. As shown in Scheme 1.15a, 9,9-bis(6′-bromohexyl)-2,7-divinylfluorene **70** was obtained by heating the mixture of **67** and tributylvinyltin in toluene using $Pd(PPh_3)_2Cl_2$ as catalyst and 2,6-di-*tert*-butylphenol as the inhibitor. Subsequent quaternization of **70** with trimethylamine in a mixture of THF/water afforded the monomer 9,9-bis(6′-(*N*,*N*,*N*-trimethylammonium) hexyl)-2,7-divinylfluorene dibromide **71**. Finally, the ammonium **P57** was obtained via $Pd(OAc)_2/P(o\text{-tolyl})_3$-catalyzed direct Heck coupling polymerization of **71** and 4,7-dibromo-2,1,3-benzothiazole **72** in a solvent mixture containing DMF/H_2O/TEA (v/v/v = 2/1/2) [55].

A postpolymerization method was also reported by Wang's group using Heck coupling reaction. As shown in Scheme 1.15b, alkylation of **42** with 1,6-dibromohexane and K_2CO_3 in acetone afforded **73**. Heck reaction between **73** and the divinyl monomer **74** led to the neutral polymer **P58**. The presence of the active bromide atom of **P58** allows the facile synthesis of **P59** through quaternization with trimethylamine [56].

Another approach to synthesize poly(fluorene vinylene)s is through the Witting polymerization method [57]. As shown in Scheme 1.15c, the key monomer 2,7-dicarbaldehyde-9,9-bis(6′-bromohexyl)fluorene **75**, was obtained by treatment of **67** with BuLi followed by the addition of anhydrous DMF. The Witting–Horner condensation reaction between **75** and 1,4-bis(diethylphosphinatylmethyl)phenylene

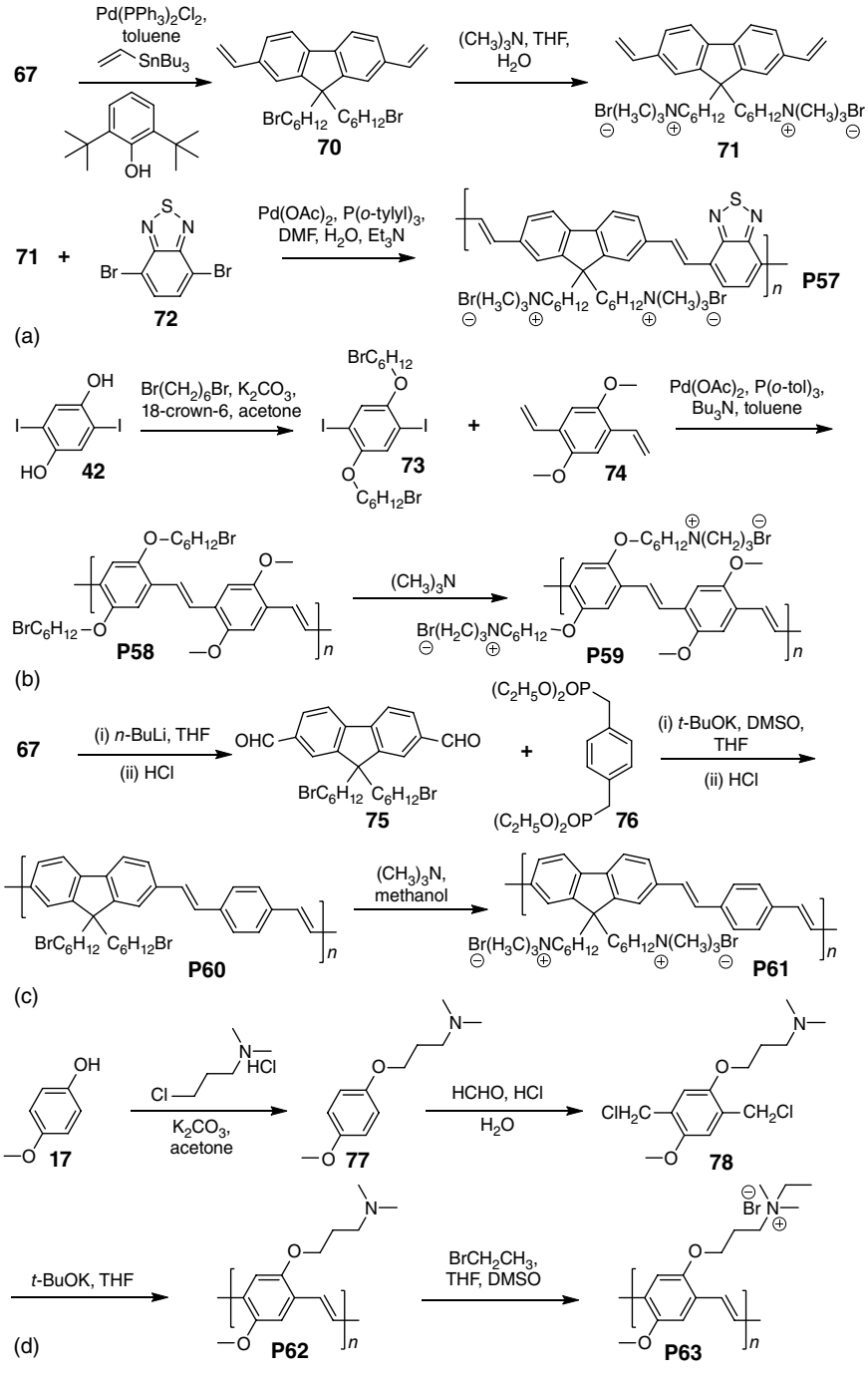

Scheme 1.15 Synthesis of ammonium CPEs **P57**, **P59**, **P61**, and **P63** with double-bonded backbones.

76 in dry THF in the presence of *t*-BuOK led to the precursor **P60**, which was converted to ammonium **P61** via quaternization with trimethylamine in chloroform/methanol.

Gilch coupling reaction was also employed by Shen's group to synthesize ammonium poly(*p*-phenylene vinylene)s [58]. As shown in Scheme 1.15d, 3-(4-methoxyphenoxy)-*N*,*N*-dimethylpropan-1-amine **77** was synthesized through Williamson etherification of **17** by refluxing in acetone with 3-chloropropyldimethylamine and K_2CO_3. Chlorination of **77** with a 37% formalin solution in concentrated hydrochloric acid resulted in the key monomer **78**. Gilch reaction of **78** was performed in THF in the presence of *t*-BuOK to yield the precursor polymer **P62**, which was treated with bromoethane in a mixture of THF/DMSO to give the ammonium poly(*p*-phenylene vinylene) **P63**.

Sonogashira reaction was often used to prepare ammonium CPEs with triple-bonded backbones. As shown in Scheme 1.16a, quaternization of **67** with trimethylamine in THF/water yielded the ammonium monomer **79**, which was directly copolymerized with 4,7-diethynyl-2,1,3-benzothiadiazole **28** to yield **P64** via Sonogashira reaction using $Pd(PPh_3)_4$/CuI as catalysts in a mixed solution of DMF/H_2O/diisopropylamine (v/v/v = 2/1/1.5) [32].

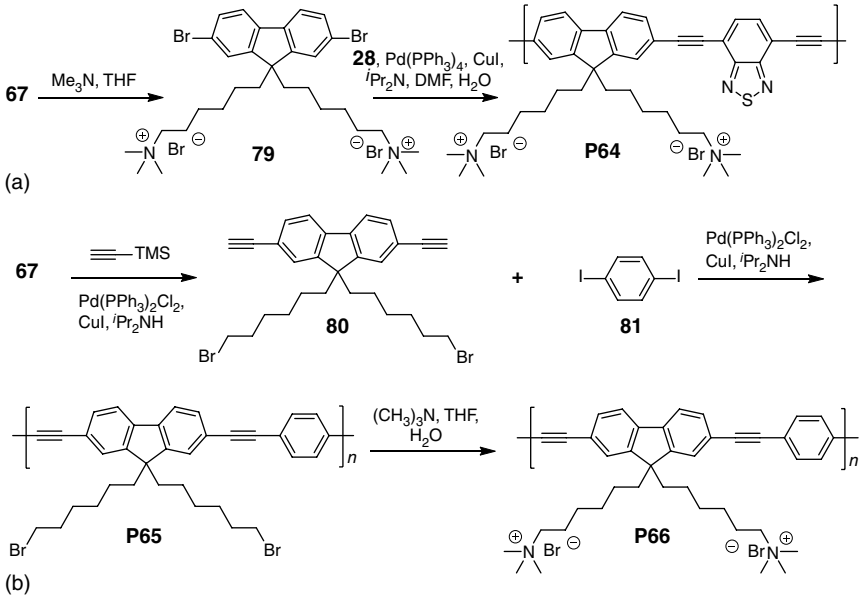

Scheme 1.16 Synthesis of ammonium polyfluorenes **P64** and **P66** with triple-bonded backbones.

Another approach to synthesize poly(fluorene ethynylene)s is via postpolymerization. As shown in Scheme 1.16b, the reaction between **67** and trimethylsilyl acetylene using $Pd(PPh_3)_2Cl_2$/CuI as catalysts followed by trimethylsilyl deprotection in a basic solution led to 9,9-bis(6-bromohexyl)-2,7-diethynylfluorene **80**. The ethynyl and bromide groups were kept intact during the reactions. **80** was copolymerized with 1,4-diiodobenzene **81**

through $Pd(PPh_3)_4$/CuI-catalyzed Sonogashira reaction in a mixture of toluene/diisopropylamine (v/v = 2/1) to yield **P65**. Quaternization of **P65** with trimethylamine afforded the ammonium **P66** [59].

Apart from the above-discussed linear cationic CPEs, Liu's group also reported hyperbranched ammonium polyfluorenes. For example, **P67** was synthesized through 2 steps from **80**. As shown in Scheme 1.17, $CpCo(CO)_2$- catalyzed homopolycyclotrimerization of **80** with UV irradiation led to hyperbranched neutral **P67**, which was converted to **P68** after treatment with trimethylamine [60].

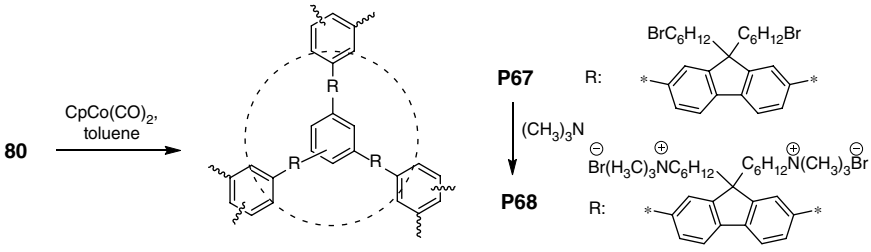

Scheme 1.17 Synthesis of hyperbranched CPE **P68**.

1.2.2.2 Pyridinium CPEs

Pyridinium CPEs are generally obtained through quaternization between pyridine and active halogen atoms (e.g., Br). As shown in Scheme 1.18a, Fukuhara and Inoue reported pyridinium polythiophene **P69** through treatment of **P40**

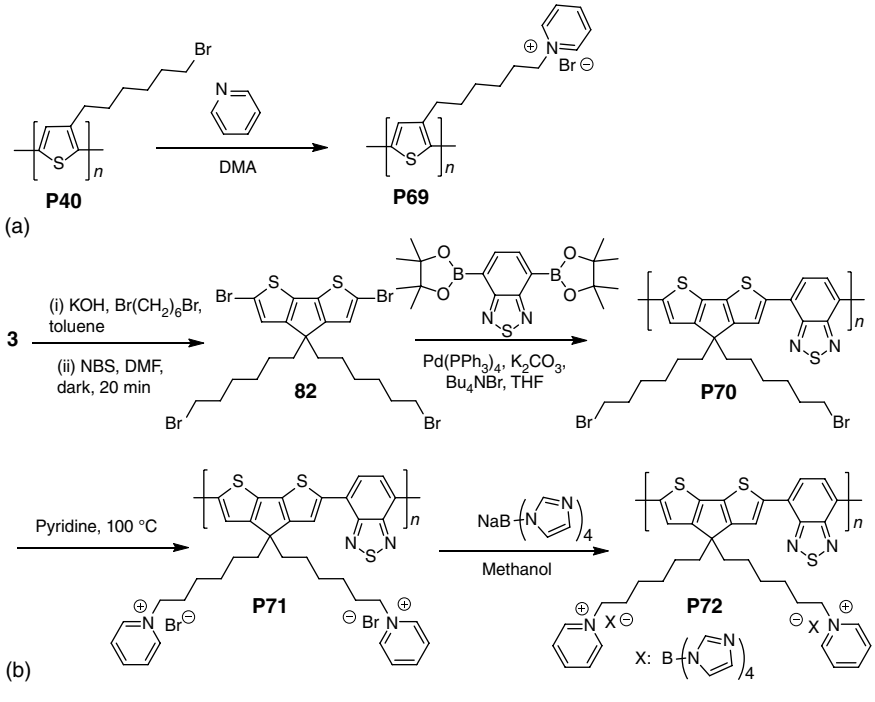

Scheme 1.18 Synthesis of pyridinium CPEs **P69**, **P71**, and **P72**.

with pyridine in *N*,*N*-dimethylacetamide (DMA) [61]. Bazan's group also reported pyridinium CPEs **P71** and **P72** with narrow band gap (Scheme 1.18b) [62]. Starting from **3**, alkylation with 1,6-dibromohexane and KOH followed by bromination of the intermediate using *N*-bromosuccinimide yielded the dibromide-substituted cyclopentadithiophene **82**. Suzuki polymerization between **82** and the bis-boronate ester of benzothiadiazole generated the neutral precursor polymer **P70**. Quaternization of **P70** with pyridine led to the pyridinium **P71**. In addition, bromide counter ion in **P71** has also been further exchanged with the large tetrakis(1-imidazolyl)borate (BIm_4^-) to yield **P72**.

1.2.2.3 Phosphonium CPEs

In addition to the ammonium and pyridinium salt, cationic CPEs with other types of charges (e.g., phosphonium) have also been reported. As shown in Scheme 1.19a, quaternization of the neutral polymer **P40** with 1-methyl-imidazole or trimethylphosphine led to **P73** or **P74**, respectively [63]. The obtained CPEs are insoluble in common organic solvents (e.g., THF, chloroform, dichloromethane, and toluene) but readily soluble in water. Using a similar strategy, **P75** was treated with PPh_3 to yield the corresponding phosphonium **P76** (Scheme 1.19b) [64].

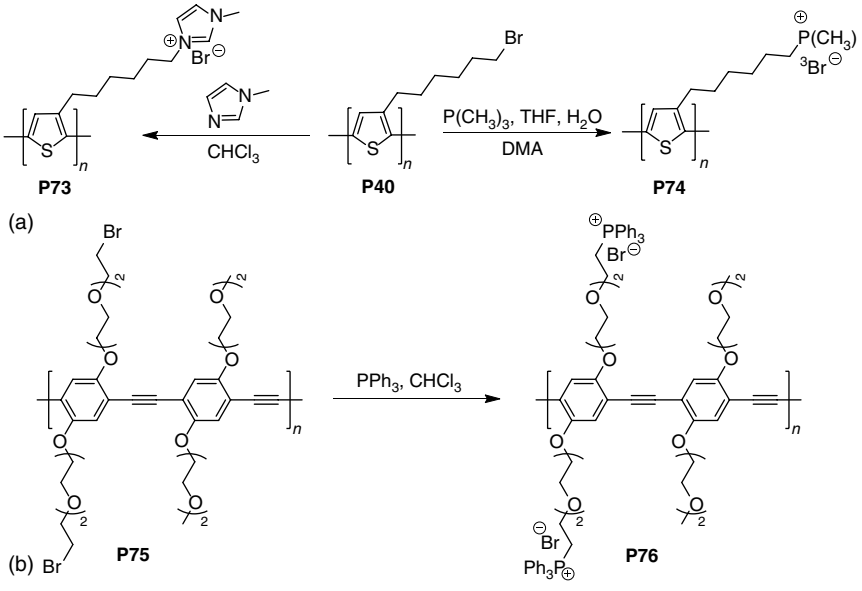

Scheme 1.19 Synthesis of cationic CPEs **P73**, **P74,** and **P76**.

1.2.3 Zwitterionic CPEs

Different from anionic and cationic CPEs, zwitterionic CPEs contain side groups with anionic and cationic functionalities that are covalently linked with each other. Zwitterionic polythiophenes have been synthesized by Konradsson's

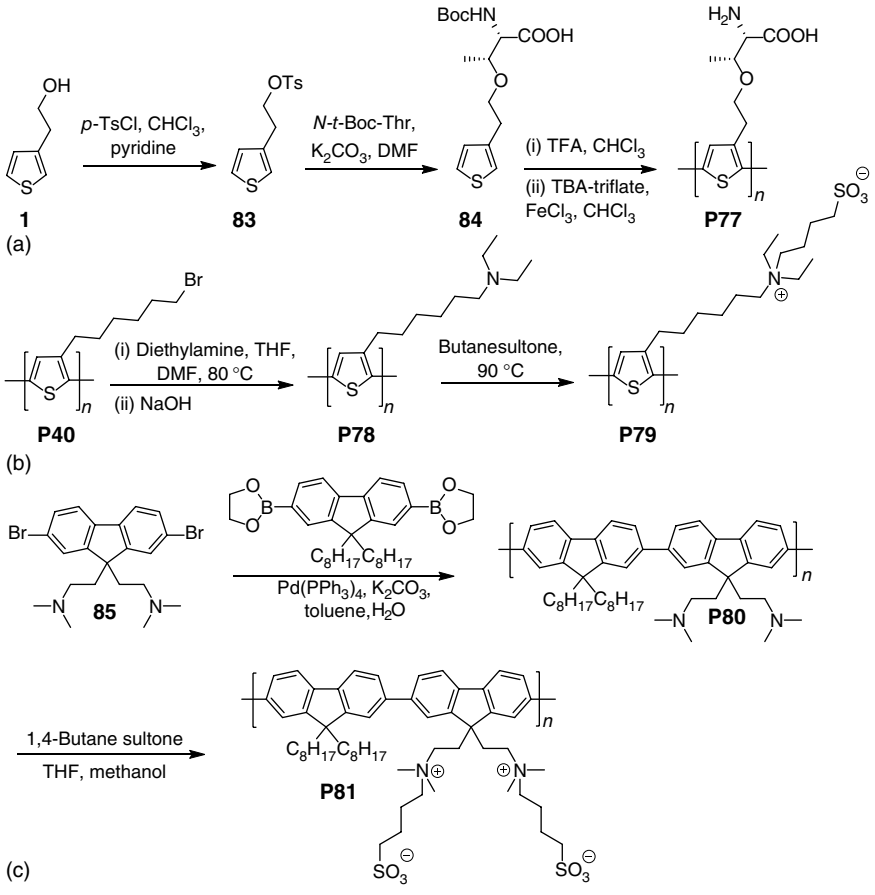

Scheme 1.20 Synthesis of zwitterionic CPEs **P77**, **P79**, and **P81**.

group. As shown in Scheme 1.20a, **1** was tosylated with *p*-TsCl in the presence of pyridine to give a thiophene derivative **83**. Alkylation of **83** with a Boc-protected amino acid, *N-t*-Boc-Thr, yielded the key monomer **84**. After Boc-deprotection with trifluoroacetic acid, $FeCl_3$-catalyzed oxidative polymerization of the product gave the zwitterionic polythiophene **P77** [65].

Another type of zwitterionic polythiophene **P79** was also synthesized. As shown in Scheme 1.20b, the precursor polymer **P40** first reacted with diethylamine in a mixture of THF/DMF to give **P78**, which was converted to **P79** using 1,4-butane sultone as the quaternization agent and solvent [66].

In 2011, Huck's group reported a zwitterionic polyfluorene as the charge injection layer for high-performance polymer light-emitting diodes [67]. As shown in Scheme 1.20c, the Pd-mediated Suzuki polymerization between **85** and di-boronate ester fluorene yielded a neutral polymer **P80**. After quaternization of **P80** using 1,4-butane sultone in a THF/methanol solvent mixture, **P81** was obtained with near 100% conversion of the tertiary amines into sulfobetaine zwitterionic groups [67].

1.3 Neutral WSCPs

In the previous section, we have described the various approaches to synthesize CPEs with different charge signs. In this section, we will briefly discuss the synthesis of neutral WSCPs. Neutral WSCPs contain neutral polar functionalities, for example, oligo(ethylene glycol) segments, that compensate for the hydrophobic nature of the conjugated backbones. Neutral WSCPs often exhibit high fluorescence quantum yield, good water solubility, and strong resistance to nonspecific interactions. As shown in Scheme 1.21a, Bazan's group reported the synthesis of a neutral WSCP **P82** using the complex *cis*-(bromo)(phenyl)[1,2-bis(diphenylphosphino)ethane]nickel as the initiator and **86** as the monomer in the presence of isopropylmagnesium chloride–lithium chloride, followed by quenching the polymerization with [2-(trimethylsilyl)ethynyl]magnesium bromide [11]. Owing to the incorporation of octakis(ethylene glycol) side chains, **P82** exhibited good solubility in water and high-fluorescence quantum yield (80%). In addition, each **P82** chain possesses one terminal silylacetylene group, which allowed further conjugation with functional components via click reaction. This provides a versatile strategy to fabricate ideal fluorescent probes for biosensing applications.

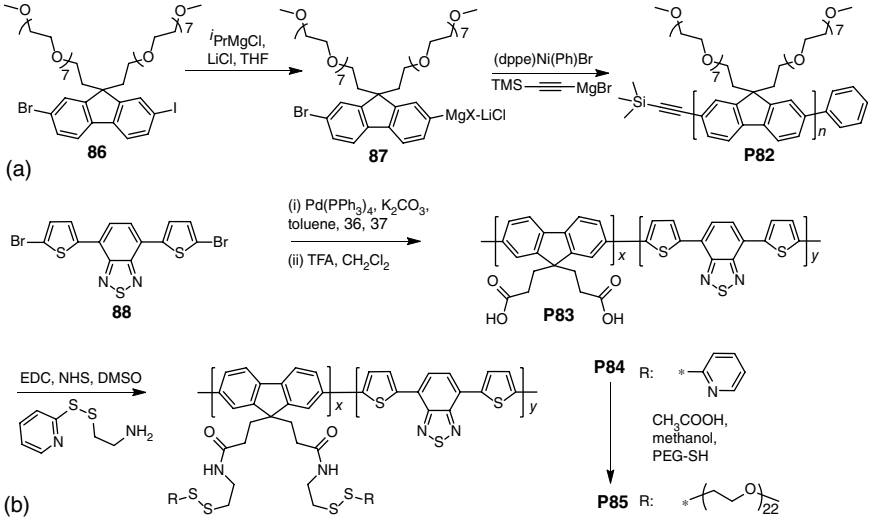

Scheme 1.21 Synthesis of neutral WSCPs **P82** and **P85**.

Meanwhile, Huang's group reported a postpolymerization method to synthesize WSCP **P85** with oligo(ethylene glycol) side chains [68]. As shown in Scheme 1.21b, Suzuki polymerization of monomers **36**, **37**, and **88** followed by deprotection of ester groups with trifluoroacetic acid yielded **P83**. Subsequently, **P83** was modified with 2-(pyridyldithio)ethylamine through amidation to yield **P84**, which was converted to **P85** through the replacement of pyridine units with PEG-SH chains.

Bunz's group also used Sonogashira reaction to prepare neutral water soluble poly(*p*-phenylene ethynylene) **P87** [69]. As shown in Scheme 1.22, Pd-catalyzed Sonogashira coupling between **89** and **90** furnished the neutral polymer **P86**, which was deprotected *in situ* and subjected to a cupper catalyzed 1,3-dipolar cycloaddition with azide-functionalized sugar resulting in **P87**. Because of the presence of polar side chains (sugar and oligo(ethylene glycol)), **P87** can be freely dissolved in water.

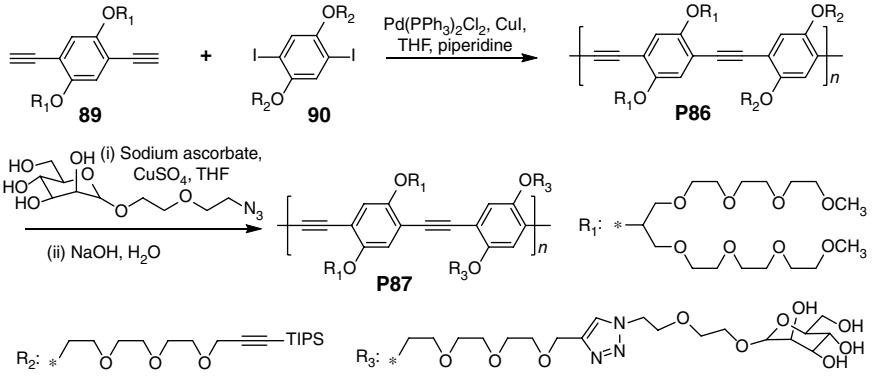

Scheme 1.22 Synthesis of neutral WSCP **P87**.

Liu's group developed another strategy to prepare WSCPs using hyperbranched polyglycerol as brush due to its good biocompatibility [70]. This method involves the combination of "grafting from" strategy and living ring-opening polymerization technique. As shown in Scheme 1.23, Starting from **P88**, reaction with NaN_3 in a mixture of THF/DMF afforded **P89**. Subsequent click reaction with propargyl alcohol led to the macroinitiator **P90**, which was used to incorporate hyperbranched polyglycerol as brush via ring-opening polymerization technique, yielding **P91** with good water

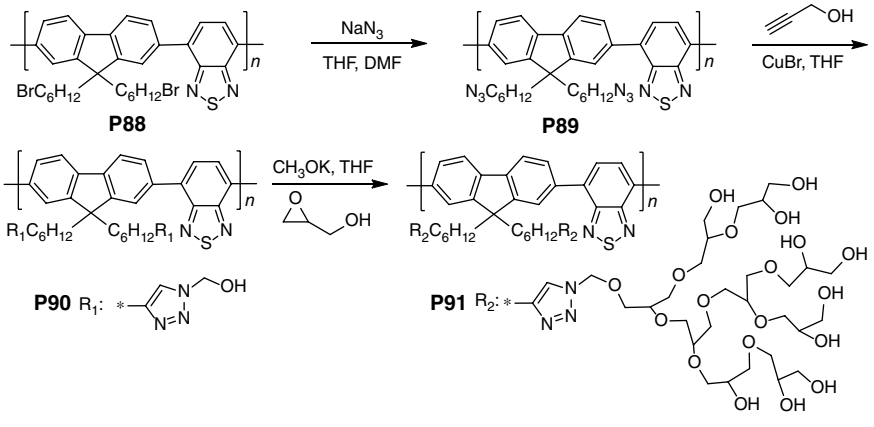

Scheme 1.23 Synthesis of neutral WSCP **P91** with HPG brush.

solubility. In addition, the same group also reported many CPs with poly(ethylene glycol) brush through click reaction between poly(ethylene glycol) and neutral precursor CP [71–73].

1.4 Fabrication of CPNPs

Compared to the chemical synthesis of CPs, preparation of CPNPs directly from organic solvent-soluble CPs represents another strategy to bring CPs into aqueous media. To simplify the discussion, all the NPs prepared from organic soluble CPs are termed as CPNPs in this chapter. The most widely used approaches for CPNPs synthesis include reprecipitation, miniemulsion, and nanoprecipitation [9, 12, 74]. In the following section, we choose some specific examples to illustrate each method by discussing their advantages and disadvantages. Scheme 1.24 shows the chemical structures of representative CPs and amphiphilic materials used for CPNP preparation.

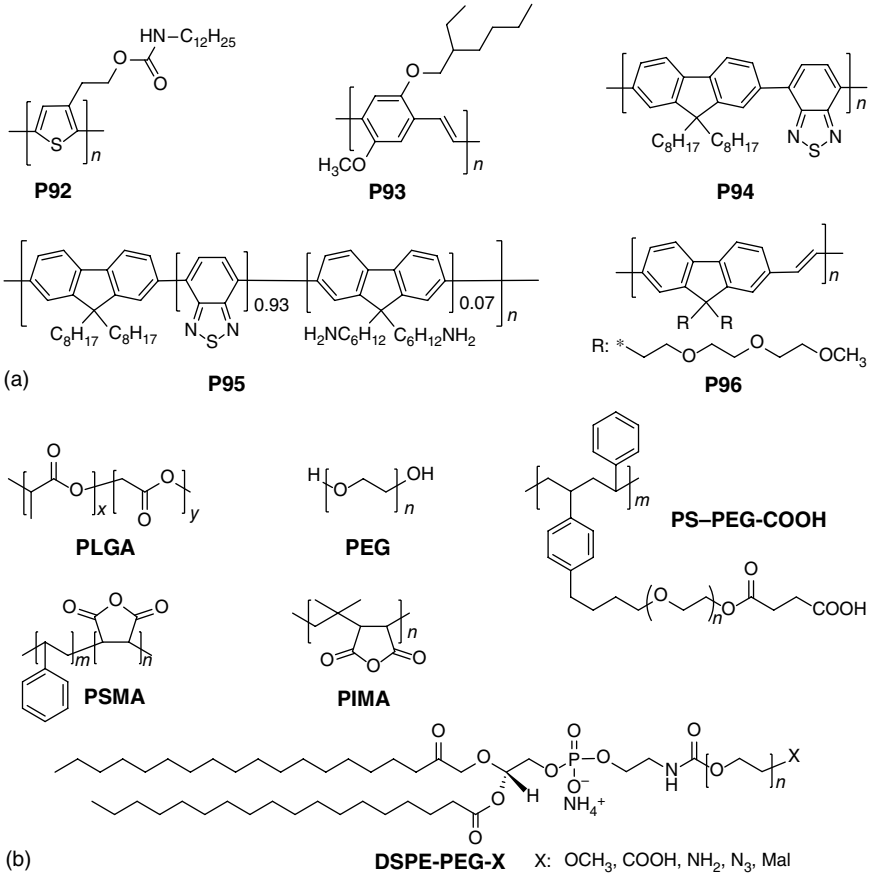

Scheme 1.24 Representative chemical structures of CPs and amphiphilic materials used for CPNP preparation.

1.4.1 Reprecipitation

Reprecipitation method was first applied to CPs by Masuhara's group [75]. In a typical reprecipitation method schematically shown in Scheme 1.25, a small amount of hydrophobic CP is dissolved in a water-miscible solvent (e.g., THF). Next, the organic solution is rapidly injected into excess water under vigorous stirring or sonication. The large solubility discrepancy of the CP in two solvents as well as the hydrophobic interactions between polymer chains induces the nanoparticle formation during the organic solvent evaporation. This method does not involve the use of any additives such as surfactants. Using this method, Masuhara's group prepared **P92** NPs with sizes ranging from 40 to 420 nm by injecting a solution of **P92** in THF into vigorously stirred distilled water [75]. The size can be tuned by changing the concentration of **P92** in THF or the temperatures of water (e.g., from 20 to 80 °C). The lower concentration provided the smaller size. The obtained CPNPs exhibited size-dependent spectroscopic properties.

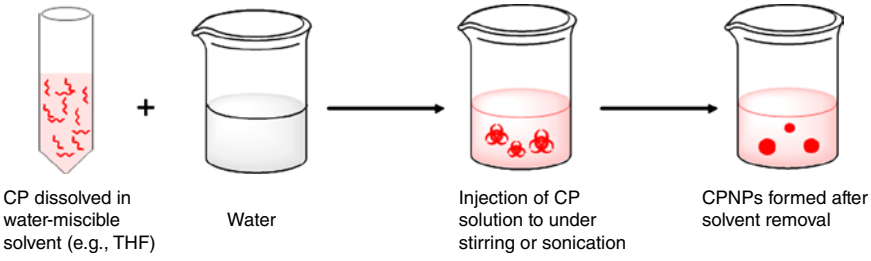

Scheme 1.25 Schematic illustration of the preparation of CPNPs using reprecipitation method.

Subsequently, McNeill's group reported a modified procedure to prepare CPNPs with the sizes ranging from 5 to 30 nm [76]. In this specific case, 2 ml of **P93** in THF with a very low concentration (0.005 wt%) was added quickly to 8 ml of deionized water under sonication conditions. After evaporation of the THF under vacuum, filtration with a 0.2 μm membrane filter was performed to afford **P93** NPs with major sizes between 5 and 10 nm. **P92** and **P93** NPs exhibit spherical shape. This method is applicable to a wide range of CPs that are soluble in water-miscible organic solvents. In addition, it is possible to adjust the particle size via tuning the CP concentration or selecting CPs with appropriate molecular weight. However, due to the inherent hydrophobic nature of CP, the obtained CPNPs tend to aggregate into large sized particles, thus precipitating from water. Therefore, these CPNPs were only obtained with a very low concentration (e.g., 0.005%), and could not be stored for a long period.

1.4.2 Miniemulsion

Miniemulsions are specially formulated heterophase systems consisting of stable nanodroplets in a continuous phase (e.g., water). In a typical miniemulsion procedure illustrated in Scheme 1.26, the CP dissolved in a water-immiscible organic

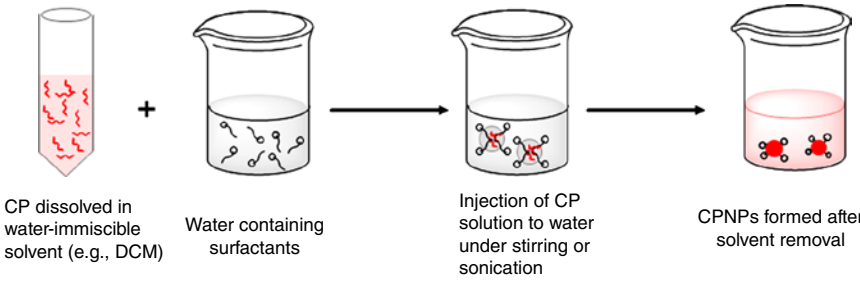

Scheme 1.26 Schematic illustration of the preparation of CPNPs using miniemulsion method.

solvent (e.g., dichloromethane, chloroform) is added to an aqueous solution containing an appropriate surfactant. The mixture is treated with ultrasonication to form stable miniemulsions containing small organic droplets of the CP solution. After solvent evaporation, the droplets collapse to form stable water-dispersible CPNPs. Compared to the reprecipitation method, the miniemulsion method employs surfactant to form and stabilize droplets. The sizes of formed CPNPs via this method vary from 2 to 500 nm, depending on the nature and concentration of the polymer and surfactant used.

Using the miniemulsion method, Liu's group reported a generic strategy to prepare a series of multicolor CPNPs with emission spanning from 400 to 700 nm, using Food and Drug Administration (FDA)-approved poly(DL-lactide-*co*-glycolide) (PLGA) as the encapsulation matrix, and poly(vinyl alcohol) (PVA) as the emulsifier [77]. Herein, we still choose **P93** as an example. In this case, a dichloromethane solution containing **P93** and PLGA was poured into an aqueous solution containing PVA. After sonicating the mixture, the resulting emulsion was stirred at room temperature to remove the solvent. Then, **P93** NPs were obtained after careful washing and centrifugation to remove the emulsifier and free **P93** molecules. Although the resultant CPNPs show good colloidal stability in water, their sizes are in the range of 240–270 nm and the encapsulation efficiencies are relatively low (~45%).

Meanwhile, Green's group reported a simple strategy to synthesize a series of PEG encapsulated CPNPs with emission spanning from blue to green, yellow, and red [78]. Using **P94** as an example, the dilute **P94** solution in dichloromethane (40 ppm by weight) was added dropwise to an aqueous PEG solution while stirring vigorously with ultrasonication. After sequential evaporation of the remaining dichloromethane, filtration with filter paper, and centrifugation, the **P94** NPs were obtained with mean diameters ranging from 2 to 3 nm and a quantum yield of ~12%. The presence of PEG is essential to stabilize the formed NPs, as the **P94** NPs prepared without PEG are not stable. However, a considerable amount of fluorescence quenching was observed in the small CPNPs.

Compared to the straightforward strategy to synthesize CPNPs from preprepared CPs, another strategy to synthesize CPNPs is miniemulsion polymerization. This method generally employs water-tolerance reactions, such as Sonogashira, Suzuki, and $FeCl_3$-catalyzed oxidative polymerization reactions.

Generally, the appropriate monomers are dispersed in surfactant-containing aqueous solution under vigorous stirring to form stable nanodroplets. During this process, the hydrophobic monomers are embedded in the interior. After addition of appropriate catalyst, polymerization and nanoparticle formation are achieved concurrently. This strategy will be discussed in detail in the next chapter.

1.4.3 Nanoprecipitation

Nanoprecipitation is a modification of the reprecipitation method, and has become the most commonly used approach for the preparation of CPNPs. In a typical procedure as shown in Scheme 1.27, CP and amphiphilic encapsulation matrix are first dissolved well in a water-miscible organic solvent (e.g., THF). The resulting solution is then quickly added into a water phase under sonication to form a stable nanoparticle dispersion. After organic solvent removal, the matrix encapsulated CPNPs were obtained. During nanoparticle formation, the hydrophobic components of the matrix and CPs are likely embedded into the NP core while the hydrophilic segments of the matrix are oriented to the aqueous environment. The NPs prepared by this method show better colloidal stability than those obtained from reprecipitation. The particle size and optical and surface chemical properties of the CP NPs can be adjusted by changing the CPs, amphiphilic matrix, and other related parameters.

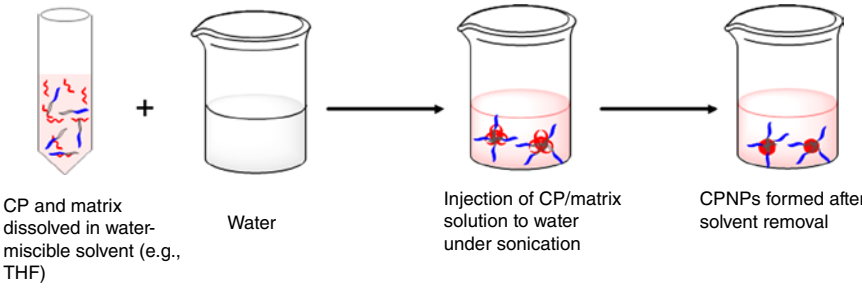

Scheme 1.27 Schematic illustration of the preparation of CPNPs using nanoprecipitation method.

In 2010, Chiu's group synthesized CPNPs based on **P94** via the nanoprecipitation method using a functional, amphiphilic, comb-like poly(styrene-*g*-ethylene oxide) (PS–PEG-COOH) as an encapsulation matrix [79]. PS–PEG-COOH consists of a hydrophobic polystyrene backbone and several hydrophilic PEG side chains terminated with carboxylic acid. Briefly, a precursor THF solution with a constant **P94** concentration and PS–PEG-COOH/**P94** fractions ranging from 0 to 20 wt% was quickly added to water in a bath sonicator to afford carboxylic-functionalized CPNPs of **P94**. During NP formation, the hydrophobic polystyrene segment and **P94** are most likely embedded inside the NPs, while the hydrophilic PEG chains and carboxylic acid groups extend outside into the aqueous environment. Moreover, the PEG chains not only function as a biocompatible layer to minimize nonspecific absorption, but also provide a steric barrier against nanoparticle aggregation and

carboxyl groups for further conjugation. The obtained CPNPs were determined by dynamic light scattering (DLS) to have an average diameter of 15 nm and a quantum yield of 30% in water. Replacement of PS–PEG-COOH with unfunctionalized PS–PEG did not cause any noticeable effects on particle size and morphology. In addition, increase of the concentration of **P94** in THF solution produced larger sized NPs. The absorption and emission of NPs based on **P94** show size-independent features.

Later on, the same group reported another strategy to prepare **P94** NPs using poly(styrene-*co*-maleic anhydride) (PSMA) as an encapsulation matrix [80]. The preparation procedure is similar to that of PS–PEG-COOH encapsulated **P94** NPs. During NP formation, the hydrophobic polystyrene units of PSMA and **P94** were anchored inside the particles while the hydrophilic maleic anhydride units were most likely localized on the NP surface and hydrolyzed in the aqueous environment to produce carboxylate groups on the NP surface for further conjugations. The obtained **P94** NPs show comparable size and fluorescence quantum yield to PS–PEG-COOH encapsulated **P94** NPs.

The nanoprecipitation method discussed above has two drawbacks: (i) The matrices are likely to dissociate from the formed NPs and (ii) it is difficult to achieve CPNPs with sizes smaller than 10 nm. To solve these problems, Chiu's group further developed a cross-linking strategy to synthesize stable CPNPs based on **P95**. In this case, poly(isobutylene-*alt*-maleic anhydride) (PIMA) was chosen as matrix and cross-linker [81]. PIMA, which has multiple reactive units, first reacts with the amine-functionalized **P95** to form covalent cross-links. Then, the resultant product dissolved in THF was injected quickly into Milli-Q water under sonication to afford **P95** NPs with carboxylic groups on the particle surface. As compared to the **P94** NPs, **P95** NPs showed lower fluorescence quantum yield (21% vs 30%) but better colloidal stability.

PEG-functionalized lipid is another matrix commonly used for CP encapsulation. The first lipid-PEG encapsulated **P94** NPs were reported by Christensen's group in 2011 [82]. They synthesized a series of lipid-PEG (PEG M_r = 2000, 1000, 500) with carboxy, biotin, or methoxy end groups. To synthesize **P94** NPs, a dilute solution of **P94** in THF was rapidly added to a ninefold volume of water containing lipid-PEG under continuous mild sonication. During this process, the aliphatic side chains on the **P94** interact with the hydrophobic lipid-PEG tail and are inserted into the NP core, while the hydrophilic PEG groups protrudes out into the aqueous media. The DLS diameters of the formed NPs are 20–30 nm, and are insensitive to the variation in the PEG length and end groups. However, the obtained **P94** NPs have low concentration and moderate fluorescence quantum yield (~18%). Subsequently, Liu's group modified this method to synthesize CPNPs based on a wide variety of preprepared CPs for bioapplications using the matrix of 1,2-distearoyl-*sn*-glycero-3-phosphoethanolamine (DSPE)-PEG_{2000} with different terminal functional groups, such as carboxylic acid, amine, azide, and maleimide [83].

Apart from PS- and lipid-derivatives, some proteins or peptides were also used as matrix to synthesize CPNPs via nanoprecipitation [84, 85]. For example, Liu's group used bovine serum albumin (BSA) as a polymer matrix to prepare **P96** NPs due to its good biocompatibility and nontoxicity [84]. The NP synthesis

started with the addition of a THF solution containing **P96** into a BSA aqueous solution under sonication, which was followed by cross-linking with glutaraldehyde and THF evaporation. The formed **P96** NPs exhibit DLS in the size of ~160 nm and carboxylic groups on the surface.

Encapsulation of CPs with silica shell is also an effective approach to synthesize CPNPs. Liu's group first reported on the synthesis of SiO_2@CP@SiO_2 NPs at room temperature without specific CP design or silane modification [86]. Using **P94** as an example, the THF solution of **P94** was first poured into a mixture of ethanol/water (v/v = 9/1) under sonication. As THF evaporates, **P94** formed small dots. Subsequently, a silica precursor, tetraethyl orthosilicate (TEOS) as well as ammonia was injected into the resulting mixture with vigorous stirring. After 12 h, an amine-functionalized silica precursor, 3-aminopropyl triethoxysilane (APTES), was added to modify the obtained SiO_2@**P94**@SiO_2 NPs with amine groups on surface. It was noted that the resulting NPs were ~70 nm in diameter with a quantum yield of 27% in water. The authors used four different CPs to prepare silica encapsulated NPs in their study, demonstrating that this method can be applied to any CPs that are soluble in organic solvents.

1.5 Conclusion

This chapter describes the commonly used strategies to bring CPs into aqueous media for biological applications. The water-soluble or water-dispersible CPs can be realized via either chemical modification of the conjugated backbones and side chains for CPEs and neutral WSCPs or by preparation of CP-based CPNPs. According to their chemical structures, the synthesis of CPEs and neutral WSCPs involves two aspects: construction of conjugated backbones and incorporation of charged or polar side chains. The conjugated backbones have been built through well-established polymerization methods, which are typically catalyzed with organometallic complexes or bases, while the functional side chains can be obtained through either direct polymerization or postpolymerization methods. For the preparation of CPNPs, three strategies are generally employed to encapsulate organic-soluble CPs and bring them in aqueous media, namely, reprecipitation, miniemulsion, and nanoprecipitation. Despite the great success in bringing organic-soluble CPs into water in the past decades, there is much to be done to understand how molecular packing and polymer aggregation affect their optical properties and how CP structures and performance can be optimized in order to meet the requirements for existing as well as new applications.

References

1 Pei, Q., Yu, G., Zhang, C., Yang, Y., and Heeger, A.J. (1995) *Science*, **269**, 1086.
2 Friend, R., Gymer, R., Holmes, A., Burroughes, J., Marks, R., Taliani, C., Bradley, D., Dos Santos, D., Bredas, J., and Lögdlund, M. (1999) *Nature*, **397**, 121–128.

3 Grimsdale, A.C., Leok Chan, K., Martin, R.E., Jokisz, P.G., and Holmes, A.B. (2009) *Chem. Rev.*, **109**, 897–1091.
4 Cheng, Y.-J., Yang, S.-H., and Hsu, C.-S. (2009) *Chem. Rev.*, **109**, 5868–5923.
5 Huang, F., Wu, H., and Cao, Y. (2010) *Chem. Soc. Rev.*, **39**, 2500–2521.
6 Liu, B. and Bazan, G.C. (2004) *Chem. Mater.*, **16**, 4467–4476.
7 Feng, L., Zhu, C., Yuan, H., Liu, L., Lv, F., and Wang, S. (2013) *Chem. Soc. Rev.*, **42**, 6620–6633.
8 Zhu, C.L., Liu, L.B., Yang, Q., Lv, F.T., and Wang, S. (2012) *Chem. Rev.*, **112**, 4687–4735.
9 Li, K. and Liu, B. (2012) *J. Mater. Chem.*, **22**, 1257–1264.
10 Pinto, M.R. and Schanze, K.S. (2002) *Synthesis*, **2002**, 1293–1309.
11 Traina, C.A., Bakus, R.C. 2nd, and Bazan, G.C. (2011) *J. Am. Chem. Soc.*, **133**, 12600–12607.
12 Tuncel, D. and Demir, H.V. (2010) *Nanoscale*, **2**, 484–494.
13 Pu, K.-Y., Shi, J., Cai, L., Li, K., and Liu, B. (2011) *Biomacromolecules*, **12**, 2966–2974.
14 Patil, A., Ikenoue, Y., Wudl, F., and Heeger, A. (1987) *J. Am. Chem. Soc.*, **109**, 1858–1859.
15 Masuda, H. and Kaeriyama, K. (1992) *Die Makromol.Chem., Rapid Commun.*, **13**, 461–465.
16 Viinikanoja, A., Lukkari, J., Ääritalo, T., Laiho, T., and Kankare, J. (2003) *Langmuir*, **19**, 2768–2775.
17 Zotti, G., Zecchin, S., Schiavon, G., and Berlin, A. (2001) *Macromolecules*, **34**, 3889–3895.
18 Xue, C., Cai, F., and Liu, H. (2008) *Chem.– Eur. J.*, **14**, 1648–1653.
19 Rubio-Magnieto, J., Azene, E.G., Knoops, J., Knippenberg, S., Delcourt, C., Thomas, A., Richeter, S., Mehdi, A., Dubois, P., Lazzaroni, R., Beljonne, D., Clement, S., and Surin, M. (2015) *Soft Matter*, **11**, 6460–6471.
20 Zotti, G., Zecchin, S., Schiavon, G., Vercelli, B., Berlin, A., and Porzio, W. (2004) *Chem. Mater.*, **16**, 2091–2100.
21 Faid, K. and Leclerc, M. (1996) *Chem. Commun.*, 2761–2762.
22 Bellina, F., Carpita, A., and Rossi, R. (2004) *Synthesis*, **2004**, 2419–2440.
23 Rulkens, R., Schulze, M., and Wegner, G. (1994) *Macromol. Rapid Commun.*, **15**, 669–676.
24 Child, A.D. and Reynolds, J.R. (1994) *Macromolecules*, **27**, 1975–1977.
25 Shi, S. and Wudl, F. (1990) *Macromolecules*, **23**, 2119–2124.
26 Gu, Z., Shen, Q.D., Zhang, J., Yang, C.Z., and Bao, Y.J. (2006) *J. Appl. Polym. Sci.*, **100**, 2930–2936.
27 Gu, Z., Bao, Y.-J., Zhang, Y., Wang, M., and Shen, Q.-D. (2006) *Macromolecules*, **39**, 3125–3131.
28 Xie, B., Bagui, M., Guo, R., Li, K., Wang, Q., and Peng, Z. (2007) *J. Polym. Sci. A Polym. Chem.*, **45**, 5123–5135.
29 Zhang, W., Zhu, L., Qin, J., and Yang, C. (2011) *J. Phys. Chem. B*, **115**, 12059–12064.
30 Chinchilla, R. and Nájera, C. (2007) *Chem. Rev.*, **107**, 874–922.
31 Huang, F., Wang, X., Wang, D., Yang, W., and Cao, Y. (2005) *Polymer*, **46**, 12010–12015.

32 Pu, K.-Y. and Liu, B. (2010) *J. Phys. Chem. B*, **114**, 3077–3084.
33 Zhao, X., Pinto, M.R., Hardison, L.M., Mwaura, J., Müller, J., Jiang, H., Witker, D., Kleiman, V.D., Reynolds, J.R., and Schanze, K.S. (2006) *Macromolecules*, **39**, 6355–6366.
34 McCullough, R.D., Ewbank, P.C., and Loewe, R.S. (1997) *J. Am. Chem. Soc.*, **119**, 633–634.
35 Xing, C., Xu, Q., Tang, H., Liu, L., and Wang, S. (2009) *J. Am. Chem. Soc.*, **131**, 13117–13124.
36 Wallow, T.I. and Novak, B.M. (1991) *J. Am. Chem. Soc.*, **113**, 7411–7412.
37 Rau, I.U. and Rehahn, M. (1993) *Polymer*, **34**, 2889–2893.
38 Zhang, Y., Liu, B., and Cao, Y. (2008) *Chem.–Asian J.*, **3**, 739–745.
39 Peng, Z.H., Xu, B.B., Zhang, J.H., and Pan, Y.C. (1999) *Chem. Commun.*, 1855–1856.
40 Fujii, A., Sonoda, T., Fujisawa, T., Ootake, R., and Yoshino, K. (2001) *Synth. Met.*, **119**, 189–190.
41 Slaven, W.T. IV, Li, C.-J., Chen, Y.-P., John, V.T., and Rachakonda, S.H. (1999) *J. Macromol. Sci.—Pure Appl. Chem.*, **36**, 971–980.
42 Kim, I.B., Dunkhorst, A., Gilbert, J., and Bunz, U.H.F. (2005) *Macromolecules*, **38**, 4560–4562.
43 Qin, C., Wu, X., Gao, B., Tong, H., and Wang, L. (2009) *Macromolecules*, **42**, 5427–5429.
44 Qin, C., Wong, W.-Y., and Wang, L. (2010) *Macromolecules*, **44**, 483–489.
45 Pinto, M.R., Kristal, B.M., and Schanze, K.S. (2003) *Langmuir*, **19**, 6523–6533.
46 Qin, C., Cheng, Y., Wang, L., Jing, X., and Wang, F. (2008) *Macromolecules*, **41**, 7798–7804.
47 Ho, H.A., Boissinot, M., Bergeron, M.G., Corbeil, G., Doré, K., Boudreau, D., and Leclerc, M. (2002) *Angew. Chem.*, **114**, 1618–1621.
48 Zhai, L. and McCullough, R.D. (2002) *Adv. Mater.*, **14**, 901–905.
49 Gutacker, A., Adamczyk, S., Helfer, A., Garner, L.E., Evans, R.C., Fonseca, S.M., Knaapila, M., Bazan, G.C., Burrows, H.D., and Scherf, U. (2010) *J. Mater. Chem.*, **20**, 1423–1430.
50 Balanda, P.B., Ramey, M.B., and Reynolds, J.R. (1999) *Macromolecules*, **32**, 3970–3978.
51 Ramey, M.B., Ann Hiller, J., Rubner, M.F., Tan, C., Schanze, K.S., and Reynolds, J.R. (2005) *Macromolecules*, **38**, 234–243.
52 Stork, M., Gaylord, B.S., Heeger, A.J., and Bazan, G.C. (2002) *Adv. Mater.*, **14**, 361–366.
53 Yang, R., Wu, H., Cao, Y., and Bazan, G.C. (2006) *J. Am. Chem. Soc.*, **128**, 14422–14423.
54 Zhang, Z., Fan, Q., Sun, P., Liu, L., Lu, X., Li, B., Quan, Y., and Huang, W. (2010) *Macromol. Rapid Commun.*, **31**, 2160–2165.
55 Pu, K.Y., Cai, L.P., and Liu, B. (2009) *Macromolecules*, **42**, 5933–5940.
56 Yuan, H.X., Liu, Z., Liu, L.B., Lv, F.T., Wang, Y.L., and Wang, S. (2014) *Adv. Mater.*, **26**, 4333–4338.
57 He, F., Ren, X., Shen, X., and Xu, Q.-H. (2011) *Macromolecules*, **44**, 5373–5380.
58 Zhang, Y., Yang, Y., Wang, C.C., Sun, B., Wang, Y., Wang, X.Y., and Shen, Q.D. (2008) *J. Appl. Polym. Sci.*, **110**, 3225–3233.

59 Pu, K.-Y., Pan, S.Y.-H., and Liu, B. (2008) *J. Phys. Chem. B*, **112**, 9295–9300.
60 Pu, K.-Y., Li, K., Shi, J., and Liu, B. (2009) *Chem. Mater.*, **21**, 3816–3822.
61 Fukuhara, G. and Inoue, Y. (2011) *J. Am. Chem. Soc.*, **133**, 768–770.
62 Henson, Z.B., Zhang, Y., Nguyen, T.-Q., Seo, J.H., and Bazan, G.C. (2013) *J.Am. Chem. Soc.*, **135**, 4163–4166.
63 Rubio-Magnieto, J., Thomas, A., Richeter, S., Mehdi, A., Dubois, P., Lazzaroni, R., Clément, S., and Surin, M. (2013) *Chem. Commun.*, **49**, 5483–5485.
64 Twomey, M., Mendez, E., Manian, R.K., Lee, S., and Moon, J.H. (2016) *Chem. Commun. (Camb.)*, **52**, 4910–4913.
65 Aslund, A., Herland, A., Hammarstrom, P., Nilsson, K.P.R., Jonsson, B.H., Inganas, O., and Konradsson, P. (2007) *Bioconjug. Chem.*, **18**, 1860–1868.
66 Costa, T., de Azevedo, D., Stewart, B., Knaapila, M., Valente, A.J.M., Kraft, M., Scherf, U., and Burrows, H.D. (2015) *Polym. Chem.*, **6**, 8036–8046.
67 Fang, J., Wallikewitz, B.H., Gao, F., Tu, G., Muller, C., Pace, G., Friend, R.H., and Huck, W.T. (2011) *J. Am. Chem. Soc.*, **133**, 683–685.
68 Li, J., Tian, C., Yuan, Y., Yang, Z., Yin, C., Jiang, R., Song, W., Li, X., Lu, X., Zhang, L., Fan, Q., and Huang, W. (2015) *Macromolecules*, **48**, 1017–1025.
69 Phillips, R.L., Kim, I.-B., Carson, B.E., Tidbeck, B.r., Bai, Y., Lowary, T.L., Tolbert, L.M., and Bunz, U.H. (2008) *Macromolecules*, **41**, 7316–7320.
70 Zhou, L., Geng, J., Wang, G., Liu, J., and Liu, B. (2013) *Polym. Chem.*, **4**, 5243–5251.
71 Pu, K.Y., Li, K., and Liu, B. (2010) *Adv. Funct. Mater.*, **20**, 2770–2777.
72 Liu, J., Ding, D., Geng, J., and Liu, B. (2012) *Polym. Chem.*, **3**, 1567–1575.
73 Liu, J., Geng, J., and Liu, B. (2013) *Chem. Commun.*, **49**, 1491–1493.
74 Pecher, J. and Mecking, S. (2010) *Chem. Rev.*, **110**, 6260–6279.
75 Kurokawa, N., Yoshikawa, H., Hirota, N., Hyodo, K., and Masuhara, H. (2004) *Chemphyschem*, **5**, 1609–1615.
76 Szymanski, C., Wu, C.F., Hooper, J., Salazar, M.A., Perdomo, A., Dukes, A., and McNeill, J. (2005) *J. Phys. Chem. B*, **109**, 8543–8546.
77 Li, K., Pan, J., Feng, S.S., Wu, A.W., Pu, K.Y., Liu, Y., and Liu, B. (2009) *Adv. Funct. Mater.*, **19**, 3535–3542.
78 Hashim, Z., Howes, P., and Green, M. (2011) *J. Mater. Chem.*, **21**, 1797–1803.
79 Wu, C., Schneider, T., Zeigler, M., Yu, J., Schiro, P.G., Burnham, D.R., McNeill, J.D., and Chiu, D.T. (2010) *J. Am. Chem. Soc.*, **132**, 15410–15417.
80 Wu, C., Jin, Y., Schneider, T., Burnham, D.R., Smith, P.B., and Chiu, D.T. (2010) *Angew. Chem. Int. Ed.*, **49**, 9436–9440.
81 Yu, J., Wu, C., Zhang, X., Ye, F., Gallina, M.E., Rong, Y., Wu, I.C., Sun, W., Chan, Y.H., and Chiu, D.T. (2012) *Adv. Mater.*, **24**, 3498–3504.
82 Kandel, P.K., Fernando, L.P., Ackroyd, P.C., and Christensen, K.A. (2011) *Nanoscale*, **3**, 1037–1045.
83 Liu, J., Feng, G., Ding, D., and Liu, B. (2013) *Polym. Chem.*, **4**, 4326–4334.
84 Ding, D., Li, K., Qin, W., Zhan, R., Hu, Y., Liu, J., Tang, B.Z., and Liu, B. (2013) *Adv. Healthc. Mater.*, **2**, 500–507.
85 Almeida, C.S., Herrmann, I.K., Howes, P.D., and Stevens, M.M. (2015) *Chem. Mater.*, **27**, 6879–6889.
86 Geng, J., Liu, J., Liang, J., Shi, H., and Liu, B. (2013) *Nanoscale*, **5**, 8593–8601.

2

Direct Synthesis of Conjugated Polymer Nanoparticles

Sibel Ciftci and Alexander J. C. Kuehne

DWI – Leibniz Institute for Interactive Materials, Forckenbeckstr. 50, 52056, Aachen, Germany

2.1 Introduction

Conjugated polymer nanoparticles (CPNs) are powerful fluorescent semiconductor materials, which excel through simple fabrication and processing techniques, their great potential for electro- and photoluminescent applications, and their high conductivity as compared to conventional polymers. Furthermore, CPNs show extraordinary resistance toward photo-oxidation and photo-bleaching and exhibit low cytotoxicity [1–4].

These characteristics render CPNs interesting candidates for fluorescent probes and vehicles in biomedical imaging [5–7]. CPNs often surpass molecular fluorescent dyes and dye-doped dielectric particles in their high photoluminescence quantum yield, through the absence of blinking and improved photostability [5–11]. Further applications of CPNs are in the area of electronic and electroluminescent devices or as composites in organic conductive threads and fibers [12].

Currently, there exists a plethora of CPNs, which can be categorized by their molecular composition, fabrication techniques, and their properties. One can distinguish first, CPNs which are produced for charge transport applications, and secondly, CPNs which are developed for tunable and efficient luminescence properties.

CPNs for charge transport applications are often based on polythiophenes (P3HT and PEDOT) and synthesized by aqueous oxidative polymerization. Particles formed from polythiophene are of great interest due to their low oxidation potential, crystallinity, and environmental stability [13]. Further, CPNs known for their good conductivity are composed of polyaniline (PANI), polypyrrole (PPy), and polyacetylene (PA) (see Figure 2.1). PANI and PPy are conjugated polymers that are also accessible by oxidative polymerization mostly in an aqueous reaction medium. By contrast, PA requires transition metal catalysis for polymerization. PA is sensitive to moisture and oxygen [14]. CPNs from these polymers find application mainly in electromagnetic shielding and anticorrosion agents for metals as well as in electronic devices and components.

Conjugated Polymers for Biological and Biomedical Applications, First Edition. Edited by Bin Liu

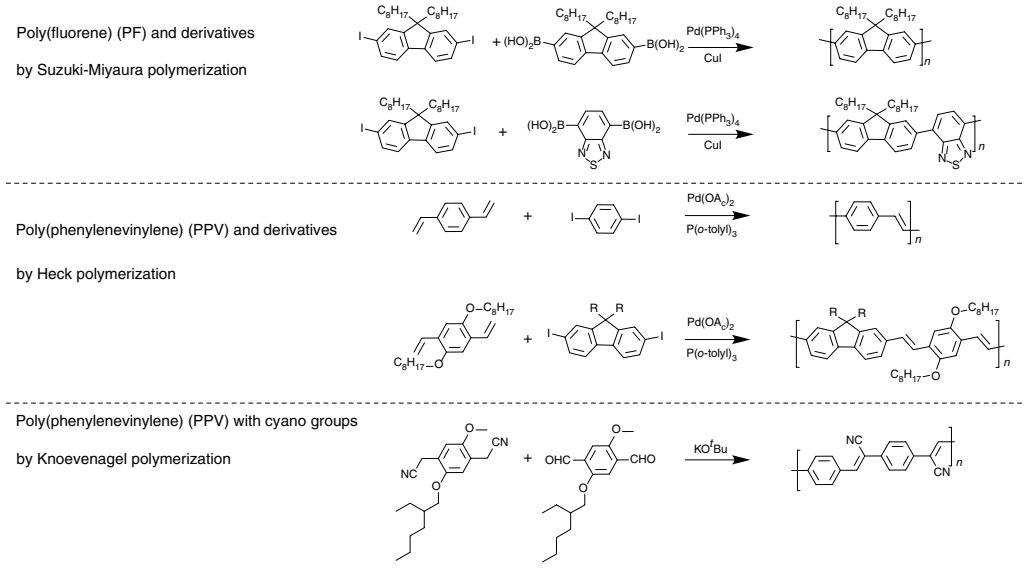

Figure 2.1 Common conjugated polymers, their derivatives, and polymerization types.

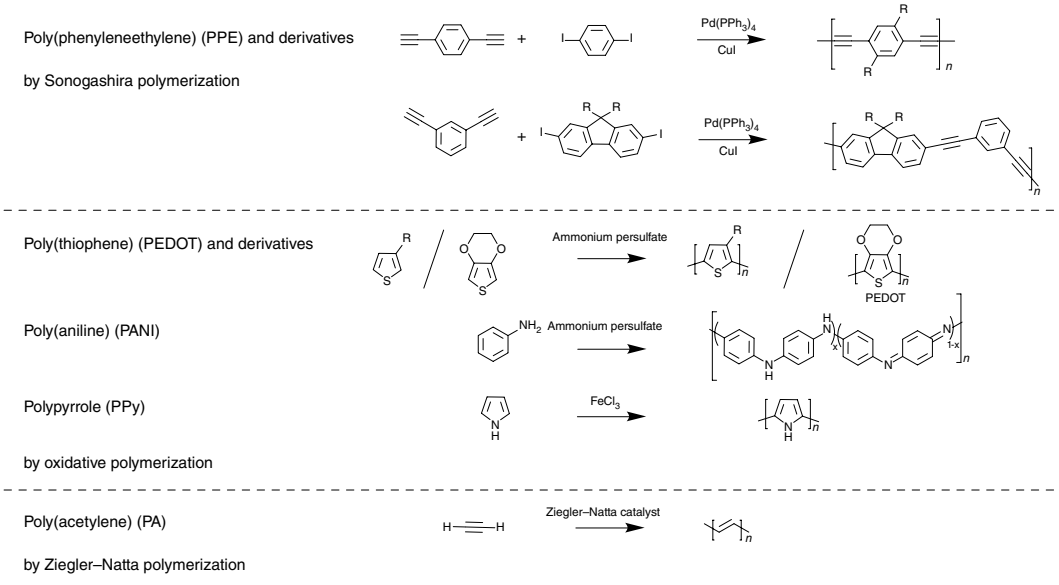

Figure 2.1 (*Continued*)

Furthermore, these nonfluorescent low electronic bandgap CPNs have shown great potential for utilization as photoacoustic contrast agents for biomedical imaging and diagnostics [15, 16].

By contrast, CPNs with larger electronic band gaps are highly luminescent and can be tuned in their spectral excitation and emission profiles as well as their quantum efficiencies by varying the monomer composition [17]. The emission of CPNs can be varied over a broad spectral range from the deep-blue into the near-infrared spectrum. CPNs can be prepared from polythiophenes, polyfluorene, polyphenylene–vinylenes, and polyphenylene–acetylenes and more complex copolymers of the aforementioned units. These types of CPNs often exhibit outstanding photoluminescence characteristics and optical properties [14].

Polyfluorenes, poly(phenylene–vinylenes) (PPV) and poly(arylene–acetylenes) are typically synthesized via Palladium-catalyzed cross-coupling polymerizations (see Figure 2.1) [18–20]. Polyfluorene- based CPNs usually exhibit high quantum yields and are high-potential candidates for application in biomedical probes. Alternatively, PPV CPNs can be produced via metathesis polycondensation (acyclic diene metathesis, ADMET) in an aqueous medium [21]. The photoluminescence properties can be improved by cyano-substituting the PPVs. [22] Such CPNs are usually prepared following Knoevenagel-type dispersion polycondensation [23]. Particles composed of phenylene–vinylene or phenylene–acetylene polymers can easily be surface functionalized with thiol-functionalized biomolecules using click-chemistry (see Figure 2.1) [24]. Attaching biological recognition motifs to the CPNs renders them suitable for specific and targeted bioimaging applications.

Besides the possibility to easily surface functionalize CPNs, there are several other requirements for CPNs to render them suitable for bioimaging and cell tracking applications: (i) the particles should ideally be monodisperse and spherical in shape. Monodisperse particles secure specific labeling of only the targeted type of cells, especially in multicomponent united cell structures. Different cells exhibit different particle uptake kinetics and monodisperse CPNs prevent unspecific uptake by the nontargeted type of cells [25, 26]. (ii) in order to maintain comparability between different CPNs and different cells in cell culture and cell tracking experiments, the particles should be uniformly spherical to avoid uptake of oblong particles prior to the uptake of differently shaped particles. To reach this aim, it is very important to adjust the synthetic environment for the preparation of CPNs. (iii) The particles should exhibit low cytotoxicity. Owing to their hydrophobic and polymeric nature, CPNs usually exhibit either very low cytotoxicity or no cytotoxicity.

Several methods exist to create CPNs. The techniques range from direct *in situ* polymerization to form particles to postpolymerization techniques, where the conjugated polymer is first synthesized and only subsequently transformed into a particle shape. There exist a few articles on conjugated polymer particles, which review the particle characteristics and highlight their applications also in the biomedical fields [2, 5, 14, 27]. While these articles give insight into the different tunable material properties, little attention is paid to the preparative techniques. Furthermore, inconsistent terminology and sometimes inept (because confusing) jargon is used in the literature to describe the synthetic

and preparative techniques. Here, we will give an overview on the different techniques to prepare CPNs and we will categorize the preparation methods by the underlying physicochemical and synthetic aspects. For selected CPNs we will also discuss their properties and performance relevant to biomedical application.

2.2 Generation of CPNs

CPN can be produced using a variety of preparative techniques. This chapter will give an overview of the different methods and discuss their prevailing advantages and disadvantages. First and foremost, we categorize the methods into two fundamental strategies: *post-polymerization methods* and *direct polymerization techniques* in disperse hetero-phase systems. As a basic principle, the insolubility of conjugated polymers in polar solvents is exploited in all preparative techniques.

In postpolymerization techniques, the conjugated polymer is first prepared in a nonpolar medium, which is a good solvent for the resulting conjugated polymer. These conjugated polymers are then "shaped" into colloidal particles *via* precipitation or emulsification techniques [2]. As a result, CPNs can be generated from commercially available and purified polymers by dispersion in a polar nonsolvent. By contrast, in direct polymerization techniques the CPNs are generated *in situ* during polymer synthesis. Dispersion polymerization or polymerization in miniemulsion are established methods for the preparation of CPNs [17, 28]. While direct polymerization techniques offer better control over the shape and dispersity of the particles, the postpolymerization techniques are more flexible in terms of the type of the conjugated polymer materials and their purity, as these are prepared in a stand-alone and separate reaction step, which allows for intermediate purification steps.

2.2.1 Postpolymerization Techniques

Three prominent postpolymerization techniques are typically employed to prepare CPNs. In *nanoprecipitation* (also often termed reprecipitation or injection method) and *miniemulsification* the conjugated polymer is dissolved in a good (nonpolar) solvent. This solution is then dispersed in a (polar) solvent, which is a poor solvent for the conjugated polymer, where either droplets of the polymer solution are formed or the polymer precipitates (Figure 2.2). The third postpolymerization method is a *self-assembly* method, which is based on intermolecular attraction, for example, Coulomb interactions (Figure 2.2). In the following text, we will describe these methods in more detail.

2.2.1.1 Nanoprecipitation

Since the nanoprecipitation technique is discussed elsewhere in this book, we will only briefly discuss nanoprecipitation for completeness in the context of this chapter. In the nanoprecipitation method, a previously synthesized conjugated polymer (CP) is dissolved in a good solvent [29]. This polymer solution is then strongly

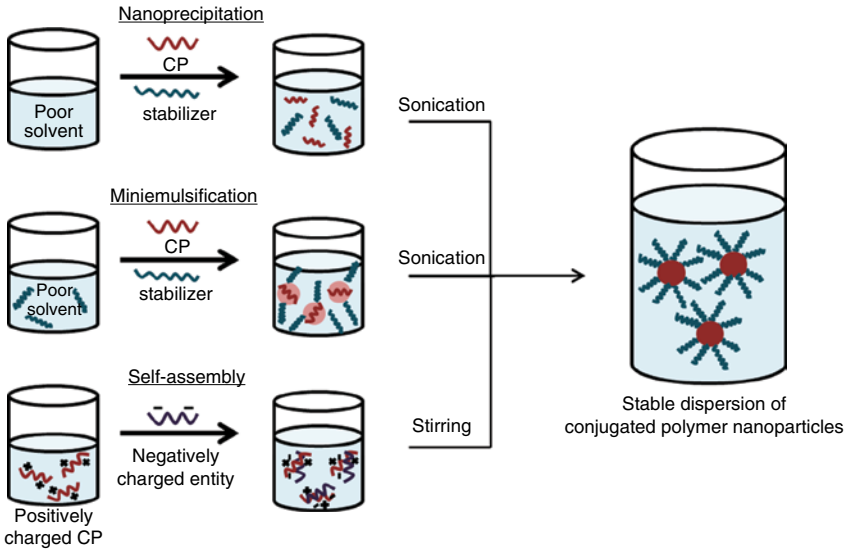

Figure 2.2 Schematic representations of the nanoprecipitation, miniemulsification, and self-assembly methods.

diluted or added quickly to an excess of a poor solvent (often water). When both solvents are miscible, then the polymer precipitates into small and spherical aggregates. Owing to the rapid increase in polarity upon injection of the polymer solution into the polar solvent (decrease of the solvent hydrophobicity), phase inversion occurs and the polymer chains collapse to form nanoparticles. CPNs are obtained as dispersions in the poor solvent [30]. The size of the resulting CPNs can be tuned by varying the concentration of the polymer in solution. Ultrasonication is often used to improve mixing of the polymer solution with the poor solvent and further reduce the nanoparticle size. The mechanism of particle stabilization in the resulting dispersion is unclear, since surfactants are often not applied in the preparation of CPNs [29]. However, charge accumulation on the surface of the particles is assumed to prevent aggregation and provide stabilization [14]. Owing to thermodynamically favorable surface to volume ratio, the formed nanoparticles are spherical. Polythiophene nanoparticles are among the first particles that have been produced via nanoprecipitation (see Figure 2.3b,d) [31]. Depending on the concentration of conjugated polymer in solution, very small CPNs can be generated, down to the point where each particles consists (predominantly) of only a single polymer chain. Singe polymer particles have been prepared from poly(2-methoxy-5-((2-ethylhexyl)oxy)-*p*-phenylenevinylene) (MEH-PPV). These MEH-PPV CPNs are stable in aqueous dispersion. The diameters of CPNs range from 5 to 30 nm (see Figure 2.3a) [29]. The particles are so small that they are often termed conjugated polymer dots inspired by the nomenclature of inorganic quantum dots.

Most recently, hybrid nanoparticles have been created by the described nanoprecipitation method (Figure 2.3c) [32]. These particles consist of a poly-[(9,9-dioctylfluorenyl-2,7-diyl)-*alt*-(1,4-benzo(2,1′,3)-thiadiazole)] (F8BT) conjugated polymer shell seeded onto silica-coated gold nanorods as cores. For the

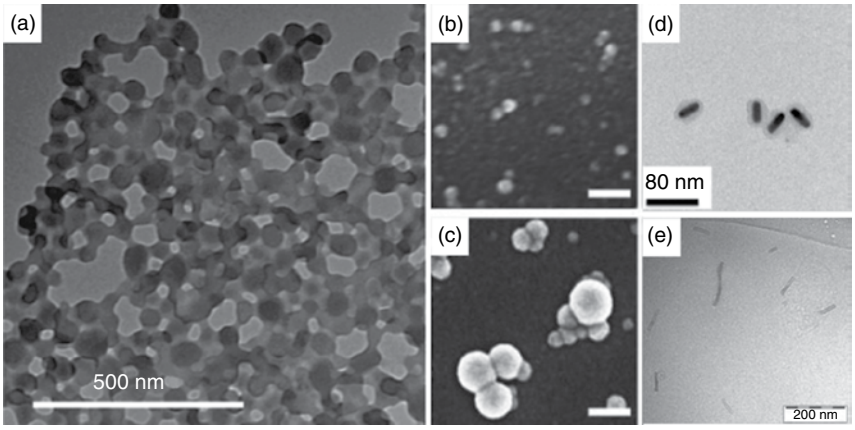

Figure 2.3 Electron microscopy images of CPNs synthesized by nanoprecipitation: (a) MEH-PPV CPNs. (Reprinted (adapted) with permission from Ref. [29]. Copyright 2005, American Chemical Society.) (b, c) Polythiophene CPNs, the scale bars represent 200 nm. (Reproduced (in part) with permission from Ref. [31]. Copyright 2004, Wiley-VCH.) (d) (F8BT) Conjugated polymer shell seeded onto silica coated gold nanorods. (Reprinted (adapted) with permission from Ref. [32]. Copyright 2016, American Chemical Society.) (e) Rod-like CPNs. (Reprinted (adapted) with permission from Ref. [33]. Copyright 2002, American Chemical Society.)

generation of these hybrid particles the F8BT polymer is dissolved in THF and silica-coated gold nanoparticles are added. This mixture is then injected quickly into deionized water (type I) and mixed by ultrasonication. Silica-gold nanorods coated with a shell of F8BT are obtained as a dispersion in water. THF can be removed at reduced pressure. These hybrid core–shell particles have potential for biological sensing and imaging applications and are promising for resolving problems in long-term tracking as well as selective imaging applications [32].

CPNs can also be produced as rods by the nanoprecipitation technique (see Figure 2.3e). When using rigid-backbone polymers with, for example, acetylene moieties (e.g., poly(phenylene-acetylenes), the conjugated polymer crystallizes during phase inversion, resulting in rod-like particles and other anisometric shapes. The mixing rate during precipitation has paramount influence on the particle shape. Rapid mixing leads to the kinetically trapped more spherical particles, whereas slowly mixing results in anisometric particle shapes. The size of the crystalline CPNs can be controlled by adjusting the molecular weight of the rigid-backbone conjugated polymer [33].

2.2.1.2 Miniemulsification

In general, emulsions are systems where liquid droplets are suspended in a continuous phase, in which the droplets are immiscible. Miniemulsification (depending on the droplet size also often termed nanoemulsification) [34] describes the method to produce stabilized droplets using high shear rates for example in high-pressure homogenizers and via ultrasonication [35]. To generate small and stable droplets, and reduce Ostwald-ripening, droplet coalescence, and flocculation, surfactants are added to provide stabilization. In a classical miniemulsion, sodium dodecyl sulfate (SDS) is used to stabilize oil droplets in

water. Miniemulsification is the most commonly applied method to generate CPNs, because this method is reproducible and exhibits high tolerance toward different environmental changes such as temperature and concentration. In contrast to the nanoprecipitation approach, here, the dispersed phase (conjugated polymer solution) and the continuous phase (poor solvent for the polymer) are not miscible. Typically, the conjugated polymer is dissolved in chloroform or toluene and added to an excess of the aqueous phase with dissolved surfactant. The mixture is then sheared until small droplets are formed and all available surfactant is engaged in stabilizing the droplet interfaces. Simultaneously, temperature is applied to the mixture in order to evaporate the organic solvent and produce CPNs dispersed in water. The concentration of the polymer solution has an impact on the diameter of the resulting nanoparticles; however, the amount of added surfactant is the decisive factor for the resulting nanoparticle size. The average size of the CPNs generated by this method ranges from 30 to 500 nm (see Figure 2.4a) [2, 14, 35].

The surfactant can also be utilized to support surface functionalization. As such, polyethylene glycolated phospholipids have been applied for stabilization of a miniemulsified conjugated polymer solution. This method leads to glycophospholipid-functionalized CPNs with an average diameter of 100 nm. Owing to their functionalization these particles are attractive candidates for targeted biological fluorescence imaging. These particles have been used to label HeLa cells (see Figure 2.4b,c) [36].

Miniemulsifications can also be utilized to prepare CPNs that consist of mixtures of conjugated polymers; for example polyfluorenes and polytriarylamines combined in the same particle [37, 38]. Alternatively, such hybrid nanomaterials can also be prepared by coating CPNs with a second functional semiconductor. For example, phosphorescent dyes (triplet emitters such as tris(bipyridine) ruthenium(II) complexes) can be attached to the surface of CPNs. Such hybrid particles with sizes between 70 and 140 nm are synthesized by mixing a diluted SDS-stabilized CPN dispersion with an aqueous solution of the tris(bipyridine) ruthenium(II) complexes. This work represents the first exploration of organic singlet–triplet hybrid nanoparticles offering encouraging possibilities for phosphorescent particles and devices from aqueous media (see Figure 2.4d) [37].

2.2.1.3 Microfluidics

To gain better control over the mixing processes, the postpolymerization techniques discussed earlier can also be performed in microfluidic channels, for example on lab-on-a-chip devices. Microfluidic techniques allow for continuous-flow production of particles as opposed to the earlier described batch processes. Constraining chemical and physical processes to the microscale reduces environmental effects, such as concentration gradients and diffusion. For the generation of emulsions and dispersions, microfluidics can improve the monodispersity of the droplets or the resulting particles [39]. The different phases with surfactant/stabilizer and conjugated polymer are injected into the channel geometry by means of tubes and then combined in a T- or cross-channel junction. The conjugated polymer solution is combined either with a miscible solvent, where the polymer *nanoprecipitates* or with a nonmiscible phase,

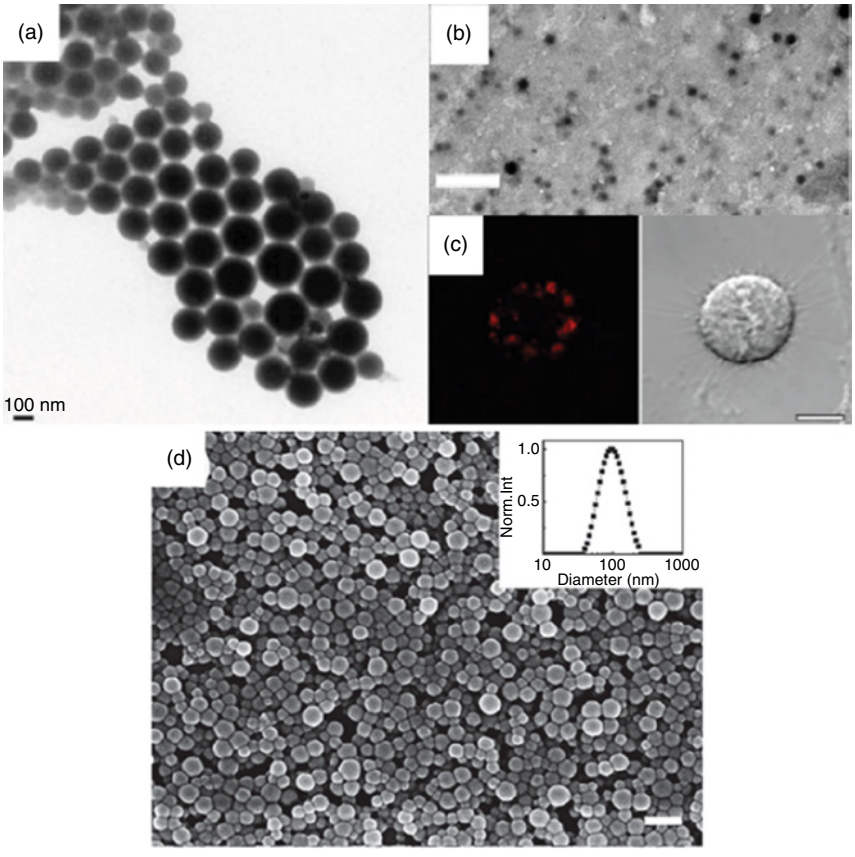

Figure 2.4 CPNs synthesized by miniemulsification: (a) transmission electron microscope image of poly(*p*-phenylene) nanoparticles. (Reproduced (in part) with permission from Ref. [35]. Copyright 2002, Wiley-VCH.) (b) Transmission electron micrograph of poly(phenylene–ethynylene) nanoparticles. The scale bar represents 500 nm, and (c) confocal microscope image (left) and bright field image (right) of a HeLa cell incubated with polyethylene glycolated phospholipid-functionalized CPNs, the scale bar represents 10 µm. (Reprinted (adapted) with permission from Ref. [36]. Copyright 2010, American Chemical Society.) (d) Scanning electron microscopy image of polyfluorene particles. The scale bar is 200 nm. Inset: dynamic light scattering profile of a poly(fluorene) particle dispersion. (Reproduced (in part) with permission from Ref. [37]. Copyright 2016, Wiley-VCH.)

where a *miniemulsion* of the polymer solution is generated drop-by-drop at the channel junction. The microfluidic channel geometries are usually produced by soft lithography, where a relief of the channel geometry is replicated using a thermally curable silicone (PDMS). However, PDMS swells in contact with nonpolar solvents and the device performance deteriorates over time. This problem can be circumvented by coating the PDMS device with hydrophobic Parylene-C in a chemical vapor deposition process [40]. To prevent wetting of the dispersed phase and produce droplets of the polymer solution, the Parylene-C-coated microfluidic chip is exposed to an oxygen plasma to render the channel surface hydrophilic [40]. A polyfluorene in toluene solution can be

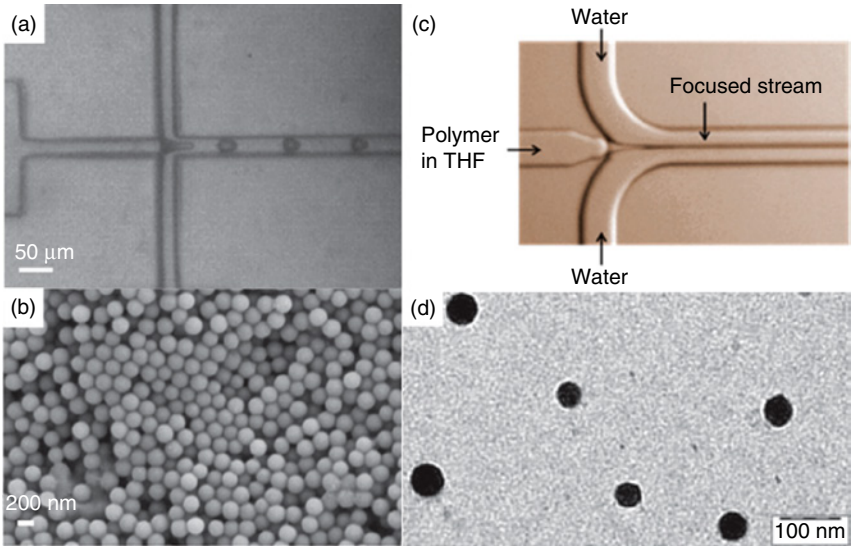

Figure 2.5 Comparison of microfluidic processes: (a) miniemulsification and (b) obtained particles. (Reproduced (in part) with permission from Ref. [40]. Copyright 2011, The Royal Society of Chemistry.) (c) Microfluidic nanoprecipitation and (d) obtained particles. (Reproduced (in part) with permission from Ref. [41]. Copyright 2012, The Royal Society of Chemistry.)

emulsified in such a device drop-by-drop, leading to monodisperse droplets of the polyfluorene solution in water with diameters in the range of 10–50 µm. Polyvinylalcohol is applied as a stabilizer in the continuous aqueous phase (see Figure 2.5a). The generated droplets are collected off-chip in an excess of the continuous phase with stabilizer and the toluene is evaporated slowly to obtain monodisperse conjugated polymer particles with diameters of a few hundred nanometers and up to several microns (see Figure 2.5b). The size can be controlled by varying the polymer concentration in the dispersed phase [40].

Alternatively, the nanoprecipitation method can be applied on chip. To do so, blockcopolymers with a conjugated block (poly(fluorene–acetylene) and a hydrophilic block (polyethyleneglycol) have been applied. The microfluidic nanoprecipitation of these block-copolymers results in sterically stabilized CPNs with diameters around 50 nm (see Figure 2.5d). The hydrophilic block plays an important role for the particle stabilization. Without the hydrophilic block no stable CPN dispersions can be obtained. The presynthesized block-copolymer is dissolved in THF and injected into the microfluidic chip. On chip, the conjugated block-copolymer solution is focused by two streams of the continuous aqueous phase at a channel cross-junction and the block-copolymer precipitates into small CPNs (Figure 2.5c) [41].

While microfluidics facilitates continuous-flow formulation and polymerization, the drawback of this technique is clearly low throughput of a single microchannel device due to the volumetric confinement to the microscale. However, the improved emulsification and precipitation conditions lead to improved

uniformity and monodispersity in comparison to the previously described batch processes (at otherwise comparable conditions).

The low throughput of microfluidic devices can be obviated by parallelizing the channel geometry and by using multiple channel junctions connected to the same inlets and outlets to increase the overall throughput [42–44]. Such parallelized channel geometries have to be carefully designed and engineered to avoid introduction of pressure-drop and flow-rate variations between the channel junctions, which would jeopardize the positive effects in microfluidics [45].

2.2.1.4 Self-Assembly

So far, we have discussed postpolymerization methods for CPNs, where a conjugated polymer solution is combined with a second phase, in which the conjugated polymer is immiscible. Alternatively, molecular self-assembly can be used for particle generation. For this, positively and negatively charged building blocks are applied, at least one of which is a conjugated polymer. The respective oppositely charged building blocks are individually dissolved or dispersed in aqueous media. These media are combined and the oppositely charged building blocks attract each other due to Coulomb interactions and aggregate into particles (see Figure 2.2). The particles can be recovered by centrifugation [1, 46]. This preparation method allows the creation of functionalized CPNs. Antibacterial CPNs can be prepared by combining an anionic polythiophene and a cationic porphyrin, which adsorb to Gram-positive and Gram-negative bacteria. Under white light illumination, these particles generate singlet oxygen and can be used in photodynamic therapy to effectively kill bacteria and cancer cells [47]. Furthermore, CPNs with antitumor activity have been produced by combining a cationic pentathiophene together with the anionic anticancer drug chlorambucil [48, 49].

2.2.2 Direct Polymerization in Heterogeneous Systems

Hitherto, the preparation strategies toward CPNs have been postpolymerization techniques. The conjugated polymer is first synthesized in solution and particles are generated from the conjugated polymer solution in a subsequent process. Alternatively, the CPNs can be prepared from monomers *in situ* during polymerization in a single step. Such direct polymerization techniques facilitate a wide range of nanoparticle architectures, sizes, and morphologies. Popular representatives for the preparation of monodisperse submicrometer particles are *dispersion polymerization* and *emulsion polymerization* as well as *polymerization in mini- and microemulsion*.

In emulsion-based techniques, the monomers are not soluble in the continuous phase. By contrast, in the dispersion polymerization procedure the monomer is soluble in the continuous phase. The polymer, which is produced during dispersion polymerization, then becomes insoluble to produce particles. As a result, dispersion polymerization requires careful selection of the reaction medium to meet these requirements. Depending on the quality of surfactants and stabilizers chosen, these emulsion- as well as dispersion polymerization can deliver monodisperse CPNs. The different approaches will be discussed in the

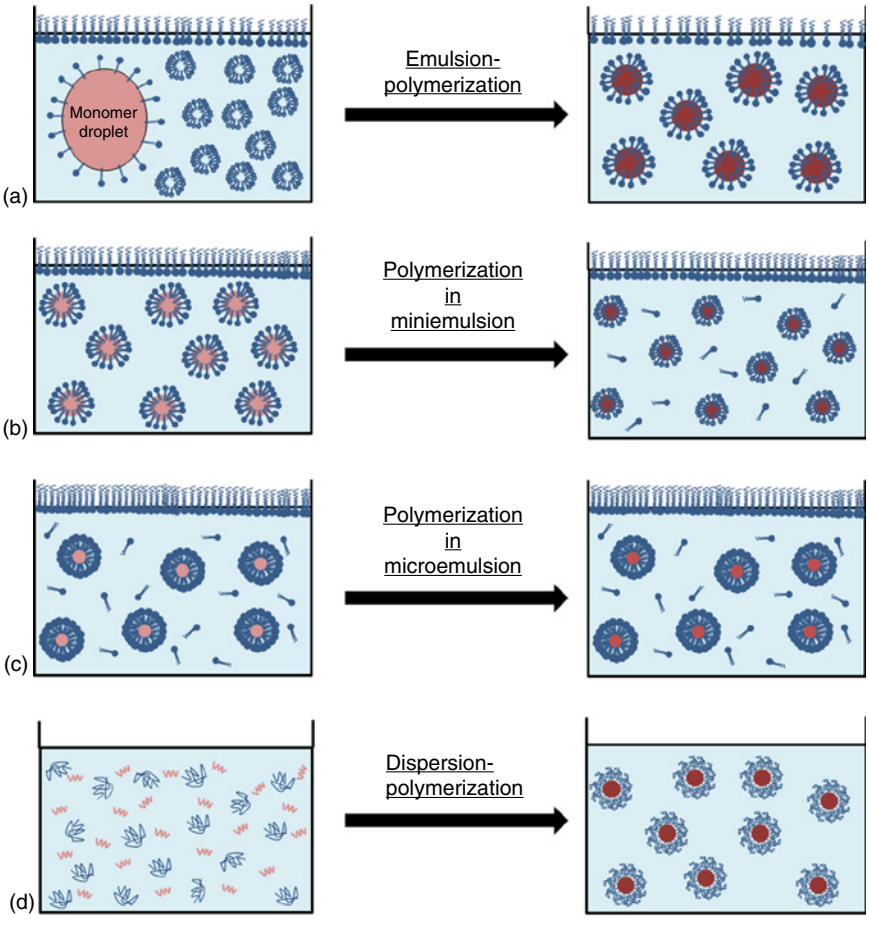

Figure 2.6 Schematic of the described direct particle preparation methods: (a) emulsion polymerization (b) polymerization in mini- and (c) microemulsion and (d) dispersion polymerization.

following sections (see Figure 2.6 for an overview of the different direct polymerization methods for the generation of CPNs).

2.2.2.1 Emulsion Polymerization

An emulsion polymerization consists of a liquid monomer phase and a second continuous phase (often water). The continuous phase contains surfactant (at a concentration above the critical micelle concentration) and, depending on the type of reaction, an initiator. At the beginning of the polymerization the monomer droplets exist as large reservoir droplets in the continuous phase. Surfactant micelles are present in the continuous phase. The monomer has a limited solubility in the continuous phase, so that a small fraction of monomer is dissolved and initiation of the chain-growth mechanism can occur. Small oligomers begin to form, which are even less soluble than the monomer and therefore diffuse into the micelles. Here, chain growth continues as the monomer diffuses into the

micelles and is consumed in the polymerization. Also, newly formed oligomers constantly enter the micelles and react with the growing polymer inside the micelles so that in radical chain-growth polymerization two radicals will terminate (by combination). These micelles are then dormant and "waiting" for a new radical to diffuse in and continue polymerization. On average, an equilibrium is established between micelles with an actively growing chain and dormant micelles [50]. This process upholds until the monomer reservoir droplets are exhausted. Because of the equilibrium, all micelle-hosted particles grow continuously over the time of conversion and monodisperse particles can be obtained [51, 52]. There is vast literature on CPNs reporting production via emulsion polymerization; however, the reader should be warned that in most cases the term is being misused for a polymerization in mini- or microemulsion, which follows a completely different mechanism and will be discussed later.

The majority of conjugated polymers is prepared from monomers, which are solids even at elevated temperatures. So, these monomers cannot be applied in emulsion polymerization. As a result, there are only few examples for CPNs generated via emulsion polymerization. One way to work around this problem is to prepare fluorescent monomers with an extended π-conjugated system that bears a polymerizable unit susceptible to free radical polymerization. Fluorescent nanoparticles can be prepared by adding this fluorescent macromonomer to an emulsion polymerization of styrene or acrylates (see Figure 2.7a). However, we wish to point out, that following this pathway, no conjugated polymer backbone is obtained [53]. Ethylenedioxythiophene (EDOT) is a liquid monomer, which represents the building block of PEDOT, a well-known conjugated polymer used for plastic electrodes. EDOT is polymerized by chemical oxidation following a chain-growth mechanism. EDOT is only partially water soluble making it ideal for emulsion polymerization [54]. PEDOT-based CPNs have been reported as excellent candidates for photothermal therapy (see Figure 2.7c,d) [55].

Owing to the lack of liquid conjugated monomers a modification of the emulsion polymerization is applied, where solvent is added to dissolve the solid

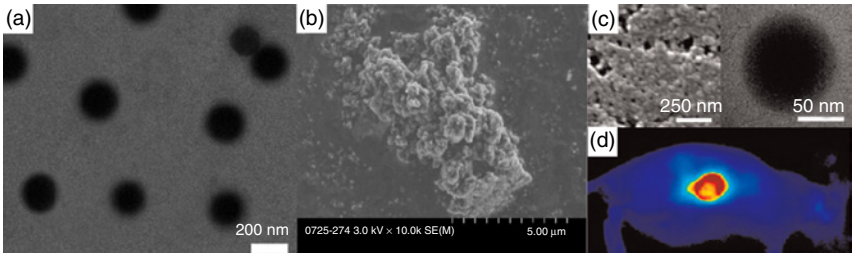

Figure 2.7 Nanoparticles synthesized by emulsion polymerization: (a) TEM image of fluorescent nanoparticles. (Reproduced (in part) with permission from Ref. [53]. Copyright 2014, The Royal Society of Chemistry.) (b) SEM image of PEDOT particles. (Reprinted (adapted) with permission from Ref. [54]. Copyright 2005, Elsevier.) (c) SEM image of PEODT nanoparticles deposited on a silicon substrate (left) and TEM image of a single PEDOT nanoparticle (right). (d) *In vivo* fluorescence image of a tumor bearing mice after injection of PEDOT nanoparticles. (Reprinted (adapted) with permission from Ref. [55]. Copyright 2012, American Chemical Society.)

monomers and perform the polymerization in a miniemulsion. This has become a versatile technique for the creation of CPNs with desired morphology and functionality. Polymerization in miniemulsion is fundamentally different from the emulsion polymerization mechanism and will be explained in the following section [50].

2.2.2.2 Polymerization in Miniemulsion

The droplets of the miniemulsion are at least one order of magnitude smaller than the reservoir droplets in emulsion polymerization. As such they have a much higher surface area per unit volume, which is stabilized by a surfactant. The droplets formed here are kinetically stable and persist over the entire polymerization process. This method is facilitated (like the previously described miniemulsification in the postpolymerization section) by using a suitable surfactant and high shear mixing such as ultrasonication or high pressure homogenization (Ultra-Turrax®, Microfluidizer®, etc.). The polymerization takes place in the suspended droplets with each droplet acting as a nanoreactor, which determines the resulting particle size (through the monomer concentration). Each miniemulsion droplet produces one individual CPN after complete conversion. This means that the state of the initially formed miniemulsion predicts the resulting particle dispersion and that no interaction between the droplets should occur. High droplet density without free surfactant prevents unwanted polymerization outside of the droplets. Miniemulsification is by far the most used method as it allows direct polymerization inside of the generated droplet nanoreactors as well as postpolymerization particle generation as discussed earlier. Because each droplet represents an isolated reaction container, a variety of different types of polymerization can be applied. These range from anionic-, cationic-, ring-opening and other chain-growth polymerizations to step-growth polymerizations, and most prominently Palladium-catalyzed cross-coupling reactions, which are widely used for the generation of CPNs [19]. Miniemulsion droplets are stable and range from 50 to 500 nm in size. However, usually the droplet size distribution is broad. This can be circumvented by using tailored surfactants with dedicated steric demand toward the continuous phase. Often, costabilizers are applied as osmotic pressure agents to completely inhibit Ostwald ripening [14].

PPV CPNs have been generated by miniemulsion polymerization using 1,4-dialkyl substituted divinylbenzene, which is polymerized via metathesis using a Ruthenium catalyst in an aqueous miniemulsion. The size of the obtained particles is around 110 nm [56]. Polyfluorene nanoparticle dispersions have been produced using Suzuki–Miyaura cross-coupling polymerization (see Figure 2.8b) [57]. Polymerization in miniemulsion also allows generation of well-defined hybrid particles. For example, Cadmium selenide (CdSe) quantum dot/polyfluorene hybrid particles have been prepared by mixing a diluted dispersion of CdSe quantum dots with the fluorene monomer solution. Subsequently, this mixture has been miniemulsified in an aqueous stabilizer solution. The obtained hybrid particles consist of only one quantum dot per nanoparticle, and show Förster resonance energy transfer from the polymer shell into the quantum dot core (see Figure 2.8a). Such hybrid particles are attractive candidates for use in cell-labeling and biological/biomedical applications, because of their enhanced

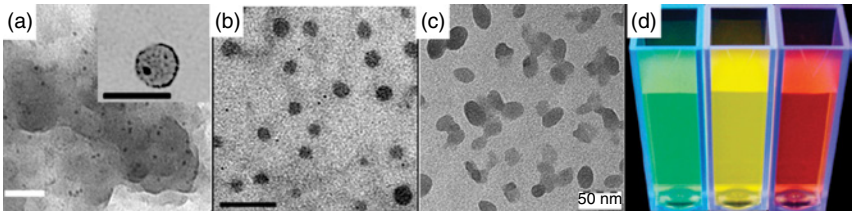

Figure 2.8 TEM images of CPNs synthesized by polymerization in miniemulsion. (a) Polyfluorene/quantum dot hybrid nanoparticles. Inset displays an individual core/shell hybrid particle. The scale bars represent 50 nm, and (b) poly(fluorene) nanoparticles (the scale bar represents 100 nm). (Reprinted (adapted) with permission from Ref. [57]. Copyright 2012, American Chemical Society.) (c) Poly(acetylene) nanoparticles synthesized by Glaser coupling, and (d) CPN dispersions with tunable emission colors. (Reprinted (adapted) with permission from Ref. [28]. Copyright 2009, American Chemical Society.)

photostability and stable photoluminescence due to the energy transfer process [58]. Furthermore, polyaniline CPNs can be produced in direct and inverse miniemulsions [50, 59]. Similarly to PEDOT, polyaniline is synthesized by oxidative polymerization. To perform the direct miniemulsion polymerization, a solution of aniline is dispersed in water using SDS as the surfactant and ammonium peroxodisulfate as the oxidation agent. After miniemulsification, an additional polymeric stabilization agent is added to provide colloidal stability during polymerization. For the inverse miniemulsion polymerization an aniline salt and concentrated HCl are dispersed in cyclohexane together with a block-co-polymer stabilizer. Potassium peroxodisufate in hydrogen peroxide solution acts as the oxidation agent. This oxidation solution is also miniemulsified in a mixture of cyclohexane and stabilizer. Both miniemulsions are then combined. Polymerization occurs due to mass exchange processes (e.g., Ostwald ripening) between the monomer droplets and the droplets containing the oxidation agent [59]. These polyaniline particles present ideal candidates for photothermal treatment of cancer and for photoacoustic imaging [60].

By contrast, step-growth polycondensation is applied in oxidative Glaser coupling to produce poly(arylene–diacetylene) nanoparticles. Here, air can be used as an oxidation agent at room temperature together with a dinonylbipyridine ligated copper(I/II) catalyst [61]. This catalyst system resides in the organic monomer phase rather than the aqueous continuous phase. Using only one monomer for the polymerization simplifies the polymerization procedure since the stoichiometry problem is circumvented. Diethynyl-substituted monomers can be copolymerized using Glaser coupling. When conjugated monomers with different electronic bandgaps are applied, nanoparticles with tunable emission spectra are obtained (see Figure 2.8d) [28].

2.2.2.3 Polymerization in Microemulsion

In contrast to miniemulsion, a microemulsion forms spontaneously and is kinetically as well as thermodynamically stable. Mini- and microemulsion require the same ingredients: a dispersed phase as reaction medium, a continuous phase, and a surfactant to provide stability. However, the crucial difference is the ratio

of surfactant to the dispersed phase. High surfactant concentrations produce microemulsions with much smaller droplet sizes [34], usually below 100 nm because the interfacial tension at the oil/water interface is reduced to almost zero [62]. Therefore, one characteristic feature of microemulsions is an apparently clear phase, which forms without the need for high shear. Microemulsions are mainly used to produce particles with diameters between 5 and 50 nm (conjugated polymer dots) [63]. The resulting particles are completely covered by surfactant. Microemulsification has been used to generate CPNs from polyacetylenes. The particles exhibit optical activity due to a helical alignment of the polyacetylene chains in the particles. The microemulsion polymerization is facilitated by SDS as a surfactant together with dimethylformamide (DMF) used here as a cosurfactant [64]. Also, polypyrrole CPNs have been generated by polymerization in microemulsion. The obtained nanoparticles exhibit diameters between 60 and 90 nm and show variable conductivity depending on the polymerization conditions. Again, the tendency to form ordered arrangements or crystalline domains within the particle governs the physical properties such as conductivity. When the microemulsion polymerization is carried out at low temperatures, the particles become smaller with higher conductivities [65]. Here, SDS and dodecyl benzyl sulfonic acid (DBSA) are used as components of the surfactant system.

2.2.2.4 Dispersion Polymerization

In contrast to all previously discussed techniques, dispersion polymerization starts out as a homogeneous reaction mixture with a single phase. The solvent for this technique needs to be good for the initial reaction ingredients, namely the monomers, polymeric stabilizers (and optionally surfactants), catalysts and if necessary an initiator. However, to obtain particles, the solvent needs to be poor for the resulting polymer. After starting the polymerization, the polymer chains start to grow in the reaction medium. While the molecular weight increases, the solubility of the polymer decreases until the critical molecular weight is reached and phase separation occurs. The precipitated polymer chains coagulate and form nuclei, which are stabilized against further aggregation by the added stabilizer. These nuclei act as seed particles for growing polymer chains in solution approaching the critical molecular weight. Thus, the seeds grow by condensation of these later precipitating polymers until maximal conversion is achieved [17, 51, 66].

PEDOT particles have been synthesized by oxidative dispersion polymerization in aqueous medium. Many different oxidation agents have been tested to obtain optimized dispersion polymerization conditions. It has been proven, that Iron(III)-*p*-toluene sulfonate as an oxidant leads to a high yield of PEDOT nanoparticles with high conductivity. Furthermore, various end-functionalized poly(ethyleneoxide) stabilizers (PEO) have been explored as reactive stabilizers. Thiophene, fluorene, and pyrrole have been applied as terminal functionalities and it has been found that the conjugated termini stabilize the PEDOT nanoparticles; however, the type of end-group does not have any significant effect on the, stability, size, and morphology of the PEDOT CPNs [13].

Palladium-catalyzed cross-coupling polymerizations such as Suzuki–Miyaura can be performed following the dispersion polymerization protocol. Dispersion

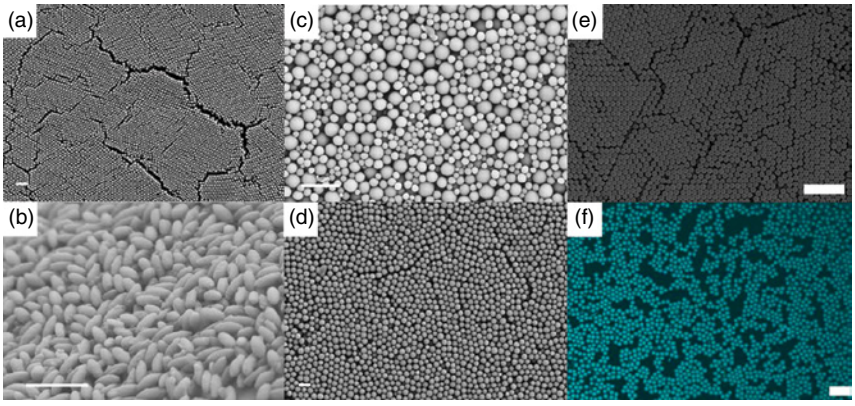

Figure 2.9 Images of CPNs synthesized by dispersion polymerization: Scanning electron micrograph images of (a) monodisperse particles of F8BT, (b) ellipsoidal particles of stretched monodisperse F8BT particles, (c) bidisperse particles of F8BT, (d) monodisperse polyfluorene particles produced by Suzuki–Miyaura dispersion polymerization. (Reprinted (adapted) with permission from Ref. [17]. Copyright 2012, Macmillan Publishers Ltd.: Nature Photonics.) (e) Monodisperse poly(phenylene–vinylene) particles produced by Heck dispersion polymerization, (f) confocal microscopy image of PPV particles. (Reprinted (adapted) with permission from Ref. [20]. Copyright 2016, American Chemical Society.) (The scale bars in (a)–(d) represent 2 µm and in (e) and (f) they represent 10 µm).

polymerization is performed in 1-propanol with tetrakis(triphenylphosphine) Palladium as catalyst and potassium *tert*-butoxide as base. To stabilize the resulting particles poly(vinylpyrrolidone-*co*-vinyl acetate) and the nonionic surfactant (Triton X-45) are applied. The resulting CPNs are monodisperse and can be tuned in size, simply by adjusting the monomer concentration. When a certain monomer concentration is exceeded, bidisperse and polydisperse sets of particles are obtained, due to secondary nucleation (see Figure 2.9c). The emission characteristics and shape of the particles can be tuned by varying the respective monomer units [17]. Furthermore, light switchable CPNs can be created by Suzuki–Miyaura dispersion polymerization using light-responsive azobenzene monomers. These particles display switchable fluorescence, which might be useful for stochastics-based localization super-resolution microscopy [67]. In a similar approach, also poly(carbazole-*alt*-benzothiadiazole) nanoparticles have been synthesized by Suzuki–Miyaura dispersion polymerization [68]. The stabilizer (here: polyvinylpyrrolidone) concentration influences the size of the resulting particles. Reducing the stabilizer concentration leads to particles with a larger diameter as less nuclei are stabilized during the crucial phase of particle formation. The effect of stabilizer concentration on the particle size has also been observed for the synthesis of polypyrrole particles with ethylhydroxyethylcellulose as a stabilizer [69]. Furthermore, it was found that the concentration of the polymeric stabilizer can influence the crystallinity of the resulting CPNs in polyfluorenes [70].

The reported conditions for Suzuki–Miyaura dispersion polymerization have also been applied to other Pd-catalyzed cross-coupling polymerizations. Heck dispersion polymerization produces highly monodisperse conjugated

polymer particles with an arylene–vinylene repeat unit (see Figure 2.9e,f). This step-growth polymerization is performed using Palladium acetate and a phosphine ligand as catalyst system and triethylamine as base. It is surprising that step-growth polymerizations like Suzuki–Miyaura, Heck and Sonogashira produce such highly uniform particles, despite the fact that polycondensation usually produces polymers with a high polydispersity index ($Đ = 2$). To unravel the mechanism behind particle formation and clarify why polycondensation can yield monodisperse particles, kinetic studies have been conducted [19]. Early nucleation allows for phase inversion of low molecular weight species, which are still uniform in their molecular weight. In step-growth polymerization the polydispersity increases linearly with the degree of conversion (from 1 to 2). The nucleating species are oligomers (for fluorene-*co*-divinylbenzene coupling on average hexamers). These oligomers precipitate together with terminally bound Palladium catalyst and further solid state coupling produces increased molecular weight in the final product [19].

In a similar manner, Sonogashira dispersion polymerization has been developed for the preparation of monodisperse nanoparticles bearing an acetylene unit in the backbone. These moieties are accessible on the surface of the resulting CPNs [24]. These particles can be easily functionalized using thiol-click chemistry making use of these surficial acetylene bonds. Functionalization with biological recognition motifs (such as arginine–glycine–aspartate peptides (RGD)) results in particles representing candidates for fluorescent probes. These probes can be targeted toward specific cells with over-expressed integrins (to which the RGD binds) for application in biomedical imaging (see Figure 2.10).

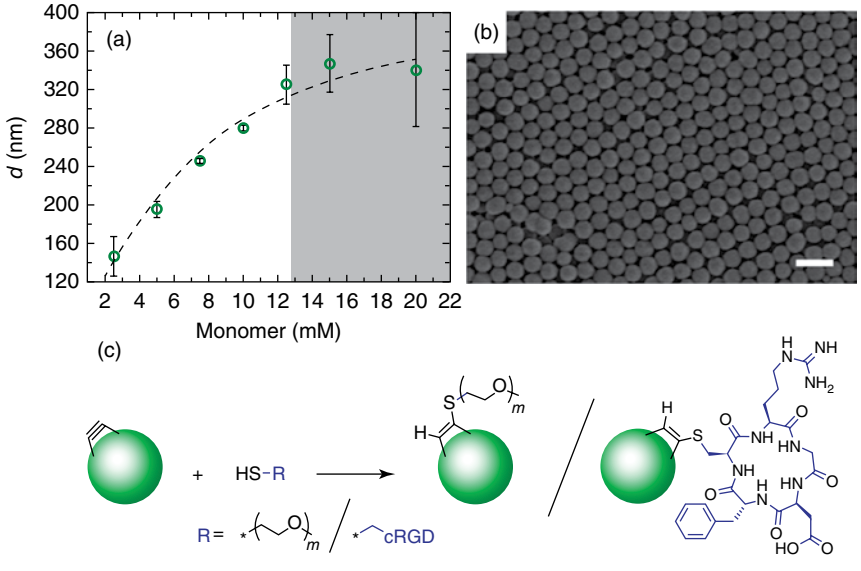

Figure 2.10 CPNs produced via Sonogashira coupling: (a) evolution of particle size with increasing monomer loading, (b) scanning electron microscope image of CPNs generated by Sonogashira dispersion polymerization (the scale bar represents 10 µm), (c) functionalization of CPNs with PEG and peptide (cRGD) by thiol-yne click chemistry. (Reproduced (in part) with permission from Ref. [24]. Copyright 2015, The Royal Society of Chemistry.)

2.3 Conclusion

Conjugated polymer particles offer high fluorescence brightness, low dispersity in size, and surface functionizability enabling a variety of imaging applications in the fields of biological analysis and biomedical imaging. They can be used for fluorescence microscopy in cell culture, fluorescence molecular tomography (FMT), photoacoustic imaging and photothermal and photodynamic therapy [1, 55, 71–74].

A variety of post- and direct polymerization techniques for CPNs preparation have been reported. Numerous functionalization methods have been developed to link specific biomolecular recognition motifs to CPNs and enable a variety of targeted imaging techniques. Furthermore, such functionalities promote solubility of the CPNs in water [8]. Application of CPNs for biomedical imaging requires colloidal stability and prevention of nonspecific interactions [75]. This can be realized by encapsulation of the particles in, for example, polyethyleneglycol (PEG) coronas. PEG is often used to impart solubility of colloids in water. It is possible to subsequently link specific functional elements such as peptides, glycans, or antibodies to the surface of the particles by click reactions or other coupling techniques [1, 24, 36, 76]. Another possibility to obtain surface functionalized CPNs is by using functionalized monomers. However, some of the biological recognition motifs will be buried in the bulk of the particle [24, 77, 78].

Although a large variety of conjugated polymer materials, preparation protocols, and surface functionalization protocols are available the biggest obstacle for transfer of CPNs into real world biomedical and clinical applications lies in the size of the CPNs. There exist only few examples in the literature, where the particles are small enough (<5 nm) to warrant renal excretion and therefore avoid accumulation of the particles in the body. Consequently, in the future, new developments toward biodegradable conjugated polymer particles are required [79]. Such particles would enable long circulation times in the body as they start out with a particle diameter larger than the pores of the kidney membrane. After degradation, the particle fragments or molecular degradation products would be smaller than 5 nm and be excretable via the renal system. Such biodegradable CPNs could then be applied in the clinic for *in vivo* and first-in-man studies. These CPNs would present the new imaging probes for a variety of fluorescence- and photoacoustic-based imaging techniques and colloidal photodynamic, photothermal, and drug-delivery therapies of the future.

References

1 Feng, L., Zhu, C., Yuan, H. *et al.* (2013) Conjugated polymer nanoparticles: preparation, properties, functionalization and biological applications. *Chem. Soc. Rev.*, **42**, 6620–6633.

2 Tuncel, D. and Demir, H.V. (2010) Conjugated polymer nanoparticles. *Nanoscale*, **2**, 484–494.

3 Burroughes, J.H., Bradley, D.D.C., Brown, A.R. *et al.* (1990) Light-emitting diodes based on conjugated polymers. *Nature*, **347**, 539–541.

4 Hide, F., Diaz-Garcia, M., and Schwartz, B. (1996) Semiconducting polymers: anew class of solid-state laser materials. *Science*, **273**, 1833–1836.

5 Wu, C. and Chiu, D.T. (2013) Highly fluorescent semiconducting polymer dots for biology and medicine. *Angew. Chem. Int. Ed.*, **52**, 3086–3109.

6 Howes, P., Thorogate, R., Green, M. *et al.* (2009) Synthesis, characterisation and intracellular imaging of PEG capped BEHP-PPV nanospheres. *Chem. Commun.*, **18**, 2490–2492.

7 Wu, C., Schneider, T., Zeigler, M. *et al.* (2010) Bioconjugation of ultrabright semiconducting polymer dots for specific cellular targeting. *J. Am. Chem. Soc.*, **132**, 15410–15417.

8 Fernando, L.P., Kandel, P.K., Yu, J. *et al.* (2010) Mechanism of cellular uptake of highly fluorescent conjugated polymer nanoparticles. *Biomacromolecules*, **11**, 2675–2682.

9 Wu, C., Bull, B., Szymanski, C. *et al.* (2008) Multicolor conjugated polymer dots for biological fluorescence imaging. *ACS Nano*, **2**, 2415–2423.

10 Wu, C., Hansen, S.J., Hou, Q. *et al.* (2011) Design of highly emissive polymer dot bioconjugates for in vivo tumor targeting. *Angew. Chem. Int. Ed.*, **50**, 3430–3434.

11 Ye, F., Wu, C., Jin, Y. *et al.* (2012) A compact and highly fluorescent orange-emitting polymer dot for specific subcellular imaging. *Chem. Commun.*, **48**, 1778–80.

12 Jang, J., Oh, J.H., and Stucky, G.D. (2002) Fabrication of ultrafine conducting polymer and graphite nanoparticles. *Angew. Chem. Int. Ed.*, **41**, 4016–4019.

13 Mumtaz, M., Lecommandoux, S., Cloutet, E., and Cramail, H. (2008) Synthesis of calibrated poly(3,4-ethylenedioxythiophene) latexes in aqueous dispersant media. *Langmuir*, **24**, 11911–11920.

14 Pecher, J. and Mecking, S. (2010) Nanoparticles of conjugated polymers. *Chem. Rev.*, **110**, 6260–6279.

15 Stejskal, J. (2001) Colloidal dispersions of conducting polymers. *J. Polym. Mater.*, **18**, 225–258.

16 Zha, Z., Deng, Z., Li, Y. *et al.* (2013) Biocompatible polypyrrole nanoparticles as a novel organic photoacoustic contrast agent for deep tissue imaging. *Nanoscale*, **5**, 4462–4467.

17 Kuehne, A.J.C., Gather, M.C., and Sprakel, J. (2012) Monodisperse conjugated polymer particles by Suzuki–Miyaura dispersion polymerization. *Nat. Commun.*, **3**, 1088.

18 Liu, B., Yu, W.L., Lai, Y.H., and Huang, W. (2003) Synthesis of polyfluorene derivatives through polymer reaction. *Opt. Mater.*, **21**, 125–133.

19 Ciftci, S. and Kuehne, A.J.C. (2015) Monodisperse conjugated polymer particles via Heck coupling – a kinetic study to unravel particle formation in step-growth dispersion polymerization. *Macromolecules*, **48**, 8389–8393.

20 Mikosch, A., Ciftci, S., and Kuehne, A.J.C. (2016) Colloidal crystal lasers from monodisperse conjugated polymer particles via bottom-up coassembly in a sol–gel matrix. *ACS Nano*, **10**, 10195–10201.

21 Schwendeman, J.E., Church, A.C., and Wagener, K.B. (2002) Synthesis and catalyst issues associated with ADMET polymerization. *Adv. Synth. Catal.*, **344** (6–7), 597–613.

22 Greenham, N.C., Moratti, S.C., Bradley, D.D.C. *et al.* (1993) Efficient light-emitting diodes based on polymers with high electron affinities. *Nature*, **365**, 628–630.

23 Ciftci, S., Mikosch, A., Haehnle, B. *et al.* (2016) Silica core/conjugated polymer shell particles via seeded Knoevenagel dispersion polymerization – laser action in whispering gallery mode resonators. *Chem. Commun.*, **52**, 14222–14225.

24 Anwar, N., Rix, A., Lederle, W., and Kuehne, A.J.C. (2015) RGD-decorated conjugated polymer particles as fluorescent biomedical probes prepared by Sonogashira dispersion polymerization. *Chem. Commun.*, **51**, 9358–9361.

25 Dash, B.C., Réthoré, G., Monaghan, M. *et al.* (2010) The influence of size and charge of chitosan/polyglutamic acid hollow spheres on cellular internalization, viability and blood compatibility. *Biomaterials*, **31**, 8188–8197.

26 Florez, L., Herrmann, C., Cramer, J.M. *et al.* (2012) How shape influences uptake: interactions of anisotropic polymer nanoparticles and human mesenchymal stem cells. *Small*, **8**, 2222–2230.

27 Kuehne, A.J.C. (2017) Conjugated polymer nanoparticles toward in vivo theranostics – focus on targeting, imaging, therapy, and the importance of clearance. *Adv. Biosyst.*, **1**, 1700100, DOI: 10.1002/adbi.201700100

28 Baier, M.C., Huber, J., and Mecking, S. (2009) Fluorescent conjugated polymer nanoparticles by polymerization in miniemulsion. *J. Am. Chem. Soc.*, **131**, 14267–14273.

29 Szymanski, C., Wu, C., Hooper, J. *et al.* (2005) Single molecule nanoparticles of the conjugated polymer MEH-PPV, preparation and characterization by near-field scanning optical microscopy. *J. Phys. Chem. B*, **109**, 8543–8546.

30 Hitoshi, K., Hirokazu, K., Shuji, O. *et al.* (1996) Size-dependent colors and luminescences of organic microcrystals. *Jpn. J. Appl. Phys.*, **35**, 221–223.

31 Kurokawa, N., Yoshikawa, H., Hirota, N. *et al.* (2004) Size-dependent spectroscopic properties and thermochromic behavior in poly(substituted thiophene) nanoparticles. *Chem. Phys. Chem*, **5**, 1609–1615.

32 Luo, W., Wu, M., Li, S. *et al.* (2016) Nanoprecipitation of fluorescent conjugated polymer onto the surface of plasmonic nanoparticle for fluorescence/dark-field dual-modality single particle imaging. *Anal. Chem.*, **88**, 6827–6835.

33 Schütze, F., Krumova, M., and Mecking, S. (2015) Size control of spherical and anisotropic fluorescent polymer nanoparticles via precise rigid molecules. *Macromolecules*, **48**, 3900–3906.

34 McClements, D.J. (2012) Nanoemulsions versus microemulsions: terminology, differences, and similarities. *Soft Matter*, **8**, 1719–1729.

35 Landfester, K., Montenegro, R., Scherf, U. *et al.* (2002) Semiconducting polymer nanospheres in aqueous dispersion prepared by a miniemulsiun process. *Adv. Mater.*, **14**, 651–655.

36 Howes, P., Greenff, M., Levitt, J. *et al.* (2010) Phospholipid encapsulated semiconducting polymer nanoparticles: their use in cell imaging and protein attachment. *J. Am. Chem. Soc.*, **132**, 3989–3996.

37 Bandyopadhyay, S., Métivier, R., Pallavi, P. *et al.* (2016) Conjugated polymer nanoparticle-triplet emitter hybrids in aqueous dispersion: fabrication and fluorescence quenching behavior. *Macromol. Rapid Commun.*, **37**, 271–277.

38 Kietzke, T., Neher, D., Landfester, K. *et al.* (2003) Novel approaches to polymer blends based on polymer nanoparticles. *Nat. Mater.*, **2**, 408–412.

39 Karnik, R., Gu, F., Basto, P. *et al.* (2008) Microfluidic platform for controlled synthesis of polymeric nanoparticles. *Nano Lett.*, **8**, 2906–2912.

40 Kuehne, A.J.C. and Weitz, D.A. (2011) Highly monodisperse conjugated polymer particles synthesized with drop-based microfluidics. *Chem. Commun.*, **47**, 12379–12381.

41 Schütze, F., Stempfle, B., Jüngst, C. *et al.* (2012) Fluorescent conjugated block copolymer nanoparticles by controlled mixing. *Chem. Commun.*, **48** (15), 2104–2106.

42 Romanowsky, M.B., Abate, A.R., Rotem, A. *et al.* (2012) High throughput production of single core double emulsions in a parallelized microfluidic device. *Lab Chip*, **12**, 802–807.

43 Nisisako, T. and Torii, T. (2008) Microfluidic large-scale integration on a chip for mass production of monodisperse droplets and particles. *Lab Chip*, **8**, 287–293.

44 Kim, S.-H., Kim, J.W., Kim, D.-H. *et al.* (2013) Enhanced-throughput production of polymersomes using a parallelized capillary microfluidic device. *Microfluid. Nanofluidics*, **14**, 509–514.

45 Femmer, T., Jans, A., Eswein, R. *et al.* (2015) High-throughput generation of emulsions and microgels in parallelized microfluidic drop-makers prepared by rapid prototyping. *ACS Appl. Mater. Interfaces*, **7**, 12635–12638.

46 Robin, M.P. and O'Reilly, R.K. (2015) Strategies for preparing fluorescently labelled polymer nanoparticles. *Polym. Int.*, **64**, 174–182.

47 Xing, C., Xu, Q., Tang, H. *et al.* (2009) Conjugated polymer/porphyrin complexes for efficient energy transfer and improving light-activated antibacterial activity. *J. Am. Chem. Soc.*, **131**, 13117–13124.

48 Yang, G., Liu, L., Yang, Q. *et al.* (2012) A multifunctional cationic pentathiophene: synthesis, organelle-selective imaging, and anticancer activity. *Adv. Funct. Mater.*, **22**, 736–743.

49 Chong, H., Nie, C., Zhu, C. *et al.* (2012) Conjugated polymer nanoparticles for light-activated anticancer and antibacterial activity with imaging capability. *Langmuir*, **28**, 2091–2098.

50 Landfester, K. (2009) Miniemulsion polymerization and the structure of polymer and hybrid nanoparticles. *Angew. Chem. Int. Ed.*, **48**, 4488–4507.

51 Arshady, R. (1992) Suspension, emulsion, and dispersion polymerization: a methodological survey. *Colloid Polym. Sci.*, **270**, 717–732.

52 Chern, C.S. (2006) Emulsion polymerization mechanisms and kinetics. *Prog. Polym. Sci.*, **31**, 443–486.

53 Zhang, X., Zhang, X., Yang, B. *et al.* (2014) Fabrication of water-dispersible and biocompatible red fluorescent organic nanoparticles via PEGylation of aggregate induced emission enhancement dye and their cell imaging applications. *Polym. Chem.*, **5**, 399–404.

54 Lei, Y., Oohata, H., Kuroda, S.I. *et al.* (2005) Highly electrically conductive poly(3,4-ethylenedioxythiophene) prepared via high-concentration emulsion polymerization. *Synth. Met.*, **149**, 211–217.

55 Cheng, L., Yeng, K., and Liu, Z. (2012) Organic stealth nanoparticles for highly effective in vivo near-infrared photothermal therapy of cancer. *ACSNano*, **6**, 5605–5613.

56 Pecher, J. and Mecking, S. (2008) Poly(*p*-phenylene vinylene) nanoparticles by acyclic diene metathesis (ADMET) polycondensation in aqueous emulsion. *Polym. Prepr.*, **49**, 363–364.

57 Negele, C., Haase, J., Leitenstorfer, A., and Mecking, S. (2012) Polyfluorene nanoparticles and quantum dot hybrids via miniemulsion polymerization. *ACS Macro Lett.*, **1**, 1343–1346.

58 Jares-Erijman, E.A. and Jovin, T.M. (2003) FRET imaging. *Nat. Biotechnol.*, **21**, 1387–1395.

59 Marie, E., Rothe, R., Antonietti, M., and Landfester, K. (2003) Synthesis of polyaniline particles via inverse and direct miniemulsion. *Macromolecules*, **36**, 3967–3973.

60 Wang, J., Yan, R., Guo, F. *et al.* (2016) Targeted lipid–polyaniline hybrid nanoparticles for photoacoustic imaging guided photothermal therapy of cancer. *Nanotechnology*, **27**, 1–10.

61 Siemsen, P., Livingston, R.C., and Diederich, F. (2000) Acetylenic coupling: a powerful tool in molecular construction. *Angew. Chem. Int. Ed.*, **39**, 2632–2657.

62 Antonietti, M. and Landfester, K. (2002) Polyreactions in miniemulsions. *Prog. Polym. Sci.*, **27**, 689–757.

63 Antonietti, M., Basten, R., Lohmann, S. *et al.* (1995) Polymerization in microemulsions – a new approach to ultrafine, highly functionalized polymer dispersions. *Macromol. Chem. Phys.*, **196**, 441–466.

64 Deng, J., Chen, B., Luo, X., and Yang, W. (2009) Synthesis of nano-latex particles of optically active helical substituted polyacetylenes via catalytic microemulsion polymerization in aqueous systems. *Macromolecules*, **42**, 933–938.

65 Rehung-U-Rai, A., Prom-Jun, A., Prissanaroon-Ouajai, W., and Ouajaj, S. (2008) Synthesis of highly conductive polypyrrole nanoparticles via microemulsion polymerization. *J. Metal Mater. Miner.*, **18**, 27–31.

66 Kawaguchi, S. and Ito, K. (2005) Dispersion polymerization. *Adv. Polym. Sci.*, **175**, 299–328.

67 Anwar, N., Willms, T., Grimme, B., and Kuehne, A.J.C. (2013) Supporting information: light-switchable and monodisperse conjugated polymer particles. *ACS Macro Lett.*, **2**, 766–769.

68 Parrenin, L., Brochon, C., Hadziiannou, G., and Cloutet, E. (2015) Low bandgap semiconducting copolymer nanoparticles by Suzuki cross-coupling polymerization in alcoholic dispersed media. *Macromol. Rapid Commun.*, **36**, 1816–1821.

69 Mandal, T.K. and Mandal, B.M. (1999) Dispersion polymerization of pyrrole using ethylhydroxyethylcellulose as a stabilizer. *J. Polym. Sci. Part A*, **37**, 3723–3729.

70 Rosencrantz, R.R., Rahimi, K., and Kuehne, A.J.C. (2014) Morphology control in poly(9,9-di-*n*-octyl-2,7-fluorene) spherulite particles prepared via dispersion polymerization. *J. Phys. Chem. B*, **118**, 6324–6328.

71 Kim, J., Lee, E., Hong, Y. *et al.* (2015) Self-doped conjugated polymeric nanoassembly by simplified process for optical cancer theragnosis. *Adv. Funct. Mater.*, **25**, 2260–2269.

72 Ge, J., Jia, Q., Liu, W. *et al.* (2015) Red-emissive carbon dots for fluorescent, photoacoustic, and thermal theranostics in living mice. *Adv. Mater.*, **27**, 4169–4177.

73 Pu, K., Mei, J., Jokerst, J.V. *et al.* (2015) Diketopyrrolopyrrole-based semiconducting polymer nanoparticles for in vivo photoacoustic imaging. *Adv. Mater.*, **27**, 5184–5190.

74 Feng, G., Fang, Y., Liu, J. *et al.* (2016) Multifunctional conjugated polymer nanoparticles for image-guided photodynamic and photothermal therapy. *Small*, **13**, 1–12.

75 Wu, C., Peng, H., Jiang, Y., and McNeill, J. (2006) Energy transfer mediated fluorescence from blended conjugated polymer nanoparticles. *J. Phys. Chem. B*, **110**, 14148–14154.

76 Wu, C., Jin, Y., Schneider, T. *et al.* (2010) Ultrabright and bioorthogonal labeling of cellular targets using semiconducting polymer dots and click chemistry. *Angew. Chem. Int. Ed.*, **49**, 9436–9440.

77 Feng, X., Tang, Y., Duan, X. *et al.* (2010) Lipid-modified conjugated polymer nanoparticles for cell imaging and transfection. *J. Mater. Chem.*, **20**, 1312.

78 Xing, C., Liu, L., Tang, H. *et al.* (2011) Design guidelines for conjugated polymers with light-activated anticancer activity. *Adv. Funct. Mater.*, **21**, 4058–4067.

79 Repenko, T., Rix, A., Ludwanowski, S., Go, D., Kiessling, F., Lederle, W., and Kuehne, A.J.C. (2017) Bio-degradable highly fluorescent conjugated polymer nanoparticles for bio-medical imaging applications. *Nat. Commun.*, **8**, 470, DOI: 10.1038/s41467-017-00545-0

3

Conjugated Polymer Nanoparticles and Semiconducting Polymer Dots for Molecular Sensing and *In Vivo* and Cellular Imaging

Xu Wu[1,2] *and Daniel T. Chiu*[1,2]

[1]*University of Washington, Department of Chemistry, Seattle, Washington 98195, USA*
[2]*University of Washington, Department of Bioengineering, Seattle, Washington 98195, USA*

3.1 Introduction

The development of luminescent nanoparticles has resulted in effective research tools for fluorescence sensing and imaging as well as for biomedical diagnosis and drug delivery [1–3]. Compared with the small organic dyes, the luminescent nanoparticles exhibit brighter and more stable fluorescent properties, which overcome the intrinsic limitations of the conventional dyes [4–6]. Moreover, the controllable physiochemical properties, such as size, surface potential, and easy surface modification, expand the applications of the luminescent nanoparticles in biomedical fields [7]. For example, quantum dots (Qdots) [8], dye-doped silica nanoparticles [9, 10], and upconversion nanoparticles [11] have attracted much attention as fluorescent probes. Particularly, Qdots are one of the best known luminescent nanoparticles and have been widely used in biological applications in the past few decades [12, 13]. Qdots possess broad absorption bands and narrow emission width, and excellent photostability and brightness compared with conventional fluorescent dyes. However, the intrinsic heavy-metal toxicity limits the applications of Qdots in biomedical applications, especially for *in vivo* imaging and drug delivery.

To generate bright and biocompatible fluorescent probes, nanoparticles based on conjugated polymers are promising candidates [14–16]. Conjugated polymers show excellent light-harvesting and light-amplifying properties because of their large π-conjugated backbones and delocalized electronic structures [15, 17, 18]. Nanoparticles composed of conjugated polymers, called conjugated polymer nanoparticles (CPNs), have exceptional photophysical properties, such as large extinction coefficients, excellent photostability, adjustable emission wavelength, and high single-particle brightness. In the past decade, CPNs have been utilized in optoelectronic and biomedical fields, thanks to their excellent optical properties [19–22]. Within the general category of CPNs is a special subset called semiconducting polymer dots (Pdots). To qualify

Conjugated Polymers for Biological and Biomedical Applications, First Edition. Edited by Bin Liu

as Pdots, the CPNs should satisfy three criteria. First, the nanoparticle size should be less than about 30 nm to be consistent with the concept of "dot." Second, the nanoparticle should contain more than 50% of semiconducting polymers to ensure high single-particle brightness. Finally, the interior of the nanoparticle should be hydrophobic. Therefore, nanoparticles that do not satisfy these three criteria are referred to as CPNs.

We will first focus our discussion on the preparation, characterization, and bioconjugation of CPNs and Pdots. Then, we will move on to discussing molecular sensing and cellular imaging, including fluorescence imaging and photoacoustic imaging. In the last section, we will summarize the work done with theranostic agents based on CPNs and Pdots. Our goal is to provide an overview of the photophysical properties and preclinical validations of the fluorescent nanoprobes based on CPNs and Pdots.

3.2 Preparation, Characterization, and Functionalization

3.2.1 Preparation

The optical properties of CPNs and Pdots are mainly determined by the conjugated polymers. The design and synthesis of conjugated polymers is the critical first step for the preparation of CPNs and Pdots. The second step is the preparation of nanoparticles with these conjugated polymers.

Conjugated polymers are often based on four basic backbone structures: poly(fluorene) (PF), poly(*p*-phenylenevinylene) (PPV), poly(*p*-phenyleneethynylene) (PPE), and poly(thiophene) (PT). For synthesis of these conjugated polymers, Suzuki coupling, Heck coupling, and Sonogashira coupling as well as oxidative polymerization and microwave-based polymerization, are widely used.

There are three main methods to prepare CPNs using conjugated polymers (Scheme 3.1), namely, the nanoprecipitation method, mini-emulsion method, and self-assembly method [23]. For the nanoprecipitation method, the conjugated polymers are first dissolved in a water-miscible organic solvent, such as THF. Then, the conjugated polymer solution is rapidly added to an excess of water under ultrasonic dispersion. The CPNs form because the significant change of solvent polarity causes the conjugated polymers to aggregate [24, 25]. The size of the CPNs can be controlled by adjusting the polymer concentration and the addition of amphiphilic polymers. Our group developed a series of functionalized CPNs by using the nanoprecipitation method and applied them to cell labeling and molecular sensing. CPNs prepared by the nanoprecipitation method typically have an average diameter of ~20 nm or less and are thus usually Pdots.

In contrast to the nanoprecipitation method, the mini-emulsion method requires a water-immiscible organic solvent, such as dichloromethane, to first dissolve the conjugated polymers. A surfactant is also needed to form the emulsion droplets under ultrasonication. However, the size of the CPNs prepared by miniemulsion methods is usually larger than 40 nm.

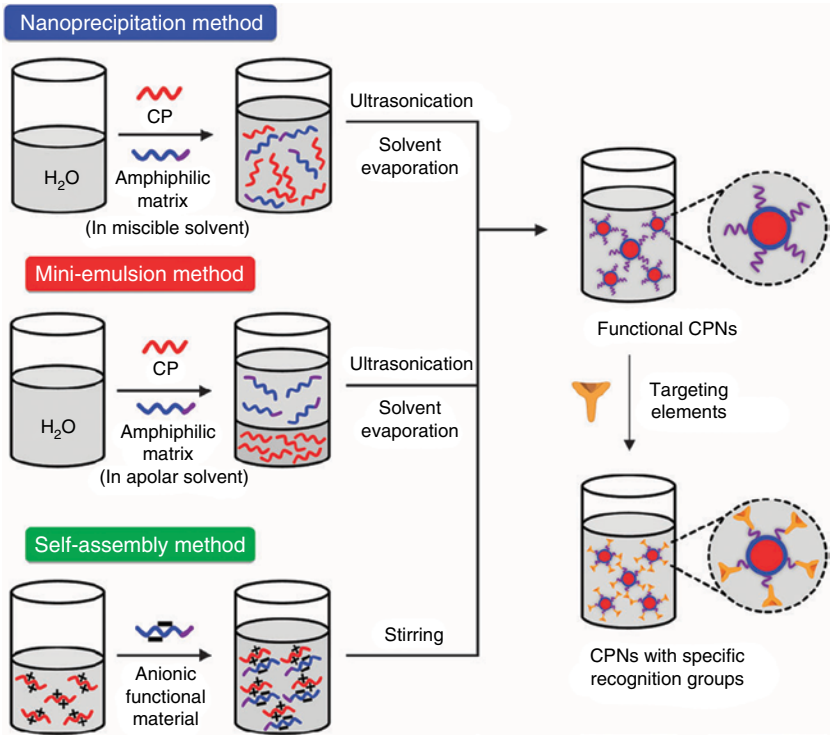

Scheme 3.1 The preparation of CPNs with three different methods, including nanoprecipitation, miniemulsion, and self-assembly method. (Reprinted with permission from Ref. [23]. Copyright 2013, Royal Society of Chemistry.)

By using self-assembly, oppositely charged conjugated polymers and coassembling reagents are first dissolved in water. Then, the solutions are mixed together under stirring in a certain ratio. This method can be applied only for water-soluble conjugated polymers. Wang and coworkers prepared CPNs using the self-assembly method to obtain CPNs of about 100 nm diameter after centrifugation for light-activated, targeted-tumor therapy [26].

3.2.2 Characterization

Given the applications of CPNs in biomedical fields, both optical properties and physiochemical properties are extremely important. First of all, the size of CPNs not only determines their brightness and photostability, but it also affects their interaction with cells and biodistribution *in vivo*. Therefore, tunability of the size of CPNs is always an important consideration during the preparation. The miniemulsion method typically produces CPNs in the range of 40–500 nm in diameter by adjusting the conjugated polymer and surfactant concentrations in the solution mixture. Usually, CPNs prepared by the miniemulsion method contains a small portion of conjugated polymers, thus resulting in low brightness compared with Pdots. In some studies, conjugated polymers were loaded within

poly(DL-lactide-*co*-glycolide) (PLGA) particles at 1 wt% [27]. In another procedure, the phospholipid matrix was used to encapsulate conjugated polymers with a fluorophore concentration of approximately 8.5 wt% [28]. In these examples, the content of conjugated polymers was quite low, such that the brightness of the resultant CPNs was not comparable with the brightness offered by Pdots that contain more than 50% of conjugated polymers.

Optical properties, including absorption, emission, quantum yield, brightness, and photostability, are critical aspects in the preparation of CPNs for biological imaging and sensing. The CPNs usually show blue-shifted absorption spectra and red-shifted emission spectra in comparison to that of the polymer in an organic solvent. In the past decade, CPNs with different emission wavelengths from the UV region to the near-infrared (NIR) region were successfully produced by designing specific conjugated polymers or by blending different polymers into CPNs. For example, we developed a series of multicolor fluorescent Pdots that emitted from 520 to 690 nm of the electromagnetic spectrum by inserting different boron dipyrromethene (BODIPY) units into the backbone of the conjugated polymers [29]. Compared with water-soluble inorganic quantum dots, Pdots usually showed roughly 10 to 100 times larger absorption cross-section, which was on the order of about 10^{-13} cm^2. CPNs usually exhibit roughly three orders of magnitude greater brightness than that of the conventional organic fluorescent dyes because of the strong light-harvesting capability of conjugated polymers [30, 31]. Recently, we also developed NIR Pdots for cell imaging by either doping NIR fluorophores into Pdots [32] or by incorporating squaraine units into the backbone of the conjugated polymers [33]. Those Pdots showed higher brightness and photostability than the corresponding Qdots and organic dyes with similar emission wavelengths, which suggest that they are promising for use in biological imaging both *in vitro* and *in vivo*.

McNeil and coworkers first demonstrated the excellent two-photon fluorescent properties of CPNs. The two-photon action cross-sections of CPNs in their work was as high as 2.0×10^5 GM, which is the largest value for a 20-nm-diameter nanoparticle and was three to four orders of magnitude higher than that of the conventional fluorescent dyes [19].

For fluorescent probes, photostability is critical for cellular imaging, especially for long-term imaging and single-molecule imaging. The traditional fluorescent dyes, such as fluorescein isothiocyanate (FITC), often suffer from serious photobleaching and photoblinking. The photostability can be characterized by the photobleaching quantum yield (φ_B), which is in the range of 10^{-4}–10^{-6} for typical fluorescent dyes. In contrast, the φ_B of CPNs is estimated to be in the range of 10^{-7}–10^{-10}, which is about three to four orders of magnitude lower than that of fluorescent dyes. Considering these excellent optical properties, CPNs have been attracting attention for applications such as cell labeling, fluorescence imaging, and molecular sensing.

3.2.3 Functionalization

Besides the excellent optical properties of CPNs and Pdots, easy functionalization and controllable surface chemistry are also important for widespread

applications in biomedical imaging and sensing. There are mainly three strategies to functionalize CPNs or Pdots for biological applications, which are the direct functionalization method, the amphiphilic polymer coprecipitation method, and the encapsulation method.

For the direct functionalization method, conjugated polymers are first covalently modified with functional groups, such as carboxyl and amino groups, in the initial polymer synthesis. Pdots are then formed using these polymers, which contain functional groups directly available for bioconjugation. For example, we synthesized a series of poly[(9,9-dioctylfluorenyl-2,7-diyl)-*co*-(1,4-benzo-{2,10,3}-thiadazole)] (PFBT) polymers with side-chain carboxylic acid groups with different molar ratios of approximately 2%, 14%, and 50% (Figure 3.1) [34]. All of the Pdots prepared from these polymers were easily functionalized with antibodies for cell labeling and fluorescence imaging. However, we found that the stability and fluorescence performance of these CPNs were affected by the degree of hydrophilic functionalization. With the increase of the ratio of carboxylic acid groups in the PFBT polymers, the quantum yield of Pdots decreased from 30% to 17% and the brightness of Pdots also decreased. Moreover, the Pdots with higher carboxylic acid groups showed strong nonspecific cellular labeling. Thus, the density of hydrophilic groups on the conjugated polymers should be carefully controlled based on the requirement of the applications.

The second strategy is the amphiphilic polymer coprecipitation method. In this strategy, the conjugated polymers are blended with a small amount of amphiphilic polymers that contain functional groups for further modification. For instance, PS–PEG-COOH, an amphiphilic comb-like polystyrene polymers, was used to functionalize the highly fluorescent PFBT Pdots for cellular imaging and labeling (Figure 3.2a) [30]. Another widely used amphiphilic polymer, poly (styrene-*co*-maleic anhydride) (PSMA) polymer, was used to blend with a

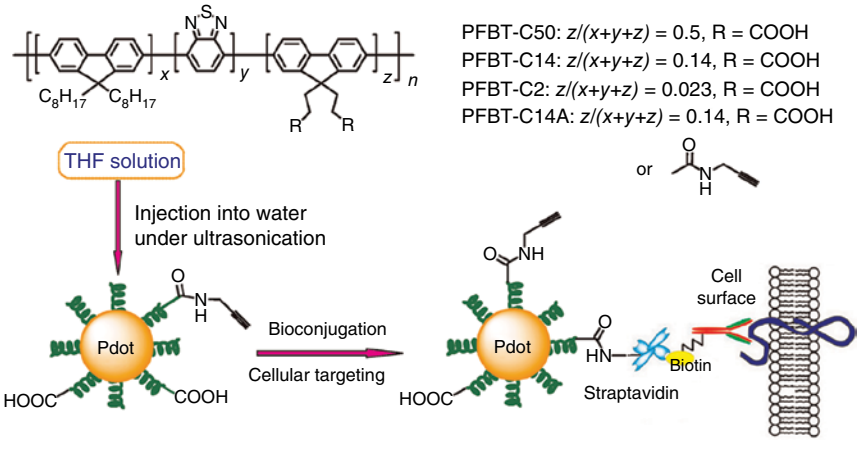

Figure 3.1 Direct functionalization of Pdots with different side-chain carboxyl groups. Bioconjugation was performed on the carboxyl groups. The Pdot-bioconjugates were specific for cellular labeling. (Reprinted with permission from Ref. [34]. Copyright 2012, American Chemical Society.)

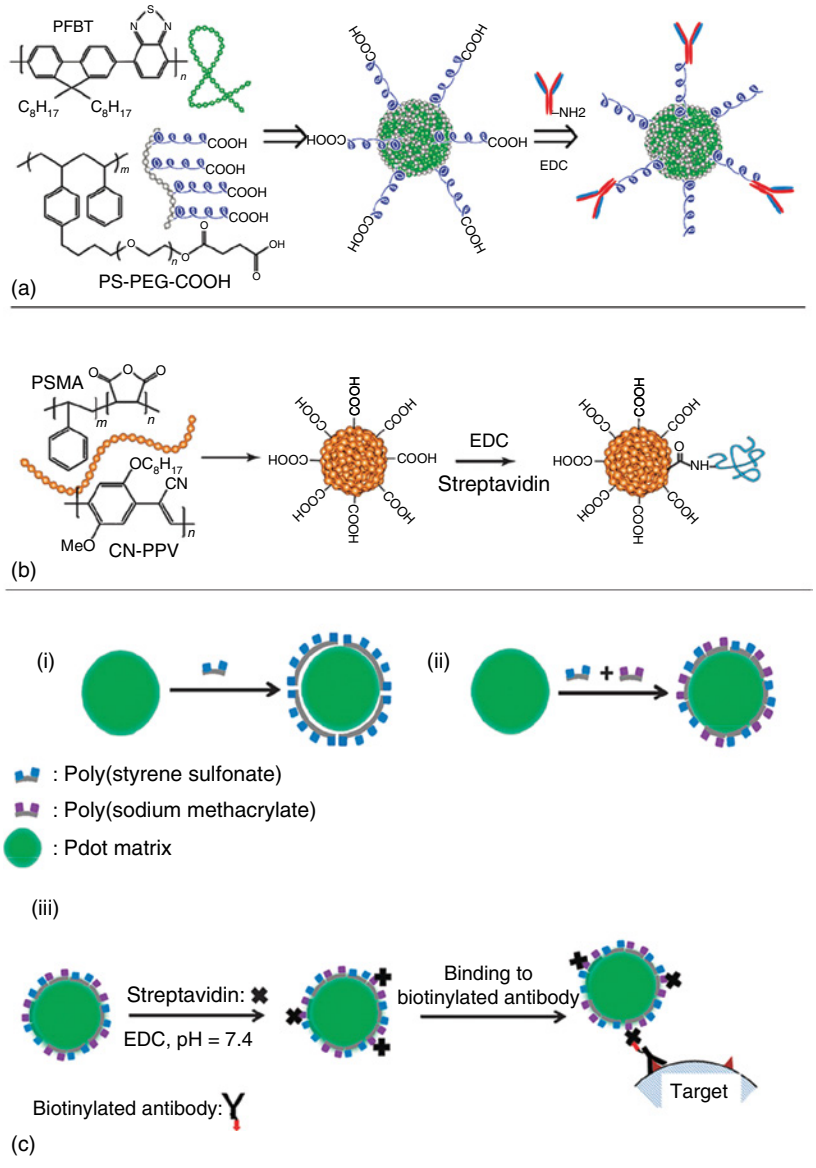

Figure 3.2 (a) Surface functionalization of PFBT Pdots with the amphiphilic polymer PS–PEG-COOH. (Reprinted with permission from Ref. [30]. Copyright 2010, American Chemical Society.) (b) Surface functionalization of CNPPV Pdots with the amphiphilic polymer PSMA. (Reprinted with permission from Ref. [35]. Copyright 2012, Royal Society of Chemistry.) (c) Encapsulation of Pdots with polyelectrolytes. (i–ii) Schematic illustration of Pdots encapsulation by one or two polyelectrolytes. (iii) Bioconjugation of streptavidin onto the surface of the polyelectrolytes encapsulated Pdots for cell labeling and imaging. (Reprinted with permission from Ref. [36]. Copyright 2012, Royal Society of Chemistry.)

conjugated polymer to form Pdots (Figure 3.2b) [35]. The biomolecules could be further attached on the surface through the carboxyl groups on the surface of Pdots during the preparation in water. In one of our studies, we first modified the surface of Pdots with a clickable group and then biorthogonal labeling using click chemistry so that we could specifically target cells [37].

The last strategy to functionalize CPNs or Pdots is the encapsulation method, which is quite similar to functionalization of inorganic nanoparticles, such as quantum dots, oxide nanoparticles, and gold nanoparticles. The widely used encapsulation materials include silica [38], phospholipid, and the PLGA polymer [27]. Also, we used polyelectrolytes to encapsulate Pdots to improve colloidal stability and to facilitate further Pdot modifications [36]. Figure 3.2c shows the encapsulation of Pdots with two different polyelectrolytes, poly(styrene sulfonate), and poly (sodium methacrylate). Compared with the bared Pdots, the polyelectrolytes encapsulated Pdots showed dramatically improved colloidal stability in both PBS buffer and concentrated metal ions solution. The functional groups introduced via polyelectrolyte encapsulation allowed for successful bioconjugation with streptavidin for cell labeling and imaging.

3.3 Molecular Sensing

CPNs and Pdots are well suited for development of sensors because they have high brightness and efficient modulation of energy transfer.

3.3.1 Metal-Ion Sensing

Metal ion detection has attracted much interest because metal ions play important roles in water pollution and some biological pathways. By using the bright fluorescence of CPNs, several biologically or environmentally relevant ions, such as Cu^{2+}, Fe^{2+}, and Hg^{2+}, were detected. In 2011, we developed a simple Pdot platform for sensitive, ratiometric Cu^{2+} and Fe^{2+} detection that used carboxyl-functionalized PFBT Pdots [39]. With addition of Cu^{2+}, the Pdots aggregated and caused fluorescence quenching. The addition of the Fe^{2+} had similar fluorescence quenching behavior. However, the Cu^{2+}-induced fluorescence quenching of Pdots was reversible with addition of ethylenediaminetetraacetic acid (EDTA), while the Fe^{2+}-induced aggregation was not reversible. This reversibility with EDTA could be used for discriminating Cu^{2+} and Fe^{3+}. Similarly, Wang and coworkers fabricated a sensor for detection of Fe^{3+} in water based on the aggregation-induced fluorescence quenching of Pdots in the presence of Fe^{3+} [40]. By doping a molecular dye, rhodamine spirolactam (RB-SL), into PFBT Pdots, Harbron and coworkers developed a ratiometric mercury ion sensor that reached a sensitivity as low as 0.7 ppb [41]. As shown in Figure 3.3, a nonfluorescent dye RB-SL was doped in PFBT Pdots, and this RhB-SL dye would only restore its fluorescence when it was exposed to mercury ions, generating fluorescent RB-Hg. In this sensor, the rhodamine dye was used as a FRET acceptor and the PFBT was used as a donor. By using the strong light-harvesting capability of Pdots, the fluorescence intensity and sensitivity of the sensor were greatly

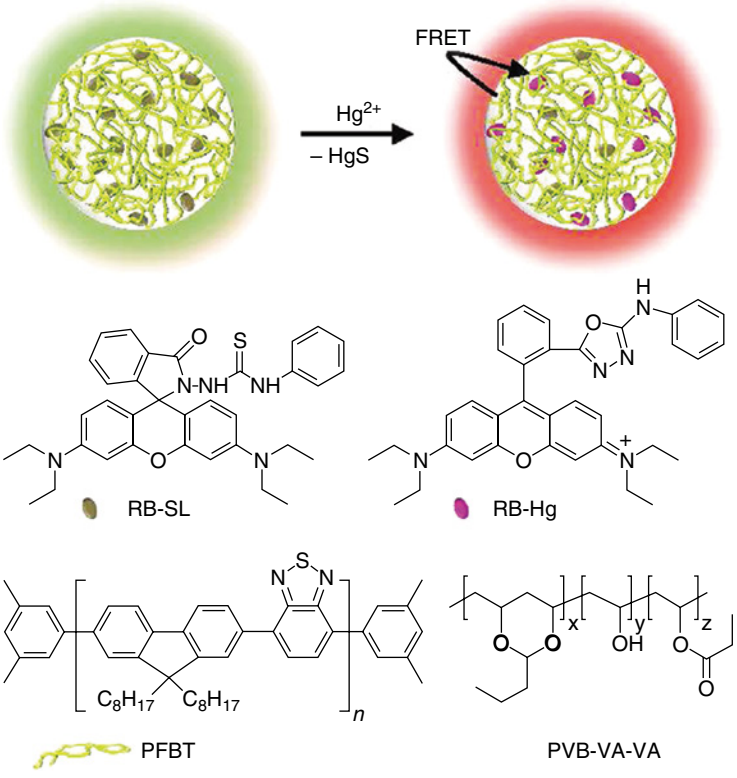

Figure 3.3 Rhodamine spirolactam-doped CPNs for mercury ion detection. (Reprinted with permission from Ref. [41]. Copyright 2012, American Chemical Society.)

enhanced. Recently, Chan and coworkers developed a ratiometric sensor based on Pdots for Pb^{2+} ions [42]. The Pdots were modified with polydiacetylenes; the detection signal was visible to the naked eye, promoting the preparation of easy-to-read test strips for field use.

3.3.2 Oxygen and Reactive Oxygen Species Detection

CPNs and Pdots can also be used for monitoring the oxygen and reactive oxygen species (ROS). In 2009, Wu and coworkers doped an oxygen-sensitive fluorophore platinum(II) octaethylporphine (PtOEP) into poly(9,9-dihexylfluorene) (PDHF) Pdots (Figure 3.4a) [43]. PtOEP worked as an energy acceptor, which emitted strong fluorescence at 650 nm when oxygen content was low. The PDHF Pdots worked as a host for the PtOEP and the energy donor when they were excited at 350 nm. With this platform, Wu and coworkers recently developed a sensor for glucose (Figure 3.4b) [44]. They modified the oxygen-consuming enzyme glucose oxidase on the surface of the Pdots as the molecular recognition element for glucose. In the presence of glucose, the glucose oxidase consumed the oxygen around Pdots, which induced the fluorescence enhancement of PtOEP. They investigated the application for long-term continuous glucose monitoring

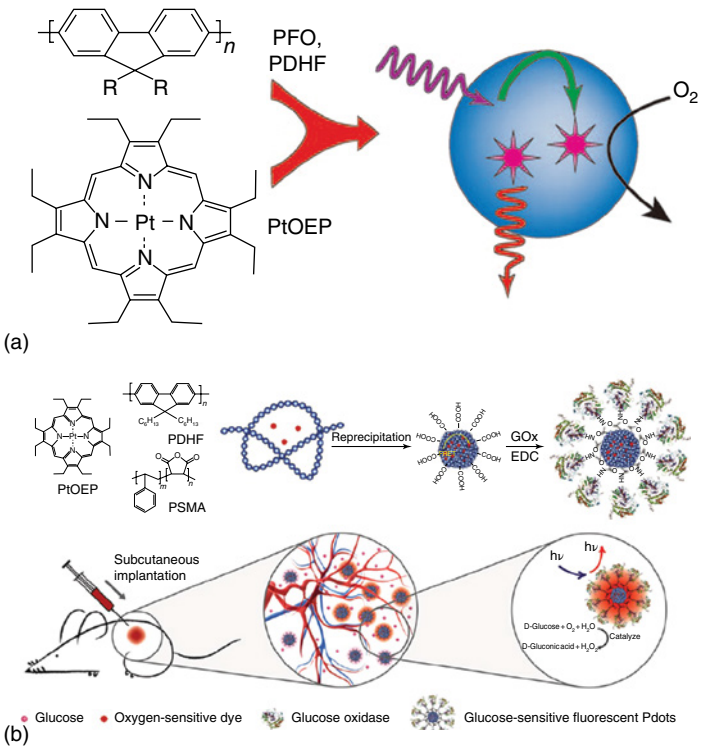

Figure 3.4 (a) Schematic illustration of the conjugated polymer dots for oxygen sensing. (Reprinted with permission from Ref. [43]. Copyright 2009, Wiley-VCH.) (b) Schematic illustration of the formation of oxygen-sensitive Pdots with glucose-oxidase modification for the monitoring of glucose levels *in vivo*. (Reprinted with permission from Ref. [44]. Copyright 2016, American Chemical Society.)

by implanting the sensor in mice. This platform might also be expanded to other important biological molecules by adjusting the modified enzymes.

Huang and coworkers recently reported a dual-emissive CPNs for oxygen sensing by doping oxygen-sensitive dye platinum(II) porphyrin into a fluorene-based conjugated polyelectrolyte with an oxygen-insensitive blue fluorescence [45]. The self-assembled small CPNs were successfully applied to imaging oxygen in a mouse model to study the tumor hypoxia.

CPNs were also used for the detection of ROS by using their excellent optical properties and easy surface modification. Instead of fluorescence, chemiluminescence (CL) and electrochemiluminescence (ECL) were used more often for the fabrication of CPNs for ROS detection. For instance, Wang and coworkers first reported CL in MEH-PPV CPNs modified with horseradish peroxidase [46]. When the chemiluminescent system was formed in the presence of luminol and H_2O_2, CL resonance energy transfer (CRET) took place. With the subsequent FRET, the Pdots emitted detectable luminescence, which was related to the concentration of H_2O_2. Pu and coworkers also fabricated chemiluminescent CPNs for ultrasensitive imaging of H_2O_2 *in vivo* [47]. As shown in Figure 3.5a, a

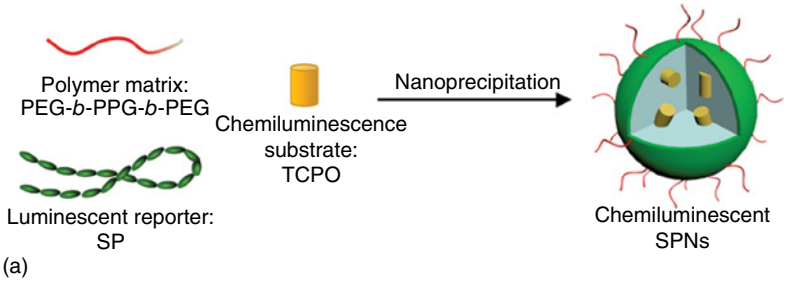

(a)

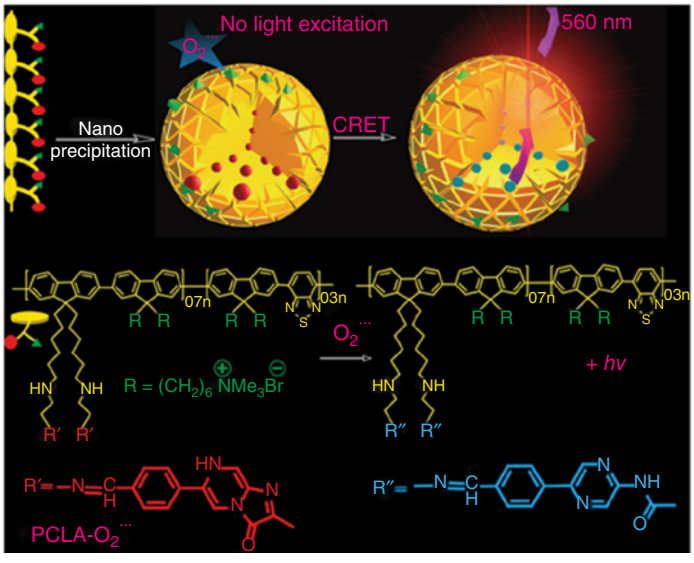

(b)

Figure 3.5 (a) Schematic of the preparation of CL CPNs for H_2O_2 detection by doping the chemiluminescent substrate into the CPNs through hydrophobic interactions. (Reprinted with permission from Ref. [47]. Copyright 2016, American Chemical Society.) (b) Schematic illustration of CL CPNs for detection of superoxide anion by grafting conjugated polymer with imidazopyriazinone. (Reprinted with permission from Ref. [48]. Copyright 2016, American Chemical Society.)

chemiluminescence substrate, TCPO, was doped into the CPNs through hydrophobic interactions. With the optimized CPNs, the chemiluminescence quantum yield could be enhanced to 2.30×10^{-2} einsteins mol^{-1} and the limit of detection for H_2O_2 was as low as 5 nM. Furthermore, by doping a naphthalocyanine dye into the CPNs with the TCPO, the resulting CPNs showed strong NIR luminescence responding to H_2O_2 due to the intraparticle CRET. These CPNs could be used for the ultrasensitive imaging of H_2O_2 in the mouse models. In addition, Tang and coworkers [48] modified the conjugated polymer PFBT with quaternary ammonium groups and an imidazopyriazinone moiety in the branches, which was used as the precursor to form CPNs (Figure 3.5b). The CL of imidazopyrazinone unit, which could be triggered by superoxide anion $(O_2)^-$, worked as the energy donor. The conjugated polymer was excited through CRET and showed bright luminescence due to the excellent light-amplifying

property of CPNs. The result from the detection $(O_2)^-$ *in vitro* and *in vivo* indicated that this CL-based CPN sensor was a promising alternative for ultralow level $(O_2)^-$ imaging.

3.3.3 pH and Temperature Monitoring

By carefully designing energy transfer between the pH-sensitive dyes and the semiconducting polymer, our group developed a ratiometric methodology for pH sensing and imaging based on Pdots [49]. In this work, poly(2,5-di(3′,7′-dimethyloctyl)phenylene-1,4-ethynylene) (PPE) Pdots were used as the donor because their emission (420–490 nm) has good overlap with the absorption spectrum of the pH-indicator FITC. Three different routes were tested to conjugate the FITC to the surface of PPE Pdots (Figure 3.6). Efficient FRET was observed in all of the final products made by these three routes. When the pH-sensitive Pdots were excited at 390 nm, two main emission peaks from FITC

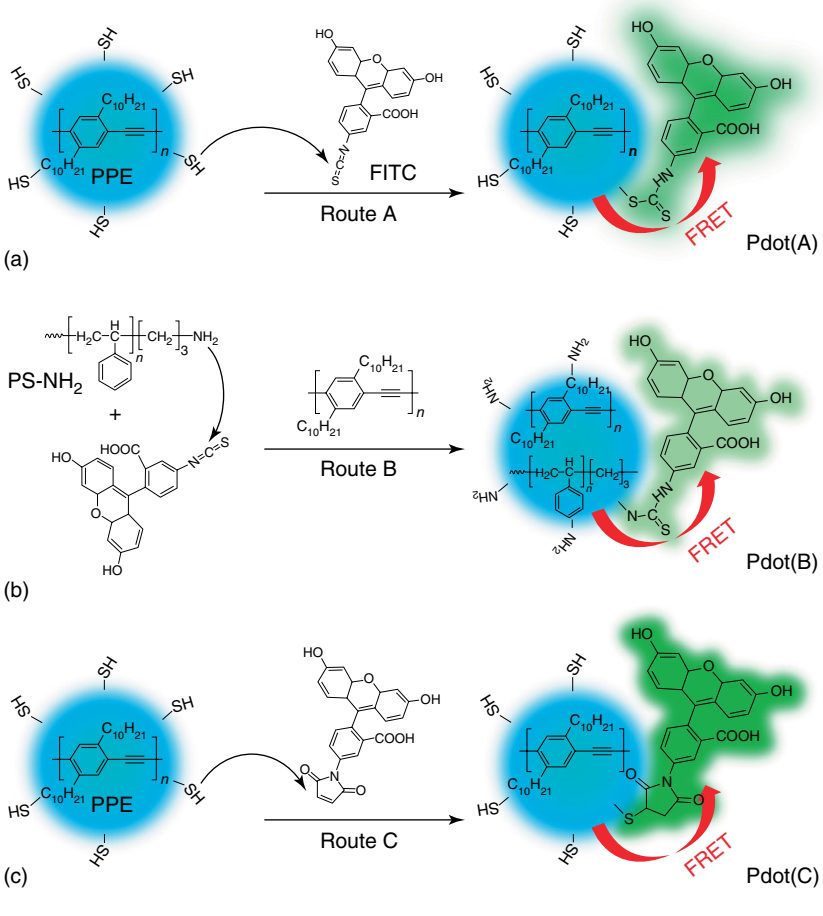

Figure 3.6 Schematic illustrating three routes to prepare pH-sensitive Pdots. (Reprinted with permission from Ref. [49]. Copyright 2011, American Chemical Society.)

(λ_{em} = 513 nm) and PPE (λ_{em} = 440 nm) were observed. However, the peak of PPE was unchanged by varying the pH. In contrast, the intensity of FITC peak decreased when the pH changed from 8 to 5. In the range of pH 5–8, the ratio of fluorescence intensity of FITC to PPE showed linear relationship and reversibility to pH. Of all the three routes, the Pdots from route A showed the highest pH detection sensitivity. Furthermore, HeLa cells were used to test cellular pH monitoring by using this ratiometric sensor. Quantitative measurement of the intracellular pH was studied by incubating the Pdots with cells, which indicated that the average pH of the cancer cells was about 5.0, which was consistent with other reports.

In a similar way, we also developed a platform to monitor the temperature in cells [50]. As shown in Figure 3.7, a temperature-sensitive dye, Rhodamine B (RhB), was attached to an amino-terminated polystyrene polymer (PS–NH_2). Then, the temperature-sensitive Pdots (RhB–Pdots) were formed by blending PFBT or PFPV with PS–RhB. In this platform, the semiconducting polymer acted as the energy donor and the RhB was used as the acceptor. The strong light-harvesting ability and amplified energy transfer capability of RhB–Pdots ensured that this system showed excellent temperature sensitivity and high brightness for cellular imaging. The RhB–Pdots showed linear fluorescence

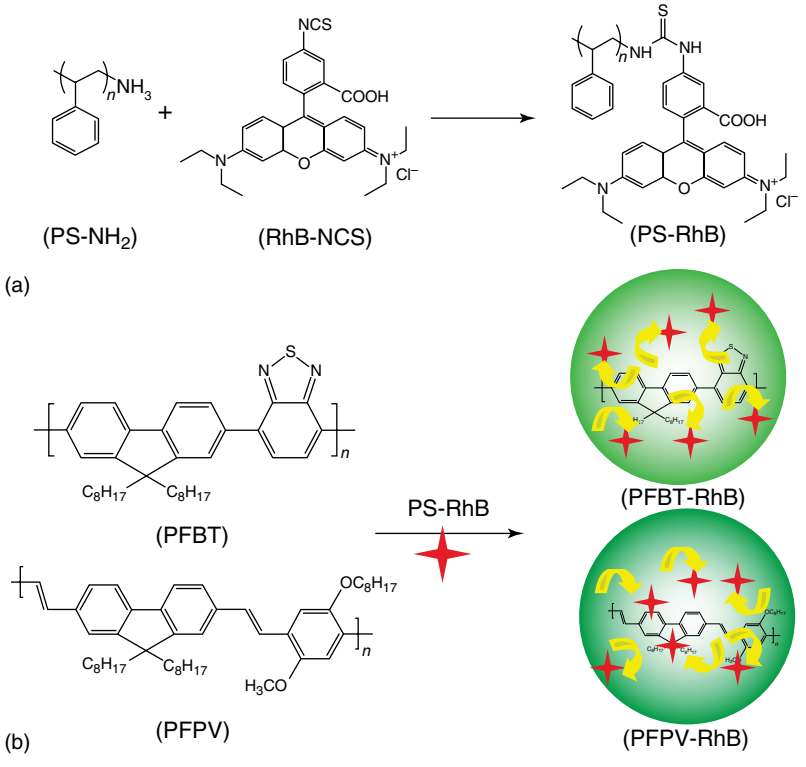

Figure 3.7 Preparation of RhB–Pdots for temperature sensing. (Reprinted with permission from Ref. [50]. Copyright 2011, American Chemical Society.)

response in the range of 10–70 °C. The ratiometric assay ensured the robust behavior for cellular imaging. We finally employed RhB–Pdots for temperature monitoring in HeLa cells and the fluorescence imaging showed accurate temperature determination in good agreement with the results measured by a thermocouple.

3.3.4 Sensing of Other Molecules

CPNs were also used to detect biomolecules based on energy transfer [3, 51]. For instance, Swager and coworkers fabricated highly fluorescent PPE polymer nanoparticles for the detection of protease [52]. As shown in Figure 3.8, the red fluorescent perylene unit was randomly inserted into the backbone of the PPE polymer; reactive succinimide groups were used to terminate the polymer. Then, the short peptide was introduced to form cross-linked CPNs by reacting with

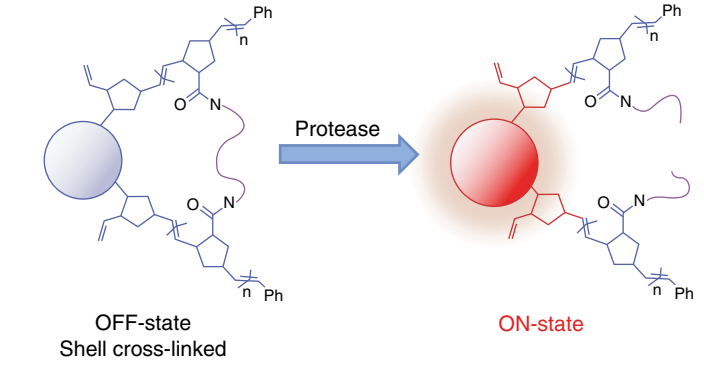

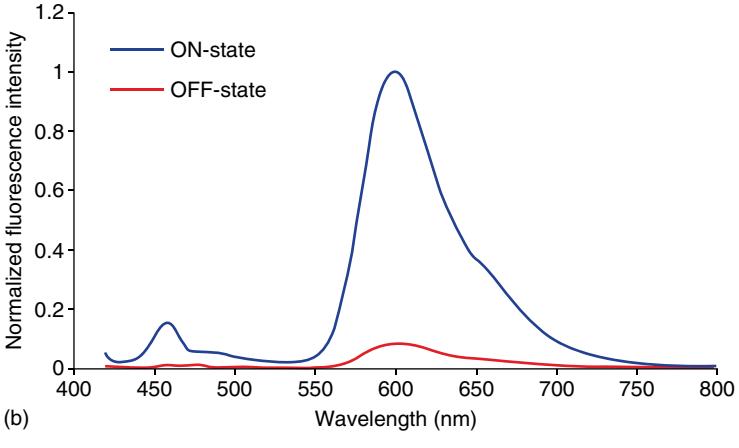

Figure 3.8 Protease detection using CPNs. (a) Sensing scheme for protease. The cross-linked CPNs showed quenched state. The cleavage of the linker by protease released the strain and turned on the fluorescence. (b) Fluoresce spectra of the cross-linked CPNs before (red) and after (blue) incubation with trypsin. (Reprinted with permission from Ref. [52]. Copyright 2012, American Chemical Society.)

succinimide groups on the PPE polymer. Therefore, the cross-linked CPNs showed a fluorescence "OFF-State" due to the strong self-quenching. Upon the presence of protease, the tightly aggregated and quenched CPNs restored the fluorescence emission because the peptide cross-linkers were cleaved and the strain released. A 15-fold enhancement of fluorescence intensity was observed with incubation of protease under physiological conditions.

In another work by Chen and coworkers, a FRET system between PFO Pdots and Au nanoparticles was fabricated for carcinoembryonic antigen (CEA) detection [53]. In this system, both PFO Pdots and Au nanoparticles, which were complementary to a CEA aptamer, were modified with DNA,. The fluorescence of PFO Pdots was quenched by the Au nanoparticles through FRET. In the presence of CEA, the FRET system was destroyed due to the stronger binding force between CEA and the aptamer. Thus, the aptamer was released and the fluorescence of PFO Pdots recovered. Therefore, the fluorescence intensity enhancement can quantitatively monitor CEA protein concentrations. Recently, they also developed another FRET system based on PFO Pdots and a metal organic framework (MOF) for the detection of the protease MMP-2 [54]. In this platform, the PFO Pdots were modified with a polypeptide chain, which contained a specific MMP-2 substrate domain and a π-rich motif. In the presence of MOF, the PFO Pdots were absorbed to MOF through the π-rich motif and had their fluorescence quenched. The PFO Pdots were released from MOF by the cleavage of the MMP-2 and the fluorescence recovered. The fluorescence recovery was proportional to the concentration of MMP-2 in the range of 0.1–2.5 $\mathrm{pg\,ml^{-1}}$ under optimal conditions.

Besides large biomolecules, such as proteins, CPNs were also used to detect other important small biomolecules. For example, Chen and coworkers developed an anodic ECL system based on PFO Pdots for the detection of melamine [55]. Melamine is widely used in the chemical industry. However, it has been added to baby food and formula illegally due to its high nitrogen content, which harms infants. Therefore, it is important to develop sensitive methods to detect melamine. In this report, the ECL signal of PFO Pdots-$C_2O_4^{2-}$ system was efficiently quenched by melamine, which showed a wide linear range from 9.0×10^{-11} to 1.1×10^{-8} M. Nitroaromatics, such as trinitrophenol and *p*-nitrophenol, were also found to be efficient quenchers for CPNs [56]. Therefore, Xi and coworkers used the electron-transfer-induced fluorescence quenching phenomenon of CPNs for the qualitative detection and quantitative analysis of nitroaromatics [56].

CPNs were also used for the anion detection and imaging [57]. As shown in Figure 3.9a, Chan and coworkers developed Pdots doped with coumarin dye for ratiometric and sensitive fluoride-anion detection [58]. In this case, coumarin dye in quenched state was doped into the PPE Pdots. Therefore, the whole system exhibited only PPE fluorescence. After the treatment of fluoride anions, the quenched coumarin was unprotected and showed high fluorescence because of the energy transfer from PPE to coumarin. The results indicated that this method can specifically monitor the concentration of fluoride anions in the range from 0 to 160 μM. Other similar anions showed no interference for fluoride detection (Figure 3.9b).

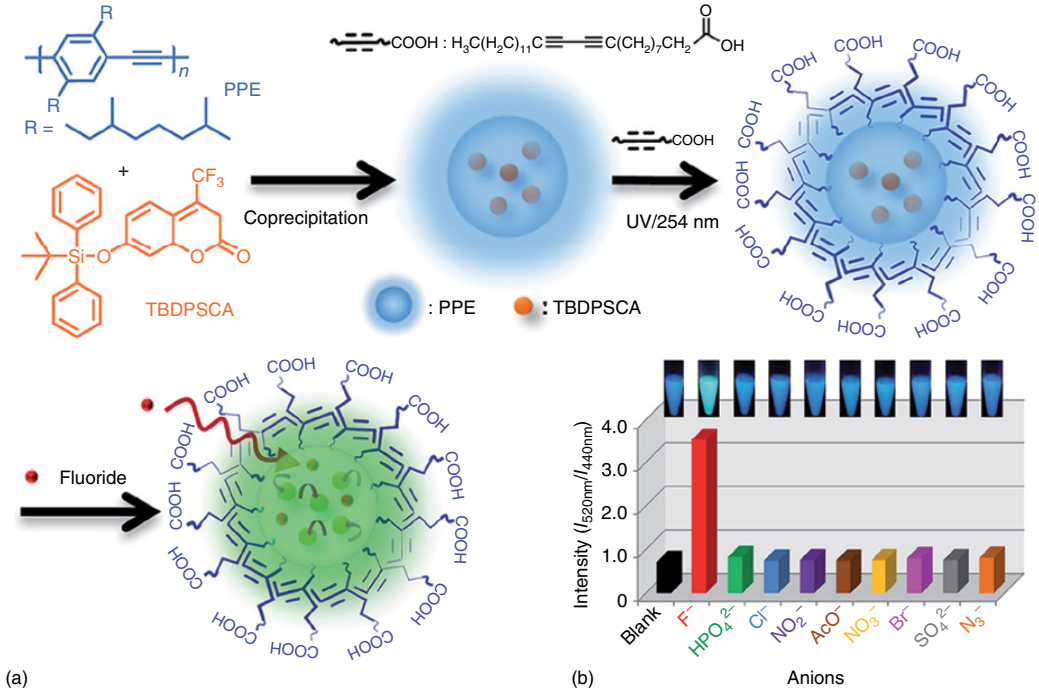

Figure 3.9 (a) Schematic showing the sensing of fluoride anion by coprecipitation of PPE and coumarin. (b) Fluorescent tubes of the selective detection of fluoride anion over other anions under a 365 nm lamp. (Reprinted with permission from Ref. [58]. Copyright 2014, Royal Society of Chemistry.)

3.4 Cellular Imaging

3.4.1 Fluorescence Imaging

3.4.1.1 *In Vitro* Imaging

Researchers have been drawn to CPNs for both nonspecific and specific fluorescence imaging because of their optical properties, including excellent photostability, high fluorescence brightness, easy modification, and low cytotoxicity. *In vitro* cellular imaging can be demonstrated using nonspecific interactions. For example, the bare CPNs without any encapsulation layer were used to demonstrate the feasibility of cellular fluorescence imaging by nonspecific cellular uptake via endocytosis. Wang and coworkers synthesized an amphiphilic-conjugated polythiophene derivative (PT-Boc) and formed CPNs with an average diameter of 700 nm in water [59]. Human lung epithelial (A549) cells were incubated with PT-Boc CPNs for 10 h at 37 °C and then washed with PBS buffer before taking images. The results showed that the PT-Boc CPNs were mainly in the cytoplasm and had significant perinuclear enrichment. CPNs embedded within another particle matrix was also used for cellular imaging. For example, Liu and coworkers prepared highly fluorescent PLGA nanoparticles loaded with conjugated polymer (CPL NPs) for cellular imaging [60]. After incubation with MCF-7 breast-cancer cells, confocal images showed that these CPL NPs were internalized in cytoplasm around the nuclei, indicating efficient cellular uptake.

Specific imaging required the modification of the surface of CPNs with some recognition elements, such as an antibody, aptamer, or peptide. One of the methods for bioconjugation is to use covalent chemistry binding. Our group developed a series of ultrabright Pdots as target probes for specific cellular imaging. In this platform, Pdots were formed by blending conjugated polymers with amphiphilic polymers, including PS–PEG-COOH and PSMA, which exhibited carboxyl groups on the surface of Pdots in water. Then, through the (1-ethyl-3-(3-dimethylaminopropyl)-carbodiimide) (EDC) conjugation between carboxyl groups on Pdots and amino groups on the antibody or streptavidin, these biomolecules were conjugated onto Pdots for specific labeling. By using this method, we successfully and specifically labeled a cell surface marker (EpCAM receptor and biotin) on living MCF-7 cells using different Pdots. As shown in Figure 3.10, we prepared three multicolor narrow emissive Pdots based on BODIPY units and performed the bioconjugation and specific cellular targeting on MCF-7 cells [29]. The fluorescence imaging and flow cytometry results indicated that these BODIPY-based multicolor Pdots are promising for multiplexed biological fluorescence imaging.

NIR-emissive fluorescence probes are highly desirable for both *in vitro* and *in vivo* imaging because of their low background fluorescence and deep penetration depth. We designed and synthesized several NIR Pdots for cellular imaging. In the first case, NIR dyes were directly doped into the Pdots to be used for NIR cellular imaging. However, the potential limitations of dye leakage for long-term imaging prompted us to pursue other NIR-emissive Pdots [32]. As shown in Figure 3.11, NIR-emissive squaraine units were inserted into the backbone of the conjugated polymers to solve the leakage problem [33]. Because of

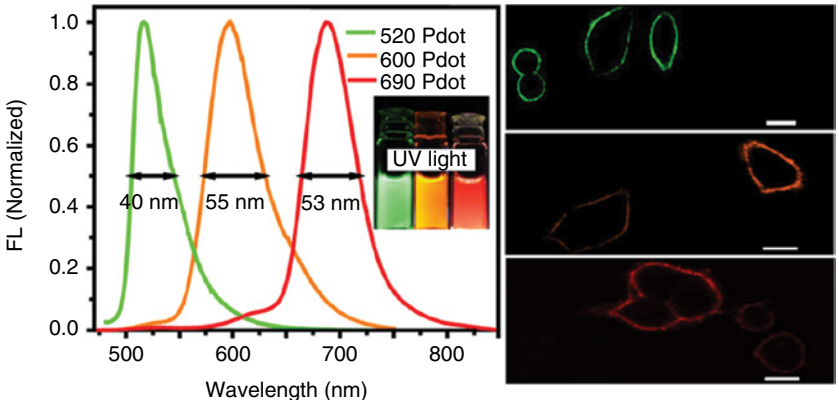

Figure 3.10 BODIPY-based multicolor Pdots with narrow emission for fluorescence imaging of the EpCAM receptors on the surface of MCF-7 cells. (Reprinted with permission from Ref. [29]. Copyright 2013, American Chemical Society.)

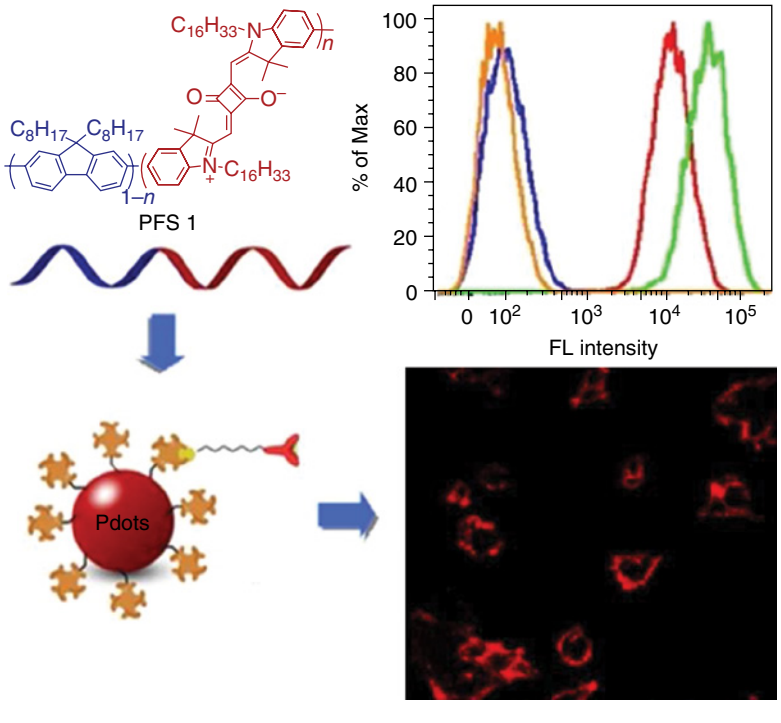

Figure 3.11 Preparation of squaraine-based Pdots with narrow NIR fluorescence emission for specific cellular labeling. (Reprinted with permission from Ref. [33]. Copyright 2014, American Chemical Society.)

through-bond-energy transfer in the polymer, highly bright and narrow-band NIR-emissive Pdots were formed with a quantum yield as high as 0.30 and large Stokes shift of ~340 nm. Compared with Qdots705, the NIR-emissive Pdots demonstrated bright fluorescence imaging ability on MCF-7 cells for EpCAM

labeling. In another example, we prepared highly fluorescent NIR-emissive Pdots by cascade FRET and carefully designed the ratio of donors, acceptors, and energy transfer units [61]. The NIR-emissive Pdots with narrow emission around 710–720 nm were obtained with high quantum yields. Single-particle fluorescence measurements of these NIR-emissive Pdots showed that they were several times brighter than Qdots705. After the bioconjugation of streptavidin onto the surface of these NIR-emissive Pdots, they effectively labeled EpCAM receptors on the surface of MCF-7 cells.

3.4.1.2 *In Vivo* Imaging

In contrast to *in vitro* fluorescence imaging, *in vivo* fluorescence imaging holds greater challenges because of photon-limiting interferences, including scattering, absorption, and autofluorescence. To overcome these limitations, NIR-emissive probes were one of the main directions that researchers pursued. Compared with the traditional organic NIR dyes, NIR-emissive CPNs are more promising because of their low toxicity, high brightness, and easy modification [62]. For instance, we fabricated highly fluorescent NIR-emissive Pdots for *in vivo*, targeted imaging of tumors [31]. As shown in Figure 3.12, a visible-light-harvesting polymer (PFBT) and a deep-red emitting polymer (PF-DBT5) were blended to form the intra-particle-energy-transfer NIR-emissive Pdots. In this system, PFBT was used as the donor and PF-DBT5 was used as the acceptor, with an efficient 650-nm emission and a quantum yield of 0.56. By conjugating

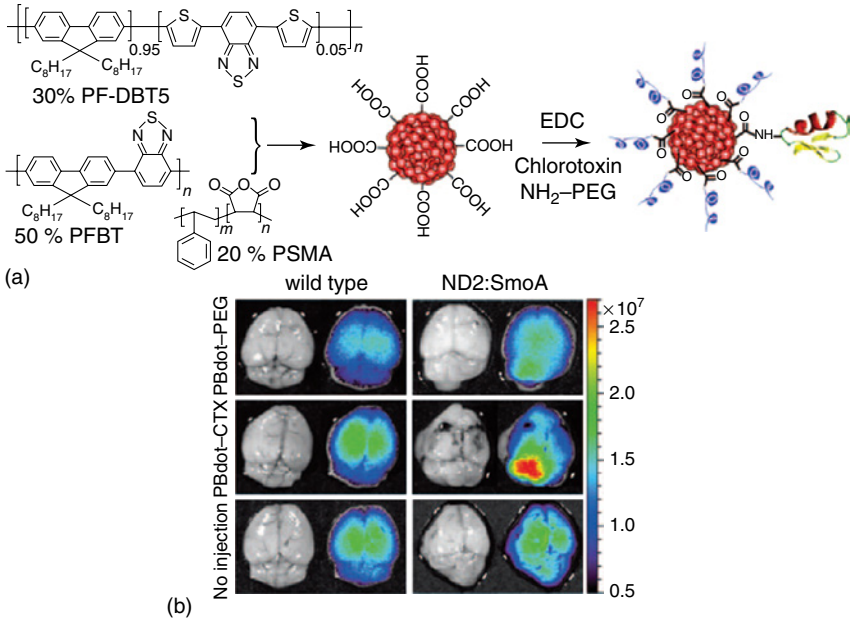

Figure 3.12 (a) Schematic illustrating the formation of blended NIR-emissive Pdots conjugated with CTX for brain tumor imaging. (b) Fluorescence imaging of the healthy wild type mice (left) and medulloblastoma tumors in ND2:SmoA mice (right) after tail-vein injection of the Pdots. (Reprinted with permission from Ref. [31]. Copyright 2011, Wiley-VCH.)

a targeting peptide, chlorotoxin (CTX), onto the Pdots, the *in vivo* fluorescence imaging showed the specific targeting to malignant brain tumors.

In another work, Rao and coworkers developed NIR-emissive CPNs by conjugating an NIR dye onto the surface of the CPNs [63]. Two peaks at 678 and 818 nm from conjugated polymer and NIR dye were present through the FRET from polymer to dye in the original state. Upon exposure to reactive oxygen and nitrogen species (RONS), the FRET pair was interrupted, resulting in the enhancement of the 678 nm emission of CPNs and decrease of 818 nm emission of the NIR dye. With these ratiometric-responsive nanoparticles, Rao and coworkers demonstrated the real-time *in vivo* imaging of the RONS pool at inflammation sites in mice.

In order to solve the problem of the strong autofluorescence from living tissues under short-wavelength irradiation, Rao and coworkers also developed self-luminescing NIR-emissive CPNs for *in vivo* lymph-node mapping and tumor imaging [64]. As shown in Figure 3.13, an NIR dye, NIR775, was coprecipitated with MEP-PPV conjugated polymer to form NIR-emissive CPNs (RET1IR). Then, RET1IR was modified with Luc8, which emitted blue light at 480 nm upon addition of its substrate coelenterazine. Through the bioluminescence resonance energy transfer (BRET) and then followed by FRET, the NIR755 was irradiated to emit fluorescence in the NIR range. To target tumor tissues, a small peptide, RGD peptide, was coated onto the surface of nanoparticles to form RET2IR@cRGD. The fluorescence from *in vivo* imaging of the RET2IR@cRGD in mice indicated that the self-luminescing BRET-FRET NIR-emissive CPNs are promising for *in vivo* imaging applications, such as lymph-node mapping and tumor imaging.

3.4.2 Photoacoustic Imaging

CPNs show excellent fluorescent properties for both *in vitro* and *in vivo* imaging. However, fluorescence imaging suffers from the intrinsic limitations of poor spatial resolution and limited tissue penetration. In contrast, photoacoustic imaging modality, which is based on the photoacoustic effect upon optical excitation, can overcome the optical diffusion limit and provide deeper tissue imaging and higher spatial resolution. Therefore, many photoacoustic contrast agents, such as small-molecule dyes, inorganic nanoparticles, carbon nanotubes, and porphysomes, were developed for photoacoustic imaging. The great optical properties of CPNs also have been used for photoacoustic imaging [65]. Pu, Rao, and coworkers developed a series of photoacoustic probes based on semiconducting CPNs in the past decade [66–72]. For more details about the photoacoutics imaging using CPNs, please refer to the Chapter titled "π-Conjugated/Semiconducting Polymer Nanoparticles for Photoacoustic Imaging" authored by Dr Kaiyi Pu in this book.

3.4.3 Multimodality Imaging

The development of multimodality imaging contrast has attracted much attention because it can get more precise diagnosis information; the different modes of imaging also can compensate for each other to some extent. CPNs were used for the fabrication of the multimodal imaging agents. Taking advantage of the

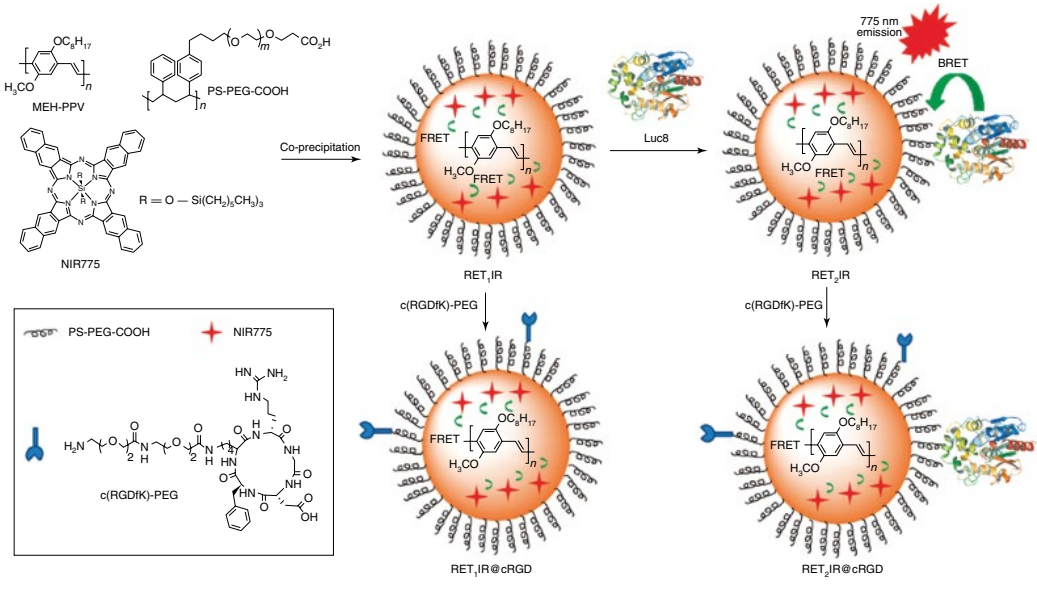

Figure 3.13 Schematic of self-luminescing BRET-FRET NIR-emissive CPNs for *in vivo* imaging. (Reprinted with permission from Ref. [64]. Copyright 2012, Nature Publishing Group.)

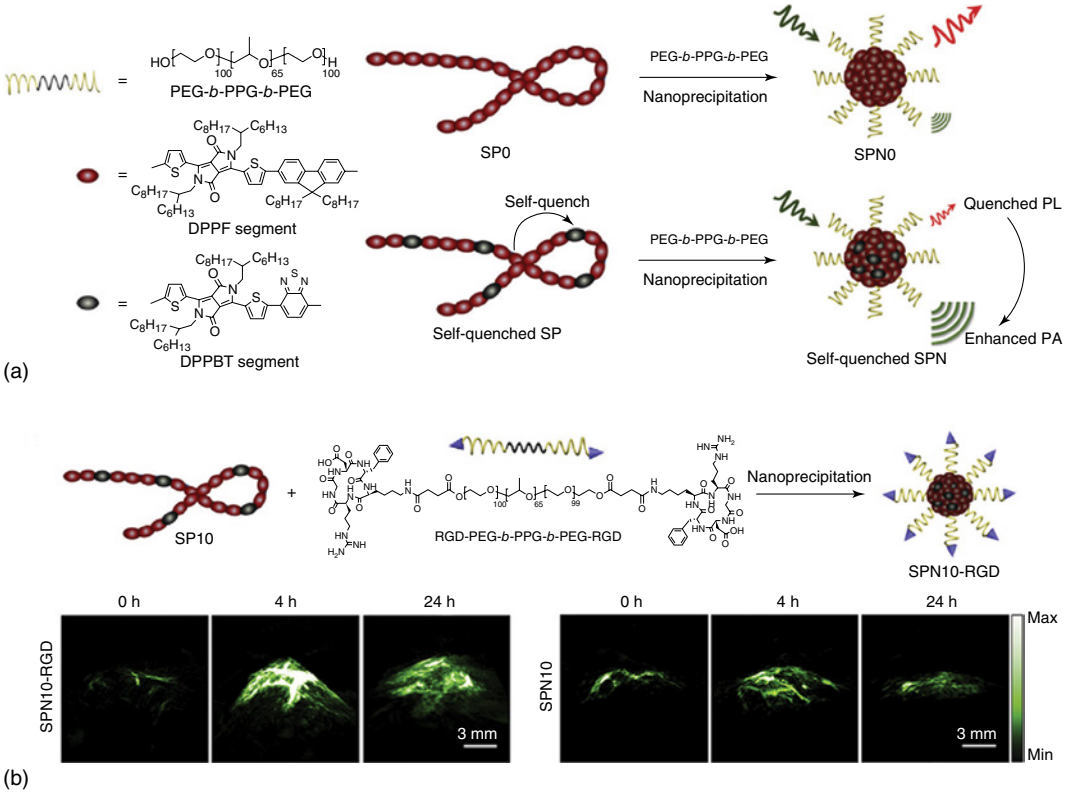

Figure 3.14 (a) Schematic illustration of the preparation of self-quenched CPNs through nanoprecipitation. (b) Bioconjugation of the RGD on the surface of the self-quenched CPNs and photoacoustic images of tumors after systemic injection of the self-quenched CPNs-RGD (SPN10-RGD) and the bare CPNs (SPN10). (Reprinted with permission from Ref. [70]. Copyright 2017, Elsevier Ltd.)

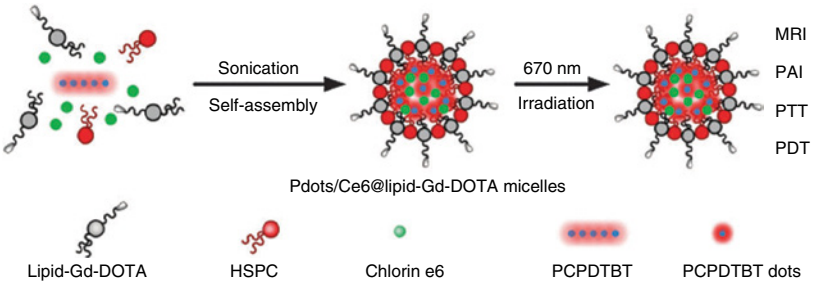

Figure 3.15 Schematic illustration of multifunctional theranostic CPNs for liver cancer diagnosis and therapy. (Reprinted with permission from Ref. [74]. Copyright 2015, Royal Society of Chemistry.)

intrinsic fluorescence and photoacoustic signals from the CPNs, Pu, Rao, and coworkers reported dual-mode fluorescence and photoacoustic imaging *in vivo* (Figure 3.14) [66].

CPNs also have been used for dual-mode fluorescence and magnetic resonance imaging (MRI). Green and coworkers prepared aqueous bifunctional CPNs using conjugated polymers, amphiphilic phospholipids, and a gadolinium-containing lipid for fluorescence and MRI [73]. The product was characterized with the fluorescence quantum yields, extinction coefficients, and MRI T_1-weighted relaxation times in water. After incubation with HeLa cells and murine macrophage-like J774 cells, the bifunctional CPNs showed excellent fluorescence imaging capacity by microscopy. However, the investigation of the MRI imaging ability of the CPNs in cells and *in vivo* was not done in this report. Liu and co-workers developed Pdots packaged in lipid micelles as a theranostic agent for liver-cancer imaging and therapy [74]. As shown in Figure 3.15, a lipid-Gd-DOTA as the MRI contrast agent, conjugated polymer (PCPDTBT), chlorine6 (Ce6) as photosensitizer, and HSPC were used to form multifunctional CPNs with sonication and self-assembly. Under the irradiation of a 670 nm laser, the CPNs could be used for fluorescence imaging, photoacoustic imaging, photodynamic therapy, and photothermal therapy for liver cancer imaging and therapy. The content of Gd in the CPNs allowed the usage for MRI. The results of this report indicated that the CPNs might be used as a promising theranostic agent for cancer diagnosis and therapy.

3.5 Conclusion

The chapter summarizes the development of CPNs over the past decade for molecular sensing and cellular imaging. CPNs exhibit excellent optical properties, such as high photostability, strong light-harvesting ability, low cytotoxicity, and high brightness. These properties have allowed their successful applications for biomedical analysis and imaging. Besides their excellent fluorescence properties, CPNs also were demonstrated to have superior capabilities in photoacoustic imaging over gold nanorods and carbon nanotubes. We hope this chapter will

help readers to understand the current advances in CPNs for molecular sensing and imaging, which in turn will help disseminate the use of CPNs in biology and medicine.

Acknowledgment

We gratefully acknowledge support from the National Institute of Health (CA186798), the Solid Tumor Translational Research of Fred Hutchinson Cancer Research Center, and the University of Washington.

References

1 Evanko, D. (2005) Focus on fluorescence imaging. *Nat. Methods*, **2**, 901.
2 Wu, C. and Chiu, D.T. (2013) Highly fluorescent semiconducting polymer dots for biology and medicine. *Angew. Chem. Int. Ed.*, **52**, 3086–3109.
3 Chan, Y.-H. and Wu, P.-J. (2015) Semiconducting polymer nanoparticles as fluorescent probes for biological imaging and sensing. *Part. Part. Syst. Charact.*, **32**, 11–28.
4 Wu, X., Wu, M., and Zhao, J.X. (2014) Recent development of silica nanoparticles as delivery vectors for cancer imaging and therapy. *Nanomed. Nanotechnol. Biol. Med.*, **10**, 297–312.
5 Lim, S.Y., Shen, W., and Gao, Z. (2015) Carbon quantum dots and their applications. *Chem. Soc. Rev.*, **44**, 362–381.
6 Kairdolf, B.A., Smith, A.M., Stokes, T.H., Wang, M.D., Young, A.N., and Nie, S. (2013) Semiconductor quantum dots for bioimaging and biodiagnostic applications. *Annu. Rev. Anal. Chem.*, **6**, 143–162.
7 Wolfbeis, O.S. (2015) An overview of nanoparticles commonly used in fluorescent bioimaging. *Chem. Soc. Rev.*, **44**, 4743–4768.
8 Zhou, J., Yang, Y., and Zhang, C.Y. (2015) Toward biocompatible semiconductor quantum dots: from biosynthesis and bioconjugation to biomedical application. *Chem. Rev.*, **115**, 11669–11717.
9 Caltagirone, C., Bettoschi, A., Garau, A., and Montis, R. (2015) Silica-based nanoparticles: a versatile tool for the development of efficient imaging agents. *Chem. Soc. Rev.*, **44**, 4645–4671.
10 Vivero-Escoto, J.L., Huxford-Phillips, R.C., and Lin, W. (2012) Silica-based nanoprobes for biomedical imaging and theranostic applications. *Chem. Soc. Rev.*, **41**, 2673–2685.
11 Zhou, J., Liu, Z., and Li, F. (2012) Upconversion nanophosphors for small-animal imaging. *Chem. Soc. Rev.*, **41**, 1323–1349.
12 Michalet, X., Pinaud, F.F., Bentolila, L.A., Tsay, J.M., Doose, S., Li, J.J. *et al.* (2005) Quantum dots for live cells, in vivo imaging, and diagnostics. *Science*, **307**, 538–544.
13 Gao, X., Cui, Y., Levenson, R.M., Chung, L.W., and Nie, S. (2004) In vivo cancer targeting and imaging with semiconductor quantum dots. *Nat. Biotechnol.*, **22**, 969–976.

14 Kim, S., Lim, C.K., Na, J., Lee, Y.D., Kim, K., Choi, K. *et al.* (2010) Conjugated polymer nanoparticles for biomedical in vivo imaging. *Chem. Commun.*, **46**, 1617–1619.

15 Jiang, Y. and McNeill, J. (2016) Light-harvesting and amplified energy transfer in conjugated polymer nanoparticles. *Chem. Rev.*, **117**, 838–859.

16 Pecher, J. and Mecking, S. (2010) Nanoparticles of conjugated polymers. *Chem. Rev.*, **110**, 6260–6279.

17 Zhu, C., Liu, L., Yang, Q., Lv, F., and Wang, S. (2012) Water-soluble conjugated polymers for imaging, diagnosis, and therapy. *Chem. Rev.*, **112**, 4687–4735.

18 Massey, M., Wu, M., Conroy, E.M., and Algar, W.R. (2015) Mind your P's and Q's: the coming of age of semiconducting polymer dots and semiconductor quantum dots in biological applications. *Curr. Opin. Biotechnol.*, **34**, 30–40.

19 Wu, C., Szymanski, C., Cain, Z., and McNeill, J. (2007) Conjugated polymer dots for multiphoton fluorescence imaging. *J. Am. Chem. Soc.*, **129**, 12904–12905.

20 Wu, C., Bull, B., Szymanski, C., Christensen, K., and McNeill, J. (2008) Multicolor conjugated polymer dots for biological fluorescence imaging. *ACS Nano*, **2**, 2415–2423.

21 Kaeser, A. and Schenning, A.P. (2010) Fluorescent nanoparticles based on self-assembled pi-conjugated systems. *Adv. Mater.*, **22**, 2985–2997.

22 Peng, H.S. and Chiu, D.T. (2014) Soft fluorescent nanomaterials for biological and biomedical imaging. *Chem. Soc. Rev.*, **44**, 4699–4722.

23 Feng, L., Zhu, C., Yuan, H., Liu, L., Lv, F., and Wang, S. (2013) Conjugated polymer nanoparticles: preparation, properties, functionalization and biological applications. *Chem. Soc. Rev.*, **42**, 6620–6633.

24 Yu, J., Wu, C., Zhang, X., Ye, F., Gallina, M.E., Rong, Y. *et al.* (2012) Stable functionalization of small semiconducting polymer dots via covalent cross-linking and their application for specific cellular imaging. *Adv. Mater.*, **24**, 3498–3504.

25 Sun, W., Yu, J., Deng, R., Rong, Y., Fujimoto, B., Wu, C. *et al.* (2013) Semiconducting polymer dots doped with europium complexes showing ultranarrow emission and long luminescence lifetime for time-gated cellular imaging. *Angew. Chem. Int. Ed.*, **52**, 11294–11297.

26 Chong, H., Nie, C., Zhu, C., Yang, Q., Liu, L., Lv, F. *et al.* (2012) Conjugated polymer nanoparticles for light-activated anticancer and antibacterial activity with imaging capability. *Langmuir*, **28**, 2091–2098.

27 Li, K., Liu, Y., Pu, K.-Y., Feng, S.-S., Zhan, R., and Liu, B. (2011) Polyhedral oligomeric silsesquioxanes-containing conjugated polymer loaded PLGA nanoparticles with trastuzumab (Herceptin) functionalization for HER2-positive cancer cell detection. *Adv. Funct. Mater.*, **21**, 287–294.

28 Howes, P., Green, M., Levitt, J., Suhling, K., and Hughes, M. (2010) Phospholipid encapsulated semiconducting polymer nanoparticles: their use in cell imaging and protein attachment. *J. Am. Chem. Soc.*, **132**, 3989–3996.

29 Rong, Y., Wu, C., Yu, J., Zhang, X., Ye, F., Zeigler, M. *et al.* (2013) Multicolor fluorescent semiconducting polymer dots with narrow emissions and high brightness. *ACS Nano*, **7**, 376–384.

30 Wu, C., Schneider, T., Zeigler, M., Yu, J., Schiro, P.G., Burnham, D.R. *et al.* (2010) Bioconjugation of ultrabright semiconducting polymer dots for specific cellular targeting. *J. Am. Chem. Soc.*, **132**, 15410–15417.

31 Wu, C., Hansen, S.J., Hou, Q., Yu, J., Zeigler, M., Jin, Y. *et al.* (2011) Design of highly emissive polymer dot bioconjugates for in vivo tumor targeting. *Angew. Chem. Int. Ed.*, **50**, 3430–3434.

32 Jin, Y., Ye, F., Zeigler, M., Wu, C., and Chiu, D.T. (2011) Near-infrared fluorescent dye-doped semiconducting polymer dots. *ACS Nano*, **5**, 1468–1475.

33 Wu, I., Yu, J., Ye, F., Rong, Y., Gallina, M.E., Fujimoto, B.S. *et al.* (2014) Squaraine-based polymer dots with narrow, bright near-infrared fluorescence for biological applications. *J. Am. Chem. Soc.*, **137**, 173–178.

34 Zhang, X., Yu, J., Wu, C., Jin, Y., Rong, Y., Ye, F. *et al.* (2012) Importance of having low-density functional groups for generating high-performance semiconducting polymer dots. *ACS Nano*, **6**, 5429–5439.

35 Ye, F., Wu, C., Jin, Y., Wang, M., Chan, Y.H., Yu, J. *et al.* (2012) A compact and highly fluorescent orange-emitting polymer dot for specific subcellular imaging. *Chem. Commun.*, **48**, 1778–1780.

36 Jin, Y., Ye, F., Wu, C., Chan, Y.H., and Chiu, D.T. (2012) Generation of functionalized and robust semiconducting polymer dots with polyelectrolytes. *Chem. Commun.*, **48**, 3161–3163.

37 Wu, C., Jin, Y., Schneider, T., Burnham, D.R., Smith, P.B., and Chiu, D.T. (2010) Ultrabright and bioorthogonal labeling of cellular targets using semiconducting polymer dots and click chemistry. *Angew. Chem. Int. Ed.*, **49**, 9436–9440.

38 Wu, C., Szymanski, C., and McNeill, J. (2006) Preparation and encapsulation of highly fluorescent conjugated polymer nanoparticles. *Langmuir*, **22**, 2956–2960.

39 Chan, Y.H., Jin, Y., Wu, C., and Chiu, D.T. (2011) Copper(II) and iron(II) ion sensing with semiconducting polymer dots. *Chem. Commun.*, **47**, 2820–2822.

40 Feng, L., Guo, L., and Wang, X. (2017) Preparation, properties and applications in cell imaging and ions detection of conjugated polymer nanoparticles with alcoxyl bonding fluorene core. *Biosens. Bioelectron.*, **87**, 514–521.

41 Childress, E.S., Roberts, C.A., Sherwood, D.Y., LeGuyader, C.L., and Harbron, E.J. (2012) Ratiometric fluorescence detection of mercury ions in water by conjugated polymer nanoparticles. *Anal. Chem.*, **84**, 1235–1239.

42 Kuo, S.Y., Li, H.H., Wu, P.J., Chen, C.P., Huang, Y.C., and Chan, Y.H. (2015) Dual colorimetric and fluorescent sensor based on semiconducting polymer dots for ratiometric detection of lead ions in living cells. *Anal. Chem.*, **87**, 4765–4771.

43 Wu, C., Bull, B., Christensen, K., and McNeill, J. (2009) Ratiometric single-nanoparticle oxygen sensors for biological imaging. *Angew. Chem. Int. Ed.*, **48**, 2741–2745.

44 Sun, K., Tang, Y., Li, Q., Yin, S., Qin, W., Yu, J. *et al.* (2016) In vivo dynamic monitoring of small molecules with implantable polymer-dot transducer. *ACS Nano*, **10**, 6769–6781.

45 Zhao, Q., Zhou, X., Cao, T., Zhang, K.Y., Yang, L., Liu, S. *et al.* (2015) Fluorescent/phosphorescent dual-emissive conjugated polymer dots for hypoxia bioimaging. *Chem. Sci.*, **6**, 1825–1831.

46 Zhang, Y., Pang, L., Ma, C., Tu, Q., Zhang, R., Saeed, E. *et al.* (2014) Small molecule-initiated light-activated semiconducting polymer dots: an integrated

nanoplatform for targeted photodynamic therapy and imaging of cancer cells. *Anal. Chem.*, **86**, 3092–3099.

47 Zhen, X., Zhang, C., Xie, C., Miao, Q., Lim, K.L., and Pu, K. (2016) Intraparticle energy level alignment of semiconducting polymer nanoparticles to amplify chemiluminescence for ultrasensitive in vivo imaging of reactive oxygen species. *ACS Nano*, **10**, 6400–6409.

48 Li, P., Liu, L., Xiao, H., Zhang, W., Wang, L., and Tang, B. (2016) A new polymer nanoprobe based on chemiluminescence resonance energy transfer (CRET) for ultrasensitive imaging of intrinsic superoxide anion in mice. *J. Am. Chem. Soc.*, **138**, 2893–2896.

49 Chan, Y.H., Wu, C., Ye, F., Jin, Y., Smith, P.B., and Chiu, D.T. (2011) Development of ultrabright semiconducting polymer dots for ratiometric pH sensing. *Anal. Chem.*, **83**, 1448–1455.

50 Ye, F., Wu, C., Jin, Y., Chan, Y.H., Zhang, X., and Chiu, D.T. (2011) Ratiometric temperature sensing with semiconducting polymer dots. *J. Am. Chem. Soc.*, **133**, 8146–8149.

51 Moon, J.H., MacLean, P., McDaniel, W., and Hancock, L.F. (2007) Conjugated polymer nanoparticles for biochemical protein kinase assay. *Chem. Commun.*, **14**, 4910–4912.

52 Cordovilla, C. and Swager, T.M. (2012) Strain release in organic photonic nanoparticles for protease sensing. *J. Am. Chem. Soc.*, **134**, 6932–6935.

53 Lin, Z., Zhang, G., Yang, W., Qiu, B., and Chen, G. (2012) CEA fluorescence biosensor based on the FRET between polymer dots and Au nanoparticles. *Chem. Commun.*, **48**, 9918–9920.

54 Yang, W., Zhang, G., Weng, W., Qiu, B., Guo, L., Lin, Z. *et al.* (2014) Signal on fluorescence biosensor for MMP-2 based on FRET between semiconducting polymer dots and a metal organic framework. *RSC Adv.*, **4**, 58852–58857.

55 Lu, Q., Zhang, J., Wu, Y., and Chen, S. (2015) Conjugated polymer dots/oxalate anodic electrochemiluminescence system and its application for detecting melamine. *RSC Adv.*, **5**, 63650–63654.

56 Huang, J., Gu, J., Meng, Z., Jia, X., and Xi, K. (2015) Signal enhancement of sensing nitroaromatics based on highly sensitive polymer dots. *Nanoscale*, **7**, 15413–15420.

57 Zhao, Q., Zhang, C., Liu, S., Liu, Y., Zhang, K.Y., Zhou, X. *et al.* (2015) Dual-emissive polymer dots for rapid detection of fluoride in pure water and biological systems with improved reliability and accuracy. *Sci. Rep.*, **5**, 16420.

58 Huang, Y.-C., Chen, C.-P., Wu, P.-J., Kuo, S.-Y., and Chan, Y.-H. (2014) Coumarin dye-embedded semiconducting polymer dots for ratiometric sensing of fluoride ions in aqueous solution and bio-imaging in cells. *J. Mater. Chem. B*, **2**, 6188–6191.

59 Tang, H., Xing, C., Liu, L., Yang, Q., and Wang, S. (2011) Synthesis of amphiphilic polythiophene for cell imaging and monitoring the cellular distribution of a cisplatin anticancer drug. *Small*, **7**, 1464–1470.

60 Li, K., Pan, J., Feng, S.-S., Wu, A.W., Pu, K.-Y., Liu, Y. *et al.* (2009) Generic strategy of preparing fluorescent conjugated-polymer-loaded poly(dl-lactide-*co*-glycolide) nanoparticles for targeted cell imaging. *Adv. Funct. Mater.*, **19**, 3535–3542.

61 Zhang, X., Yu, J., Rong, Y., Ye, F., Chiu, D.T., and Uvdal, K. (2013) High-intensity near-IR fluorescence in semiconducting polymer dots achieved by cascade FRET strategy. *Chem. Sci.*, **4**, 2143–2151.

62 Shuhendler, A.J., Pu, K., Cui, L., Uetrecht, J.P., and Rao, J. (2014) Real-time imaging of oxidative and nitrosative stress in the liver of live animals for drug-toxicity testing. *Nat. Biotechnol.*, **32**, 373–380.

63 Pu, K., Shuhendler, A.J., and Rao, J. (2013) Semiconducting polymer nanoprobe for in vivo imaging of reactive oxygen and nitrogen species. *Angew. Chem. Int. Ed.*, **52**, 10325–10329.

64 Xiong, L., Shuhendler, A.J., and Rao, J. (2012) Self-luminescing BRET–FRET near-infrared dots for in vivo lymph-node mapping and tumour imaging. *Nat. Commun.*, **3**, 1193.

65 Pu, K., Chattopadhyay, N., and Rao, J. (2016) Recent advances of semiconducting polymer nanoparticles in in vivo molecular imaging. *J. Controlled Release*, **240**, 312–322.

66 Pu, K., Shuhendler, A.J., Jokerst, J.V., Mei, J., Gambhir, S.S., Bao, Z. *et al.* (2014) Semiconducting polymer nanoparticles as photoacoustic molecular imaging probes in living mice. *Nat. Nanotechnol.*, **9**, 233–239.

67 Xie, C., Zhen, X., Lei, Q., Ni, R., and Pu, K. (2017) Self-assembly of semiconducting polymer amphiphiles for in vivo photoacoustic imaging. *Adv. Funct. Mater.*, DOI: 10.1002/adfm.201605397

68 Lyu, Y., Zhen, X., Miao, Y., and Pu, K. (2017) Reaction-based semiconducting polymer nanoprobes for photoacoustic imaging of protein sulfenic acids. *ACS Nano*, **11**, 358–367.

69 Zhang, J., Zhen, X., Upputuri, P.K., Pramanik, M., Chen, P., and Pu, K. (2016) Activatable photoacoustic nanoprobes for in vivo ratiometric imaging of peroxynitrite. *Adv. Mater.*, **29**, 1–8.

70 Xie, C., Upputuri, P.K., Zhen, X., Pramanik, M., and Pu, K. (2017) Self-quenched semiconducting polymer nanoparticles for amplified in vivo photoacoustic imaging. *Biomaterials*, **119**, 1–8.

71 Pu, K., Mei, J., Jokerst, J.V., Hong, G., Antaris, A.L., Chattopadhyay, N. *et al.* (2015) Diketopyrrolopyrrole-based semiconducting polymer nanoparticles for in vivo photoacoustic imaging. *Adv. Mater.*, **27**, 5184–5190.

72 Miao, Q., Lyu, Y., Ding, D., and Pu, K. (2016) Semiconducting oligomer nanoparticles as an activatable photoacoustic probe with amplified brightness for in vivo imaging of pH. *Adv. Mater.*, **28**, 3662–3668.

73 Hashim, Z., Green, M., Chung, P.H., Suhling, K., Protti, A., Phinikaridou, A. *et al.* (2014) Gd-containing conjugated polymer nanoparticles: bimodal nanoparticles for fluorescence and MRI imaging. *Nanoscale*, **6**, 8376–8386.

74 Zhang, D., Wu, M., Zeng, Y., Liao, N., Cai, Z., Liu, G. *et al.* (2015) Lipid micelles packaged with semiconducting polymer dots as simultaneous MRI/photoacoustic imaging and photodynamic/photothermal dual-modal therapeutic agents for liver cancer. *J. Mater. Chem. B.*, **4**, 589–599.

4

Conjugated Polymers for *In Vivo* Fluorescence Imaging

Jun Li and Dan Ding

Nankai University, State Key Laboratory of Medicinal Chemical Biology, Key Laboratory of Bioactive Materials, Ministry of Education, and College of Life Sciences, 94 Weijin Road, Tianjin, 300071, China

4.1 Introduction

The emergence of *in vivo* molecular imaging probes has provided scientists and clinicians with vital information on the occurrence and development of diseases, guidance of the choices of therapy methods, and estimation of prognosis as well as evaluation of treatment effects of therapeutic agents [1–3]. In recent years, a variety of *in vivo* imaging modalities including fluorescence imaging [4], magnetic resonance imaging (MRI) [5], photoacoustic imaging [6], X-ray computed tomography (X-CT) [7], positron emission tomography (PET) [8], and single photon emission computing tomography (SPECT) [9] have been extensively investigated for the purpose of diagnostics and therapeutics of diseases. Among them, fluorescence imaging technique with superb sensitivity, excellent temporal resolution, low cost, and high safety shows unique merits in sensitive biosensing and high-contrast bioimaging *in vivo* [10]. Compared with other imaging modalities, fluorescence imaging also requires less resources and space [11]. In particular, near-infrared (NIR) light (>700 nm) has been receiving increasing attention as it allows for *in vivo* bioimaging with minimum background fluorescence, low interferential absorption, and deep tissue permeability [12]. Very recently, NIR fluorescence has been utilized for clinical image-guided cancer surgery, which holds great promise for improving cancer surgery outcomes [13]. So far, there have been many fluorescent materials such as organic fluorophores, lanthanide derivatives, carbon nanotubes, and inorganic semiconducting quantum dots (QDs) widely exploited for fabrication of *in vivo* fluorescence imaging probes [14–16]. Each material, however, suffers its own limitations, such as aggregation-caused quenching effect, low quantum yield (QY), poor photobleaching resistance, high cytotoxicity, or long-term retention in the body [17–19]. These disadvantages of conventional fluorescent materials greatly limit their practical biological applications. Exploration of alternative ones with improved properties is thus highly desirable.

Conjugated Polymers for Biological and Biomedical Applications, First Edition. Edited by Bin Liu

Conjugated polymers (CPs), that are macromolecules with π-conjugated backbones, have been widely accepted as a novel class of fluorescent materials [20–22]. As compared to conventional fluorescent materials, CPs show the combined advantages of high extinction coefficients, intense brightness, large photobleaching threshold as well as low cytotoxicity and *in vivo* toxicity [23]. Besides, the electronic characteristics of the π-delocalized backbones of CPs benefit a combination of large optical cross-section with facile inter-/intrachain excitation transfer, thus allowing for biosensing with outstanding sensitivity and minimal limit of detection [24]. Generally, CPs are hydrophobic, and thus achieving *in vivo* applications requires significant improvement of their water solubility. There have been two approaches employed for this purpose to date. One is to formulate CPs into nanoparticles (CP NPs, also referred as CP dots) by using versatile nanoengineering methods and biocompatible amphiphilic molecules as the doping matrix [25]. The other is to form conjugated polyelectrolytes (CPEs) via covalently linking charged or hydrophilic side chains to the CP backbone [26]. Since 2010, CP dots and CPEs have been largely investigated as fluorescent probes for *in vivo* bioimaging [27–29], and they exhibit intrinsic advantages over the ones based on conventional fluorescent materials. For example, the emission of CP dots has been demonstrated to be magnitudes higher than that of small-molecule organic dyes as well as tens of times larger when compared with inorganic QDs [30]. Furthermore, many studies have confirmed and highlighted the superb photostability and biostability of CP-based fluorescent probes, which are not susceptible to the overexpressed bioactive molecules in the disease tissues, such as enzymes and immune cell-secreting reactive oxygen species (ROS) [6, 31].

In this chapter, the recent progress in the development of CP-based fluorescent probes applied for *in vivo* bioimaging will be systematically summarized. As there is a vast amount of successful studies on the *in vivo* fluorescence imaging of CP-based probes, we have divided them into six parts, including *in vivo* fluorescence imaging of tumors, stimuli-responsive fluorescence imaging, *in vivo* fluorescence cell tracking, two-photon excited brain vascular imaging, dual-modality imaging of tumors *in vivo*, as well as other *in vivo* fluorescence imaging applications. Finally, a short outlook of the CP-based *in vivo* fluorescent probes in the future is given.

4.2 *In Vivo* Fluorescence Imaging of Tumors

The research on the fluorescent probes for *in vivo* tumor imaging has attracted considerable interest, as fluorescence imaging technique benefits cancer diagnosis and tumor-removal surgery in terms of extremely high sensitivity, single-cell resolution, and use of portable instruments [32]. Additionally, nanotechnology has been well accepted to advance the field of cancer diagnosis and treatment [33]. Because of the fenestrations (about 200–400 nm) of tumor vasculature associated with the rapid growth of tumor mass, the nano-sized materials (nanomaterials) can preferentially enter the tumors. On the other hand, the lack of lymphatic drainage in tumor tissues leads to decreased clearance of macromolecules (>40 kDa), which is beneficial to long-term retention of

nanomaterials within tumors. The aforementioned two physiologic signatures of tumors are together termed the enhanced permeability and retention (EPR) effect", also known as the passive tumor targeting of nanomaterials [34]. Besides, the facile surface functionalization with various active targeting ligands (folic acid (FA) and RGD peptide, etc.) makes the nanomaterials actively target tumor mass, further enhancing their tumor enrichment on the basis of EPR effect [35].

Noteworthy, NIR fluorescent CP dots that combine the advantages of CPs, NIR light, and nanotechnology have been considered to be ideal fluorescent probes for *in vivo* detection and visualization of tumors. To realize NIR fluorescence of CP, Liu and coworkers incorporated two narrow band gap monomers, 2,1,3-benzothiadiazole (BT) and 4,7-di(thiophen-2-yl)-2,1,3-benzothiadiazole (DBT) into the conjugated backbone of poly(9,9-dihexylfluorene), which afforded poly[(9,9-dihexylfluorene)-*co*-2,1,3-benzothiadiazole-*co*-4,7-di(thiophen-2-yl)-2,1,3-benzothiadiazole] (PFBTDBT10) [36]. As shown in Figure 4.1a, the energy donor rendered PFBTDBT10 with an absorption maximum at about 470 nm upon formulation into CP dots. For energy acceptor, the DBT concentration was chosen at 10 mol% to guarantee complete energy transfer from energy donor to energy acceptor segments, thus achieving intense NIR fluorescence. Moreover, the low concentration of narrower band gap monomer DBT was also beneficial to significantly inhibit aggregation-caused quenching of CP emission. Subsequent formulation of PFBTDBT10 using 1,2-distearoyl-*sn*-glycero-3-phosphoethanolamine-*N*-[methoxy(polyethylene glycol)-2000] (DSPE-PEG_{2000}) as the encapsulation matrix yielded PFBTDBT10-based CP dots (Figure 4.1b), which were spherical in shape with a mean hydrodynamic diameter of around 80 nm. By virtue of the rational molecular design of PFBTDBT10, the CP dots showed an emission peaked at 698 nm and a QY as high as 0.27 in water (Figure 4.1c). This value of QY was much higher than that of commercial QD655 in water (0.15). *In vivo* experiments revealed that the PFBTDBT10-based CP dots possessed negligible *in vivo* toxicity, relatively long *in vivo* blood circulation half-life (about 1.8 h) and good tumor passive targeting ability via EPR effect post intravenous injection of CP dots (Figure 4.1d). Noteworthy, when the CP dots were surface functionalized with an active targeting ligand, FA (Figure 4.1b), more CP-FA dots could be enriched in the tumor mass after intravenous administration due to the folate receptor-mediated active targeting effect (Figure 4.1d). Besides tumors, the intravenously injected CP dots and CP-FA dots were also significantly accumulated into reticuloendothelial system (RES) organs such as liver and spleen (Figure 4.1e). As a consequence, the bright NIR fluorescence as well as prominent passive and active targeting capability made CP-FA dots a very promising fluorescent probe for *in vivo* cancer diagnosis.

For another example, Chiu and coworkers reported a bright CP dot by coencapsulating energy donor and acceptor CPs with poly(styrene-*co*-maleic anhydride) (PSMA) as the encapsulation matrix [37]. A visible light-harvesting CP, poly[(9,9-dioctylfluorenyl-2,7-diyl)-*co*-(1,4-benzo-{2,1′,3}-thiadiazole)] (PFBT) and a far-red/NIR (FR/NIR) emitting CP (PF-DBT5) were selected as the energy donor and acceptor polymers, respectively (Figure 4.2a). At a blending ratio of 0.6 (PF-DBT5/PFBT in weight), effective intraparticle energy transfer occurred within the CP dot, as evidenced by the complete fluorescence quenching of the

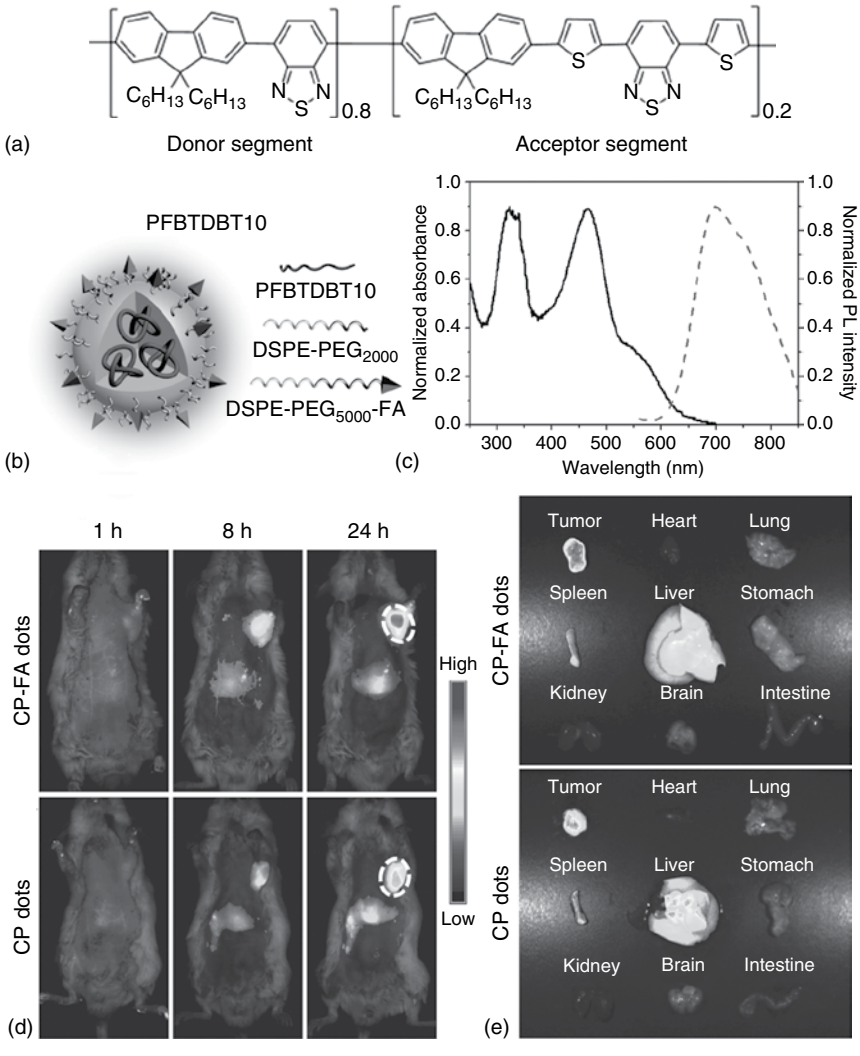

Figure 4.1 (a) Chemical structure of PFBTDBT10. (b) Schematic illustration of CP-FA dot. (c) Normalized UV–vis absorption (solid) and emission spectra (dashed) of CP dots in water (excited at 465 nm). (d) *In vivo* fluorescence imaging of H22 tumor-bearing mice at different time points after intravenous injection of CP-FA dots and CP dots, respectively. The tumor-bearing mouse model was established by subcutaneous inoculating murine hepatic H22 cancer cells into the mouse left axillary space. The white circles indicated the tumor mass. (e) *Ex vivo* fluorescence imaging of various mouse tissues at 24 h post intravenous injection of CP-FA dots and CP dots, respectively. (Adapted with permission from Ref. [36]. Copyright 2013, Wiley-VCH Verlag GmbH & Co. KGaA.)

PFBT donor and large fluorescence rise of PF-DBT5 acceptor. As a result, the CP dots displayed a QY as high as 0.56 with an emission peaked at about 650 nm and an absorption band extending to 600 nm (Figure 4.2b). To enable efficient *in vivo* tumor imaging, the CP dots were next surface functionalized with PEG and chlorotoxin (CTX) (Figure 4.2a). The CP dots were coated with PEG in order to

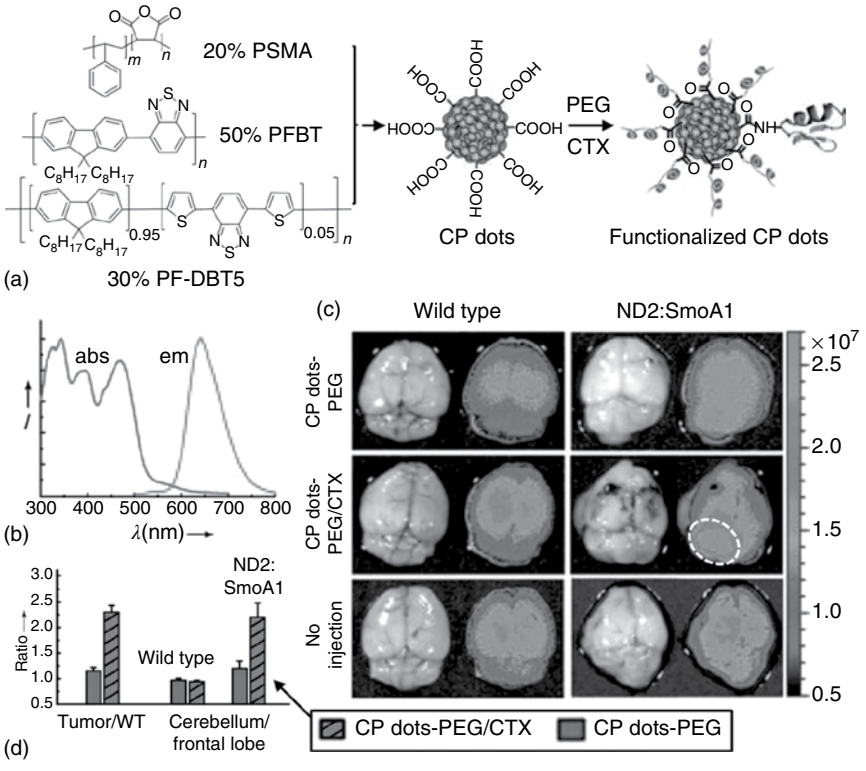

Figure 4.2 (a) Chemical structures of PSMA, PFBT, and PF-DBT5 as well as schematic illustration of formation of functionalized CP dots (CP dots-PEG/CTX). (b) UV–vis absorption and emission spectra of the CP dots. (c) *Ex vivo* fluorescence imaging of healthy brains in wild type mice and medulloblastoma tumors in ND2:SmoA1 mice at 72 h post intravenous administration of CP dots-PEG/CTX or CP dots surface functionalized with only PEG (CP dots-PEG). The white circle indicates the tumor site. (d) Tumor targeting efficiency by quantification of the fluorescence intensities in ND2:SmoA1 versus wild type mice and cerebellum versus frontal lobe. (Adapted with permission from Ref. [37]. Copyright 2011, Wiley-VCH Verlag GmbH & Co. KGaA.)

reduce the protein adsorption in blood and thus increase the blood circulation time of CP dots. On the other hand, CTX that is a 36-amino acid peptide can tightly bind to the tumors of neuroectodermal origin, endowing CP dots with good active tumor-targeting ability. The transmission electron microscopy (TEM) observation indicated the particle-like shape of the functionalized CP dots with a mean size of around 15 nm. *In vivo* studies using an *in situ* brain tumor mouse model (namely ND2:SmoA1) suggested that the CP dots functionalized with both PEG and CTX (CP dots-PEG/CTX) were able to traverse the blood–brain barrier and specifically target the malignant brain tumors (Figure 4.2c), and that CTX played a vital role in detecting brain tumor in the cerebellum in a sensitive and high-contrast manner (Figure 4.2d). Besides the aforementioned two examples, to date, there have also been many successfull studies on CP dots or CPEs utilized for *in vivo* fluorescence imaging of tumors

[38–44], indicating that they can serve as advanced fluorescent probes for *in vivo* cancer diagnosis.

4.3 Stimuli-Responsive Fluorescence Imaging

Development of intelligent fluorescent probes that can respond to stimuli in disease microenvironments is particularly valuable as they allow for conspicuous and specific *in vivo* disease detection with large signal-to-noise ratio [45, 46]. Owing to the ascendant optical properties, CPs have been extensively used as fluorescent components to design and fabricate stimuli-responsive fluorescent probes. So far, a large number of CP-based fluorescence turn-on probes and ratiometric fluorescent probes have been reported for *in vivo* bioimaging applications, whose fluorescence could specifically light up or alter when triggered by ROS, oxygen, hypoxia, or light, and so on [47–53]. For instance, Rao and coworkers developed a CP-based ratiometric fluorescent nanoprobe for imaging of ROS in inflammatory microenvironments *in vivo* [47]. As displayed in Figure 4.3a, the CP-based nanoprobe (namely NanoDRONE) was prepared by using DSPE-PEG_{2000} to encapsulate a CP, PCFDP ([9,9′-dihexyl-2,7-bis(1-cyanovinylene)fluorenylene-*alt-co*-2,5-bis(*N*,*N*′-diphenylamino)-1,4-phenylene]), which was followed by surface modification of a cyanine dye derivative IR775COOH in order to realize fluorescence resonance energy transfer (FRET) between PCFDP and IR775COOH. The NanoDRONE had a spherical morphology with a hydrodynamic diameter of about 78 nm.

The UV–vis spectra indicated that PCFDP-encapsulated NPs without modification of IR775COOH (PCFDP NPs) had an absorption maximum at 410 nm, whereas NanoDRONE possessed two absorption peaks at 410 and 788 nm (Figure 4.3b). The absorption peak at 788 nm belonged to IR775COOH. The photoluminescence (PL) spectra as displayed in Figure 4.3c revealed that PCFDP NPs had an emission peaked at 678 nm; nevertheless, upon excitation of PCFDP at 410 nm, NanoDRONE had two emission peaks at 678 and 818 nm, corresponding to the PCFDP and IR775COOH, respectively. Noteworthy, as compared to PCFDP NPs, the PCFDP emission centered at 678 nm within NanoDRONE greatly reduced for about six times, verifying the effective FRET from the PCFDP core to IR775COOH on the NP surface (Figure 4.3c). In this work, the most important reason why PCFDP was selected as the energy donor of NanoDRONE was that the PCFDP fluorescence was highly stable to ROS. Taking ClO^-, one of the most oxidative ROS for example, as depicted in Figure 4.3d, the emission of PCFDP NPs only slightly decreased in the presence of ClO^- (14 μM), which showed far better performance in resistance to ClO^- than Cy5.5 and QD655. This result manifested that PCFDP was an inert energy donor, allowing for precise ratiometric imaging and sensing of ROS. On the other hand, IR775COOH was well known to be easily degraded by ROS oxidation. Therefore, when NanoDRONE met ROS, such as $ONOO^-$, the rapid oxidation-induced degradation of surface IR775COOH revoked FRET accompanied with the fluorescence recovery of the PCFDP core (Figure 4.3e). NanoDRONE could respond to several ROS, including $ONOO^-$, ClO^-, and ·OH, with rather low limit of detection of

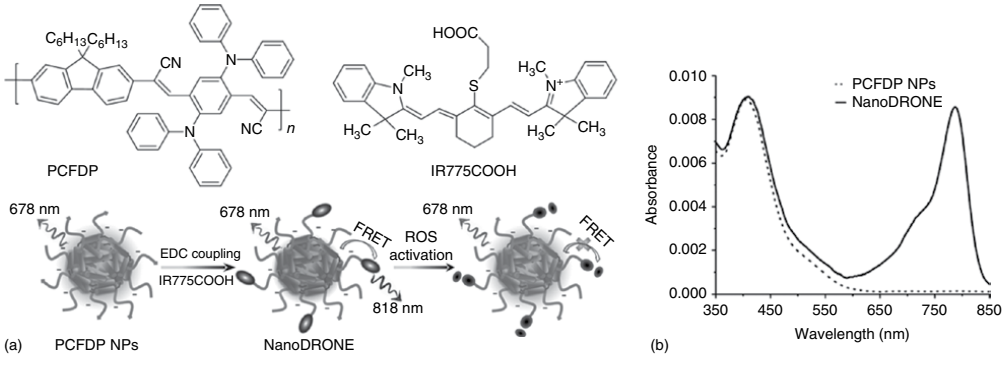

Figure 4.3 (a) Chemical structures of PCFDP and IR755COOH as well as schematic illustration of the PCFDP NPs and NanoDRONE formation and the ROS sensing. (b) UV–vis absorption and (c) emission spectra of PCFDP NPs and NanoDRONE in PBS buffer. (d) Fluorescence changes of PCFDP NPs, QD655, and Cy5.5 at 678, 655, and 693 nm, respectively, when addition of different concentrations of ClO^- in PBS. [PCFDP NPs] = [Cy5.5] = 1.0 μg; [QD655] = 20 μM. Excitation: 405 nm for PCFDP NPs; 500 nm for QD655; 630 nm for Cy5.5. (e) PL spectra of NanoDRONE in PBS buffer with and without addition of $ONOO^-$ at concentrations of 0.1, 0.2, 0.3, 0.4, and 0.5 μM, respectively. (f) Fluorescence changes of NanoDRONE (0.1 μg ml^{-1}) in the presence of various ROS in nitrogen-purged PBS. F and F_0 stood for the PL intensities at 678 nm with and without addition of 1 μM of ROS. Excitation at 405 nm. (g) *In vivo* fluorescence imaging of ROS using NanoDRONE in LPS-induced peritonitis-bearing mice. LPS was intraperitoneally administrated into the mice to establish the peritonitis-bearing mouse model. As a control, saline was also intraperitoneally injected into another group of mice. (h) Quantitative analysis of the fluorescence signals in the peritoneal cavity based on the imaging in (g). * represented $P < 0.05$ between the two groups. (Adapted with permission from Ref. [47]. Copyright 2013, Wiley-VCH Verlag GmbH & Co. KGaA.)

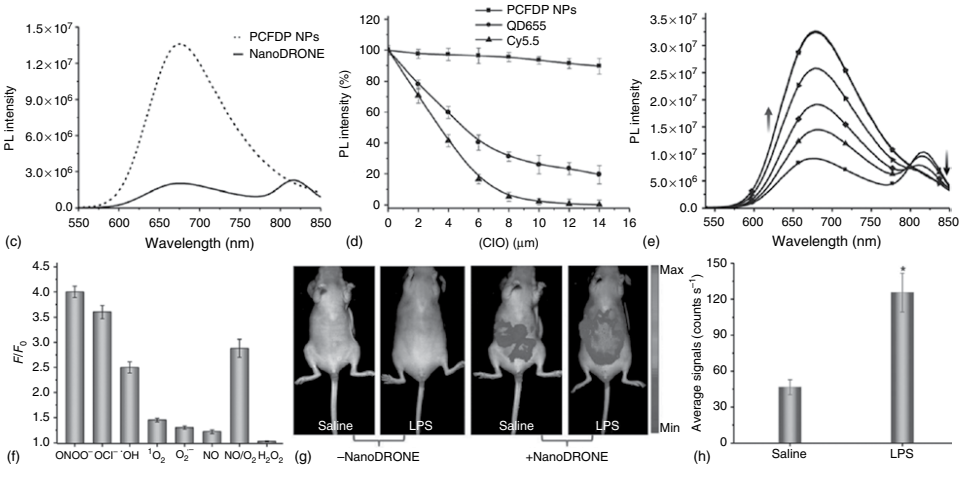

Figure 4.3 (*Continued*)

around 10 nM (Figure 4.3f). Bacterial cell wall lipopolysaccharide (LPS)-induced peritonitis-bearing mouse model was established to investigate the application of NanoDRONE in imaging ROS in live animals. Inflammatory mouse model was chosen because immune cells such as neutrophils and macrophages tended to move toward the inflammation site, followed by stimulating release of various ROS. After intraperitoneal injection of NanoDRONE into the peritonitis-bearing mice for 30 min, the fluorescence of PCFDP within NanoDRONE significantly recovered and was detected by the *in vivo* fluorescence imaging instrument. Such fluorescence at the abdomen site of peritonitis-bearing mice was much brighter than that of NanoDRONE-injected healthy mice (Figure 4.3g,h). Furthermore, intravenous administration of NanoDRONE also allowed for ratiometric fluorescence imaging of ROS with time-dependent fluorescence elevation of PCFDP and the concurrent loss of IR775COOH emission in the inflammation regions induced by bacterial infection. As a consequence, CPs hold an important advantage of high stability toward ROS, making them ideal fluorescent materials to construct smart probes for accurate *in vivo* diagnosis of endogenous ROS-associated diseases.

4.4 *In Vivo* Fluorescence Cell Tracking

Continuous and accurate *in vivo* cell tracking over a long period of time is of great significance for observing cell proliferation, migration and homing, estimation of therapeutic effect of functional cells as well as understanding cell-regenerative capability [10, 54]. Especially for stem cells, which can differentiate into specialized cells and secrete cytokines for disease treatment, their *in vivo* tracking in a long-term and accurate manner is still challenging [55]. Currently, reporter gene labeling and exogenous contrast agent labeling are the two main approaches for *in vivo* cell tracking [56]. Although the reporter gene labeling method is well accepted to be able to provide precise and quantitative information on the fate of stem cells [57], such gene transfection-based approach is hard to implement clinically. Thereby, the exogenous contrast agent labeling method has received increasing attention [58]. In recent years, iron oxide NPs have been mostly used as an exogenous agent to label different functional cells and subsequently track them *in vivo* by taking advantage of MRI [59]. However, iron oxide NPs were reported to be facilely leaky from the cells [60] and MRI modality suffers from low sensitivity to its contrast agents [61]. Therefore, a highly sensitive imaging modality together with advanced exogenous contrast agents that meet the combined requirements of high brightness, large signal-to-noise ratio, negligible interference on cell behavior and function, long retention in cells, excellent biological stability, and accurate long-term cell tracking ability remain in urgent pursuit.

Very recently, fluorescent CP dots have been applied for *in vivo* tracking of cancer cells and stem cells [62, 63]. It is encouraging that CP dots meet nearly all the above-mentioned requirements, serving as a superior exogenous cell tracker. Li and coworkers *et al*. developed a highly fluorescent CP dot for *in vivo* tracking of mesenchymal stem cells (MSCs) with a skin wound mouse model and more

importantly, for grasping how MSCs contributed to skin regeneration [63]. The CP poly(9,9-dihexylfluorene-*alt*-2,1,3-benzoxadiazole) (PFBD) was employed in this work and the CP dots (namely Tat-PFBD dots) were fabricated by a nanoprecipitation strategy using DSPE-PEG_{2000} and DSPE-PEG_{2000}-maleimide as the matrix to encapsulate PFBD, which was followed by surface conjugation with a cell-penetrating peptide (RKKRRQRRRC) derived from HIV-1 Tat protein via maleimide–thiol coupling reaction (Figure 4.4a). The Tat-PFBD dots had a mean size of about 37 nm in aqueous solution and exhibited a strong absorption peaked at 474 nm and an emission centered at 583 nm in water (Figure 4.4b). Noteworthy, the QY of Tat-PFBD dots in water is as high as 0.42. Through simple coincubation at 37 °C for 4 h, Tat-PFBD dots could be largely internalized into the cytoplasma of MSCs and realize high MSC labeling rate of 99.9% (Figure 4.4c). As compared to the QD-based commercial fluorescent cell tracker Qtracker® 585, Tat-PFBD dots showed much higher biological stability and better *in vitro* stem cell tracking ability. To set up the skin wound mouse model, a full-thickness excision wound was performed on both sides of mouse dorsal skin. Then, Tat-PFBD dot-labeled MSCs were transplanted into the left wound with Matrigel as the substrate. As the control, the same amount of MSCs without Tat-PFBD dot labeling were transplanted into the contralateral wound (right side). It was important to note that the MSCs were isolated from male FVB-luc-GFP transgenic mice, which thus expressed both luciferase and green fluorescent protein (GFP). Therefore, the *in vivo* fate of MSCs could be precisely and noninvasively revealed by bioluminescence via injection of luciferase substrate D-luciferin, which helped to verify the accuracy of exogenous Tat-PFBD dots in long-term tracking of MSCs *in vivo*. On the other hand, the MSCs expressed GFP as well, allowing for investigating, through observation of the wound skin slices, whether Tat-PFBD dots remained long enough to label the transplanted MSCs.

As shown in Figure 4.4d and e, strong fluorescent signals could be observed from the left wound site transplanted with Tat-PFBD dot-labeled MSCs, which gradually reduced over time during the skin regeneration. In the meantime, the luciferase-generated bioluminescence from left skin would site displayed similar intensity to that of right site at each day (Figure 4.4f and g), demonstrating that Tat-PFBD dot labeling had negligible interference on the bioluminescence imaging. When focusing on the left skin wound, the luciferase-generated bioluminescence had a similar signal decay trend to the Tat-PFBD dot fluorescence within a 21-day-study duration (Figure 4.4e and g), suggesting that Tat-PFBD dots were reliable for long-term *in vivo* MSC tracking. On day 21 post MSC transplantation, the left skin was sliced and the images from the slices as shown in figure indicated that around 86% of GFP-expressed transplanted MSCs were still labeled with Tat-PFBD dots (Figure 4.4h), manifesting that Tat-PFBD dots could serve as an effective exogenous contrast agent for *in vivo* tracking of transplanted MSCs in a long-term and accurate manner. More importantly, by virtue of the Tat-PFBD dot labeling, it was also reasonable to conclude that the transplanted MSCs contributed to skin regeneration through both differentiation toward endothelial cells (Figure 4.4i) and paracrine signaling (Figure 4.4j) to boost neovascularization and that MSCs did not directly differentiate into epidermal lineage *in vivo*. To sum up, CP dots exhibit combined merits in *in vivo* cell tracking in terms of high

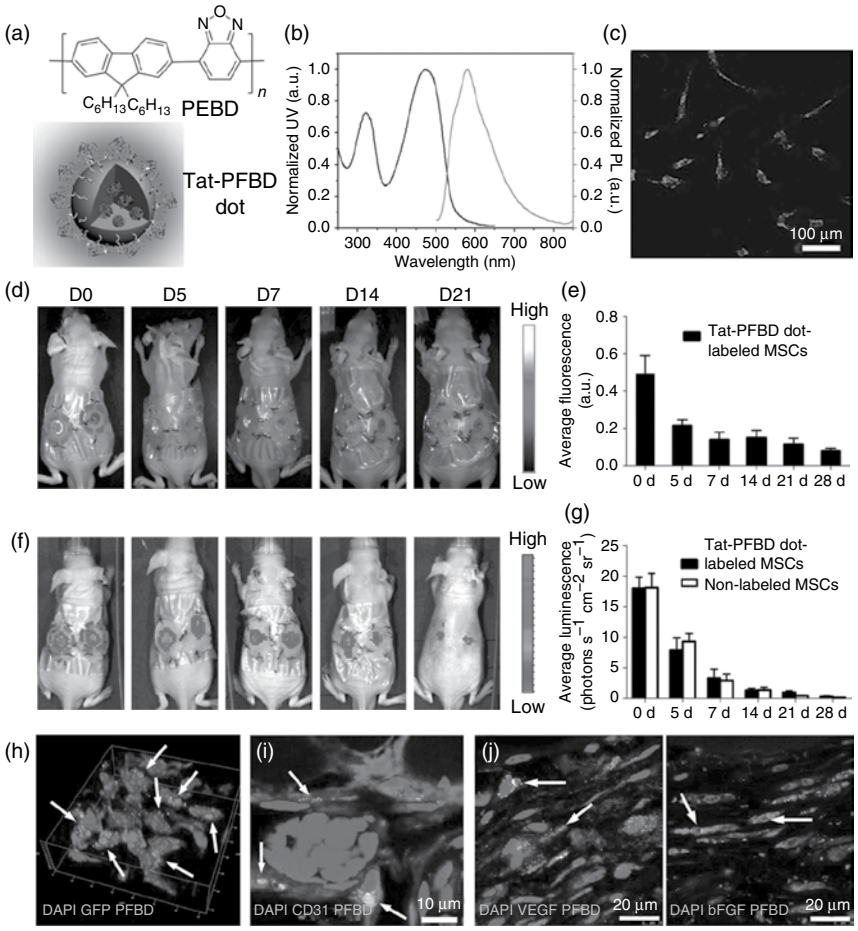

Figure 4.4 (a) Chemical structure of PFBD and schematic illustration of Tat-PFBD dot. (b) UV–vis absorption and emission spectra of Tat-PFBD dots in water. Excitation at 474 nm. (c) Confocal image of MSCs after incubation with Tat-PFBD dots (4 nM) at 37 °C for 4 h. (d) Time-dependent *in vivo* fluorescence imaging of skin wound-bearing mice. The left side wound was transplanted with Tat-PFBD dot-labeled MSCs; the right one was transplanted with nonlabeled MSCs. (e) Quantitative analysis of the fluorescence intensity change at the left wound site. (f) Corresponding *in vivo* bioluminescence imaging of the same mouse in (a). (g) Quantitative analyses of the bioluminescence intensity changes at left and right wound sites. (h–j) Confocal images of the regenerated skin from mice treated with Tat-PFBD dot-labeled MSCs for 21 days. GFP was intrinsically expressed in MSCs for (h); CD31 was costained to visualize blood vessels for (i); VEGF and bFGF was costained, respectively, to reveal paracrine cytokines of Tat-PFBD dot-labeled MSCs for (j). The white arrows indicate the Tat-PFBD dots in (h–j). 4′,6-Diamidino-2-phenylindole (DAPI) was used to stain cell nuclei in (c, h–j). (Adapted with permission from Ref. [63]. Copyright 2015, Wiley-VCH Verlag GmbH & Co. KGaA.)

fluorescence, negligible interference on cell behavior and function, superb retention within cells, and excellent biological stability and photostability as well as precise long-term cell tracking capacity, which make them hold great promise for commercialization as an advanced cell tracker in the near future.

4.5 Two-Photon Excited Brain Vascular Imaging

Two-photon fluorescence imaging (TPFI) refers to absorbing low-energy NIR light and generating high-energy visible fluorescence [64]. As compared to the one-photon fluorescence imaging with absorption wavelength lesser than that of emission, TPFI offers a clearer optical window for *in vivo* bioimaging, benefitting deeper tissue imaging with single-cell resolution [65]. To evaluate the imaging capacity of a TPFI agent, two-photon absorption (TPA) cross-section (δ) and two-photon action cross-section ($\eta\delta$; where η is the PL QY) are the two important parameters. Larger δ and $\eta\delta$ values of a TPFI agent signify the more effective TPFI and higher resolution [66]. Recently, CP dots have been verified to be ideal TPFI agents with high δ and $\eta\delta$ values [67, 68]. For instance, Liu and coworkers utilized a biocompatible triblock copolymer F127 to encapsulate PFBT and then used a silica shell for further surface protection, which afforded PFBT-F127-SiO_2 NPs (Figure 4.5a) [68]. The

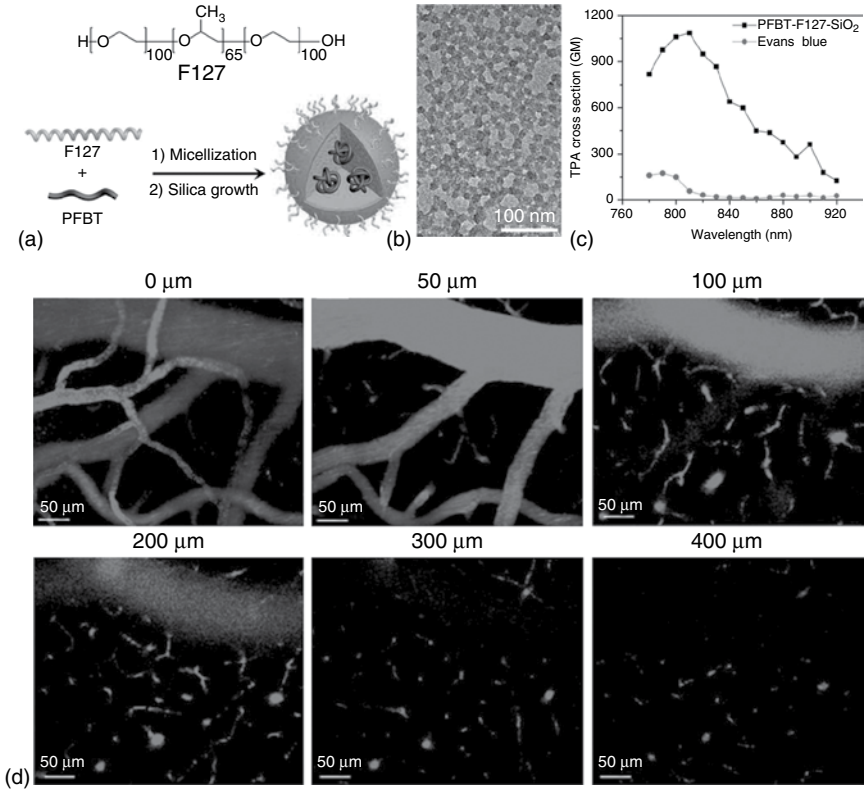

Figure 4.5 (a) Chemical structure of F127 and schematic illustration of the PFBT-F127-SiO_2 NP formation. (b) TEM image of PFBT-F127-SiO_2 NPs. (c) TPA spectra of PFBT-F127-SiO_2 NPs on the basis of CP chain concentration and Evans Blue in water. (d) Intravital TPFI of mouse brain vasculature at different vertical depths after retro-orbital injection of PFBT-F127-SiO_2. (Adapted with permission from Ref. [68]. Copyright 2014, American Chemical Society.)

resultant PFBT-F127-SiO_2 NPs were spherical in shape with uniform size of 12 nm based on TEM investigation (Figure 4.5b), which also showed excellent colloidal stability. Thanks to the F127/silica dual-protection design, PFBT-F127-SiO_2 NPs possessed a high QY of 75%, which was the highest among the currently reported PFBT-based NPs. As shown in Figure 4.5c, the PFBT-F127-SiO_2 NPs had a maximum δ (1085 GM) and $\eta\delta$ (814 GM) at 810 nm, which were much higher than those of the commercial TPFI agent, Evans Blue. The large δ and $\eta\delta$ values endowed PFBT-F127-SiO_2 NPs with excellent TPFI capability to visualize the mouse brain vasculature in a deep and high-resolution manner using two-photon microscopy (Figure 4.5d). As a consequence, the excellent performance in *in vivo* imaging of brain blood vessels makes TPFI CP dots an efficient and reliable tool for understanding the occurrence and development of brain vasculature-associated diseases (e.g., stroke and cerebral hemorrhage).

4.6 Dual-Modality Imaging of Tumors *In Vivo*

Dual-modality imaging is capable of overcoming the drawbacks of imaging modality when used alone [69]. Fluorescence imaging holds the advantage of high sensitivity; however, it cannot provide 3D information with anatomical resolution [69, 70]. Several other imaging modalities, such as MRI, X-CT, and photoacoustic imaging (PAI), show excellent spatial resolution but suffer from low sensitivity to the corresponding contrast agents [71]. Thereby, dual-modality imaging including fluorescence/MRI, fluorescence/X-CT, and fluorescence/PAI are attracting increasing attention for precise tumor diagnosis *in vivo* due to the alliance of the excellent sensitivity of fluorescence with superb spatial resolution of the other modality [72–74]. Liu and coworkers reported an iron oxides (IOs)-containing CP dot for targeted *in vivo* dual-modal fluorescence/MR imaging of tumors [75]. The dual-modality imaging CP dot, namely, FMCPNP was formed by coencapsulation of an FR/NIR fluorescent CP (poly[9,9-bis(6′-(*N*,*N*-dimethylamino)hexyl)fluorenyldivinylene-*alt*-4,7-(2,1,3,-benzothiadiazole)]; PFVBT) and DSPE-coated IOs into a mixture of poly(lactic-*co*-glycolic acid) (PLGA) and PLGA–PEG-folate (Figure 4.6a). It was noted that the DSPE coating on the IOs could effectively avoid the quenching of PFVBT fluorescence by IOs via acting as a barrier to reduce their contact. The surface folate functionalization enabled targeted *in vivo* tumor imaging via folate receptor-mediated active targeting effect. The FMCPNPs had a spherical morphology with an average hydrodynamic diameter of approximately 176 nm. UV–vis absorption and emission spectra indicated that FMCPNPs possessed absorption and emission maxima at 516 and 636 nm, respectively (Figure 4.6b). Moreover, as displayed in Figure 4.6c, FMCPNPs showed superparamagnetic behavior at 298 K with a saturated magnetization value of 3.42 emu g^{-1}, suitable for *in vivo* MRI. Employing murine hepatoma H22 tumor-bearing mouse model, *in vivo* noninvasive fluorescence imaging revealed that FMCPNPs exhibited prominent tumor uptake at 6 h post intravenous injection by virtue of both the EPR effect and folate

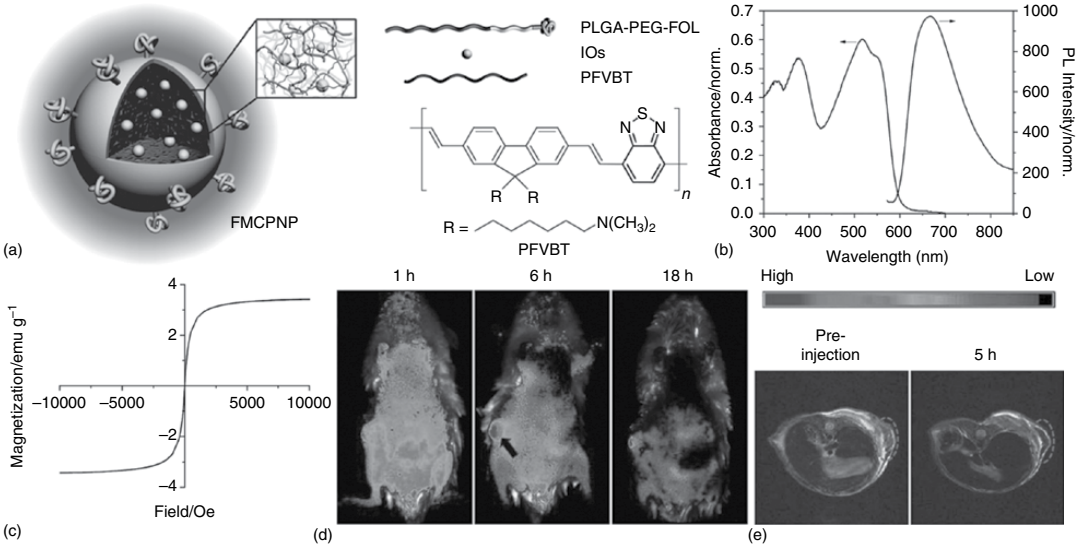

Figure 4.6 (a) Chemical structure of PFVBT and schematic illustration of the FMCPNP. (b) UV–vis absorption and emission spectra of FMCPNPs in water. Excitation at 518 nm. (c) Hysteresis curve of FMCPNPs. (d) Time-dependent *in vivo* noninvasive fluorescence imaging of mice after intravenous injection of FMCPNPs. (e) *In vivo* MRI of the same mouse in (d) preinjection and postinjection of FMCPNPs for 5 h. The arrow in (d) and the circle in (e) indicates the tumor site. (Adapted with permission from Ref. [75]. Copyright 2012, Wiley-VCH Verlag GmbH & Co. KGaA.)

receptor-mediated active targeting effect, benefitting sensitive tumor detection *in vivo* (Figure 4.6d). On the other hand, *in vivo* T_2-weighted MRI gave the spatial information on the depth of the tumor mass with anatomical resolution, by observation of the drop in MR signal (Figure 4.6e). Besides this work, several other successful examples have reasonably confirmed that CPs can serve as an ideal fluorescent component to construct dual-modal imaging nanoprobes for *in vivo* cancer diagnositics [76–79].

4.7 Other *In Vivo* Fluorescence Imaging Applications

Owing to the outstanding optical properties, CP dots and CPEs have also been applied for several other *in vivo* fluorescence imaging applications, such as sentinel lymph node (SLN) mapping [27], zebrafish imaging [80, 81], drug tracing [28], tissue engineering [82], mouse arterial blood flow tracking [83], and so on [84–88]. SLN imaging is of great importance for suppression of cancer recurrence and metastasis, as SLNs near the primary tumor are usually the host of metastatic tumor cells and are potential tumor recurrence positions [89]. To visualize SLNs in live animals, Kim and coworkers synthesized a series of cyanovinylene-backboned CP dots (namely cvPDs) with various fluorescence ranging from blue to NIR via tetrabutyl ammonium hydroxide (TBAH)-catalyzed Knoevenagel condensation in the hydrophobic core of solvent-free aqueous micelles (Figure 4.7a) [27]. NIR emissive cvPDs (NIR-cvPDs) with a high mass extinction coefficient of 21 300 $cm^2 g^{-1}$ at the absorption maximum (465 nm) were used for *in vivo* imaging applications (Figure 4.7b). *In vivo* study suggested that after intradermal injection of NIR-cvPDs (about 60 nm in diameter) into the forepaw pad of mice, NIR-cvPDs could rapidly move to SLNs along the lymphatic vessels, achieving effective SLN mapping (Figure 4.7c). Such clear SLN imaging can provide surgeons with vital information on formulating a surgery plan to eradicate cancer.

In vivo bioimaging in the second NIR window (NIR-II, 1000–1700 nm) has recently emerged as an advanced imaging modality with lower autofluorescence, higher tissue penetration, and, thus, better spatial resolution in deep tissues, as compared to bioimaging in the first NIR window (NIR-I, 750–900 nm) [1]. Dai and coworkers developed a brightly NIR-II fluorescent CP (poly(benzo[1,2-*b*:3,4-*b*′]difuran-*alt*-fluorothieno-[3,4-*b*]thiophene)) through copolymerization of an electron-donating monomer benzo[1,2-*b*:3,4-*b*′] difuran and an electron-withdrawing monomer fluorothieno-[3,4-*b*]thiophene [83]. Using DSPE–PEG as the encapsulation matrix, NIR-II emissive CP dot was yielded with a mean size of 2.9 nm measured by atomic force microscopy, which possessed an absorption and emission peak at 654 and 1047 nm, respectively. By virtue of the intense NIR-II emission and the high PL QY (about 1.7%), the CP dots enabled clear and fast imaging and tracking of real-time arterial blood flow in the mouse hind limb. This successful study reasonably demonstrated that CP is an advanced material to construct *in vivo* NIR-II fluorescent probes.

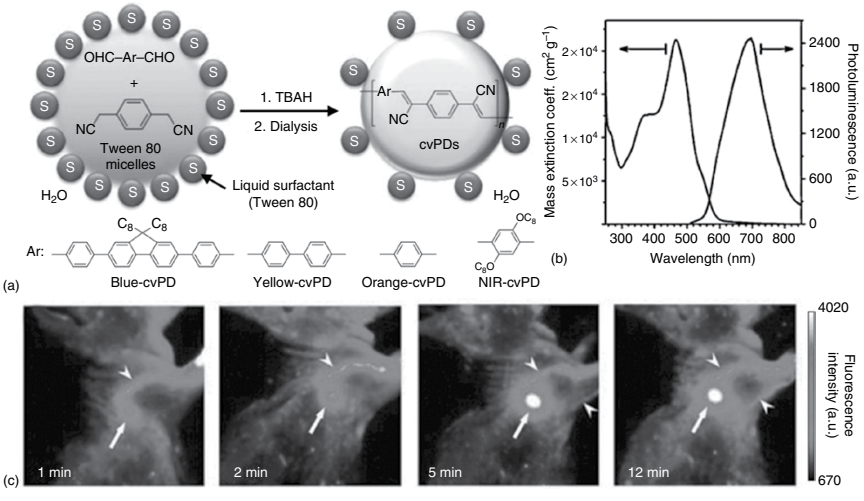

Figure 4.7 (a) Schematic illustration of the formation of various cvPDs. (b) Mass extinction coefficient and PL spectra of NIR-cvPDs in water. (c) Time-dependent *in vivo* fluorescence imaging of mice after intradermal injection of NIR-cvPDs (10 µl of 1.7 mg ml^{-1}) into the right paw. The arrows and arrowheads indicate axillary lymph node and lymphatic vessels, respectively. (Adapted with permission from Ref. [27]. Copyright 2010, Royal Society of Chemistry.)

4.8 Conclusions and Perspectives

In this chapter, the recent progress of CP-based fluorescent probes for *in vivo* bioimaging has been summarized and discussed. As compared to the *in vivo* fluorescent probes on the basis of conventional fluorescent materials, CP-based ones hold the combined advantages of high extinction coefficients, bright fluorescence, excellent photobleaching resistance, negligible fluorescence change in disease microenvironment, low cytotoxicity, and *in vivo* toxicity as well as large TPA δ and $\eta\delta$ values for TPFI, which make them a new generation of advanced *in vivo* fluorescent probes. In addition, several nanoengineering approaches provide CP-based fluorescent probes with optimal physicochemical properties and flexible surface functionalization, which result in optimized *in vivo* kinetics and biodistribution as well as prominent targeting ability, benefitting efficient *in vivo* bioimaging. It is worth emphasizing that CP dots have been demonstrated to be advantageous *in vivo* fluorescent cell trackers, which meet nearly all the necessary qualities in *in vivo* cell tracking in terms of high fluorescence, negligible interference on cell behavior and function, superb retention within cells, excellent biological stability and photostability, as well as precise long-term cell tracking capability. Future work will mainly concentrate on the development of highly fluorescent CP-based probes with longer wavelength excitation, multiphoton excitation (e.g., three-photon excitation) or emission within a second NIR window, which will be further beneficial to provide sights and insights into the biological processes in deeper tissues *in vivo*. Furthermore, CP-based fluorescent probes that can be applied for effective fluorescence imaging-guided surgery are also urgently desirable, which will hold great promise in clinical translation. In a word, the research on CPs for *in vivo* fluorescence imaging has become a popular new subject in the areas of life sciences and biomedical engineering and it is hoped that more exciting and interesting work will emerge in the near future.

References

1 Antaris, A.L., Chen, H., Cheng, K., Sun, Y., Hong, G., Qu, C., Diao, S., Deng, Z., Hu, X., Zhang, B., Zhang, X., Yaghi, O.K., Alamparambil, Z.R., Hong, X., Cheng, Z., and Dai, H. (2015) A small-molecule dye for NIR-II imaging. *Nat. Mater.*, **15**, 235–242.

2 Gao, X., Cui, Y., Levenson, R.M., Chung, L.W.K., and Nie, S. (2004) In vivo cancer targeting and imaging with semiconductor quantum dots. *Nat. Biotechnol.*, **22**, 969–976.

3 Larson, D.R., Zipfel, W.R., Williams, R.M., Clark, S.W., Bruchez, M.P., Wise, F.W., and Webb, W.W. (2003) Water-soluble quantum dots for multiphoton fluorescence imaging in vivo. *Science*, **300**, 1434–1436.

4 Ding, D., Li, K., Liu, B., and Tang, B.Z. (2013) Bioprobes based on AIE fluorogens. *Acc. Chem. Res.*, **46**, 2441–2453.

5 Mikhaylov, G., Mikac, U., Magaeva, A.A., Itin, V.I., Naiden, E.P., Psakhye, I., Babes, L., Reinheckel, T., Peters, C., Zeiser, R., Bogyo, M., Turk, V., Psakhye,

S.G., Turk, B., and Vasiljeva, O. (2011) Ferri-liposomes as an MRI-visible drug-delivery system for targeting tumours and their microenvironment. *Nat. Nanotechnol.*, **6**, 594–602.

6 Pu, K., Shuhendler, A.J., Jokerst, J.V., Mei, J., Gambhir, S.S., Bao, Z., and Rao, J. (2014) Semiconducting polymer nanoparticles as photoacoustic molecular imaging probes in living mice. *Nat. Nanotechnol.*, **9**, 233–239.

7 Leveridge, M.J., Bostrom, P.J., Koulouris, G., Finelli, A., and Lawrentschuk, N. (2010) Imaging renal cell carcinoma with ultrasonography, CT and MRI. *Nat. Rev. Urol.*, **7**, 311–325.

8 Liu, Z., Cai, W., He, L., Nakayama, N., Chen, K., Sun, X., Chen, X., and Dai, H. (2007) In vivo biodistribution and highly efficient tumour targeting of carbon nanotubes in mice. *Nat. Nanotechnol.*, **2**, 47–52.

9 Hicks, R.J. and Hofman, M.S. (2012) Is there still a role for SPECT-CT in oncology in the PET-CT era? *Nat. Rev. Clin. Oncol.*, **9**, 712–720.

10 Wu, T.J., Tzeng, Y.K., Chang, W.W., Cheng, C.A., Kuo, Y., Chien, C.H., Chang, H.C., and Yu, J. (2013) Tracking the engraftment and regenerative capabilities of transplanted lung stem cells using fluorescent nanodiamonds. *Nat. Nanotechnol.*, **8**, 682–689.

11 Waerzeggers, Y., Monfared, P., Viel, T., Winkeler, A., and Jacobs, A.H. (2010) Mouse models in neurological disorders: applications of non-invasive imaging. *Biochim. Biophys. Acta*, **1802**, 819–839.

12 Frangioni, J.V. (2003) In vivo near-infrared fluorescence imaging. *Curr. Opin. Chem. Biol.*, **7**, 626–634.

13 Vahrmeijer, A.L., Hutteman, M., van der Vorst, J.R., van de Velde, C.J.H., and Frangioni, J.V. (2013) Image-guided cancer surgery using near-infrared fluorescence. *Nat. Rev. Clin. Oncol.*, **10**, 507–518.

14 Pu, K., Li, K., and Liu, B. (2010) A molecular brush approach to enhance quantum yield and suppress nonspecific interactions of conjugated polyelectrolyte for targeted far-red/near-infrared fluorescence cell imaging. *Adv. Funct. Mater.*, **20**, 2770–2777.

15 Reisch, A. and Klymchenko, A.S. (2016) Fluorescent polymer nanoparticles based on dyes: seeking brighter tools for bioimaging. *Small*, **12**, 1968–1992.

16 Chen, M. and Yin, M. (2014) Design and development of fluorescent nanostructures for bioimaging. *Prog. Polym. Sci.*, **39**, 365–395.

17 Mei, J., Leung, N.L.C., Kwok, R.T.K., Lam, J.W.Y., and Tang, B.Z. (2015) Aggregation-induced emission: together we shine, united we soar!. *Chem. Rev.*, **115**, 11718–11940.

18 Derfus, A.M., Chan, W.C.W., and Bhatia, S.N. (2004) Probing the cytotoxicity of semiconducting quantum dots. *Nano Lett.*, **4**, 11–18.

19 Wu, W., Li, R., Bian, X., Zhu, Z., Ding, D., Li, X., Jia, Z., Jiang, X., and Hu, Y. (2009) Covalently combining carbon nanotubes with anticancer agent: preparation and antitumor activity. *ACS Nano*, **3**, 2740–2750.

20 McQuade, D.T., Pullen, A.E., and Swager, T.M. (2000) Conjugated polymer-based chemical sensors. *Chem. Rev.*, **100**, 2537–2574.

21 Liu, B. and Bazan, G.C. (2004) Homogeneous fluorescence-based DNA detection with water-soluble conjugated polymers. *Chem. Mater.*, **16**, 4467–4476.

22 Feng, L., Zhu, C., Yuan, H., Liu, L., Lv, F., and Wang, S. (2013) Conjugated polymer nanoparticles: preparation, properties, functionalization and biological applications. *Chem. Soc. Rev.*, **42**, 6620–6633.

23 Zhu, C., Liu, L., Yang, Q., Lv, F., and Wang, S. (2012) Water-soluble conjugated polymers for imaging, diagnosis, and therapy. *Chem. Rev.*, **112**, 4687–4735.

24 Feng, F., Liu, L., and Wang, S. (2010) Fluorescent conjugated polymer-based FRET technique for detection of DNA methylation of cancer cells. *Nat. Protoc.*, **5**, 1255–1264.

25 Li, K. and Liu, B. (2012) Polymer encapsulated conjugated polymer nanoparticles for fluorescence bioimaging. *J. Mater. Chem.*, **22**, 1257–1264.

26 Pu, K. and Liu, B. (2011) Fluorescent conjugated polyelectrolytes for bioimaging. *Adv. Funct. Mater.*, **21**, 3408–3423.

27 Kim, S., Lim, C.K., Na, J., Lee, Y.D., Kim, K., Choi, K., Leary, J.F., and Kwon, I.C. (2010) Conjugated polymer nanoparticles for biomedical in vivo imaging. *Chem. Commun.*, **46**, 1617–1619.

28 Ding, D., Li, K., Zhu, Z., Pu, K., Hu, Y., Jiang, X., and Liu, B. (2011) Conjugated polyelectrolyte-cisplatin complex nanoparticles for simultaneous in vivo imaging and drug tracking. *Nanoscale*, **3**, 1997–2002.

29 Li, K. and Liu, B. (2014) Polymer-encapsulated organic nanoparticles for fluorescence and photoacoustic imaging. *Chem. Soc. Rev.*, **43**, 6570–6597.

30 Jin, Y., Ye, F., Zeigler, M., Wu, C., and Chiu, D.T. (2011) Near-infrared fluorescent dye-doped semiconducting polymer dots. *ACS Nano*, **5**, 1468–1475.

31 Pu, K., Chattopadhyay, N., and Rao, J. (2016) Recent advances of semiconducting polymer nanoparticles in in vivo molecular imaging. *J. Controlled Release*, **240**, 312–322.

32 Wang, K., He, X., Yang, X., and Shi, H. (2013) Functionalized silica nanoparticles: a platform for fluorescence imaging at the cell and small animal levels. *Acc. Chem. Res.*, **46**, 1367–1376.

33 Schroeder, A., Heller, D.A., Winslow, M.M., Dahlman, J.E., Pratt, G.W., Langer, R., Jacks, T., and Anderson, D.G. (2012) Treating metastatic cancer with nanotechnology. *Nat. Rev. Cancer*, **12**, 39–50.

34 van Vlerken, L.E., Duan, Z., Little, S.R., Seiden, M.V., and Amiji, M.M. (2008) Biodistribution and pharmacokinetic analysis of paclitaxel and ceramide administrated in multifunctional polymer-blend nanoparticles in drug resistant breast cancer model. *Mol. Pharmaceutics*, **5**, 516–526.

35 Farokhzad, O.C. and Langer, R. (2009) Impact of nanotechnology on drug delivery. *ACS Nano*, **3**, 16–20.

36 Ding, D., Liu, J., Feng, G., Li, K., Hu, Y., and Liu, B. (2013) Bright far-red/near-infrared conjugated polymer nanoparticles for in vivo bioimaging. *Small*, **9**, 3093–3102.

37 Wu, C., Hansen, S.J., Hou, Q., Yu, J., Zeigler, M., Jin, Y., Burnham, D.R., McNeill, J.D., Olson, J.M., and Chiu, D.T. (2011) Design of highly emissive polymer dot bioconjugates for in vivo tumor targeting. *Angew. Chem. Int. Ed.*, **50**, 3430–3434.

38 Ahmed, E., Morton, S.W., Hammond, P.T., and Wager, T.M. (2013) Fluorescent multiblock π-conjugated polymer nanoparticles for in vivo tumor targeting. *Adv. Mater.*, **25**, 4504–4510.

39 Aoki, H., Kakuta, J., Yamaguchi, T., Nitahara, S., and Ito, S. (2011) Near-infrared fluorescent nanoparticle of low-bandgap π-conjugated polymer for in vivo molecular imaging. *Polym. J.*, **43**, 937–940.

40 Cao, F. and Xiong, L. (2016) Folic acid functionalized PFBT fluorescent polymer dots for tumor imaging. *Chin. J. Chem.*, **34**, 570–575.

41 Kim, J., Lee, E., Hong, Y., Kim, B., Ku, M., Heo, D., Choi, J., Na, J., You, J., Haam, S., Huh, Y.M., Suh, J.S., Kim, E., and Yang, J. (2015) Self-doped conjugated polymeric nanoassembly by simplified process for optical cancer theragnosis. *Adv. Funct. Mater.*, **25**, 2260–2269.

42 Xiong, L., Cao, F., Cao, X., Guo, Y., Zhang, Y., and Cai, X. (2015) Long-term-stable near-infrared polymer dots with ultrasmall size and narrow-band emission for imaging tumor vasculature in vivo. *Bioconjugate Chem.*, **26**, 817–821.

43 Ding, D., Li, K., Qin, W., Zhan, R., Hu, Y., Liu, J., Tang, B.Z., and Liu, B. (2013) Conjugated polymer amplified far-red/near-infrared fluorescence from nanoparticles with aggregation-induced emission characteristics for targeted in vivo imaging. *Adv. Healthc. Mater.*, **2**, 500–507.

44 Zhu, H., Fang, Y., Zhen, X., Wei, N., Gao, Y., Luo, K.Q., Xu, C., Duan, H., Ding, D., Chen, P., and Pu, K. (2016) Multilayered semiconducting polymer nanoparticles with enhanced NIR fluorescence for molecular imaging in cells, zebrafish and mice. *Chem. Sci.*, **7**, 5118–5125.

45 Zhuang, Y.D., Chiang, P.Y., Wang, C.W., and Tan, K.T. (2013) Environment-sensitive fluorescent turn-on probes targeting hydrophobic ligand-binding domains for selective protein detection. *Angew. Chem. Int. Ed.*, **52**, 8124–8128.

46 Kobayashi, H., Ogawa, M., Alford, R., Choyke, P.L., and Urano, Y. (2010) New strategies for fluorescent probe design in medical diagnostic imaging. *Chem. Rev.*, **110**, 2620–2640.

47 Pu, K., Shuhendler, A.J., and Rao, J. (2013) Semiconducting polymer nanoprobe for in vivo imaging of reactive oxygen and nitrogen species. *Angew. Chem. Int. Ed.*, **52**, 10325–10329.

48 Dmitriev, R.I., Borisov, S.M., Düssmann, H., Sun, S., Müller, B.J., Prehn, J., Baklaushev, V.P., Klimant, I., and Papkovsky, D.B. (2015) Versatile conjugated polymer nanoparticles for high-resolution O_2 imaging in cells and 3D tissue models. *ACS Nano*, **9**, 5275–5288.

49 Jeong, K., Park, S., Lee, Y.D., Lim, C.K., Kim, J., Chung, B.H., Kwon, I.C., Park, C.R., and Kim, S. (2013) Conjugated polymer/photochromophore binary nanococktails: bistable photoswitching of near-infrared fluorescence for in vivo imaging. *Adv. Mater.*, **25**, 5574–5580.

50 Kim, D. and Lee, T.S. (2016) Photoswitchable emission color change in nanodots containing conjugated polymer and photochrome. *ACS Appl. Mater. Interfaces*, **8**, 34770–34776.

51 Li, P., Liu, L., Xiao, H., Zhang, W., Wang, L., and Tang, B. (2016) A new polymer nanoprobe based on chemiluminescence resonance energy transfer for ultrasensitive imaging of intrinsic superoxide anion in mice. *J. Am. Chem. Soc.*, **138**, 2893–2896.

52 Seo, Y.H., Singh, A., Cho, H.J., Kim, Y., Heo, J., Lim, C.K., Park, S.Y., Jang, W.D., and Kim, S. (2016) Rational design for enhancing inflammation-responsive in

vivo chemiluminescence via nanophotonic energy relay to near-infrared AIE-active conjugated polymer. *Biomaterials*, **84**, 111–118.

53 Zhao, Q., Zhou, X., Cao, T., Zhang, K.Y., Yang, L., Liu, S., Liang, H., Yang, H., Li, F., and Huang, W. (2015) Fluorescent/phosphorescent dual-emissive conjugated polymer dots for hypoxia bioimaging. *Chem. Sci.*, **6**, 1825–1831.

54 Jokerst, J.V., Khademi, C., and Gambhir, S.S. (2013) Intracellular aggregation of multimodal silica nanoparticles for ultrasound-guided stem cell implantation. *Sci. Transl. Med.*, **5**, 117ra35.

55 Ding, D., Mao, D., Li, K., Wang, X., Qin, W., Liu, R., Chiam, D.S., Tomczak, N., Yang, Z., Tang, B.Z., Kong, D., and Liu, B. (2014) Precise and long-term tracking of adipose-derived stem cells and their regenerative capacity via superb bright and stable organic nanodots. *ACS Nano*, **8**, 12620–12631.

56 Jokerst, J.V., Thangaraj, M., Kempen, P.J., Sinclair, R., and Gambhir, S.S. (2012) Photoacoustic imaging of mesenchymal stem cells in living mice via silica-coated gold nanorods. *ACS Nano*, **6**, 5920–5931.

57 Brader, P., Serganova, I., and Blasberg, R.G. (2013) Noninvasive molecular imaging using reporter genes. *J. Nucl. Med.*, **54**, 167–172.

58 Kircher, M.F., Gambhir, S.S., and Grimm, J. (2011) Noninvasive cell-tracking methods. *Nat. Rev. Clin. Oncol.*, **8**, 677–688.

59 Ferreira, L., Karp, J.M., Nobre, L., and Langer, R. (2008) New opportunities: the use of nanotechnologies to manipulate and track stem cells. *Cell Stem Cell*, **3**, 136–146.

60 Xu, C., Miranda-Nieves, D., Ankrum, J.A., Matthiesen, M.E., Phillips, J.A., Roes, I., Wojtkiewicz, G.R., Juneja, V., Kultima, J.R., Zhao, W., Vemula, P.K., Lin, C.P., Nahrendorf, M., and Karp, J.M. (2012) Tracking mesenchymal stem cells with iron oxide nanoparticle loaded poly(lactide-*co*-glycolide) microparticles. *Nano Lett.*, **12**, 4131–4139.

61 Bridot, J.L., Faure, A.C., Laurent, S., Rivière, C., Billotey, C., Hiba, B., Janier, M., Josserand, V., Coll, J.L., Elst, L.V., Muller, R., Roux, S., Perriat, P., and Tillement, O. (2007) Hybrid gadolinium oxide nanoparticles: multimodal contrast agents for in vivo imaging. *J. Am. Chem. Soc.*, **129**, 5076–5084.

62 Liu, J., Li, K., and Liu, B. (2015) Far-red/near-infrared conjugated polymer nanoparticles for long-term in situ monitoring of liver tumor growth. *Adv. Sci.*, **2**, 1500008.

63 Jin, G., Mao, D., Cai, P., Liu, R., Tomczak, N., Liu, J., Chen, X., Kong, D., Ding, D., Liu, B., and Li, K. (2015) Conjugated polymer nanodots as ultrastable long-term trackers to understand mesenchymal stem cell therapy in skin regeneration. *Adv. Funct. Mater.*, **25**, 4263–4273.

64 Schenke-Layland, K., Riemann, I., Damour, O., Stock, U.A., and Konig, K. (2006) Two-photon microscopes and in vivo multiphoton tomographs powerful dicagnostic tools for tissue engineering and drug delivery. *Adv. Drug Delivery Rev.*, **58**, 878–896.

65 He, G.S., Tan, L.S., Zheng, Q., and Prasad, P.N. (2008) Multiphoton absorbing materials: molecular designs, characterizations, and applications. *Chem. Rev.*, **108**, 1245–1330.

66 Ding, D., Goh, C.C., Feng, G., Zhao, Z., Liu, J., Liu, R., Tomczak, N., Geng, J., Tang, B.Z., Ng, L.G., and Liu, B. (2013) Ultrabright organic dots with

aggregation-induced emission characteristics for real-time two-photon intravital vasculature imaging. *Adv. Mater.*, **25**, 6083–6088.

67 Zhang, W., Kang, J., Li, P., Liu, L., Wang, H., and Tang, B. (2016) Two-photon fluorescence imaging of sialylated glycans in vivo based on a sialic acid imprinted conjugated polymer nanoprobe. *Chem. Commun.*, **52**, 13991–13994.

68 Geng, J., Goh, C.C., Tomczak, N., Liu, J., Liu, R., Ma, L., Ng, L.G., Gurzadyan, G.G., and Liu, B. (2014) Micelle/silica co-protected conjugated polymer nanoparticles for two-photon excited brain vascular imaging. *Chem. Mater.*, **26**, 1874–1880.

69 Nam, T., Park, S., Lee, S.Y., Park, K., Choi, K., Song, I.C., Han, M.H., Leary, J.J., Yuk, S.A., Kwon, I.C., Kim, K., and Jeong, S.Y. (2010) Tumor targeting chitosan nanoparticles for dual-modality optical/MR cancer imaging. *Bioconjugate Chem.*, **21**, 578–582.

70 Xu, Q., Zhu, L., Yu, M., Feng, F., An, L., Xing, C., and Wang, S. (2010) Gadolinium(III) chelated conjugated polymer as a potential MRI contrast agent. *Polymer*, **51**, 1336–1340.

71 Feng, G. and Liu, B. (2016) Multifunctional AIEgens for future theranostics. *Small*, **12**, 6528–6535.

72 Fan, H.M., Olivo, M., Shuter, B., Yi, J.B., Bhuvaneswari, R., Tan, H.R., Xing, G.C., Ng, C.T., Liu, L., Lucky, S.S., Bay, B.H., and Ding, J. (2010) Quantum dot capped magnetite nanorings as high performance nanoprobe for multiphoton fluorescence and magnetic resonance imaging. *J. Am. Chem. Soc.*, **132**, 14803–14811.

73 Zhang, J., Li, C., Zhang, X., Huo, S., Jin, S., An, F.F., Wang, X., Xue, X., Okeke, C.I., Duan, G., Guo, F., Zhang, X., Hao, J., Wang, P.C., Zhang, J., and Liang, X.J. (2015) In vivo tumor-targeted dual-modal fluorescence/CT imaging using a nanoprobe co-loaded with an aggregation-induced emission dye and gold nanoparticles. *Biomaterials*, **42**, 103–111.

74 Geng, J., Liao, L.D., Qin, W., Tang, B.Z., Thakor, N., and Liu, B. (2015) Fluorogens with aggregation induced emission: ideal photoacoustic contrast reagents due to intramolecular rotation. *J. Nanosci. Nanotechnol.*, **15**, 1864–1868.

75 Li, K., Ding, D., Huo, D., Pu, K., Thao, N.N.P., Hu, Y., Li, Z., and Liu, B. (2012) Conjugated polymer based nanoparticles as dual-modal probes for targeted in vivo fluorescence and magnetic resonance imaging. *Adv. Funct. Mater.*, **22**, 3107–3115.

76 Ding, D., Wang, G., Liu, J., Li, K., Pu, K., Hu, Y., Ng, J.C.Y., Tang, B.Z., and Liu, B. (2012) Hyperbranched conjugated polyelectrolyte for dual-modality fluorescence and magnetic resonance cancer imaging. *Small*, **8**, 3523–3530.

77 Wang, G., Zhang, X., Liu, Y., Hu, Z., Mei, X., and Uvdal, K. (2015) Magneto-fluorescent nanoparticles with high-intensity NIR emission, T_1- and T_2-weighted MR for multimodal specific tumor imaging. *J. Mater. Chem. B*, **3**, 3072–3080.

78 Song, X., Gong, H., Yin, S., Cheng, L., Wang, C., Li, Z., Li, Y., Wang, X., Liu, G., and Liu, Z. (2014) Ultra-small iron oxide doped polypyrrole nanoparticles for in vivo multimodal imaging guided photothermal therapy. *Adv. Funct. Mater.*, **24**, 1194–1201.

79 Song, X., Liang, C., Gong, H., Chen, Q., Wang, C., and Liu, Z. (2015) Photosensitizer-conjugated albumin–polypyrrole nanoparticles for imaging-guided in vivo photodynamic/photothermal therapy. *Small*, **11**, 3932–3941.

80 Liou, S.Y., Ke, C.S., Chen, J.H., Luo, Y.W., Kuo, S.Y., Chen, Y.H., Fang, C.C., Wu, C.Y., Chiang, C.M., and Chan, Y.H. (2016) Tuning the emission of semiconducting polymer dots from green to near-infrared by alternating donor monomers and their applications for in vivo biological imaging. *ACS Macro Lett.*, **5**, 154–157.

81 Liu, H.Y., Wu, P.J., Kuo, S.Y., Chen, C.P., Chang, E.H., Wu, C.Y., and Chan, Y.H. (2015) Quinoxaline-based polymer dots with ultrabright red to near-infrared fluorescence for in vivo biological imaging. *J. Am. Chem. Soc.*, **137**, 10420–10429.

82 Wickham, A., Sjölander, D., Bergström, G., Wang, E., Rajendran, V., Hildesjö, C., Skoglund, K., Nilsson, K.P.R., and Aili, D. (2015) Near-infrared emitting and pro-angiogenic electrospun conjugated polymer scaffold for optical biomaterial tracking. *Adv. Funct. Mater.*, **25**, 4274–4281.

83 Hong, G., Zou, Y., Antaris, A.L., Diao, S., Wu, D., Cheng, K., Zhang, X., Chen, C., Liu, B., He, Y., Wu, J.Z., Yuan, J., Zhang, B., Tao, Z., Fukunage, C., and Dai, H. (2014) Ultrafast fluorescence imaging in vivo with conjugated polymer fluorophores in the second near-infrared window. *Nat. Commun.*, **5**, 4206.

84 Lv, F., Qiu, T., Liu, L., Yang, J., and Wang, S. (2016) Recent advances in conjugated polymer materials for disease diagnosis. *Small*, **12**, 696–705.

85 Klingstedt, T. and Nilsson, K.P.R. (2011) Conjugated polymers for enhanced bioimaging. *Biochim. Biophys. Acta*, **1810**, 286–296.

86 Wu, C. and Chiu, D.T. (2013) Highly fluorescent semiconducting polymer dots for biology and medicine. *Angew. Chem. Int. Ed.*, **52**, 3086–3109.

87 Peng, H.S. and Chiu, D.T. (2015) Soft fluorescent nanomaterials for biological and biomedical imaging. *Chem. Soc. Rev.*, **44**, 4699–4722.

88 Palner, M.P., Pu, K., Shao, S., and Rao, J. (2015) Semiconducting polymer nanoparticles with persistent near-infrared luminescence for in vivo optical imaging. *Angew. Chem. Int. Ed.*, **54**, 11477–11480.

89 Liang, C., Diao, S., Wang, C., Gong, H., Liu, T., Hong, G., Shi, X., Dai, H., and Liu, Z. (2014) Tumor metastasis inhibition by imaging-guided photothermal therapy with single-walled carbon nanotubes. *Adv. Mater.*, **26**, 5646–5652.

5

π-Conjugated/Semiconducting Polymer Nanoparticles for Photoacoustic Imaging

Chen Xie and Kanyi Pu

Nanyang Technological University, School of Chemical and Biomedical Engineering, N1.3-B2-05, 70 Nanyang Drive, Singapore, 637457, Singapore

5.1 Introduction

Photoacoustic (PA) imaging is a nonionizing imaging technology that combines optical excitation with ultrasonic detection [1, 2]. Compared with fluorescence imaging, PA imaging has higher spatial resolution and deeper tissue penetration because scattering of ultrasonic signals is much weaker than that of optical signals in biological tissues. When compared with ultrasonic imaging whose contrast is limited by the mechanical properties of tissues, PA imaging has better contrast because it is related to the optical properties of tissues or contrast agents [3]. As a result of combining the advantages of optical imaging with ultrasonic imaging, PA imaging can provide deep tissue penetration, high spatial resolution, and satisfactory tissue contrast [4–7]. PA imaging has been rapidly developed in the past decades by virtue of the fast development of laser technology and ultrasonic detectors [8–10]. Several types of PA imaging systems such as PA microscopy [11], PA endoscopy [12] and PA computed tomography (CT) [13, 14] have been designed for imaging objects with different dimensions ranging from a single organelle to a whole animal. A variety of studies have demonstrated the potential of PA imaging in biological applications such as vascular imaging [15], oxygen metabolism imaging [16], and breast cancer imaging [17]. However, besides very few endogenous PA contrast agents such as hemoglobin and melanin, most tissues do not contain naturally light absorbers to serve as endogenous PA contrast agents [18]. Thus, development of exogenous PA contrast agents is in high demand to obtain better contrast in the region of interest (ROI) and to fully utilize the advantages of PA imaging in life sciences.

Until now, many contrast agents have been developed for PA imaging, such as near-infrared (NIR) dyes [19–21], fluorescent proteins [22, 23], inorganic nanoparticles [24–27], two-dimensional (2D) materials [28, 29], carbon materials [30–32], and porphysomes [33–35]. However, NIR organic dyes, fluorescent proteins, and inorganic nanoparticles commonly confront the issue of poor photostability unless specific precaution or modification is undertaken [36, 37].

Conjugated Polymers for Biological and Biomedical Applications, First Edition. Edited by Bin Liu

Carbon and 2D materials generally have broad and multipeak PA spectral profiles [38, 39], which makes them difficult to be distinguished from the tissue background especially at low concentrations. Porphysomes usually possess high PA brightness and relatively narrow PA spectral profile but may have phototoxicity as they are able to generate singlet oxygen upon light irradiation [40, 41]. Therefore, development of alternative PA imaging contrast agents with high PA brightness, excellent photostability and good biocompatibility is highly demanded.

π-Conjugated/semiconducting polymers (SPs) are a series of polymers with π-electron delocalized backbones that endow SPs with optical and electronic properties [42, 43]. *π*-Conjugated/semiconducting polymer nanoparticles (SPNs) made from SPs have gained growing attention in the bioimaging field for their aqueous solubility, good biocompatibilities, and attractive optical properties [44, 45]. Until now, SPNs have been applied for fluorescence imaging including cell tracking [46], tumor target imaging [47, 48], reactive oxygen species (ROS) imaging [37] and ultrafast hemodynamic imaging [49]. SPNs have also been utilized for chemiluminescence imaging of drug-induced injury [50], *in vivo* lymph node mapping [51], and neuroinflammation [52]. Furthermore, photothermal therapy (PTT) [53, 54] and real-time activation of neurons [55] can also be achieved by taking advantage of their high photothermal conversion efficiency. With high capability of transferring photon energy into heat, SPNs are promising materials for PA imaging. Previous studies have showed that SPNs often have a better photostability than gold nanorods (GNR) and higher PA amplitude than carbon nanotubes because of their relatively high absorption coefficients [36, 37, 56]. Thus, SPNs can serve as good candidates for PA imaging.

The classification, development, detailed principles, and structures of PA instrumentations have been widely studied and reviewed [8, 10, 57, 58]. The applications of SPNs in fluorescence and chemi-/bioluminescence imaging have also been studied both *in vivo* and *in vitro* [59–63]. Therefore, this chapter will instead focus on the applications of SPNs as PA contrast agents for *in vivo* PA imaging. We will first give a brief introduction of the mechanism of PA imaging, and discuss the design strategy and preparation of SPNs for *in vivo* PA imaging, and conclude by highlighting the applications of SPNs including PA imaging of brain vasculature, tumor, lymph nodes, ROS, and multimodal imaging.

5.2 Mechanism of PA Imaging

The PA effect was first discovered by Bell in 1880 following his observation of the generation of sound owing to the absorption of modulated sunlight [64]. In PA imaging, nonionizing laser pulses are delivered into biological tissues, the irradiated tissues absorb pulsed light energy and convert it into heat, generating a local transient temperature rise and in turn an initial pressure rise because of the thermoelastic expansion. The generated thermoelastic expansion further produces wideband (MHz) ultrasonic waves, termed PA waves. Ultrasonic transducers detect the ultrasonic waves generated and are analyzed from their arrival times to produce images (Figure 5.1) [57]. A 1 mK temperature rise can induce a wave

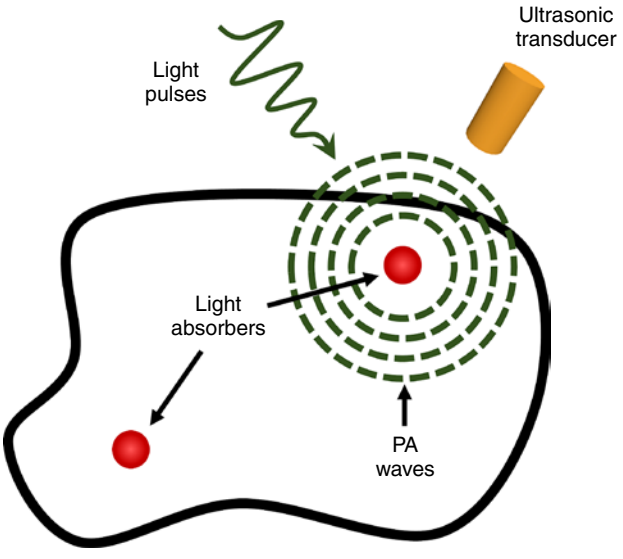

Figure 5.1 Schematic illustration of mechanism of PA imaging.

pressure rise of approximately 800 Pa, which is usually above the detection limit of the ultrasonic transducer [1]. Thus, PA imaging is able to provide high signal-to-noise ratio without damaging the tissues.

The PA pressure P can be described by the wave equation as follows [65]:

$$\left(\frac{1}{\nu^2}\frac{\partial^2}{\partial t^2} - \nabla^2\right)P = \frac{\alpha\beta}{C_p}\frac{\partial^2}{\partial t^2}I,$$

where P is related to speed of sound ν, time t, absorption coefficient α, thermal expansion coefficient β, and optical beam intensity I. The electrorestriction is ignored in the equation as PA signal in biological tissues is dominated by thermal expansion. Based on the wave equation, the magnitude of the PA pressure $|P|$ is determined by the parameters that are listed in the following equation:

$$|P| \propto \frac{\alpha\beta\nu}{C_{\mathrm{p}}}.$$

In a biological environment, the absorption coefficient α is the most important parameter and a major factor in determining the contrast of PA imaging because it may vary several orders of magnitude depending on the optical wavelength and the types of tissue. As different biological tissues have different absorption coefficients, it is feasible to reconstruct the distribution of optical energy decomposition and thus rebuild the images of the tissues. However, it will be difficult to reconstruct the image of the tissue if the absorption coefficient of the tissue is too low. In that case, exogenous PA contrast agents will be needed to generate enough contrast for PA imaging.

5.3 SPNs for PA Imaging

5.3.1 Preparation of SPNs

SPs with highly delocalized π-conjugated backbones have significant advantages over small molecular dyes because of their higher absorption coefficients, better photostability, and more red-shifted absorption [66]. SPs are usually synthesized by polymerization of one or more monomers through palladium-catalyzed coupling reactions, such as Suzuki, Heck, and Sonogashira coupling [42, 67]. To achieve satisfied tissue penetration depth for *in vivo* imaging, SPs with NIR absorption are preferred. Thus, the design strategy combines electron-rich and electron-deficient moieties together to form the electron donor–acceptor structure [68–70]. The donor–acceptor structure may significantly reduce the band gap of SPs, endowing SPs with NIR absorption capabilities[71]. In addition, based on the energy dissipation mechanism [72], the photon energy that is absorbed by chromophores will be typically dissipated through three pathways: (i) fluorescence that can be detected as optical signals, (ii) nonradiative thermal deactivation that generate heat and PA signals, and (iii) storage as long-lived species such as phosphorescence. Therefore, SPs with weak fluorescence should have relatively strong PA signals. It is generally considered that high absorption coefficient at the NIR region and high efficiency of nonradiative decay processes are two dominant features that can help obtain strong PA signals for SPs [2, 70].

To make SPs soluble in aqueous solutions, a variety of methods have been applied for the preparation of water-soluble SPNs. Structural modification is one of the conventional methods to synthesize SPNs with good water solubility [42, 66]. Some studies have reported the synthesis of semiconducting polyelectrolytes (SPEs) based on several types of SPs, such as poly(fluorene-*co*-phenylene) (PFP), poly(*p*-phenylenevinylene) (PPV) and poly(*p*-phenyleneethynylene) (PPE), through introducing charge groups into the side chains of SPs [73–75]. SPEs can coassemble with opposite charged materials into water to form SPNs [76, 77]. However, structural modification is commonly a time-consuming and complicated process to endow each promising SP with aqueous solubility. In contrast, encapsulation of SPs by amphiphilic biocompatible polymers is a more convenient strategy to convert SPs into SPNs with good water solubility. Some SPs and amphiphilic polymers used in the preparation of SPNs are listed in Scheme 5.1. To encapsulate SPs into amphiphilic polymers, nanoprecipitation and miniemulsion are the two major preparation methods that have been widely applied and studied, both of which can lead to stable and size-uniformed SPNs [78–80]. Multifunctional SPNs can also be readily prepared by coencapsulating SPs with other materials into amphiphilic polymers. Such kind of SPNs may have applications in activatable PA and multimodal imaging [36, 81, 82].

Until now, SPNs have been utilized for PA imaging of brain vasculature [83], tumor [84–87], lymph nodes [36] and some molecular mediators *in vivo* such as ROS [36] and pH [81]. Combining PA imaging with other imaging techniques, such as X-ray CT and magnetic resonance imaging (MRI), to achieve multimodal imaging has also been studied using multifunctional SPNs [88, 89].

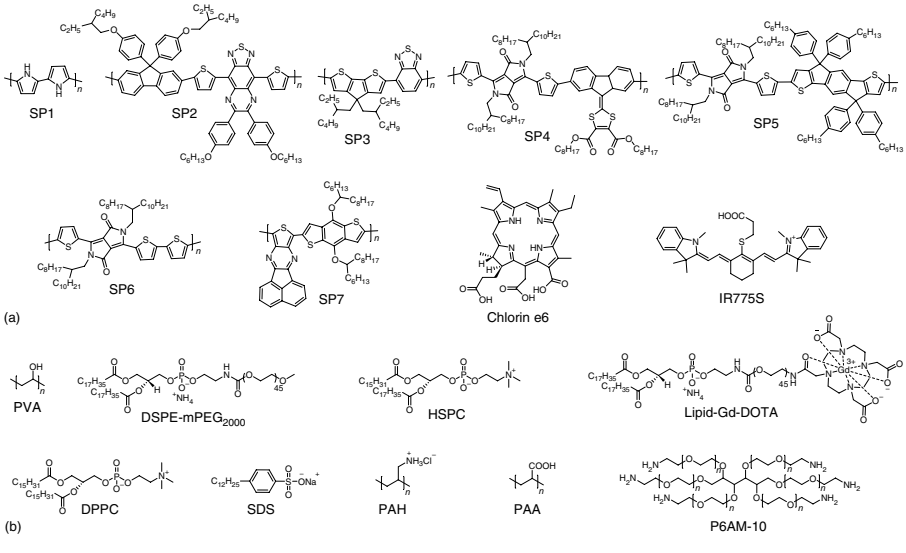

Scheme 5.1 (a) Chemical structures of some SPs and small molecules used for PA imaging. (b) Chemical structures of some amphiphilic molecules used for the preparation of SPNs.

5.3.2 PA Imaging of Brain Vasculature

New diagnostic tools for treatment of brain diseases such as brain cancer, Parkinson's disease, and Alzheimer's disease are in high demand. Conventional imaging modalities such as MRI, CT, and PET confront different obstacles for brain imaging due to their low sensitivity or limited spatial resolution [65, 90]. PA imaging has been successfully applied for studying the hemodynamic changes of the brain in living mice [5, 58]. However, interference of some intrinsic optical agents restricts the sensitivity and resolution of the PA imaging in brain vasculature. Thus, developing exogenous PA contrast agents for brain vasculature imaging is highly demanded. Original example of SPNs for PA imaging of brain vasculature was based on polypyrrole (SP1, Scheme 5.1a) based SPNs (SPN1) [83]. Some inherent features of SPN1 make them suitable for biomedical applications and PA imaging, including high conductivity, NIR absorption, good biocompatibility, and excellent stability [91, 92]. Zha *et al*. synthesized SPN1 for PA tomography imaging via chemical oxidation polymerization (Figure 5.2a). The polymerization was conducted by using $FeCl_3$ as the initiator and polyvinyl alcohol (PVA) as the stabilizer in aqueous solution. SPN1 with narrow size distribution were formed by simply introducing pyrrole monomers into the aqueous solution. After removing the impurities in the solution, the purified SPN1 with uniform diameter was obtained. The extinction spectrum of SPN1 showed a broad absorption band ranging from visible to NIR region (Figure 5.2b). The high absorption coefficient in the NIR region allowed SPN1 to be a good candidate for PA imaging. As expected, SPN1 can generate a strong PA signal when illuminated by laser pulses at 808 nm. To evaluate the feasibility of SPN1 as PA contrast agents and test the maximum PA imaging depth, tissue mimicking phantom that embedded SPN1 was prepared. The phantom was then placed under several pieces of chicken breast muscle to determine the maximum PA imaging depth. With the increase of thickness of the chicken tissue, the PA amplitude of the phantom became weaker and weaker (Figure 5.2c). Based on the experiment, the maximum imaging depth was determined as 4.3 cm, which was approximately fivefold deeper than the effective optical penetration depth. The SPN1 was then applied for *in vivo* PA imaging of brain blood vessels. After systemic administration of SPN1 through tail vein for only 5 min, the PA signal in brain vasculature of mouse increased significantly compared with the background (0 min), showing the good ability of SPN1 for PA imaging of brain vessels (Figure 5.2d). Furthermore, the enhanced contrast between blood vessels and brain parenchyma can be clearly observed even after administration for 60 min, demonstrating the long-time *in vivo* circulating properties of SPN1.

Besides SPN1, some other SPNs have also been developed for PA imaging of brain vasculature. Liu *et al*. designed and synthesized poly[9,9-bis(4-(2-ethylhexyl)phenyl)fluorene-*alt*-*co*-6,7-bis(4-(hexyloxy)phenyl)-4,9-di-(thiophen-2-yl)thiadiazolo-quinoxaline] (SP2), a SP with alternating donor–acceptor structure backbone, via Suzuki polymerization [56]. SP2-based SPNs (SPN2) were prepared by a modified precipitation method which used 1,2-distearoyl-*sn*-glycero-3-phosphoethanolamine-*N*-[methoxy(polyethylene glycol)-2000] (DSPE-$mPEG_{2000}$) as the matrix to encapsulate SP2 (Figure 5.3a).

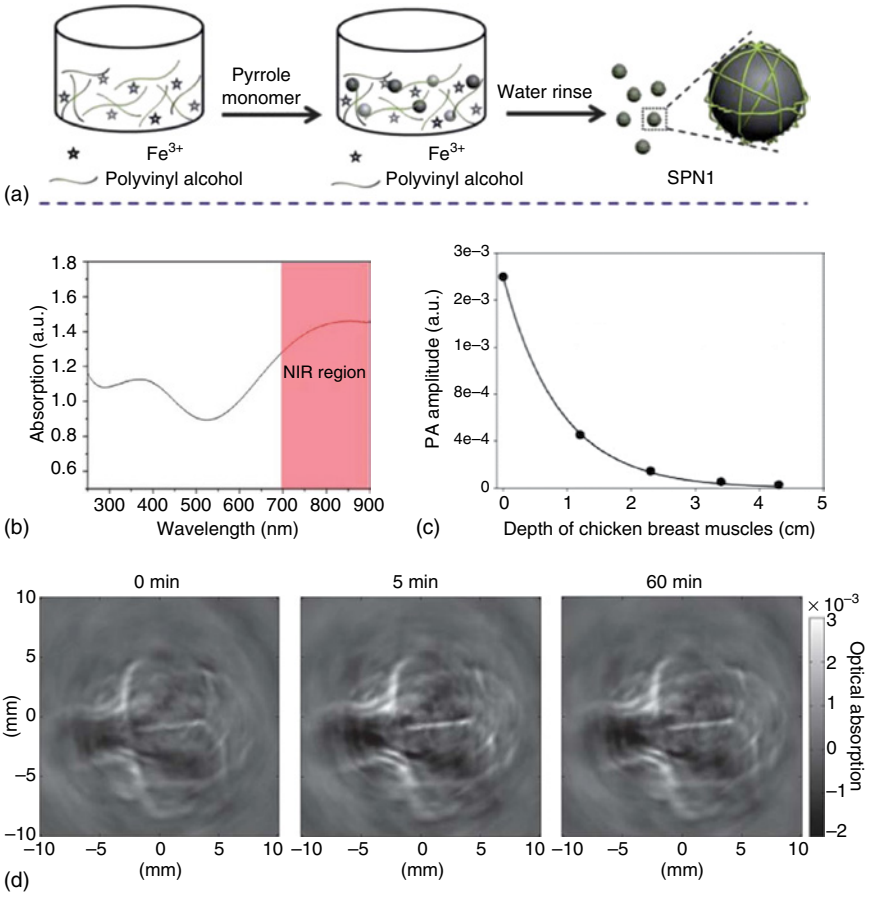

Figure 5.2 (a) Schematic illustration of preparation of SPN1. (b) Absorption spectrum of SPN1 (50 μg ml^{-1}) in water. (c) PA amplitude of SPN1 (50 μg ml^{-1}) in agar gel embedded in chicken breast muscle as a function of depth from the laser irradiated surface. (d) PA imaging of brain after systemic administration of SPN1 for 0, 5, and 60 min. (Reprinted with permission from Ref. [83]. Copyright 2013, Royal Society of Chemistry.)

SPN2 had a strong absorption peak at around 800 nm, such strong absorption in the NIR region showed suitability for PA imaging. Photostability of SPN2 was then evaluated along with GNR as the control. The absorption peak of GNR at 800 nm decreased by approximately 60% after laser irradiation for only 5 s (Figure 5.3b). In contrast, almost no change of absorption was observed for SPN2 after irradiation for the same time. No significant changes in the absorption of SPN2 was detected even after irradiation for 6 min, while the absorption peak at 800 nm almost disappeared for GNR at the same time point. These data clearly demonstrated the superior photostability of SPN2 compared to that of GNR. The PA intensities of SPN2 were measured upon illumination with an 800 nm pulse laser at different concentrations (Figure 5.3c). A linear relationship between PA intensities and the concentrations of SPN2 was clearly observed. The PA image of

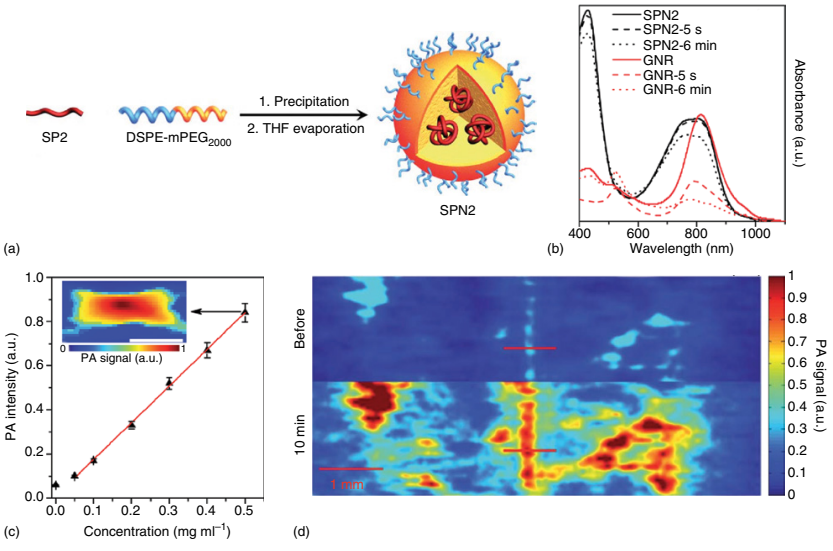

Figure 5.3 (a) Schematic illustration of the preparation of SPN2 using DSPE-mPEG$_{2000}$ as the matrix. (b) UV–vis absorption of SPN2 and GNR before and after laser irradiation for 5 s and 6 min, respectively. (c) The PA intensity as a function of concentration of SPN2. The inset figure shows the PA image of SPN2 at the concentration of 0.5 mg ml^{-1}. (d) PA images of rat cortical vasculature before and after systemic administration of SPN2 for 10 min. (Reprinted with permission from Ref. [56]. Copyright 2013, Royal Society of Chemistry.)

SPN2 at 0.5 mg mL^{-1} also showed the high PA signal generation capability of SPN2. Furthermore, SPN2 had almost no fluorescence under the excitation at 800 nm, indicating that nonradiative decay was the primary pathway of the energy dissipation process for the excitons. Thus, SPN2 was demonstrated to be a good candidate for PA imaging. The ability of SPN2 for *in vivo* PA imaging was then evaluated by cortical vasculature imaging of living rats. Before systemic administration, only weak PA signals can be detected from the brain vessels of rat because of the relatively low absorption coefficient of hemoglobin molecules at 800 nm. On the contrary, the PA signal from the blood vessels greatly enhanced after systemic administration of SPN2 for 10 min (Figure 5.3d). The enhanced contrast between blood vessels and brain parenchyma should be attributed to the strong PA signal of SPN2 circulating in the blood vessels. In addition, PA signals in the blood vessels remained almost the same after administration for 30 min, indicating the relatively long circulation time of SPN2 *in vivo*.

5.3.3 PA Imaging of Tumor

Tumor imaging is an imperative research area as diagnosis of tumor in the early stages is crucial for tumor therapy [93]. PA imaging holds great promise in tumor imaging as it can provide both high spatial resolution and deep tissue penetration [1, 94]. A variety of PA contrast agents have been applied for tumor imaging, such as organic dyes [95, 96], GNR [97], and porphyrins [98]. SPNs have also been utilized for PA imaging of tumor owing to their superior photostability and good biocompatability. Based on SP2, Balasundaram *et al.* developed folate-functionalized SPN2 (folate-SPN2), which served as a nanoprobe for PA imaging of folate receptor-positive (FR+ve) breast cancer [99]. The folate-SPN2 also had NIR absorption with strong PA intensity. The *in vivo* PA imaging results showed that folate-SPN2-treated mice had stronger PA signal in the tumor site compared with that of folate-free SPN2-treated mice, confirming the active targeting capability of folate-SPN2 to FR+ve breast cancer.

To screen SPs with excellent PA properties for tumor imaging and study the relationship between polymer structures and PA properties, Pu *et al.* designed a series of SPs (SP4–SP6) composed of diketopyrrolopyrrole (DPP) which is a widely used low band gap monomer [72]. These SPs and poly(cyclopentadithiophene-*alt*-benzothiadiazole) (SP3) that had no DPP structure were respectively transformed into SPNs by coprecipitating with DSPE-mPEG$_{2000}$ (Figure 5.4a). The PA spectra of obtained SPNs were then measured and compared with each other. It is obvious that SPN6 had a much stronger PA signal than any other SPN under the same concentration (Figure 5.4b). The PA amplitudes of SPNs at 710 nm were determined at a series of concentrations ranging from 5 to 100 μg ml^{-1}. All SPNs showed a linear relationship between PA amplitude and SPN concentration (Figure 5.4c). The PA signal of SPN6 was approximately 3.70, 5.40, and 3.20-fold higher than that of SPN3, SPN4, and SPN5 at each concentration, respectively. In addition, owing to the relatively red-shifted absorption and stronger PA amplitude of SPN6 as compared with other SPNs, only the PA amplitude of SPN6 could be detected under concentrations as low as 2 μg ml^{-1} at 850 nm. The fluorescence

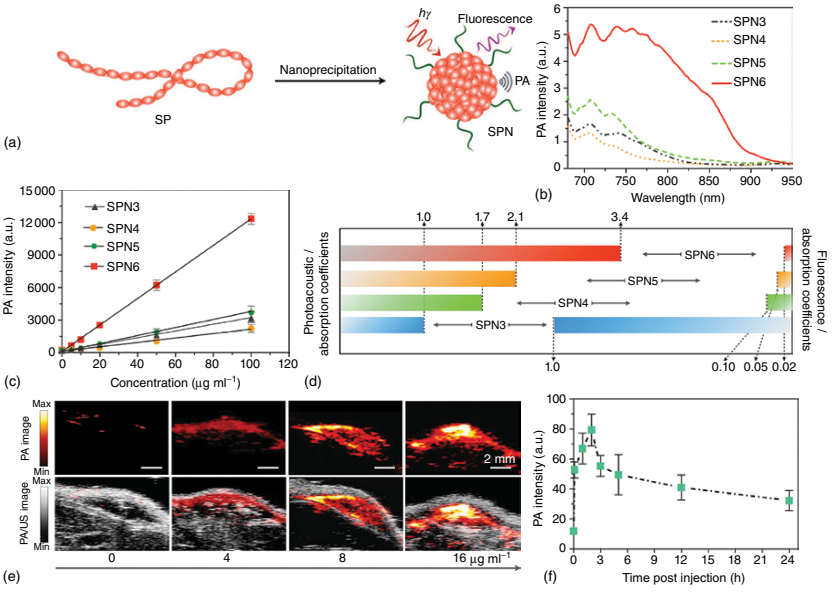

Figure 5.4 (a) Schematic illustration of preparation of SPNs via nanoprecipitation. (b) PA spectra of SPNs in 1 × PBS (pH = 7.4). (c) PA intensities of SPNs as a function of concentration in PBS (pH = 7.4). (d) Normalized PA and fluorescence intensities based on same mass extinction coefficients of SPNs at 710 nm. (e) PA and PA/ultrasound coregistered images of SPN6-matrigel inclusions in mice at different concentrations. (f) PA signals at 750 nm in tumor as a function of time after administration of SPN6. The error bars represent standard deviations of three separate measurements. (Reprinted with permission from Ref. [72]. Copyright 2015, Wiley-VCH Verlag GmbH & Co. KGaA, Weinheim.)

of SPNs showed that SPN3 had the strongest fluorescence intensity among all the SPNs, which was 20, 10, and 54-fold higher than that of SPN4, SPN5, and SPN6, respectively. To compare the optical and PA properties of SPNs, the fluorescence and PA amplitudes of SPNs at 710 nm were normalized based on their mass excitation coefficients (Figure 5.4d). SPN6 had the highest normalized PA brightness among all SPNs, which was followed by SPN4, SPN5, and SPN3. It can be observed that the order of the PA amplitudes of SPNs is contrary to that for the fluorescence intensities. This phenomenon can be explained by the mechanism of energy dissipation process described in the preceding text. As these SPNs are not phosphorescence, the fluorescence and thermal deactivation compete with each other upon light illumination. Among all the SPNs, the strongest electron donor–acceptor backbone structure endowed SPN6 with the narrowest band gap, which also induced SPN6 to favor nonradiative deactivation more. Thus, these data demonstrated that SPN6 was the best candidate for the PA imaging due to its best ability to transfer photon energy into heat among all the SPNs. The *in vivo* PA imaging capability of SPN6 was first evaluated by subcutaneous injections of SPN6 solutions into the dorsal area of mice. With the increase of the SPN6 concentration, the PA intensities in the dorsal area became stronger and stronger (Figure 5.4e). Quantification data showed linear correlation between mass concentration and PA signal of SPN6. The detection limit of SPN6 was determined as $0.6\,\mu g\,ml^{-1}$ for *in vivo* PA imaging, which was 3.3 and 14.9-times lower than that of SPN3 and GNR, respectively. Furthermore, no PA intensity loss of SPN6 was observed after exposure to 2700 laser pulses, indicating its excellent photostability. SPN6 was then applied for *in vivo* PA imaging of tumor using HeLa xenograft tumor model. After systemic administration of SPN6 through tail vein, the PA signal in the tumor site increased dramatically within a short period of time (Figure 5.4f). The PA signal in the tumor reached the maximum at 2 h post injection, which was 5.3-fold higher than the tumor background. Also, the real-time *in vivo* PA spectrum which extracted from the tumor of SPN6-injected mice resembled well with the PA spectrum in solution (Figure 5.4b), confirming that the enhancement of PA signal in the tumor area was generated from SPN6.

Based on SP3, Zhang *et al.* designed a SPN3-based theranostic nanosystem (SPN3/Ce6@lipid-Gd-DOTA micelles) for tumor which combined MRI, PA imaging, photodynamic therapy (PDT), and PTT into one micelle (Figure 5.5a) [100]. They first synthesized a gadolinium-1,4,7,10-tetraacetic acid (Gd-DOTA) conjugated [polyethylene glycol-2000]-2-distearoyl-*sn*-glycero-3-phosphoethanolamine, lipid-Gd-DOTA, based on previous literature [101]. Then, a matrix-encapsulation method was used to prepare the nanoparticles by encapsulating SP3 and chlorin e6 (Ce6) into lipid-Gd-DOTA micelles with the help of 1-palmitoyl-2-stearoyl-*sn*-glycero-3-phosphatidylcholine (HSPC) [102]. The successful preparation of SPN3/Ce6@lipid-Gd-DOTA micelles was confirmed by comparing its absorption spectrum with the absorption spectra of SPN3@lipid micelles and Ce6 (Figure 5.5b). For SPN3/Ce6@lipid-Gd-DOTA micelles, the sharp absorption peak at 405 nm can be assigned to the Soret absorption peak of Ce6, while the broad absorption peak at around 650 nm was assigned to the absorption of SP3 and the Q-band absorption of

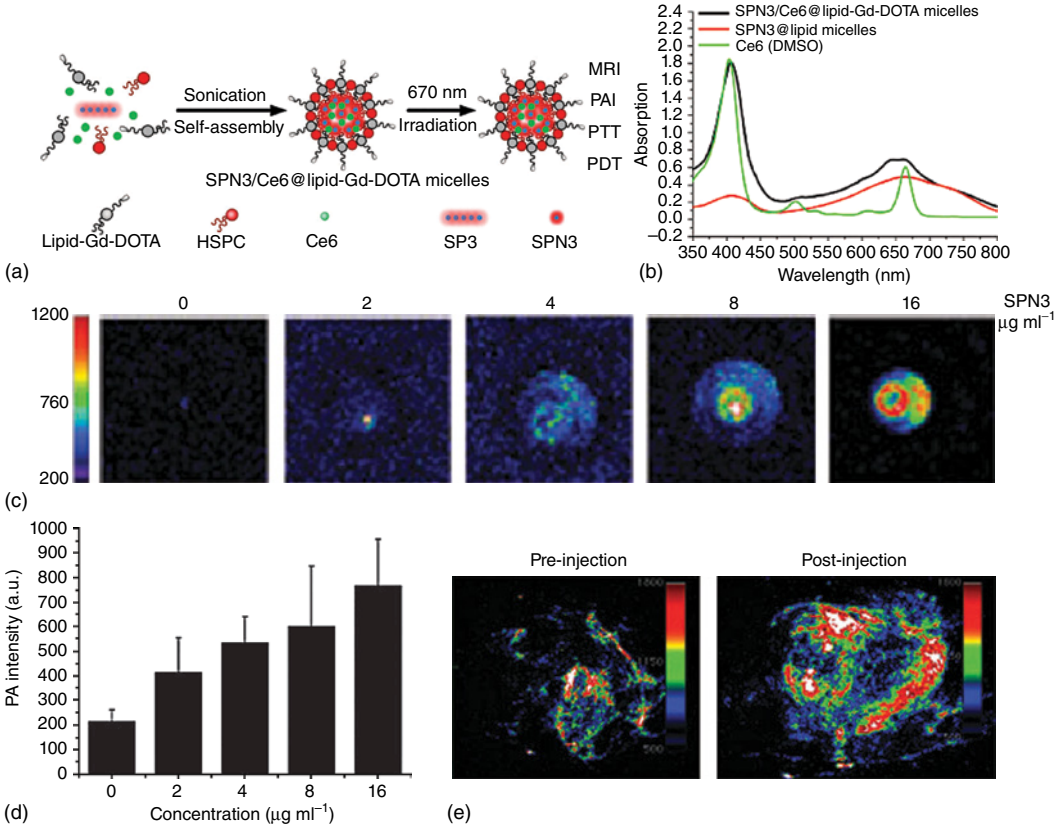

Figure 5.5 (a) Schematic illustration of preparation of SPN3/Ce6@lipid-Gd-DOTA micelles. (b) Absorption spectra of Ce6 (in DMSO), SPN3@lipid micelles, and SPN3/Ce6@lipid-Gd-DOTA micelles. (c) PA images and (d) PA intensities of SPN3/Ce6@lipid-Gd-DOTA micelles under different concentrations. (e) PA images of the tumor sites before and after intratumoral injection of SPN3/Ce6@lipid-Gd-DOTA micelles. (Reprinted with permission from Ref. [100]. Copyright 2015, Royal Society of Chemistry.)

Ce6. These data clearly indicated the successful encapsulation of SP3 and Ce6 into the micelles, and the loading efficiencies of SP3 and Ce6 were determined as 16 and 24 wt%, respectively. The PA intensities of SPN3/Ce6@lipid-Gd-DOTA micelles were then measured under different concentrations. When the concentration was increased from 0 to 16 μg ml^{-1}, the PA signal increased gradually as observed from the PA images (Figure 5.5c). The quantification results also showed that the PA intensity of SPN3/Ce6@lipid-Gd-DOTA micelles increased along with the increasing of the concentration of micelles (Figure 5.5d). Owing to the satisfying *in vitro* PA imaging capability, the SPN3/Ce6@lipid-Gd-DOTA micelles were then utilized for *in vivo* PA imaging of tumor. After intratumoral injection of SPN3/Ce6@lipid-Gd-DOTA micelles, the PA signal in the tumor site was much stronger than the PA signal in the tumor before injection (Figure 5.5e), showing the potential of *in vivo* PA imaging for SPN3/Ce6@lipid-Gd-DOTA micelles. SPN3/Ce6@lipid-Gd-DOTA micelles also showed good PDT and PTT effects owing to the relatively high photothermal conversion efficiency of SP3 and the singlet oxygen generated by Ce6. Thus, SPN3/Ce6@lipid-Gd-DOTA micelles may act as a promising theranostic agent for tumor imaging and therapy.

5.3.4 PA Imaging of Lymph Nodes

Staging of lymph nodes is important because nodal metastases in some types of cancer restrict the therapeutic options and are also a fundamental index for prognosis [103]. Several studies have been reported for PA imaging of lymph nodes by using different PA contrast agents such as gold nanocages [104, 105], dye-loaded mesoporous silica nanoparticles [106], and dye-loaded perfluorocarbon nanoparticles [107]. The first example of using SPNs for PA imaging of lymph nodes is reported by Pu *et al.* [36] SP3 and poly(acenaphthothienopyrazine-*alt*-benzodithiophene) (SP7) were encapsulated by 1,2-dipalmitoyl-*sn*-glycero-3-phosphocholine (DPPC) to form SPN3 and SPN7 through nanoprecipitation, respectively (Figure 5.6a). The narrower PA spectral profile and higher PA intensity of SPN3 compared with SPN7 made SPN3 a better candidate for PA imaging. To estimate the PA intensity of SPN3 *in vivo*, matrigel-containing solutions of SPN3, single-walled carbon nanotubes (SWNTs) or GNR under different concentrations were subcutaneously injected into living mice. Linear correlations between nanoparticle concentration and PA amplitude were observed for all nanoparticles (Figure 5.6b). It is noted that PA amplitude of SPN3 was 4.0 and 5.8-fold higher than that of SWNTs and GNR, respectively, under the same mass concentration indicating the excellent PA imaging ability of SPN3. Then, the *in vivo* lymph node tracking ability of SPN3 was tested by PA and fluorescence imaging. After systemic administration of SPN3 through tail vein for 24 h, obvious accumulations of SPN3 in brachial lymph nodes (BLNs), inguinal lymph nodes (ILNs), and superficial cervical lymph nodes (SCLNs) of the living mice were observed from the PA images (Figure 5.6c), while almost no PA signal can be detected for all lymph nodes before administration of SPN3. *Ex vivo* lymph nodes imaging in the agar phantom further confirmed the lymph nodes accumulation ability of SPN3 (Figure 5.6d). Lymph node from the SPN3-injected mice showed obvious PA signal while no PA signal was observed for the lymph node

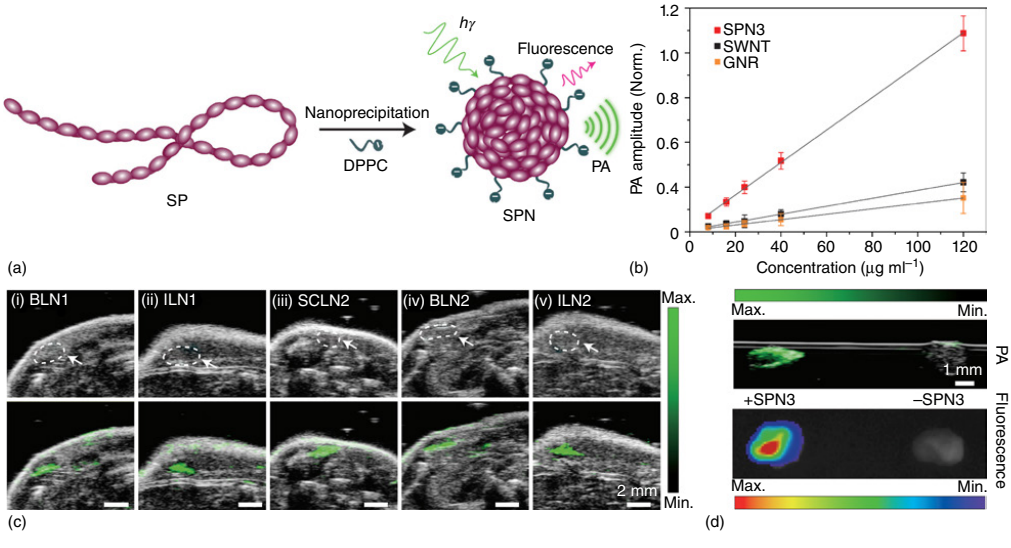

Figure 5.6 (a) Schematic illustration of preparation of SPNs through nanoprecipitation method. (b) PA amplitudes of the matrigel-containing solutions of nanoparticles in the subcutaneous dorsal area of living mice as a function of mass concentration. The background signal was 0.21 ± 0.03 a.u., which were calculated as the average PA signal in the areas where no nanoparticles were injected. $R^2 = 0.992$, 0.990, and 0.992 for SPN3, SWNTs, and GNR, respectively. (c) Ultrasound (upper) and PA/ultrasound coregistered (lower) images of lymph nodes after intravenous injection of SPN3 (50 μg mouse^{-1}). Images represent the transverse slices of the lymph nodes. The white arrows and dashed circles showed the lymph nodes. The abbreviation names BLN, ILN, and SCLN represent brachial lymph node, inguinal lymph node, and superficial cervical lymph node, respectively. (d) *Ex vivo* PA/ultrasound coregistered (top) and fluorescence/bright-field (bottom) images of resected lymph nodes from SPN3-injected mouse (left) and saline-injected mouse (right) in an agar phantom. (Reprinted with permission from Ref. [36]. Copyright 2014, Nature Publishing Group.)

from saline-injected mice under the same scale bar. Similar results were also shown in the fluorescence imaging of the lymph nodes. Quantification data revealed a 13.3-fold enhancement for PA intensity of lymph nodes from SPN3-injected mice as compared to the lymph nodes from saline-injected mice, demonstrating the superior lymph nodes' tracking capability of SPN3 *in vivo*.

5.3.5 PA Imaging of ROS

ROS is a series of critical chemical mediators that play vital roles in many pathological processes including bacterial infections, cancer, cardiovascular disease, and arthritis [108–110]. Imaging of ROS *in vivo* is a crucial but challenging task because of the lack of stability for many imaging agents in the presence of ROS. Owing to the high photostability and good resistance against ROS, SPNs have been developed for both *in vitro* and *in vivo* imaging of ROS. Owing to the excellent PA imaging capability and good tolerance for ROS, SPN3 was further utilized to design a ratiometric PA nanoprobe (RSPN) by coupling SPN3 to a ROS-sensitive NIR dye (IR775S) (Figure 5.7a) [36]. Before treatment of ROS, the PA spectrum of RSPN showed three major peaks at 700, 735, and 820 nm with almost the same intensity. Upon the addition of $ONOO^-$ or ClO^-, PA peak at 700 nm, which was attributed to SP3, almost remained the same. However, the peak at 735 nm decreased dramatically and the peak at 820 nm nearly disappeared because of the ROS-mediated oxidation of IR775S (Figure 5.7b). Therefore, the detection of $ONOO^-$ or ClO^- through ratiometric PA imaging (PA_{700}/PA_{820}) can be achieved. The capacity of RSPN to detect endogenously generated ROS was tested *in vitro* by using murine macrophage RAW264.7 cells. Strong PA signals were observed at both 700 and 820 nm for RSPN- incubated RAW264.7 cells in the resting state, resulting in $PA_{700}/PA_{820} = 1.4 \pm 0.43$. However, after pretreating cells with lipopolysaccharide (LPS) and interferon-γ (IFN-γ), PA signal at 820 nm decreased significantly due to the oxidation of IR775S by ROS which was stimulated by LPS and IFN-γ, leading to an enhancement of PA_{700}/PA_{820} to 7.3 ± 0.96. When *N*-acetylcysteine (NAC) was used to treat the cells together with LPS and IFN-γ, PA_{700}/PA_{820} returned to a relatively low level of 3.3 ± 0.78 as NAC is a free-radical scavenger that can eliminate ROS (Figure 5.7c). In addition, The ROS imaging capability was tested *in vivo* by using a murine model of zymosan-induced acute edema. PA signals were simultaneously monitored at 700 and 820 nm for both zymosan and saline-treated mice. PA amplitude at 700 nm for both zymosan and saline-treated mice nearly remained unchanged over time, as illustrated by pseudo-green color (Figure 5.7d). However, the PA amplitude at 820 nm for zymosan-treated mice decreased over time. In contrast, no obvious difference was observed for the PA amplitude at 820 nm of saline-treated mice over time. The superposition analysis showed a pseudo-color changing from yellow to green for zymosan-treated mice but not for saline-treated mice. These data showed the effectiveness of detection of ROS for RSPN both *in vitro* and *in vivo*.

5.3.6 Multimodal Imaging

Multimodal imaging has attracted great attention as it can combine the advantages of different imaging modalities [111]. To date, several studies have reported

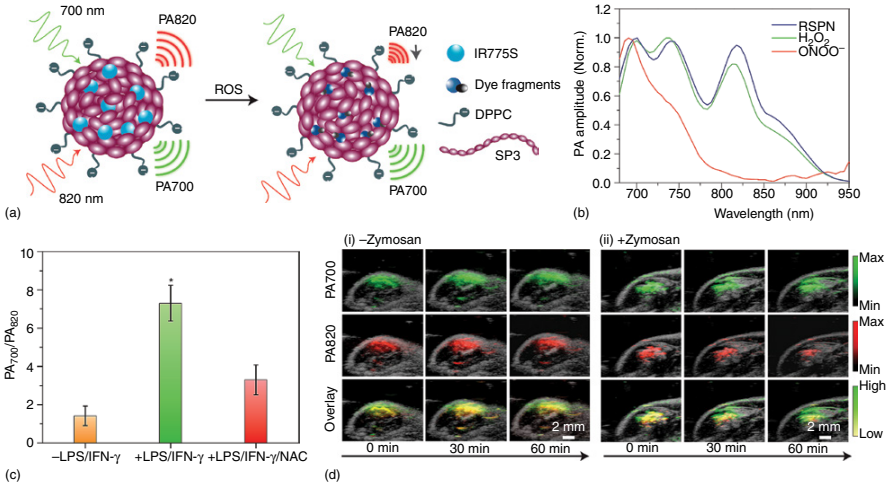

Figure 5.7 (a) Schematic illustration of RSPN probe for PA imaging of ROS. (b) Representative PA spectra of RSPN (5 μg ml^{-1}) in the absence and presence of different ROS (5 μM). (c) Quantification of PA ratio (PA_{700}/PA_{820}) for RAW264.7 cell pellets with and without LPS/IFN-γ or LPS/IFN-γ/NAC treatment. Error bars represents standard deviations from four measurements. *Statistically significant difference in PA_{700}/PA_{820} between LPS/IFN-γ treated and untreated or LPS/IFN-γ/NAC-treated cell pellets. ($^*p < 0.05$) (d) PA and ultrasound overlaid images of saline- (i) and zymosan-treated (ii) regions in the thigh of mice ($n = 3$). RSPN (3 μg in 50 μl) was intramuscularly injected into the thigh of mice after treatment of zymosan for 20 min. (Reprinted with permission from Ref. [36]. Copyright 2014, Nature Publishing Group.)

the combination of PA imaging with other imaging modalities to accomplish multimodal imaging [112]. SPNs have also been utilized for the development of multimodal imaging contrast agents by doping SPNs with other materials. Jin *et al.* developed a nanotheranostic system by encapsulating tantalum oxide nanoparticles into SPN1 described earlier [89]. The obtained SPN1-based composite nanoparticles (TaO_x@SPN1) can act as both PA- and CT-imaging agents. TaO_x@SPN1 were then utilized for bimodal *in vivo* tumor imaging. The PA signal in the tumor area increased dramatically compared with the tumor background after i.v. injection of TaO_x@SPN1 for 1 h. In addition, TaO_x@SPN1 also showed good effect of PTT owing to its high photothermal conversion efficiency.

Similarly, Song *et al.* designed SP1-coated iron oxide nanoparticles (IONP@SPN1-PEG) to achieve multimodal imaging guided PTT [88]. They first synthesized ultrasmall iron oxide nanoparticles (IONPs), and then encapsulated IONPs with SP1 to obtain SP1-coated IONPs (IONP@SPN1). To endow IONP@SPN1 with good biocompatibility, a layer-by-layer (LBL) strategy was utilized to functionalize the nanoparticles (Figure 5.8a). IONP@SPN1 was coated sequentially by poly allylamine hydrochloride (PAH), polyacrylic acid (PAA), and six-arm branched PEG (P6AM-10). The obtained IONP@SPN1-PEG exhibited excellent stability in different biological mediums, which allowed them to be used in biological applications. The absorption spectra of IONP@SPN1 and IONP@SPN1-PEG were almost the same, indicating that surface coating had no impact on the absorption of the nanoparticles (Figure 5.8b). In addition, the relatively high absorption in NIR region of IONP@SPN1-PEG showed its potential in PA imaging. IONP@SPN1-PEG was then evaluated for *in vivo* PA imaging due to its broad and high absorption in the NIR region. Before systemic administration of IONP@SPN1-PEG, PA signals can only be detected in the big vasculatures of the tumor area, which were generated from hemoglobin molecules in the blood vessels (Figure 5.8c). In contrast, the PA signals in the tumor area increased significantly after systemic administration of IONP@SPN1-PEG for 24 h, indicating that IONP@SPN1-PEG can accumulate into the tumor area and generate strong PA signals. The quantification data showed that the PA signal in the tumor site at $t = 24$ h post injection was approximately fourfold higher than the PA signal before injection (Figure 5.8d), which further confirmed the excellent PA imaging capability of IONP@SPN1-PEG. In addition, IONP@SPN1-PEG also had a strong T_2-weighted MRI signal due to the high content of IONP in the nanoparticles, endowing IONP@SPN1-PEG with great prospect for bimodal imaging. By virtue of good passive tumor targeting ability and efficient nonradiative decay process, IONP@SPN1-PEG also showed good PTT effect for tumor treatment, demonstrating its potential in bimodal imaging guided PTT of tumor.

5.4 Summary and Outlook

SPNs have shown many advantages for *in vivo* PA imaging including good biocompatibility, excellent photostability, high PA brightness and high ROS tolerance as demonstrated by the studies presented in this chapter. These properties

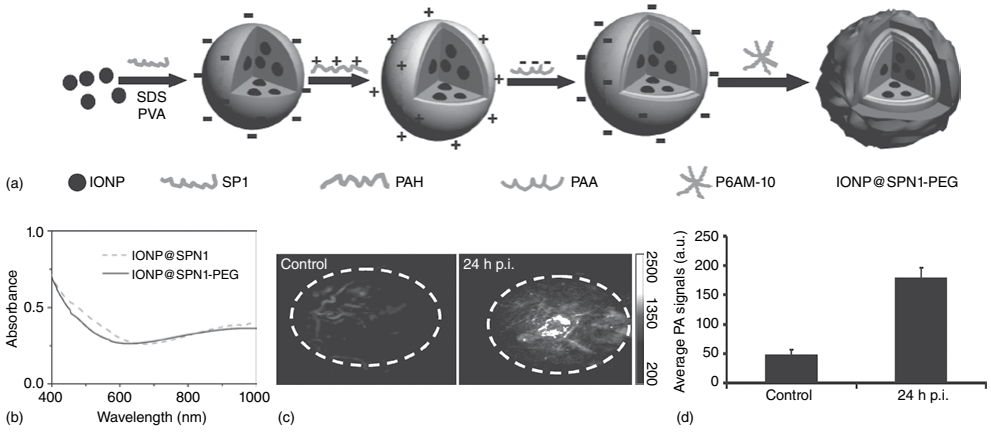

Figure 5.8 (a) Schematic illustration of fabrication process of IONP@SPN1-PEG nanocomposites. (b) Absorption spectra of IONP@SPN1 and IONP@SPN1-PEG at same concentration of SP1 (0.01 mg ml^{-1}). (c) PA images of mice before (left) and after systemic administration of IONP@SPN1-PEG for 24 h (right). (d) Quantification of PA signals from the tumor area in figure (c). (Reprinted with permission from Ref. [88]. Copyright 2013, Wiley-VCH Verlag GmbH & Co. KGaA, Weinheim.)

are important for PA imaging but not all exist in other PA contrast agents such as NIR organic dyes, inorganic nanoparticles, and 2D materials. The optical properties of SPNs are mainly determined by the SPs that are used to form the SPNs, and are usually independent of the physical properties of SPNs such as particle size, which distinguish SPNs from many inorganic nanoparticles (such as GNR) with size-dependent optical spectral properties. In addition, activatable and functional moieties can be easily encapsulated into SPNs with no influence on the optical properties of precursor SPNs, enabling activatable PA imaging and multimodal imaging. Recently, the influence of surface coating on the PA intensities of SPNs has been studied by Zhen *et al*. [113]. By coating of PEG-*b*-PPG-*b*-PEG- encapsulated SPNs with silica layer, the PA amplitude of SPNs can be increased by 1.4-fold. Mechanism studies revealed that the increased PA amplitudes can be attributed to the higher heat interfacial conductance for the interface between silica shell and water than that for the interface between SP core and water. Furthermore, owing to the high photothermal conversion efficiency of SPNs, theranostic systems based on PA imaging and PTT can also be achieved. Thus, SPNs provide a multifunctional nanoplatform that combines PA imaging with other imaging or therapy modalities for preclinical biological applications.

Although SPNs hold great promise for PA imaging and other biological applications, several critical issues should be addressed before advancing them for clinical translations. For example, although no *in vivo* toxicity of SPNs was detected in preliminary animal studies, the biodegradable properties and biological clearance of SPNs have to be fully evaluated. The long-term biosafety and *in vivo* residence time of SPNs also need to be studied. To forward the clinical translation of SPNs, complete clearance from the body within a short time after imaging is demanded. Thus, SPNs with sizes smaller than 5 nm are highly demanded as they can penetrate glomerular capillary walls and be rapidly cleared out from the body through urinary excretion. Preparation of biodegradable SPs is another possible solution as biodegradable amphiphilic polymers are available. Therefore, preparation of ultrasmall, biodegradable SPNs is highly desirable for promoting the clinical applications of SPNs.

References

1 Wang, L.V. and Hu, S. (2012) *Science*, **335**, 1458.
2 Kim, C., Favazza, C., and Wang, L.H.V. (2010) *Chem. Rev.*, **110**, 2756.
3 Zhang, Y., Hong, H., and Cai, W. (2011) *Cold Spring Harbor Protoc.*, **2011**, 1015.
4 Ntziachristos, V., Ripoll, J., Wang, L.V., and Weissleder, R. (2005) *Nat. Biotechnol.*, **23**, 313.
5 Wang, X.D., Pang, Y.J., Ku, G., Xie, X.Y., Stoica, G., and Wang, L.H.V. (2003) *Nat. Biotechnol.*, **21**, 803.
6 Zackrisson, S., van de Ven, S.M., and Gambhir, S.S. (2014) *Cancer Res.*, **74**, 979.
7 Zhang, H.F., Maslov, K., Stoica, G., and Wang, L.V. (2006) *Nat. Biotechnol.*, **24**, 848.
8 Wang, Y., Erpelding, T.N., Jankovic, L., Guo, Z., Robert, J.L., David, G., and Wang, L.V. (2012) *J. Biomed. Opt.*, **17**, 061208.

9 Xia, J. and Wang, L.V. (2014) *IEEE Trans. Biomed. Eng.*, **61**, 1380.
10 Liu, Y., Nie, L., and Chen, X. (2016) *Trends Biotechnol.*, **34**, 420.
11 Yao, J., Wang, L., Yang, J.M., Maslov, K.I., Wong, T.T., Li, L., Huang, C.H., Zou, J., and Wang, L.V. (2015) *Nat. Methods*, **12**, 407.
12 Yang, J.M., Li, C., Chen, R., Rao, B., Yao, J., Yeh, C.H., Danielli, A., Maslov, K., Zhou, Q., Shung, K.K., and Wang, L.V. (2015) *Biomed. Opt. Express*, **6**, 918.
13 Razansky, D., Buehler, A., and Ntziachristos, V. (2011) *Nat. Protoc.*, **6**, 1121.
14 Nie, L., Wang, S., Wang, X., Rong, P., Ma, Y., Liu, G., Huang, P., Lu, G., and Chen, X. (2014) *Small*, **10**, 1585.
15 Wang, L.V. (2009) *Nat. Photonics*, **3**, 503.
16 Yao, J., Maslov, K.I., Zhang, Y., Xia, Y., and Wang, L.V. (2011) *J. Biomed. Opt.*, **16**, 076003.
17 Manohar, S., Vaartjes, S.E., van Hespen, J.C.G., Klaase, J.M., van den Engh, F.M., Steenbergen, W., and van Leeuwen, T.G. (2007) *Opt. Express*, **15**, 12277.
18 Ntziachristos, V. and Razansky, D. (2010) *Chem. Rev.*, **110**, 2783.
19 Zhang, Y., Cai, X., Wang, Y., Zhang, C., Li, L., Choi, S.W., Wang, L.V., and Xia, Y. (2011) *Angew. Chem. Int. Ed.*, **50**, 7359.
20 Levi, J., Kothapalli, S.R., Ma, T.J., Hartman, K., Khuri-Yakub, B.T., and Gambhir, S.S. (2010) *J. Am. Chem. Soc.*, **132**, 11264.
21 Fan, Q.L., Cheng, K., Yang, Z., Zhang, R.P., Yang, M., Hu, X., Ma, X.W., Bu, L.H., Lu, X.M., Xiong, X.X., Huang, W., Zhao, H., and Cheng, Z. (2015) *Adv. Mater.*, **27**, 843.
22 Hoffman, R.M. (2005) *Nat. Rev. Cancer*, **5**, 796.
23 Filonov, G.S., Krumholz, A., Xia, J., Yao, J., Wang, L.V., and Verkhusha, V.V. (2012) *Angew. Chem. Int. Ed.*, **51**, 1448.
24 Chen, M., Tang, S., Guo, Z., Wang, X., Mo, S., Huang, X., Liu, G., and Zheng, N. (2014) *Adv. Mater.*, **26**, 8210.
25 Black, K.C.L., Wang, Y., Luehmann, H.P., Cai, X., Xing, W., Pang, B., Zhao, Y., Cutler, C.S., Wang, L.V., Liu, Y., and Xia, Y. (2014) *ACS Nano*, **8**, 4385.
26 Liu, J., Zheng, X., Yan, L., Zhou, L., Tian, G., Yin, W., Wang, L., Liu, Y., Hu, Z., Gu, Z., Chen, C., and Zhao, Y. (2015) *ACS Nano*, **9**, 696.
27 Ku, G., Zhou, M., Song, S., Huang, Q., Hazle, J., and Li, C. (2012) *ACS Nano*, **6**, 7489.
28 Cheng, L., Liu, J., Gu, X., Gong, H., Shi, X., Liu, T., Wang, C., Wang, X., Liu, G., Xing, H., Bu, W., Sun, B., and Liu, Z. (2014) *Adv. Mater.*, **26**, 1886.
29 Song, X.R., Wang, X., Yu, S.X., Cao, J., Li, S.H., Li, J., Liu, G., Yang, H.H., and Chen, X. (2015) *Adv. Mater.*, **27**, 3285.
30 De la Zerda, A., Zavaleta, C., Keren, S., Vaithilingam, S., Bodapati, S., Liu, Z., Levi, J., Smith, B.R., Ma, T.J., Oralkan, O., Cheng, Z., Chen, X., Dai, H., Khuri-Yakub, B.T., and Gambhir, S.S. (2008) *Nat. Nanotechnol.*, **3**, 557.
31 Kim, J.W., Galanzha, E.I., Shashkov, E.V., Moon, H.M., and Zharov, V.P. (2009) *Nat. Nanotechnol.*, **4**, 688.
32 Liu, J., Wang, C., Wang, X., Wang, X., Cheng, L., Li, Y., and Liu, Z. (2015) *Adv. Funct. Mater.*, **25**, 384.
33 Lovell, J.F., Jin, C.S., Huynh, E., Jin, H., Kim, C., Rubinstein, J.L., Chan, W.C., Cao, W., Wang, L.V., and Zheng, G. (2011) *Nat. Mater.*, **10**, 324.

34 Huynh, E., Leung, B.Y., Helfield, B.L., Shakiba, M., Gandier, J.A., Jin, C.S., Master, E.R., Wilson, B.C., Goertz, D.E., and Zheng, G. (2015) *Nat. Nanotechnol.*, **10**, 325.
35 Ng, K.K., Shakiba, M., Huynh, E., Weersink, R.A., Roxin, Á., Wilson, B.C., and Zheng, G. (2014) *ACS Nano*, **8**, 8363.
36 Pu, K., Shuhendler, A.J., Jokerst, J.V., Mei, J., Gambhir, S.S., Bao, Z., and Rao, J. (2014) *Nat. Nanotechnol.*, **9**, 233.
37 Pu, K., Shuhendler, A.J., and Rao, J. (2013) *Angew. Chem. Int. Ed.*, **52**, 10325.
38 Huang, P., Lin, J., Wang, X., Wang, Z., Zhang, C., He, M., Wang, K., Chen, F., Li, Z., Shen, G., Cui, D., and Chen, X. (2012) *Adv. Mater.*, **24**, 5104.
39 Jin, C.S., Lovell, J.F., Chen, J., and Zheng, G. (2013) *ACS Nano*, **7**, 2541.
40 Chang, K., Tang, Y., Fang, X., Yin, S., Xu, H., and Wu, C. (2016) *Biomacromolecules*, **17**, 2128.
41 Lovell, J.F., Liu, T.W., Chen, J., and Zheng, G. (2010) *Chem. Rev.*, **110**, 2839.
42 Feng, L., Zhu, C., Yuan, H., Liu, L., Lv, F., and Wang, S. (2013) *Chem. Soc. Rev.*, **42**, 6620.
43 Wu, C. and Chiu, D.T. (2013) *Angew. Chem. Int. Ed.*, **52**, 3086.
44 Pu, K., Chattopadhyay, N., and Rao, J. (2016) *J. Controlled Release*, **240**, 312.
45 Sun, K., Tang, Y., Li, Q., Yin, S., Qin, W., Yu, J., Chiu, D.T., Liu, Y., Yuan, Z., Zhang, X., and Wu, C. (2016) *ACS Nano*, **10**, 6769.
46 Pu, K., Shuhendler, A.J., Valta, M.P., Cui, L., Saar, M., Peehl, D.M., and Rao, J. (2014) *Adv. Healthc. Mater.*, **3**, 1292.
47 Wu, C., Hansen, S.J., Hou, Q., Yu, J., Zeigler, M., Jin, Y., Burnham, D.R., McNeill, J.D., Olson, J.M., and Chiu, D.T. (2011) *Angew. Chem. Int. Ed.*, **50**, 3430.
48 Zhu, H., Fang, Y., Zhen, X., Wei, N., Gao, Y., Luo, K.Q., Xu, C., Duan, H., Ding, D., Chen, P., and Pu, K. (2016) *Chem. Sci.*, **7**, 5118.
49 Hong, G., Zou, Y., Antaris, A.L., Diao, S., Wu, D., Cheng, K., Zhang, X., Chen, C., Liu, B., He, Y., Wu, J.Z., Yuan, J., Zhang, B., Tao, Z., Fukunaga, C., and Dai, H. (2014) *Nat. Commun.*, **5**, 4206.
50 Shuhendler, A.J., Pu, K., Cui, L., Uetrecht, J.P., and Rao, J. (2014) *Nat. Biotechnol.*, **32**, 373.
51 Xiong, L., Shuhendler, A.J., and Rao, J. (2012) *Nat. Commun.*, **3**, 1193.
52 Zhen, X., Zhang, C., Xie, C., Miao, Q., Lim, K.L., and Pu, K. (2016) *ACS Nano*, **10**, 6400.
53 Lyu, Y., Fang, Y., Miao, Q., Zhen, X., Ding, D., and Pu, K. (2016) *ACS Nano*, **10**, 4472.
54 Song, X., Liang, C., Gong, H., Chen, Q., Wang, C., and Liu, Z. (2015) *Small*, **11**, 3932.
55 Lyu, Y., Xie, C., Chechetka, S.A., Miyako, E., and Pu, K. (2016) *J. Am. Chem. Soc.*, **138**, 9049.
56 Liu, J., Geng, J.L., Liao, L.D., Thakor, N., Gao, X.H., and Liu, B. (2014) *Polym. Chem.*, **5**, 2854.
57 Yao, J. and Wang, L.V. (2011) *Contrast Media Mol. Imaging*, **6**, 332.
58 Hu, S. and Wang, L.V. (2010) *Front. Neuroenerg.*, **2**, 10.
59 Wu, C., Bull, B., Christensen, K., and McNeill, J. (2009) *Angew. Chem. Int. Ed.*, **48**, 2741.

60 Chan, Y.H., Wu, C., Ye, F., Jin, Y., Smith, P.B., and Chiu, D.T. (2011) *Anal. Chem.*, **83**, 1448.
61 Kim, S., Lim, C.K., Na, J., Lee, Y.D., Kim, K., Choi, K., Leary, J.F., and Kwon, I.C. (2010) *Chem. Commun.*, **46**, 1617.
62 Jeong, K., Park, S., Lee, Y.D., Lim, C.K., Kim, J., Chung, B.H., Kwon, I.C., Park, C.R., and Kim, S. (2013) *Adv. Mater.*, **25**, 5574.
63 Yu, J., Rong, Y., Kuo, C.-T., Zhou, X.-H., and Chiu, D.T. (2017) *Anal. Chem.*, **89**, 42.
64 Bell, A.G. (1880) *Am. J. Sci.*, **20**, 305.
65 Witte, R.S., Kim, K., Ashish, A., Fan, W., Kopelman, R., Kotov, N., Kipke, D., and O'Donnell, M. (2008) *Proc. SPIE Int. Soc. Opt. Eng.*, **6856**, 685614.
66 Li, K. and Liu, B. (2012) *J. Mater. Chem.*, **22**, 1257.
67 Liu, B., Wang, S., Bazan, G.C., and Mikhailovsky, A. (2003) *J. Am. Chem. Soc.*, **125**, 13306.
68 Geng, J., Li, K., Ding, D., Zhang, X., Qin, W., Liu, J., Tang, B.Z., and Liu, B. (2012) *Small*, **8**, 3655.
69 Ding, D., Liu, J., Feng, G., Li, K., Hu, Y., and Liu, B. (2013) *Small*, **9**, 3093.
70 Cui, L. and Rao, J. (2016) *WIREs Nanomed. Nanobiotechnol.* doi: 10.1002/wnan.1418
71 Marszalek, T., Li, M.M., and Pisula, W. (2016) *Chem. Commun.*, **52**, 10938.
72 Pu, K., Mei, J., Jokerst, J.V., Hong, G., Antaris, A.L., Chattopadhyay, N., Shuhendler, A.J., Kurosawa, T., Zhou, Y., Gambhir, S.S., Bao, Z., and Rao, J. (2015) *Adv. Mater.*, **27**, 5184.
73 Zhu, C., Liu, L., Yang, Q., Lv, F., and Wang, S. (2012) *Chem. Rev.*, **112**, 4687.
74 Pu, K.Y. and Liu, B. (2011) *Adv. Funct. Mater.*, **21**, 3408.
75 Duarte, A., Pu, K.Y., Liu, B., and Bazan, G.C. (2011) *Chem. Mater.*, **23**, 501.
76 Xing, C.F., Xu, Q.L., Tang, H.W., Liu, L.B., and Wang, S. (2009) *J. Am. Chem. Soc.*, **131**, 13117.
77 Yang, G.M., Liu, L.B., Yang, Q., Lv, F.T., and Wang, S. (2012) *Adv. Funct. Mater.*, **22**, 736.
78 Xie, C., Upputuri, P.K., Zhen, X., Pramanik, M., and Pu, K. (2016) *Biomaterials*, **119**, 1.
79 Li, K., Pan, J., Feng, S.S., Wu, A.W., Pu, K.Y., Liu, Y.T., and Liu, B. (2009) *Adv. Funct. Mater.*, **19**, 3535.
80 Zhang, J., Chen, H., Zhou, T., Wang, L., Gao, D., Zhang, X., Liu, Y., Wu, C., and Yuan, Z. (2017) *Nano Res.*, **10**, 64.
81 Miao, Q., Lyu, Y., Ding, D., and Pu, K. (2016) *Adv. Mater.*, **28**, 3662.
82 Liang, X.L., Li, Y.Y., Li, X.D., Jing, L.J., Deng, Z.J., Yue, X.L., Li, C.H., and Dai, Z.F. (2015) *Adv. Funct. Mater.*, **25**, 1451.
83 Zha, Z.B., Deng, Z.J., Li, Y.Y., Li, C.H., Wang, J.R., Wang, S.M., Qu, E.Z., and Dai, Z.F. (2013) *Nanoscale*, **5**, 4462.
84 Lyu, Y., Zhen, X., Miao, Y., and Pu, K. (2017) *ACS Nano*, **11**, 358.
85 Zhang, J., Yang, C., Zhang, R., Chen, R., Zhang, Z., Zhang, W., Peng, S., Chen, X., Liu, G., Hsu, C., and Lee, C. (2017) *Adv. Funct. Mater.*, **27**, 1605094.
86 Xie, C., Zhen, X., Lei, Q., Ni, R., and Pu, K. (2017) *Adv. Funct. Mater.*, **27**, 1605397.
87 Yin, C., Zhen, X., Zhao, H., Tang, Y., Ji, Y., Lyu, Y., Fan, Q., Huang, W., and Pu, K. (2017) *ACS Appl. Mater. Interfaces*, **9**, 12332.

88 Song, X.J., Gong, H., Yin, S.N., Cheng, L., Wang, C., Li, Z.W., Li, Y.G., Wang, X.Y., Liu, G., and Liu, Z. (2014) *Adv. Funct. Mater.*, **24**, 1194.
89 Jin, Y.S., Li, Y.Y., Ma, X.B., Zha, Z.B., Shi, L.L., Tian, J., and Dai, Z.F. (2014) *Biomaterials*, **35**, 5795.
90 Schneider, J.E., Bamforth, S.D., Grieve, S.M., Clarke, K., Bhattacharya, S., and Neubauer, S. (2003) *Magn. Reson. Mater. Phys., Biol. Med.*, **16**, 43.
91 Hong, J.Y., Yoon, H., and Jang, J. (2010) *Small*, **6**, 679.
92 Oh, W.K., Yoon, H., and Jang, J. (2010) *Biomaterials*, **31**, 1342.
93 Hussain, T. and Nguyen, Q.T. (2014) *Adv. Drug Delivery Rev.*, **66**, 90.
94 Mallidi, S., Luke, G.P., and Emelianov, S. (2011) *Trends Biotechnol.*, **29**, 213.
95 Zhang, J., Zhen, X., Upputuri, P.K., Pramanik, M., Chen, P., and Pu, K. (2017) *Adv. Mater.*, **29**, 1604764.
96 Miao, Q. and Pu, K. (2016) *Bioconjugate Chem.*, **27**, 2808.
97 Jokerst, J.V., Cole, A.J., Van de Sompel, D., and Gambhir, S.S. (2012) *ACS Nano*, **6**, 10366.
98 Huynh, E., Lovell, J.F., Helfield, B.L., Jeon, M., Kim, C., Goertz, D.E., Wilson, B.C., and Zheng, G. (2012) *J. Am. Chem. Soc.*, **134**, 16464.
99 Balasundaram, G., Ho, C.J.H., Li, K., Driessen, W., Dinish, U.S., Wong, C.L., Ntziachristos, V., Liu, B., and Olivo, M. (2015) *Int. J. Nanomed.*, **10**, 387.
100 Zhang, D., Wu, M., Zeng, Y.Y., Liao, N.S., Cai, Z.X., Liu, G., Liu, X.L., and Liu, J.F. (2016) *J. Mater. Chem. B*, **4**, 589.
101 Zeng, Y.Y., Zhang, D., Wu, M., Liu, Y., Zhang, X., Li, L., Li, Z., Han, X., Wei, X.Y., and Liu, X.L. (2014) *ACS Appl. Mater. Interfaces*, **6**, 14266.
102 Feng, G., Li, K., Liu, J., Ding, D., and Liu, B. (2014) *Small*, **10**, 1212.
103 McMahon, C.J., Rofsky, N.M., and Pedrosa, I. (2010) *Radiology*, **254**, 31.
104 Song, K.H., Kim, C.H., Cobley, C.M., Xia, Y.N., and Wang, L.V. (2009) *Nano Lett.*, **9**, 183.
105 Cai, X., Li, W.Y., Kim, C.H., Yuan, Y.C., Wang, L.H.V., and Xia, Y.N. (2011) *ACS Nano*, **5**, 9658.
106 Liu, Z.G., Rong, P.F., Yu, L., Zhang, X.T., Yang, C.J., Guo, F., Zhao, Y.Z., Zhou, K.C., Wang, W., and Zeng, W.B. (2015) *Mol. Pharmaceutics*, **12**, 3119.
107 Akers, W.J., Kim, C., Berezin, M., Guo, K., Fuhrhop, R., Lanza, G.M., Fischer, G.M., Daltrozzo, E., Zumbusch, A., Cai, X., Wang, L.V., and Achilefu, S. (2011) *ACS Nano*, **5**, 173.
108 Szabo, C., Ischiropoulos, H., and Radi, R. (2007) *Nat. Rev. Drug Discovery*, **6**, 662.
109 Medzhitov, R. (2008) *Nature*, **454**, 428.
110 Bauerova, K. and Bezek, A. (1999) *Gen. Physiol. Biophys.*, **18**, 15.
111 Jennings, L.E. and Long, N.J. (2009) *Chem. Commun.*, (24), 3511.
112 Shin, T.H., Choi, Y., Kim, S., and Cheon, J. (2015) *Chem. Soc. Rev.*, **44**, 4501.
113 Zhen, X., Feng, X., Xie, C., Zheng, Y., and Pu, K. (2017) *Biomaterials*, **127**, 97.

6

Conjugated Polymers for Two-Photon Live Cell Imaging

Shuang Li[1], *Xiao-Fang Jiang*[1], *and Qing-Hua Xu*[2]

[1] *South China University of Technology, School of Material Science and Engineering, State Key Laboratory of Luminescent Materials and Devices, No. 381 Wushan Road, Guangzhou, Guangdong, 510640, PR China*
[2] *National University of Singapore, Department of Chemistry, 3 Science Drive 3, Singapore, 117543, Singapore*

6.1 Introduction

Fluorescence microscopy is one of the most widely used noninvasive and powerful bioimaging tools for visualization of biological materials and pathways and events in living cells, tissues, and animals [1–3], due to its simple, fast, sensitive, reliable, and reproducible detection [4–6]. So far, the most sensitive fluorescence imaging modalities have been able to monitor biological interactions at the single-molecule level with nanometer spatial resolution [7–10], which provide more details on cellular processes. In general, detection limit, sensitivity, specificity, and reliability of fluorescence-based techniques are mainly determined by the photophysical properties of the imaging contrast agents, such as brightness, photo-stability, excitation, and emission wavelength as well as sensing modalities.

Conventional fluorescence microscopy utilizes linear one-photon absorption (1PA) processes for contrast generation, which usually uses ultraviolet–visible light as the excitation source. However, light in this region (300–650 nm) is strongly absorbed and scattered by tissues of the biological environment and generates autofluorescence, which will blur the images at greater depths. Consequently, applications of conventional one-photon excitation (1PE) fluorescence microscopy are limited to the superficial area (depth of <100 μm) of living tissues or animals. Compared to ultraviolet–visible light, far-red/near-infrared (NIR) light (650–950 nm) is favorable for imaging applications within intact tissues due to its larger tissue penetration depth and minimal interference from absorption and scattering by surrounding biological tissues and thus less photodamage to some light-sensitive novel organs [11].

Two-photon excitation microscopy (2PEM), invented by Denk *et al.* in the 1990s [12], is a revolutionary tool which has attracted great research interests in the biological imaging field. 2PEM utilizes the phenomenon of simultaneous absorption of two photons, which is called two-photon absorption (2PA). In a

Conjugated Polymers for Biological and Biomedical Applications, First Edition. Edited by Bin Liu

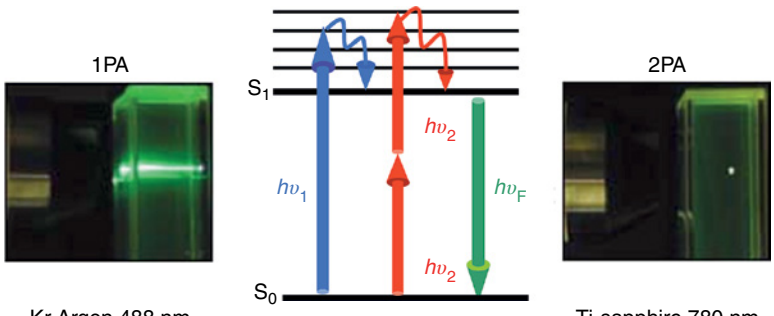

(a)

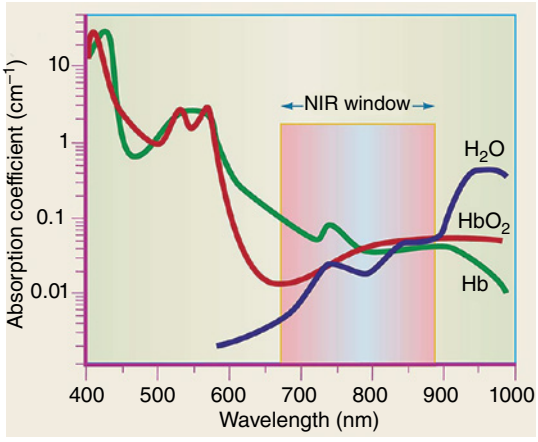

(b)

Figure 6.1 (a) Jablonski diagram illustrating 1PA, 2PA, and the related fluorescence process. Deep tissue penetration length of NIR light. (b) The NIR window for *in vivo* imaging. The spectral response of oxygenated hemoglobin, deoxygenated hemoglobin, and water varies as a function of wavelength. The red highlighted area indicates the biological optical window where adsorption due to the body is minimum. (Adapted with permission from Refs [13, 14]. Copyright 2001, 2002 Nature Publishing Group.)

2PA process, molecules are promoted to the excited state by simultaneous absorption of two photons of lower energy, as illustrated in Figure 6.1a. Compared with conventional 1PE fluorescence microscopy that utilizes light of shorter wavelength (higher energy) to excite the contrast agent, the excitation wavelength used in 2PEM usually falls in the NIR region. Light in this region is coincident with the biological transparency window (700–1100 nm), which has minimal absorption and scattering by the surrounding biological molecules (Figure 6.1b) and thus renders deeper tissue depth (up to a few centimeter) [13, 15]. As 2PA process depends quadratically on the incident light intensity, 2PA-induced fluorescence could only be observed in the focal volume of laser beam, leading to a localized excitation as shown in Figure 6.1a [14]. This localized excitation gives rise to 3D spatial resolution and greatly reduced photo-damage to living tissues. Although 2PA-/2PE-based techniques require expensive high-power excitation

sources such as pulsed lasers compared to its 1PE counterparts, the unique advantages of 2PA/2PE in deep tissue imaging applications make the investment worthwhile. 2PEM and related techniques have been developed for high-sensitivity *in vivo* imaging and measurement during the past few decades.

So far, the lack of suitable two-photon contrast agents has remained the most challenging issue that hinders the development and practical applications of 2PEM. Development of 2PA materials with large two-photon absorption cross-section (δ) values draws great research interest to enhance the efficiency of 2PA-related techniques. Various materials have been utilized as 2PEM contrast agents, including small organic molecules, dendrimers, polymers, fluorescent proteins, and inorganic materials (quantum dots and gold nanoparticles) as well as some composite materials during the past few decades [16–18]. Ideal 2PEM contrast agents require large δ and high fluorescence quantum yield (Φ_F). The product of two, $\delta\Phi_F$, is termed as two-photon action cross-section, characterizing the two-photon brightness of a fluorophore. As a 2PA process has different symmetry selection rules from that of 1PA, fluorophores that have been optimized for conventional 1PE techniques have very small δ values [19]. Versatile methods have been adopted to improve the δ values of small organic molecules at ~800 nm, the central wavelength of most readily available femtosecond laser source. δ values could be improved by optimizing molecular structures, including conjugation length, molecular planarity, intramolecular charge transfer, vibronic coupling, dimensionality of the charge-transfer network, and the electron-donating and electron-withdrawing abilities of the donor and acceptor [20–22]. Owing to the rapid development of material synthesis, π-conjugated organic molecules and conjugated polymers with δ values over 1000 GM have been widely reported [19, 23].

However, some candidates for 2PEM imaging contrast agents still suffer from some drawbacks such as poor photo-stability of organic dyes [24], cytotoxicity, and irregular blinking behaviors of quantum dots as well as low quantum yields of gold nanoparticles [25]. Among various 2PEM imaging contrast agents, conjugated polymers are excellent candidates due to their high two-photon brightness and excellent photo-stability. Conjugated polymers are organic macromolecules that are characterized by a backbone structure containing alternating double- and single-bonds, along which the delocalized π-electron can migrate via π-electron cloud overlap [26]. Since the discovery of conductive polymers in the 1970s, which was awarded the Nobel Prize in chemistry [27–34], a number of conjugated polymers have been designed and synthesized by different research groups all over the world [35, 36]. Owing to their unique electronic structures, conjugated polymers displayed exceptional photo-physical properties such as large absorption coefficient, high fluorescent quantum yield (Φ_F), and optical amplification via Förster resonance energy transfer (FRET) [37], which make them excellent light-harvesting materials and highly fluorescent imaging agents [38–42]. Combination of conjugated polymers and nanotechnology endows conjugated-polymer-based nanoparticles (CPNs) with rich properties such as amphilicity, surface functionalities, a variety of sensing moieties, and enhanced permeability [43, 44]. CPNs have been demonstrated as promising contrast agents in imaging and sensing applications due to their unique advantages

including high brightness, brilliant photo-stability, great biocompatibility, facile chemical synthesis, tunable optical properties, and various polymer chemistry as well as versatile surface modifications [26, 45–47]. In addition to their excellent linear optical properties that have been reviewed recently [26, 45–47], conjugated polymers have larger δ values compared with their small-molecule counterparts [48], which make them promising contrast agents for various 2PE-based biological applications.

However, the intrinsic hydrophobicity originating from π-conjugated backbone limits their potential applications in biological systems. For their biological applications, water-soluble conjugated polymers are needed considering the aqueous environment of biological systems. Water-soluble conjugated polymers can be obtained by modifying the π-conjugated backbones with charged side chains. In addition to chemical modification with ionic side chains, hydrophobic conjugated polymers can become soluble by using various physical approaches to fabricate water-dispersible nanoparticles [20, 26, 49, 50]. In this chapter, we will summarize the development of various water-soluble conjugated polymers and CPNs in the applications of two-photon live cell imaging.

6.2 Conjugated Polymers and CPNs as One-Photon Excitation Imaging Contrast Agents

Conjugated polymers have attracted considerate attention as fluorescent probes due to their tunable electronic and optical properties by designing different backbone structures and side chains as well as the effective conjugation length [26, 46, 47, 51]. Owing to the rapid development of design and synthesis, conjugated polymers with high Φ_F values and emission colors that span the entire range of the visible spectrum have been widely developed, including polyfluorene (such as PDHF and PFO), poly(phenylene ethynylene) (such as PPE), poly(phenylene vinylene) (such as MEH-PPV and CN-PPV), and fluorene-based copolymers (such as PFPV, PFBT, and PFDBT5) [26]. Various conjugated polyelectrolytes (CPEs) have been prepared by modifying the backbones of conjugated polymers with charged side chains to endow water solubility for biological applications [33, 37, 52]. Charged side chains, such as cationic quaternary ammonium groups, anionic carboxyl groups, sulfonic groups, and phosphate groups endow CPEs with sufficient capability to dissolve in aqueous solution for their further interactions with biomacromolecules. Charged groups or recognition elements along the backbones of CPEs provide various electrostatic and hydrophobic interactions or binding moieties of receptors with various biomolecules in living systems, which allow targeted bioimaging applications [46]. For example, Zhu *et al.* reported a positively charged fluorescent probe, poly(*p*-phenylene vinylene) derivative (PPV-1), for monitoring cell apoptosis [53]. Upon apoptosis, a series of changes such as the exposure of negatively charged phosphatidylserine and the enhancement of membrane permeability occur in the cellular membrane. Bright green fluorescence was observed for apoptotic cells, while little fluorescence was observed for intact cells due to inefficient cellular uptake. Kim *et al.* synthesized an anionic folic acid substituted PPE derivative for targeted cancer cell imaging [54]. Compared with the

counterpart polymer without folic acid groups, the folic acid functionalized PPE derivative could selectively stain KB cancer cells through receptor-mediated uptake and primarily localize in the cytoplasm.

Highly bright NIR conjugated polymers with deep tissue penetration ability have largely aroused research interest for their bioimaging applications to avoid optical interferences such as absorption, scattering, and autofluorescence. As most conjugated polymers emit in the visible range, introduction of narrow-band-gap moieties into the backbone of conjugated polymers is a good strategy to tune the emission wavelength to far-red or NIR range. Liu *et al*. synthesized a bright far-red and NIR fluorescent conjugated polymer with a Φ_F value of 25% and a large Stokes shift of ~200 nm for *in vitro* and *in vivo* imaging applications [55].

In addition to their large extinction coefficients and high Φ_F, the backbone of conjugated polymers holds the polymeric segments in close proximity, allowing for super-quenching of the fluorescence of conjugated polymers or optical amplification of analytes via FRET [39, 41, 56]. The signal amplification of analytes helps to enhance the detection sensitivity and thus accelerate the development of conjugated-polymers-based biosensing and bioimaging applications [32, 34, 37, 57–67]. By grafting conjugated polymers with specific recognition ligands, this methodology can be utilized for sensitive detection of analytes in complex biological environments such as disease-related biomarkers such as nucleic acids and proteins [52, 68–89]. For instance, Pu and Liu synthesized a new cationic polyfluorene derivative with 20 mol% 2,1,3-benzothiadiazole (BT) content via Suzuki cross-coupling polymerization for naked-eye detection and quantification of heparin [90]. Feng *et al*. designed a homogeneous, convenient and sensitive DNA methylation detection method using an optically amplifying CPE (poly((1,4-phenylene)-2,7-[9,9-bis(6′-*N*,*N*,*N*-trimethyl-ammonium)-hexylfluorene] dibromide)) [91].

In addition to chemical modification with ionic side chains, hydrophobic conjugated polymers can become soluble by using physical approaches via emulsion or reprecipitation to fabricate water-dispersible nanoparticles. Highly fluorescent CPNs represent a new class of advanced imaging contrast agents that are involved in cross-disciplinary areas of material sciences, biological sciences, and polymer chemistry. The superior properties of CPNs have drawn much research interest to the applications of CPNs as imaging contrast agents during the past few decades [26, 45, 47, 92–105]. CPNs can be prepared via direct polymerization from monomers or post polymerization. Typical post-polymerization preparation methods include reprecipitation and miniemulsion [45]. Dopant molecules could be encapsulated into CPNs either to tune the emission range [104] or to achieve multiple biomedical functionalities [20, 49, 106, 107].

Many efforts have been made to synthesize highly fluorescent CPNs for sensitive bioimaging and biosensing applications, which have been thoroughly described in a few recent review reports [26, 42, 45–47, 66]. By encapsulating various fluorophores as energy accepters and light emitters, the emission wavelengths of CPNs could be conveniently tuned. Incorporation of a copolymer into CPNs could potentially impart CPNs with versatile functionalities including biocompatibility, specific recognition, colloid stability, brightness,

and photo-stability [107]. Hydrophobicity-induced aggregation is a severe issue that reduces the brightness of conjugated polymers. To address this issue, poly (ethylene glycol) (PEG) is favorable owing to its high hydrophilicity and good biocompatibility. Many CPNs coated by PEG and PEG derivatives have been applied in biological imaging fields. For instance, Traina *et al*. synthesized fluorescent conjugated polymers with good water solubility and high Φ_F by incorporating PEG side chains [58]. Φ_F values of most hydrophobic conjugated polymers decrease significantly when they are transferred from an organic solvent into polar aqueous media because of aggregation, which could be overcome by using amphiphilic block polymers as the encapsulation matrix [108]. Specific target recognition can be achieved by surface functionalization with specific recognition elements such as peptide, sugar, protein, and antibody. For example, Liu *et al*. designed and synthesized far-red/near-IR CPNs with maleimide groups on the surface for targeted imaging of HER2-overexpressed cancer cells owing to the efficient bioconjugation between anti-HER2 affibody and maleimide groups by click reaction [96]. Ye *et al*. designed highly fluorescent CPNs with orange-emitting for specific subcellular targeting via streptavidin bioconjugation [109]. Feng *et al*. synthesized single-chain conjugated polymer dots embedded nanoparticles bearing cell penetration peptide (TAT) as surface ligands for long-term cancer cell tracing applications [98]. In this work, CPNs were fabricated by using a matrix-encapsulation method. The embedded single-chain conjugated polymers can be modulated into spherical dots with different sizes by alteration of feed concentrations as illustrated in Figure 6.2a. Single-chain conjugated polymer dots are formed upon decreasing feed concentration to 0.2 mg ml^{-1}, where the CPNs exhibit highest fluorescence quantum yield of 32%. Maleimide was introduced as the functional group of the nanoparticle surface, which favors easy conjugation with cell penetration peptide via click chemistry to preserve its biofunctions. The cellular imaging capability of TAT peptide functionalized CPNs was evaluated on MCF-7 breast cancer cells. These CPNs show high brightness and good biocompatibility, which allow cell tracing for over nine generations (Figure 6.2c), superior to commercial cell tracker Qtracker 585.

6.3 Conjugated Polymers as 2PEM Contrast Agents

Conjugated polymers display much larger δ values than their small molecule counterparts due to their delocalized π-conjugation molecular structure and the many repeat units (RUs) they contain. Significant research efforts have been made to investigate the nonlinear optical properties of conjugated polymers, including polydiacetylenes [110, 111], poly(*p*-arylenevinylenes) (PPVs), *p*-phenylene-based ladder polymers [112, 113], as well as aromatic-heterocyclic polymers such as polythiophenes [114, 115], polybenzobisazoles [116], polyquinolines [117], polyquinoxalines [118], and polyanthrazolines [119]. In recent years, several research groups have been working on the design and synthesis of novel conjugated polymers with large δ and $\delta\,\Phi_F$ values for two-photon live cell imaging [120–123]. Yang *et al.* synthesized poly(1,4-diketo-3,6-diphenylpyrrolo [3,4-*c*]pyrrole-*alt*-3,6-carbazole/2,7-fluorene) (PDCZ/PDFL) as high-performance 2PEM imaging contrast agents

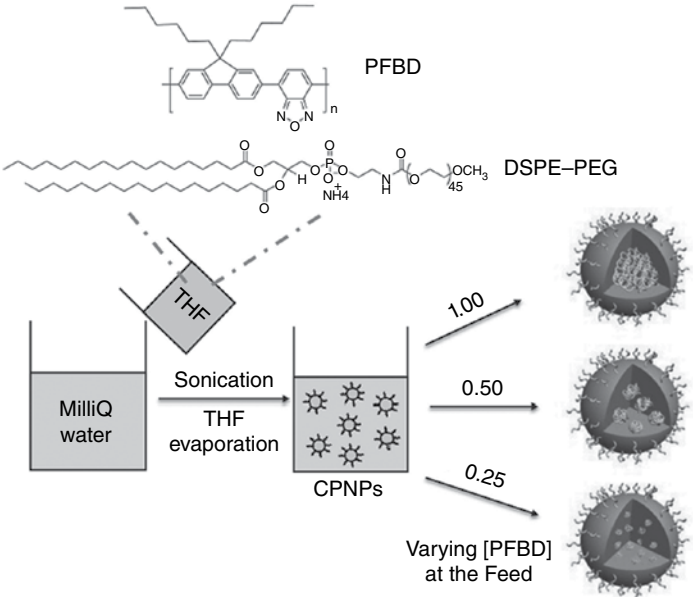

(a)

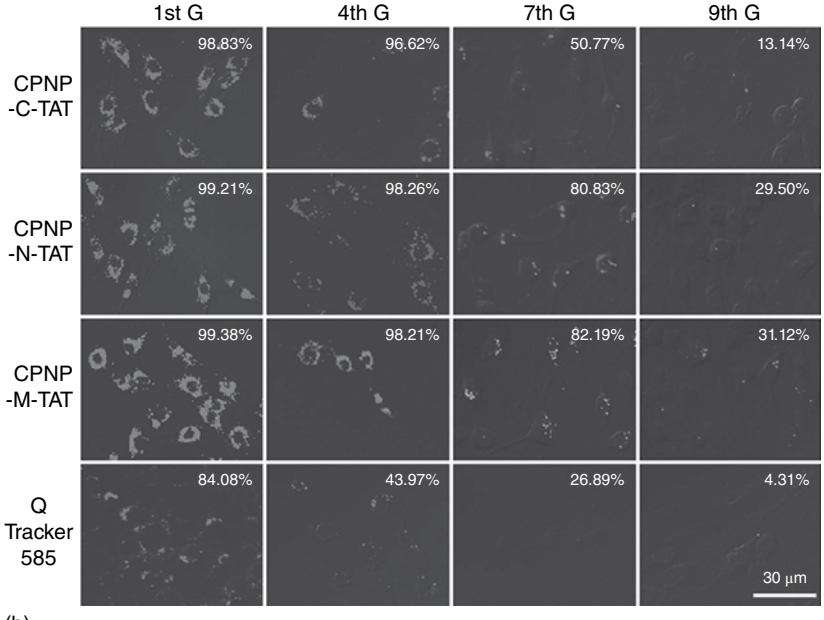

(b)

Figure 6.2 (a) Chemical structure of PFBD and DSPE–PEG, and the schematic illustration of CPN formation at different feed concentration. (b) Confocal images of MCF-7 breast cancer cells at different designated generations after overnight incubation with 2 nM of CPN-C-TAT, CPN-N-TAT, CPN-M-TAT, or Qtracker® 585 at 37 °C. (Reprinted with permission from Ref. [98]. Copyright 2014, Wiley-VCH.)

with δ values of up to 970 and 900 GM per RU for PDCZ and PDFL, respectively (Scheme 6.1a) [120]. Keller *et al.* synthesized conjugated polymers containing 4,8-bis(2-ethylhexyloxy)benzo[1,2-*b*;3,4-*b*′]-dithiophene (BDT) donor groups and thiophene with various electron-withdrawing acceptor groups (Scheme 6.1b) [121]. They demonstrated that conjugated polymers with strong electron-withdrawing acceptors possess large δ values. Li *et al.* synthesized two novel pyrrole-based conjugated polymers emitting strong yellow-green and orange fluorescence with Φ_F values of 46% and 33% and δ values of 2392 and 1938 GM per RU, respectively (CP1 and CP2 in Scheme 6.1c) [122]. Huang *et al.* synthesized two cross-conjugated polymers with large δ values for metal ion sensing, poly[(9,9-di-*n*-hexylfluorene-2,7-diyl)-*alt*-*co*-(2-(4-(*N*,*N*-(dibutylamino) styryl) benzene)-1,4-diyl)] (CP3 in Scheme 6.1d) and poly[(9,9-di-*n*-hexylfluorene-2,7-diyl)-*alt*-*co*-(2,5-bis(4-(*N*,*N*-(dibutylamino)styryl) benzene) -1,4-diyl)] (CP4 in Scheme 6.1d) [123]. The D-π-D conjugated side chains on the latter polymer endow it with a large δ value of 1440 GM per RU in THF at 740 nm. Zhou *et al.* synthesized two series of hyperbranched conjugated polymers based on alkyl-modified 2,4,6-tris(thiophen-2-yl)-1,3,5-triazine central units linked through fluorene bridges of different lengths via Suzuki coupling, as summarized in Scheme 6.1e (P and P′) [124]. By introducing the alkyl group at the thienyl group in 2,4,6-tris(thiophen-2-yl)-1,3,5-triazine unit, polymers with high molecular weight and enhanced δ were obtained.

Despite the excellent two-photon optical properties of conventional conjugated polymers, the intrinsic hydrophobicity originating from the π-conjugated backbone limits their potential applications in biological systems. Water solubility is required for their applications as 2PEM contrast agents. Water-soluble conjugated polymers can be obtained by modifying the π-conjugated backbones with charged (anionic or cationic) side chains [46]. McRae *et al.* used an anionic carboxylated PPE derivative as a nonspecific low-affinity binding element for cellular imaging under both one-photon and two-photon excitation [125]. The PPE backbones were functionalized either with positively charged tetraalkylammonium groups (PPE 1) or with negatively charged carboxylated (PPE 2) (Figure 6.3) as nonspecific low-affinity binding elements. Polymer PPE 1 and PPE 2 showed bright 2PEF combined with good photo-stability that renders them well suited for 2PEM (Figure 6.3a). PPE 2 can selectively stain the extracellular matrix protein fibronectin of fibroblast cells, which was ascribed to the interactions between the carboxyl groups of PPE 2 and the positively charged extended area within fibronectin repeats 12–14, a location involved in the binding of heparin. Moreover, the internalization of PPE 2 became more efficient upon prolonged incubation, which was ascribed to the partial prevention of transportation of PPE 2 into live cells because of its negatively charged side chains. Stabo-Eeg *et al.* reported Φ_F and δ values of three CPEs: POMT, POWT, and PTAA (Figure 6.3) in three different pH buffer systems for monitoring structural changes in proteins [126]. POMT was found to have the highest Φ_F value of circa 0.10 at pH 2.0. The δ values of POMT and POWT was found to be more than 18–25 times and 7–11 times that of fluorescein, respectively. POMT has been further utilized as contrast agents for 2PEM to distinguish conformational differences between amyloid fibrils formed reduced and nonreduced insulin recorded in spectrally resolved images (Figure 6.3b).

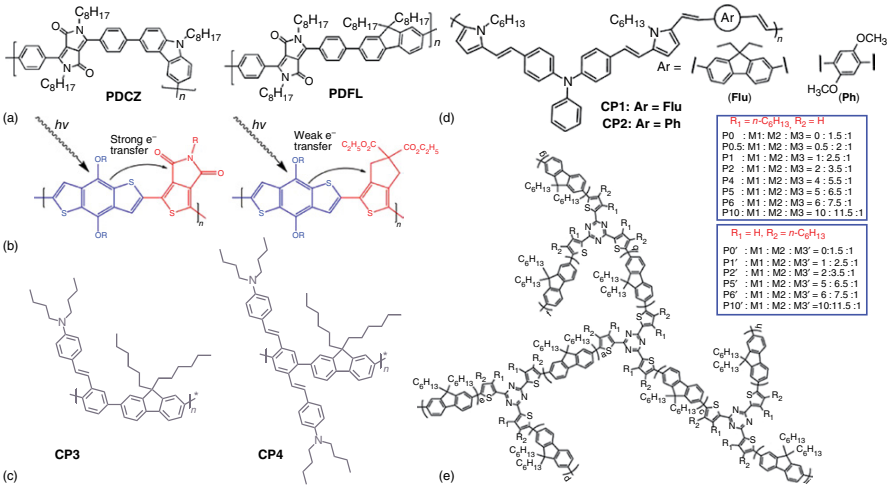

Scheme 6.1 Highly fluorescent two-photon conjugated polymers. (Reproduced with permission from Refs [120–124]. Copyright 2007, 2011, 2014, 2016, American Chemical Society, 2014 Wiley-VCH.)

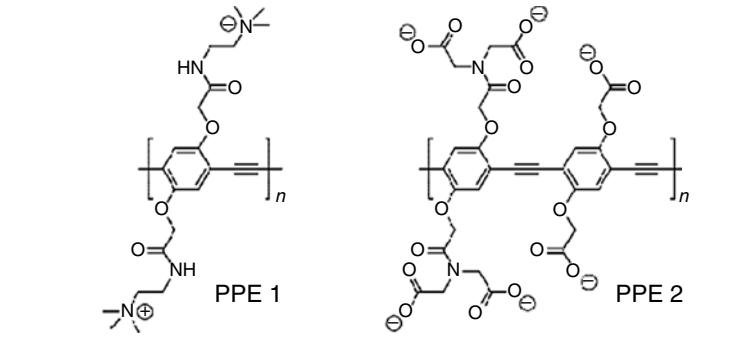

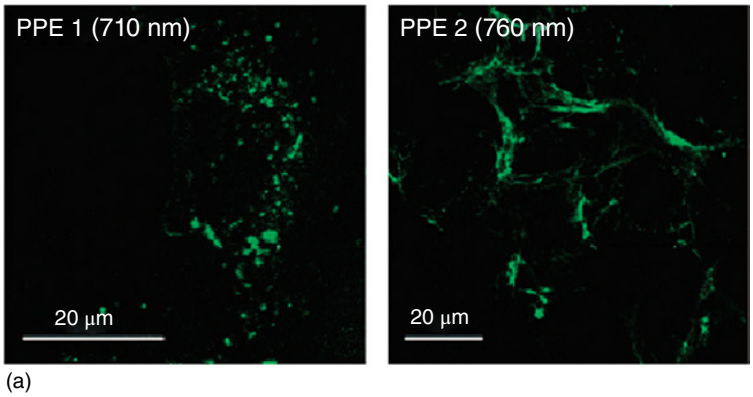

(a)

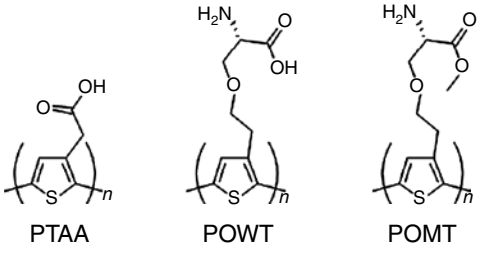

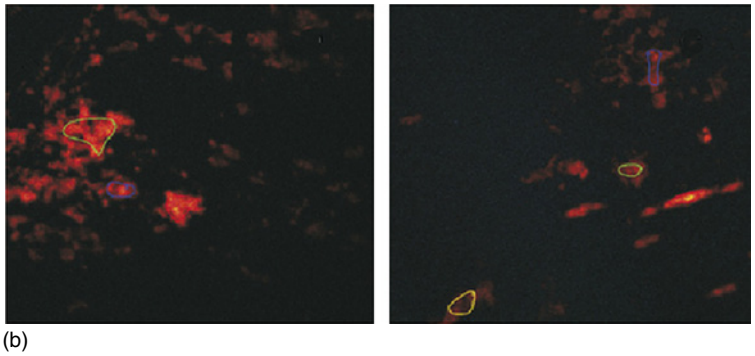

(b)

Figure 6.3 Chemical structures of PPE 1, PPE 2, PTAA, POWT, and POMT. (a) 2PEM of PPE derivatives interacting with live mouse fibroblast cells. Cells were incubated with PPE 1 (left, $\lambda_{ex} = 710$ nm) or PPE 2 (right, $\lambda_{ex} = 760$ nm) in DMEM at 37 °C for 4 h. (b) Micrographs of insulin amyloid aggregates stained with POMT. 2PEM of reduced (left) and nonreduced insulin amyloid at 820 nm. (Reprinted with permission from Refs [125, 126]. Copyright 2008, American Chemical Society, 2007 Elsevier B.V.)

Two-photon optical properties and applications of various polyfluorene-based cationic conjugated polymers (CCPs, Scheme 6.2) have also been widely explored for their 2PE-based applications [21, 127–129]. PFP is a commercially available conjugated polymer, which has been widely used in various 1PE-based light-harvesting materials for biosensing [57]. Even though it could act as two-photon light harvesting materials to enhance two-photon emission of small molecules by tens of times [127, 128], its δ value per RU is still quite small: only 8.4 GM per RU at 800 nm. To further improve the performance of these CCPs as two-photon light-harvesting materials, He *et al*. designed and synthesized two water-soluble polyfluorene-based CCPs in PFE and PFV (Scheme 6.2) [129]. The δ values of these CCPs at 800 nm have been significantly improved by inserting ethynylene and vinylene groups as the bridges, which extends the conjugation length and electron delocalization. Larger conjugation of PFE and PFV and better coplanarity of PFV lead to a larger extent of charge separation and, thus, a larger δ value. The δ values of PFE (with ethynylene bridge) and PFV (with the vinylene bridge) at 800 nm are eight times and 36 times of that of PFP, respectively. However, the Φ_F values of PFP, PFE, and PFV are 9.8%, 9.8%, and 3.0%, which are significantly lower than the corresponding neutral precursors in organic solvents (48%, 60%, and 48% for PFP-Br, PFE-Br, and PFV-Br in THF, respectively) likely due to formation of aggregates and aggregation-induced quenching of intrachain singlet exciton [130, 131]. Later in 2013, Shen *et al*. designed a series of polyfluorene-vylevynylene-phenylene type CCPs by introducing two kinds of substituents into the backbone

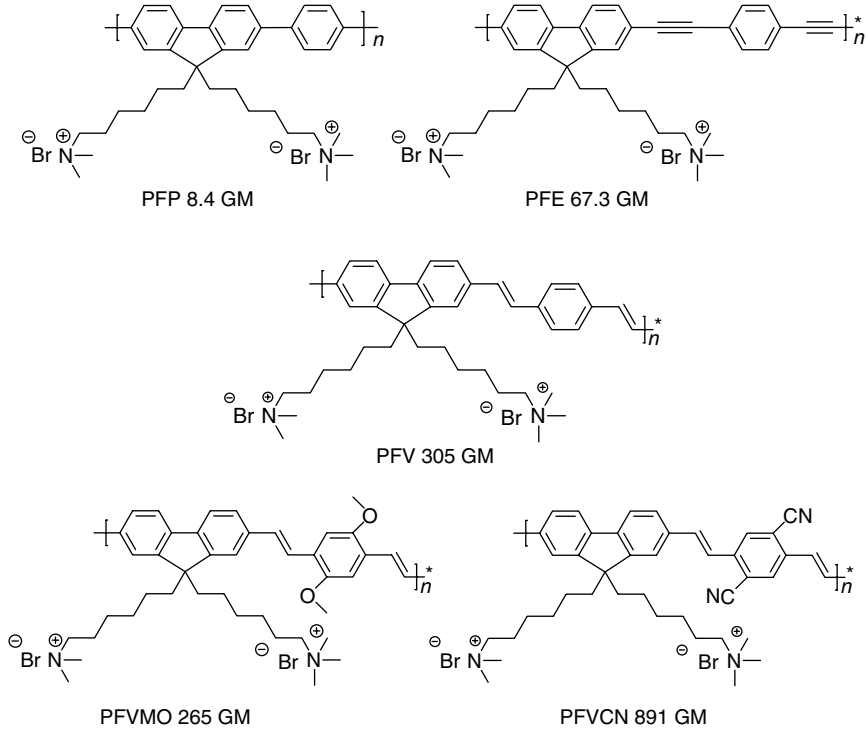

Scheme 6.2 Molecular structures and δ values per RU at 800 nm of a few polyfluorene-based cationic conjugated polymers.

[21]. By introducing an electron-donating methoxy group and electron-withdrawing cyano group into the phenyl ring of a polymer backbone for PFVMO and PFVCN (Scheme 6.2), respectively, the δ values were significantly improved. Among three polymers, PFVCN was found to possess the highest Φ_F and a much larger δ value than PFVMO and the unsubstituted PFV (Figure 6.4). Notably, PFVCN remains a relatively high Φ_F value (20%) in water owing to the formation of an excimer-like state via interchain interaction [132]. The maximum δ value per RU reached 370, 390, and 891 GM for PFV, PFVMO, and PFVCN, respectively. The δ value per RU was enhanced by ~2.4 folds by introducing strong electron-withdrawing cyano group into the phenyl ring of the backbone, which was ascribed to increased conjugation length due to electron-withdrawing effects of cyano group and less degree of distortion from planarity. The $\delta\Phi_F$ values were calculated to be 128, 115, and 2673 GM per molecule for PFV, PFVMO, and PFVCN. Owing to its large δ value and high Φ_F, PFVCN has high two-photon brightness so that 2PE fluorescence of PFVCN in water dispersion can be directly visualized with the naked eye (Figure 6.4a inset). In addition, these three CCPs displayed low dark cytotoxicity by monitoring the metabolic viability of HeLa cells (Figure 6.4d). 2PEM cell imaging experiments using PFV, PFVMO, and PFVCN were conducted on HeLa cancer cells under excitation at 810 nm using a two-photon laser scanning confocal microscopy, which demonstrate that these CCPs, in particular PFVCN, can act as promising agents for 2PEM cell imaging with high contrast ratios.

6.4 Conjugated-Polymer-Based Nanoparticles (CPNs) as 2PEM Contrast Agents

CPNs containing tens of polymer chains with large δ values per nanoparticle have been proved to be an ideal probe for 2PEM long-term intracellular imaging owing to the superior biocompatibility and nonblinking property compared with quantum dots [103]. Owing to the excellent properties of CPNs, many researchers have been motivated to explore simple and universal strategies to prepare highly efficient CPNs for various 2PE-based sensing and imaging applications [26, 42, 45]. Water-soluble CPNs can be prepared from hydrophobic conjugated polymers, CPEs, and hybrid materials such as dye-doped CPNs and polymer-doped silica NPs. Herein we summarize some strategies that have been widely utilized to prepare highly fluorescent water-soluble CPNs.

6.4.1 CPNs Prepared from Hydrophobic Conjugated Polymers

The intrinsic hydrophobicity originating from π-conjugated backbone limits the potential applications of conjugated polymers in biological systems. Water soluble CPNs can be prepared from hydrophobic conjugated polymers by a variety of methods such as reprecipitation method and microemulsion [26, 45, 47, 105]. Wu *et al.* reported CPNs with δ values of as high as 2.0×10^5 GM per particle (20 nm in diameter, Figure 6.5a) [103]. These CPNs were prepared by polyfluorene derivative (PDHF), copolymer (PFPV) and polyphenylenevinylene derivative

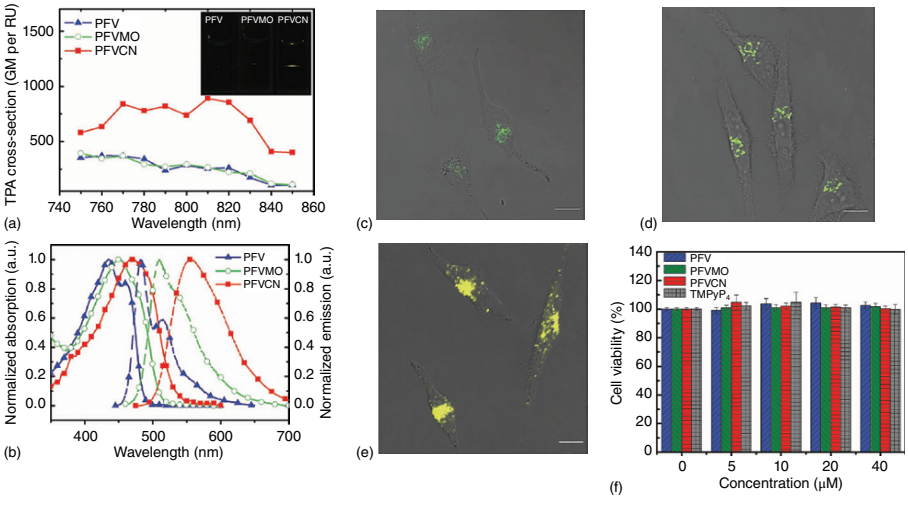

Figure 6.4 (a) Wavelength-dependent $\delta\Phi_F$ (per RU) values of PFV, PFVMO, and PFVCN in water. The inset shows their photographs under fs laser excitation at 810 nm. (b) Normalized absorption (solid lines) and fluorescence spectra (dash lines) of PFV, PFVMO, and PFVCN in water. Overlaid images of 2PEF and bright-field images of HeLa cancer cells treated with PFV (c), PFVMO (d), and PFVCN (e) for 3 h. Scale bar: 10 μm. (f) Metabolic viability of HeLa cells after incubation with PFV, PFVMO, PFVCN, and TMPyP4 of different concentrations (in RU for polymers) for 24 h. (Reproduced with permission from Ref. [21]. Copyright 2013, Wiley-VCH.)

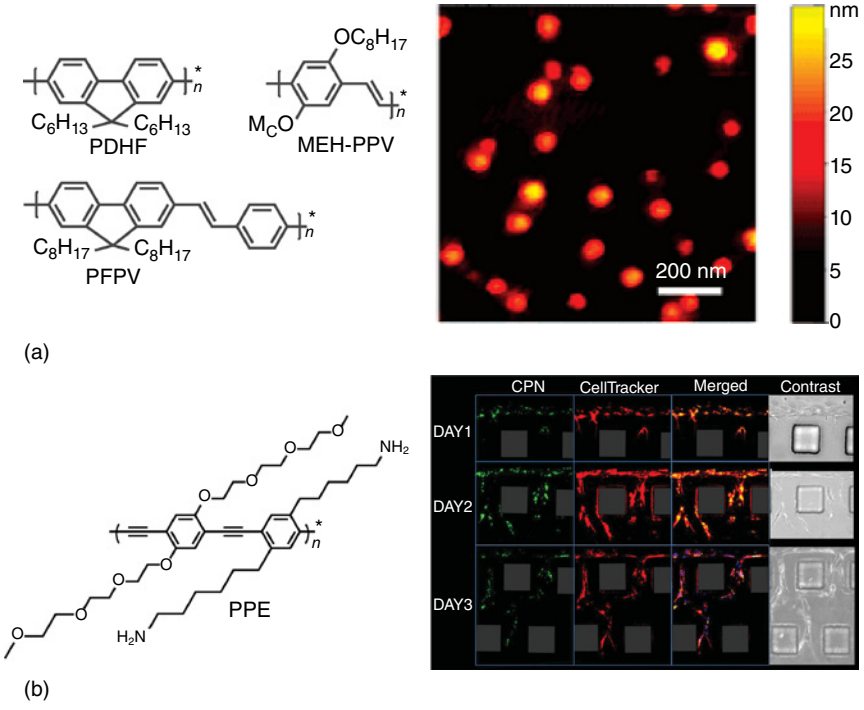

Figure 6.5 Chemical structures of PDHF, MEH-PPV, PFPV, and PPE. (a) Photograph of fluorescence from aqueous CPNs dispersions under 2PE by a 800 nm mode-locked Ti:sapphire laser. (b) Fluorescence images (days 1, 2, and 3) of cultured cells in a microfluidic device. 2PE images showing projection of capillary structures through 80 mm of the central gel region. (Reproduced with permission from Refs [103, 133]. Copyright 2007, American Chemical Society, 2009 Wiley-VCH.)

(MEH-PPV) using a reprecipitation method. The particle size could be controlled from 5 to 50 nm by varying the concentration of feed solution. The $\delta\Phi_F$ values of as-prepared CPNs are 3–4 orders of magnitude higher than the values of conventional fluorescence dyes, and an order of magnitude higher than those of inorganic quantum dots. Moon and coworkers utilized hydrophobic conjugated polymers to fabricate CPNs using ultrafiltration of an amine-containing poly(*p*-phenylene ethynylene) (PPE, Figure 6.5b) solution to obtain transparent yellow colored CPNs with size down to 8 nm [133]. These CPNs exhibited excellent stability during the first three months of storage. The $\delta\Phi_F$ values ranged from 100 to 11 000 GM per particle with maximum at ~730 nm. The biocompatibility of these CPNs was examined by long-term monitoring of capillary formation in a microfluidic device, indicating their potential for *in vitro* or *in vivo* imaging applications. Mecking and coworkers reported the preparation of fluorescent CPNs based on poly(arylene ethynylene) (Figure 6.6, poly-1–5) by a direct polymerization method involving Sonogashira coupling in an aqueous miniemulsion [134]. These CPNs exhibited sizes in the range of 60–120 nm, and δ values ranging from 10^6 to 10^7 GM. The applications of these CPNs for multiphoton fluorescence imaging applications have been further demonstrated.

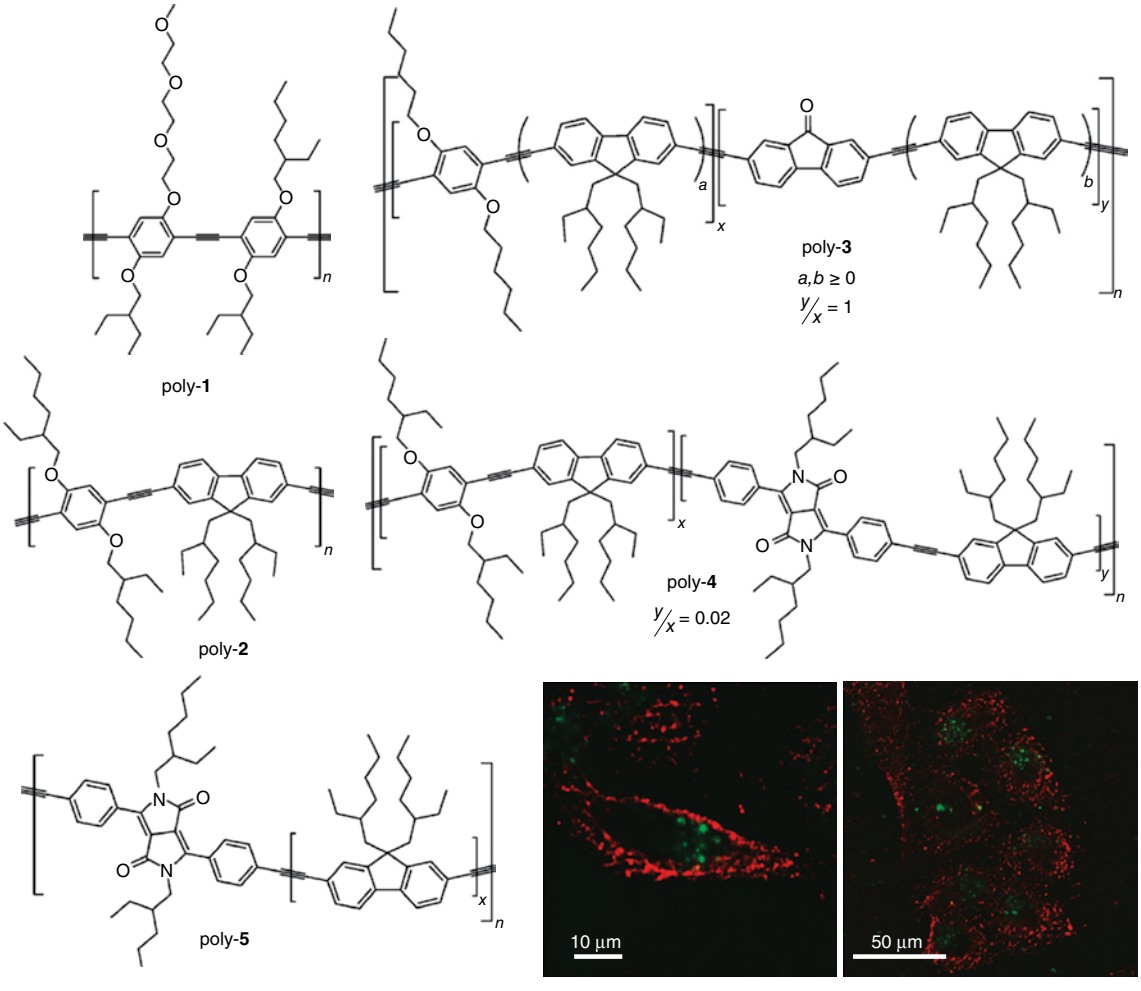

Figure 6.6 Chemical structures of poly-1 to poly-5. Confocal fluorescence micrographs of fixed HeLa cells labeled with poly-1 (green, inside) and poly-4 (red, outside) NPs excited at 780 nm. (Reproduced with permission from Ref. [134]. Copyright 2010, American Chemical Society.)

To achieve deep tissue imaging, both deep penetration of excitation light and effective collection of fluorescence signals from deep tissues are essential. Fluorescence contrast agents with both relatively long excitation and emission wavelengths are favorable for *in vivo* imaging applications due to less absorption and scattering by the intact tissue as well as less autofluorescence from the biological environment. Red-emitting fluorophores with large δ values and high Φ_F are ideal for 2PEM agents for deep tissue imaging. Significant efforts have been made in preparing red-emitting CPNs. However, red emitters generally have a large conjugation system, which makes them floppy and prone to aggregation in aqueous media via π–π stacking and hydrophobic interactions, thus leading to significantly reduced Φ_F [32, 59]. To mitigate the aggregation, chemical introduction of narrow-band-gap moieties into conjugated polymer backbones [55, 135] have been utilized to obtain CPNs that emit in the far-red or near-IR range. In these CPNs, energy transfer from conjugated polymers to narrow-band-gap moieties resulted in significantly red-shifted emission.

Chromophores based on the structure of bis(diphenylaminostyryl)benzene (DPSB) have D-π-D structures with large δ values [123]. Inspired by this material, Liu *et al*. designed and synthesized a series of DPSB-based conjugated polymers, including linearly copolymer M1 and cross-copolymer S1 by copolymerization of DPSB units and fluorene units (Figure 6.7a) [23]. The dithienylbenzothiadiazole (DTBT) units were introduced into the backbones as energy acceptor to red shift the emission of the conjugated polymer to far-red region. The conjugated polymers were constructed as a D-π-A-π-D structure to improve δ values (M2 and S2). Water-soluble CPNs based on these polymers were prepared by using poly(styrene-*co*-maleic anhydride) (PSMA) as the encapsulation matrix. Through optimization of the polymer/matrix mass ratio and the initial feed concentration of the polymer solution, a high Φ_F of 24% was achieved for these red-emitting CPNs in water. δ and $\delta\Phi_F$ values of these polymers at 750 nm reached up to 1000 and 190 GM per RU in aqueous media, 2.5×10^5 GM and 4.7×10^4 GM per nanoparticle, respectively (Figure 6.7). These nanoparticles displayed excellent photostability and biocompatibility. Their applications as 2PEM fluorescence probes for cell membrane imaging have been demonstrated in three different cell lines (HepG2 cancer cells, HeLa cancer cells, and NIH/3T3 cells) by using a laser scanning confocal microscope under femtosecond laser excitation at 750 nm. Strong fluorescence was observed from the cell membrane for all three types of cells. Apparently, these CPNs were found to be advantageous over the commercial probe, CellMask Deep Red Plasma membrane stain, for their potential applications in 2PEM bioimaging.

6.4.2 CPNs Prepared from Conjugated Polyelectrolytes (CPEs)

Water-soluble CPNs can also be constructed from CPEs. Owing to their aromatic backbones, most CPEs are partially hydrophobic despite their ionic water-soluble side chains. A method to generate self-assembled CPNs in aqueous media is to attach high-hydrophilic or amphiphilic components to the side chains of CPEs, such as PEG. For example, Liu *et al*. utilized PEG_{1000}-COOH as a side chain due to its brilliant hydrophilicity, biocompatibility and resistance to nonspecific

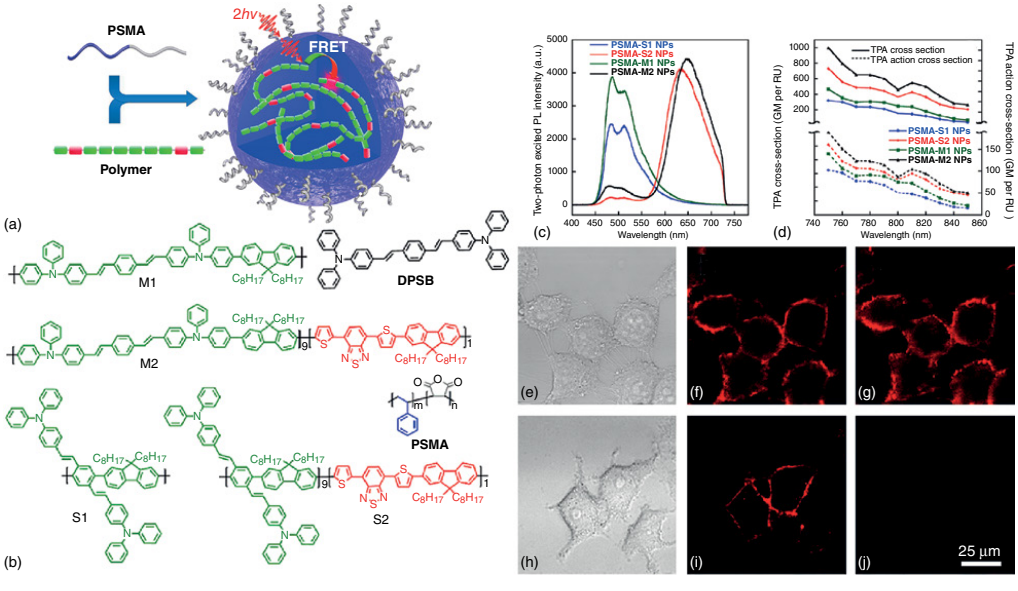

Figure 6.7 (a) Illustrative preparation procedures of CPNs; (b) chemical structures of DPSB, encapsulation matrix PSMA, and polymer S1, S2, M1, M2; (c) 2PE fluorescence spectra of CPNs with the same concentration (2.5 μM RU) in water dispersion, λ_{EX} = 810 nm; (d) wavelength-dependent δ and $\delta\Phi_F$ values per RU for different CPNs; (e–j) Bright-field (e, h), 1PE fluorescence (f, i) and 2PE fluorescence (g. j) images of HepG2 cells after incubation with PMSA-M2 CPNs (top line) and CellMask Deep Red Plasma membrane stain (bottom line). λ_{EX} is 405 (f), 650 (i), and 750 nm (g and j), respectively. (Reproduced with permission from Ref. [23]. Copyright 2015, American Chemical Society.)

adsorption of biomolecules [136]. The grafted CPE (PFBDDBT10–PEG1000-COOH) was dispersed in water to self-assemble into CPNs with a mean diameter of 55 nm. In addition, CPNs can also be fabricated via a nanoprecipitation method by adding its DMSO solution to water under sonication [55]. In this case, the nanoparticle sizes are tunable from 49 to 39 and 27 nm when the CPE concentrations vary from 0.5 to 0.25 and 0.17 mg ml^{-1}. Two methods generate CPNs with size ranging from 20 to 70 nm and relatively homogeneous sizes. As the self-assembly is a thermodynamically controlled process, the size and morphology of the obtained CPNs prepared from grafted CPEs are sensitive to solution conditions such as concentration, ionic strength, and temperature [137].

In 2015, Dmitriev *et al*. prepared a class of CPNs by using the "precipitation" technique for high-resolution O_2 imaging in cells and 3D tissue models under 2PE [138]. They prepared CPNs by dissolving the polymer in a "good" solvent and rapidly adding an excess of water to it. The CPNs consist of a substituted conjugated polymers (polyfluorene or poly(fluorene-*alt*-benzothiadiazole)) acting as a FRET antenna and a fluorescent reference with covalently bound phosphorescent metalloporphyrin (PtTFPP, PtTPTBPF), as illustrated in Figure 6.8. The CPNs display enhanced two-photon brightness, good compatibility with ratio-metric and lifetime-based imaging modes, and low toxicity for cells. The "zwitter-ionic" NPs show high cell-staining efficiency, while their cell entry mechanisms differ for the different 3D models.

6.4.3 CPNs Prepared by Hybrid Materials

Red-emitting fluorophores with large δ values and high Φ_F are ideal for 2PEM agents for deep tissue imaging. In addition to chemically introducing narrow band-gap moiety into the polymer backbone, physical blending of conjugated polymers with red-emitting fluorophores [139] is a flexible method to obtain CPNs that emit in the far-red/NIR range. Conjugated polymers have large δ values and high Φ_F. However, most conjugated polymers generally emit in the visible range. FRET could be utilized to further extend the red shift between the excitation and emission wavelengths. Most importantly, FRET from conjugated polymers results in fluorescence amplification of the energy acceptors, which has been widely utilized for various biological applications with enhanced efficiency [57, 140]. 2PE-based FRET from conjugated polymers with large δ values to red-emitting dyes with high Φ_F could potentially realize near-IR excitation and red emission for sensitive detection to enable highly efficient 3D deep tissue imaging [107, 127, 128]. Encapsulating organic dyes into CPNs can tune the fluorescence properties of CPNs. Inside these CPNs, highly efficient FRET process from the excited conjugated polymer matrix to the dye dopant enhances the brightness of the dye dopant [23, 46, 57, 58, 107, 141]. Based on this concept, Li *et al*. utilized the reprecipitation method to encapsulate organic dyes into conjugated polymers to fabricate highly fluorescent red-emitting CPNs (Figure 6.9a) [141]. In these CPNs, hydrophobic conjugated polymers PFV-Br with a δ value of 256 GM per RU at 800 nm was selected as the two-photon light-harvesting material. Hydrophobic fluorophore magnesium phthalocyanine (MgPc), which emits at 680 nm with a high Φ_F value (~30%) was selected as the

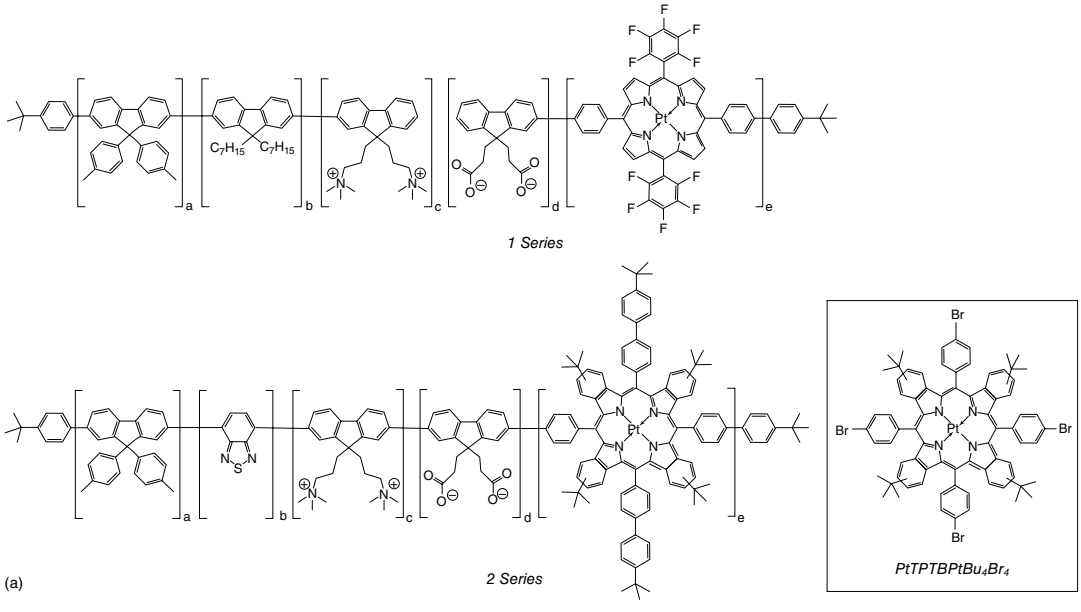

Figure 6.8 (a) Structure of the O_2-sensitive conjugated polymer, (b) their conformation in organic solvent and in nanoparticle form after precipitation with water, TEM image of the resulting NPs, and ratio-metric intensity imaging of NPs in MEF cells exposed to different O_2 at 37 °C and treated with inhibitor of respiration. (Adapted with permission from Ref. [138]. Copyright 2015, American Chemical Society.)

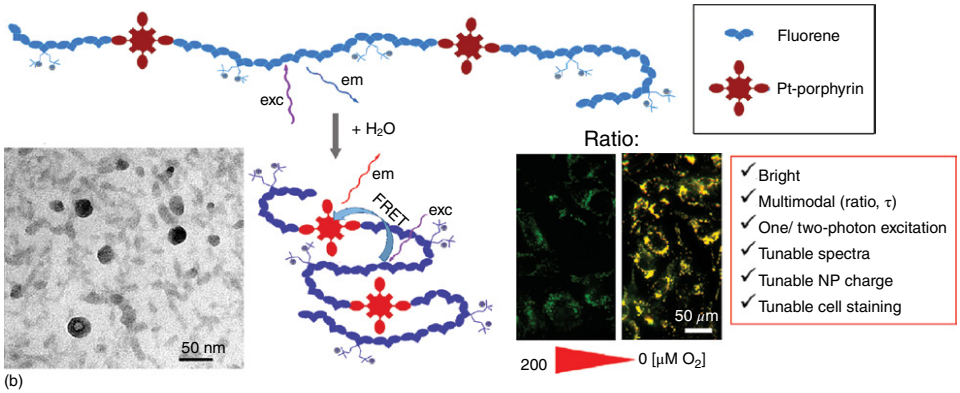

(b)

Figure 6.8 (*Continued*)

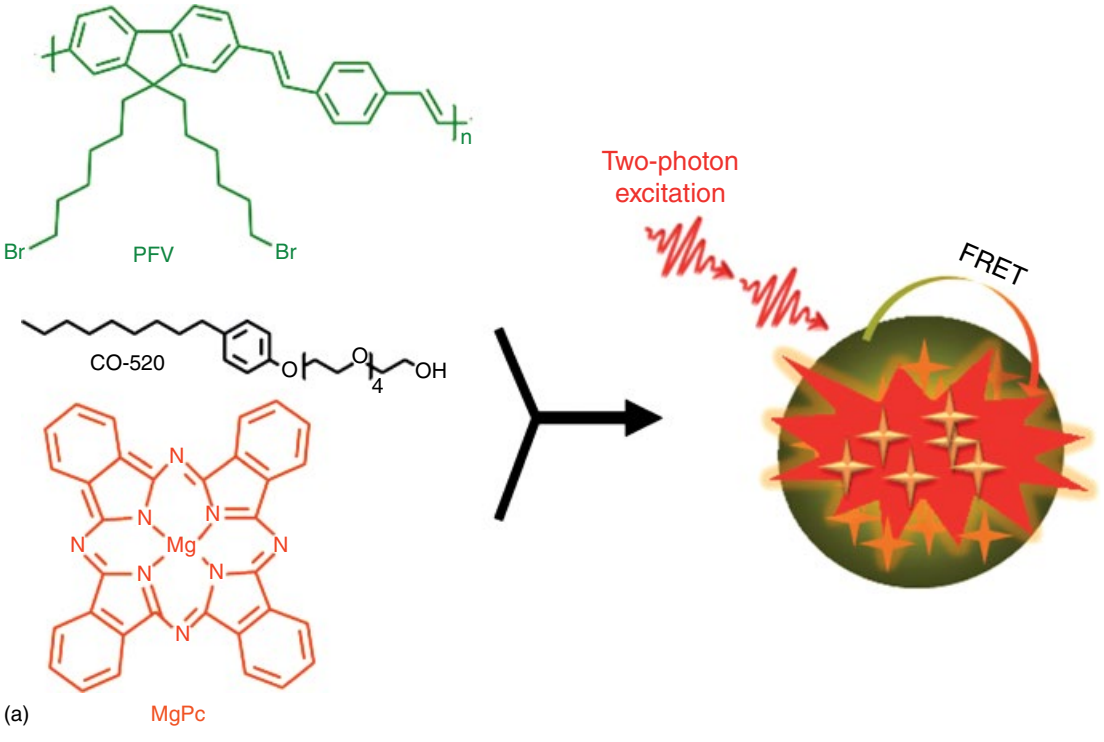

Figure 6.9 (a) Schematic preparation procedures of MgPc/PFV NPs; 1PE (b) and 2PE (c) fluorescence spectra of PFV NPs and MgPc/PFV NPs. Excitation wavelengths for 1PE and 2PE are 437 and 800 nm, respectively; (d) cell viability assay of HepG2 cancer cells treated with MgPc(0.75%)/PFV NPs and MgPc NPs containing the same amount of MgPc for 8 h; (e) overlaid 2PE fluorescent images and bright-field images of HepG2 cancer cells after incubation with 2 μM MgPc(0.75%)/PFV NPs. The nanoparticle concentration is in terms of the PFV per RU. (Reproduced with permission from Ref. [141]. Copyright 2014, American Chemical Society.)

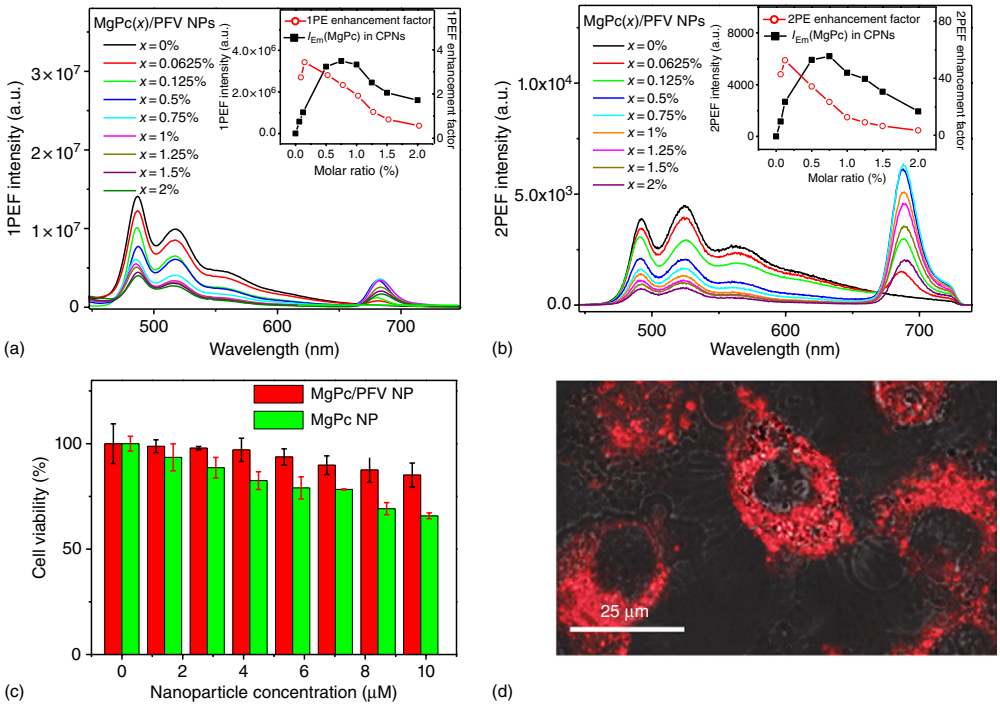

Figure 6.9 (*Continued*)

model for red-emitting dyes to demonstrate the concept of preparation of CPNs that display high 2PE brightness in the far red/NIR region for 2PEM live cell imaging. A nonionic surfactant was introduced into the CPNs to stabilize the CPNs in water dispersion, reduce cytotoxicity meanwhile accelerate cell uptake (Figure 6.9). These MgPc-/PFV-based nanoparticles display an effective δ value of up to 4300 GM (per MgPc) at 800 nm. 1PE and 2PE fluorescence intensities of MgPc were enhanced by up to ~3.4 and ~54 times, respectively. The doping concentration was adjusted to optimize red emission of the CPNs by monitoring 1PE and 2PE fluorescence of the CPNs. After encapsulation into CPNs, the 2PE fluorescence of MgPc was significantly enhanced. Meanwhile, the reduced cytotoxicity of MgPc was demonstrated by monitoring the cell viability of HepG2 cancer cells as shown in Figure 6.9d. The 2PEM cancer cell imaging capability of the as-prepared CPNs was conducted on a two-photon laser scanning confocal microscope by using femtosecond laser pulses at 800 nm (Figure 6.9e). They have also prepared CPNs by using another red-emitting dye, Nile red, as a doping material and energy acceptor using the same reprecipitation method. This concept could become a general approach to the preparation of two-photon excitation red-emitting materials for deep-tissue live-cell imaging with high contrast.

Another far-red emitting hybrid CPNs (~730 nm) were prepared by using conjugated polymer P-F8-DPSB as two-photon light harvesting materials (Figure 6.10). NIR emitting dye, DPA-PR-PDI served as the energy acceptor and copolymer, FA-F127, served as stabilizing agent and provided selective targeting moiety [142]. The hybrid CPNs possess a δ value up to 2.3×10^6 GM per particle at 800 nm. The large δ of the conjugated polymer, high Φ_F (up to 45%), and efficient energy transfer from the conjugated polymer to NIR-emitting fluorophore (up to 90%) imparted these hybrid CPNs fluorescence imaging ability with penetration depth up to 1200 μm. The practicability of the hybrid CPNs for fluorescence imaging was demonstrated in HeLa cells.

Silica NPs loaded with CPs could also be utilized for 2PE imaging applications. In 2010, Parthasarathy *et al*. reported that an anionic CPE, $PPESO_3$, exhibited moderately strong 2PA in the near-IR region with an onset at ~800 nm and δ value of ~400 GM at 690 nm [143]. This anionic CPE has been further utilized to prepare $PPESO_3$-coated silica nanoparticles as 2PEM contrast agents in HeLa cells with largely improved resolution compared to 1PE fluorescence microscopy. Aparicio-Ixta *et al*. prepared conjugated polymer-containing silica nanoparticles that displayed a high Φ_F value (~0.75), large δ value of 8686 GM per polymer chain at 740 nm, good photo-stability and viability [144]. Geng *et al*. developed a micelle/silica coprotection strategy to stabilize and prevent aggregation of conjugated polymers inside the silica nanoparticles [145]. The poly(9,9-dihexylfluorene-*alt*-2,1,3-benzothiadiazole) (PFBT)- loaded CPNs showed a δ value of 1085 GM at 810 nm based on polymer chain concentration and an emission maximum at 545 nm with a high Φ_F value of 75%. The prepared PFBT CPNs have shown good colloid stability and photo-stability as well as benign biocompatibility, which have been further applied to visualize the mouse brain vasculature through intravital 2PEM brain vascular imaging with high contrast (Figure 6.11).

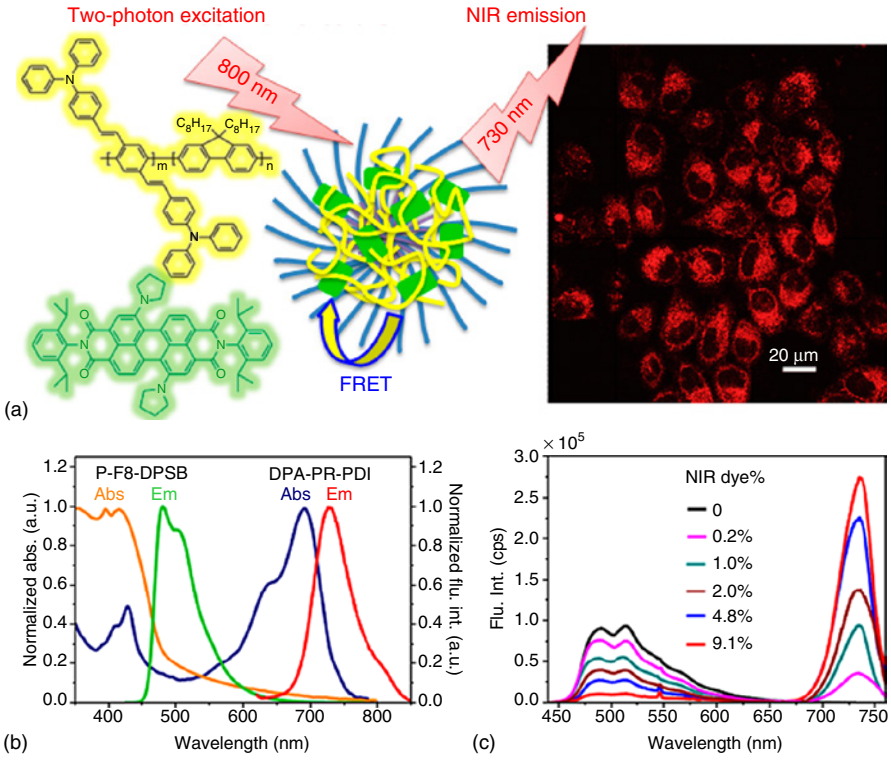

Figure 6.10 (a) Chemical structures of the CP with 2PEF feature (P-F8-DPSB), NIR fluorescent dye (DPA-PR-PDI) used for the construction of the hybrid CPNs and 2PEF imaging of HeLa cells; (b) normalized absorption and fluorescence emission spectra of P-F8-DPSB polymer and DPA-PR-PDI in THF solution; (c) fluorescence emission spectra of the hybrid P-F8-DPSB/DPA-PR-PDI NPs with various polymer/dye ratios upon 800 nm excitation. (Reproduced with permission from Ref. [142]. Copyright 2015, American Chemical Society.)

6.5 Conclusions and Outlook

Recent advances of water-soluble conjugated polymers and CPNs have greatly fostered their practical applications in 2PEM for live cell imaging. Development of new conjugated polymer materials with high two-photon brightness (large two-photon absorption cross-sections and high fluorescence quantum yields) and red emitting dyes with high quantum yields are still of vital importance to design highly efficient CPN-based 2PE fluorescence probes. Other important directions include target selectivity to certain cell lines and improved biocompatibility by smart design on the surface functionalization of CPNs and integration of drug delivery techniques such as light, enzyme, or pH-responsive nanoparticle surface. The progress in molecular design, nanoparticle preparation, and pharmacokinetics will foster the practical applications of conjugated polymers and CPNs as 2PEM contrast agents in live cells or intact tissues. In addition, encapsulating light-activated

drugs such as photosensitizers for photodynamic therapy will render enhanced therapeutic effects at the same time [20, 107]. In combination with 2PE imaging capability of CPNs, this could facilitate development of ideal drugs for imaging-guided two-photon photodynamic therapy and endow new opportunities in potential clinical applications [20, 21, 106, 128].

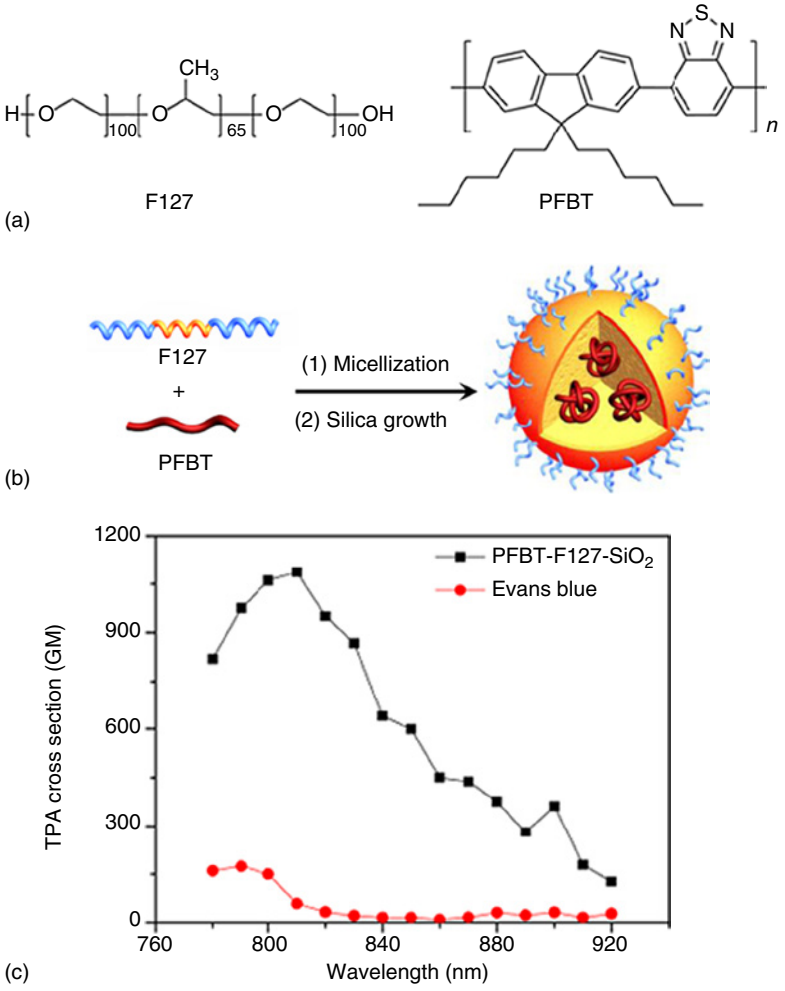

Figure 6.11 (a) Chemical structure of F127 and PFBT; (b) schematic illustration of the fabrication of PFBT-F127-SiO_2 NPs. (c) 2PA spectra of PFBT-F127-SiO_2 NPs (based on CP chain concentration) and Evans blue in water. (d) UV–vis (dash-dotted line) and PL (solid line) spectra of PFBT-F127-SiO_2 NPs (red) and PFBT-DSPE NPs (black) at 25 μg ml^{-1} of PFBT. Fluorescence decay curves of PFBT-F127-SiO_2 NPs (red) and PFBT-DSPE NPs (black). (e) Intravital TPFI of PFBT-F127-SiO_2 NPs stained blood vessels of mice brain at various depths (A–G) and the respective Z-projected image (H) as well as 3D image (I). Scale bar: 50 μm. (Reproduced with permission from Ref. [145]. Copyright 2014, American Chemical Society.)

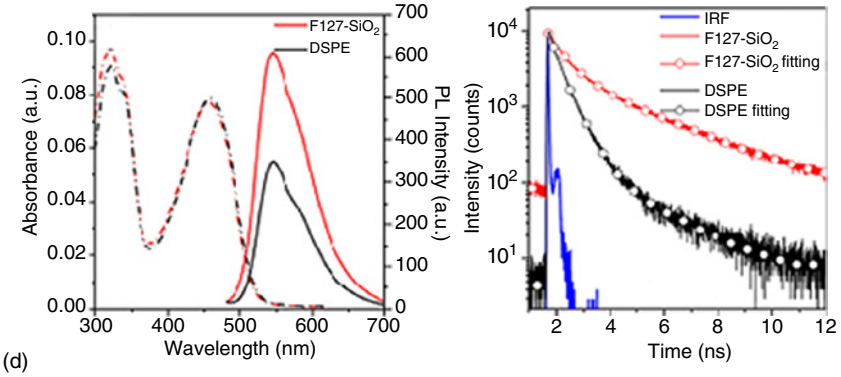

(d)

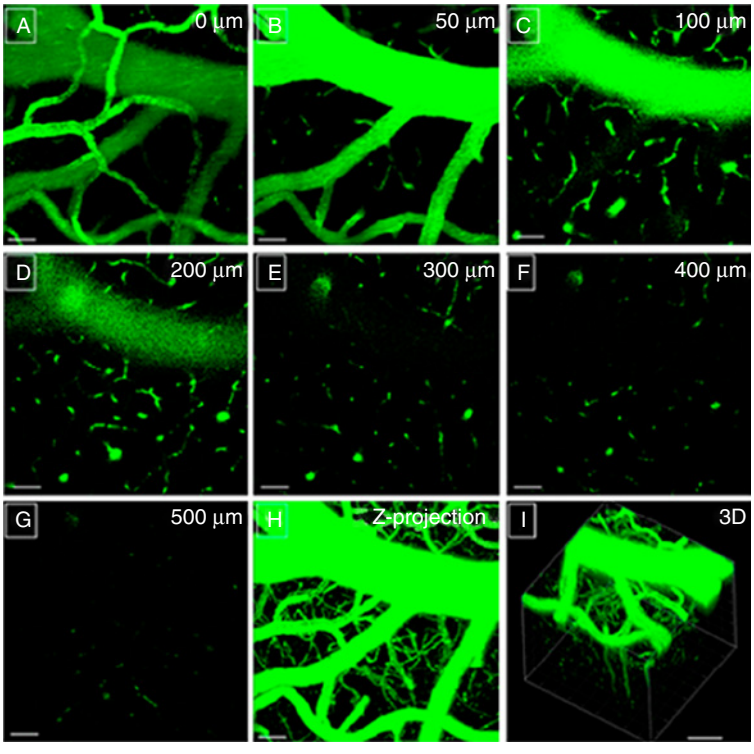

(e)

Figure 6.11 (*Continued*)

References

1 Jackson, R., Oda, R.P., Bhandari, R.K., Mahon, S.B., Brenner, M., Rockwood, G.A., and Logue, B.A. (2014) Development of a fluorescence-based sensor for rapid diagnosis of cyanide exposure. *Anal. Chem.*, **86**, 1845–1852.

2 Chattopadhyay, P.K., Price, D.A., Harper, T.F., Betts, M.R., Yu, J., Gostick, E., Perfetto, S.P., Goepfert, P., Koup, R.A., De Rosa, S.C. *et al.* (2006) Quantum dot

semiconductor nanocrystals for immunophenotyping by polychromatic flow cytometry. *Nat. Med.*, **12**, 972–977.
3 Ranasinghe, R.T. and Brown, T. (2011) Ultrasensitive fluorescence-based methods for nucleic acid detection: towards amplification-free genetic analysis. *Chem. Commun.*, **47**, 3717–3735.
4 Agard, D., Hiraoka, Y., Shaw, P., and Sedat, J.W. (1989) Fluorescence microscopy in three dimensions. *Methods Cell Biol.*, **30**, 353–377.
5 Gu, M., Sheppard, C.J.R., and Gan, X. (1991) Image formation in a fiber-optical confocal scanning microscope. *J. Opt. Soc. Am. A*, **8**, 1755–1761.
6 Gustafsson, M.G.L. and Webb, W.W. (2005) Nonlinear structured-illumination microscopy: wide-field fluorescence imaging with theoretically unlimited resolution. *Proc. Natl. Acad. Sci. USA*, **102**, 13081–13086.
7 Yildiz, A., Forkey, J.N., McKinney, S.A., Ha, T., Goldman, Y.E., and Selvin, P.R. (2003) Myosin V walks hand-over-hand: single fluorophore imaging with 1.5-nm localization. *Science*, **300**, 2061–2065.
8 Xie, X.S., Yu, J., and Yang, W.Y. (2006) Living cells as test tubes. *Science*, **312**, 228–230.
9 Moerner, W.E. (2007) New directions in single-molecule imaging and analysis. *Proc. Natl. Acad. Sci. USA*, **104**, 12596–12602.
10 Huang, B., Wang, W., Bates, M., and Zhuang, X. (2008) Three-dimensional super-resolution imaging by stochastic optical reconstruction microscopy. *Science*, **319**, 810–813.
11 Weissleder, R. and Ntziachristos, V. (2003) Shedding light onto live molecular targets. *Nat. Med.*, **9**, 123–128.
12 Denk, W., Strickler, J.H., and Webb, W.W. (1990) Two-photon laser scanning fluorescence microscopy. *Science*, **248**, 73–76.
13 Weissleder, R. (2001) A clearer vision for *in vivo* imaging. *Nat. Biotechnol.*, **19**, 316–317.
14 Cahalan, M.D., Parker, I., Wei, S.H., and Miller, M.J. (2002) Two-photon tissue imaging: seeing the immune system in a fresh light. *Nat. Rev. Immunol.*, **2**, 872–880.
15 Helmchen, F. and Denk, W. (2005) Deep tissue two-photon microscopy. *Nat. Methods*, **2**, 932–940.
16 Yao, S. and Belfield, K.D. (2012) Two-photon fluorescent probes for bioimaging. *Eur. J. Org. Chem.*, **2012**, 3199–3217.
17 Zijlstra, P., Chon, J.W.M., and Gu, M. (2009) Five-dimensional optical recording mediated by surface plasmons in gold nanorods. *Nature*, **459**, 410–413.
18 Larson, D.R., Zipfel, W.R., Williams, R.M., Clark, S.W., Bruchez, M.P., Wise, F.W., and Webb, W.W. (2003) Water-soluble quantum dots for multiphoton fluorescence imaging *in vivo*. *Science*, **300**, 1434–1436.
19 Pawlicki, M., Collins, H.A., Denning, R.G., and Anderson, H.L. (2009) Two-photon absorption and the design of two-photon dyes. *Angew. Chem. Int. Ed.*, **48**, 3244–3266.
20 Shen, X., Li, L., Wu, H., Yao, S.Q., and Xu, Q.-H. (2011) Photosensitizer-doped conjugated polymer nanoparticles for simultaneous two-photon imaging and two-photon photodynamic therapy in living cells. *Nanoscale*, **3**, 5140–5146.

21 Shen, X., Li, L., Min Chan, A.C., Gao, N., Yao, S.Q., and Xu, Q.-H. (2013) Water-soluble conjugated polymers for simultaneous two-photon cell imaging and two-photon photodynamic therapy. *Adv. Opt. Mater.*, **1**, 92–99.

22 Guan, Z., Polavarapu, L., and Xu, Q.-H. (2010) Enhanced two-photon emission in coupled metal nanoparticles induced by conjugated polymers. *Langmuir*, **26**, 18020–18023.

23 Liu, P., Li, S., Jin, Y., Qian, L., Gao, N., Yao, S.Q., Huang, F., Xu, Q.-H., and Cao, Y. (2015) Red-emitting DPSB-based conjugated polymer nanoparticles with high two-photon brightness for cell membrane imaging. *ACS Appl. Mater. Interfaces*, **7**, 6754–6763.

24 Medintz, I.L., Uyeda, H.T., Goldman, E.R., and Mattoussi, H. (2005) Quantum dot bioconjugates for imaging, labelling and sensing. *Nat. Mater.*, **4**, 435–446.

25 Resch-Genger, U., Grabolle, M., Cavaliere-Jaricot, S., Nitschke, R., and Nann, T. (2008) Quantum dots versus organic dyes as fluorescent labels. *Nat. Methods*, **5**, 763–775.

26 Wu, C. and Chiu, D.T. (2013) Highly fluorescent semiconducting polymer dots for biology and medicine. *Angew. Chem. Int. Ed.*, **52**, 3086–3109.

27 Heeger, A.J. (2001) Semiconducting and metallic polymers: the fourth generation of polymeric materials (nobel lecture). *Angew. Chem. Int. Ed.*, **40**, 2591–2611.

28 Shirakawa, H. (2001) The discovery of polyacetylene film: the dawning of an era of conducting polymers (nobel lecture). *Angew. Chem. Int. Ed.*, **40**, 2574–2580.

29 MacDiarmid, A.G. (2001) Nobel lecture: "synthetic metals": a novel role for organic polymers. *Rev. Mod. Phys.*, **73**, 701–712.

30 Chen, J. and Cao, Y. (2009) Development of novel conjugated donor polymers for high-efficiency bulk-heterojunction photovoltaic devices. *Acc. Chem. Res.*, **42**, 1709–1718.

31 Grimsdale, A.C., Leok Chan, K., Martin, R.E., Jokisz, P.G., and Holmes, A.B. (2009) Synthesis of light-emitting conjugated polymers for applications in electroluminescent devices. *Chem. Rev.*, **109**, 897–1091.

32 Thomas, S.W. III, Joly, G.D., and Swager, T.M. (2007) Chemical sensors based on amplifying fluorescent conjugated polymers. *Chem. Rev.*, **107**, 1339–1386.

33 Duarte, A., Pu, K.-Y., Liu, B., and Bazan, G.C. (2011) Recent advances in conjugated polyelectrolytes for emerging optoelectronic applications. *Chem. Mater.*, **23**, 501–515.

34 Liu, B. and Bazan, G.C. (2004) Homogeneous fluorescence-based DNA detection with water-soluble conjugated polymers. *Chem. Mater.*, **16**, 4467–4476.

35 Coakley, K.M. and McGehee, M.D. (2004) Conjugated polymer photovoltaic cells. *Chem. Mater.*, **16**, 4533–4542.

36 Günes, S., Neugebauer, H., and Sariciftci, N.S. (2007) Conjugated polymer-based organic solar cells. *Chem. Rev.*, **107**, 1324–1338.

37 Gaylord, B.S., Heeger, A.J., and Bazan, G.C. (2002) DNA detection using water-soluble conjugated polymers and peptide nucleic acid probes. *Proc. Natl. Acad. Sci. USA*, **99**, 10954–10957.

38 Tan, C., Atas, E., Müller, J.G., Pinto, M.R., Kleiman, V.D., and Schanze, K.S. (2004) Amplified quenching of a conjugated polyelectrolyte by cyanine dyes. *J. Am. Chem. Soc.*, **126**, 13685–13694.

39 Fan, C., Plaxco, K.W., and Heeger, A.J. (2003) Electrochemical interrogation of conformational changes as a reagentless method for the sequence-specific detection of DNA. *Proc. Natl. Acad. Sci. USA*, **100**, 9134–9137.

40 Ren, X. and Xu, Q.-H. (2009) Label-free DNA sequence detection with enhanced sensitivity and selectivity using cationic conjugated polymers and picogreen. *Langmuir*, **25**, 43–47.

41 Chen, L., McBranch, D.W., Wang, H.-L., Helgeson, R., Wudl, F., and Whitten, D.G. (1999) Highly sensitive biological and chemical sensors based on reversible fluorescence quenching in a conjugated polymer. *Proc. Natl. Acad. Sci. USA*, **96**, 12287–12292.

42 Duan, X., Liu, L., Feng, F., and Wang, S. (2009) Cationic conjugated polymers for optical detection of DNA methylation, lesions, and single nucleotide polymorphisms. *Acc. Chem. Res.*, **43**, 260–270.

43 Lucky, S.S., Soo, K.C., and Zhang, Y. (2015) Nanoparticles in photodynamic therapy. *Chem. Rev.*, **115**, 1990–2042.

44 Moon, J.H., McDaniel, W., Maclean, P., and Hancock, L.F. (2007) Live-cell-permeable poly(*p*-phenylene ethynylene). *Angew. Chem. Int. Ed.*, **46**, 8223–8225.

45 Feng, L., Zhu, C., Yuan, H., Liu, L., Lv, F., and Wang, S. (2013) Conjugated polymer nanoparticles: preparation, properties, functionalization and biological applications. *Chem. Soc. Rev.*, **42**, 6620–6633.

46 Zhu, C., Liu, L., Yang, Q., Lv, F., and Wang, S. (2012) Water-soluble conjugated polymers for imaging, diagnosis, and therapy. *Chem. Rev.*, **112**, 4687–4735.

47 Li, K. and Liu, B. (2012) Polymer encapsulated conjugated polymer nanoparticles for fluorescence bioimaging. *J. Mater. Chem.*, **22**, 1257–1264.

48 He, G.S., Tan, L.-S., Zheng, Q., and Prasad, P.N. (2008) Multiphoton absorbing materials: molecular designs, characterizations, and applications. *Chem. Rev.*, **108**, 1245–1330.

49 Shen, X., He, F., Wu, J., Xu, G.Q., Yao, S.Q., and Xu, Q.-H. (2011) Enhanced two-photon singlet oxygen generation by photosensitizer-doped conjugated polymer nanoparticles. *Langmuir*, **27**, 1739–1744.

50 Wu, C., Peng, H., Jiang, Y., and McNeill, J. (2006) Energy transfer mediated fluorescence from blended conjugated polymer nanoparticles. *J. Phys. Chem. B*, **110**, 14148–14154.

51 Kim, J. and Swager, T.M. (2001) Control of conformational and interpolymer effects in conjugated polymers. *Nature*, **411**, 1030–1034.

52 Feng, F.D., He, F., An, L.L., Wang, S., Li, Y.H., and Zhu, D.B. (2008) Fluorescent conjugated polyelectrolytes for biomacromolecule detection. *Adv. Mater.*, **20**, 2959–2964.

53 Zhu, C., Yang, Q., Liu, L., and Wang, S. (2011) A potent fluorescent probe for the detection of cell apoptosis. *Chem. Commun.*, **47**, 5524–5526.

54 Kim, I.-B., Shin, H., Garcia, A.J., and Bunz, U.H.F. (2007) Use of a folate–PPE conjugate to image cancer cells *in vitro*. *Bioconjugate Chem.*, **18**, 815–820.

55 Liu, J., Geng, J., and Liu, B. (2013) A bright far-red and near-infrared fluorescent conjugated polyelectrolyte with quantum yield reaching 25%. *Chem. Commun.*, **49**, 1491–1493.

56 Pinto, M.R. and Schanze, K.S. (2004) Amplified fluorescence sensing of protease activity with conjugated polyelectrolytes. *Proc. Natl. Acad. Sci. USA*, **101**, 7505–7510.

57 Wang, S., Gaylord, B.S., and Bazan, G.C. (2004) Fluorescein provides a resonance gate for FRET from conjugated polymers to DNA intercalated dyes. *J. Am. Chem. Soc.*, **126**, 5446–5451.

58 Traina, C.A., Bakus, R.C., and Bazan, G.C. (2011) Design and synthesis of monofunctionalized, water-soluble conjugated polymers for biosensing and imaging applications. *J. Am. Chem. Soc.*, **133**, 12600–12607.

59 Wu, C., Bull, B., Szymanski, C., Christensen, K., and McNeill, J. (2008) Multicolor conjugated polymer dots for biological fluorescence imaging. *ACS Nano*, **2**, 2415–2423.

60 Heeger, P.S. and Heeger, A.J. (1999) Making sense of polymer-based biosensors. *Proc. Natl. Acad. Sci. USA*, **96**, 12219–12221.

61 Wang, Y. and Liu, B. (2009) Conjugated polymer as a signal amplifier for novel silica nanoparticle-based fluoroimmunoassay. *Biosens. Bioelectron.*, **24**, 3293–3298.

62 Pu, K.-Y. and Liu, B. (2009) Optimizing the cationic conjugated polymer-sensitized fluorescent signal of dye labeled oligonucleotide for biosensor applications. *Biosens. Bioelectron.*, **24**, 1067–1073.

63 Pu, K.Y., Li, K., and Liu, B. (2010) A molecular brush approach to enhance quantum yield and suppress nonspecific interactions of conjugated polyelectrolyte for targeted far-red/near-infrared fluorescence cell imaging. *Adv. Funct. Mater.*, **20**, 2770–2777.

64 Pu, K.Y. and Liu, B. (2011) Fluorescent conjugated polyelectrolytes for bioimaging. *Adv. Funct. Mater.*, **21**, 3408–3423.

65 He, F., Tang, Y., Wang, S., Li, Y., and Zhu, D. (2005) Fluorescent amplifying recognition for DNA G-quadruplex folding with a cationic conjugated polymer: a platform for homogeneous potassium detection. *J. Am. Chem. Soc.*, **127**, 12343–12346.

66 Feng, X., Liu, L., Wang, S., and Zhu, D. (2010) Water-soluble fluorescent conjugated polymers and their interactions with biomacromolecules for sensitive biosensors. *Chem. Soc. Rev.*, **39**, 2411–2419.

67 Liu, X., Tang, Y., Wang, L., Zhang, J., Song, S., Fan, C., and Wang, S. (2007) Optical detection of mercury(II) in aqueous solutions by using conjugated polymers and label-free oligonucleotides. *Adv. Mater.*, **19**, 1471–1474.

68 An, L.L., Tang, Y.L., Feng, F.D., He, F., and Wang, S. (2007) Water-soluble conjugated polymers for continuous and sensitive fluorescence assays for phosphatase and peptidase. *J. Mater. Chem.*, **17**, 4147–4152.

69 Feng, F.D., Tang, Y.L., He, F., Yu, M.H., Duan, X.R., Wang, S., Li, Y.L., and Zhu, D.B. (2007) Cationic conjugated polymer/DNA complexes for amplified fluorescence assays of nucleases and methyltransferases. *Adv. Mater.*, **19**, 3490–3495.

70 Feng, F.D., Tang, Y.L., Wang, S., Li, Y.L., and Zhu, D.B. (2007) Continuous fluorometric assays for acetylcholinesterase activity and inhibition with conjugated polyelectrolytes. *Angew. Chem. Int. Ed.*, **46**, 7882–7886.

71 Zhu, Q., Zhan, R.Y., and Liu, B. (2010) Homogeneous detection of trypsin in protein mixtures based on fluorescence resonance energy transfer between anionic conjugated polymer and fluorescent probe. *Macromol. Rapid Commun.*, **31**, 1060–1064.

72 Feng, G.X., Liang, J., and Liu, B. (2013) Hyperbranched conjugated polyelectrolytes for biological sensing and imaging. *Macromol. Rapid Commun.*, **34**, 705–715.

73 Wang, Y., Zhan, R., Li, T., Pu, K.-Y., Wang, Y., Tan, Y.C., and Liu, B. (2012) Fluorescence and visual detection of single nucleotide polymorphism using cationic conjugated polyelectrolyte. *Langmuir*, **28**, 889–895.

74 Wang, Y. and Liu, B. (2007) Silica nanoparticle assisted DNA assays for optical signal amplification of conjugated polymer based fluorescent sensors. *Chem. Commun.*, (34), 3553–3555.

75 Li, K. and Liu, B. (2009) Conjugated polyelectrolyte amplified thiazole orange emission for label free sequence specific DNA detection with single nucleotide polymorphism selectivity. *Anal. Chem.*, **81**, 4099–4105.

76 Zhang, Y., Wang, Y., and Liu, B. (2009) Peptide-mediated energy transfer between an anionic water-soluble conjugated polymer and Texas red labeled DNA for protease and nuclease activity study. *Anal. Chem.*, **81**, 3731–3737.

77 Wang, J. and Liu, B. (2009) Fluorescence resonance energy transfer between an anionic conjugated polymer and a dye-labeled lysozymeaptamer for specific lysozyme detection. *Chem. Commun.*, (17), 2284–2286.

78 Pu, K.-Y., Zhan, R., and Liu, B. (2010) Conjugated polyelectrolyte blend as perturbable energy donor–acceptor assembly with multicolor fluorescence response to proteins. *Chem. Commun.*, **46**, 1470–1472.

79 Liang, J., Li, K., and Liu, B. (2013) Visual sensing with conjugated polyelectrolytes. *Chem. Sci.*, **4**, 1377–1394.

80 Sun, C., Gaylord, B.S., Hong, J.W., Liu, B., and Bazan, G.C. (2007) Application of cationic conjugated polymers in microarrays using label-free DNA targets. *Nat. Protoc.*, **2**, 2148–2151.

81 Li, K., Pu, K.-Y., Cai, L., and Liu, B. (2011) Phalloidin-functionalized hyperbranched conjugated polyelectrolyte for filamentous actin imaging in living HeLa cells. *Chem. Mater.*, **23**, 2113–2119.

82 Pu, K.-Y. and Liu, B. (2010) Fluorescence turn-on responses of anionic and cationic conjugated polymers toward proteins: effect of electrostatic and hydrophobic interactions. *J. Phys. Chem. B*, **114**, 3077–3084.

83 Pu, K.-Y., Shi, J., Cai, L., Li, K., and Liu, B. (2011) Affibody-attached hyperbranched conjugated polyelectrolyte for targeted fluorescence imaging of HER2-positive cancer cell. *Biomacromolecules*, **12**, 2966–2974.

84 Pu, K.Y. and Liu, B. (2009) Intercalating dye harnessed cationic conjugated polymer for real-time naked-eye recognition of double-stranded DNA in serum. *Adv. Funct. Mater.*, **19**, 1371–1378.

85 Liu, B. and Bazan, G.C. (2006) Synthesis of cationic conjugated polymers for use in label-free DNA microarrays. *Nat. Protoc.*, **1**, 1698–1702.

86 Wang, Y., Zhang, Y., and Liu, B. (2010) Conjugated polyelectrolyte based fluorescence turn-on assay for real-time monitoring of protease activity. *Anal. Chem.*, **82**, 8604–8610.

87 Yu, D., Zhang, Y., and Liu, B. (2008) Interpolyelectrolyte complexes of anionic water-soluble conjugated polymers and proteins as platforms for multicolor protein sensing and quantification. *Macromolecules*, **41**, 4003–4011.

88 Li, K. and Liu, B. (2010) Water-soluble conjugated polymers as the platform for protein sensors. *Polym. Chem.*, **1**, 252–259.

89 Liu, B. and Bazan, G.C. (2005) Methods for strand-specific DNA detection with cationic conjugated polymers suitable for incorporation into DNA chips and microarrays. *Proc. Natl. Acad. Sci. U.S.A.*, **102**, 589–593.

90 Pu, K.-Y. and Liu, B. (2008) A multicolor cationic conjugated polymer for naked-eye detection and quantification of heparin. *Macromolecules*, **41**, 6636–6640.

91 Feng, F., Liu, L., and Wang, S. (2010) Fluorescent conjugated polymer-based FRET technique for detection of DNA methylation of cancer cells. *Nat. Protoc.*, **5**, 1255–1264.

92 Feng, X., Lv, F., Liu, L., Tang, H., Xing, C., Yang, Q., and Wang, S. (2010) Conjugated polymer nanoparticles for drug delivery and imaging. *ACS Appl. Mater. Interfaces*, **2**, 2429–2435.

93 Xu, Z.Z., Liao, Q., Wu, Y.S., Ren, W.L., Li, W., Liu, L.B., Wang, S., Gu, Z.J., Zhang, H.L., and Fu, H.B. (2012) Water-miscible organic J-aggregate nanoparticles as efficient two-photon fluorescent nano-probes for bio-imaging. *J. Mater. Chem.*, **22**, 17737–17743.

94 Yuan, Y., Wang, Z., Cai, P., Liu, J., Liao, L.-D., Hong, M., Chen, X., Thakor, N., and Liu, B. (2015) Conjugated polymer and drug co-encapsulated nanoparticles for chemo- and photo-thermal combination therapy with two-photon regulated fast drug release. *Nanoscale*, **7**, 3067–3076.

95 Feng, G., Ding, D., Li, K., Liu, J., and Liu, B. (2014) Reversible photoswitching conjugated polymer nanoparticles for cell and *ex vivo* tumor imaging. *Nanoscale*, **6**, 4141–4147.

96 Liu, J., Feng, G., Ding, D., and Liu, B. (2013) Bright far-red/near-infrared fluorescent conjugated polymer nanoparticles for targeted imaging of HER2-positive cancer cells. *Polym. Chem.*, **4**, 4326–4334.

97 Ding, D., Liu, J., Feng, G.X., Li, K., Hu, Y., and Liu, B. (2013) Bright far-red/near-infrared conjugated polymer nanoparticles for *in vivo* bioimaging. *Small*, **9**, 3093–3102.

98 Feng, G.X., Li, K., Liu, J., Ding, D., and Liu, B. (2014) Bright single-chain conjugated polymer dots embedded nanoparticles for long-term cell tracing and imaging. *Small*, **10**, 1212–1219.

99 Zhou, L., Geng, J., Wang, G., Liu, J., and Liu, B. (2012) Facile synthesis of stable and water-dispersible multihydroxy conjugated polymer nanoparticles with tunable size by dendritic cross-linking. *ACS Macro Lett.*, **1**, 927–932.

100 Li, K., Ding, D., Huo, D., Pu, K.Y., Ngo, N.P.T., Hu, Y., Li, Z., and Liu, B. (2012) Conjugated polymer based nanoparticles as dual-modal probes for targeted *in vivo* fluorescence and magnetic resonance imaging. *Adv. Funct. Mater.*, **22**, 3107–3115.

101 Li, K., Liu, Y.T., Pu, K.Y., Feng, S.S., Zhan, R.Y., and Liu, B. (2011) Polyhedral oligomeric silsesquioxanes-containing conjugated polymer loaded PLGA nanoparticles with trastuzumab (Herceptin) functionalization for HER2-positive cancer cell detection. *Adv. Funct. Mater.*, **21**, 287–294.

102 Ding, D., Li, K., Zhu, Z., Pu, K.-Y., Hu, Y., Jiang, X., and Liu, B. (2011) Conjugated polyelectrolyte-cisplatin complex nanoparticles for simultaneous *in vivo* imaging and drug tracking. *Nanoscale*, **3**, 1997–2002.

103 Wu, C., Szymanski, C., Cain, Z., and McNeill, J. (2007) Conjugated polymer dots for multiphoton fluorescence imaging. *J. Am. Chem. Soc.*, **129**, 12904–12905.

104 Jin, Y., Ye, F., Zeigler, M., Wu, C., and Chiu, D.T. (2011) Near-infrared fluorescent dye-doped semiconducting polymer dots. *ACS Nano*, **5**, 1468–1475.

105 Peng, H.S. and Chiu, D.T. (2015) Soft fluorescent nanomaterials for biological and biomedical imaging. *Chem. Soc. Rev.*, **44**, 4699–4722.

106 Grimland, J.L., Wu, C., Ramoutar, R.R., Brumaghim, J.L., and McNeill, J. (2011) Photosensitizer-doped conjugated polymer nanoparticles with high cross-sections for one- and two-photon excitation. *Nanoscale*, **3**, 1451–1455.

107 Shen, X., Li, S., Li, L., Yao, S.Q., and Xu, Q.-H. (2015) Highly efficient, conjugated-polymer-based nano-photosensitizers for selectively targeted two-photon photodynamic therapy and imaging of cancer cells. *Chem. Eur. J.*, **21**, 2214–2221.

108 Tian, Y., Chen, C.Y., Cheng, Y.J., Young, A.C., Tucker, N.M., and Jen, A.K.Y. (2007) Hydrophobic chromophores in aqueous micellar solution showing large two-photon absorption cross sections. *Adv. Funct. Mater.*, **17**, 1691–1697.

109 Ye, F., Wu, C., Jin, Y., Wang, M., Chan, Y.H., Yu, J., Sun, W., Hayden, S., and Chiu, D.T. (2012) A compact and highly fluorescent orange-emitting polymer dot for specific subcellular imaging. *Chem. Commun.*, **48**, 1778–1780.

110 Carter, G.M., Hryniewicz, J.V., Thakur, M.K., Chen, Y.J., and Meyler, S.E. (1986) Nonlinear optical processes in a polydiacetylene measured with femtosecond duration laser pulses. *Appl. Phys. Lett.*, **49**, 998–1000.

111 Rao, D.N., Chopra, P., Ghoshal, S.K., Swiatkiewicz, J., and Prasad, P.N. (1986) Third-order nonlinear optical interaction and conformational transition in poly-4-BCMU polydiacetylene studied by picosecond and subpicosecond degenerate four wave mixing. *J. Chem. Phys.*, **84**, 7049–7050.

112 Lindle, J.R., Bartoli, F.J., Hoffman, C.A., Kim, O.K., Lee, Y.S., Shirk, J.S., and Kafafi, Z.H. (1990) Nonlinear optical properties of benzimidazobenzophenanthroline type ladder polymers. *Appl. Phys. Lett.*, **56**, 712–714.

113 Yu, L., Chen, M., and Dalton, L.R. (1990) Ladder polymers: recent developments in syntheses, characterization, and potential applications as electronic and optical materials. *Chem. Mater.*, **2**, 649–659.

114 Perepichka, I.F., Perepichka, D.F., Meng, H., and Wudl, F. (2005) Light-emitting polythiophenes. *Adv. Mater.*, **17**, 2281–2305.

115 Barbarella, G., Melucci, M., and Sotgiu, G. (2005) The versatile thiophene: an overview of recent research on thiophene-based materials. *Adv. Mater.*, **17**, 1581–1593.

116 Lee, C.Y.C., Swiatkiewicz, J., Prasad, P.N., Mehta, R., and Bai, S.J. (1991) Third order non-linear optical properties of poly-*p*-phenylene benzobisthiazole and its novel composite with Zytel processed via methane sulphonic acid solution extrusion. *Polymer*, **32**, 1195–1199.

117 Agrawal, A.K., Jenekhe, S.A., Vanherzeele, H., and Meth, J.S. (1992) Third-order nonlinear optical properties of conjugated rigid-rod polyquinolines. *J. Phys. Chem.*, **96**, 2837–2843.

118 Kimball, B.R., Nakashima, M., Roach, J.F., Jaglowski, J.A.J., Aranda, F.J., and Rao, D.V.G.L.N. (1996) Optical power limiting in solutions of polyphenylquinoxalines. *SPIE's 1996 International Symposium on Optical Science, Engineering, and Instrumentation, Denver, CO, United States*, pp. 190–201.

119 Yu, L. and Dalton, L.R. (1990) Synthesis and characterization of new polymers exhibiting large optical nonlinearities. I. Ladder polymers from 3,6-disubstituted 2,5-dichloroquinone and tetraaminobenzene. *Macromolecules*, **23**, 3439–3444.

120 Yang, C., Zheng, M., Li, Y., Zhang, D., Xue, S., and Yang, W. (2014) Poly(1,4-diketo-3,6-diphenylpyrrolo[3,4-*c*]pyrrole-*alt*-3,6-carbazole/2,7-fluorene) as high-performance two-photon dyes. *J. Polym. Sci., Part A: Polym. Chem.*, **52**, 944–951.

121 Keller, B., McLean, A., Kim, B.-G., Chung, K., Kim, J., and Goodson, T. (2016) Ultrafast spectroscopic study of donor–acceptor benzodithiophene light harvesting organic conjugated polymers. *J. Phys. Chem. C*, **120**, 9088–9096.

122 Li, Q., Zhong, C., Huang, J., Huang, Z., Pei, Z., Liu, J., Qin, J., and Li, Z. (2011) Conjugated polymers with pyrrole as the conjugated bridge: synthesis, characterization, and two-photon absorption properties. *J. Phys. Chem. B*, **115**, 8679–8685.

123 Huang, F., Tian, Y., Chen, C.-Y., Cheng, Y.-J., Young, A.C., and Jen, A.K.Y. (2007) Cross-conjugated polymers with large two-photon absorption cross-sections for metal ion sensing. *J. Phys. Chem. C*, **111**, 10673–10681.

124 Zhou, P., Zhong, C., Chen, X., Qin, J., Mariz, I., and Maçôas, E. (2014) New kind of hyperbranched conjugated polymers containing alkyl-modified 2,4,6-tris(thiophen-2-yl)-1,3,5-triazine unit for enhancing two-photon absorption. *Macromolecules*, **47**, 6679–6686.

125 McRae, R.L., Phillips, R.L., Kim, I.-B., Bunz, U.H.F., and Fahrni, C.J. (2008) Molecular recognition based on low-affinity polyvalent interactions: selective binding of a carboxylated polymer to fibronectin fibrils of live fibroblast cells. *J. Am. Chem. Soc.*, **130**, 7851–7853.

126 Stabo-Eeg, F., Lindgren, M., Nilsson, K.P.R., Inganäs, O., and Hammarström, P. (2007) Quantum efficiency and two-photon absorption cross-section of conjugated polyelectrolytes used for protein conformation measurements with applications on amyloid structures. *Chem. Phys.*, **336**, 121–126.

127 Tian, N. and Xu, Q.-H. (2007) Enhanced two-photon excitation fluorescence by fluorescence resonance energy transfer using conjugated polymers. *Adv. Mater.*, **19**, 1988–1991.

128 Wu, C. and Xu, Q.-H. (2009) Enhanced one- and two-photon excitation emission of a porphyrin photosensitizer by FRET from a conjugated polyelectrolyte. *Macromol. Rapid Commun.*, **30**, 504–508.

129 He, F., Ren, X., Shen, X., and Xu, Q.-H. (2011) Water-soluble conjugated polymers for amplification of one- and two-photon properties of photosensitizers. *Macromolecules*, **44**, 5373–5380.

130 Ho, H.-A. and Leclerc, M. (2004) Optical sensors based on hybrid aptamer/conjugated polymer complexes. *J. Am. Chem. Soc.*, **126**, 1384–1387.

131 Zhao, X., Pinto, M.R., Hardison, L.M., Mwaura, J., Müller, J., Jiang, H., Witker, D., Kleiman, V.D., Reynolds, J.R., and Schanze, K.S. (2006) Variable band gap poly(arylene ethynylene) conjugated polyelectrolytes. *Macromolecules*, **39**, 6355–6366.

132 Schwartz, B.J. (2003) Conjugated polymers as molecular materials: how chain conformation and film morphology influence energy transfer and interchain interactions. *Annu. Rev. Phys. Chem.*, **54**, 141–172.

133 Rahim, N.A.A., McDaniel, W., Bardon, K., Srinivasan, S., Vickerman, V., So, P.T.C., and Moon, J.H. (2009) Conjugated polymer nanoparticles for two-photon imaging of endothelial cells in a tissue model. *Adv. Mater.*, **21**, 3492–3496.

134 Pecher, J., Huber, J., Winterhalder, M., Zumbusch, A., and Mecking, S. (2010) Tailor-made conjugated polymer nanoparticles for multicolor and multiphoton cell imaging. *Biomacromolecules*, **11**, 2776–2780.

135 Ding, D., Liu, J., Feng, G., Li, K., Hu, Y., and Liu, B. (2013) Fluorescence imaging: bright far-red/near-infrared conjugated polymer nanoparticles for *in vivo* bioimaging. *Small*, **9**, 3092.

136 Dobrovolskaia, M.A. and McNeil, S.E. (2007) Immunological properties of engineered nanomaterials. *Nat. Nanotechnol.*, **2**, 469–478.

137 Sheiko, S.S., Sumerlin, B.S., and Matyjaszewski, K. (2008) Cylindrical molecular brushes: synthesis, characterization, and properties. *Prog. Polym. Sci.*, **33**, 759–785.

138 Dmitriev, R.I., Borisov, S.M., Düssmann, H., Sun, S., Müller, B.J., Prehn, J., Baklaushev, V.P., Klimant, I., and Papkovsky, D.B. (2015) Versatile conjugated polymer nanoparticles for high-resolution O_2 imaging in cells and 3D tissue models. *ACS Nano*, **9**, 5275–5288.

139 Wu, C., Hansen, S.J., Hou, Q., Yu, J., Zeigler, M., Jin, Y., Burnham, D.R., McNeill, J.D., Olson, J.M., and Chiu, D.T. (2011) Design of highly emissive polymer dot bioconjugates for *in vivo* tumor targeting. *Angew. Chem. Int. Ed.*, **50**, 3430–3434.

140 Xu, Q.-H., Wang, S., Korystov, D., Mikhailovsky, A., Bazan, G.C., Moses, D., and Heeger, A.J. (2005) The fluorescence resonance energy transfer (FRET) gate: a time-resolved study. *Proc. Natl. Acad. Sci. USA*, **102**, 530–535.

141 Li, S., Shen, X., Li, L., Yuan, P., Guan, Z., Yao, S.Q., and Xu, Q.-H. (2014) Conjugated-polymer-based red-emitting nanoparticles for two-photon excitation cell imaging with high contrast. *Langmuir*, **30**, 7623–7627.

142 Lv, Y., Liu, P., Ding, H., Wu, Y., Yan, Y., Liu, H., Wang, X., Huang, F., Zhao, Y., and Tian, Z. (2015) Conjugated polymer-based hybrid nanoparticles with two-photon excitation and near-infrared emission features for fluorescence bioimaging within the biological window. *ACS Appl. Mater. Interfaces*, **7**, 20640–20648.

143 Parthasarathy, A., Ahn, H.-Y., Belfield, K.D., and Schanze, K.S. (2010) Two-photon excited fluorescence of a conjugated polyelectrolyte and its application in cell imaging. *ACS Appl. Mater. Interfaces*, **2**, 2744–2748.

144 Aparicio-Ixta, L., Ramos-Ortiz, G., Pichardo-Molina, J.L., Maldonado, J.L., Rodriguez, M., Tellez-Lopez, V.M., Martinez-Fong, D., Zolotukhin, M.G., Fomine, S., Meneses-Nava, M.A. *et al.* (2012) Two-photon excited fluorescence of silica nanoparticles loaded with a fluorene-based monomer and its cross-conjugated polymer: their application to cell imaging. *Nanoscale*, **4**, 7751–7759.

145 Geng, J.L., Goh, C.C., Tomczak, N., Liu, J., Liu, R.R., Ma, L., Ng, L.G., Gurzadyan, G.G., and Liu, B. (2014) Micelle/silica co-protected conjugated polymer nanoparticles for two-photon excited brain vascular imaging. *Chem. Mater.*, **26**, 1874–1880.

7

Water-Soluble Conjugated Polymers for Sensing and Imaging Applications

Xingfen Liu[1], *Wei Huang*[1,2], *and Quli Fan*[1]

[1] *Key Laboratory for Organic Electronics and Information Displays & Jiangsu Key Laboratory for Biosensors, Institute of Advanced Materials (IAM), Jiangsu National Synergistic Innovation Center for Advanced Materials (SICAM), Nanjing University of Posts & Telecommunications, 9 Wenyuan Road, Nanjing, 210023, China*
[2] *Key Laboratory of Flexible Electronics (KLOFE) & Institute of Advanced Materials (IAM), Jiangsu National Synergistic Innovation Center for Advanced Materials (SICAM), Nanjing Tech University (NanjingTech), 30 South Puzhu Road, Nanjing, 211816, China*

7.1 Introduction

Conjugated polymers (CPs) with large π-conjugated backbones and delocalized electronic structures exhibit efficient coupling between opto-electronic segments, and have been widely applied in opto-electronic devices in the past decade [1]. Meanwhile, water-soluble conjugated polymers (WSCPs) with various hydrophilic moieties are endowed with powerful capabilities that can be used in aqueous biological systems [2–4]. As is known, upon light irradiation, excitons in the CPs can be transferred to lower energy/electron acceptor sites efficiently, resulting in quenched fluorescence of CPs or amplified signals of acceptors [5]. This makes them a class of promising fluorescence probes for highly sensitive sensing of DNA, RNA, protein, enzyme, tumor marker, inhibitor, ion, photosensitizer, bacteria, pathogen, and even tumor cells [2–4, 6].

Conjugated polymer nanoparticles (CPNs) with small size (tens of nanometer) combine the properties of CPs and nanoparticles and define a new class of promising fluorescence probe for bioimaging [5]. Compared with conventional organic dyes and inorganic semiconducting quantum dots, CPNs display several distinguishing features, such as high brightness, excellent photostability, low cytotoxicity, large absorption cross-section, and versatile surface modification. Owing to the above advantages, numerous exciting advancements have been achieved in imaging (NIR, two-photo, multicolor, photoacoustic, and multimodal imaging), drug/gene delivery, and imaging-guided cancer therapy [4, 7]. In this chapter, we mainly focus on the biological applications of WSCPs in sensing and imaging. Challenges and outlook in this field will also be discussed. The preparation, properties, functionalization, and other biomedical applications of CPs can be found in other literatures [2–4, 6].

Conjugated Polymers for Biological and Biomedical Applications, First Edition. Edited by Bin Liu

7.2 Conjugated Polymers for Sensing

WSCPs, as biosensing materials, have many advantages over other luminescent materials because of their excellent light-harvesting capability, high quantum yield, and unique polymer chain conformation. Four main sensing mechanisms are always used for the design of optical sensors: (i) Föster resonance energy transfer (FRET) between CPs and chromophores; (ii) superquenching of CPs; (iii) conformational effects of CPs; and (iv) aggregation-induced optical changes. While developing highly specific and sensitive sensing strategies, water-soluble polyfluorene (PF), polythiophene (PT), and poly(phenylene ether) (PPE) derivatives have often been used to design fluorescent sensors for various analytes of interest.

7.2.1 Sensing Based on FRET

7.2.1.1 One-Step FRET

Bazan and Heeger research group pioneered investigations using FRET between CPs and fluorophores to detect DNA [8]. In that classic assay, a neutral peptide nucleic acid (PNA) was selected as a probe because of its ability to form specific complexes with DNA, and also because the PNA/DNA complex is tighter than the analogous DNA/DNA complex [9]. A cationic conjugated polyfluorene derivative (**CP 1**) was used as an energy donor in this scheme. As shown in Figure 7.1a, a PNA strand labeled with a chromophore (PNA-C*) was used as the probe; here, the C* acts as an energy acceptor because it has a strong spectral overlap with **CP 1**. In the absence of DNA, there are no electrostatic interactions between **CP 1** and PNA-C*, and the distance between **CP 1** and C* is too great for efficient FRET to occur. Addition of complementary ssDNA allows the PNA to hybridize and endows the PNA-C* with multiple negative charges that could then bind with **CP 1** via electrostatic interactions to form a complex. Hence, the new average distance between **CP 1** and C* allows for FRET to take place. However, if noncomplementary ssDNA is added, the PNA-C* is unable to hybridize and electrostatic complexation occurs only between **CP 1** and DNA. As a result, the distance is too large for FRET to occur. Excitation of **CP 1** provides fluorescence emission that is more than 25 times higher than that obtained by exciting the C*, allowing detection of target DNA at a concentration of 10 pM with a standard fluorometer. Furthermore, Bazan's group developed a strategy for the detection of single nucleotide polymorphisms (SNPs) with fluorescein-labeled peptide nucleic acid (PNA-FL), **CP 2**, and single-strand-specific S1 nuclease enzyme [10]. Long ssDNA target sequences were digested by S1 nuclease, leaving intact only those regions that hybridize to the PNA probe. Any PNA/DNA mismatches resulted in complete DNA digestion. Therefore, FRET from **CP 2** to fluorescein (FL) occurs only for the perfect PNA-FL/DNA complex.

Although PNA has many advantages as a probe, it is more expensive than DNA for practical use. Bazan's group developed a complementary method that relies upon a more traditional DNA probe and **CP 1** for DNA hybridization detection [11]. This offers many possibilities for the design of strategies for the detection of DNA-related issues, such as hybridization, conformation alternation, and methylation of DNA. Wang's group reported a convenient, sensitive, and label-free

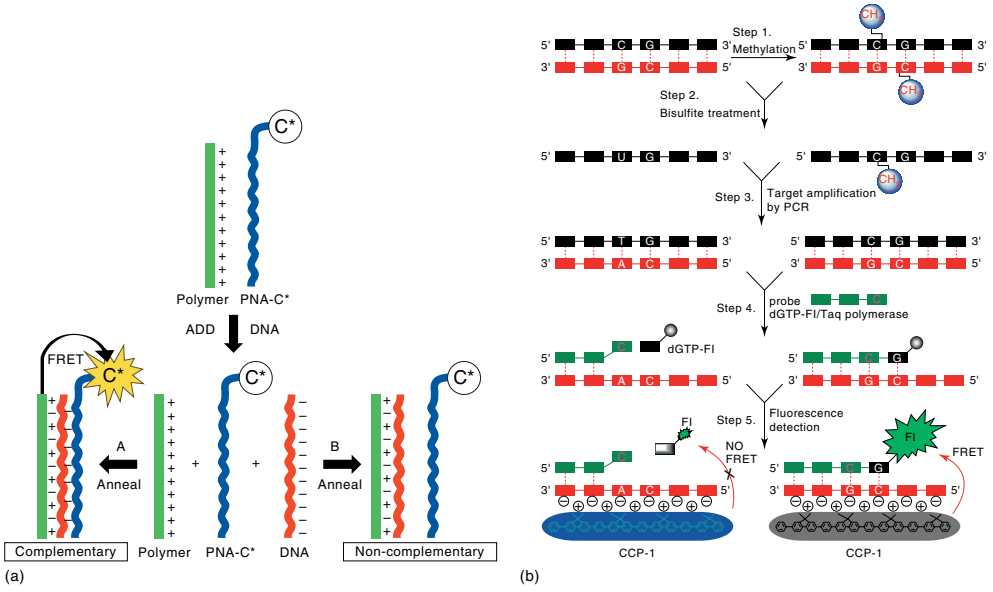

Figure 7.1 (a) Scheme of the DNA detection based on FRET between **CP 1** and PNA-C*. (Reprinted with permission from Ref. [8]. Copyright 2002, National Academy of Sciences, U.S.A.) (b) Scheme of the detection of DNA methylation based on FRET between dGTP-Fl and **CP 2**. (Reprinted with permission from Ref. [12]. Copyright 2008, American Chemical Society.)

method to determine the DNA methylation status of CpG sites of plasmid and human colon cancer cell [12] Figure 7.1b. The system relies on the remarkable optical amplification of cationic conjugated polyelectrolytes (**CP 2**) and highly selective single base extension reaction. The higher FRET efficiency between **CP 2** and fluorescein-labeled dGTP (dGTP-Fl) is correlated to the incorporation of dGTP-Fl into the DNA probe by single base extension reaction when the target/probe pair is complementary at the methylation site. As low as 1% methylation status can be determined by this method. Since **CP 2** acts as an indicator of the methylation status in the "mix and detect" assay, the turn-on response of fluorescence is rapid and sensitive. Additionally, strategies for the sensitive and selective detection of adenosine deaminase (ADA) and its inhibitor [13], thrombin [14], and transcription factor [15] were developed based on the dye-labeled DNA probe and the subsequent high efficient FRET from CPs to dyes.

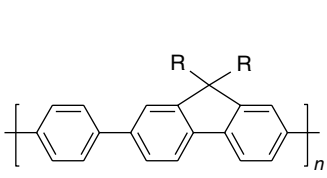

CP 1 R = $(CH_2)_6\overset{+}{N}Me_3\overset{-}{I}$

CP 4 R = $(CH_2)_6\overset{+}{N}Me_3\overset{-}{Br}$

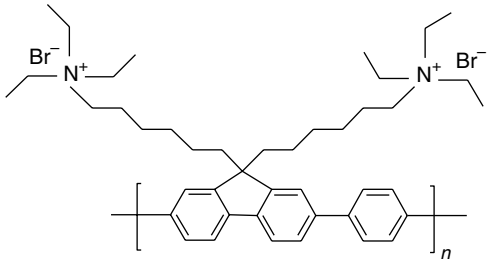

CP 2

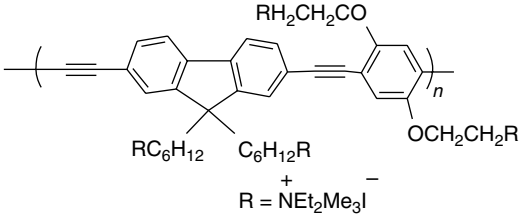

R = $\overset{+}{N}Et_2Me_3\overset{-}{I}$

PFEP

Label-free biosensors have several advantages compared with labeled ones, such as low cost, simpler procedures, and time saving. Using dyes that can intercalate into the DNA duplex or G-quadruplex is another popular strategy based on the FRET between CPs and dyes. Huang's group reported an ultrasensitive label-free biosensor for assaying of sequence-specific DNA-binding protein (DBP) based on **PFEP**, shown in Figure 7.2a [16]. A key transcription factor, nuclear factor-kappa B (NF-κB), was used as a model target. A series of label-free DNA probes bearing one or two protein-binding sites were designed for specific identification of the target protein. In the presence of the target, the binding DBP protects the probe from digestion by exonuclease III, resulting in high efficient FRET due to strong electrostatic interactions between **PFEP** and the DNA probe. By using label-free hairpin DNA or dsDNA containing two binding sites as the probe, as low as 1 pg ml^{-1} of NF-κB in HeLa nuclear extracts can be detected, which is 10 000-fold more sensitive than the previously reported methods. The approach also allows naked-eye detection by observing the fluorescent color of

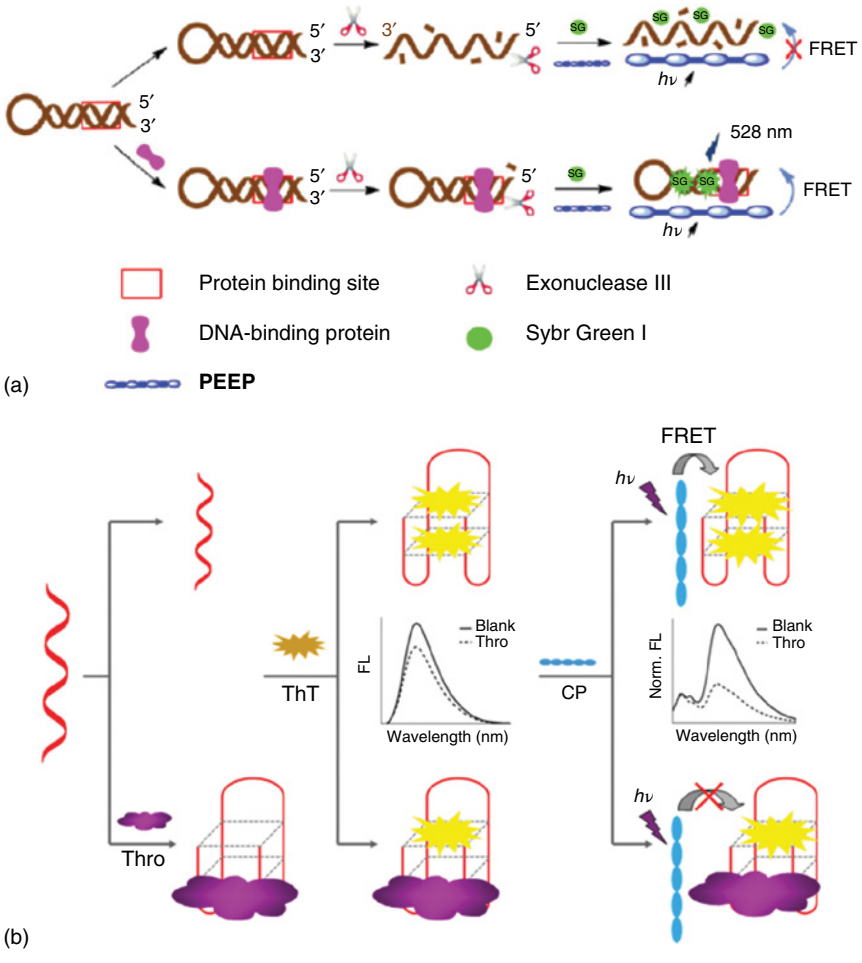

Figure 7.2 (a) Scheme of label-free detection of DNA-binding protein based on the FRET between PFEP and Sybr Green I. (Reprinted with permission from Ref. [16]. Copyright 2013, Elsevier.) (b) Scheme of the label-free detection of thrombin based on G-quadruplex specific dye (ThT). (Reprinted with permission from Ref. [17]. Copyright 2015, American Chemical Society.)

solutions with the assistance of a hand-held UV lamp. Recently, a new FRET system that uses a special dye, thioflavin T (ThT) as an energy acceptor and **PFEP** as an energy donor was developed for protein detection [17]. As shown in Figure 7.2b, in the absence of the target, ThT induces the aptamer to form a G-quadruplex and intercalates into it with strong fluorescence. Strong electrostatic attraction between the negatively charged G-quadruplex and positively charged **PFEP** allows a short donor–acceptor distance, resulting in a high FRET signal. However, in the presence of the target, a G-quadruplex/thrombin complex formed first, followed by the intercalation of ThT into the G-quadruplex. A long distance exists between the donor and acceptor due to the strong steric hindrance from the large-sized thrombin, which leads to a low FRET signal.

Other strategies were also developed for the detection of important substance and cancer cells [18, 19]. For example, Rotello's group reported supramolecular

complexes of a family of positively charged **CP 3-1**,**2**,**3**,**4** and green fluorescent protein (GFP), and created a FRET-based ratiometric biosensor array, as shown in Figure 7.3 [19]. Selective multivalent interactions of the CPs with mammalian cell surfaces caused differential change in FRET signals, providing a fingerprint signature for each cell type. The resulting fluorescence signatures allowed the identification of 16 different cell types as well as the discrimination between healthy, cancerous, and metastatic cells, with the same genetic background. The utility of the biosensor was further demonstrated in the detection of blinded unknown samples, where 121 of 128 samples were correctly identified. This selectivity-based sensor stratified diverse cell types in minutes, using only 2000 cells, without requiring specific biomarkers or cell labeling.

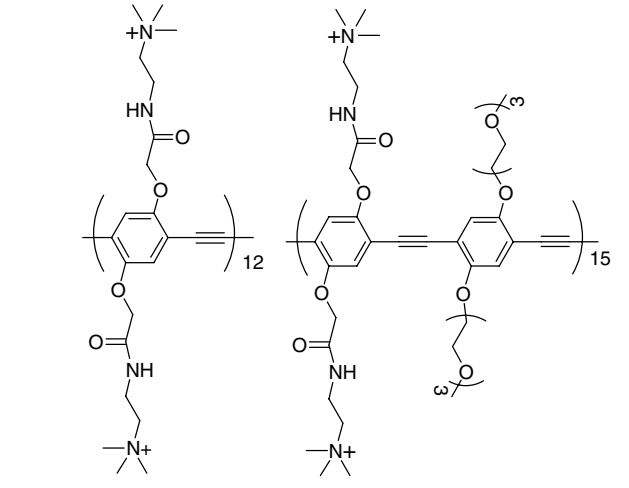

CP 3-1 CP 3-2

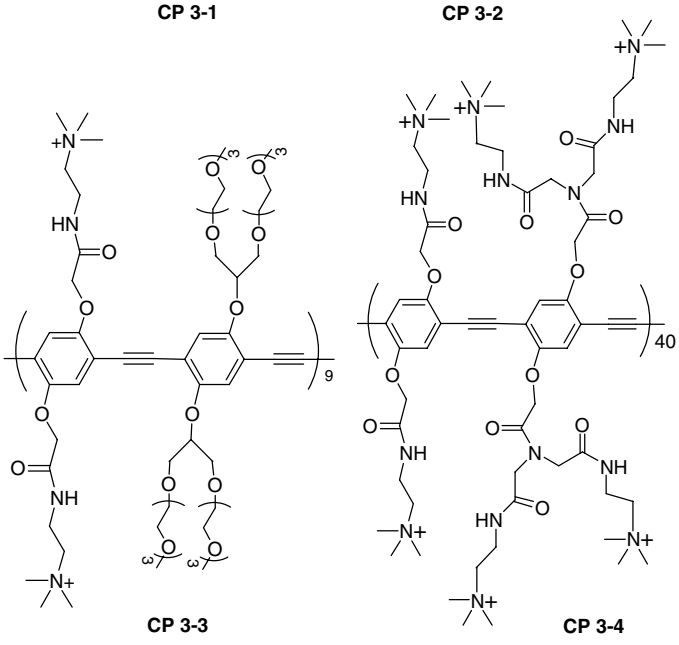

CP 3-3 CP 3-4

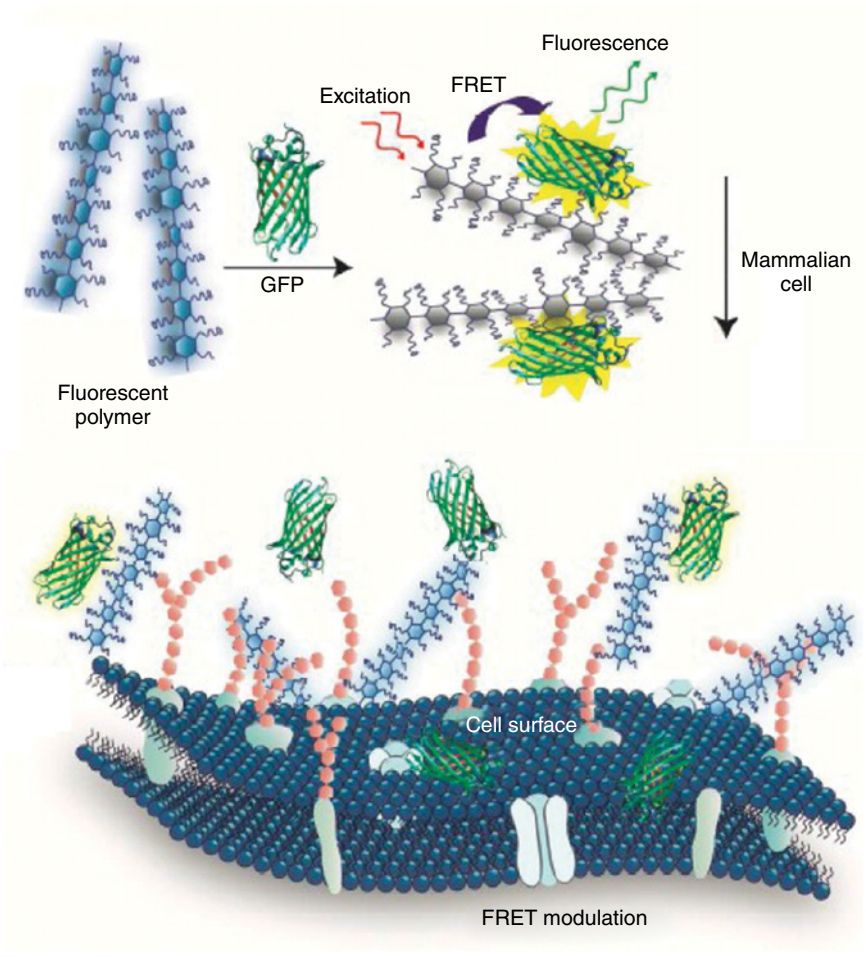

Figure 7.3 Schematic illustration of FRET-based cell sensing using CP-GFP complexes. (Reprinted with permission from Ref. [19]. Copyright 2016, American Chemical Society.)

7.2.1.2 Two-Step FRET

Bazan and coworkers first designed a two-step FRET strategy to improve the performance of the ssDNA-based assay [20]. Ethidium bromide (EB) is known to have an increased fluorescence quantum yield upon intercalation between the stacked bases of dsDNA. Theoretically, the energy transfer from **CP 1** to EB would take place when EB intercalated into the dsDNA. However, the authors did not observe efficient FRET even though the distance and spectral overlap between **CP 1** and EB were appropriate for a high rate of FRET. They suspected that the reason for this inefficient energy transfer was a nearly orthogonal arrangement of donor and acceptor transition dipole moments. When Fl is attached to one terminus of the dsDNA, there is efficient FRET from **CP 1** through Fl to EB. Fluorescence decay kinetics and fluorescence anisotropy measurements showed that the proximity and conformational freedom of Fl provide a

FRET gate to dyes intercalated within dsDNA. They further studied the two-step energy transfer process by using pump-dump-emission spectroscopy and time-correlated single-photon counting, and found that including Fl as an intermediate "FRET gate" provided a much more efficient energy transfer to EB, with an eightfold amplification relative to direct excitation of the intercalator [21].

In a cascade FRET process, CP and dyes have alternative fluorescence, which is appropriate for the design of a DNA logic gate. Huang's group reported an optical-logic system based on **PFEP**/DNA/intercalating dyes assembly for label-free detection of conformational conversion of DNA i-motif structure [22]. Multiple logic gates operating in parallel were simulated by taking advantage of the pH-driven conformational conversion of DNA i-motif structure and the two-step FRET process in this assembly. This logic system does not require any chemical modification or oligonucleotide labeling, which offers the advantages of simplicity and cost efficiency. What is important is that the logic gates can be switched back and forth by addition of H^+ and OH^-, which makes operation easy and feasible to realize system reset. Recently, a new biosensor based on **CP 4** and FRET was reported for adenosine deaminase (ADA) detection [23]. In the absence of ADA, the aptamer forms a hairpin-like conformation with adenosine, which is far from its complementary single-stranded DNA (DNAc-Fl). When **CP 4** is excited at 380 nm, Fl emits strong green fluorescence via one-step FRET while EB has no fluorescence. After addition of ADA, adenosine is hydrolyzed to inosine and subsequently dsDNA is formed between the aptamer and DNAc-Fl, followed by EB intercalating into dsDNA. Once **CP 4** is excited, EB will emit strong yellow fluorescence after a two-step FRET from **CP 4** to Fl and from Fl to EB. The sensitive ADA detection is realized with a low detection limit of 0.5 U/L by measuring the FRET ratio of EB to Fl.

7.2.2 Sensing Based on Superquenching of CPs

Fluorescence of CPs can be quenched by protein, peptide, gold nanoparticle (AuNPs), graphene oxide (GO), and even bacteria via energy/electron transfer, which provides many possibilities for the design of highly sensitive sensors. The quenching capacity of a quencher is often evaluated by the Stern–Volmer constant, K_{sv}. Under conditions where all other variables are held constant, the higher the K_{sv}, the lower the concentration of the quencher required to achieve fluorescence quenching.

7.2.2.1 Analytes-Induced Quenching

Early in 2002, Fan *et al.* discovered the superquenching of **MBL-PPV** by cytochrome *c* (cyt *c*) with a super-high K_{sv} excess of $10^8\,M^{-1}$ [24]. They proposed that efficient fluorescence quenching relies on the formation of a conjugated polymer–quencher complex driven by attractive Coulomb interactions. In view of this fact, Liu's group developed a fluorescence "turn-on" assay for monitoring protease activity on the basis of **PFP-CO_2Na** [25]. The fluorescence of **PFP-CO_2Na** was significantly quenched by cyt *c* due to complexation-mediated electron transfer between the polymer and protein. K_{sv} was calculated to be $\sim 1.32 \times 10^7\,M^{-1}$. The complex of **PFP-$CO_2$Na**/cyt *c* was used as a substrate. When trypsin was added to the substrate, a gradual recovery of the fluorescence intensity for

PFP-CO_2Na was observed due to trypsin-catalyzed hydrolysis of cyt *c*. The digestion converts positively charged cyt *c* to negatively charged heme-containing fragments at pH 8.9, which disturbs the complexation of the **PFP-CO_2Na**/heme center due to electrostatic repulsion between the fragments and the polymer. The limit of detection (LOD) of trypsin is ~1.7 nM and k_{cat}/K_m is calculated to be 5350 $M^{-1}s^{-1}$, which make it possible to monitor trypsin in real time.

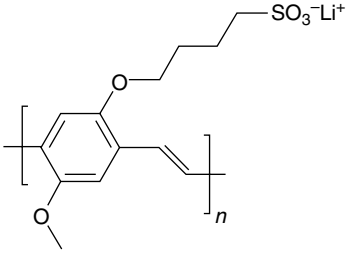

MBL-PPV

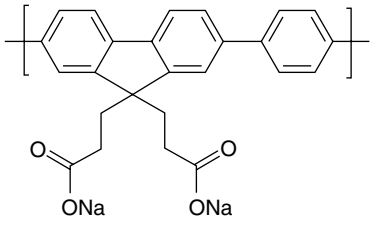

PFP-CO_2Na

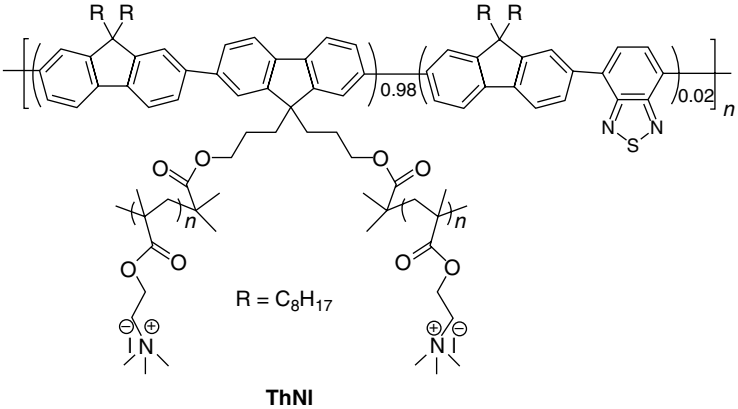

ThNI

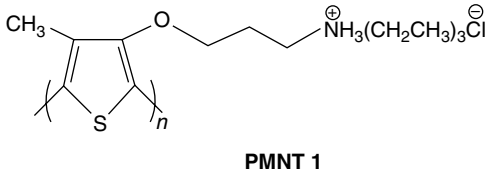

PMNT 1

Taking advantage of the light-harvesting properties of CPs, a new fluorescent biosensor was designed to screen α-glucosidase inhibitors (AGIs) by using *para*-nitrophenyl-α-D-glucopyranoside (PNPG) as s substrate [26]. In the presence of α-glucosidase, PNPG was hydrolyzed by α-glucosidase and 4-nitrophenol was released. The fluorescence of **CP 4** was quenched efficiently by anionic 4-nitrophenol (K_{sv} is 3.7×10^5 M^{-1}) presumably via the process of photo-induced electron transfer (PET) or energy transfer under experimental conditions (pH 7.4). Upon addition of AGIs, α-glucosidase is inactivated by AGIs. Therefore, PNPG cannot be cleaved by α-glucosidase and a recovery of fluorescence was observed.

Water-soluble conjugated polyelectrolyte brush has a superbranched molecular structure and highly charged side chains, which endow them more possibilities to interact with oppositely charged biomolecules. Recently, our group reported a rapid, specific and label-free method for the detection of tumor marker, human α-fetoprotein (AFP), based on the selective superquenching of **ThNI** [27]. The positively charged ThNI exists as monodispersed nanoparticles, and it gives bright blue fluorescence in aqueous solution. Interestingly, the fluorescence of ThNI can be significantly quenched by AFP and the K_{sv} is estimated to be $2.44 \times 10^8\,M^{-1}$. The method is highly selective and sensitive with a LOD of 2 nM for AFP in an artificial mixture.

Recently, Xing and coworkers found the fluorescence quenching of polythiophene derivative (**PMNT 1)** by bacteria, and developed a strategy for high-throughput screening of photodynamic antimicrobial chemotherapy photosensitizers (PSs) [28]. In the absence of PS, the bacteria grow exponentially and can be coated tightly by **PMNT 1** through electrostatic and hydrophobic interactions between **PMNT 1** and negatively charged bacteria, resulting in the formation of aggregates and the fluorescence quenching of **PMNT 1**. In the presence of PS, the bacteria can be efficiently killed and the fluorescence of **PMNT 1** is not affected, leading to original and strong fluorescence of **PMNT 1**. The bacterial number can be detected quantitatively by **PMNT 1** via various fluorescence quenching efficiencies. The LOD for *Escherichia coli* is 3.0×10^5 Cfu. The photodynamic antimicrobial chemotherapy (PACT) efficacy of six different PSs toward the antibiotic resistant *E. coli* was examined in a high-throughput fashion for PS screening. Results demonstrated that PSs of TMPyP, TBO, and MB are superefficient in killing *E. coli* cells with white-light irradiation and no fluorescence quenching was observed. However, negatively charged PSs of HP and PC cannot lead to efficient reduction of the cell viability in PACT, demonstrating that electrostatic repulsion between anionic PS and the surface of *E. coli* leads to less adsorption of PS to *E. coli*.

7.2.2.2 Gold Nanoparticles-Induced Superquenching

Heeger's group first reported the superquenching of cationic polyfluorene by AuNPs with a K_{sv} approaching $10^{11}\,M^{-1}$, which is several orders of magnitude larger than any previously reported CP–quencher pair, and 9–10 orders of magnitude larger than small molecule dye–quencher pairs [29]. Based on the superquenching of AuNPs to the fluorescence of CPs, various sensors were developed for the detection of proteins. Su and coworkers constructed a hybrid sensor using AuNPs and five kinds of CPs (**CCPE-410**, **CCPE-470**, **CCPE-630**, **ACPE-430**, **ACPE-560**) for the detection of protein–DNA interactions [30]. Through a proper selection of CPs in terms of charge properties relative to the charge of dsDNA–AuNPs and emission wavelengths relative to the AuNP extinction peak, the hybrid sensors can be constructed into "light-on," "light-off," and "two-way" models (Figure 7.4). Protein binding can be detected by fluorescence recovery, fluorescence quenching, or both ways. The "two-way" sensor allows for detection of proteins of any charge properties or unknown charge properties. With estrogen receptor (ERα and ERβ), their consensus DNA element, and all 15 possible singly mutated elements, the authors demonstrated the accuracy of the hybrids sensors

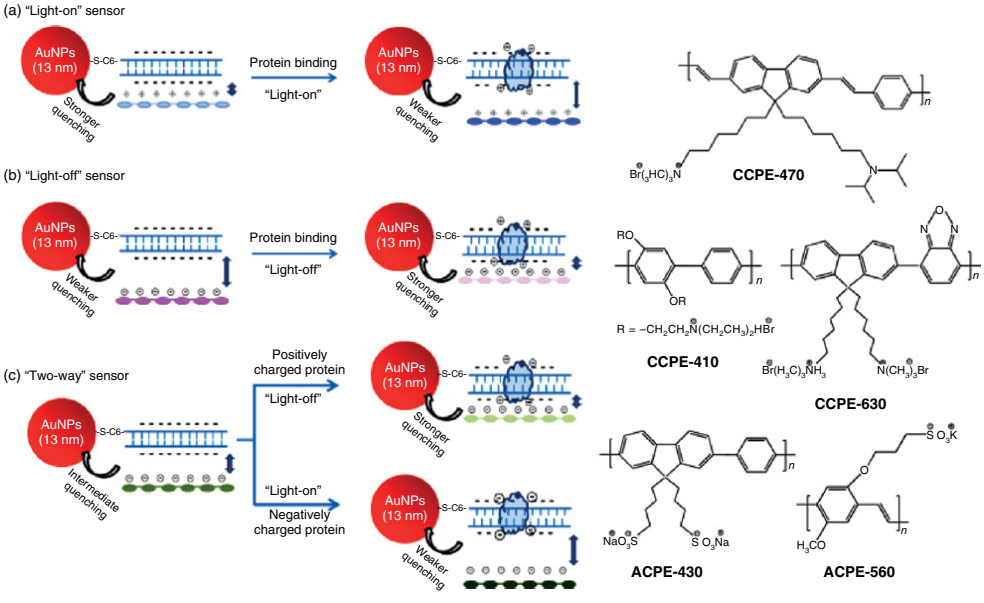

Figure 7.4 Schematic drawings of (a) "light-on," (b) "light-off," and (c) "two-way" hybrid sensors for the detection of protein-DNA interactions by fluorescence recovery, fluorescence quenching, or both ways. (Reprinted with permission from Ref. [30]. Copyright 2013, American Chemical Society.)

for determination of binding affinity constant, binding stoichiometry, and site- and nucleotide-specific binding energy matrix. The *in vitro* binding energy determined by the hybrid sensors correlates very well with the energy matrix computed from *in vivo* genome-wide ERα binding data (rank correlation coefficient 0.98).

Recently, Liu's group reported a tumor-responsive nanoprobe based on a hybrid of **PFBT 1** and AuNPs [31]. A pH triggered charge-reversible polymer and **PFBT 1** were sequentially deposited onto the AuNP surface through electrostatic interactions. In physiological conditions (pH ≈ 7.4), the hybrid probe is almost nonfluorescent due to the superquenching of **PFBT 1** by AuNPs via energy/charge transfer and efficient exciton migration along the polymer backbone. When exposed to acidic extracellular microenvironments in tumor ($pH_e \approx 6.5$), the acid-labile amides hydrolyze into primary amines. The generated amine groups result in strong electrostatic repulsion between **PFBT 1** and AuNPs, leading to recovered probe fluorescence.

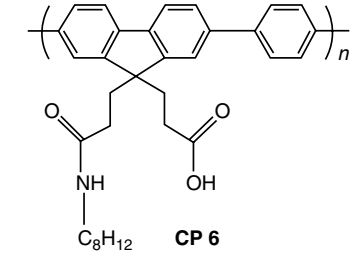

CP 6

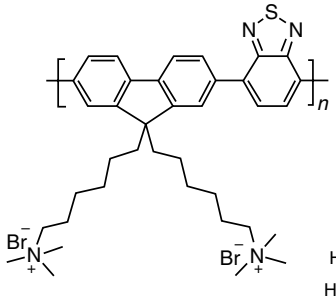

PFBT 1

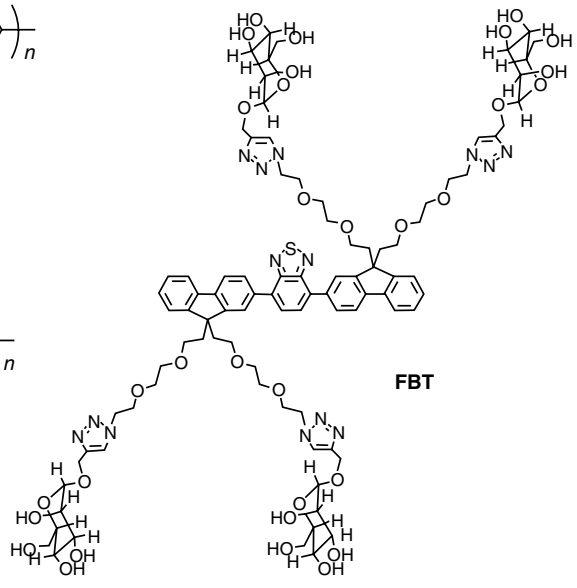

FBT

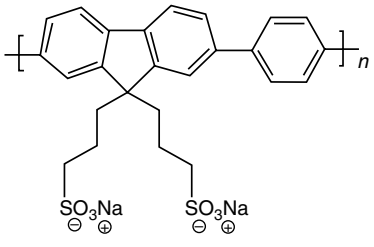

CP 5–1

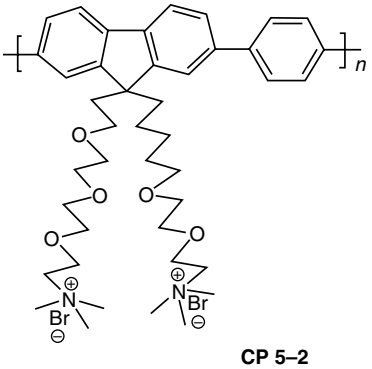

CP 5–2

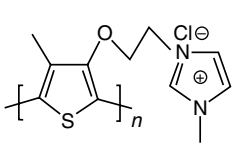

CP 5–3

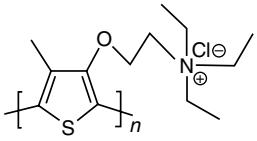

CP 5–4

7.2.2.3 Graphene Oxide-Induced Superquenching

A GO-based bioassay was developed by using a conjugated oligomer as probe for light-up detection of Concanavalin A (Con A) and *E. coli* [32]. **FBT** has a high density of α-mannose side chains and a relatively short backbone, which endows it good water solubility. By virtue of the fluorescence quenching capability of GO, the background fluorescence is low, which ultimately leads to efficient visual detection of Con A and *E. coli* with high sensitivity and selectivity. Furthermore, Fan's group investigated the interactions between GO and various CPs possessing different structures and charges [33]. They found that the charge and the molecular structure of CPs (**CP5-1, 2, 3, 4**) play important roles in GO–CPs interactions. Among them, electrostatic interactions, π–π interaction, and cation-π bonding are dominant driving forces. Based on this, a sensitive homogeneous sensor was developed for DNA and RNA detection with a detection limit of 50 pM DNA and RNA, which increased the sensitivity 40-fold as compared to the corresponding GO-free sensors (Figure 7.5A).

Wang's group developed a hybrid probe of GO and cationic **CP 4** for the detection of the conformation transition of calmodulin (CaM) [34]. The conformation of CaM changes from closed configuration to an open one, converting to a claviform dumbbell-shaped biomolecule upon Ca^{2+}-binding. The stronger hydrophobic interaction and weaker electrostatic repulsion lead to more CaM adsorption to the surface of GO upon binding with Ca^{2+} than that of CaM in the absence of Ca^{2+} (apoCaM), resulting in much farther proximity between **CP 4** and green fluorescent protein labeled at the N-terminus of CaM and therefore much weaker FRET efficiency for **CP 4**/Ca^{2+}/CaM as compared with that of **CP 4**/apoCaM in the presence of GO. The assembly of CaM with GO is quantitatively and reversibly controlled by Ca^{2+} ions (Figure 7.5B).

7.2.3 Sensing Based on Conformation Conversion

PT and polydiacetylene (PDA) are two classes of special polymers in view of the conformation-sensitive property to initiate discernible signal changes by naked eyes [35, 36]. Leclerc's group pioneered DNA detection based on the conformational effects of photoactive PT derivative (**PMNT 2**) [37]. As shown in Figure 7.6A and B, the random-coil conformation of **PMNT 2** is highly fluorescent with a yellow color in aqueous solution, which corresponds to a less-conjugated, nonplanar form with absorption at 392 nm. Upon addition of ssDNA (X1) to **PMNT 2**, the color of the solution changed from yellow to red in about 5 min due to the formation of a so-called "duplex" between **PMNT 2** and the ssDNA probe, a process driven by electrostatic attraction. This duplex

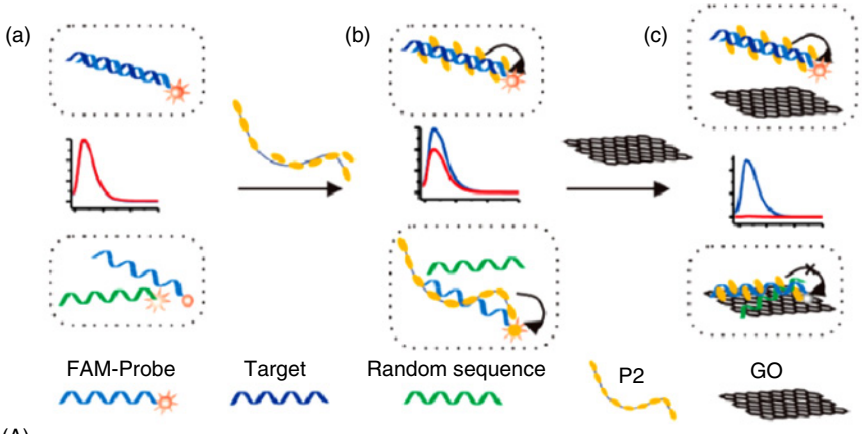

(A)

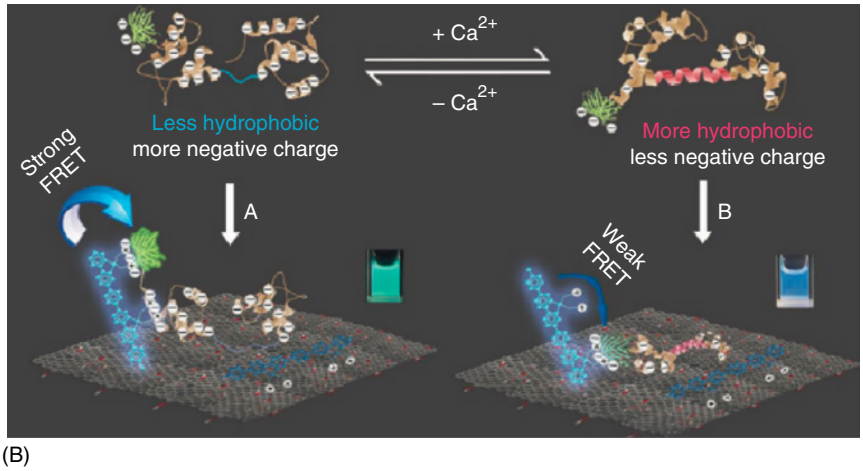

(B)

Figure 7.5 (A) Schematic presentation of DNA analysis with the GO–CPs hybrid system. (Reprinted with permission from Ref. [33]. Copyright 2015, American Chemical Society.) (B) Scheme of a GO and CP 4 hybrid probe for the detection of conformation changes of calmodulin (CaM). (Reprinted with permission from Ref. [34]. Copyright 2015, Wiley-VCH Verlag GmbH & Co. KGaA.)

corresponds to a highly conjugated planar form with absorption at 520 nm and strongly quenched fluorescence. However, when cDNA (Y1) was added to the red mixture, the solution became yellow, with fluorescence recovery presumably caused by the formation of a new "triplex" complex that formed via complexation of **PMNT 2** with the hybridized dsDNA. The biosensor has good selectivity and can distinguish one- and two-base mismatch targets clearly. The limit of fluorometric detection for DNA was 20 fM, which represents an improvement of seven orders of magnitude over the colorimetric assay. Based on the conformational change of PT, we also developed colorimetric and fluorometric strategies for the simple and sensitive detection of mercury ion, and pH-driven conformational conversion of DNA i-motif structure [38, 39].

Sim and coworkers developed a PDA liposome-based multiplex biosensor array for well-known water and food-borne pathogens detection [40]. The fabricated biosensor was able to perform the simultaneous and quantitative detection of six species of pathogens.

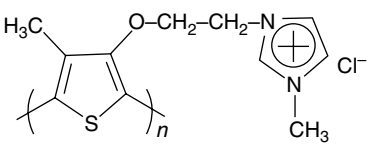

PMNT 2

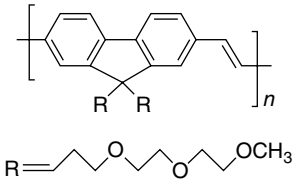

PFV

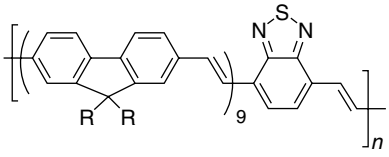

PFVBT

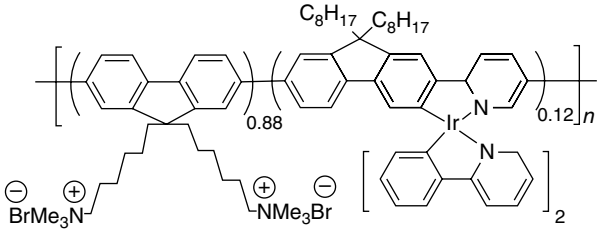

CP 7

7.2.4 Sensing Based on Aggregation of Conjugated Polymers

The fluorescence of CPs is significantly related to the aggregation of polymer chains. Xia and coworkers designed a type of bipolar probe that comprises hydrophilic DNA and hydrophobic **CP 6** unit [41]. In aqueous solution, micelles with a hydrophobic **CP 6** core and a hydrophilic DNA shell were formed. The aggregation-caused quenching (ACQ) effect suppresses the fluorescence of **CP 6**. Adding telomerase, the hydropathical profile of the bipolar probes is drastically regulated, resulting in the collapse of micelles and the liberating of fluorescent **CP 6** simultaneously (Figure 7.7a). The probe was used in both mimic systems and real urine samples (38 samples). Sensitive and specific detection of telomerase was achieved and clear classification for normal people and cancer patients was obtained. The bipolar probe can also be used for detecting Hg^{2+} ions based on signal-off mechanism by changing the aggregate state of hydrophobic parts, which is beneficial for an ACQ effect (Figure 7.7b).

Fan's group synthesized a cationic polyfluorene derivative **CP 7** containing an iridium complex ($(ppy)_2Ir(FlPy)$) as the energy acceptor [42]. The polymer shows efficient intrinsic FRET in aqueous solution due to the solubility-limitation-caused

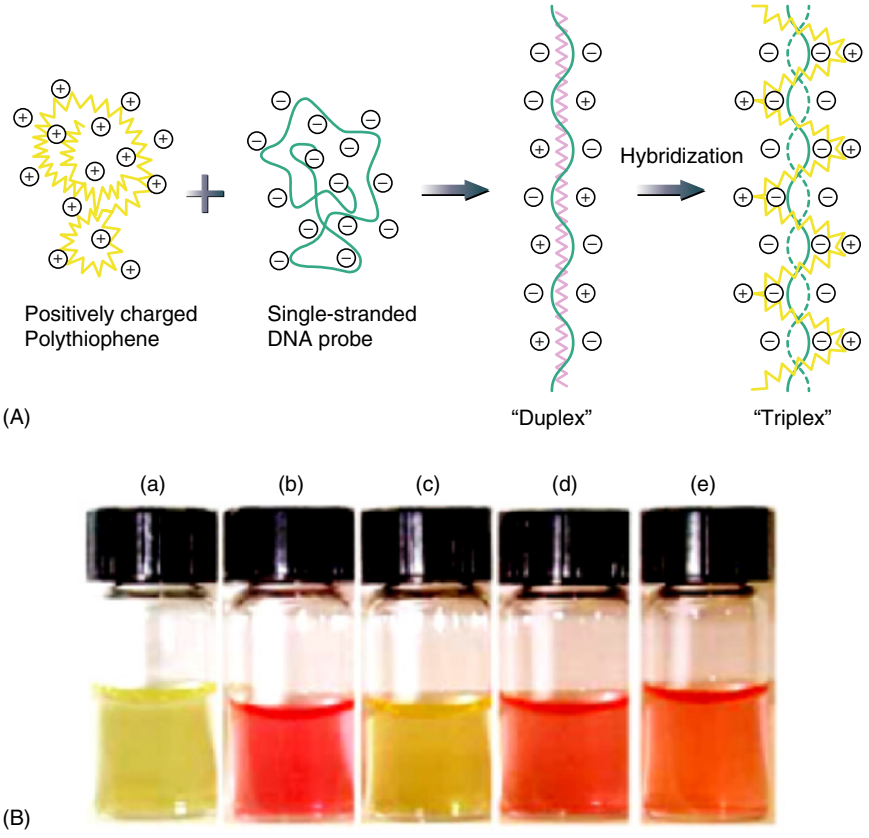

Figure 7.6 (A) Schematic description of the formation of polythiophene/single-stranded nucleic acid duplex and polythiophene/hybridized nucleic acid triplex forms. (B) Photographs of solutions of (a) polythiophene, (b) polythiophene/X1 duplex, (c) polythiophene/X1/Y1 triplex, (d) polythiophene/X1/Y2 mixture, and (e) polythiophene/X1/Y3 mixture. (Reprinted with permission from Ref. [37]. Copyright 2002, Wiley-VCH Verlag GmbH & Co. KGaA.)

polymer aggregation. Thus, at a relatively high concentration, **CP 7** emits dual-emissive red phosphorescence upon donor excitation. Investigation of the emission responses of **CP 7** toward proteins reveals a unique weakened FRET process from the main segments to the $(ppy)_2Ir(FlPy)$ units in the presence of histone instead of other proteins. With such a selective weakened FRET process, the emission color of **CP 7** solution turns from red to lilac only in the presence of histone, allowing for visual discrimination of histone. Moreover, the linearity of this weakened FRET of **CP 7** also enables effective quantification of histone with an LOD of 60 nM.

7.3 Imaging of Conjugated Polymers

Bioimaging techniques, such as magnetic resonance imaging (MRI), optical imaging, and computed tomography (CT) have been successfully utilized in clinical applications. Fluorescent CPs, with plenty of absorbance repeat units,

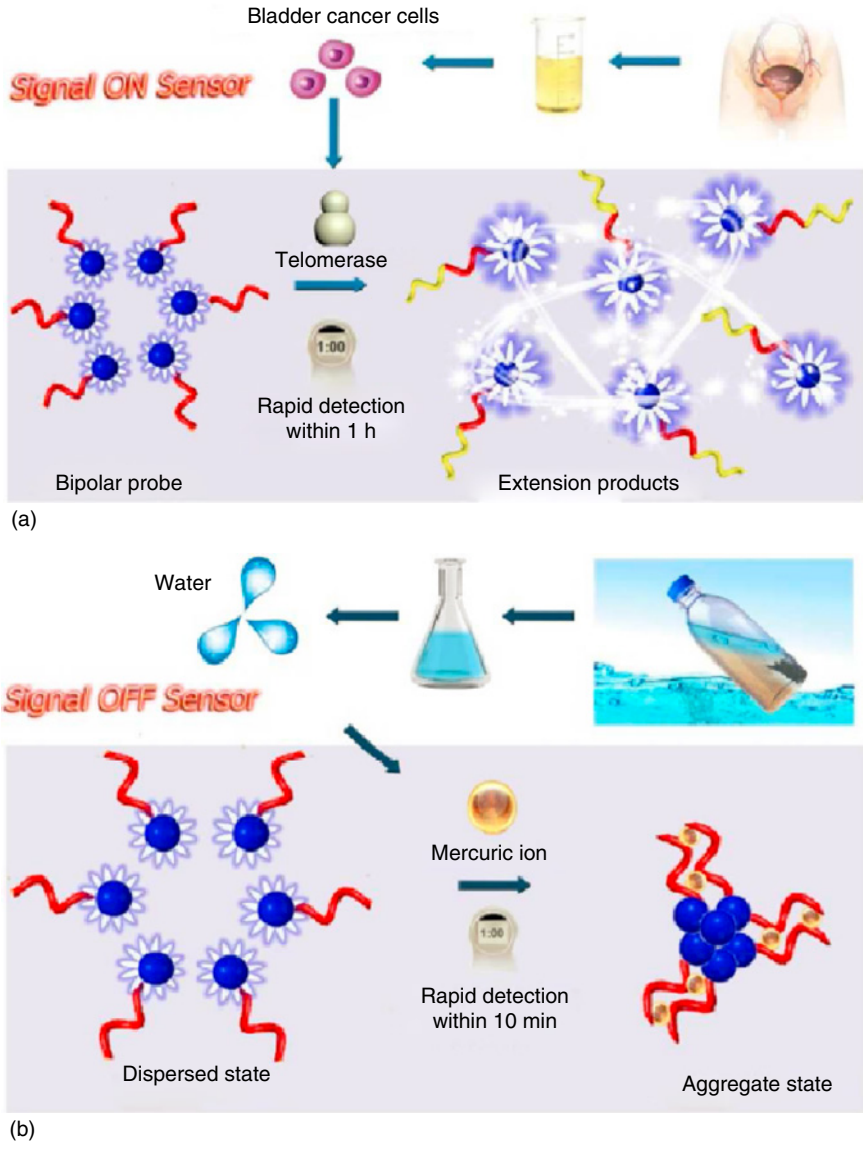

Figure 7.7 (a) Schematic illustration of telomerase activity detection using the hydrophilic/hydrophobic properties of the bipolar probes. (b) Schematic illustration of the strategy of Hg^{2+} detection by tuning the aggregate state of the bipolar probe. (Reprinted with permission from Ref. [41]. Copyright 2015, American Chemical Society.)

possess extremely strong light-harvesting ability and attract many interests in optical imaging. Recently, Liu *et al.* [43], Wang and coworkers [44], Huang and coworkers [45], Chiu and coworkers [46], and other groups reported various strategies to produce CPNs or CP dots for *in vitro* and *in vivo* imaging. These CPNs show high brightness, good photostability, and low cytotoxicity, which

make them promising candidates for new generation fluorescence imaging probes. Multimodal imaging can provide complementary information for reliable monitoring and tracking of biological objects, which now has been the subject of extensive research in the field of bioimaging.

7.3.1 Single-Modal Imaging

7.3.1.1 Fluorescence Imaging

Fluorescence-based optical imaging is indispensable for investigating the biological processes in living systems due to their high spatial and temporal resolution. CPNs can be used for nonspecific imaging via enhanced permeability and retention (EPR) effect and specific imaging by modification of CPNs. During the early period of CPNs-based fluorescence imaging, researchers mainly focused on nonspecific imaging based on the EPR effect of cancer cells. Nonspecific imaging relies on nonspecific cellular uptake of CPNs without specific targeting elements, and CPNs are mainly located in the cytoplasm. Good biocompatibility and low cytotoxicity are two basic requirements for CPNs to be used in bioimaging. Recently, various CPNs with different structures were developed to improve the biocompatibility, aggregation, brightness, and photostability. Wang and coworkers synthesized a neutral amphiphilic **PT-Boc** to improve the biocompatibility of CPNs for cell imaging [47]. The **PT-Boc** self-aggregates in water and forms spherical CPNs with an average diameter of 700 nm. The CPNs possess high photostability and low cytotoxicity for A549 cells. Cell imaging investigation revealed that the CPNs locate in the cytoplasm of A549 cells, especially in the perinuclear region.

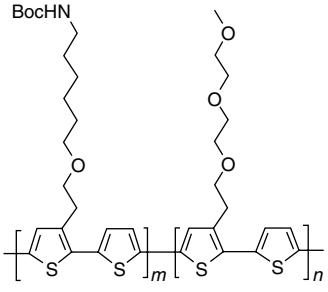

PT-Boc

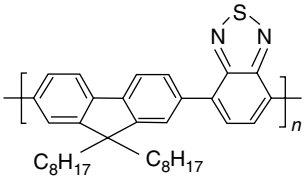

PFBT 2

DSSN+

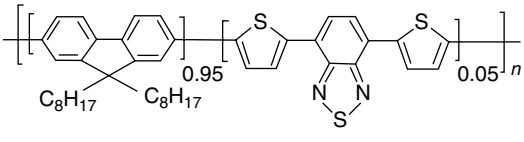

PF-DBT5

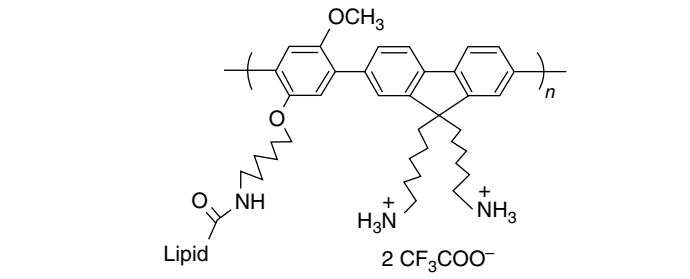

PFPL

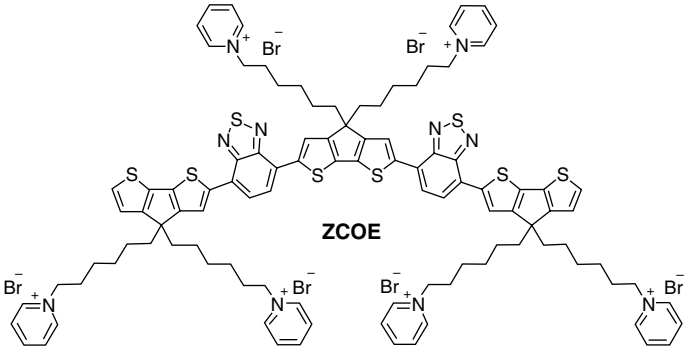

In comparison with nonspecific imaging, specific imaging requires CPNs to carry some specific recognition elements such as peptide, sugar, protein, and antibody to improve the selectivity and the bonding efficiency of CP dots. Chiu and coworkers developed a new set of CP dots with azido or alkyne groups on the surface, and further achieved the labeling of specific cellular targets by click reaction [48]. The **PFBT 2**-based CP dots exhibit high brightness, and excellent photostability in complicated biological media. CP dots with alkyne group can selectively tag MCF-7 cell by azido-bearing artificial monosaccharide (GalNAz) pathway. During the same period, lipid-modified CPN based on polyfluorene derivative (**PFPL**) was developed for cell imaging and transfection [49]. **PFPL** is amphiphilic and has two unique structural features. First, the lipid is designed as a side chain in consideration of the fact that the lipid is biocompatible and can enter the cytoplasm easily and also provides protective layers to CP backbones. Second, the ammonium pendant groups can interface with genes that offer **PFPL** as a vector for gene delivery. The **PFPL** forms uniform nanoparticles in water with a size of about 50 nm and they exhibit excellent photostability and little cytotoxicity. It can easily enter the cytoplasm via endocytosis (within 4 h) and can be used for cell imaging. **PFPL** can also deliver plasmids (pCX-EGFP) into lung cancer cells (A549) for transcription and translation. Thus, one can directly track the entrance of plasmids into cells and the expression of GFP proteins using fluorescence microscopy. Additionally, Christensen and coworkers prepared four different PEG lipid-coated CPNs with different terminal groups (biotin and carboxyl moieties) [50]. The highly stable CPNs with sizes of 21–26 nm display improved hydrophilicity, high quantum yield and good biocompatibility. In comparison to CPNs without PEG lipid end groups, CPNs with biotinylated PEG lipid can efficiently bond to streptavidin-coated glass slides. Moreover, the

specific imaging of surface receptor CD16/32 of J774A.1 cells was achieved by using biotinylated anti-CD16/32 mAb as a primary binding element and streptavidin as a sandwich bridge molecule. These results indicate that PEG lipid-functionalized CPNs can be applied in specific imaging and sensing. Recently, CPNs modified with antibody and RGD were also reported for fast, convenient, and highly sensitive live cell imaging [51, 52].

7.3.1.2 Far-Red and NIR Imaging

Far-red/near-infrared probes attract considerable research interests because they provide minimal autofluorescence, low photodamage, and high tissue penetration, which is of high importance for *in vivo* biological applications. In 2010, Kim and coworkers realized *in vivo* real-time sentinel lymph node (SLN) imaging using CPNs with a cyanovinylene backbone by intradermal injection [53]. In view of the visibility feature of near-infrared CPNs under UV light, the technique provides a visual way to precisely determine the position of two axillary SLNs. To overcome the drawback of low quantum yield of CPNs in the red/near-infrared region, Chiu and coworkers prepared CPNs composed of a high-harvesting **PFBT 2** (donor), deep-red emission **PF-DBT5** (acceptor), and functional poly(styrene-*co*-maleic anhydride) (PSMA) [46]. These CP dots with an average diameter of 15 nm exhibit large absorptivity ($3.0 \times 10^7\,cm^{-1}\,M^{-1}$ at 488 nm) and high quantum yield (0.56 in water) and maximal emission at 650 nm due to the efficient intraparticle energy transfer in the polymer blend. After covalently linking with neuroectodermal tumor-targeted ligand chlorotoxin (CTX) and PEG, the CTX-CPNs can specifically target and accumulate in the ND2:SmoA1 site after injection for both symptomatic ND2:SmoA1 and wild type. Histological analysis shows that PBdot-CTX can better target the cerebellum of SND:SmoA1 mice than that of wild-type mouse. However, there is no obvious difference for PBdot-CTX (with targeted element) and PBdot-PEG (without targeted element) in SND:SmoA1 mice. The biodistribution profile of CTX-CP dots after 72 h post injection shows remarkable uptake in the liver, uptake also occurs in other organs (such as the spleen).

Bazan's group synthesized two NIR-emitting conjugated oligoelectrolytes, **DSSN+** and **ZCOE** [54, 55]. **DSSN+** contains four long-axis-terminating pendant ionic groups, which mimic the distribution of hydrophilic and hydrophobic components of a lipid bilayer, whereas **ZCOE** contains six evenly distributed pendant ionic groups across its π-conjugated backbone, making it more hydrophilic and less likely to persist in a hydrophobic lipid environment. The λ_{em} values of **DSSN+** exhibit a ~118 nm hypsochromic shift as the solvent is shifted from polar (λ_{em} is 594 nm in water) to nonpolar (λ_{em} is 476 nm in toluene). The photoluminescence spectra of **ZCOE** exhibits a weak, broad, and featureless emission band stretching from ~650 to 1000 nm. The emission maximum exhibits a 36 nm hypsochromic shift as solvent polarity decreases from chloroform (758 nm) to toluene (722 nm) and is accompanied by an increase in quantum yield from ~3% to ~5%. Imaging investigation demonstrated that **DSSN+** accumulated in the lipid membranes of cells (Figure 7.8a). **ZCOE** exhibits diffuse staining of *E. coli* cells, whereas it displays internal staining of select yeast cells which also show propidium iodide staining, indicating **ZCOE** is a "dead" stain for this organism. Staining of mammalian cells (COS-1 cells) reveals complete internalization of **ZCOE** through endocytosis, as supported by co-localization with LysoTracker and late endosome markers (Figure 7.8b).

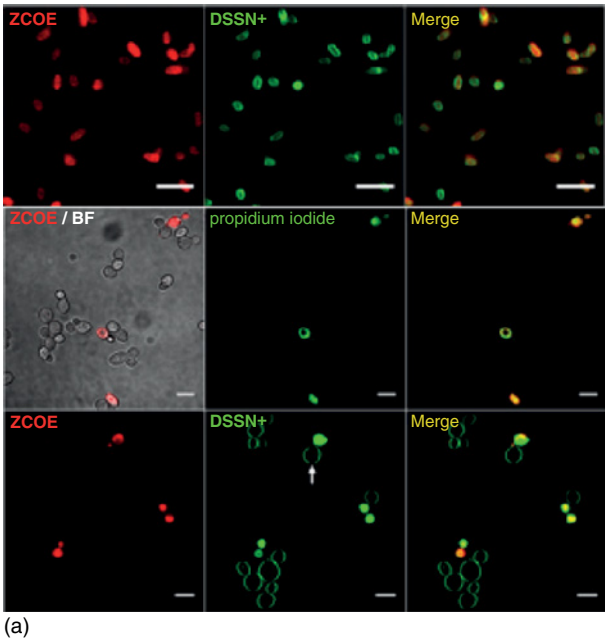

(a)

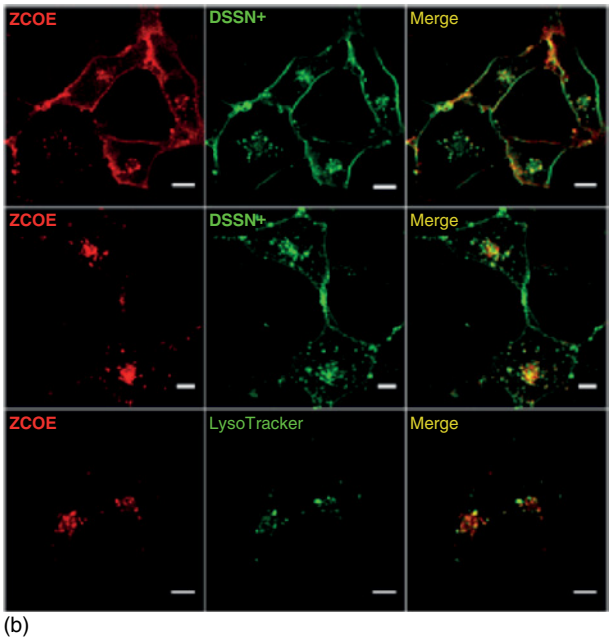

(b)

Figure 7.8 (a) First row: single-plane confocal micrograph of *E. coli* cells stained with ZCOE and DSSN+. Scale bars are 5 µm. Second and third row: two single-plane confocal and bright-field (BF) micrographs of yeast cells stained with ZCOE, propidium iodide, and DSSN+. Arrow indicates axial attenuated emission from DSSN+ when illuminated by the polarized light. Four scale bars are 10 µm. (b) Single-plane confocal micrographs of COS-1 cells stained with ZCOE (Top). Dual stain with DSSN+ imaged soon after staining and after ~12 h (middle). Dual stain with LysoTracker Green applied 12 h after ZCOE (bottom). Scale bars are 10 µm. (Reprinted with permission from Ref. [54]. Copyright 2014, American Chemical Society.)

More recently, Yang and coworkers synthesized three types of new NIR fluorescent conjugated oligoelectrolytes (**Q-FlTBTTFl**, **Q-FlBBTFl**, and **Q-FlTBBTTFl**) with quaternized ammonium ionic groups in their side chains for water solubility [56]. The emission wavelength is modulated in the range of 600–1300 nm, by adjusting the intramolecular charge transfer. The conjugated oligoelectrolytes show remarkably larger Stokes shifts (147–276 nm) compared to commercial rhodamine and cyanine dyes in water, avoiding self-quenching and interference from the excitation backscattered light. The photoluminescence QY was improved substantially by up to 27.8% in water. In vitro and in vivo images of a mouse xenograft model treated with the **Q-FlBBTFl**/vesicular exhibit a substantially stronger fluorescence signal at the tumor site than at the other organs, illustrating the potential as an NIR fluorescent imaging agent for the diagnosis of cancer.

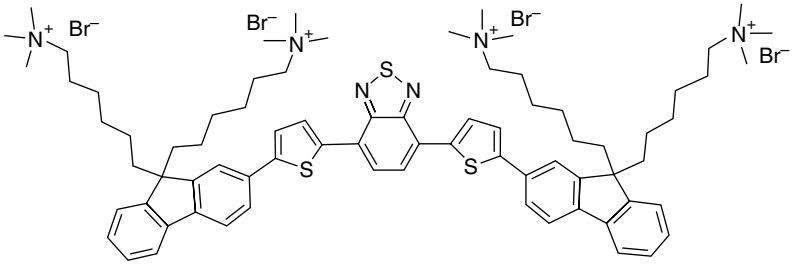

Q-FlTBTTFl

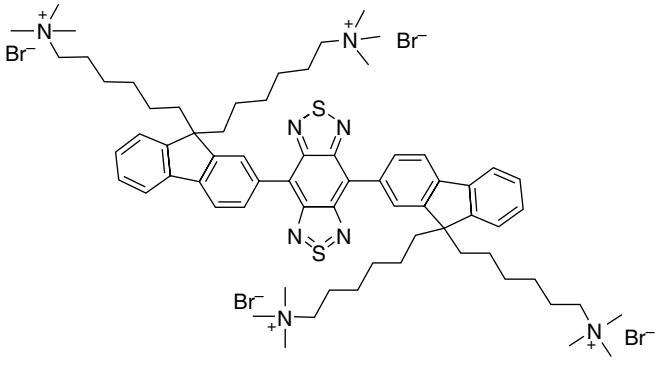

Q-FlBBTFl

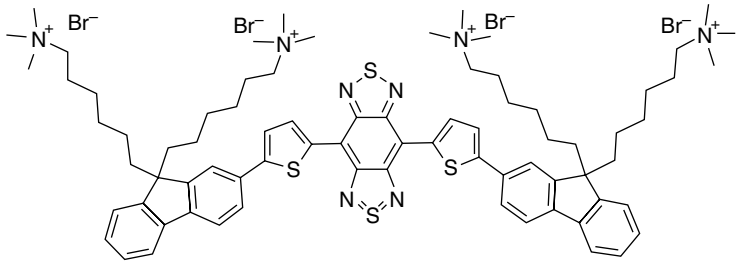

Q-FlTBBTTFl

As a recent development, fluorescence imaging in the second near-infrared window (NIR-II, 1000–1700 nm) has attracted great interest due to reduced photon scattering of long-wavelength photons, deeper tissue penetration, and high spatial resolution. Dai and coworkers reported traumatic brain injury imaging in the second near-infrared window with a molecular fluorophore [57] (Figure 7.9). The fluorophore **IR-E1** with bright emission in the NIR-II window in aqueous solution was synthesized by molecular engineering approaches. The QY of **IR-E1** was ≈0.7% under 808 nm excitation, which was twofold of carbon nanotubes (CNTs). High magnification NIR-II dynamic imaging demonstrated that in the injured region, the blood perfusion front moved in an ultraslow manner at a speed of ≈0.002 mm s^{-1}. The authors also observed blood perfusion into single vessels (Figure 7.9f–i). Perfusion into a vessel at ≈25–30 min post injection of the NIR-II dye was observed (Figure 7.9f–h and red arrows), which was a remarkably long time for blood circulation to reach the vessel. The speed of the blood flow in the single vessel was measured to be as low as ≈0.02 mm s^{-1}. This pathology brain imaging could be used as a biomarker in drug trials or the clinic and as a target for therapeutic invention.

7.3.1.3 Two-Photon Imaging

Two-photon fluorescence imaging (2PFI) has recently attracted great research interest as a noninvasive technique to investigate complex biological issues. As 2PFI is usually excited by near-infrared lasers (700–1000 nm), it shows obvious advantages in deeper penetration depth, lower autofluorescence, less scattering, and reduced phototoxicity as compared with conventional one-photon excited technique. Moon's group reported on CPNs' superior 2P characteristics and 2P imaging of endothelial cells in a model tissue culture system [58]. They synthesized CPNs with very small size (8 nm) and extremely large 2P cross-sections (1000 and 11 000 GM with a maximum at about 730 nm) and excellent photostability. These cross-sections are at least 2–3 orders of magnitude higher than conventional organic fluorophores. The hydrophilicity and nontoxicity of CPNs allow for long-term monitoring of angiogenesis by endothelial cells in a tissue model. Schanze's group reported $PPESO_3$-coated silica nanoparticles (300 nm) for two-photon excited fluorescence cell imaging [59]. They demonstrated that two-photon fluorescence imaging shows improved resolution compared to one-photon microscopy. It is possible to detect the emission from individual $PPESO_3$-coated nanoparticles in the 2PFI. The particles appear to be preferentially localized in endosomes in the cytosolic region of the cell.

Recently, to improve the QY as well as 2P action cross-section of CPNs, Liu's group developed micelle/silica coprotected CPNs for two-photon excited brain vascular imaging [60] (Figure 7.10). The **PFBT 3** loaded nanoparticles (PFBT-F127-SiO_2 NPs) showed a 2P absorption cross-section of 1085 GM at 810 nm based on polymer chain concentration and an emission maximum at 545 nm with a high fluorescence QY of 75%. The fluorescence lifetime investigation reveals that the high fluorescence QY is mainly due to reduced polymer aggregation and minimized environment influence on the fluorescence of CP. The synthesized **PFBT 3** NPs show good colloid stability and photostability as well as benign biocompatibility, which was further applied to visualize the mouse brain

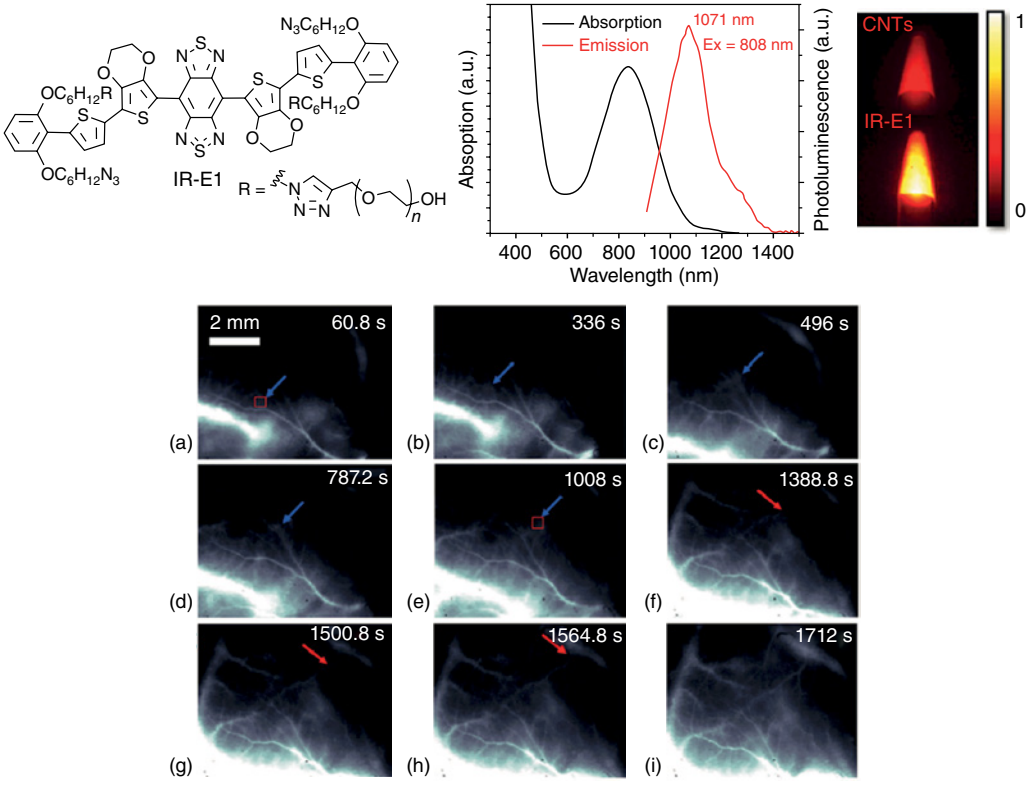

Figure 7.9 Molecular structure, UV–vis absorption and fluorescence emission spectra of IR-E1 (upper left two figures). Fluorescence imaging of a typical Hipco CNT and IR-E1 (upper right figure). NIR-II dynamic imaging of hypoperfusion in a TBI mouse at single-vessel resolution. (a–f) Video rate dynamic image frames recorded in the injured region of a TBI mouse (2 h after TBI) in the hypoperfusion phase with 300 ms exposure time in the NIR-II window (>1300 nm) after intravenous injection of IR-E1 (10 mg kg^{-1}), showing ultraslow blood perfusion from the transverse sinus region (bright lower-left region) into the injured region. Blue arrow points to the perfusion front over which the signal traveled. (f–h) A single vessel was observed to be perfused over ≈2.9 min. Red arrows point to the blood flow in front of the vessel. (Reprinted with permission from Ref. [57]. Copyright 2016, Wiley-VCH Verlag GmbH & Co. KGaA.)

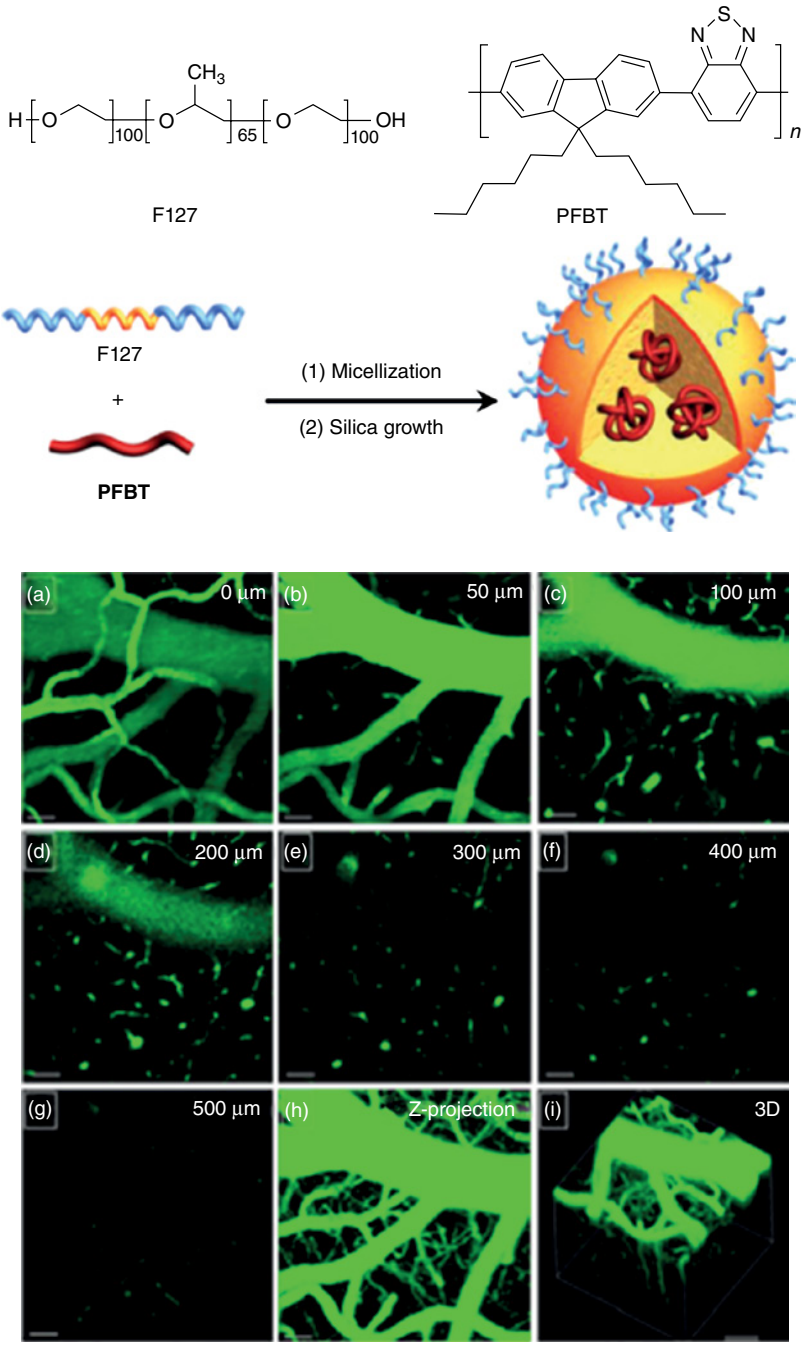

Figure 7.10 Chemical structures of F127 and PFBT, schematic illustration of the fabrication of PFBT-F127-SiO_2 NPs, and intravital TPFI of PFBT-F127-SiO_2 NPs stained blood vessels of mice brain at depth of 0 μm (a), 50 μm (b), 100 μm (c), 200 μm (d), 300 μm (e), 400 μm (f), and 500 μm (g), and the respective Z-projected image (h) as well as 3D image (i). All the images share the same scale bar of 50 μm. (Reprinted with permission from Ref. [60]. Copyright 2014, American Chemical Society.)

vasculature through intravital two-photon excited brain vascular imaging with high contrast. The major blood vessels as well as the smaller capillaries in the pia mater could be visualized with the help of PFBT-F127-SiO_2 NPs. In addition, no obvious aggregates were observed in brain blood vessels, owing to the poly(ethylene oxide) segments on the surface of NPs blocking nonspecific binding. More importantly, microvasculature deep in the brain that lies beyond the pia matter (500 μm) could still be detected with high resolution (Figure 7.10g). As a control, no fluorescence was detected from the brain blood vessels before PFBT-F127-SiO_2 NPs were administered. The Z-projected (Figure 7.10h) and 3D reconstruction (Figure 7.10i) images illustrate that the probe can efficiently label the blood vasculature under *in vivo* conditions.

7.3.1.4 Multicolor Imaging

Multicolor imaging makes it possible for more than one target to be visualized simultaneously in the same cell, thus allowing several events to be captured in a single snapshot with reduced amount of reagents, consumables, and samples. Recently, development of multiplex imaging has become more and more important in cell counting, cell sorting, and clinical diagnostics. Early in 2008, McNeill and coworkers reported a variety of highly fluorescent CPNs (**PFO**, **PPE**, **PFPV**, **PFBT**, **MEHPPV**) for fluorescence imaging in live cells [61] (Figure 7.11). These nanoparticles exhibit small particle diameters, extraordinary fluorescence brightness, and excellent photostability. The absorption bands of these CPNs ranging from 350 to 550 nm, depending on the polymer. Analysis of the UV–vis absorption spectra at a known particle concentration indicated that the peak absorption cross-section of single particles (~15 nm diameter) was on the order of $\sim 10^{-13}\,cm^2$. The fluorescence spectra are shown in Figure 7.11a and the quantum yields range from a few percent to as high as 40%, depending on the polymer. Single particle fluorescence imaging and kinetic studies indicate much higher emission rates ($\sim 10^8\,s^{-1}$) and little or no blinking of the nanoparticles as compared to results for single dye molecules and quantum dots. Analysis of single particle photobleaching trajectories reveals excellent photostability — as many as 10^9 or more photons emitted per nanoparticle prior to irreversible photobleaching. Fluorescence decay kinetics demonstrated that the lifetime of PFPV and MEHPPV dots were determined to be ~130 ps, while β-phase PFO and PFBT dots showed longer lifetimes around ~270 and ~600 ps, respectively. PPE dots display complex fluorescence decay kinetics, the 440 nm emission peak shows a single exponential decay with time constant of 242 ps, while the 480 nm emission exhibits a biexponential decay with time constants of 276 ps and 1.56 ns. The fluorescence images clearly indicate internalization of the CP dots by the cells, and show perinuclear labeling and brightly fluorescent vacuoles and organelles (e.g., pinosomes and lysosomes) (Figure 7.11b). More diffuse nanoparticle fluorescence was observed in the cytoplasm, possibly indicating that some of the CPNs crossed cell membranes. Nanoparticle uptake via endocytosis was observed in live macrophage cells.

Electrostatic interactions and hydrophobic interaction between charged CPs and oppositely charged biomolecules are important factors to be considered for the fabrication of multifunctional nanoparticles. Wang and coworkers reported

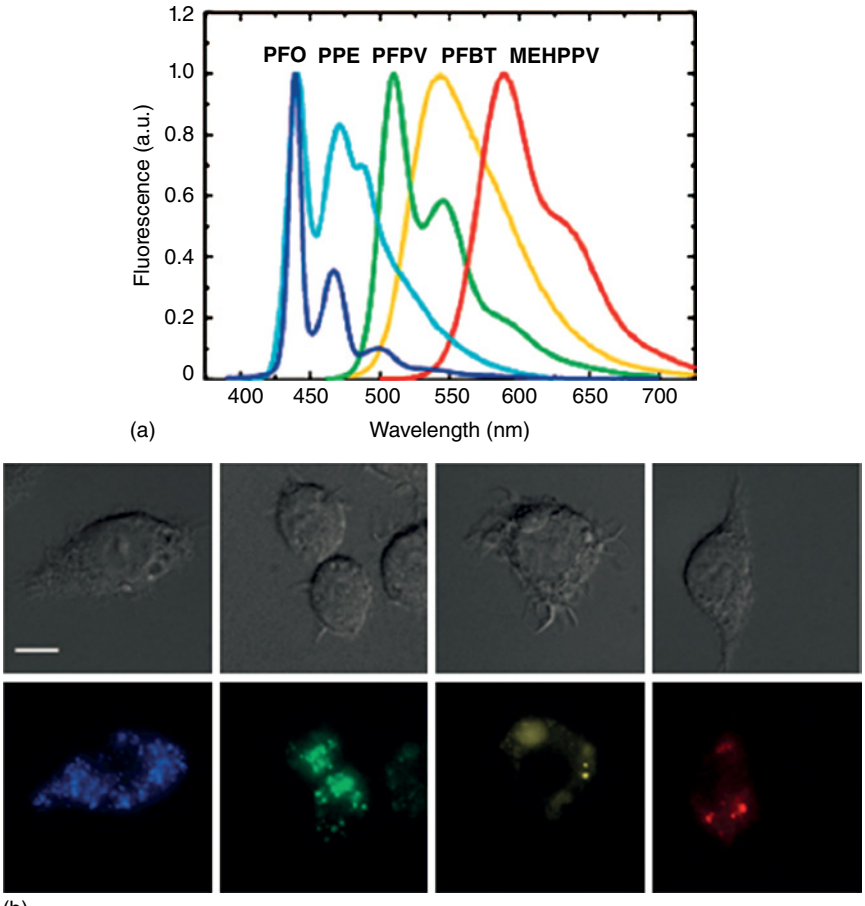

Figure 7.11 (a) Fluorescence spectra of various conjugated polymer dots. (b) Differential interference contrast (DIC) images (top), and fluorescence images (bottom) of macrophage cells labeled with PPE, PFPV, PFBT, and MEHPPV dots, respectively. The scale bar is 10 µm. (Reprinted with permission from Ref. [61]. Copyright 2008, American Chemical Society.)

multispectral microparticles formed by bacteria-mediated assemblies of CPN for cell imaging and barcoding [44] (Figure 7.12). The bacteria-CPN microparticles exhibit multicolor emissions by tuning FRET efficiencies among CPNs under single excitation wavelength. Large Stokes shifts up to 170 nm were observed for these microparticles. As is known, the biological membrane of an *E. coli* cell is mainly composed of lipid and protein. Thus, the amphiphilic CPs can bind to the outer surface membrane of *E. coli* through electrostatic attraction and hydrophobic interaction, which kept three polymers in close proximity to allow efficient intermolecular FRET. The blue-emitting **P1** acts as the donor for green-emitting **P2** and red-emitting **P4**, green-emitting **P2** acts as the acceptor for blue-emitting polymer and the donor for red-emitting polymer, while red-emitting **P4** acts as the acceptor for green-emitting and red-emitting polymers. Therefore, intermolecular multistep FRET occurs in *E. coli*-polymer

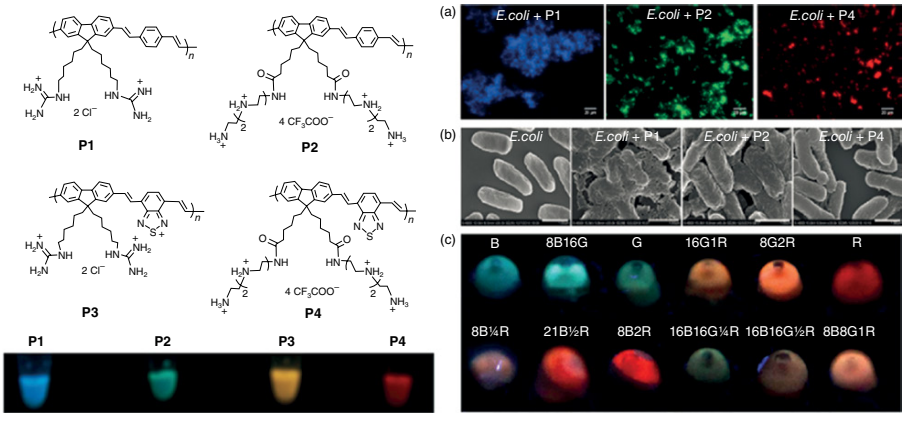

Figure 7.12 Chemical structures and the emission colors of **P1**, **P2**, **P3**, and **P4**. (a) Fluorescence microscope images of *E. coli*-CPN microparticles. The excitation wavelength is 380/30 nm for **P1**, 455/70 nm for **P2**, and 540/40 nm for **P4**. The scale bar is 20 µm. (b) SEM images of *E. coli* and *E. coli*-CPN microparticles. The scale bar is 1.0 µm. (c) Various color-barcoded microparticles by mixing the *E. coli* and the CPNs. The image was taken under 365 nm UV light. (Reprinted with permission from Ref. [44]. Copyright 2012, Wiley-VCH Verlag GmbH & Co KGaA.)

microparticles upon the excitation of the blue-emitting polymer **P1** with a short excitation wavelength. For **P1**, the absorption maximum is at 371 nm, and the emission displays a maximum peak at 472 nm with a QY of 21%. The maximum absorption of **P2** is 380 nm, and emission maximum is 475 nm with a QY of 10%. The maximum absorption is 425 nm for **P3** and 475 nm for **P4**, and emission maximum is 589 nm for **P3** and 625 nm for **P4**. Through regulating the proportions of **P1**, **P2**, and **P4** on *E. coli* cells, various color-barcoded microparticles can be obtained. Owing to the low cytotoxicity and tunable emission color, these CPNs/*E. coli* microparticles are successfully employed for cell imaging and optical barcoding.

Fan's group constructed a multicolor fluorescence probe by encapsulating rare-earth ion-doped upconversion nanoparticles (UCNPs) with grafted CP brushes [62]. A concept of dual-upconversion was proposed in this study. Taking advantage of the structure and optical properties of a polyfluorene derivative (PFNBr), the authors integrated the UCNPs with PFNBr via van der Waals interactions to acquire excellent water solubility, stability, and dual-upconversion. The absorption maximum of PFNBr encapsulated on the surface of $NaYF_4$:Yb–Er in aqueous solution was observed to be slightly blue shifted and the absorption profile was broadened. However, after encapsulation, the intensity ratio of the red and green emission peaks increased from 0.577 for pure $NaYF_4$:Yb–Er to 0.889 for $NaYF_4$:Yb–Er@PFNBr. The $NaYF_4$:Yb–Er@PFNBr exhibits multicolor fluorescence when NIR excitation is adjusted to different wavelengths. The $NaYF_4$:Yb–Er@PFNBr is highly resistant to photobleaching because the photoluminscence intensity remains almost unchanged under 30 min of continuous wavelength NIR irradiation. According to the images from the green channel (500–560 nm) and red channel (630–680 nm), the $NaYF_4$:Yb–Er@PFNBr nanocomposites were efficiently internalized into HepG-2 cells rather than merely staining the membrane surface.

Recently, peptide or antibody was conjugated on the CPNs to realize targeted imaging for several kinds of cells simultaneously. Liu's group reported a general approach to prepare CP dots embedded silica nanoparticles (SiO_2@CP@SiO_2) for targeted HER2-positive cellular imaging [63]. Four CPs (**PFP**, **PFVP**, **PFBT**, **PFBTDBT**) are employed to demonstrate the versatility of the developed strategy, yielding fluorescent silica NPs with emission across the visible spectra range (Figure 7.13). Field emission transmission electron microscopy investigation reveals that the entanglement between hydrophobic CPs and the aminopropyl groups of 3-aminopropyl triethoxysilane contributes to the successful encapsulation of CPs into a silica matrix. The synthesized NPs exhibit excellent physical stability and good photostability. The amine groups on surfaces benefit from further conjugation for biological applications. Through reaction with a peptide (GGHAHFG) that is specific to the HER2 receptor, the synthesized NPs were successfully applied for targeted cellular imaging of HER2-overexpressed SKBR-3 breast cancer cells.

Wang's group reported multicolor CPNs bioconjugated with antibodies for targeted cell imaging and specific cell detection [64] (Figure 7.14). CPNs with an average diameter of ~30 nm exhibit good photostability, low cytotoxicity, and phototoxicity. Compared with primary antibody-modified CPNs, amplified

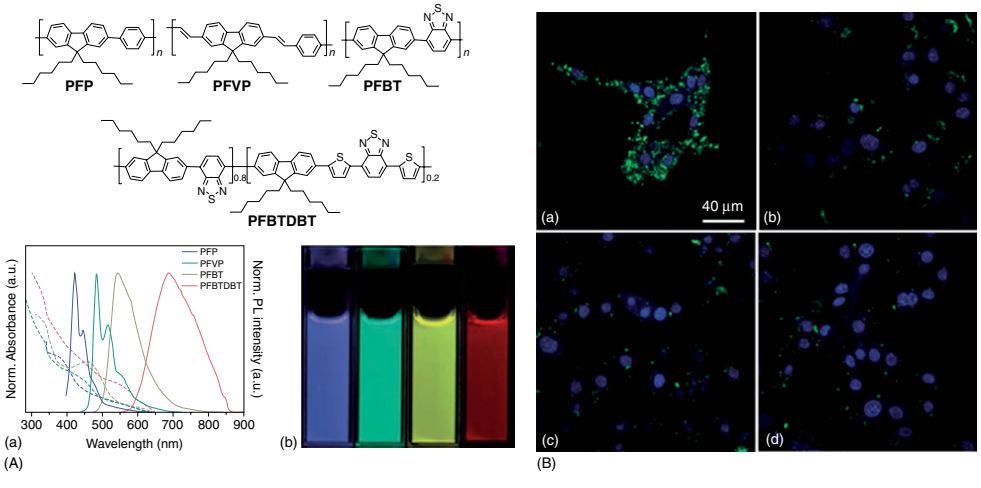

Figure 7.13 (A) Chemical structures, normalized UV–vis absorption (dashed line) and PL spectra (solid line), and photographs under a hand-held UV lamp (excited at 365 nm) of SiO_2@CP@SiO_2 NPs. (B) Confocal fluorescence images of SKBR-3 breast cancer cells (a and b) and NIH/3T3 fibroblast cells (c and d) after 2 h incubation with SiO_2@PFBT@SiO_2-Pep (a and c) and SiO_2@PFBT@SiO_2-COOH (b and d) NP suspensions at 100 mg ml^{-1} NPs at 37 °C. All images have the same scale bar of 40 μm. (Reprinted with permission from Ref. [63]. Copyright 2013, Royal Society of Chemistry.)

imaging signal to target tumor cells is realized through the second antibody strategy. The emission spectra maxima for P1, P2, P3, and P4 are 422, 500, 540, and 670 nm, respectively. Emission QYs vary depending on the electron acceptor unit in the polymer backbones (3–78%). Upon excitation at 360 nm, the shorter wavelength-emissive polymers were anticipated to act as the donor for longer wavelength-emissive ones (acceptors), through interchain multistep FRET process. Thus, by varying the mixing ratio of the polymers, multicolor emission can be regulated through FRET among the four polymers under one excitation wavelength. CPNs with carboxyl groups on the surface were prepared by a modified coprecipitation method based on hydrophobic interactions of CPs and PSMA. The surface carboxyl groups can then be modified with antibodies (Figure 7.14a). For these CPNs, CPs P1–P4 are the light-emitting vectors with tunable emission colors from blue to red; and PSMA acts as a coating and a source of carboxyl functionalities. To amplify the imaging signal for tumor cells, a second antibody (IgG) strategy was used by modifying CPNs with IgG. Compared with P3/PSMA/anti-EpCAM CPNs, the imaging signal for MCF-7 cells was observed to be significantly enhanced through the second antibody strategy (Figure 7.14b).

Furthermore, Huang's group reported a series of CPNs with tunable photoluminescence colors. Carboxylate groups on the side chain were covalently conjugated with specific molecules such as streptavidin (SA), IgG, and poly(ethylene glycol) [65]. The resultant PPVseg–SA CPNs show efficient labeling ability in specific cellular imaging. Stevens's group developed a strategy to modulate cellular uptake of CPNs using modular amphiphilic peptide capping ligands [66]. More recently, Wang and coworkers designed a membrane probe based on a water-soluble polyfluorene (PF-DBT-BIMEG) [67]. The probe shows a strong affinity toward lipid membranes owing to the high charge density from abundant imidazolium moieties together with moderate rigidity and hydrophobicity derived from the conjugated backbone. Upon binding with a membrane, the interchain FRET of the probe was substantially enhanced, which resulted in the emission of both blue and red fluorescence. This is favorable for dual-color imaging.

7.3.2 MultiModal Imaging

7.3.2.1 MRI/Fluorescence Imaging

MRI is a noninvasive method for tumor detection that offers high physiological and anatomical resolution. However, the detection sensitivity of MRI is relatively low. The combination of MRI and optical imaging modalities provide possibilities to overcome this drawback due to the high sensitivity of fluorescence imaging. Superparamagnetic iron oxide nanocrystals and Gd^{3+} are always encapsulated in the core of nanocomposites for magnetic manipulation and MR imaging. In 2012, Liu and coworkers reported a CP and iron oxide-based nanoparticles (FMCPNPs) for *in vivo* FR/NIR fluorescence and MRI [68] (Figure 7.15). PFVBT was designed and synthesized as the fluorescent polymer. The iron oxide nanoparticles in the core provided T_2-weighted MRI, whereas the amphiphilic oligomers on the surface of the nanoparticles introduced good water solubility, biocompatibility, and cancer-targeting. The lipid coated on iron oxides can effectively separate the CP

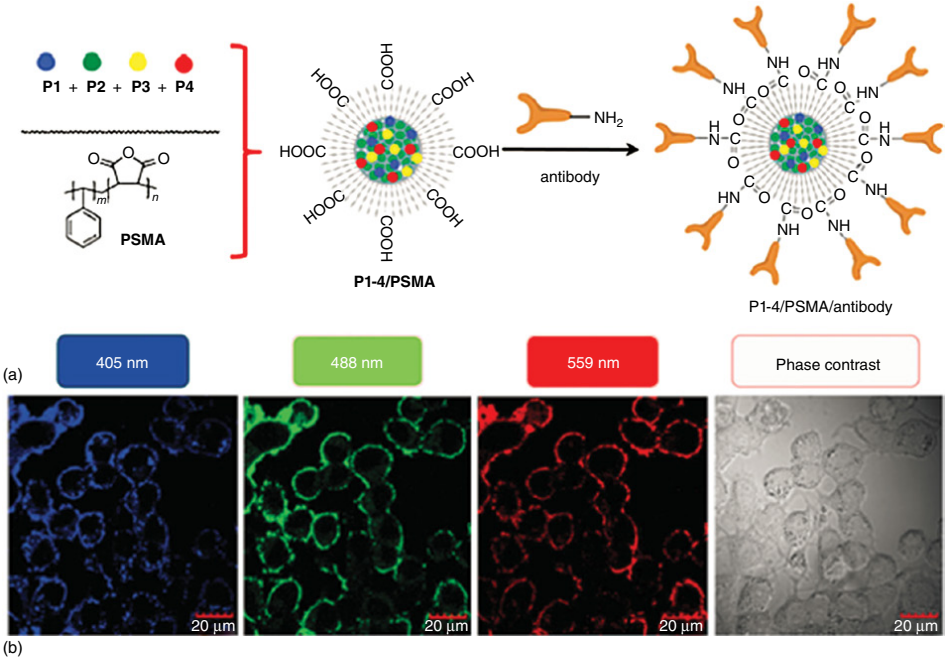

Figure 7.14 (a) The preparation of multicolor CPNs (P1–4/PSMA) and their modification with an antibody. (b) Multichannel fluorescence images of MCF-7 cells with P1–4/PSMA/anti-EpCAM CPNs. The excitation wavelengths are 405 nm, 488 nm, and 559 nm. (Reprinted with permission from Ref. [64]. Copyright 2014, Wiley-VCH Verlag GmbH & Co. KGaA.)

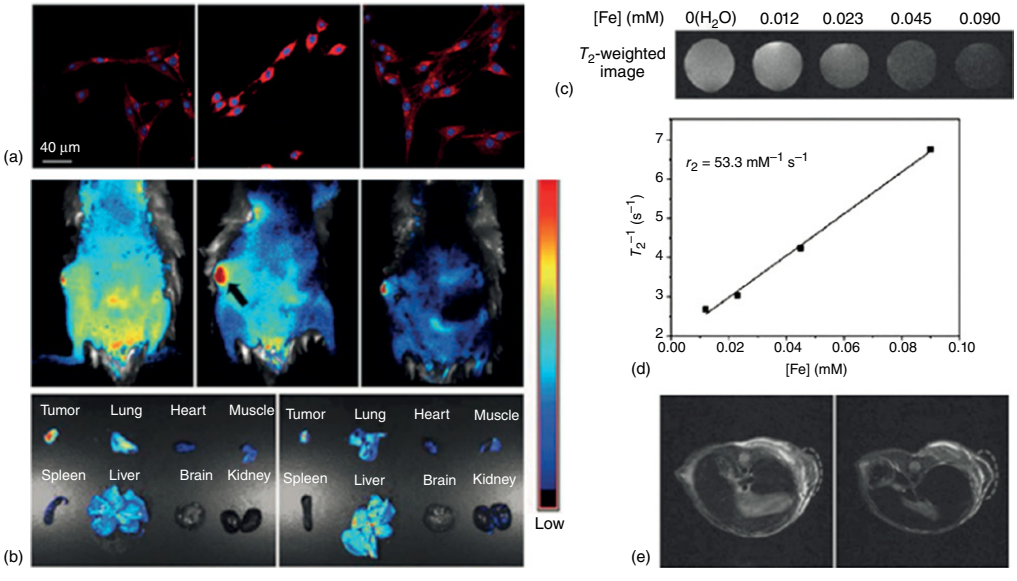

Figure 7.15 (a) Confocal images of the MCF-7 breast cancer cells after 4 h incubation with the MCPNP (left), FMCPNP (middle), and free folic acid-pretreated MCF-7 breast cancer cells after 4 h incubation with 0.25 mg ml^{-1} of FMCPNPs (right). The nuclei were stained by DAPI. (b) *In vivo* fluorescence images of mouse injected with FMCPNPs acquired at 1, 6, and 18 h post injection (upper). Fluorescence images of various organs from the mice treated with FMCPNPs (left) and MCPNPs (right), respectively, at 12 h post injection. (c) T_2-weighted MR images of FMCPNPs in water. (d) T_2 relaxivity plot of aqueous suspension of FMCPNPs. (e) Representative *in vivo* MR images of mouse pre injection (left) and post injection with FMCPNPs for 5 h (right). (Reprinted with permission from Ref. [68]. Copyright 2012, Wiley-VCH Verlag GmbH & Co. KGaA.)

from iron oxides to minimize fluorescence quenching. *In vivo* fluorescence imaging illustrated that although the FMCPNPs are widely dispersed among the whole body of mouse at 1 h post injection, they have a tendency to be enriched in the tumor tissue over time due to folate receptor-mediated active targeting effect (Figure 7.15b). The fluorescence intensity at the tumor site at 6 h post injection is ~1.9 times of that at 1 h post injection. Some intense red fluorescent spots are clearly observed in the tumor slice, verifying the prominent uptake of FMCPNPs in the tumor. T_2-weighted MRI shows that signal intensity decreases with increased concentration of FMCPNPs, indicating that the NPs can shorten the spin–spin relaxation time (Figure 7.15d). *In vitro* studies reveal that these dual-modal NPs can serve as an effective probe to achieve targeted imaging of MCF-7 breast cancer cells without obvious cytotoxicity. *In vivo* MRI demonstrated that an obvious drop in the MR signal is observed at the tumor site at 5 h post injection, indicating the prominent tumor uptake of NPs, which is in good accordance with the fluorescence imaging study (Figure 7.15e).

Fan's group also fabricated a MRI/fluorescence imaging probe (MNPs@PFPANa) by conjugating an anionic grafted conjugated polyelectrolyte (PFPAA) on the surface of Fe_3O_4 nanoparticles through ligand exchange with oleic acid [69]. These nanoparticles with a mean hydrodynamic diameter of ~26 nm showed good water solubility and stability, with no precipitation observed in eight months. In addition, these nanoparticles exhibited superparamagnetic properties with a saturation magnetization (Ms) of 20 emu g^{-1}, which is sufficient for bioapplications. Upon incubation with macrophage cells for 48 h, the nanoparticles showed good biocompatibility and low toxicity. Confocal microscopy results revealed that MNPs@PFPANa can be retained in cytoplasm with high fluorescence. Furthermore, they reported folate receptor-targeted multifunctional fluorescent magnetic nanoparticles (FMNPs) composed of cores containing iron oxide nanocrystals and amphiphilic oligo(*p*-phenyleneethynylene) (OPE) shells with multimodal imaging capability [45]. The 2P action cross-section of OPE–PEG–FA was calculated to 2362 GM in methanol with laser excitation at 720 nm. Two-photo imaging demonstrated that the MNPs@OPE-PEG-FA were preferentially targeted to the cancer cells and can be perfectly internalized into the cytoplasm rather than adhered to the cell membrane due to folate receptor-mediated endocytosis. The targeted dual-mode imaging of cancer cells was further performed *in vivo* using an animal tumor model. Compared with the images before MNPs injection, an obvious decrease of signal intensity can be detected 4 h after injection using both MNPs@OPE–PEG-NH_2 and MNPs@OPE–PEG–FA. In addition, the MRI T_2 signals of the tumor area displayed significant negative enhancement when MNPs@OPE–PEG–FA were applied.

Gadolinium ion (Gd^{3+})-containing material is another common agent for MRI. Liu's group synthesized a Gd^{3+}-chelated hyperbranched conjugated polyelectrolyte (HCPE-Gd) nanospheres with an average diameter of ~42 nm [70] (Figure 7.16). Owing to the presence of PEG spacer, the chelation of Gd^{3+} ions showed negligible effects to the optical properties of HCPE, and a QY of 10% in aqueous solution was obtained. The relaxivity (R_1), referred to $1/T_1$ per unit concentration of agent, was compared between HCPE–Gd and clinically used MR agent

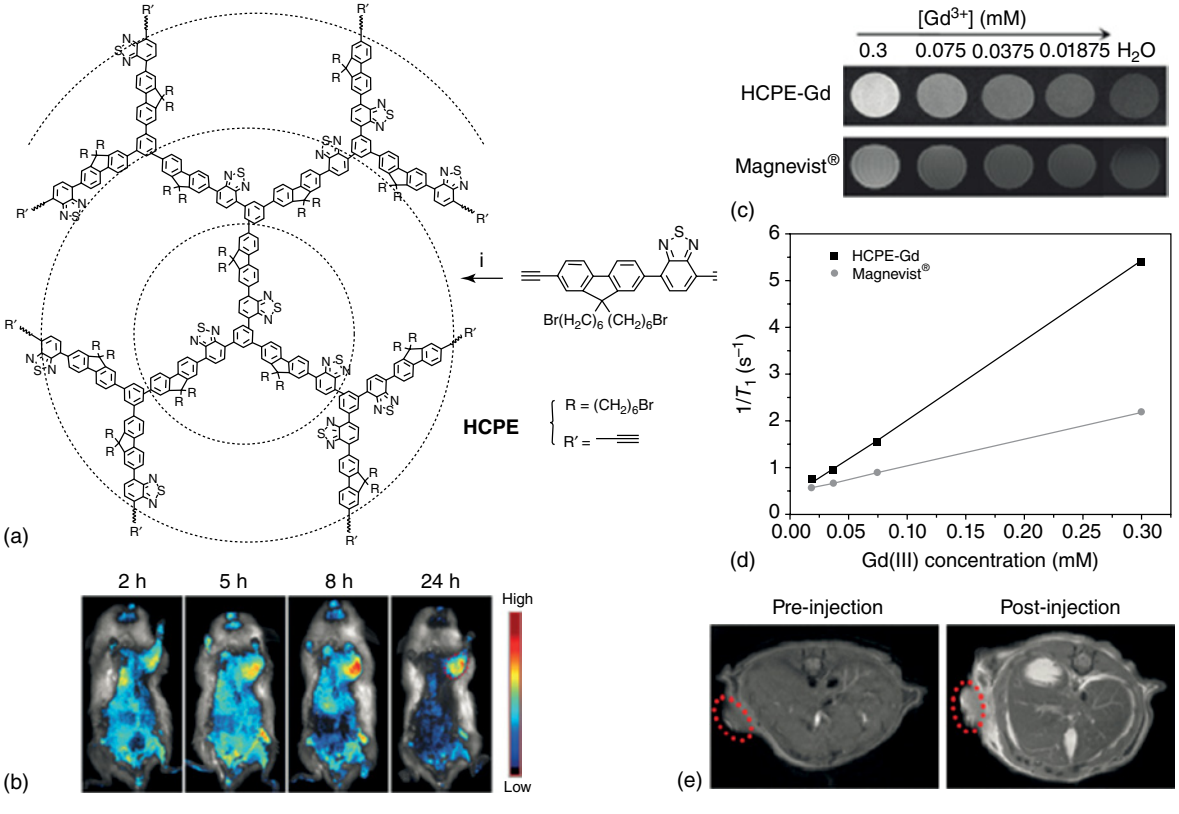

Figure 7.16 (a) Chemical structure of HCPE. (b) *In vivo* noninvasive fluorescence imaging of H_{22} tumor-bearing mice after intravenous injection of HCPE-Gd. (c) T_1-weighted MR images of HCPE–Gd and Magnevist at various concentrations of Gd(III). (d) Water proton longitudinal relaxation rate ($1/T_1$) of HCPE–Gd and Magnevist as a function of Gd(III) concentration. (e) T_1-weighted MR images of H_{22} tumor-bearing mice after intravenous injection of HCPE-Gd at 0 and 6 h post injection. The red circles indicate the tumor site. (Reprinted with permission from Ref. [70]. Copyright 2012, Wiley-VCH Verlag GmbH & Co. KGaA.)

Magnevist (Figure 7.16c,d). The R_1 values were calculated to be 16.8 and 5.7 $mM^{-1}s^{-1}$ for HCPE-Gd and Magnevist, respectively, indicating the higher MRI sensitivity of HCPE–Gd than that of Magnevist. The *in vitro* fluorescence image of MCF-7 cancer cells shows the effective internalization of HCPE–Gd into MCF-7 breast cancer cells. The *in vivo* fluorescence/MR dual-modal imaging was conducted after injection of HCPE–Gd to H_{22} tumor-bearing mice via tail vein. Figure 7.16e shows the T_1-weighted MR images before and after HCPE–Gd injection, where the MR signal in tumor tissue is much stronger at 6 h post injection as compared with that before injection. Further fluorescence and MR imaging studies on hepatoma H_{22} tumor-bearing mouse model revealed that HCPE–Gd can serve as an efficient optical/MR dual-modal imaging nanoprobe for *in vivo* cancer diagnosis.

7.3.2.2 Fluorescence/Dark-Field Imaging

AuNPs could scatter visible and near-infrared light upon excitation of their surface plasmon oscillation, which makes them suitable as a contrast agent for dark-field imaging [71, 72]. Liu's group reported CP and AuNPs coloaded PLGA nanocomposites with eccentric internal nanostructure for dual-modal targeted cellular imaging [73] (Figure 7.17). Conjugated polymer **PFVBT** with far-red fluorescence is selected for fluorescence imaging. AuNPs of 5 nm diameter with strong scattering signal is used for dark-field imaging. Poly(lactide-*co*-glycolide (PLGA) is chosen as the polymer matrix because it is nontoxic and biodegradable with high cellular uptake efficiency. Folate is used to modify the composite for targeting tumor recognition, FPAuBT NCs and PAuBT NCs are used to denote the AuNP and **PFVBT** coloaded PLGA nanocomposites with and without folic acid at the surface. Here, F stands for folate, P stands for PLGA, BT stands for **PFVBT**, and NC stands for nanocomposite. Upon excitation at 520 nm, **PFVBT** has an emission maximum at 620 nm with an emission tail extended to 850 nm, allowing for FR/NIR fluorescence imaging. Due to the eccentric location of AuNPs [74, 75] (upper pictures in Figure 7.17b), the fluorescence of **PFVBT** is well maintained in the nanocomposite. The authors attributed this to the evaporation-induced phase separation between the Au NPs and polymer matrix. Cytotoxicity investigation of FPBT NCs and FPAuBT NC2s (FPAuBT NCs with 2 mg AuNPs at the feed) demonstrated that there is no obvious cytotoxic effect at low concentration (<400 nM). When the concentration increases to 800 nM, the cell viabilities slightly reduce to ~ 93% and 87% for cells upon incubation with FPBT NCs and FPAuBT NCs for 48 h. CLSM fluorescence imaging demonstrated that the folic acid groups at the nanocomposite surface favor its cellular uptake due to the receptor mediated uptake of FPBT NCs and FPAuBT NCs for MCF-7 cell lines (Figure 7.17a). The dark-field microscopic images of MCF-7 breast cancer cells after 2.5 h incubation in the medium containing FPAuBT NCs demonstrated that the light resulting from AuNPs is predominately accumulated inside the cell cytoplasm, which makes individual cell easily identifiable in the dark-field microscopic image (bottom pictures in Figure 7.17b). In addition, MCF-7 breast cancer cells incubated with PAuBT NCs without folic acid at the surface show a relative weak brightness, which is consistent with the results obtained from CLSM images.

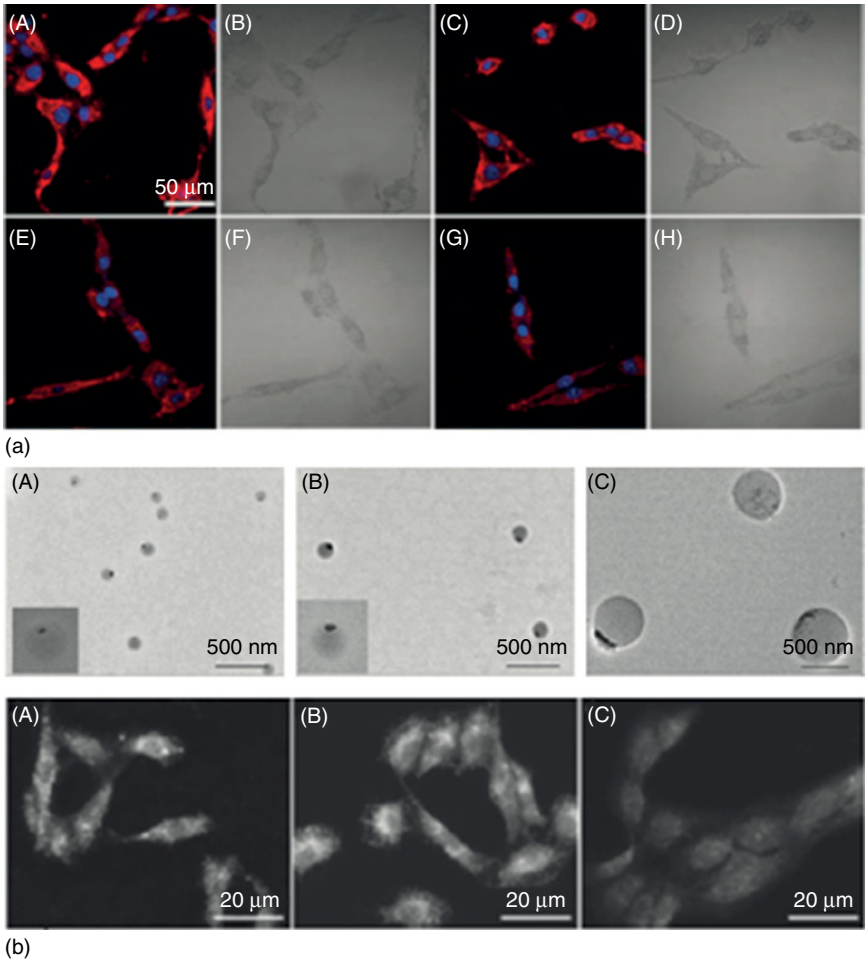

Figure 7.17 (a) CLSM fluorescence and bright-field images of fixed MCF-7 breast cancer cells after 2.5 h incubation with FPBT NC (A, B), FPAuBT NC2 (C, D), PBT NC (E, F), and PAuBT NC (G, H). (b) FE-TEM images of FPAuBT NCs prepared by encapsulation of 1 mg PFVBT with 1 mg (A), 2 mg (B), and 4 mg (C) of Au NPs, respectively, in PLGA matrix (upper). Dark-field microscopic images of MCF-7 breast cancer cells after 2.5 h incubation with FPAuBT NC2s (A) and PAuBT NC2s (B) and control cells without nanocomposites (C) (bottom). (Reprinted with permission from Ref. [73]. Copyright 2012, Wiley-VCH Verlag GmbH & Co. KGaA.)

Based on the above research, Xiao and coworkers reported a multilayer nanoprobe for fluorescence/dark-field dual-modality single particle imaging [76] (Figure 7.18). The fluorescent conjugated polymer **PFBT** was precipitated onto the surface of silica-coated plasmonic gold nanorods with a thin layer of silver (noted as SSGNRs). The metal core was used to provide plasmonic signal for dark-field imaging. A silica shell (<10 nm) was designed as the screening material to decrease the nonradiative energy transfer from the **PFBT** to the metal core. Compared with the fluorescence intensity of regular **PFBT** polymer dots without the metal core, the fluorescence intensity of the polymer was enhanced around twofold after

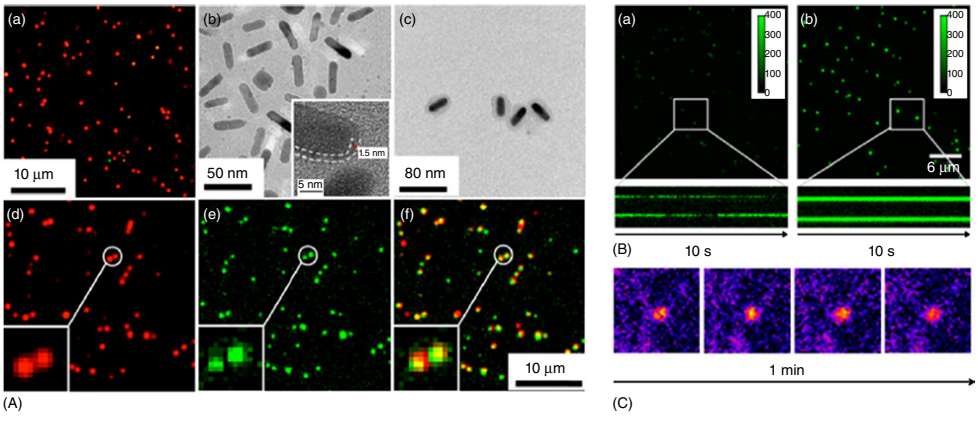

Figure 7.18 (A) Color dark-field (a) and TEM images of silver-coated GNRs (b). TEM imaging of silica-coated SGNR (c). The dark-field (d) and fluorescence (e) images of PFBT-coated SSGNRs. The merged image from the dark-field (red) and fluorescence (green) channels (f). (B) Single particle fluorescence imaging of regular PFBT nanoparticles (a) and PFBT-SSGNRs (b) represent intensity tracks as a function of time from individual nanoparticles. (C) Representative single particle dark-field images of PFBT-SSGNRs on cell membrane as a function of time. (Reprinted with permission from Ref. [76]. Copyright 2016, American Chemical Society.)

assembling onto the silica-decorated metal nanorod surface. The authors attributed the metal-enhanced fluorescence effect to the strongly magnified electromagnetic effect close to the nanoparticles. Similar improved fluorescence effect was also observed at the single molecule level. On the dark-field image, the SSGNRs particles exhibited nearly uniform color as well as intensity distribution, indicative of the good colloidal stability of the nanoparticle. The *epi*-fluorescence imaging demonstrated that bright fluorescent spots from the scattering points were detectable. Tracking of PFBT-SSGNRs in living cells demonstrated that without PFBT-SSGNRs, some bright spots were observable from the dark-field image, which could be assigned to signals from vesicles or organelles inside the cell. While no discernible signal was noted from the fluorescence mode (in the wavelength range of 550–600 nm), negligible background noise was demonstrated under this imaging condition. After co-incubation with HeLa cells for 2 h, the amount of bright spots on the cell membrane was greatly increased in contrast to the blank control, which was also observed in fluorescence mode. As a consequence, long-term and reliable single particle imaging and tracking can be realized by toggling between fluorescence and dark-field mode interactively.

7.3.2.3 MRI/Photoacoustic Imaging

Dai and coworkers reported PEGylated polypyrrole nanoparticles conjugated with gadolinium chelates (Gd–PEG–PPy NPs) for dual-modal MRI/PA imaging and photothermal therapy of cancer [77]. The Gd–PEG–PPy nanoparticles of 70 nm exhibit a high T_1 relaxivity coefficient of 10.61 l $mM^{-1}s^{-1}$, more than twice as high as that of the relating free Gd^{3+} complex (4.21 l $mM^{-1}s^{-1}$). T_1-weighted MR images showed enhanced brightness in the range of Gd^{3+} concentrations from 18.75 to 300×10^{-6} M. T_1 relaxation time increases with the increasing of Gd^{3+} concentrations and the trend is well fit by a linear line within the analyzed range of Gd^{3+} concentrations. MR imaging for the tumors in living mice demonstrated that large amount of Gd–PEG–PPy NPs circulated in the blood and then accumulated at the tumor site, which proved the high efficiency of tumor targeting of these nanoparticles. Compared with intrinsic tumor image with only big vasculatures visible before injection, the photoacoustic image showed greater clarity and significant increase in the photoacoustic signal in the tumor after 24 h intravenous injection of Gd–PEG–PPy NPs. Furthermore, by incorporating a photosensitizer with semiconducting polymer dots, researchers fabricated multifunctional Pdots/Ce6@lipid-Gd–DOTA micelles for MRI/photoacoustic dual-modal imaging and photodynamic therapy [78]. The Pdots/Ce6@lipid-Gd–DOTA micelles exhibited extremely low cytotoxicity, and had excellent MR- and PA-imaging contrast-enhancement ability, which could simultaneously offer anatomical information and morphological information on tumors.

7.4 Challenges and Outlook

In terms of the biological applications of CPs, numerous exciting advancements have been made by virtue of the unique light-harvesting and fluorescence emission properties. Various highly sensitive strategies were developed for the

detection of DNA, protein, metal ions, peptide, and enzyme, as well as pH, reactive oxygen species (ROS), and telomerase in live cells. Owing to the excellent photostability, low cytotoxicity, and high brightness, CPNs have attracted great attention recently. CPNs-based fluorescence imaging, NIR imaging, and multimodal imaging were widely developed for *in vitro* and *in vivo* imaging of tumor cells, drug delivery, and imaging-guided cancer therapy.

In spite of the encouraging progress, limitations that prevent further development of these CPs and their practical applications still exist. For example, general fluorescence imaging still has low signal to noise ratio, limited tissue penetration depth, and low spatial and temporal resolution. In addition, CPNs for NIR imaging still have relatively low quantum yield. More importantly, distributions of CPNs in other organs during *in vivo* imaging cannot be avoided due to the nonspecific interactions between CPNs and biomolecules.

However, a very bright future for CPs can still be expected as a result of the rapid development in this field. WSCPs are expected to display functions in more sophisticated and more in-depth biological systems. Future study will focus on, but not be limited to, the following directions: (i) developing new CPs with NIR emission, especially in NIR-II window, is a promising strategy to improve penetration depth and spatial and temporal resolution due to the decreased light scattering interference and low autofluorescence of NIR light; (ii) for practical applications, the metabolic processes and pathways of CPNs *in vivo* are two important issues that should be investigated since the current fluorescent probe has suboptimal excretion kinetics; (iii) interactions between CPNs and biomolecules should be fully investigated before practical applications because this may lower the specificity *in vivo*. Looking ahead, we sincerely hope that a large number of innovative ideas can be inspired by current results and many exciting research will be achieved in the near future.

References

1 Heeger, A.J. (2001) *Angew. Chem. Int. Ed.*, **40**, 2591.
2 Zhu, C.L., Liu, L.B., Yang, Q., Lv, F.T., and Wang, S. (2012) *Chem. Rev.*, **112**, 4687.
3 Feng, G.X., Liang, J., and Liu, B. (2013) *Macromol. Rapid Commun.*, **34**, 705.
4 Feng, L.H., Zhu, C.H., Yuan, H.X., Liu, L.B., Lv, F.T., and Wang, S. (2013) *Chem. Soc. Rev.*, **42**, 6620.
5 Thomas, S.W., Joly, G.D., and Swager, T.M. (2007) *Chem. Rev.*, **107**, 1339.
6 Liu, X.F., Fan, Q.L., and Huang, W. (2011) *Biosens. Bioelectron.*, **26**, 2154.
7 Pu, K.Y. and Liu, B. (2011) *Adv. Funct. Mater.*, **21**, 3408.
8 Gaylord, B.S., Heeger, A.J., and Bazan, G.C. (2002) *Proc. Natl. Acad. Sci. USA*, **99**, 10954.
9 Egholm, M., Buchardt, O., Christensen, L., Behrens, C., Freier, S.M., Driver, D.A., Berg, R.H., Kim, S.K., Norden, B., and Nielsen, P.E. (1993) *Nature*, **365**, 566.
10 Gaylord, B.S., Massie, M.R., Feinstein, S.C., and Bazan, G.C. (2005) *Proc. Natl. Acad. Sci. USA*, **102**, 34.

11 Gaylord, B.S., Heeger, A.J., and Bazan, G.C. (2003) *J. Am. Chem. Soc.*, **125**, 896.
12 Feng, F.D., Wang, H.Z., Han, L.L., and Wang, S. (2008) *J. Am. Chem. Soc.*, **130**, 11338.
13 Wang, C., Tang, Y., and Guo, Y. (2014) *ACS Appl. Mater. Interfaces*, **6**, 21686.
14 Liu, X.F., Shi, L., Hua, X.X., Huang, Y.Q., Su, S., Fan, Q.L., Wang, L.H., and Huang, W. (2014) *ACS Appl. Mater. Interfaces*, **6**, 3406.
15 Liu, X.F., Ouyang, L., Huang, Y.Q., Feng, X.M., Fan, Q.L., and Huang, W. (2012) *Polym. Chem.*, **3**, 703.
16 Liu, X.F., Ouyang, L., Cai, X.H., Huang, Y.Q., Feng, X.M., Fan, Q.L., and Huang, W. (2013) *Biosens. Bioelectron.*, **41**, 218.
17 Liu, X.F., Hua, X.X., Fan, Q.L., Chao, J., Su, S., Huang, Y.Q., Wang, L.H., and Huang, W. (2015) *ACS Appl. Mater. Interfaces*, **7**, 16458.
18 Wang, Y.X., Li, S.L., Feng, L.H., Nie, C.Y., Liu, L.B., Lv, F.T., and Wang, S. (2015) *ACS Appl. Mater. Interfaces*, **7**, 24110.
19 Rana, S., Elci, S.G., Mout, R., Singla, A.K., Yazdani, M., Bender, M., Bajaj, A., Saha, K., Bunz, U.H.F., Jirik, F.R., and Rotello, V.M. (2016) *J. Am. Chem. Soc.*, **138**, 4522.
20 Wang, S., Gaylord, B.S., and Bazan, G.C. (2004) *J. Am. Chem. Soc.*, **126**, 5446.
21 Xu, Q.H., Wang, S., Korystov, D., Mikhailovsky, A., Bazan, G.C., Moses, D., and Heeger, A.J. (2005) *Proc. Natl. Acad. Sci. USA*, **102**, 530.
22 Li, J., Huang, Y.Q., Qin, W.S., Liu, X.F., and Huang, W. (2011) *Polym. Chem.*, **2**, 1341.
23 Wang, C., Tang, Y.L., Liu, Y., and Guo, Y. (2014) *Anal. Chem.*, **86**, 6433.
24 Fan, C.H., Plaxco, K.W., and Heeger, A.J. (2002) *J. Am. Chem. Soc.*, **124**, 5642.
25 Wang, Y., Zhang, Y., and Liu, B. (2010) *Anal. Chem.*, **82**, 8604.
26 Cao, A., Tang, Y., and Liu, Y. (2012) *ACS Appl. Mater. Interfaces*, **4**, 3773.
27 Liu, X.F., Shi, L., Zhang, Z.Y., Fan, Q.L., Huang, Y.Q., Su, S., Fan, C.H., Wang, L.H., and Huang, W. (2015) *Analyst*, **140**, 1842.
28 Li, R.H., Niu, R.M., Qi, J.J., Yuan, H.B., Fan, Y.B., An, H.L., Yan, W.M., Li, H.R., Zhan, Y., and Xing, C.F. (2015) *ACS Appl. Mater. Interfaces*, **7**, 14569.
29 Fan, C.H., Wang, S., Hong, J.W., Bazan, G.C., Plaxco, K.W., and Heeger, A.J. (2003) *Proc. Natl. Acad. Sci. USA*, **11**, 6297.
30 Lukman, S., Aung, K.M., Liu, J., Liu, B., and Su, X.D. (2013) *ACS Appl. Mater. Interfaces*, **5**, 12725.
31 Yuan, Y.Y., Ding, D., Li, K., Liu, J., and Liu, B. (2014) *Small*, **10**, 1967.
32 Wang, L.H., Pu, K.Y., Li, J., Qi, X.Y., Li, H., Zhang, H., Fan, C.H., and Liu, B. (2011) *Adv. Mater.*, **23**, 4386.
33 Li, F., Chao, J., Li, Z.H., Xing, S., Su, S., Li, X.X., Song, S.P., Zuo, X.L., Fan, C.H., Liu, B., Huang, W., Wang, L.H., and Wang, L.H. (2015) *Anal. Chem.*, **87**, 3877.
34 Yuan, H.B., Qi, J.J., Xing, C.F., An, H.L., Niu, R.M., Zhan, Y., Fan, Y.B., Yan, W.M., Li, R.H., Wang, B., and Wang, S. (2015) *Adv. Funct. Mater.*, **25**, 4412.
35 Ho, H.A., Najari, A., and Leclerc, M. (2008) *Acc. Chem. Res.*, **41**, 168.
36 Ahn, D.J. and Kim, J.M. (2008) *Acc. Chem. Res.*, **41**, 805.
37 Ho, H.A., Boissinot, M., Bergeron, M.G., Corbeil, G., Dore, K., Boudreau, D., and Leclerc, M. (2002) *Angew. Chem. Int. Ed.*, **41**, 1548.
38 Liu, X.F., Tang, Y.L., Wang, L.H., Zhang, J., Song, S.P., Fan, C.H., and Wang, S. (2007) *Adv. Mater.*, **19**, 1471.

39 Wang, L.H., Liu, X.F., Yang, Q., Fan, Q.L., Song, S.P., Fan, C.H., and Huang, W. (2010) *Biosens. Bioelectron.*, **25**, 1838.

40 Park, C.H., Kim, J.P., Lee, S.W., Jeon, N.L., Yoo, P.J., and Sim, S.J. (2009) *Adv. Funct. Mater.*, **19**, 3703.

41 Jia, Y.M., Zuo, X.L., Lou, X.D., Miao, M., Cheng, Y., Min, X.H., Li, X.C., and Xia, F. (2015) *Anal. Chem.*, **87**, 3890.

42 Sun, P.F., Lu, X.M., Fan, Q.L., Zhang, Z.Y., Song, W.L., Li, B., Huang, L., Peng, J.W., and Huang, W. (2011) *Macromolecules*, **44**, 8763.

43 Li, K., Pan, J., Feng, S.S., Wu, W.Q., Pu, K.Y., Liu, Y.T., and Liu, B. (2009) *Adv. Funct. Mater.*, **19**, 3535.

44 Feng, X.L., Yang, G.M., Liu, L.B., Lv, F.T., Yang, Q., Wang, S., and Zhu, D.B. (2012) *Adv. Mater.*, **24**, 637.

45 Yin, C., Hong, B.B., Gong, Z.C., Zhao, H., Hu, W.B., Lu, X.M., Li, J., Li, X., Yang, Z., Fan, Q.L., Yao, Y.Y., and Huang, W. (2015) *Nanoscale*, **7**, 8907.

46 Wu, C.F., Hansen, S.J., Hou, Q., Yu, J.B., Zeigler, M., Jin, Y.H., Burnham, D.R., McNeill, J.D., Olson, J.M., and Chiu, D.T. (2011) *Angew. Chem. Int. Ed.*, **50**, 3430.

47 Tang, H.W., Xing, C.F., Liu, L.B., Yang, Q., and Wang, S. (2011) *Small*, **7**, 1464.

48 Wu, C.F., Jin, Y.H., Schneider, T., Burnham, D.R., Smith, P.B., and Chiu, D.T. (2010) *Angew. Chem. Int. Ed.*, **49**, 9436.

49 Feng, X.L., Tang, Y.L., Duan, X.R., Liu, L.L., and Wang, S. (2010) *J. Mater. Chem.*, **20**, 1312.

50 Kandel, P.K., Fernando, L.P., Ackroyd, P.C., and Christensen, K.A. (2011) *Nanoscale*, **3**, 1037.

51 Lee, K., Lee, J., Jeong, E.J., Kronk, A., Elenitoba-Johnson, K.S.J., Lim, M.S., and Kim, J. (2012) *Adv. Mater.*, **24**, 2479.

52 Anwar, N., Rix, A., Lederle, W., and Kuehne, A.J.C. (2015) *Chem. Commun.*, **51**, 9358.

53 Kim, S., Lim, C.K., Na, J., Lee, Y.D., Kim, K., Choi, K., Leary, J.F., and Kwon, I.C. (2010) *Chem. Commun.*, **46**, 1617.

54 Thomas, A.W., Henson, Z.B., Du, J., Vandenberg, C.A., and Bazan, G.C. (2014) *J. Am. Chem. Soc.*, **136**, 3736.

55 Garner, L.E., Park, J., Dyar, S.M., Chworos, A., Sumner, J.J., and Bazan, G.C. (2010) *J. Am. Chem. Soc.*, **132**, 10042.

56 Woo, S.J., Park, S., Jeong, J.E., Hong, Y., Ku, M., Kim, B.Y., Jang, H., Heo, S.C., Wang, T., Kim, K.H., Yang, J., Kim, J.H., and Woo, H.Y. (2016) *ACS Appl. Mater. Interfaces*, **8**, 15937.

57 Zhang, X.D., Wang, H., Antaris, A.L., Li, L., Diao, S., Ma, R., Nguyen, A., Hong, G., Ma, Z., Wang, J., Zhu, S.J., Castellano, J.M., Wyss-Coray, T., Liang, Y., Luo, J., and Dai, H. (2016) *Adv. Mater.*, **28**, 6872.

58 Rahim, N.A.A., McDaniel, W., Bardon, K., Srinivasan, S., Vickerman, V., So, P.T.C., and Moon, J.H. (2009) *Adv. Mater.*, **21**, 3492.

59 Parthasarathy, A., Ahn, H.Y., Belfield, K.D., and Schanze, K.S. (2010) *ACS Appl. Mater. Interfaces*, **2**, 2744.

60 Geng, J.L., Goh, C.C., Tomczak, N., Liu, J., Liu, R.R., Ma, L., Ng, L.G., Gurzadyan, G.G., and Liu, B. (2014) *Chem. Mater.*, **26**, 1874.

61 Wu, C.F., Bull, B., Szymanski, C., Christensen, K., and McNeill, J. (2008) *ACS Nano*, **2**, 2415.

62 Hu, W.B., Lu, X.M., Jiang, R.C., Fan, Q.L., Zhao, H., Deng, W.X., Zhang, L., Huang, L., and Huang, W. (2013) *Chem. Commun.*, **49**, 9012.

63 Geng, J.L., Liu, J., Liang, J., Shi, H.B., and Liu, B. (2013) *Nanoscale*, **5**, 8593.

64 Feng, L.H., Liu, L.B., Lv, F.T., Bazan, G.C., and Wang, S. (2014) *Adv. Mater.*, **26**, 3926.

65 Bao, B.Q., Ma, M.F., Chen, J., Yuwen, L.H., Weng, L.X., Fan, Q.L., Huang, W., and Wang, L.H. (2014) *ACS Appl. Mater. Interfaces*, **6**, 11129.

66 Almeida, C.S., Herrmann, I.K., Howes, P.D., and Stevens, M.M. (2015) *Chem. Mater.*, **27**, 6879.

67 Cui, Q.L., Wang, X.Y., Yang, Y., Li, S.L., Li, L.D., and Wang, S. (2016) *Chem. Mater.*, **28**, 4661.

68 Li, K., Ding, D., Huo, D., Pu, K.Y., Thao, N.N.P., Hu, Y., Li, Z., and Liu, B. (2012) *Adv. Funct. Mater.*, **22**, 3107.

69 Lu, X.M., Jiang, R.C., Yang, M.H., Fan, Q.L., Hu, W.B., Zhang, L., Yang, Z., Deng, W.X., Shen, Q.M., Huang, Y.Q., Liu, X.F., and Huang, W. (2014) *J. Mater. Chem. B*, **2**, 376.

70 Ding, D., Wang, G., Liu, J.Z., Li, K., Pu, K.Y., Hu, Y., Ng, J.C.Y., Tang, B.Z., and Liu, B. (2012) *Small*, **8**, 3523.

71 El-Sayeda, I.H., Huang, X.H., and El-Sayed, M.A. (2006) *Cancer Lett.*, **239**, 129.

72 Hu, Y., Chen, Q., Ding, Y., Li, R.T., Jiang, X.Q., and Liu, B.R. (2009) *Adv. Mater.*, **21**, 3639.

73 Geng, J.L., Li, K., Pu, K.Y., Ding, D., and Liu, B. (2012) *Small*, **8**, 2421.

74 Kietzke, T., Neher, D., Kumke, M., Ghazy, O., Ziener, U., and Landfester, K. (2007) *Small*, **3**, 1041.

75 Chen, T., Yang, M.X., Wang, X.J., Tan, L.H., and Chen, H.Y. (2008) *J. Am. Chem. Soc.*, **130**, 11858.

76 Luo, W.J., Wu, M., Li, S., Xu, Y.L., Ye, Z.J., Wei, L., Chen, B., Xu, Q.H., and Xiao, L.H. (2016) *Anal. Chem.*, **88**, 6827.

77 Liang, X.L., Li, Y.Y., Li, X.D., Jing, L.J., Deng, Z.J., Yue, X.L., Li, C.H., and Dai, Z.F. (2015) *Adv. Funct. Mater.*, **25**, 1451.

78 Zhang, D., Wu, M., Zeng, Y.Y., Liao, N.S., Cai, Z.X., Liu, G., Liu, X.L., and Liu, J.F. (2016) *J. Mater. Chem. B*, **4**, 589.

8

Conjugated Polymers for Gene Delivery

Joong Ho Moon[1] *and Kenry*[2]

[1]*Florida International University, Department of Chemistry and Biochemistry, 11200 SW 8th Street, Miami, FL, 33199, USA*
[2]*National University of Singapore, Department of Chemical and Biomolecular Engineering, 4 Engineering Drive 4, Singapore, 117585, Singapore*

8.1 Introduction

Gene therapy has emerged as one of the most attractive strategies in combating various physiological conditions and diseases [1–3], including neurodegenerative diseases, hematological diseases, antiviral diseases, hereditary genetic disorders, and cancer. Delivery of genetic materials including deoxyribonucleic acid (DNA) or ribonucleic acid (RNA) into target tissue or cells is crucial to achieve the therapeutic purpose. Despite its tremendous potential, the effective translation of gene therapy into clinical applications is still hampered by various biological challenges. Poor delivery efficiency is the biggest challenge. The highly negatively charged phosphodiesters backbone of nucleotides are prone to fast degradation by various nucleases and render them difficult to penetrate though the membrane of negatively charged lipid bilayers. To overcome these barriers, the genetic materials are often conjugated with or encapsulated within nanocarriers [2, 4]. Nanocarriers with low toxicity provide necessary protection against the endonucleases, targeting function to target tissues, and efficient cellular entries.

Current gene delivery methods can be broadly classified into viral and nonviral systems [5–7]. Viral system typically utilizes recombinant viruses as the vector for the delivery of genetic materials. In spite of its high transfection efficiency, the virus-mediated delivery system may induce high immunogenicity, inflammation, carcinogenicity, and random genetic integration. Because of this, the viral gene delivery system has found limited clinical implementation. As a safer alternative, recent years have witnessed the increasing development of synthetic nonviral vectors for gene delivery. As compared to their viral counterparts, the nonviral carriers display the necessary biocompatibility, biodegradability, controlled release, lower immunogenicity, and greater large-scale manufacturing possibility.

Positively charged synthetic carriers [8, 9], such as cationic polymers (e.g., poly L-lysine (PLL) [10], polyethylene imine (PEI) [11–14], poly methacrylates (PMA) [15–17], poly(amido amine) (PAA) [18–21], and poly(glycoamidoamine)

Conjugated Polymers for Biological and Biomedical Applications, First Edition. Edited by Bin Liu

[22, 23], and cationic lipids [24–27] have been widely demonstrated for the delivery of genetic materials including plasmid deoxyribonucleic acid (pDNA), mRNA, micro ribonucleic acid (miRNA), and small interfering ribonucleic acid (siRNA) (Figure 8.1) [2]. The electrostatic interactions between negatively charged nucleic acids and positively charged polymers allow the formation of uniform and stable polyplexes, which can protect nucleic acids from nuclease degradation. While the efficient delivery of pDNA has been demonstrated with these carriers, the siRNA delivery efficiency is relatively low. This inefficiency is mainly attributed to the structural differences between siRNA and pDNA, resulting in different complexation behaviors [28]. In general, pDNA has a length of several kilo nucleotides and a characteristic molecular topography that enables it to flexibly condense into nanometer-sized particles upon interaction with the positively charged carriers. On the other hand, the structurally rigid and short siRNA interacts in a disorderly fashion with the carriers. Inefficient condensation leads to larger complex sizes, complex instability, and poor siRNA protection from nucleases, resulting in a decreased delivery efficiency and knockdown efficiency. Moreover, the abundant positive charges in the carrier may always raise cellular toxicity issues [29]. This is because the positive charges strongly interact with the negatively charged membrane, causing cellular toxicity.

It is important to highlight that these delivery methods are less capable of long-term imaging and tracking of gene delivery and release in a real-time setting. In fact, the noninvasive visualization of the gene delivery process is crucial for monitoring the therapeutic process and improving current therapeutic protocols. To overcome this, fluorescent imaging agents, primarily organic fluorescent dyes, and quantum dots (QDs), have been developed and attached to the gene vectors or used directly for the delivery process to be tracked using fluorescence microscopic techniques. However, functional organic fluorescent dyes often suffer from low signal intensity, poor photostability, and they typically induce significant photobleaching and cytotoxicity. Similarly, despite their attractive optical properties with tunable emission and superior brightness and photostability, QDs display severe cytotoxicity through the leaching of metallic ions and generation of reactive oxygen species (ROS). As such, the design and development of novel multifunctional agents with outstanding luminescence, simultaneous therapeutic and molecular imaging capabilities, improved transfection efficiency, and negligible cytotoxicity are of utmost importance.

8.2 Fundamental Properties of Conjugated Polymers

Conjugated polymers (CPs) are synthetic organic materials with π-conjugated and delocalized electronic backbones. Owing to the highly delocalized π-electron system and configurable side chains, CPs exhibit unique electrical conductivity, outstanding photophysical properties (e.g., excellent fluorescence quantum yield, molar absorptivity, photostability, and energy transfer efficiency), and exceptional biophysical properties (e.g., high cellular entry and low cytotoxicity). These attractive properties render CPs multifunctional and highly suitable for numerous biomedical applications, including biosensing [30–33], bioimaging [34, 35], and

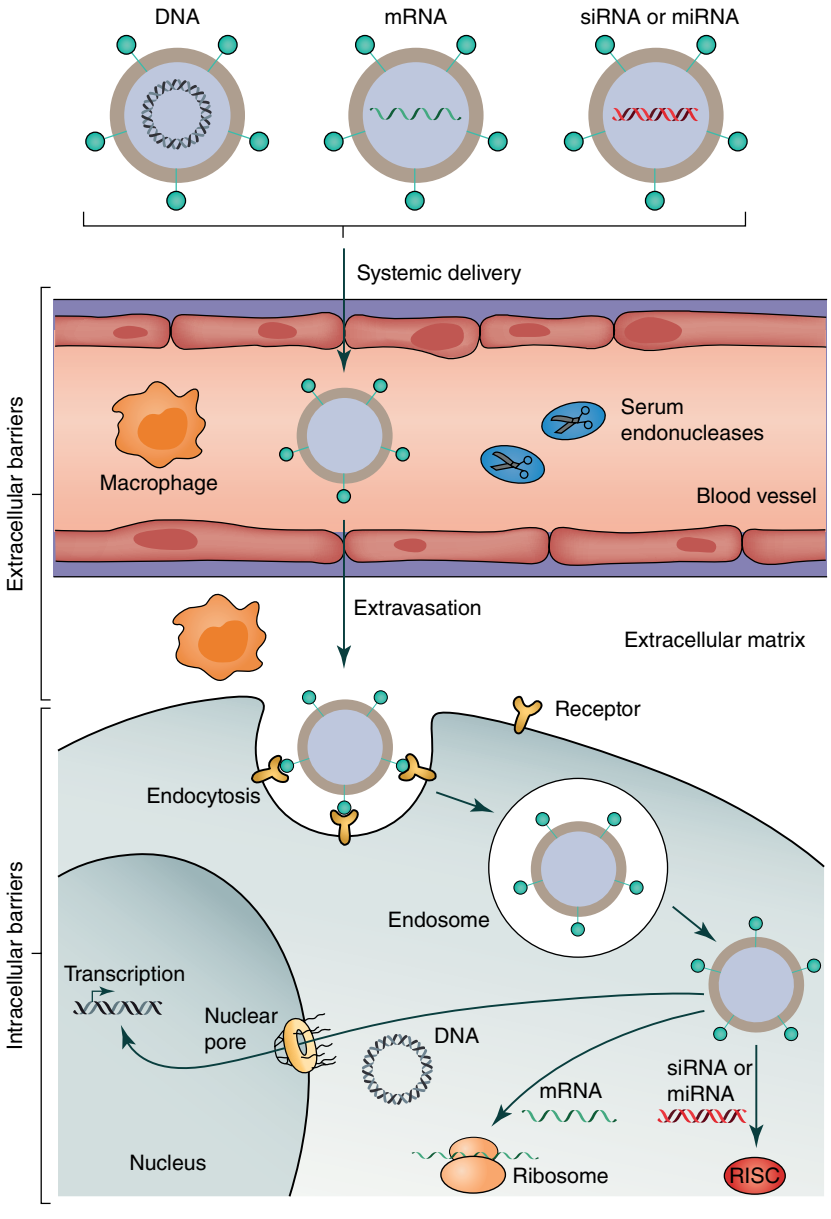

Figure 8.1 Obstacles hampering the effective delivery of nucleic acids by nonviral carriers. Various nonviral agents may be used to deliver different genetic materials, such as DNA, mRNA, and small interfering RNA (siRNA) or microRNA (miRNA). For successful gene delivery, the nonviral vectors need to protect these genetic materials from enzymatic degradation in cellular environments and rapid renal clearance from the circulation system. These nonviral gene carriers must also facilitate the cellular endocytic internalization and endosomal escape of the nucleic acids. Both siRNA and miRNA have to be encapsulated by the RNA-induced silencing complex (RISC) while mRNA must associate with the translational machinery. DNA, in contrast, has to be transported into the nucleus to induce its function. (Adapted with permission from Ref. [2]. Copyright 2014, Macmillan Publishers Limited.)

importantly, gene delivery [36]. Depending on their backbone structures, CPs can be categorized into numerous types [36] including poly(*p*-phenyleneethynylene) (PPE), poly(*p*-phenylenevinylene) (PPV), poly(fluorenyldivinylene) (PFV), poly(fluorine-*co*-phenylene) (PFP), polythiophene (PT), and polydiacetylene (PDA).

As synthetic macromolecules possessing rigid hydrophobic backbones and exhibiting intrinsic fluorescence, CPs are highly promising for improving gene transfection efficiency. In fact, the intrinsic fluorescent nature of CPs, which originates from the aromatic π-electrons conjugated along the backbones, will be highly advantageous in delivery tracking and cellular studies as the need for additional carrier labeling can be eliminated [37]. While the side chains of CPs are able to attract anionic nucleic acids [38–40], the integral hydrophobic backbones of cationic CPs are capable of stabilizing the ionic complex, cellular interaction and following uptake of the complexes, and endosomal release of genetic materials, further improving the delivery efficiency. Indeed, hydrophobicity has been recognized as an integral characteristic of the cationic carriers that improves the whole delivery process [12, 41–43]. The backbone rigidity and hydrophobicity also contribute to unique self-assembly processes, offering aggregation structure, and surface property controls that are pivotal for optimizing cellular interactions and entries. Finally, CPs containing primary amines exhibit low charge-to-molecular weight ratios (~1/380 for a PPE with ethylene oxide side chains), which contribute to their low cytotoxicity as compared to conventional polymers (i.e., PEI) that have high charge-to-molecular weight ratios (~1/43) [44].

It is noteworthy that the pristine CPs may not be used directly and effectively for biological applications owing to their poor solubility in aqueous solutions. Nevertheless, this may be overcome through the introduction of different functional groups along the conjugated backbone to regulate the physical properties of CPs. Through the incorporation of charged (i.e., cationic or anionic) pendant groups or hydrophilic polar side chains along the polymeric backbones, various water-soluble CPs or conjugated polyelectrolytes (CPEs) have been synthesized. Alternatively, conjugated polymer nanoparticles (CPNs) have also been synthesized via the self-assembly of nonaqueous-soluble CPs in aqueous solution, which often coupled with a stabilization with block copolymers or amphiphilic surfactants. In fact, up to date, a vast majority of the demonstrated *in vivo* applications of CPs are based on CPNs owing to the flexibility in CP selection, facile synthesis, and doping of CPs, excellent luminescence and photostability, and controllable nanoparticle size for improved biophysical properties. Because of these tunable physicochemical/biophysical properties, the fluorescent CPEs and CPNs have been regarded as highly promising biomaterials for cellular labeling, delivery, and monitoring applications.

8.3 Intracellular Targeting, Cytotoxicity, and Biodegradability of Conjugated Polymers

The gene transfection efficiency is directly influenced by the cellular entry pathways of the carriers. Therefore, a deep understanding of the entry pathways of synthetic carriers is pivotal to improve the overall efficiency of the labeling and

delivery processes. Carriers having both hydrophobic units and positive charges are known to exhibit efficient initial interaction with negatively charged hydrophobic lipids in the cellular membrane, resulting in improved entry into cells [45]. During the entry processes, the nature of the surface properties and sizes of the carriers influence the entry pathways [46, 47]. Two well-known mechanisms of nanoparticle entry are endocytosis (i.e., receptor-mediated or nonreceptor-medicated) and direct entry (i.e., membrane fusion or receptor-mediated). The entry mechanism for various synthetic polymers is known to be primarily endocytosis through initial interaction of positively charged polymers with the negatively charged cellular membrane [48, 49]. Polymers modified with cell surface receptors exhibit enhanced endocytosis. Although endocytosis is a significant uptake mechanism in mammalian cells, genes entrapped in endosomes or lysosomes decrease the transfection efficiency due to either the recycling of endosome contents to the cell surface or the degradation processes in acidic lysosomes. Therefore, modulating cellular entry pathways through detailed mechanistic studies as a function of hydrophobicity and charge density is crucial for a successful gene delivery. For example, as a mimic of the high-density lipoprotein that directly delivers hydrophobic cholesterol to cytosol, a peptide-phospholipid nanocarrier was synthesized for the direct delivery of hydrophobic drugs or surrogates [50]. In this direct delivery mechanism, hydrophobicity of the carrier plays an important role in cellular entry.

This has, indeed, been further confirmed in a recent study that investigated the surface morphological changes of the human cervical cancer cells, that is, HeLa cells, upon their interactions with CPNs [51]. The positively charged CPNs possessed a hydrodynamic diameter of 56 nm and induced negligible cytotoxicity up to a concentration of 40×10^{-6} M. After a short incubation with CPNs for 1 h, evident changes to the surface morphology of HeLa cells could be observed. More clearly, the cellular membrane post-CPN treatment displayed submicrometer to micrometer interconnected protrusions and pits. However, with further incubation, these features disappeared from the cell membrane. Evidently, these surface morphological variations were significantly influenced by the CPN concentrations and incubation times. Interestingly, HeLa cells incubated with positively charged PEI under similar conditions did not display any cell surface morphological changes. Contrary to PEI, CPNs possess positively charged side chains and rigid hydrophobic aromatic backbone. As such, the cell surface morphological changes in the presence of CPNs might be due to the active endocytosis of CPNs facilitated by their efficient hydrophobic interactions with the negatively charged hydrophobic cellular membrane. Furthermore, it was highly likely that the endocytosis process started when CPNs attached to and aggregated on the cell membrane surface. These cluster aggregations further enhanced the surface attachment of CPNs before they were actively internalized by the cells. All these suggest the critical role of the hydrophobicity of CPNs in mediating their cellular interactions and the subsequent efficient cellular entry and endocytosis.

As the surface of a cell comprises hydrophobic membrane lipids and negatively charged proteoglycans, the amphiphilicity of CPEs and CPNs is a factor paramount in mediating their cellular interactions and subsequent cellular entry.

In addition, other physical properties of these nanostructures, particularly their size and shape, are highly anticipated to influence their labeling and delivery efficiencies. More clearly, nanoparticles with large surface area-to-volume ratios are expected to display shape- and size-dependent cellular interactions and targeting efficiency. This was shown in a recent study investigating the cellular interactions of core–shell nanoparticles [52]. In the study, the core–shell CP-hyaluronic acid (CP-HA) nanoparticles were fabricated when a semiflexible poly(phenylenebutadiynylene) (PPB) was complexed with a linear polysaccharide HA. The fluorescent core-shell nanoparticles were observed to display high specificity toward cancer cells owing to the specific HA binding to the surface receptors of these cells. In contrast, in normal cells, the core–shell nanoparticles exhibited low specificity. Taken together, functional and structural modifications of CPs-based nanostructures followed by systematic investigations to control the cellular entry pathways will have significant impact on designing gene or drug delivery vehicles with desired properties for enhanced cellular applications.

An efficient release from the carriers and endosomes has also been shown to improve the transfection efficiency [53]. Indeed, the delivery efficiency of the gene vectors may be decreased if they experience endocytosis-mediated cellular entry through endosomes. Although nonendocytosis-based delivery is ideally demanded for drug and gene delivery, proportions of genes delivered via endocytosis, especially via clathrin-medicated endocytosis (CME), are quite high because CME involves continuous uptake of nutrients, intercellular communications, and signal transduction [45]. Therefore, efficient endosome escaping mechanisms should be considered for improving the transfection efficiency using synthetic carriers. This is because genes residing in endosomes and lysosomes may be transported back to the surrounding extracellular environments or be subjected to degradation without reaching cytosol. In fact, alternative cellular entry mechanisms of CPNs, possibly caveolae-mediated endocytosis (CvME) and micropinocytosis, ought to be explored as they tend to escape the lysosomal degradation processes. Interestingly, pH-sensitive, fusogenic, peptide-modified lipids are known to destabilize the endosomal membrane via structural transition from a bilayer to an inverted hexagonal structure [54, 55]. Derived from viruses, fusogenic peptides increase hydrophobicity upon structural transitioning at the endosomal pH [56, 57]. Various amine-containing polymers aid escape by increasing the influx of ions in the endosome, leading to swelling or rupturing of the membrane (i.e., proton sponge hypothesis) [14, 58]. Although structural changes of hydrophobically modified synthetic carriers in acidic endosomes are not ordered compared with those of peptides or liposomes, increased hydrophobicity from the structural changes results in improved endosomal escaping efficiency, while maintaining low toxicity. Disulfide-containing carriers are used to modulate hydrophobicity and charge density in endosomes [21, 57, 59]. Disulfide bonds in the carriers are rapidly reduced by reductive intracellular environments due to the high glutathione concentration (~10 mM) [60], resulting in de-aggregation of the carriers. De-aggregation of carriers weakens ionic interaction between the carrier and nucleic acids and changes the local hydrophobicity.

In general, gene carriers and their payloads may be trafficked into different cellular organelles depending on their cellular entry pathways. An appropriate

modulation of their cellular interactions and entry pathways are, therefore, anticipated to enhance the overall intracellular applications and efficiency of the gene carriers. Several studies have demonstrated the regulation of entry pathways and localizations of CPs through the alteration of their self-assembly characteristic. In one such work, the cellular entry mechanisms of positively charged primary amine-containing CPNs into human cervical cancer cells (HeLa cells), were investigated [61]. CPNs were taken up by the cancer cells primarily through an energy-dependent mechanism although a small proportion of CPNs entered the cells via energy-independent entry pathways. Intriguingly, for the energy-dependent pathway, the CPNs were internalized mainly via the CvME as verified through the reduced uptake of CPNs by cancer cells treated with the CvME inhibitor genistein as well as the high colocalization of CPNs with the protein caveloin-1 present in caveolae. Also, it was noted that CPNs did not induce any cytotoxicity. With outstanding photophysical properties, noncytotoxicity, and nondestructive cellular entry pathways, the multifunctional CPNs are highly promising for minimizing payload degradation during the delivery process.

In addition to cellular entry pathways, the overall functional performance, particularly the labeling and delivery efficiency, of CPNs and CPEs are significantly influenced by their subcellular localizations and cytotoxicity, which are dependent on the chemical structures of their backbones and side chains [62]. The surface properties of CPNs can be modulated by modification of the side chain and backbone of the corresponding CPs, which will influence the cellular interactions, cellular entry, and subsequent subcellular localizations. CPNs comprising primary amines displayed high Golgi localization with negligible cytotoxicity [62]. In contrast, a reduced Golgi localization with a higher cytotoxicity could be observed with the addition of short ethylene oxide and tertiary amine side chains, respectively.

Other factors influencing the overall delivery efficiency of CPs are their backbone flexibility and biodegradability [63–65]. For instance, CPs with smaller fragments resulting from intracellular degradation will facilitate an improved release of payloads. As such, there arises a need to develop flexible CPs with high biodegradability and preserved photophysical excellence. Interestingly, the biodegradability of CPs may be tuned by manipulating their self-assembly properties through the addition of degradable linkers. Recently, the synthesis of biodegradable CPs with tunable backbone flexibility and preserved photophysical properties has been reported [63]. In this work, a series of highly fluorescent and flexible PPEs were synthesized through the incorporation of disulfide-comprising nonconjugated monomers under optimized polymerization conditions. In fact, through controlled variation of the amount of flexible biodegradable monomeric linkers incorporated along the backbone of fully aromatic PPE under Sonogashira cross-coupling reaction conditions, the PPE backbone flexibility could be tuned. It was observed that the self-assembly characteristics of the rigid and flexible PPE-based nanoparticles upon complexation with polysaccharides were distinctively different. Interestingly, it was further noted that even with the addition of flexible monomers up to 50% into the backbone, the modified PPEs displayed similar photophysical properties to those of the fully conjugated PPEs.

In a separate work, an improvement to the structural and photophysical characteristics of PPBs through controlling the polymeric backbone flexibility has

been demonstrated [64]. High molecular weight polar side chain-containing PPBs of about 38 000 g mol^{-1} were prepared based on the reaction between the deactivated aryl bromide linker and an alkyne monomer under the coupling conditions mediated by palladium and copper. The enhanced PPB properties were ascribed to the doping of the PPB backbone with a small quantity of nonconjugating, flexible phenyleneethynylenes (PEs) units (i.e., PE-doped PPB or PE-d-PPB) as the newly synthesized PE-d-PPBs were highly promising for fluorescent live cell imaging.

For cellular organelles with additional membranes, particularly mitochondria, the need for further membrane penetration will inevitably reduce the delivery and labeling efficiency of carriers. Nevertheless, a recent study has reported the specific localization and efficient targeting of mitochondria of live cancer cells using biodegradable CPNs (Figure 8.2) [65]. The biodegradable polymeric nanoparticles were synthesized from the self-assembly of disulfide-containing CPs (Figure 8.2a). More clearly, the nonconjugated degradable linkers were introduced along the conjugated polymeric backbones to generate biodegradable CPs possessing photophysical properties similar to those of fully conjugated CPs. Indeed, the self-assembly behavior of the CPs was modulated through the modification of their backbones with flexible linkers, which eventually altered their cellular entry pathways. Upon cellular uptake, the disassembling and intracellular degradation of CPNs into low molecular weight conjugated oligomers (COs) occurred. The resultant fluorescent COs were then effectively trafficked to target and label mitochondria. To confirm this, the subcellular localization of CPNs were evaluated in which a nonbiodegradable CPN was prepared and used as control. It was termed CPN-2 while the biodegradable CPN was termed CPN-1. To further enhance their hydrophilicity, both CPNs were complexed with the negatively charged HA. The Pearson's correlation coefficient (PCC) was used as a quantitative colocalization metric. The characteristic mitochondrial granular patterns and a high PCC value of 0.78 were noted from the biodegradable CPN-1/HA complex, while the nonbiodegradable CPN-2/HA complex displayed a low PCC value of 0.37 accompanied by punctuated spots in its fluorescence image patterns (Figure 8.2b). This suggests the high and low mitochondrial colocalizations of CPN-1/HA and CPN-2/HA complexes, respectively. Moreover, the high-specific mitochondrial localization of CPN-1 was further verified through fluorescence spectroscopic analysis of the mitochondrial fraction of the live HeLa cells (Figure 8.2c). Through the mechanistic study, it was proposed that the mitochondria-specific localization of biodegradable CPNs was achieved via macropinocytosis followed by the intracellular degradation of CPNs to low molecular weight COs.

8.4 Plasmid DNA (pDNA) Delivery

Complexation of nucleic acids with synthetic polymers into small and stable complexes requires the intricate balance between charge density and hydrophobicity. The positively charged polymers with hydrophobic moieties are less water soluble than the intact cationic polymers and thus, assemble into lipid-like

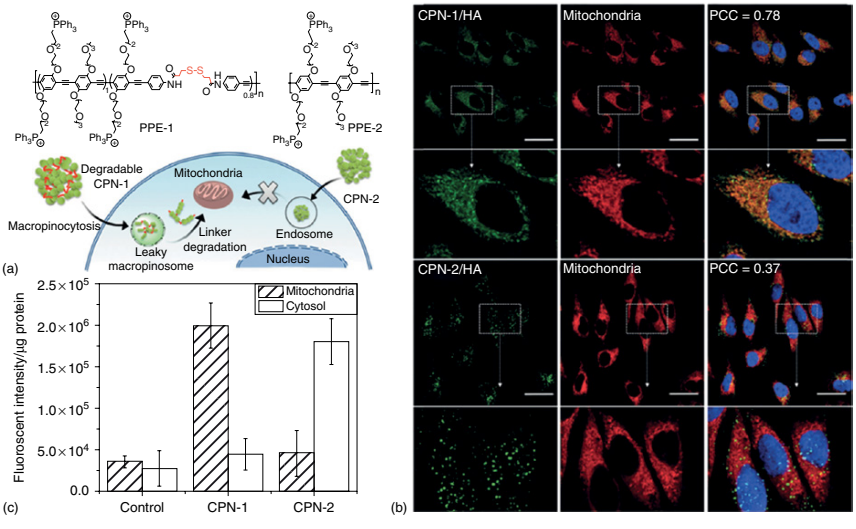

Figure 8.2 Specific intracellular targeting of conjugated polymer nanoparticles toward mitochondria. (a) Chemical structures of PPEs in the presence and absence of biodegradable linkers on the polymeric backbones (i.e., PPE-1 and PPE-2, respectively) accompanied by a schematic illustration demonstrating the cellular entry of biodegradable CPN (i.e., CPN-1), followed by its mitochondrial localization. (b) Fluorescence microscopic images showing the CPN/HA-incubated HeLa cells (green). The mitochondria and nuclei of the HeLa cells were stained in red and blue, respectively. Scale bars represent 20 μm. (c) Signal intensity of the fluorescently-stained mitochondria and cytosol of HeLa cells treated with CPNs. The higher fluorescent intensity of mitochondria of HeLa cells incubated with CPN-1 shows the specific localization of CPN-1 toward mitochondria. (Adapted with permission from Ref. [65]. Copyright 2016, The Royal Society of Chemistry.)

aggregations to form a stable and protective complex. The preaggregated hydrophobically modified polymers retain enough positive charge density to electrostatically attract nucleic acids and to cooperate with hydrophobic units in the aggregates for endosomolytic activities to release nucleic acids upon delivery [53]. Hydrophobic modifications of PEIs (high or low molecular weights or branched) [12, 42, 66], PAA [43], or poly aspartamides [41] have been reported to improve nucleic acid delivery. To modulate the cellular behaviors of the polymers, researchers introduce endosomolytic peptides [67, 68], hydrophobic amino acids (tyrosine or tryptophan) [11], alkyl acrylate [42, 66], ketalized acrylate [12], or steroids [41] into the side chains. Conclusively, balanced charge density and hydrophobicity are crucial to achieve small complex sizes, high nucleic acid loading density, high complex stability, and better protection of nucleic acids.

Branched polyethyleneimines (PEIs) with high molecular weight (e.g., 25 kDa branched PEIs) are known to be efficient gene delivery vehicles *in vitro* and *in vivo*. Despite their excellent transfection efficiency, PEIs are found to induce significant cytotoxicity. This may be attributed to their high amine density, which mediates the formation of necrosis-inducing polymer aggregates on the cellular membrane. To reduce their cytotoxicity, PEIs were modified with fluorescent, hyperbranched conjugated polyelectrolytes (HCPEs) for simultaneous gene transfection and imaging [69]. In the study, HCPEs were first synthesized through a simple cyclotrimerization of dialkynyl monomers catalyzed by $CpCo(CO)_2$. The as-prepared HCPEs with intrinsic fluorescent cores comprised highly emissive repeating units of fluorene–phenylene–fluorene. These HCPEs were next grafted with two branched PEIs with low molecular weights (i.e., PEI600 and PEI1800) via PEG linkers to generate PEI-conjugated HCPEs (i.e., HCPEPEI-1 and HCPEPEI-2, respectively), and their simultaneous utilization as both pDNA carriers and fluorescent contrast agents for tracking the pDNA delivery were subsequently evaluated. The HCPEPEI-1 and HCPEPEI-2 conjugates were capable of condensing pDNA at the low N/P ratios of 2 and 1, respectively, where the N/P ratios refer to the molar ratios of amine to phosphate in cationic polymers and pDNA, respectively. The as-synthesized nanostructures displayed low cytotoxicity and possessed optimal sizes ranging from 70 to 150 nm and positive zeta potentials, which could mediate efficient cellular uptake. Both HCPEs-DNA polyplexes were successfully taken up by the fibroblast-like COS-7 cells, resulting in effective gene transfections. HCPEPEI-2 exhibited a higher gene transfection efficiency than HCPEPEI-1, which might be ascribed to the higher amine density in HCPEPEI-2 than in HCPEPEI-1, enabling enhanced DNA binding and the formation of smaller and compact polyplexes.

In another study, the synthesis of an intrinsically fluorescent water-soluble cationic polyfluorene (CCP) and its application for highly efficient pDNA delivery and imaging have been demonstrated [70]. The highly fluorescent nature with an approximately 43% quantum yield in aqueous solution coupled with the excellent photostability of CCP facilitated the real-time tracking of the pDNA delivery and transfection processes. Furthermore, as a delivery vector for pDNA, CCP was capable of encapsulating and protecting pDNA from nuclease degradation. The transfection efficiency of CCP was reported to be as high as 92% at the

system employed, which significantly surpassed that of commercial transfection vectors, such as PEI and lipofectamine 2000.

Separately, fluorescent nanoparticles with good solubility have been prepared from the π-conjugated oligomers OFBT-A with 4,7-(9,9′-bis(6-adenine hexyl) fluorenyl)-2,1,3-benzothiadiazole units, which were modified with the mildly hydrophilic nucleotide adenine (A) groups on their side chains [71]. They were used as functional oligonucleotide vehicles carrying the single-stranded DNA labeled with TR-T5 fluorescent dyes. In particular, OFBT-A/TR-T5 nanocomposites possessed a wide range of working pH spanning from 3 to 9.5 and they exhibited high stability in solution with high ionic strength up to 500 mM. The appropriate physical size coupled with the close-to-neutral surface of the nanocomposites facilitated the enhanced uptake of short TR-DNA by A549 lung cancer cells. Also, OFBT-A/TR-T5 nanocomposites displayed a much lower cytotoxicity than OFBT-A nanoparticles.

In a different example, several cationic polythiophene derivatives were developed for gene regulation, specifically for the photounwinding of supercoiled pDNA under white light exposure (400–800 nm), through the generation of ROS [72]. In general, DNA supercoiling refers to the underwinding or overwinding of a strand of DNA. It plays a crucial role in numerous genetic processes, including transcription and gene replication. In this work, the electrostatic interactions between the positively charged CPs and the negatively charged pDNA facilitated the formation of CP-pDNA nanocomplexes. Upon the irradiation of white light, the cationic CPs were excited and they sensitized the surrounding oxygen molecules to generate ROS, which damaged and efficiently unwound the supercoiled pDNA into a relaxed state. It was revealed that the gene expression level of the unwound relaxed pDNA was significantly downregulated and decreased as compared to that of the pDNA with intact supercoiled structure.

Gene expression may be regulated at various levels through different methods, such as DNA modification and regulations of transcription and translation. In a recent investigation, DNA alkylation and gene regulation were achieved through the application of polyfluorene derivative comprising pendent alkylating chlorambucil moieties (PFP-Cbl), where Cbl is a chemical typically used for DNA modification in cancer therapy [73]. With the addition of Cbl onto their side chains, the resultant CPs were endowed with abundant alkylating groups. Incubated directly with DNA *in vitro*, PFP-Cbl with multivalent binding sites could enhance DNA alkylating reaction and improve DNA cross-linking. Moreover, PFP-Cbl was able to significantly downregulate the gene expression of luciferase reporter plasmid, as verified through the *in vitro* transcription and translation tests as well as the transfection of p-EGFP plasmid. Also, the self-luminous nature of PFP-Cbl enabled the tracing of the cellular internalization of the PFP-Cbl-plasmid complexes.

A recent report has demonstrated the preparation of a series of well-defined 2,6-bis(1-methylbenzimidazolyl)pyridinyl (BIP)-terminated ethanolamine-functionalized poly(glycidyl methacrylate) (BIP-PGEA) cationic nanoparticles with low molecular weight and their application for the efficient codelivery of drug and gene (Figure 8.3) [74]. The hydrophobic π-conjugated BIP core of the nanoparticles was able to encapsulate an aromatic, water-insoluble anticancer drug

[i.e.,10-hydroxy camptothecin (CPT)], while the PGEA periphery was capable of condensing pDNA efficiently (Figure 8.3a). The high transfection efficiency of BIP-PGEA nanoparticles surpassed that of linear PGEA and branched PEI. The evaluation of the antitumor effect of the BIP-PGEA-CPT nanoparticles on HepG2 cells was then conducted. When treated with only CPT, the viability of HepG2 cells was about 94.5 ± 6.4%, indicating the negligible cytotoxicity of CPT (Figure 8.3b). A similar phenomenon was observed from the cells treated with only the pro-drug 5-FC in which the cellular viability was largely maintained (Figure 8.3c). HepG2 cell treated with BIP-PGEA2 nanoparticles, on the other hand, started to display a reduced viability as compared to the 5-FC- and CPT-treated cells (Figure 8.3d). Nevertheless, when CPT was loaded onto BIP-PGEA2 nanoparticles, those cells incubated with these nanocomplexes exhibited reduced viability at roughly 51.9 ± 2.3% (Figure 8.3e). A significant toxicity was observed when HepG2 cells were incubated with BIP-PGEA2/CD/5-FC nanoparticles (Figure 8.3f). Eventually, the cellular viability of HepG2 cells reached the lowest at approximately 24.3 ± 1.8% when they were treated with BIP-PGEA2-CPT/CD/5-FC nanoparticles (Figure 8.3g). This might be attributed to the synergistic antitumor effect of the CD/5-FC gene/prodrug suicide system as well as the chemotherapeutic effect of antitumor drug CPT. Conclusively, BIP-PGEA-CPT nanoparticles possessed a strong synergistic antitumor effect on HepG2 cells when they were utilized in the BIP-PGEA-CPT-mediated suicide gene therapy system containing cytosine deaminase/5-fluorocytosine (CD/5-FC).

8.5 Small Interfering RNA (siRNA) Delivery

RNA interference (RNAi) [75–77] is a process by which small RNA molecules regulate gene expression by the sequence-specific degradation of messenger RNA (mRNA) (i.e., inhibition of proteins from mRNA), resulting in the knockdown of the corresponding protein. Chemically synthesized or endogenously produced small RNAs binding to RNA-induced silencing complex (RISC) produce the antisense RNA strands, which specifically hybridize to target mRNA followed by degradation. Endogenously generated miRNA is an abundant class of single-stranded small RNA with a length of 18–25 nucleotides, which regulates genes associated with most cellular processes, including differentiation, proliferation, and apoptosis,

Figure 8.3 Development of polycation-based nanoparticles with low molecular weight for the effective co-delivery of drug and pDNA. (a) Schematic illustration showing the synthesis of BIP-PGEA-CPT/pDNA complexes. (b–g) HepG2 cells incubated with: (b) free antitumor drug CPT with a concentration of 4.5 μg ml^{-1} equal that of CPT in BIP-PGEA2/CPT nanoparticles at an N/P ratio of 25, (c) free prodrug 5-FC, with a concentration of 80 μg ml^{-1}, (d) BIP-PGEA2 nanoparticles, (e) BIP-PGEA2-CPT nanoparticles, (f) BIP-PGEA2/CD/5-FC nanoparticles, with a 5-FC concentration of 80 μg ml^{-1} and at an N/P ratio of 25, and (g) BIP-PGEA2-CPT/CD/5-FC nanoparticles, with a 5-FC concentration of 80 μg ml^{-1} and at an N/P ratio of 25. The results demonstrated the strong synergistic antitumor effect induced by BIP-PGEA-CPT nanoparticles on HepG2 cells. (Adapted with permission from Ref. [74]. Copyright 2014, American Chemical Society.)

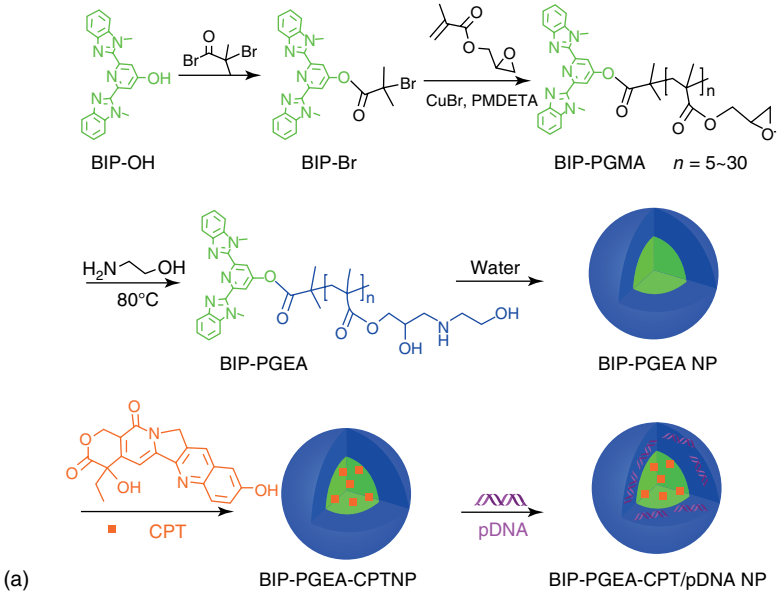
BIP-OH
BIP-Br
CuBr, PMDETA
BIP-PGMA
n = 5~30
H2N
OH
80°C
BIP-PGEA
Water
BIP-PGEA NP
CPT
pDNA
BIP-PGEA-CPTNP
BIP-PGEA-CPT/pDNA NP

(a)

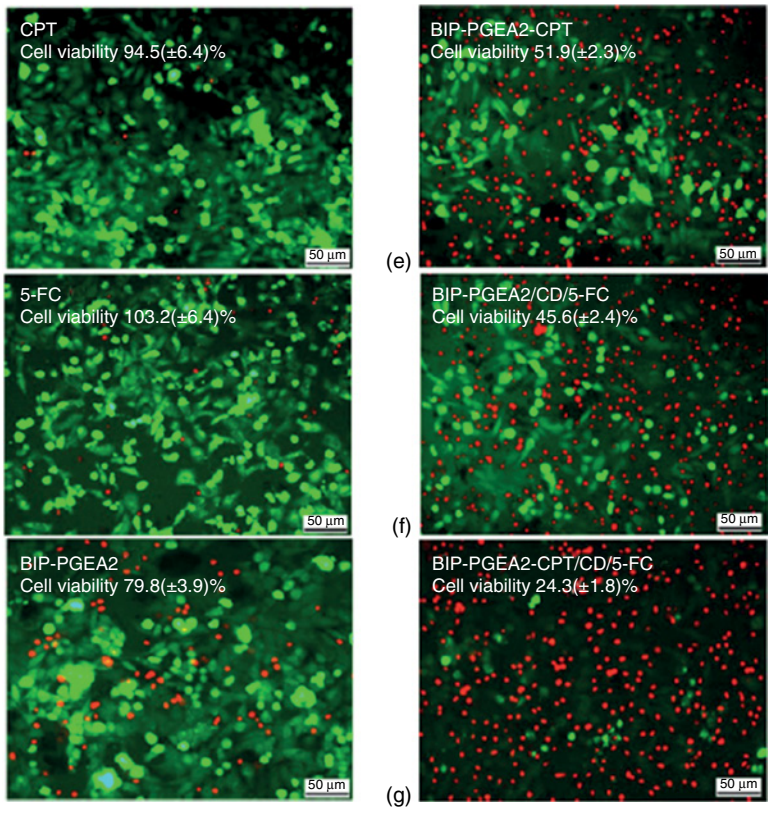
CPT
Cell viability 94.5(±6.4)%
5-FC
Cell viability 103.2(±6.4)%
BIP-PGEA2
Cell viability 79.8(±3.9)%
BIP-PGEA2-CPT
Cell viability 51.9(±2.3)%
BIP-PGEA2/CD/5-FC
Cell viability 45.6(±2.4)%
BIP-PGEA2-CPT/CD/5-FC
Cell viability 24.3(±1.8)%
50 μm

(b) (c) (d) (e) (f) (g)

by interacting with the translational machinery [78, 79]. Owing to its high specificity and efficiency, the rapidly growing RNAi technology is an extremely versatile tool to analyze gene functions in various organisms and cells. Specific knockdown of gene expression associated with diseases has led to extensive efforts to develop RNAi as a therapeutic intervention in disease-causing gene expression pathways in humans [80–82]. Because abnormal protein expression levels or their unique profiles are closely associated with various diseases including genetic disorders, neurodegenerative diseases, and cancers, RNAi technology is a highly efficient therapeutic tool for those conventionally nondrugable genes [83, 84]. In spite of the tremendous potential of RNAi, numerous challenges still hinder the successful applications of RNAi for the study of gene function and disease therapeutics.

RNAi requires efficient delivery of optimal amounts of small RNA to target tissues or cells with minimal toxic side effect [85–87]. The delivery requirement is not only because RNA itself cannot penetrate and cross the cellular membrane and physiological barriers due to its high negative charge, hydrophilicity, and small size, but also because RNA molecules are highly unstable and vulnerable to enzymatic degradation in cellular environments as well as to rapid kidney filtration from the circulatory system. Because of this labile degradation by endogenous nucleases, unprotected oligonucleotides possess an extremely short half-life *in vivo*. Also, after a cellular uptake, RNA molecules must be able to escape the endosome to enter the cytosol in order to promote its therapeutic effect.

For successful translation into clinical applications, safe and efficient deliveries of therapeutic RNA to targeted cells and tissues coupled with efficient gene silencing are necessary. Considerable efforts have been devoted in the past two decades to address and overcome various challenges, especially in exploring and identifying suitable nanomaterials. An ideal RNA carrier should exhibit several characteristics: high RNA binding and loading density, high RNA protection capability, efficient cellular entry and trafficking, low cellular toxicity, and efficient RNA release in cytosol. Target specificity and ideal pharmacokinetic properties of carriers are also required for *in vivo* applications [88, 89]. Viral carriers, such as adenoviral and retroviral constructs, have been used for cell-specific delivery of RNA [90]. Although viral delivery has been successfully used for many cell types with high efficiency, safety concerns associated with host immune responses against viral proteins necessitate the development of a safer therapeutic RNA delivery vehicle. Positively charged fluorescent CPs have gained much attention owing to their distinctive photophysical and biophysical properties. While the side chains of CPs can attract negatively charged nucleic acids, the hydrophobic backbones can stabilize the ionic complex, cellular uptake of the complexes, and endosomal release of RNA. To enhance complexation, siRNA protection, and cytocompatibility, various hydrophobic moieties have recently been linked to the side chains of CPs. The excellent photophysical characteristics of CPs also enable a long-term real-time visualization of the delivery process.

For evaluating the gene expression mechanism at the single cell level, the delivery of artificial siRNAs to plant protoplasts has been conventionally achieved using electroporation [91, 92]. However, extensive loss of viable protoplasts may result from the use of this technique. Alternatively, viral vectors and polyethylene glycol have been used for siRNA delivery. A noteworthy advancement in the

delivery of siRNAs to plant protoplasts has been demonstrated with the use of CPNs. As compared to viral vectors, CPNs/siRNA complexes are anticipated to deliver siRNAs for gene expression knockdown with higher safety in the absence of viral pathogenesis. Most recently, fluorescent CPNs were prepared for the effective delivery of siRNA to tobacco BY-2 plant protoplasts to knockdown of a specific gene in protoplasts [93]. Within 2 h of delivery, CPNs were found in the protoplasts. CPNs induced negligible cytotoxicity on protoplasts, as evidenced from the protoplasts maintaining their viability in the presence of CPNs over a course of 72 h. siRNAs targeting particular genes in the pathway of cellulose biosynthesis was delivered by CPNs, resulting in the successful downregulation of the cell wall synthase as confirmed by the reverse transcription quantitative polymerase chain reaction (RT-qPCR). In this demonstration, CPNs were successfully used as a potent transfection vehicle for the delivery of siRNAs to plant protoplasts, while the siRNA uptake process was fluorescently monitored.

Soon after the first demonstration of CPNs for siRNA delivery in plant cells, the same CPNs were also successfully used for the efficient target gene knockdown in mammalian cells [94]. The amphiphilic CPNs of the loose aggregation of the amine-comprising PPEs in water formed stable complexes, protected siRNA, and delivered it to the cells. In addition to the gel retardation assay, which revealed the complete complexation of siRNA with CPNs, the intrinsic fluorescent nature of CPNs allowing the facile monitoring of complexation was tracked through fluorescent changes. siRNA delivery was also visualized by using fluorescently labeled siRNA, confirming the siRNA delivery by CPNs. The CPN/siRNA complexes localized effectively inside the live HeLa cells, and the biologically active siRNA targeting β-actin successfully knocked down the expression of the target gene. The downregulated protein expression was then quantified by the western blotting, and the CPN-mediated gene regulation efficiency was found to be ~94%.

Conjugated polythiophenes were grafted with the low molecular weight PEI-1.8k for the development of cationic fluorescent copolymers as self-tracking siRNA carriers [95]. In fact, the low molecular weight PEI-1.8K served as a gene-condensing vector that enabled the formation of positively charged nanocomplexes with siRNA with high stability and low cytotoxicity. On the other hand, the rigid polythiophene with hydrophobic hexyl groups endowed the copolymer with a fluorescent label-free capability and increased the cell membrane permeability, resulting in the enhancement of siRNA transport across cell and endosomal membranes. The cellular uptake of the polymer/siRNA nanocomplexes was high beyond 80% and they localized efficiently inside A549 cells. Delivered via copolymers at a suitable dose, siRNA could cause considerable knockdown of the target protein. Interestingly, a higher knockdown efficiency of 52.8% with negligible cytotoxicity could be achieved with the use of siRNA complexes comprising copolymers with higher hydrophobicity, as revealed through a luciferase knockdown assay performed *in vitro* in A549-luc cells. This suggests the significant role of the hydrophobicity of the thiophene backbone and the alkyl side chain of the polymers in improving the cellular uptake and siRNA delivery performance. As such, the PEI-*co*-polythiophenes copolymers possess tremendous potential as an efficient self-tracking siRNA delivery vehicle with minimal cytotoxicity.

CPs may also be used for the regulation of gene-based drug resistance. In one of the first such studies, a cationic dendritic polyfluorene (PFP) was designed for the binding, encapsulation, and effective delivery of siRNA [96]. As a gene carrier, PFP was able to protect siRNA from nuclease degradation. Importantly, as an siRNA transfection vector, PFP could efficiently induce multidrug resistance reversal and improve drug sensitivity, as demonstrated in the application of PFP for the targeted delivery of siRNA to doxorubicin-resistant MCF-7 human breast cancer cells.

Recently, monodispersed brush-like CPE nanoparticles (PFNBrs) have been synthesized for the development of a PFNBr/siRNA nanocomplex-based delivery platform with dual functions of carrying siRNA and tracking its delivery process (Figure 8.4) [97]. The cationic CPE nanoparticles with unique brush-like molecular structure possessed lower proportion of sturdy backbone of polyfluorene and high density of flexible side chains consisting of polymethylmethacrylate derivatives (Figure 8.4a). The buried fluorene backbone enabled the PFNBr nanoparticles to display and maintain a strong and stable photophysical performance as a functional reporter capable of visualizing payload delivery and distribution and cellular imaging. The positively charged multibranched side chains with extended spatial structural conformation, on the other hand, endowed the CPE nanostructures the ability to carry and protect the oppositely charged siRNA. As such, based on electrostatic interactions, the cationic brush-like CPE nanostructures were able to form highly stable complexes with the negatively charged siRNA molecules and condense them for endocytic cellular internalization. Indeed, this was verified through the *in vitro* cellular uptake assay. Specifically, the free negatively charged siRNA could hardly penetrate into PANC-1 cells, demonstrating that the anionic siRNA alone was inhibited from cellular internalization (Figure 8.4b). The cationic PFNBr nanoparticles, in comparison, could simply penetrate and localize inside the cells (Figure 8.4c). Impressively, by generating positively charged PFNBr/siRNA complexes through the electrostatic interactions between siRNA molecules and PFNBr nanoparticles, a significant enhancement in cellular internalization and siRNA localization could be achieved (Figure 8.4d). This indicates the versatility of the CPE nanostructures as both efficient siRNA carriers and fluorescent reporters. In fact, as an siRNA nanocarrier, PFNBr nanoparticles exhibited a superior payload loading capacity of 1 mol polymer to above 32.5 mol siRNA, and enhanced siRNA protection. As a result, the concentration of carriers in the system could be decreased from $\mu mol\,l^{-1}$ to $nmol\,l^{-1}$, which was considerably lower than those of other CP-based delivery systems. Impressively, with a minimal dose in the range of $nmol\,l^{-1}$, the PFNBr/siRNA nanocomplexes effectively entered the cells and released siRNA to induce high gene silencing efficiency with no noticeable cytotoxicity. Specifically, only $20\,nmol\,l^{-1}$ nanocomplexes carrying $200\,nmol\,l^{-1}$ siPlk1 transfected into PANC-1 cells were required to knockdown targeted Plk1 mRNA effectively with a high efficiency of 23.9%. Conclusively, the brush-like cationic CPE nanoparticle-based siRNA delivery system is highly promising for the development of novel therapeutic platforms based on nucleic acids.

The endosome has been known as the primary physiological barrier hampering an effective gene transfection process. Endosomal disruption, consequently, may be necessary and beneficial to increase the transfection effectiveness. In recent years,

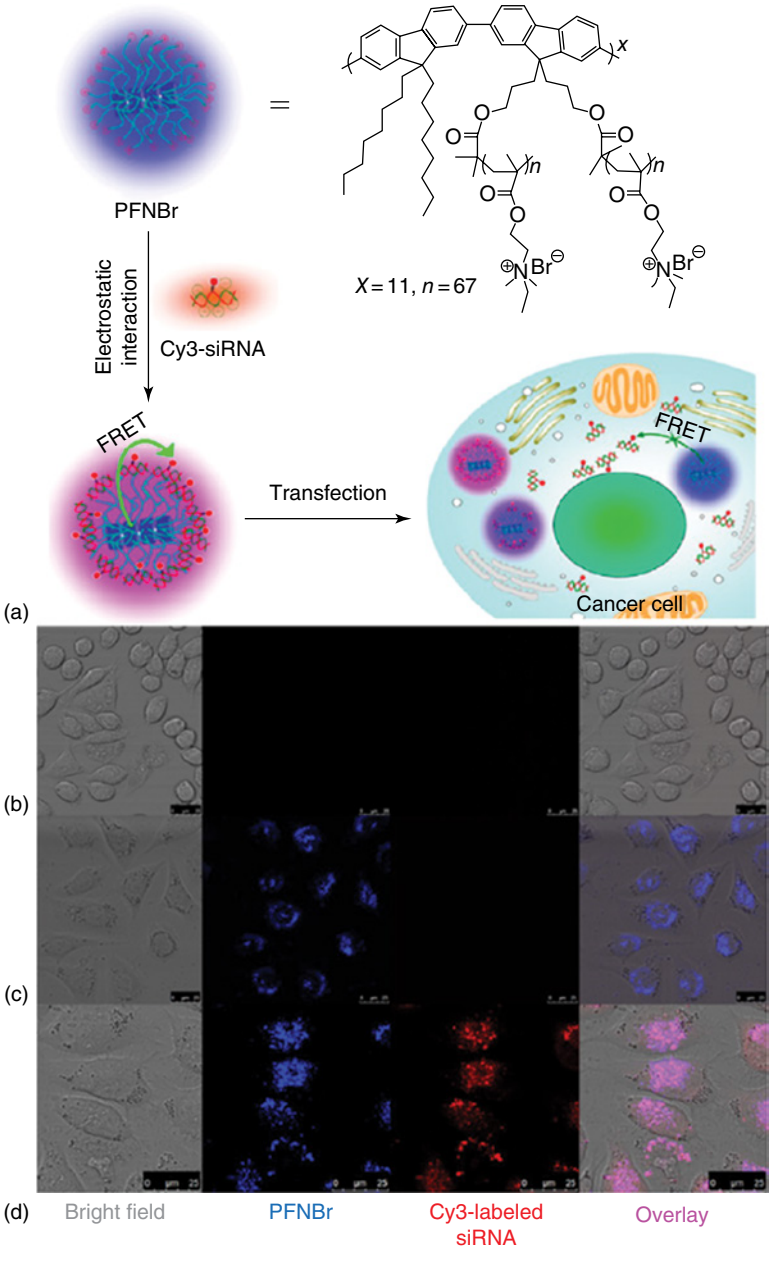

Figure 8.4 Brush-like cation conjugated polyelectrolyte nanoparticles for the effective visualized delivery of siRNA. (a) Schematic illustration showing the delivery of siRNA using PFNBr. (b–d) Confocal microscopy images of PANC-1 cells incubated with individual Cy3-labeled siRNAs, CPNs, and their polyplexes for 4 h, illustrating their cellular internalization: (b) Cy3-labeled siRNA (100 nmol l^{-1}); (c) PFNBr (40 nmol l^{-1}); (d) Cy3-labeled siRNA (100 nmol l^{-1}) and PFNBr (40 nmol l^{-1}). PFNBr and cy3-labeled siRNA were represented in blue and red, respectively. (Adapted with permission from Ref. [97]. Copyright 2013, American Chemical Society.)

photochemistry-based approaches have garnered increasing interests for potential applications in photoresponsive drug release or photothermal and photodynamic therapies [98–100] due to their excellent spatiotemporal resolution, noninvasive nature, and biosafety [101–104]. In one of the latest studies, the cationic PPV derivative was used for the construction of a multifunctional platform for the white light-enhanced endosomal escape-based delivery of siRNA (Figure 8.5) [105]. The CPE with cationic and amphipathic characteristics was able to self-assemble with siRNA and deliver it into target cells effectively (Figure 8.5a). Interestingly, upon white light irradiation, the cationic PPV was able to photosensitize the surrounding oxygen molecules to generate ROS, which could photochemically disturb the endosomal membrane, leading to an enhanced endosomal escape of siRNA. Because of this, siRNA was able to escape enzymatic degradation and the siRNA influx into the cytoplasm for RNAi would be increased, thereby enhancing the gene silencing efficiency of siRNA. Also, the siRNA delivery and intracellular localization processes could be imaged with PPV owing to its high fluorescence emission and good photostability. It was noted that the HeLa cells treated with the PPV-siRNA polyplexes emitted fluorescence Cy5-labeled siRNA and PPV (Figure 8.5b). At the same time, the fluorescence of both Cy5-labeled siRNA and PPV overlapped with that of Lysotracker, indicating the colocalization of the polyplexes with endosome. Upon white light irradiation, siRNA molecules distributed across the cytoplasm of the light-irradiated cells. This suggests the occurrence of the white light-enhanced endosomal escape of siRNA. In fact, from the single-cell imaging performed after another 20 h incubation post white light irradiation, it could be observed that a majority of siRNA molecules had escaped from the endosome (Figure 8.5c). Additionally, the PPV-siRNA polyplexes exhibited a significantly higher transfection efficiency of 93.7 ± 5% as compared to both 25 kDa PEI and lipofectamine 2000 with transfection efficiencies of 28.8 ± 13% and 77.0 ± 9%, respectively (Figure 8.5d). Finally, as revealed through the luciferase assay with HeLa-Luc cells, the gene silencing efficiency of the white light-irradiated PPV-siRNA polyplexes was significantly higher than those of siRNA, 25 kDa PEI, and even the PPV-siRNA polyplexes without the white light exposure (Figure 8.5e). Altogether, these suggest the advantages of PPV as an siRNA vector as well as the application of photochemistry coupled with PPV for enhanced gene therapeutic effects.

8.6 Conclusions and Outlook

To summarize, recent years have witnessed the increasing development and applications of intrinsically fluorescent cationic CPs for the delivery of genetic materials, particularly pDNA and siRNA, for potential gene therapy in combating various physiological conditions and diseases. Owing to their excellent structural and photobiophyscial properties, the positively charged CPs, as nonviral gene vectors, possess high potential as multifunctional gene delivery material exhibiting efficient gene knockdown or expression with imaging and tracking functions. CPs are synthetic macromolecules possessing highly delocalized π-conjugated backbones and charged flexible side chains enabling effective bindings with the negatively charged nucleic acids and facilitating formation of stable

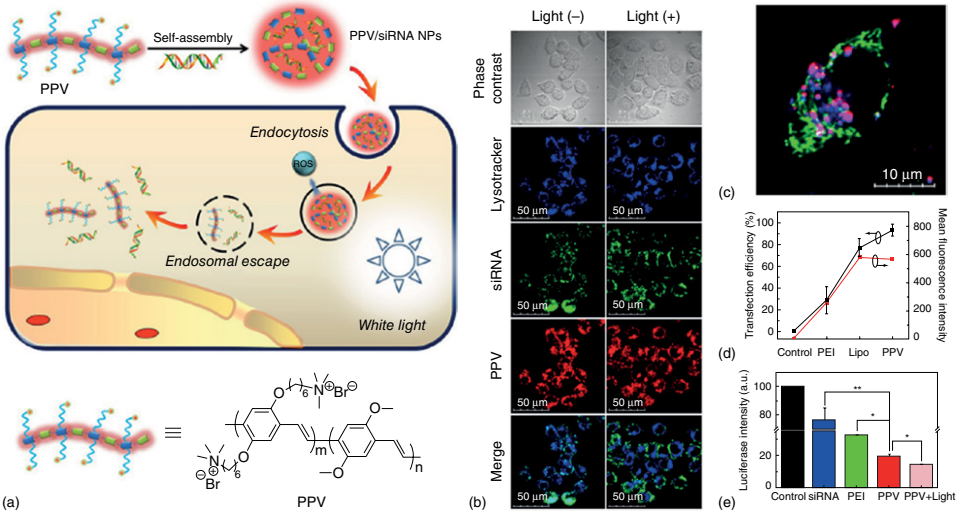

Figure 8.5 Multifunctional poly(*p*-phenylene vinylene)-based structure for the light-enhanced delivery of siRNA. (a) Schematic illustration demonstrating the high siRNA delivery based on the white light-facilitated endosomal escape approach. (b) Endosomal escape of PPV/siRNA polyplexes in the absence and presence of white light irradiation. (c) Colocalization of the PPV/siRNA polyplexes with endosome after another 20 h incubation post white light irradiation. Lysotracker, siRNA, and PPV were represented in blue, green, and red, respectively. (d) Transfection efficiency of PPV/siRNA polyplexes with respect to those of positive controls, that is, PEI and lipofectamine 2000. (e) Luciferase intensity measured from HeLa-Luc cells after a 24 h incubation with PPV/siRNA polyplexes at 1 μg anti-Luc siRNA. (Adapted with permission from Ref. [105]. Copyright 2016, Wiley-VCH Verlag GmbH & Co.)

CP/gene polyplexes. The fluorescent backbones also serve as light-harvesting units useful for visualizing and monitoring of the cellular internalization and localization processes of the polyplexes. The configurable hydrophilic polar side chains of CPs offer the high dispersibility and solubility in aqueous solution, which is highly advantageous for their further interactions with biomacromolecules, drugs, microorganisms, and cells. Concurrently, the low molecular weight side chains containing primary amines also contribute to the minimal cytotoxicity of CPs. Overall, as a result of the highly delocalized π-electron system and configurable side chains, CPs exhibit outstanding physicochemical properties, notably excellent fluorescence quantum yield, robust photostability, tunable spectral properties, versatile surface chemistry, high cellular entry, high cytocompatibility, and low cytotoxicity. These attractive properties, therefore, render CPs highly suitable as gene vectors for the effective delivery of these genetic materials and imaging of their cellular uptake and localization.

Nevertheless, despite all the promising structural and photobiophysical features coupled with potential gene delivery applications, several challenges remain for the translation of CPs into real clinical applications. Firstly, further development and characterization of the identified CP-based nanostructures for the effective delivery of specific genetic materials, such as pDNA, mRNA, miRNA, or siRNA, are crucial in order to achieve the desired therapeutic effects. Till date, a majority of the reported studies are still explorative in nature. As such, more stringent standards and experimental parameters need to be upheld in further evaluating the characteristics and overall feasibility of CPs for gene delivery applications. Secondly, it is crucial to highlight that most of the reported studies are still at the proof-of-concept stage and based on *in vitro* evaluations. In fact, the *in vivo* biological behaviors of CPs have not been well characterized and elucidated. Specifically, the *in vivo* circulation times, biodistribution, targeting capability and efficiency, localization behavior, and cytocompatibility of CPs are still minimally studied and understood. It is crucial to mention that the *in vitro* and *in vivo* CP behaviors and performances may vary significantly and the obtained *in vitro* results may not be predictive and accurate if they are to be translated directly for *in vivo* applications. Evident gaps clearly still exist. Unless these are bridged, the clinical applications of CPs for gene delivery will remain only as a vision and may not be realized. Encouragingly, in the last several years, we have witnessed the slow but steady progresses being made to fill the gaps. More efforts are clearly necessary in these directions. However, we foresee that once these challenges have been overcome, the future outlooks of the applications, clinical translations, and even commercialization of CP-based multifunctional gene therapeutic platforms are bright and encouraging.

References

1 Somia, N. and Verma, I.M. (2000) Gene therapy: trials and tribulations. *Nat. Rev. Genet.*, **1**, 91–99.

2 Yin, H., Kanasty, R.L., Eltoukhy, A.A., Vegas, A.J., Dorkin, J.R., and Anderson, D.G. (2014) Non-viral vectors for gene-based therapy. *Nat. Rev. Genet.*, **15**, 541–555.

3 Naldini, L. (2015) Gene therapy returns to centre stage. *Nature*, **526**, 351–360.
4 Xu, H., Li, Z., and Si, J. (2014) Nanocarriers in gene therapy: a review. *J. Biomed. Nanotechnol.*, **10**, 3483–3507.
5 Al-Dosari, M.S. and Gao, X. (2009) Nonviral gene delivery: principle, limitations, and recent progress. *AAPS J.*, **11**, 671.
6 Nayerossadat, N., Maedeh, T., and Ali, P.A. (2012) Viral and nonviral delivery systems for gene delivery. *Adv. Biomed. Res.*, **1**, 27.
7 Ramamoorth, M. and Narvekar, A. (2015) Non viral vectors in gene therapy- an overview. *J. Clin. Diagn. Res.*, **9**, GE01–GE06.
8 Langer, R. and Tirrell, D.A. (2004) Designing materials for biology and medicine. *Nature*, **428**, 487–492.
9 Pack, D.W., Hoffman, A.S., Pun, S., and Stayton, P.S. (2005) Design and development of polymers for gene delivery. *Nat. Rev. Drug Discov.*, **4**, 581–593.
10 Inoue, Y., Kurihara, R., Tsuchida, A., Hasegawa, M., Nagashima, T., Mori, T., Niidome, T., Katayama, Y., and Okitsu, O. (2008) Efficient delivery of siRNA using dendritic poly(l-lysine) for loss-of-function analysis. *J. Controlled Release*, **126**, 59–66.
11 Creusat, G., Rinaldi, A.-S., Weiss, E., Elbaghdadi, R., Remy, J.-S., Mulherkar, R., and Zuber, G. (2010) Proton sponge trick for pH-sensitive disassembly of polyethylenimine-based siRNA delivery systems. *Bioconjugate Chem.*, **21**, 994–1002.
12 Shim, M.S. and Kwon, Y.J. (2009) Acid-responsive linear polyethylenimine for efficient, specific, and biocompatible siRNA delivery. *Bioconjugate Chem.*, **20**, 488–499.
13 Mao, S., Neu, M., Germershaus, O., Merkel, O., Sitterberg, J., Bakowsky, U., and Kissel, T. (2006) Influence of polyethylene glycol chain length on the physicochemical and biological properties of poly(ethylene imine)-*graft*-poly(ethylene glycol) block copolymer/SiRNA polyplexes. *Bioconjugate Chem.*, **17**, 1209–1218.
14 Akinc, A., Thomas, M., Klibanov, A.M., and Langer, R. (2005) Exploring polyethylenimine-mediated DNA transfection and the proton sponge hypothesis. *J. Gene Med.*, **7**, 657–663.
15 van de Wetering, P., Moret, E.E., Schuurmans-Nieuwenbroek, N.M.E., van Steenbergen, M.J., and Hennink, W.E. (1999) Structure–activity relationships of water-soluble cationic methacrylate/methacrylamide polymers for nonviral gene delivery. *Bioconjugate Chem.*, **10**, 589–597.
16 Hinrichs, W.L.J., Schuurmans-Nieuwenbroek, N.M.E., van de Wetering, P., and Hennink, W.E. (1999) Thermosensitive polymers as carriers for DNA delivery. *J. Controlled Release*, **60**, 249–259.
17 Felber, A.E., Castagner, B., Elsabahy, M., Deleavey, G.F., Damha, M.J., and Leroux, J.-C. (2011) siRNA nanocarriers based on methacrylic acid copolymers. *J. Controlled Release*, **152**, 159–167.
18 Lin, C., Zhong, Z., Lok, M.C., Jiang, X., Hennink, W.E., Feijen, J., and Engbersen, J.F.J. (2007) Novel bioreducible poly(amido amine)s for highly efficient gene delivery. *Bioconjugate Chem.*, **18**, 138–145.
19 Christensen, L.V., Chang, C.-W., Kim, W.J., Kim, S.W., Zhong, Z., Lin, C., Engbersen, J.F.J., and Feijen, J. (2006) Reducible poly(amido ethylenimine)s

designed for triggered intracellular gene delivery. *Bioconjugate Chem.*, **17**, 1233–1240.

20 Zugates, G.T., Anderson, D.G., Little, S.R., Lawhorn, I.E.B., and Langer, R. (2006) Synthesis of poly(β-amino ester)s with thiol-reactive side chains for DNA delivery. *J. Am. Chem. Soc.*, **128**, 12726–12734.

21 Ou, M., Wang, X.-L., Xu, R., Chang, C.-W., Bull, D.A., and Kim, S.W. (2008) Novel biodegradable poly(disulfide amine)s for gene delivery with high efficiency and low cytotoxicity. *Bioconjugate Chem.*, **19**, 626–633.

22 Srinivasachari, S., Liu, Y., Zhang, G., Prevette, L., and Reineke, T.M. (2006) Trehalose click polymers inhibit nanoparticle aggregation and promote pDNA delivery in serum. *J. Am. Chem. Soc.*, **128**, 8176–8184.

23 Fichter, K.M., Ingle, N.P., McLendon, P.M., and Reineke, T.M. (2013) Polymeric nucleic acid vehicles exploit active interorganelle trafficking mechanisms. *ACS Nano*, **7**, 347–364.

24 Spagnou, S., Miller, A.D., and Keller, M. (2004) Lipidic carriers of siRNA: differences in the formulation, cellular uptake, and delivery with plasmid DNA. *Biochemistry*, **43**, 13348–13356.

25 Akinc, A., Zumbuehl, A., Goldberg, M., Leshchiner, E.S., Busini, V., Hossain, N., Bacallado, S.A., Nguyen, D.N., Fuller, J., Alvarez, R., Borodovsky, A., Borland, T., Constien, R., de Fougerolles, A., Dorkin, J.R., Narayanannair Jayaprakash, K., Jayaraman, M., John, M., Koteliansky, V., Manoharan, M., Nechev, L., Qin, J., Racie, T., Raitcheva, D., Rajeev, K.G., Sah, D.W.Y., Soutschek, J., Toudjarska, I., Vornlocher, H.-P., Zimmermann, T.S., Langer, R., and Anderson, D.G. (2008) A combinatorial library of lipid-like materials for delivery of RNAi therapeutics. *Nat. Biotechnol.*, **26**, 561–569.

26 Tagalakis, A.D., He, L., Saraiva, L., Gustafsson, K.T., and Hart, S.L. (2011) Receptor-targeted liposome-peptide nanocomplexes for siRNA delivery. *Biomaterials*, **32**, 6302–6315.

27 Xue, H.-Y. and Wong, H.-L. (2011) Solid lipid–PEI hybrid nanocarrier: an integrated approach to provide extended, targeted, and safer siRNA therapy of prostate cancer in an all-in-one manner. *ACS Nano*, **5**, 7034–7047.

28 Gary, D.J., Puri, N., and Won, Y.-Y. (2007) Polymer-based siRNA delivery: perspectives on the fundamental and phenomenological distinctions from polymer-based DNA delivery. *J. Controlled Release*, **121**, 64–73.

29 Fischer, D., Li, Y., Ahlemeyer, B., Krieglstein, J., and Kissel, T. (2003) *In vitro* cytotoxicity testing of polycations: influence of polymer structure on cell viability and hemolysis. *Biomaterials*, **24**, 1121–1131.

30 McQuade, D.T., Pullen, A.E., and Swager, T.M. (2000) Conjugated polymer-based chemical sensors. *Chem. Rev.*, **100**, 2537–2574.

31 Thomas, S.W., Joly, G.D., and Swager, T.M. (2007) Chemical sensors based on amplifying fluorescent conjugated polymers. *Chem. Rev.*, **107**, 1339–1386.

32 Alvarez, A., Costa-Fernández, J.M., Pereiro, R., Sanz-Medel, A., and Salinas-Castillo, A. (2011) Fluorescent conjugated polymers for chemical and biochemical sensing. *TrAC Trends Anal. Chem.*, **30**, 1513–1525.

33 Zhang, X., Wang, C., Wang, P., Du, J., Zhang, G., and Pu, L. (2016) Conjugated polymer-enhanced enantioselectivity in fluorescent sensing. *Chem. Sci.*, **7**, 3614–3620.

34 Zhu, C., Liu, L., Yang, Q., Lv, F., and Wang, S. (2012) Water-soluble conjugated polymers for imaging, diagnosis, and therapy. *Chem. Rev.*, **112**, 4687–4735.

35 Qian, C.-G., Zhu, S., Feng, P.-J., Chen, Y.-L., Yu, J.-C., Tang, X., Liu, Y., and Shen, Q.-D. (2015) Conjugated polymer nanoparticles for fluorescence imaging and sensing of neurotransmitter dopamine in living cells and the brains of zebrafish larvae. *ACS Appl. Mater. Interfaces*, **7**, 18581–18589.

36 Yang, G., Lv, F., Wang, B., Liu, L., Yang, Q., and Wang, S. (2012) Multifunctional non-viral delivery systems based on conjugated polymers. *Macromol. Biosci.*, **12**, 1600–1614.

37 Tzeng, S.Y. and Green, J.J. (2013) Subtle changes to polymer structure and degradation mechanism enable highly effective nanoparticles for siRNA and DNA delivery to human brain cancer. *Adv. Healthc. Mater.*, **2**, 468–480.

38 Gaylord, B.S., Heeger, A.J., and Bazan, G.C. (2003) DNA hybridization detection with water-soluble conjugated polymers and chromophore-labeled single-stranded DNA. *J. Am. Chem. Soc.*, **125**, 896–900.

39 Ding, L., Chi, E.Y., Schanze, K.S., Lopez, G.P., and Whitten, D.G. (2010) Insight into the mechanism of antimicrobial conjugated polyelectrolytes: lipid headgroup charge and membrane fluidity effects. *Langmuir*, **26**, 5544–5550.

40 Doré, K., Dubus, S., Ho, H.-A., Lévesque, I., Brunette, M., Corbeil, G., Boissinot, M., Boivin, G., Bergeron, M.G., Boudreau, D., and Leclerc, M. (2004) Fluorescent polymeric transducer for the rapid, simple, and specific detection of nucleic acids at the zeptomole level. *J. Am. Chem. Soc.*, **126**, 4240–4244.

41 Kim, H.J., Ishii, A., Miyata, K., Lee, Y., Wu, S., Oba, M., Nishiyama, N., and Kataoka, K. (2010) Introduction of stearoyl moieties into a biocompatible cationic polyaspartamide derivative, PAsp(DET), with endosomal escaping function for enhanced siRNA-mediated gene knockdown. *J. Controlled Release*, **145**, 141–148.

42 Philipp, A., Zhao, X., Tarcha, P., Wagner, E., and Zintchenko, A. (2009) Hydrophobically modified oligoethylenimines as highly efficient transfection agents for siRNA delivery. *Bioconjugate Chem.*, **20**, 2055–2061.

43 Convertine, A.J., Diab, C., Prieve, M., Paschal, A., Hoffman, A.S., Johnson, P.H., and Stayton, P.S. (2010) pH-responsive polymeric micelle carriers for siRNA drugs. *Biomacromolecules*, **11**, 2904–2911.

44 Richards Grayson, A.C., Doody, A.M., and Putnam, D. (2006) Biophysical and structural characterization of polyethylenimine-mediated siRNA delivery *in vitro*. *Pharm. Res.*, **23**, 1868–1876.

45 Khalil, I.A., Kogure, K., Akita, H., and Harashima, H. (2006) Uptake pathways and subsequent intracellular trafficking in nonviral gene delivery. *Pharmacol. Rev.*, **58**, 32.

46 Nel, A.E., Madler, L., Velegol, D., Xia, T., Hoek, E.M.V., Somasundaran, P., Klaessig, F., Castranova, V., and Thompson, M. (2009) Understanding biophysicochemical interactions at the nano-bio interface. *Nat. Mater.*, **8**, 543–557.

47 Tan, S.J., Jana, N.R., Gao, S., Patra, P.K., and Ying, J.Y. (2010) Surface-ligand-dependent cellular interaction, subcellular localization, and cytotoxicity of polymer-coated quantum dots. *Chem. Mater.*, **22**, 2239–2247.

48 Hillaireau, H. and Couvreur, P. (2009) Nanocarriers' entry into the cell: relevance to drug delivery. *Cell. Mol. Life Sci.*, **66**, 2873–2896.

49 Sahay, G., Alakhova, D.Y., and Kabanov, A.V. (2010) Endocytosis of nanomedicines. *J. Controlled Release*, **145**, 182–195.

50 Zhang, Z., Cao, W., Jin, H., Lovell, J.F., Yang, M., Ding, L., Chen, J., Corbin, I., Luo, Q., and Zheng, G. (2009) Biomimetic nanocarrier for direct cytosolic drug delivery. *Angew. Chem. Int. Ed.*, **48**, 9171–9175.

51 Shan, Y., Panday, N., Myoung, Y., Twomey, M., Wang, X., Li, W., Celik, E., Moy, V., Wang, H., Moon, J.H., and He, J. (2016) Scanning ion conductance microscopic study for cellular uptake of cationic conjugated polymer nanoparticles. *Macromol. Biosci.*, **16**, 599–607.

52 Twomey, M., Na, Y., Roche, Z., Mendez, E., Panday, N., He, J., and Moon, J.H. (2013) Fabrication of core–shell nanoparticles via controlled aggregation of semiflexible conjugated polymer and hyaluronic acid. *Macromolecules*, **46**, 6374–6378.

53 Varkouhi, A.K., Scholte, M., Storm, G., and Haisma, H.J. (2011) Endosomal escape pathways for delivery of biologicals. *J. Controlled Release*, **151**, 220–228.

54 Hafez, I.M. and Cullis, P.R. (2001) Roles of lipid polymorphism in intracellular delivery. *Adv. Drug Delivery Rev.*, **47**, 139–148.

55 Cullis, P.R., Hope, M.J., and Tilcock, C.P.S. (1986) Lipid polymorphism and the roles of lipids in membranes. *Chem. Phys. Lipids*, **40**, 127–144.

56 Min, S.-H., Kim, D.M., Kim, M.N., Ge, J., Lee, D.C., Park, I.Y., Park, K.C., Hwang, J.-S., Cho, C.-W., and Yeom, Y.I. (2010) Gene delivery using a derivative of the protein transduction domain peptide, K-Antp. *Biomaterials*, **31**, 1858–1864.

57 Baumhover, N.J., Anderson, K., Fernandez, C.A., and Rice, K.G. (2010) Synthesis and *in vitro* testing of new potent polyacridine–melittin gene delivery peptides. *Bioconjugate Chem.*, **21**, 74–83.

58 Sonawane, N.D., Szoka, F.C., and Verkman, A.S. (2003) Chloride accumulation and swelling in endosomes enhances DNA transfer by polyamine-DNA polyplexes. *J. Biol. Chem.*, **278**, 44826–44831.

59 Breunig, M., Hozsa, C., Lungwitz, U., Watanabe, K., Umeda, I., Kato, H., and Goepferich, A. (2008) Mechanistic investigation of poly(ethylene imine)-based siRNA delivery: disulfide bonds boost intracellular release of the cargo. *J. Controlled Release*, **130**, 57–63.

60 Meister, A. (1991) Glutathione deficiency produced by inhibition of its synthesis, and its reversal; applications in research and therapy. *Pharmacol. Ther.*, **51**, 155–194.

61 Lee, J., Twomey, M., Machado, C., Gomez, G., Doshi, M., Gesquiere, A.J., and Moon, J.H. (2013) Caveolae-mediated endocytosis of conjugated polymer nanoparticles. *Macromol. Biosci.*, **13**, 913–920.

62 Mendez, E. and Moon, J.H. (2013) Side chain and backbone structure-dependent subcellular localization and toxicity of conjugated polymer nanoparticles. *Chem. Commun.*, **49**, 6048–6050.

63 Vokatá, T., Twomey, M., Mendez, E., and Moon, J.H. (2015) Synthesis of biodegradable conjugated polymers with controlled backbone flexibility. *J. Polym. Sci., Part A: Polym. Chem.*, **53**, 1403–1412.

64 Vokatá, T. and Moon, J.H. (2013) Synthesis of phenyleneethynylene-doped poly(*p*-phenylenebutadiynylene)s for live cell imaging. *Macromolecules*, **46**, 1253–1259.

65 Twomey, M., Mendez, E., Manian, R.K., Lee, S., and Moon, J.H. (2016) Mitochondria-specific conjugated polymer nanoparticles. *Chem. Commun.*, **52**, 4910–4913.

66 Zintchenko, A., Philipp, A., Dehshahri, A., and Wagner, E. (2008) Simple modifications of branched PEI lead to highly efficient siRNA carriers with low toxicity. *Bioconjugate Chem.*, **19**, 1448–1455.

67 Lundberg, P., El-Andaloussi, S., Sütlü, T., Johansson, H., and Langel, Ü. (2007) Delivery of short interfering RNA using endosomolytic cell-penetrating peptides. *FASEB J.*, **21**, 2664–2671.

68 Meyer, M., Philipp, A., Oskuee, R., Schmidt, C., and Wagner, E. (2008) Breathing life into polycations: functionalization with pH-responsive endosomolytic peptides and polyethylene glycol enables siRNA delivery. *J. Am. Chem. Soc.*, **130**, 3272–3273.

69 Wang, G., Yin, H., Yin Ng, J.C., Cai, L., Li, J., Tang, B.Z., and Liu, B. (2013) Polyethyleneimine-grafted hyperbranched conjugated polyelectrolytes: synthesis and imaging of gene delivery. *Polym. Chem.*, **4**, 5297–5304.

70 Feng, X., Lv, F., Liu, L., Yang, Q., Wang, S., and Bazan, G.C. (2012) A highly emissive conjugated polyelectrolyte vector for gene delivery and transfection. *Adv. Mater.*, **24**, 5428–5432.

71 Wang, X., He, F., Li, L., Wang, H., Yan, R., and Li, L. (2013) Conjugated oligomer-based fluorescent nanoparticles as functional nanocarriers for nucleic acids delivery. *ACS Appl. Mater. Interfaces*, **5**, 5700–5708.

72 Yang, G., Yuan, H., Zhu, C., Liu, L., Yang, Q., Lv, F., and Wang, S. (2012) New conjugated polymers for photoinduced unwinding of DNA supercoiling and gene regulation. *ACS Appl. Mater. Interfaces*, **4**, 2334–2337.

73 Nie, C., Zhu, C., Feng, L., Lv, F., Liu, L., and Wang, S. (2013) Synthesis of a new conjugated polymer for DNA alkylation and gene regulation. *ACS Appl. Mater. Interfaces*, **5**, 4549–4554.

74 Zhao, Y., Yu, B., Hu, H., Hu, Y., Zhao, N.-N., and Xu, F.-J. (2014) New low molecular weight polycation-based nanoparticles for effective codelivery of pDNA and drug. *ACS Appl. Mater. Interfaces*, **6**, 17911–17919.

75 Zamore, P.D., Tuschl, T., Sharp, P.A., and Bartel, D.P. (2000) RNAi: double-stranded RNA directs the ATP-dependent cleavage of mRNA at 21 to 23 nucleotide intervals. *Cell*, **101**, 25–33.

76 Elbashir, S.M., Harborth, J., Lendeckel, W., Yalcin, A., Weber, K., and Tuschl, T. (2001) Duplexes of 21-nucleotide RNAs mediate RNA interference in cultured mammalian cells. *Nature*, **411**, 494–498.

77 Hannon, G.J. (2002) RNA interference. *Nature*, **418**, 244–251.

78 Bartel, D.P. (2009) MicroRNAs: target recognition and regulatory functions. *Cell*, **136**, 215–233.

79 Carthew, R.W. and Sontheimer, E.J. (2009) Origins and mechanisms of miRNAs and siRNAs. *Cell*, **136**, 642–655.

80 Castanotto, D. and Rossi, J.J. (2009) The promises and pitfalls of RNA-interference-based therapeutics. *Nature*, **457**, 426–433.

81 Kim, D.H. and Rossi, J.J. (2007) Strategies for silencing human disease using RNA interference. *Nat. Rev. Genet.*, **8**, 173–184.

82 Dorsett, Y. and Tuschl, T. (2004) SiRNAs: applications in functional genomics and potential as therapeutics. *Nat. Rev. Drug Discov.*, **3**, 318–329.

83 Chan, J.A., Krichevsky, A.M., and Kosik, K.S. (2005) MicroRNA-21 is an antiapoptotic factor in human glioblastoma cells. *Cancer Res.*, **65**, 6029.

84 Turchinovich, A., Weiz, L., Langheinz, A., and Burwinkel, B. (2011) Characterization of extracellular circulating microRNA. *Nucleic Acids Res.*, **39**, 7223–7233.

85 Xia, H., Mao, Q., Paulson, H.L., and Davidson, B.L. (2002) siRNA-mediated gene silencing *in vitro* and *in vivo*. *Nat. Biotechnol.*, **20**, 1006–1010.

86 Whitehead, K.A., Langer, R., and Anderson, D.G. (2009) Knocking down barriers: advances in siRNA delivery. *Nat. Rev. Drug Discov.*, **8**, 129–138.

87 Green, J.J., Langer, R., and Anderson, D.G. (2008) A combinatorial polymer library approach yields insight into nonviral gene delivery. *Acc. Chem. Res.*, **41**, 749–759.

88 Behlke, M.A. (2006) Progress towards *in vivo* use of siRNAs. *Mol. Ther.*, **13**, 644–670.

89 Akhtar, S. and Benter, I.F. (2007) Nonviral delivery of synthetic siRNAs *in vivo*. *J. Clin. Invest.*, **117**, 3623–3632.

90 Qin, X.-F., An, D.S., Chen, I.S.Y., and Baltimore, D. (2003) Inhibiting HIV-1 infection in human T cells by lentiviral-mediated delivery of small interfering RNA against CCR5. *Proc. Natl. Acad. Sci. USA*, **100**, 183–188.

91 Fisk, H.J. and Dandekar, A.M. (2004) Electroporation: introduction and expression of transgenes in plant protoplasts, in *Transgenic Plants: Methods and Protocols* (ed. L. Peña), Humana Press, Totowa, NJ, pp. 79–90.

92 Davey, M.R., Anthony, P., Power, J.B., and Lowe, K.C. (2005) Plant protoplasts: status and biotechnological perspectives. *Biotechnol. Adv.*, **23**, 131–171.

93 Silva, A.T., Nguyen, A., Ye, C., Verchot, J., and Moon, J.H. (2010) Conjugated polymer nanoparticles for effective siRNA delivery to tobacco BY-2 protoplasts. *BMC Plant Biol.*, **10**, 291.

94 Moon, J.H., Mendez, E., Kim, Y., and Kaur, A. (2011) Conjugated polymer nanoparticles for small interfering RNA delivery. *Chem. Commun.*, **47**, 8370–8372.

95 He, P., Hagiwara, K., Chong, H., Yu, H.-H., and Ito, Y. (2015) Low-molecular-weight polyethyleneimine grafted polythiophene for efficient siRNA delivery. *Biomed. Res. Int.*, **2015**, 9.

96 Feng, X., Lü, F., Liu, L., and Wang, S. (2013) MDR1-targeted siRNA delivery with cationic dendritic conjugated polymers. *Chin. Sci. Bull.*, **58**, 2762–2766.

97 Jiang, R., Lu, X., Yang, M., Deng, W., Fan, Q., and Huang, W. (2013) Monodispersed brush-like conjugated polyelectrolyte nanoparticles with efficient and visualized SiRNA delivery for gene silencing. *Biomacromolecules*, **14**, 3643–3652.

98 Ferris, D.P., Zhao, Y.-L., Khashab, N.M., Khatib, H.A., Stoddart, J.F., and Zink, J.I. (2009) Light-operated mechanized nanoparticles. *J. Am. Chem. Soc.*, **131**, 1686–1688.

99 Xing, C., Xu, Q., Tang, H., Liu, L., and Wang, S. (2009) Conjugated polymer/porphyrin complexes for efficient energy transfer and improving light-activated antibacterial activity. *J. Am. Chem. Soc.*, **131**, 13117–13124.

100 Yuan, Y., Liu, J., and Liu, B. (2014) Conjugated-polyelectrolyte-based polyprodrug: targeted and image-guided photodynamic and chemotherapy with on-demand drug release upon irradiation with a single light source. *Angew. Chem. Int. Ed.*, **53**, 7163–7168.

101 Seward, H.E. and Bagshaw, C.R. (2009) The photochemistry of fluorescent proteins: implications for their biological applications. *Chem. Soc. Rev.*, **38**, 2842–2851.

102 Riggsbee, C.W. and Deiters, A. (2010) Recent advances in the photochemical control of protein function. *Trends Biotechnol.*, **28**, 468–475.

103 Monti, S. and Manet, I. (2014) Supramolecular photochemistry of drugs in biomolecular environments. *Chem. Soc. Rev.*, **43**, 4051–4067.

104 Nussinovitch, U. and Gepstein, L. (2015) Optogenetics for *in vivo* cardiac pacing and resynchronization therapies. *Nat. Biotechnol.*, **33**, 750–754.

105 Li, S., Yuan, H., Chen, H., Wang, X., Zhang, P., Lv, F., Liu, L., and Wang, S. (2016) Cationic poly(p-phenylene vinylene) materials as a multifunctional platform for light-enhanced siRNA delivery. *Chem. Asian J.*, **11**, 2686–2689.

9

Conductive Polymer-Based Functional Structures for Neural Therapeutic Applications

Kenry and Bin Liu

National University of Singapore, Department of Chemical and Biomolecular Engineering, 4 Engineering Drive 4, Singapore, 117585, Singapore

9.1 Introduction

The nervous system is one of the most important physiological systems possessing several central and crucial functions, such as the proper regulation and maintenance of cognitive and neuronal functions [1–4]. Because of this, injuries to the nervous system, such as spinal cord and peripheral nerve injury, may result in tremendous negative biological consequences, including neurodegenerative disorders of the brain and spinal cord as well as peripheral nerve lesions. At the same time, the malfunctions of other physiological systems requiring close nervous controls may occur, leading to the possibility of lifelong disabilities [5, 6].

Numerous methods have been actively investigated for the medical therapy of damaged or injured nervous systems [7–10]. These strategies typically seek to direct and improve the regeneration of nerve fibers and axons, which will aid the repair of neuronal systems with associated functional recovery. One recent example includes neural therapy and regenerative medicine [9, 10]. As an increasingly explored alternative to conventional transplantation strategies, neural therapy, tissue engineering, and regenerative medicine aim to overcome the limitations of current clinical treatments for compromised tissue and organ functions [11]. To achieve this, the controlled interactions between synthetic biomaterials and functional structures with various biological entities are necessary. As a result, neural therapy and regenerative medicine emphasize on innovative and rational designs and development of novel synthetic biomaterials analogous to the native three-dimensional extracellular matrix (ECM) in regulating and achieving the desired cellular behavior and tissue progression [12–15].

Fundamentally, advanced neural therapies rely on the synergistic combination of biomaterials, drug delivery, and cell therapy strategies. A key ingredient that influences the outcome of neural therapy and functional recovery is the physicochemical properties, particularly the electrical property, of the synthetic conduits. This is because many neuronal cells and tissues in the human body are

Conjugated Polymers for Biological and Biomedical Applications, First Edition. Edited by Bin Liu

intrinsically responsive to electrical stimuli and are actively involved in the transmission of electrochemical signals in the nervous system. In fact, several studies have reported that electrical stimulation serves as an efficient cue to stimulate neuronal activities. As such, the development of stimulus-responsive biomaterials with tunable properties is highly desirable for successful neural therapies.

Recent years have seen the emergence of a new class of electroactive biomaterials, that is, electrically conductive polymers [16–19], capable of directly facilitating electrical, electromechanical, and/or electrochemical stimulations to neural cells. In fact, conductive polymeric materials have attracted tremendous interest in recent years due to their unique physiochemical properties [20]. These include excellent electrical conductivity, high conductivity-to-weight ratio, and outstanding manipulation of electrical stimulus. One of the most important features of conductive polymers is the possibility to tune their physicochemical characteristics for particular applications through surface functionalization with numerous biological moieties, such as enzymes, antibodies, and other biological molecules. These properties may be further modulated post-material synthesis via external stimuli, including pH and light [21, 22]. Conductive polymers may also be endowed with biodegradability and biocompatibility based on the same approach. Interestingly, the versatile conductive polymers may be synthesized into different functional structures, such as hydrogels, microfibers, and nanofibers. Consequently, conductive polymers and their associated functional structures are promising and may possess numerous potential bioapplications [16–18], notably in the different areas of neural therapy, such as electrostimulated drug delivery system, tissue engineering scaffolds, and neural implants (Figure 9.1).

9.2 Conductive Polymer-Based Functional Structures

9.2.1 Conductive Polymers

Since the first synthesis of electrically conductive polymers several decades ago [23], specifically in the mid-1970s, active research into conductive polymers have been increasingly carried out to unravel and exploit their unusual physicochemical features for a plethora of complex applications [18]. Conductive polymers are synthetic organic polymers possessing the characteristic physical and chemical properties of common polymers as well as the electrical and optical features of metals and inorganic semiconductors [16, 18, 19, 24, 25]. More clearly, conductive polymers exhibit a unique combination of positive features of both conventional polymers and metals, that is, ease of synthesis and flexibility in processing of organic polymers as well as the electronically active nature and charge-conducting capability similar to that of metals. Consequently, this class of polymeric materials has been widely utilized in the microelectronics industry for light-emitting diodes, batteries, photovoltaic devices, and electrochromic displays [26, 27]. Interestingly, more recently, conductive polymers

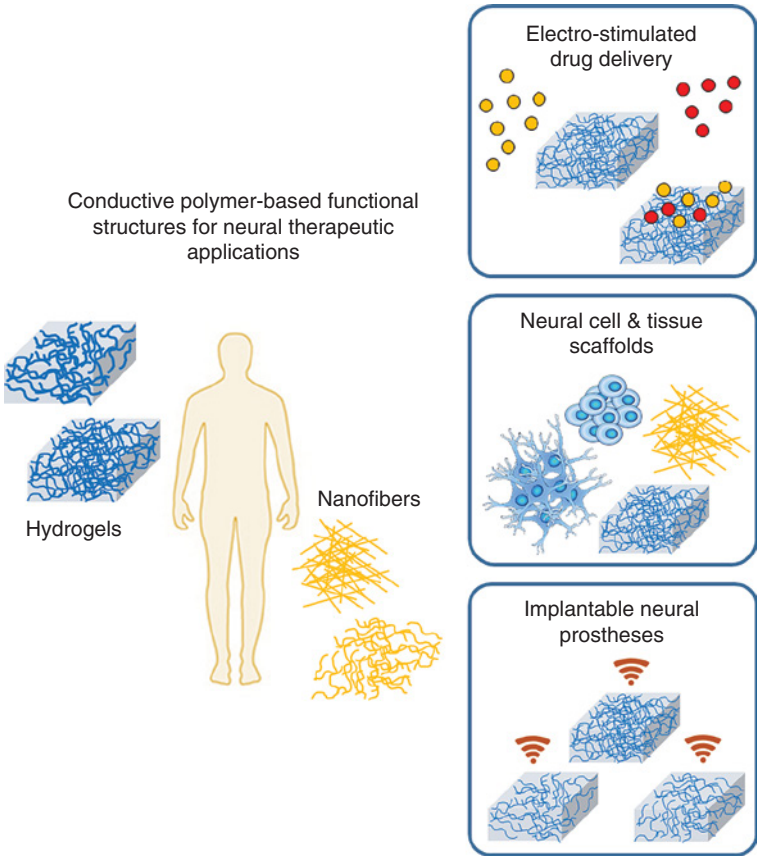

Figure 9.1 Conductive polymer-based functional structures, such as hydrogels and nanofibers, for various applications in neural therapeutic applications, specifically electrostimulated drug delivery, neural cell and tissue scaffolds, and implantable neural prostheses.

have also been increasingly exploited for biomedical applications after the identification of their biocompatibility with many biomolecules [28–32]. This is because it is possible to chemically functionalize conductive polymers with different physiologically relevant species to improve their overall functionality to meet the needs of specific bioapplications [19]. Moreover, the flexibility in processing conducting polymers and manipulating them into various forms, such as hydrogels and nanofibers, and numerous functional devices, including electrodes and implantable scaffolds, further render them attractive as constituents of advanced systems designed to communicate with electrically sensitive physiological tissues, such as in brains and nerves, for different therapeutic purposes. As such, the stimulus-responsive conductive polymers are highly promising in biomedicine.

Conductive polymers are also identified as conjugated polymers due to their unique backbone structure, which comprises alternating single and double C—C bonds (i.e., C═C) and loosely held electrons in their backbones [23, 33]

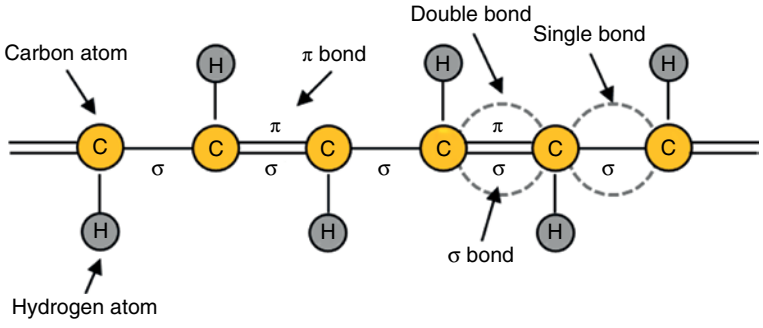

Figure 9.2 Conjugated backbone structure of conducting polymer comprising alternating single and double bonds, in which π bond facilitates the delocalization of electrons while σ bond maintains the strength of the chain.

(Figure 9.2). Structurally, the atoms in the polymeric chain are held together by σ bonds and every atom in the polymeric backbone is involved in a weaker π bond. The conjugated backbone possesses a high degree of π-orbital overlap. Conjugated polymers by themselves are generally not conductive and possess an overall electrically neutral system. To overcome the energy barrier and to endow conductivity to these polymeric structures, dopant molecules are introduced into conjugated polymers. In fact, it is through this doping process that conjugated polymers are imparted their highly conducting nature. In principle, doping refers to a charge transfer mechanism in which unbound charge carriers are generated through the addition or removal of electrons from the backbone of conjugated polymers. Through the doping process, the neutral polymer chains can either be reduced (i.e., n-type doping) or oxidized (i.e., p-type doping) to render them negatively or positively charged, respectively [16, 19, 33, 34]. When the polymer is subjected to reduction, an electron charge carrier is generated through the introduction of an electron in the conduction band. In contrast, a hole charge carrier is created through the removal of an electron from the valence band when the polymer is subjected to oxidation. Both n- and p-type dopants encompass a wide range of molecules, including small salt ions (e.g., Br^-, Cl^-, and NO_3^-) and large dopants (e.g., polymers, peptides, and hyaluronic acid) [16, 33]. The presence of the π-orbital system within the conjugated polymeric backbone further enhances the charge carrier mobility. The doping process is significantly dependent on various elements, such as charge carrier length, chain length, conjugation length, charge transfer to adjacent molecules, and so on.

In fact, the electrical conductivity of conductive polymers as well as their unique electronic properties, such as high electron affinity and low ionization potential, arise because of the existence of conjugated double bonds along their backbone. Because of this conjugated backbone system, conductive polymers are intrinsically rigid and display high stiffness. Conductive polymers possess hydrophobic backbone that facilitates the π–π stacking of the chains, owing to the presence of aromatic rings in the conjugated backbone.

The potential biomedical applications of electroactive conductive polymers have been widely reported, notably as neural probes and neural prostheses for

neural activity stimulation and modulation, neural sensing, as well as for electrostimulated controlled drug release and delivery, and neural tissue engineering [35–38]. An attractive feature of conductive polymers important for these bioapplications is their capability to regulate the cellular behaviors of various electrically sensitive cells, such as the cellular growth and migration of nerve cells, through controlled local delivery of electrical stimulation and modulation [39–41]. This is beneficial for the repair and regeneration of damaged tissues, highlighting the applicability of conductive polymers in neural tissue engineering and regenerative medicine. Separately, the introduction of biologically active dopants may endow conductive polymers the versatility of stimuli-responsive biomaterials as they are capable of providing both electrical and biological cues necessary for interfacing with neural cells and directing their cellular activities, underlining the great potential conductive polymers possess for neural therapeutic applications.

To date, the most commonly explored conductive polymers for biomedical applications are polypyrrole (PPy), polyaniline (PANi), and polythiophene (PTh) and its derivatives poly(3,4-ethylenedioxythiophene) (PEDOT) [42, 43] (Figure 9.3). Importantly, good biocompatibility of these conductive polymers with cells and tissues has been demonstrated in both *in vitro* and *in vivo* systems [28–32].

As one of the most extensively investigated conductive polymers, PPy is a synthetic polymer possessing many outstanding physicochemical qualities [44, 45]. These include high electrical conductivity and ion exchange capacity, excellent chemical and environmental stability, flexible preparation and facile surface modification, and good *in vitro* and *in vivo* biocompatibility [45–48]. Importantly, PPy is stimulus-responsive which means that its properties may be dynamically manipulated through the application of an electric potential. However, it is important to note that once synthesized, PPy is less processable, nonthermoplastic, highly brittle, mechanically rigid, and insoluble due to the high degree of conjugation in its molecular backbone [33, 49–51]. As such, PPy is more commonly optimized and modified into a more processable and manageable form before being used as a structural material. For example, the unmodified form of PPy may be doped with small molecules anions or functionalized with bioactive molecules to endow it with attractive qualities suitable for biomedical

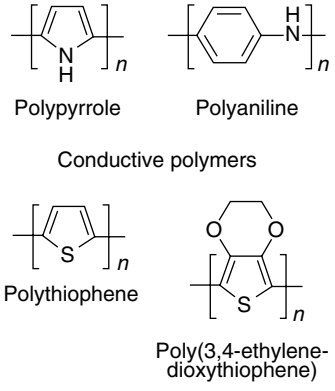

Figure 9.3 Common conductive polymers with their chemical structures, that is, polypyrrole (PPy), polyaniline (PAni), polythiophene (PTh), and poly(3,4-ethylenedioxythiophene) (PEDOT), used for biomedical applications, specifically for neural therapy and regenerative medicine.

applications. Because of this, the doped PPy has been explored in a wide range of bioapplications, notably in drug delivery systems, neural tissue engineering and regenerative medicine, and as a smart biomaterial for the construction of neural probes and nerve guidance channels [52–55].

After PPy, PANi is the next most widely examined conductive polymer. Commonly known as aniline black, PANi emerges as the acidic condition-induced oxidative product of aniline [19, 33]. Based on the degree of oxidation, PANi may exist in numerous forms, that is, the fully reduced leucoemeraldine base, the fully oxidized pernigraniline base, and the half-oxidized emeraldine base [19, 33]. Among these three forms, the emeraldine base is the most conductive and stable form of PANi. As a conductive polymer, PANi displays various advantages, including structural form diversity, high environmental stability, facile synthesis, and importantly, versatile capability to switch electrically between its different states of conductivity and resistivity through the doping/de-doping process [56, 57]. In comparison to that of PPy, the exploration into the potential biomedical applications of PANi has developed relatively slower. This is because the bioapplications of PANi are largely hampered by its low solubility, challenging processability, lack of flexibility, and nonbiodegradability. Nevertheless, with increasing evidences showing the ability of PANi and its derivatives in facilitating cell growth and differentiation as well as their good *in vitro* and *in vivo* biocompatibility [30, 31], PANi and its variants have been more actively explored for controlled drug delivery, neural probing, and tissue engineering applications.

In addition to PPy and PANi, there are several other conductive polymers that are recently investigated for biomedical applications, such as PTh and its derivative PEDOT [19, 33]. PEDOT, in general, possesses similar, if not more superior, properties as PPy. As one of the most attractive PTh derivatives, PEDOT has outstanding electrical conductivity, chemical stability, and versatility of side chain functionalization, supporting its practical utilization in biomedicine. PEDOT is typically prepared through the polymerization of the 3,4-ethylenedioxythiophene bicyclic monomer [19]. In contrast to PTh, PEDOT possesses lower band gap, oxidation and reduction potential, and improved overall properties, as across the 3- and 4-positions of its heterocyclic ring, there is a dioxyalkylene bridging group [19]. As a result, it displays better electrical conductivity and thermal stability as compared to PPy. For its potential bioapplications, PEDOT has been demonstrated as a smart material for biosensing, as an electroactive scaffold for cell culture, and as a neural electrode for neural probing [33]. Interestingly, PEDOT has been developed as an electroconductive biomaterial possessing direct and functional contact with the electrically active neural tissues and nervous system. For example, PEDOT has been polymerized around living neural cells for the fabrication of hybrid neural cell-templated conductive polymer electrode [58]. More clearly, PEDOT was utilized as a neural electrode by *in situ* polymerizing and interfacing it with the surrounding brain tissue. As the PEDOT filaments extended sufficiently far to breach the surrounding glial scar, sensitive contacts with the neuron plasma membrane could be formed. To enhance its biological interactions with neurons, PEDOT has been electrochemically

codoped with the biologically active nerve growth factor (NGF). For instance, PC-12 cells have been observed to adhere and possess extended neurites on the NGF-modified PEDOT film [46]. This strategy may be further explored for the rational design and development of conductive polymer-based materials capable of both electrical and biological stimulations for neural therapy applications.

9.2.2 Conductive Polymer-Based Hydrogels

Since their emergence in the early 1950s, polymer hydrogels have held great importance in the field of biomaterials [59]. In general, hydrogels are three-dimensional networks of polymers generated from highly hydrophilic cross-linked monomers. Hydrogels possess high water content and porous internal architecture and display high elasticity. Because of the imbibement of large quantity of water, hydrogels appear as elastic networks with their interstitial space effectively filled with water. This imbibed water may be free or bound. Interestingly, in response to external environmental stimuli, hydrogels can easily alter their shape and size either through the imbibement or through the expulsion of free water. Also, hydrogels are capable of imbibing other monomeric and polymerizable species into their interstices. These reactive species will then occupy the void spaces and interact with the pendant moieties or chain segments of the hydrogels. Hydrogels possess several intrinsic characteristics, such as soft elastomeric nature, low interfacial tension, and swelling capacity, which is beneficial across a wide range of biomedical applications, notably for drug delivery systems, tissue engineering, and regenerative medicine. Specifically, frictional and mechanical irritations may be minimized because of the soft elastomeric characteristic of hydrogels; protein adsorption, cell adhesion, and biofouling may be reduced because of the low interfacial tension; and permeability for low molecular weight metabolites and drug molecules may be increased due to the swelling capacity of hydrogels. Intriguingly, the use of hydrogels as synthetic scaffolds is even more attractive if they can be endowed with electrical properties such that they are capable of simultaneously mimicking the native ECM architecture and providing electrical stimulation for enhancing cell–cell communication.

In recent years, the polymerization of conductive polymers within the hydrogel networks has been shown to create a novel class of stimuli-responsive electroconductive hydrogels with tailored physicochemical properties [22]. This group of multifunctional hybrid networks has a three-dimensional hydrated architecture of the conventional insulating polymers as well as the electrical functionality of conductive electroactive polymers. Specifically, they merge the hydration, swellability, rapid ion mobility and small molecule diffusivity, and biocompatibility of the polymeric hydrogels with the outstanding electrical conductivity and electrochemical redox controlling capability of conductive polymers. In order to mimic the native ECM, the electroconductive hydrogels may be fabricated in various dimensions and functionalized with bioactive molecules. In addition, electroconductive hydrogels may assume the form in which the dominant or continuous constituent is the hydrogels within which the conductive polymers polymerize or vice versa.

Preparation of electroconductive hydrogels for biomedical applications has been increasingly reported recently [22]. For example, a polymeric composite formed from PPy and poly(methylmethacrylate) (PMMA) was synthesized as a controlled drug delivery vehicle [60]. In other instances, PPy was prepared electrochemically within the p(HEMA) hydrogels [61] or formed into a hydrogel in the presence of PMAS dopant [62]. Separately, a PPy-mucopolysaccharide electroconductive hydrogel composite had also been synthesized and demonstrated to be capable of releasing bound proteins when it was subjected to an electrical potential, rendering it attractive for controlled drug release and neural tissue engineering applications [63]. In addition to PPy, the conductive polymer PANi has also been used to form electroconductive hydrogels. For instance, an electrically conductive hydrogel composite was prepared by dispersing and polymerizing PANi nanoparticles in a polyvinyl pyrrolidone (PVP) hydrogel, followed by the irradiation-induced PVP cross-linking [22]. An electroactive PANi-polyacrylamide hydrogel composite was synthesized for controlled drug delivery through the electropolymerization of PANi within an insulating polyacrylamide hydrogel matrix with varying pore sizes [64]. In another example, a cross-linked polyelectrolyte hydrogel, poly(2-acrylamido-2-methyl propane sulfonic acid) (PAMPS), was used to trap PANi for the preparation of an electroconductive hydrogel network [65].

9.2.3 Conductive Polymer-Based Nanofibers

Besides electroconductive hydrogels, conductive polymers have also been widely explored for the fabrication of other functional structures, that is, nanofibers. In fact, conductive polymer-based nanofibers have been increasingly assessed as functional structures for the development of neural tissue engineering scaffolds owing to their capability to contract and relax with respect to applied electrical potential as well as to electrically stimulate neural cells and tissues. At the same time, the integration of neural tissues at the electrode interface can be improved with conductive polymer-based scaffolds. Among the many available conductive polymers, PPy and PANi are most commonly used for the fabrication of conductive polymer-based composite nanofibers. The physicochemical properties of these composite nanofibrous scaffolds may be further optimized through various post-synthesis treatments, such as blending, physical coating, and/or surface functionalization with biologically active species (e.g., growth factors and ECM molecules).

In a recent study, electrically conductive PPy/poly(DL-lactide-*co*-glycolide) (PPy/PLGA) nanofibers were fabricated for nerve tissue engineering [66]. It was observed that these composite nanofibers facilitated the growth and differentiation of rat pheochromocytoma PC-12 cells and improved the formation of neurites through electrical stimulation. In contrast to randomly oriented nanofibers, the aligned nanofibers induced the formation of cells with longer neurites. Furthermore, the surface of PPy could be modified with nerve growth factor in order to enhance the electrical and biological stimulations to neurons for the regeneration of axons [67]. Additionally, in a separate report, composite PANi/polyethylene oxide (PANI/PEO) nanofibers were synthesized for neural therapy [68].

9.3 Synthesis and Functionalization of Conductive Polymer-Based Functional Structures

9.3.1 Synthesis and Doping of Conductive Polymers

In general, conductive polymers may be synthesized through two primary routes, that is, chemical and electrochemical strategies [16, 19]. The synthesis of conductive polymers based on chemical strategy typically relies on either condensation polymerization or addition polymerization. In brief, during the chemical synthesis of conductive polymers, especially PPy, PANi, and PTh, the monomers of these polymers, namely pyrrole, aniline, and thiophene, respectively, are first oxidized to produce radical cations. These cations will react with neutral monomers to generate dimers (i.e., oligomer of two monomers) after oxidation and deprotonation. Following this, the oxidation of dimers will take place to yield dimeric radical cations. The combination of these dimeric radical cations with new neutral monomers can generate trimers (i.e., oligomers of three monomers). Through these continuous reactions, the polymeric chains grow, leading to the formation of conductive polymers.

Interestingly, chemical polymerization enables the creation of almost all types of conductive polymers in a scale-up throughput. It also affords numerous possible routes for the facile fabrication of a range of conductive polymers and their associated composites, the covalent modification of polymeric backbone, and importantly, the option for covalent functionalization after the synthesis of conductive polymers. For example, through chemical synthesis, common conductive polymers such as PPy can be easily combined with various polymers, including PMMA, poly(D,L-lactide) (PDLLA), polystyrene (PS), polyvinylchloride (PVC), and polyurethane (PU), to generate polymeric composites [19, 51, 69]. Nevertheless, the electrical conductivity of the chemically synthesized polymers is known to be lower than that of their counterparts prepared electrochemically. At the same time, the conductivity of the conductive polymers fabricated through chemical methods is highly dependent on several factors, such as solvent type and purity, relative concentrations of the oxidants and reagents, stirring rate, and reaction time and temperature, rendering the repeatability and reliability of chemical synthesis challenging [70–72].

The electrochemical polymerization of conductive polymers, in contrast, is typically carried out in the presence of electrical current applied via electrodes placed in a monomer-containing solution. In addition, this solution contains the solvent and doping agent necessary for the electrochemical synthesis of conductive polymers. As an electrical current is applied, the monomers deposit and undergo oxidization on the working electrode. Subsequently, they form insoluble polymer chains. The electrochemical synthesis of conductive polymers can be performed based on three distinct strategies, that is, galvanostatic, potentiostatic, and potentiodynamic polymerization strategies [19, 46, 73]. Through galvanostatic polymerization, the electrode current is controlled while the electrical potential of the electrodes changes. On the other hand, the electrode potential is controlled while the electrode current changes with the application of potentiostatic polymerization strategy. The potentiodynamic

electrochemical polymerization produces conductive polymers with different surface morphology as compared to those polymerized under galvanostatic and potentiostatic conditions.

In general, electrochemical polymerization affords the fast *in situ* deposition of conductive polymers. In addition, it is capable of generating thin film polymer with controlled morphology and thickness down to 20 nm, while polymers in thick film or powder form are typically obtained with chemical polymerization. Furthermore, as the properties of the fabricated polymeric film are highly dependent on the electrode system, deposition charge and time, the solvent, the doping agent, and the temperature, they may be tailored accordingly. Electrochemical synthesis also enables the concurrent entrapment of molecules and doping during the synthesis process. Unfortunately, the electrochemical polymerization of conductive polymers is only possible if their monomers can be oxidized under an electrical potential. As such, there is a limited number of dopants that can be used for electrochemical polymerization and thus, limited type of conductive polymers that can be electrochemically prepared, although common conductive polymers (e.g., PPy, PANi, PTh, and PEDOT) can either be chemically or electrochemically polymerized. Also, it may be challenging to remove the synthesized polymeric films from the electrodes and functionalize these conductive polymers covalently after the process of synthesis.

The electrical conductivity of the conductive polymers is typically endowed through a doping process in which charge carriers are introduced into the polymers [19]. This doping process normally takes place while the polymers are being synthesized and may be performed chemically or electrochemically. Nevertheless, electrochemical doping is necessary if the polymers are to be doped with biological molecules as most of these dopants are incapable of the redox chemistry required in chemical synthesis. The electrical conductivity of the doped polymers is strongly dependent on the amount and the different types of dopants used. These dopants behave distinctively and will affect the electrical conductivity and structural properties of the doped polymers differently.

9.3.2 Fabrication of Electroconductive Hydrogels

In general, electroconductive hydrogels can be synthesized based on two primary fabrication approaches. The first strategy relies on the chemical or electrochemical polymerization of conductive monomers in a presynthesized insulating hydrogel template to fabricate a hybrid polymeric network (Figure 9.4). The reactive monomers may comprise a mixture of the precursors of both hydrogels and conductive polymers. Together with thermal- or photo-labile free radical initiators, these reactive monomers can be mixed into a single prepolymer cocktail. Subsequently, this cocktail may be subjected to various treatments to generate different hydrogel functional forms, such as prepared as microspheres, cast into thin film, spun as nanofibers, or spun-applied to electrodes. In electrochemical polymerization, the hydrogel form (e.g., microsphere, film, or fiber) has to be applied to either a metallic or semiconducting electrode. An appropriate potential with respect to a reference electrode will then be applied to this electrode to begin the polymerization process. In contrast to electrochemical polymerization,

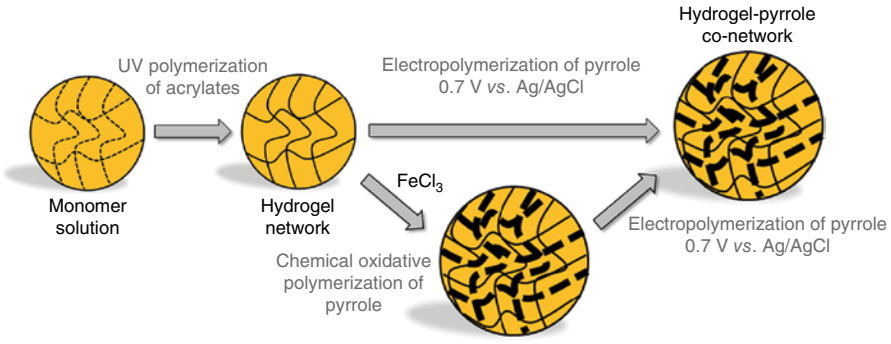

Figure 9.4 General strategies for the synthesis of electroconductive polymer-based hydrogels based on electrochemical and chemical oxidative polymerization approaches.

substrate is typically not required in the chemical oxidative polymerization of hydrogel. In fact, this process can advance as long as the hydrogel form is immersed in an appropriate solution consisting of initializing oxidants, such as $FeCl_3$.

The second electroconductive hydrogel fabrication strategy blends the precursor monomers and subjects them to a step-wise or simultaneous polymerization to generate the single component conductive hydrogel. The self-assembly of the conjugated polymeric chains or introduction of chemically cross-linkable and water soluble moieties in the polymeric backbone plays a crucial role in this fabrication strategy. Importantly, with this second synthetic approach, conductive polymers serve as the continuous constituent in the hydrogel network. Ultimately, the electroconductive hydrogel network comprises a conventional hydrogel matrix physically entrapping the conductive polymer chains.

9.3.3 Electrospinning of Conductive Polymer-Based Nanofibers

Electrospinning is one of the most established and widely used strategies for the synthesis of micro- and nanoscale fibers [74, 75]. In fact, it is a robust and versatile electrostatic-based technique that enables the facile synthesis of fibers from a wide range of polymers, with diameters spanning from a few micrometers down to 10 nm [76]. Based on this strategy, a high-voltage electrostatic field is first generated between a syringe nozzle and a counter electrode. As the polymer solution is ejected from the syringe, a charged jet is drawn from this solution. Subsequently, the evaporation of solvent occurs as the jet accelerates toward a collector counter electrode. This eventually results in the formation of continuous nanofibers on the grounded target. Interestingly, using electrospinning, synthetic scaffolds analogous to ECM can be prepared easily. These scaffolds comprise nanofibers with high surface area-to-volume ratio and excellent mechanical and structural property. Importantly, they can support the attachment and growth of cells, rendering these nanofibrous scaffolds attractive for biomedical applications in neural tissue engineering and regenerative medicine.

Conductive polymers have been actively assessed as the base materials for the fabrication of nanofibers through electrospinning [66, 74, 76, 77]. In general, sole conductive polymers may be electrospun by themselves. Nevertheless, this process

needs the use of conductive polymers that are soluble in organic solvents (e.g., PPy) [74]. The synthesized nanofibers may not be applicable for biological utilizations due to the chemical conditions (e.g., dissolution in hot sulfuric acid and doping) required for the preparation of the conductive polymer nanofibers (e.g., PANi nanofibers). As such, conductive polymers tend to be blended with spinnable polymers as carrier materials (e.g., PS, poly(ethylene oxide), and poly(vinyl cinnamate)) before the process of electrospinning for the synthesis of polymeric composite nanofibers [74]. Another commonly adopted strategy is to coat conductive polymers on the electrospun nanofibers [78]. For example, fibroin fibers were coated with PPy and the resultant composite nanofibers were capable of facilitating the adherence and growth of fibroblasts and mesenchymal stem cells. Separately, PPy-coated PLGA nanofibers were prepared and demonstrated to support the proliferation and differentiation of hippocampal neurons and PC-12 cells [66].

9.3.4 Functionalization and Modification of Conductive Polymer-Based Functional Structures

The design and development of biologically active surfaces is one of the most important endeavors in the field of biomaterials. This is because the interactions between biological systems and biomaterials normally occur at the interface. Consequently, various techniques for surface modification, functionalization, and ligand immobilization have been established for generating biomaterial surface having bioactive species that can facilitate the interactions of biomaterials with a wide variety of biomolecules and cells. Numerous attempts have been made to optimize and enhance the physicochemical properties (e.g., conductivity, hydrophobicity, surface roughness, degradability, and biocompatibility) of conductive polymer-based functional structures for neural therapeutic applications. One of the primary modification strategies exploits the incorporation of biologically active dopant molecules, such as proteins, peptides, and ECM molecules, into the conductive polymer-based structures to endow them with specific features or functionalities, including higher affinity for binding with cell adhesion moieties to enhance the adhesion, growth, and differentiation of neural cells on these functional structures.

The functionalization of conductive polymers may generally be realized through the same doping process that endows the conductive polymers their conductivity. This may be typically exploited utilizing a wide range of charged bioactive dopant molecules, such as collagen, chitosan, dextran sulfate, heparin, hyaluronic acid, and growth factors [16, 17]. Nevertheless, it is important to highlight that several drawbacks, including low loading capacity, are evident with the use of doping. In addition, depending on the type of biological dopants, biomolecule doping of conductive polymers may induce certain effects on their physical properties, such as changes in the overall surface roughness of the doped polymeric structures. To negate these constraints, surface immobilization of biomolecules on conductive polymers has recently been exploited. Generally, the surface immobilization of biological moieties on conductive polymer-based functional structures may be realized through several ways, notably, physical adsorption, entrapment, and covalent binding [33].

Biomolecules may be functionalized on the surface of conductive polymers through physical adsorption. This may be achieved through the static interactions between the charged biomolecules and polymer matrix, biomolecules may physically adsorb on the polymer surface. Notwithstanding its simplicity, the physical adsorption of biomolecules is highly sensitive to pH, resulting in the compromised conductivity of the functionalized polymeric structures. Separately, biomolecules may also be physically entrapped within the conductive polymers. This may be realized by mixing the functionalizing biomolecules with the monomer, solvent, and dopant prior to the synthesis process, and then subjecting the mixture to electrochemical polymerization, upon which the functionalizing biomolecules around the electrode will be encapsulated into the growing polymer. This approach is primarily aimed at large biomolecules (e.g., DNA and enzymes) as once entrapped, these biomolecules may not be able to easily escape from the encapsulating polymers.

In addition to physical adsorption and entrapping, biologically active species may also be covalently grafted to the monomer of conductive polymers. Through covalent bonding, the long-term stability of the functionalized conductive polymers will be enhanced as the biological moieties will attach strongly to the polymers and may not be detached easily. Nevertheless, as chemical reactions form an integral part in covalent binding, the activity and performance of the covalently modified conductive polymers may be affected, unlike those of functional structures modified based on the simple physical adsorption and entrapping processes, which permit the introduction of biomolecules in the absence of chemical reaction.

Lastly, the modification of conductive polymer-based functional structures may be achieved via surface topographical patterning. It is well known that topographical characteristics, such as surface roughness, of cellular and tissue scaffolds play a significant role in influencing numerous cellular behaviors, especially adhesion, proliferation, and differentiation. As such, it is anticipated that with appropriate surface topographical modifications, the desired physical guidance of axonal orientation and direction vital for neural tissue engineering and regenerative medicine can be realized.

9.4 Applications of Conductive Polymer-Based Functional Structures for Neural Therapies

9.4.1 Electrostimulated Drug Delivery

Electrostimulated drug delivery refers to a programmed drug release mechanism controlled through the application of an electrical voltage or current [79, 80]. In recent years, conductive polymer-based functional structures have been increasingly exploited for controlled drug released and delivery. This is because conductive polymer-based structures generally have high porosity and delocalized charge centers which, in response to reduction or oxidation, enable counter-ion diffusion and electromigration within the polymer body [81–83]. Combined with biologically active drug molecules, the loaded electroactive polymer systems can be engineered such that the release, delivery, exchange, or movement gating

of specific drug molecules is achieved in a programmed fashion or on demand via electrostimulation, which may take the form of electroactive gating or electropumping [84]. Electroactive gating may be established when the oxidation state of the polymeric membrane is varied while a constant electric field is maintained on its two sides. In contrast, when the drug concentration accumulates within the polymeric membrane while on either side of the membrane a concentration gradient remains constant, electropumping may be realized.

Conductive polymers are typically oxidized and possess a positively charged backbone after polymerization. To maintain electroneutrality, the positive charges have to be balanced with anions. Because of this, the negatively charged anionic drug molecules can be simply introduced into the conductive polymers during the synthesis and polymerization processes. Nevertheless, the backbone of the conductive polymers becomes neutral upon reduction, triggering the release of the anionic drug molecules. Interestingly, the positively charged cationic drug molecules may also be loaded into the conductive polymer network. This may be realized by utilizing the hydrophobic and electrostatic interactions between the conductive polymer backbone, the cationic drug, and the anionic counter ion. Otherwise, the positively charged drug molecules may be introduced into the conductive polymers after the synthesis process, specifically after the reduction of the conductive polymer network. In fact, conductive polymers lose their positive charges when they are reduced. As a result, the conductive polymer backbone attracts the cationic drugs and these positively charged molecules interact with the anionic counter ions that have been entrapped physically within the polymeric matrix. The drug loading efficiency of the conductive polymers is strongly dependent on the molecular weight of the counter ions. More clearly, when the counter ions possess a large molecular weight, a high drug loading capacity may be realized, and vice versa.

Nonetheless, it is important to note that the development and use of individual pristine conductive polymers, such as PPy, PANi, and PTh, as drug delivery platforms are hampered by numerous limitations. These include intrinsically low drug loading capacity, passive diffusion-induced and anion exchange-induced loss of loaded drug molecules, low oxidative stability of pristine conductive polymers, low diffusion coefficients of the loaded and released drug molecules, reduced drug eluting capability, and the unpredictable nature and poor control of the drug binding and release kinetics. As such, for electrostimulated drug release to be effectively performed beyond small drug molecules under low concentrations, conductive polymers with enhanced molecular porosity and improved diffusion coefficient for counter anions are needed. To address these shortcomings, electroconductive hydrogels capable of rapid switching have been developed. Electroconductive hydrogels may generally experience physical or chemical transitions upon the application of electric field and therefore, may serve as responsive drug delivery vehicles. The backbone charge and the conductive polymer scaffold volume may be easily tuned by varying the redox state of the conductive polymer. Consequently, with this mechanism, drug molecules can be delivered in a controlled manner. Importantly, with electroconductive hydrogel, the electrostimulated drug delivery system possesses high molecule loading capacity and is capable of operating with low voltage actuation.

9.4.2 Neural Cell and Tissue Scaffolds for Neural Regeneration

Neural tissue engineering and regenerative medicine seek to replace, repair, and/or reconstruct the compromised, damaged, or lost neural tissue functions [9–11]. To this end, the effective repair and/or regeneration of functional neuronal tissues and organs rely on the controlled and synergistic interplay between neural cells, growth factors, and scaffolds to promote and direct neuronal cell outgrowth and differentiation. More specifically, in neural tissue engineering, three-dimensional functional tissues suitable for implantation are generated through the seeding and regeneration of neural cells on synthetic biomimetic scaffolds. Interestingly, among these integral components of neural tissue engineering, neural cell and tissue scaffolds are arguably the easiest to control and modify [12, 14]. An ideal cell and tissue scaffold for neural tissue engineering ought to possess the structural and biological functions similar to those of the native physiological ECM. This scaffold has to be capable of manipulating cellular behaviors in directing the specific repair and regeneration of target tissues and organs. Furthermore, the scaffold should possess high mechanical strength and flexibility to provide mechanical support for proliferating neuronal cells and, at the same time, be able to provide physiological signals to guide axonal growth. Also, tissue engineering scaffold should possess high porosity with large surface area-to-volume ratio, excellent biodegradability, and biocompatibility, for effective cell and tissue regeneration [85].

In general, successful neurite outgrowth and axonal elongation for an effective neural regeneration is significantly dependent on numerous factors, such as cellular microenvironment, scaffold morphology and topography, and external stimulations (e.g., mechanical and electrical stimulations). Patterned ECM nanostructures have been shown to be capable of providing directional cues [86]. However, the neural regeneration process *in vivo* may be limited as the therapeutic levels of growth stimulating signals may not be maintained. Separately, axonal growth has been promoted through the delivery of growth factors, including nerve growth factor and brain-derived neurotrophic factor, to the injury sites, and through the surface functionalization of biomaterial-based scaffolds using proteins and peptides [87, 88]. Nonetheless, the use of these approaches present several limitations as the molecular bioactivity may not be well retained and the localized delivery to the injury sites may not be well controlled. Electrical stimulation has been reported to be an effective cue for promoting cell proliferation and differentiation and to improve the overall neural regeneration process [24]. This is because specific physiological functions, such as signaling of the nervous system, are heavily regulated through bioelectricity. As a result, the electrically conductive polymers have emerged as a suitable candidate for the construction of synthetic bioactive scaffolds for neural tissue engineering.

In fact, it is anticipated that conductive polymer-based scaffolds are able to electrically stimulate electrosensitive cells, modulate certain cellular behaviors, and regulate the process of cellular regeneration. This has also been demonstrated by several studies, in which conductive polymers have been observed to exert encouraging cellular influence in facilitating and modulating the regeneration of certain electrically sensitive tissues, including nerves [24, 77]. Among all pristine

conductive polymers, PANi and its derivatives have been the most actively investigated polymers for tissue engineering and regenerative medicine. While conductive polymers hold numerous attractive features for the construction of tissue engineering scaffolds capable of electrical stimulation, their use is still hampered by primary concerns regarding their non-negligible cytotoxicity and poor degradation characteristics.

To address these concerns, conductive polymers have been increasingly integrated into a cross-linked porous hydrogel matrix that serves to mitigate the overexposure of conductive polymers to cells [69]. In fact, the combination of conductive polymers and porous hydrogel matrix possesses great potential for neural regenerative medicine. Together, conductive polymers serve to provide electrical stimuli required by the electroresponsive neural cells and tissues while the preformed hydrogel network offers a hydrated and porous environment needed for nutrient exchange as well as the mechanical integrity to support cell adhesion and proliferation. Consequently, increasing efforts have been directed to developing electroconductive hydrogels to promote neuronal cell and tissue growth and reconstruction, including axonal outgrowth for the efficient regeneration of peripheral nerve in the nervous system. For example, PANi has been synthesized within polyethyleneglycol diacrylate (PEGDA) for the formation of superporous PANi/PEGDA hybrid scaffolds with high *in vitro* stability and decreased cytotoxicity as well as capable of offering intrinsic signaling necessary for stimulating neurite outgrowth [89]. More clearly, PANi was precipitated *in situ* in PEGDA solution and then cross-linked for the fabrication of electroconductive PANi/PEGDA macroporous hydrogels to facilitate nerve regeneration process. In another example, PANi was mixed with poly(L-lactic acid) (PLLA) and then electrospun to fabricate composite PLLA/PANi nanofiber-based scaffolds for the *in vitro* electrical stimulation of nerve stem cells [77]. Besides, conductive polymers have also been incorporated into other chemically cross-linked hydrogel, such as alginate, gelatin, poly(hydroxyethylmethacrylate) (pHEMA), polyacrylamide (PAAM), poly(2-acrylamido-2-methylpropanesulfonic acid) (PAMPS), polyacrilic acid (PAA), polyvinylpyrrolidone (PVP) [65, 90–94], to generate composite polymeric scaffolds for neural tissue engineering and regenerative medicine.

9.4.3 Implantable Biosensors and Neural Prostheses

The applications of both short- and long-term implantable biosensors and prostheses are highly useful for a wide range of clinical utilities [73]. In fact, the acquisition of real-time metabolic and physiological data is important for evaluating the immediate and long-term impacts of clinical and personalized medicine. For instance, an implantable biosensor capable of detecting the existence and quantifying the real-time concentration of neural disease-related biomolecules would be of significant interest and useful for neural therapy, in particular for early neural disease detection and outcome prediction of patient treatments. Because of this, implantable biosensors capable of detecting and quantifying plethora of physiologically relevant metabolites and biomarkers have been actively developed. In addition to implantable biosensors, another

class of synthetic devices that possesses great potential in neural therapeutic applications is neural prosthesis. In general, neural prostheses are assistive devices engineered to restore damage or lost neural functions. These implanted devices rely significantly on efficient electrical communication with the central nervous system for the effective executions of their functions. Some examples of neural prostheses include prostheses for artificial limb motor control, optoelectronic prostheses for damaged visual restoration, artificial cochlear for auditory sensory function restoration, and neurostimulators for pain relief and bladder control [95–98].

For these artificial implantable medical devices, a crucial factor affecting their clinical effectiveness is their ability to realize effective long-term implantation under physiological conditions within the body. However, numerous challenges lie ahead to hamper this implementation. For example, for implantable biosensors, the electrode surfaces play an important role in maintaining the sensor specificity as they serve as the active sites for the immobilization of specific enzymes. The immobilized enzymes will catalyze the formation of electrochemically active species from the target biomolecules necessary for biosensing. As such, the electrode surfaces need to be resistant to unwanted biomolecule adsorption, denaturation, and biofouling. This is because all these nonspecific biological events will induce an appreciable decrease in the sensor current response and reduced signal-to-noise ratio [99]. To address this issue, hydrogels have been exploited as biosensor coating materials. For instance, considerable resistance to biomolecule adsorption has been reported with the use of a hydrogel conetwork poly(HEMA-*co*-PEGMA-MPC) synthesized from biomimetic and highly hydrophilic monomers [22]. In fact, the hydration features, rigidity, and mechanical strength of the eventual polymerized hydrogels may be tailored by tuning the individual monomer ratios in the hydrogel composition. This is crucial as, with appropriate hydration and elastic modulus similar to those of living tissues, fibrous encapsulation may be reduced once the hydrogel-coated assistive devices are implanted. Nevertheless, these hydrogels display high interfacial electrical impedances as, while they are ionically conductive, they are not electronically conductive. Crucially, both implantable biosensors and neural prosthetic devices in the peripheral and central nervous system will benefit from an electrode-to-tissue interface having low interfacial impedance and high electrical mobility. As a result, hydrogel networks have been increasingly blended with conductive polymers in engineering stimuli-responsive, multifunctional electroconductive hydrogels with reduced interfacial impedances. PPy is one of the most exploited pristine conductive polymers for this purpose due to its ease of polymerization through chemical oxidation or electropolymerization, and biocompatibility [35, 36]. In fact, PPy has been widely blended with acrylate-based hydrogel to form a conetwork of electroconductive hydrogel.

As compared to the use of conductive polymer PPy on its own, the addition of PPy into a hydrogel network provides numerous advantages. This is because the pristine conductive polymer possesses a switching speed which is dependent on its intercalation into a semi-crystalline polymer as well as the counter anion dopant diffusivity. Furthermore, the conductive polymer on its own displays

rather weak mechanical properties and may simply break apart or detach from the metal surface easily when subjected to external forces. This is crucial because damaging forces may always present when the electrodes are first implanted into the neural tissues or when they are in contact with the neural tissues over time due to micromotions. Consequently, with the incorporation of conductive polymer, for example, PPy, within a hydrogel matrix, the new hybrid electroconductive hydrogel will possess excellent electrochemistry, low electrical impedance, outstanding mechanical strength, and low cytotoxicity. In fact, with these attractive features, electroconductive hydrogels comprising a poly(HEMA)-based hydrogel component and a PPy conductive polymer conetwork have been widely exploited for the surface modification of long-term implantable neural electrodes and prosthetic devices.

9.5 Summary and Outlook

Neural cells and tissues in the nervous systems are sensitive and responsive to electrical charge or current. This may be seen from the integral role played by the action potential generated at the synapse in regulating neural communication. This suggests that a conductive neural scaffold capable of introducing electrical stimuli may be highly relevant and useful for facilitating neurite outgrowth and nerve regeneration. Because of this, conductive polymers and their associated functional structures have emerged as suitable electroactive biomaterials for numerous neural therapeutic applications. While conductive polymers, notably PPy, PANi, and PTh, possess numerous outstanding physicochemical properties, such as high electrical conductivity, excellent chemical stability, versatile surface chemistry and ease of modification, and good biocompatibility, their biomedical utilizations may be limited by their hydrophobicity, mechanical brittleness, poor processability, and nondegradability. To overcome these shortcomings, conductive polymers have often been mixed with degradable polymers, such as chitosan, collagen, gelation, heparin, polyurethane, poly(lactide-*co*-glycolide), polylactide (PLA), polycaprolactone (PCL), and poly(lactide-*co*-polycaprolactone) (PLA-co-PCL), to fabricate polymeric blends and composites with enhanced physicochemical features [18], particularly increased solubility and mechanical strength.

The incorporation of conductive polymers within a prefabricated hydrophilic hydrogel network has also been extensively investigated as another alternative to circumvent the drawbacks of individual pristine conductive polymers. In fact, the electroconductive hydrogels represent unique smart multifunctional biomaterials with tailored architectures which combine and retain the responsive attributes of both electroactive polymers and hydrophilic hydrogels. With their low interfacial impedance, excellent electrical stimulation, and low voltage actuation, electroconductive hydrogels are capable of controlled release of drug biomolecules on demand, directing cell alignment, proliferation, and differentiation. Specifically, the introduction of conductive polymer-based functional structures into biological systems is promising as conductive hydrogel- or conductive nanofiber-based scaffolds can serve as the physical substrates for cell attachment, growth, and regeneration. More importantly, it permits the controlled and

localized delivery of electrical stimuli to specific injury sites in order to promote cell growth and tissue repair. With their considerable *in vivo* biocompatibility, electroconductive hydrogels are highly desirable for use in implantable biosensors and neural prosthetic devices, such as deep brain stimulation electrodes.

Despite all the promising signs, it is important to note that there exist several challenges that need to be overcome before conductive polymer-based functional structures may find widespread neural therapeutic applications and even commercialization. First, more efforts are needed to enhance the intrinsic physicochemical features and properties of individual pristine conductive polymers. This could be realized through the design and development of a novel class of conjugated polymers possessing high solubility, excellent electron transport, and side functional groups that may be utilized as cross-linking sites, modified with specific bioactive molecules, or functionalized with biodegradable linkers. Second, while conductive polymer-based functional structures have been shown to possess tremendous potential in numerous neural therapeutic applications, a majority of these studies have been conducted in an *in vitro* setting. It is crucial to highlight that the *in vitro* device functions and performances may be significantly different from those under *in vivo* condition. As such, more systematic and robust *in vivo* investigations on the feasibility of conductive polymers and their associated functional structures for neural therapeutic applications are necessary. Important parameters that require special attention in these studies include the *in vivo* biodegradability, cytotoxicity, and biocompatibility of conductive polymers and their functional structures. Only when the relevant observations and parameters have been established, the potential applications of conductive polymers for neural therapy may be confirmed.

In summary, conductive polymers and their associated functional structures, such as hydrogels and nanofibers have shown great potentials in different areas of neural therapeutic applications, notably in electrostimulated drug delivery, neural tissue engineering and regenerative medicine, and implantable biosensors and neural prostheses. Overall, with major challenges anticipated to be addressed in the near future and considering the vast potential of conductive polymer-based functional structures, we foresee an exciting prospect for the utilization of conductive polymers for neural therapeutic applications and commercialization.

References

1 Franklin, R.J. and Blakemore, W.F. (1990) The peripheral nervous system–central nervous system regeneration dichotomy: a role for glial cell transplantation. *J. Cell Sci.*, **95** (2), 185.

2 Huebner, E.A. and Strittmatter, S.M. (2009) Axon regeneration in the peripheral and central nervous systems. *Results Probl. Cell Differ.*, **48**, 339.

3 Bougea, A., Anagnostou, E., Konstantinos, G., George, P., Triantafyllou, N., and Kararizou, E. (2015) A systematic review of peripheral and central nervous system involvement of rheumatoid arthritis, systemic lupus erythematosus, primary Sjorgen's syndrome, and associated immunological profiles. *Int. J. Chronic Dis.*, **2015**, 11.

4 Reinhold, A.K. and Rittner, H.L. (2017) Barrier function in the peripheral and central nervous system—a review. *Eur. J. Physiol.*, **469** (1), 123.

5 Choi, D.W. (1988) Glutamate neurotoxicity and diseases of the nervous system. *Neuron*, **1** (8), 623.

6 Lee, H.-Y., Fu, Y.-H., and Ptáček, L.J. (2015) Episodic and electrical nervous system disorders caused by nonchannel genes. *Annu. Rev. Physiol.*, **77** (1), 525.

7 Sharifi, M.S. (2013) Treatment of neurological and psychiatric disorders with deep brain stimulation; raising hopes and future challenges. *Basic Clin. Neurosci.*, **4** (3), 266.

8 Gessler, D.J. and Gao, G. (2016) Gene therapy for the treatment of neurological disorders: metabolic disorders, in *Gene Therapy for Neurological Disorders: Methods and Protocols* (ed. F.P. Manfredsson), Springer, New York, p. 429.

9 Schmidt, C.E. and Leach, J.B. (2003) Neural tissue engineering: strategies for repair and regeneration. *Annu. Rev. Biomed. Eng.*, **5** (1), 293.

10 Gu, X., Ding, F., and Williams, D.F. (2014) Neural tissue engineering options for peripheral nerve regeneration. *Biomaterials*, **35** (24), 6143.

11 Langer, R. and Vacanti, J.P. (1993) Tissue engineering. *Science*, **260** (5110), 920.

12 Subramanian, A., Krishnan, U.M., and Sethuraman, S. (2009) Development of biomaterial scaffold for nerve tissue engineering: biomaterial mediated neural regeneration. *J. Biomed. Sci.*, **16** (1), 108.

13 O'Brien, F.J. (2011) Biomaterials & scaffolds for tissue engineering. *Mater. Today*, **14** (3), 88.

14 Ai, J., Kiasat-Dolatabadi, A., Ebrahimi-Barough, S., Ai, A., Lotfibakhshaiesh,N., Norouzi-Javidan, A., Saberi, H., Arjmand, B., and Aghayan, H.R. (2014) Polymeric scaffolds in neural tissue engineering: a review. *Arch. Neurosci.*, **1** (1), 15.

15 Sensharma, P., Madhumathi, G., Jayant, R.D., and Jaiswal, A.K. (2017) Biomaterials and cells for neural tissue engineering: current choices. *Mater. Sci. Eng. C*. doi: 10.1016/j.msec.2017.03.264

16 Guimard, N.K., Gomez, N., and Schmidt, C.E. (2007) Conducting polymers in biomedical engineering. *Prog. Polym. Sci.*, **32** (8–9), 876.

17 Bendrea, A.-D., Cianga, L., and Cianga, I. (2011) Review paper: progress in the field of conducting polymers for tissue engineering applications. *J. Biomater. Appl.*, **26** (1), 3.

18 Guo, B., Glavas, L., and Albertsson, A.-C. (2013) Biodegradable and electrically conducting polymers for biomedical applications. *Prog. Polym. Sci.*, **38** (9), 1263.

19 Balint, R., Cassidy, N.J., and Cartmell, S.H. (2014) Conductive polymers: towards a smart biomaterial for tissue engineering. *Acta Biomater.*, **10** (6), 2341.

20 Shirakawa, H. (2001) The discovery of polyacetylene film: the dawning of an era of conducting polymers. *Synth. Met.*, **125** (1), 3.

21 Huang, L., Zhuang, X., Hu, J., Lang, L., Zhang, P., Wang, Y., Chen, X., Wei, Y., and Jing, X. (2008) Synthesis of biodegradable and electroactive multiblock polylactide and aniline pentamer copolymer for tissue engineering applications. *Biomacromolecules*, **9** (3), 850.

22 Guiseppi-Elie, A. (2010) Electroconductive hydrogels: synthesis, characterization and biomedical applications. *Biomaterials*, **31** (10), 2701.

23 Shirakawa, H., Louis, E.J., MacDiarmid, A.G., Chiang, C.K., and Heeger, A.J. (1977) Synthesis of electrically conducting organic polymers: halogen derivatives of polyacetylene, (CH). *J. Chem. Soc., Chem. Commun.*, (16), 578.

24 Kotwal, A. and Schmidt, C.E. (2001) Electrical stimulation alters protein adsorption and nerve cell interactions with electrically conducting biomaterials. *Biomaterials*, **22** (10), 1055.

25 Lakard, B., Ploux, L., Anselme, K., Lallemand, F., Lakard, S., Nardin, M., and Hihn, J.Y. (2009) Effect of ultrasounds on the electrochemical synthesis of polypyrrole, application to the adhesion and growth of biological cells. *Bioelectrochemistry*, **75** (2), 148.

26 Stenger-Smith, J.D. (1998) Intrinsically electrically conducting polymers: synthesis, characterization, and their applications. *Prog. Polym. Sci.*, **23** (1), 57.

27 Long, Y.-Z., Li, M.-M., Gu, C., Wan, M., Duvail, J.-L., Liu, Z., and Fan, Z. (2011) Recent advances in synthesis, physical properties and applications of conducting polymer nanotubes and nanofibers. *Prog. Polym. Sci.*, **36** (10), 1415.

28 Wang, X., Gu, X., Yuan, C., Chen, S., Zhang, P., Zhang, T., Yao, J., Chen, F., and Chen, G. (2004) Evaluation of biocompatibility of polypyrrole *in vitro* and *invivo*. *J. Biomed. Mater. Res. A*, **68A** (3), 411.

29 Ramanaviciene, A., Kausaite, A., Tautkus, S., and Ramanavicius, A. (2007) Biocompatibility of polypyrrole particles: an *in vivo* study in mice. *J. Pharm. Pharmacol.*, **59** (2), 311.

30 Wang, C.H., Dong, Y.Q., Sengothi, K., Tan, K.L., and Kang, E.T. (1999) *In vivo* tissue response to polyaniline. *Synth. Met.*, **102** (1), 1313.

31 Humpolicek, P., Kasparkova, V., Saha, P., and Stejskal, J. (2012) Biocompatibility of polyaniline. *Synth. Met.*, **162** (7–8), 722.

32 Zhao, H., Zhu, B., Sekine, J., Luo, S.-C., and Yu, H.-H. (2012) Oligoethylene-glycol-functionalized polyoxythiophenes for cell engineering: syntheses, characterizations, and cell compatibilities. *ACS Appl. Mater. Interfaces*, **4** (2), 680.

33 Ghasemi-Mobarakeh, L., Prabhakaran, M.P., Morshed, M., Nasr-Esfahani, M.H., Baharvand, H., Kiani, S., Al-Deyab, S.S., and Ramakrishna, S. (2011) Application of conductive polymers, scaffolds and electrical stimulation for nerve tissue engineering. *J. Tissue Eng. Regener. Med.*, **5** (4), e17.

34 Ravichandran, R., Sundarrajan, S., Venugopal, J.R., Mukherjee, S., and Ramakrishna, S. (2010) Applications of conducting polymers and their issues in biomedical engineering. *J. R. Soc. Interface*, **7** (Suppl. 5), S559.

35 Cui, X., Wiler, J., Dzaman, M., Altschuler, R.A., and Martin, D.C. (2003) *In vivo* studies of polypyrrole/peptide coated neural probes. *Biomaterials*, **24** (5), 777.

36 George, P.M., Lyckman, A.W., LaVan, D.A., Hegde, A., Leung, Y., Avasare, R., Testa, C., Alexander, P.M., Langer, R., and Sur, M. (2005) Fabrication and biocompatibility of polypyrrole implants suitable for neural prosthetics. *Biomaterials*, **26** (17), 3511.

37 Wadhwa, R., Lagenaur, C.F., and Cui, X.T. (2006) Electrochemically controlled release of dexamethasone from conducting polymer polypyrrole coated electrode. *J. Controlled Release*, **110** (3), 531.

38 Svirskis, D., Travas-Sejdic, J., Rodgers, A., and Garg, S. (2010) Electrochemically controlled drug delivery based on intrinsically conducting polymers. *J. Controlled Release*, **146** (1), 6.

39 Wong, J.Y., Langer, R., and Ingber, D.E. (1994) Electrically conducting polymers can noninvasively control the shape and growth of mammalian cells. *Proc. Natl. Acad. Sci. USA*, **91** (8), 3201.

40 Collazos-Castro, J.E., Polo, J.L., Hernández-Labrado, G.R., Padial-Cañete, V., and García-Rama, C. (2010) Bioelectrochemical control of neural cell development on conducting polymers. *Biomaterials*, **31** (35), 9244.

41 Quigley, A.F., Razal, J.M., Thompson, B.C., Moulton, S.E., Kita, M., Kennedy, E.L., Clark, G.M., Wallace, G.G., and Kapsa, R.M.I. (2009) A conducting-polymer platform with biodegradable fibers for stimulation and guidance of axonal growth. *Adv. Mater.*, **21** (43), 4393.

42 Das, T.K. and Prusty, S. (2012) Review on conducting polymers and their applications. *Polym.-Plast. Technol. Eng.*, **51** (14), 1487.

43 Rivnay, J., Owens, R.M., and Malliaras, G.G. (2014) The rise of organic bioelectronics. *Chem. Mater.*, **26** (1), 679.

44 Ateh, D.D., Navsaria, H.A., and Vadgama, P. (2006) Polypyrrole-based conducting polymers and interactions with biological tissues. *J. Royal Soc. Interface*, **3** (11), 741.

45 Li, Y., Neoh, K.G., and Kang, E.-T. (2004) Plasma protein adsorption and thrombus formation on surface functionalized polypyrrole with and without electrical stimulation. *J. Colloid Interface Sci.*, **275** (2), 488.

46 Kim, D.H., Richardson-Burns, S.M., Hendricks, J.L., Sequera, C., and Martin, D.C. (2007) Effect of immobilized nerve growth factor on conductive polymers: electrical properties and cellular response. *Adv. Funct. Mater.*, **17** (1), 79.

47 George, P.M., LaVan, D.A., Burdick, J.A., Chen, C.Y., Liang, E., and Langer, R. (2006) Electrically controlled drug delivery from biotin-doped conductive polypyrrole. *Adv. Mater.*, **18** (5), 577.

48 Zhang, X. and Manohar, S.K. (2004) Bulk synthesis of polypyrrole nanofibers by a seeding approach. *J. Am. Chem. Soc.*, **126** (40), 12714.

49 Bousalem, S., Mangeney, C., Chehimi, M.M., Basinska, T., Miksa, B., and Slomkowski, S. (2004) Synthesis, characterization and potential biomedical applications of *N*-succinimidyl ester functionalized, polypyrrole-coated polystyrene latex particles. *Colloid Polym. Sci.*, **282** (12), 1301.

50 Lee, J.-W., Serna, F., Nickels, J., and Schmidt, C.E. (2006) Carboxylic acid-functionalized conductive polypyrrole as a bioactive platform for cell adhesion. *Biomacromolecules*, **7** (6), 1692.

51 Meng, S., Rouabhia, M., Shi, G., and Zhang, Z. (2008) Heparin dopant increases the electrical stability, cell adhesion, and growth of conducting polypyrrole/poly(l,l-lactide) composites. *J. Biomed. Mater. Res. A*, **87A** (2), 332.

52 Geetha, S., Rao, C.R.K., Vijayan, M., and Trivedi, D.C. (2006) Biosensing and drug delivery by polypyrrole. *Anal. Chim. Acta*, **568** (1–2), 119.

53 Sharma, M., Waterhouse, G.I.N., Loader, S.W.C., Garg, S., and Svirskis, D. (2013) High surface area polypyrrole scaffolds for tunable drug delivery. *Int. J. Pharm.*, **443** (1–2), 163.

54 Huang, Z.-B., Yin, G.-F., Liao, X.-M., and Gu, J.-W. (2014) Conducting polypyrrole in tissue engineering applications. *Front. Mater. Sci.*, **8** (1), 39.

55 Nectow, A.R., Marra, K.G., and Kaplan, D.L. (2012) Biomaterials for the development of peripheral nerve guidance conduits. *Tissue Eng. Part B, Rev.*, **18** (1), 40.

56 Guo, Y., Li, M., Mylonakis, A., Han, J., MacDiarmid, A.G., Chen, X., Lelkes, P.I., and Wei, Y. (2007) Electroactive oligoaniline-containing self-assembled monolayers for tissue engineering applications. *Biomacromolecules*, **8** (10), 3025.

57 Cullen, D.K., Ankur, R.P., John, F.D., Douglas, H.S., and Bryan, J.P. (2008) Developing a tissue-engineered neural-electrical relay using encapsulated neuronal constructs on conducting polymer fibers. *J. Neural Eng.*, **5** (4), 374.

58 Sarah, M.R.-B., Jeffrey, L.H., and David, C.M. (2007) Electrochemical polymerization of conducting polymers in living neural tissue. *J. Neural Eng.*, **4** (2), L6.

59 Ulijn, R.V., Bibi, N., Jayawarna, V., Thornton, P.D., Todd, S.J., Mart, R.J., Smith, A.M., and Gough, J.E. (2007) Bioresponsive hydrogels. *Mater. Today*, **10** (4), 40.

60 Nikpour, M., Chaouk, H., Mau, A., Chung, D.J., and Wallace, G. (1999) Porous conducting membranes based on polypyrrole–PMMA composites. *Synth. Met.*, **99** (2), 121.

61 Brahim, S. and Guiseppi-Elie, A. (2005) Electroconductive hydrogels: electrical and electrochemical properties of polypyrrole–poly(HEMA) composites. *Electroanalysis*, **17** (7), 556.

62 Gilmore, K.J., Kita, M., Han, Y., Gelmi, A., Higgins, M.J., Moulton, S.E., Clark, G.M., Kapsa, R., and Wallace, G.G. (2009) Skeletal muscle cell proliferation and differentiation on polypyrrole substrates doped with extracellular matrix components. *Biomaterials*, **30** (29), 5292.

63 Hodgson, A.J., Gilmore, K., Small, C., Wallace, G.G., Mackenzie, I.L., Aoki, T., and Ogata, N. (1994) Reactive supramolecular assemblies of mucopolysaccharide, polypyrrole and protein as controllable biocomposites for a new generation of 'intelligent biomaterials'. *Supramol. Sci.*, **1** (2), 77.

64 Lira, L.M. and Córdoba de Torresi, S.I. (2005) Conducting polymer–hydrogel composites for electrochemical release devices: synthesis and characterization of semi-interpenetrating polyaniline–polyacrylamide networks. *Electrochem. Commun.*, **7** (7), 717.

65 Siddhanta, S.K. and Gangopadhyay, R. (2005) Conducting polymer gel: formation of a novel semi-IPN from polyaniline and crosslinked poly(2-acrylamido-2-methyl propanesulphonicacid). *Polymer*, **46** (9), 2993.

66 Lee, J.Y., Bashur, C.A., Goldstein, A.S., and Schmidt, C.E. (2009) Polypyrrole-coated electrospun PLGA nanofibers for neural tissue applications. *Biomaterials*, **30** (26), 4325.

67 Gomez, N. and Schmidt, C.E. (2007) Nerve growth factor-immobilized polypyrrole: bioactive electrically conducting polymer for enhanced neurite extension. *J. Biomed. Mater. Res. A*, **81A** (1), 135.

68 Norris, I.D., Shaker, M.M., Ko, F.K., and MacDiarmid, A.G. (2000) Electrostatic fabrication of ultrafine conducting fibers: polyaniline/polyethylene oxide blends. *Synth. Met.*, **114** (2), 109.

69 Shi, G., Rouabhia, M., Wang, Z., Dao, L.H., and Zhang, Z. (2004) A novel electrically conductive and biodegradable composite made of polypyrrole nanoparticles and polylactide. *Biomaterials*, **25** (13), 2477.

70 Cao, Y., Andreatta, A., Heeger, A.J., and Smith, P. (1989) Influence of chemical polymerization conditions on the properties of polyaniline. *Polymer*, **30** (12), 2305.

71 Kudoh, Y., Akami, K., and Matsuya, Y. (1998) Chemical polymerization of 3,4-ethylenedioxythiophene using an aqueous medium containing an anionic surfactant. *Synth. Met.*, **98** (1), 65.

72 Calvo, P.A., Rodríguez, J., Grande, H., Mecerreyes, D., and Pomposo, J.A. (2002) Chemical oxidative polymerization of pyrrole in the presence of *m*-hydroxybenzoic acid- and *m*-hydroxycinnamic acid-related compounds. *Synth. Met.*, **126** (1), 111.

73 Wallace, G.G., Smyth, M., and Zhao, H. (1999) Conducting electroactive polymer-based biosensors. *TrAC Trends Anal. Chem.*, **18** (4), 245.

74 Chronakis, I.S., Grapenson, S., and Jakob, A. (2006) Conductive polypyrrole nanofibers via electrospinning: electrical and morphological properties. *Polymer*, **47** (5), 1597.

75 Kenry and Lim, C.T. (2017) Nanofiber technology: current status and emerging developments. *Prog. Polym. Sci.* doi: 10.1016/j.progpolymsci.2017.03.002

76 Sawicka, K.M. and Gouma, P. (2006) Electrospun composite nanofibers for functional applications. *J. Nanopart. Res.*, **8** (6), 769.

77 Prabhakaran, M.P., Ghasemi-Mobarakeh, L., Jin, G., and Ramakrishna, S. (2011) Electrospun conducting polymer nanofibers and electrical stimulation of nerve stem cells. *J. Biosci. Bioeng.*, **112** (5), 501.

78 Aznar-Cervantes, S., Roca, M.I., Martinez, J.G., Meseguer-Olmo, L., Cenis, J.L., Moraleda, J.M., and Otero, T.F. (2012) Fabrication of conductive electrospun silk fibroin scaffolds by coating with polypyrrole for biomedical applications. *Bioelectrochemistry*, **85**, 36.

79 LaVan, D.A., McGuire, T., and Langer, R. (2003) Small-scale systems for *in vivo* drug delivery. *Nat. Biotechnol.*, **21** (10), 1184.

80 Staples, M., Daniel, K., Cima, M.J., and Langer, R. (2006) Application of micro- and nano-electromechanical devices to drug delivery. *Pharm. Res.*, **23** (5), 847.

81 Epstein, A.J., Joo, J., Kohlman, R.S., Du, G., MacDiarmid, A.G., Oh, E.J., Min, Y., Tsukamoto, J., Kaneko, H., and Pouget, J.P. (1994) Inhomogeneous disorder and the modified drude metallic state of conducting polymers. *Synth. Met.*, **65** (2), 149.

82 Patil, R., Harima, Y., Yamashita, K., Komaguchi, K., Itagaki, Y., and Shiotani, M. (2002) Charge carriers in polyaniline film: a correlation between mobility and *in situ* ESR measurements. *J. Electroanal. Chem.*, **518** (1), 13.

83 Kang, S.D. and Snyder, G.J. (2017) Charge-transport model for conducting polymers. *Nat. Mater.*, **16** (2), 252.

84 Wu, J., Mullett, W.M., and Pawliszyn, J. (2002) Electrochemically controlled solid-phase microextraction based on conductive polypyrrole films. *Anal. Chem.*, **74** (18), 4855.

85 Hutmacher, D.W. (2000) Scaffolds in tissue engineering bone and cartilage. *Biomaterials*, **21** (24), 2529.

86 Houchin-Ray, T., Swift, L.A., Jang, J.-H., and Shea, L.D. (2007) Patterned PLG substrates for localized DNA delivery and directed neurite extension. *Biomaterials*, **28** (16), 2603.

87 Wang, H.-J., Lin, Z.-X., Liu, X.-M., Sheng, S.-Y., and Wang, J.-Y. (2005) Heparin-loaded zein microsphere film and hemocompatibility. *J. Controlled Release*, **105** (1–2), 120.

88 Higuchi, A., Shirano, K., Harashima, M., Yoon, B.O., Hara, M., Hattori, M., and Imamura, K. (2002) Chemically modified polysulfone hollow fibers with vinylpyrrolidone having improved blood compatibility. *Biomaterials*, **23** (13), 2659.

89 Guarino, V., Alvarez-Perez, M.A., Borriello, A., Napolitano, T., and Ambrosio, L. (2013) Conductive PANi/PEGDA macroporous hydrogels for nerve regeneration. *Adv. Healthc. Mater.*, **2** (1), 218.

90 Dispenza, C., Presti, C.L., Belfiore, C., Spadaro, G., and Piazza, S. (2006) Electrically conductive hydrogel composites made of polyaniline nanoparticles and poly(*N*-vinyl-2-pyrrolidone). *Polymer*, **47** (4), 961.

91 Dai, T., Qing, X., Lu, Y., and Xia, Y. (2009) Conducting hydrogels with enhanced mechanical strength. *Polymer*, **50** (22), 5236.

92 Abidian, M.R. and Martin, D.C. (2009) Multifunctional nanobiomaterials for neural interfaces. *Adv. Funct. Mater.*, **19** (4), 573.

93 Smirnov, M.A., Bobrova, N.V., Dmitriev, I.Y., Bukolšek, V., and Elyashevich, G.K. (2011) Electroactive hydrogels based on poly(acrylic acid) and polypyrrole. *Polym. Sci. Ser. A*, **53** (1), 67.

94 Liu, Y., Hu, J., Zhuang, X., Zhang, P., Wei, Y., Wang, X., and Chen, X. (2012) Synthesis and characterization of novel biodegradable and electroactive hydrogel based on aniline oligomer and gelatin. *Macromol. Biosci.*, **12** (2), 241.

95 Taylor, D.M., Tillery, S.I.H., and Schwartz, A.B. (2002) Direct cortical control of 3D neuroprosthetic devices. *Science*, **296** (5574), 1829.

96 Schwartz, A.B. (2004) Cortical neural prosthetics. *Annu. Rev. Neurosci.*, **27**(1), 487.

97 Daniel, P., Alexander, V., Phil, H., and Stephen, B. (2005) Design of a high-resolution optoelectronic retinal prosthesis. *J. Neural Eng.*, **2** (1), S105.

98 Chikar, J.A., Hendricks, J.L., Richardson-Burns, S.M., Raphael, Y., Pfingst, B.E., and Martin, D.C. (2012) The use of a dual PEDOT and RGD-functionalized alginate hydrogel coating to provide sustained drug delivery and improved cochlear implant function. *Biomaterials*, **33** (7), 1982–1990.

99 Saldarriaga Fernández, I.C., van der Mei, H.C., Lochhead, M.J., Grainger, D.W., and Busscher, H.J. (2007) The inhibition of the adhesion of clinically isolated bacterial strains on multi-component cross-linked poly(ethylene glycol)-based polymer coatings. *Biomaterials*, **28** (28), 4105–4112.

10

Conjugated Polymers for Photodynamic Therapy

Thangaraj Senthilkumar and Shu Wang

Institute of Chemistry, Chinese Academy of Sciences, Key Laboratory of Organic Solids, Zhongguancun North First Street 2, Beijing, 100190, PR China

10.1 Introduction

10.1.1 Photodynamic Therapy – Concept and History

Photodynamic therapy (PDT) is the photochemistry-based modality using a photosensitizer (PS), light source, and tissue oxygen for killing of diseased cells. A PS is the chemical molecule involved in a photochemical reaction that absorbs light at particular wavelengths to produce reactive molecular species such as singlet oxygen ($^1O_2$) or a reactive radical. The concept of combining light with a chemical agent has had a long history since ancient times. Three thousand years ago, sunlight-activated repigmentation of vitiligo was used by ancient Chinese, Indians, and Egyptians [1–3]. The developments that are made in the evolution of PDT including milestone achievements are listed out in Figure 10.1. Hematoporphyrin-based PS systems had been developed for various cancer treatments during 1900–2000 AD. As of today, many PSs are available for the treatment of diseases such as tumor targeting and killing, antimicrobial activities, various acnes and related diseases, vascular targeting, and ophthalmology.

10.1.2 Outline of the PDT Process

The PDT approach is remote-controlled light activation after the delivery of inert components and therefore, it is desired to be advantageous over invasive surgical treatments, radiation therapy, and chemotherapy. The major components of PDT are namely (i) PS, (ii) light of specific wavelength to activate the PS, and (iii) tissue Oxygen. In a typical PDT process, the PS is administrated into the body through an intravenous injection followed by light illumination leading to the cell or tissue death, which is schematically represented in Figure 10.2a and b. It is noted that PS are in circulation in body fluids for

Conjugated Polymers for Biological and Biomedical Applications, First Edition. Edited by Bin Liu

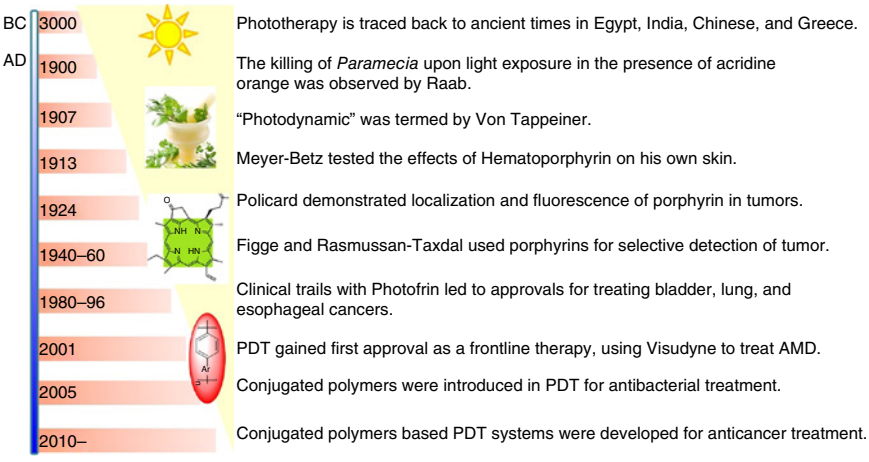

Figure 10.1 A timeline of selected milestones in the historical development of PDT.

considerable periods of time prior to light activation. During the time of circulation, the PS is accumulated in the targeted location. For the purpose of schematic representation it has been limited to show that PS is only accumulated in the targeted region whereas in actual cases there are chances for the accumulation of PS in the other parts of the body. In the final step, the light source having the appropriate wavelength to excite the PS is illuminated upon the targeted region. The excited PS emits fluorescence energy that is transferred to tissue oxygen in order to produce reactive molecular species that are responsible for cell death.

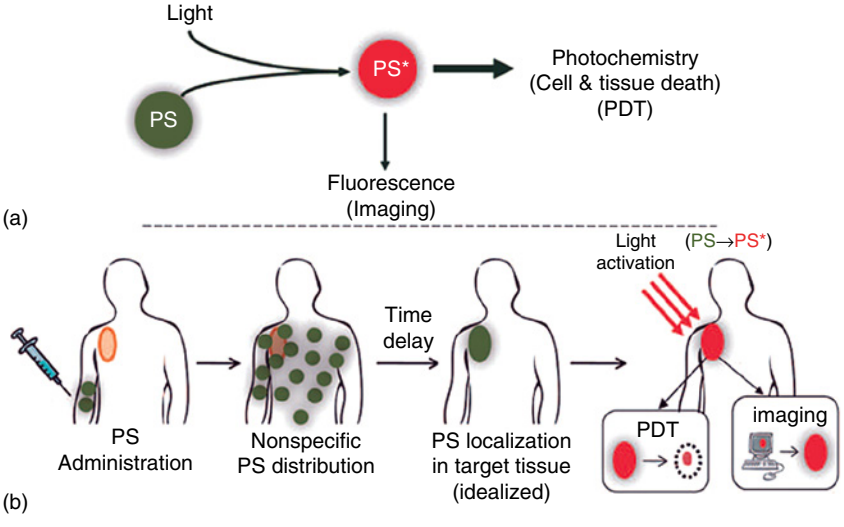

Figure 10.2 Schematic representation of PDT process. (Adapted from Ref. [3]. Copyright 2010, American Chemical Society.)

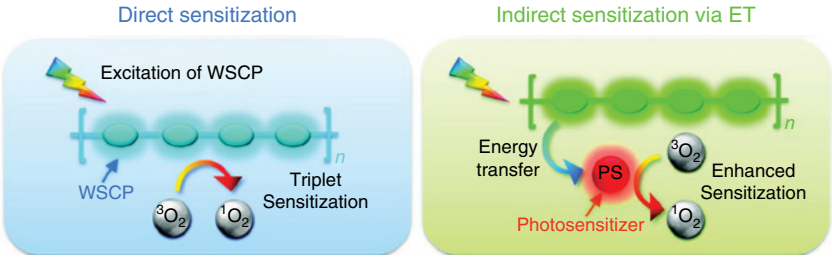

Figure 10.3 Two types of oxygen sensitization mechanism provided by CPs. (Adapted from Ref. [4]. Copyright 2012, American Chemical Society.)

10.1.3 Role of Conjugated Polymers in PDT

Small molecule based PS have been predominantly used in PDT treatment for many decades. However, they posed serious challenges in terms of absorption cross-section, solubility, and low enhanced permeation and retention (EPR) effect. There was great demand for candidates that could meet the pitfalls of small molecule based PS. When conjugated polymers (CPs) came into light, researchers explored CPs as PSs by taking advantage of large absorption cross-section, easy functionalization, and prominent EPR effect. Based on the emission wavelength of CPs, there are two types of sensitization modes as depicted in Figure 10.3. Type I: Direct sensitization: emission energy is directly transferred from the CP to tissue Oxygen and Type II: CPs act as energy transfer systems to PSs such as porphyrin derivatives to generate singlet oxygen ($^1O_2$) production. Additionally, CP provides a multitargeting platform for selective recognition of microorganisms and tumor sites with the functionalization of specific receptors. For example, quaternary ammonium (QA) group in the hydrogel matrix is reported to suppress the growth of microorganisms [5]. The accumulation of CPs toward target site can be controlled through specific binding groups so as to eliminate nonspecific toxicity to normal tissue. The design aspects of CP and choice of light source will be elaborated in Section 10.1.5. Excellent reviews that cover all the aspects of design, synthesis of CPs and their application in imaging, diagnosis, and therapy including photodynamic therapy are available in literature [4, 6, 7].

10.1.4 Photochemistry Behind the PDT Process

The photochemical mechanism involved in the PDT process can be explained step by step through the Jablonski diagram as shown in Figure 10.4 and there are detailed reviews discussing photochemistry, lifetime, and generation of singlet oxygen [3, 8–10]. Step 1: PS absorbs appropriate wavelength light required for excitation to electronically excited singlet state ($^1PS^*$). Step 2: From the singlet state the excited state PS undergoes intersystem crossing to attain excited triplet state $^3PS^*$, which favors energy transfer to tissue oxygen. Step 3: A photochemical reaction is taking place between $^3PS^*$ and oxygen molecules ($^3O_2$) to produce $^1O_2$ as cytotoxic agent. Singlet oxygen is highly reactive because two highest energy electrons reside together in the same antibonding orbital in opposite spin [11].

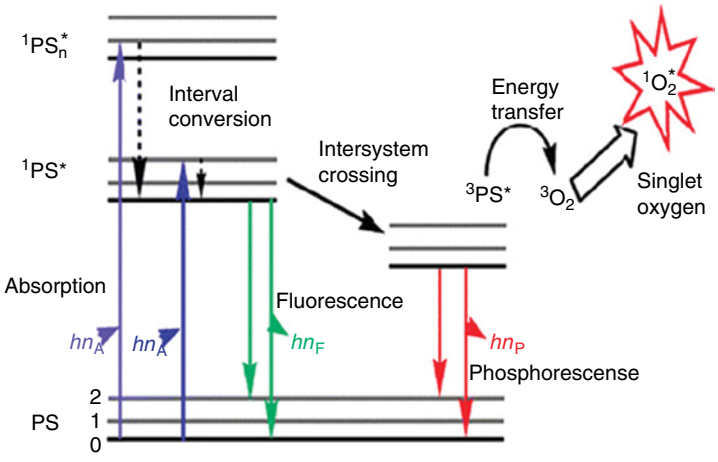

Figure 10.4 Jablonski diagram showing the formation of singlet oxygen. (Adapted from Ref. [8]. Copyright 2011, Royal Society of Chemistry.)

How can highly reactive species be chosen for PDT? Will these reactive species not affect normal cell in neighbor sites to tumor sites? These obvious questions arising in readers' minds can be clarified by singlet oxygen diffusion in cellular media. The lifetime of singlet oxygen is three orders of magnitude lower in *in vivo* conditions than the lifetime in external conditions, which is approximately 1–3 μs in a water medium [11]. In cellular systems, the lifetime of singlet oxygen is a gradient function within the same cell. The value of lifetime is around 100 ns in the lipid membranes and in the cytoplasm, the lifetime is at a maximum value of 250 ns. These results predict that the diffusion range of $^1O_2$ is being limited considerably upto 45 nm in cellular media [12]. As the diameter of human cells ranges from approximately 10 to 100 μm, the diffusion of $^1O_2$ cannot exceed beyond a single cell length. Therefore, the site where the primary generation of $^1O_2$ occurs can alone be prone to attack by reactive species. This feature highlights the chances of controlled killing of diseased cells without causing toxicity to the adjacent normal cells and thus, choice of singlet oxygen generation is allowed in PDT.

10.1.5 Design Aspects of Effective PDT

To achieve effective treatment, any strategy should be inbuilt with features such as noninvasive, negligible toxicity to normal cells and selective binding to the target site. PDT requires three important design aspects to meet the standards of an effective treatment.

i) The penetration depth of an external light source into the tissue is an important factor for reaching the target site and for operating with minimum toxicity to normal tissue. There is a relationship between the excitation wavelength of PS and the ability of the penetration profile, which is demonstrated in Figure 10.5. The lights sources such as UV (below 400 nm) and blue and green light cannot penetrate the deeper tissue because of higher scattering

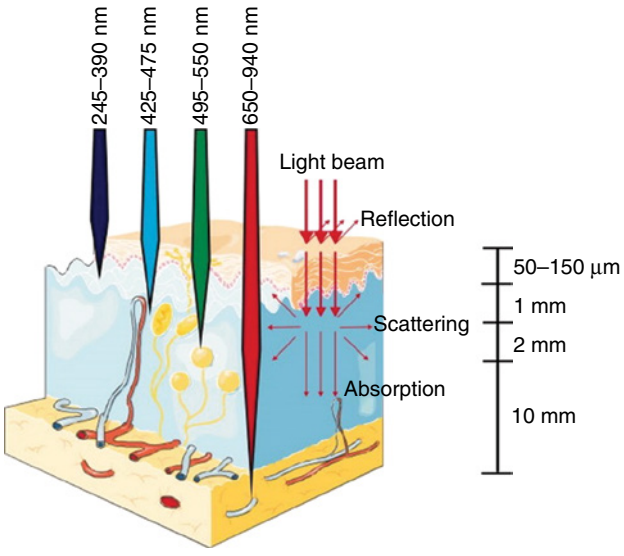

Figure 10.5 Light penetration through tissue. The penetration depth of typical light is dominated by the rates of absorption, scattering, transmission, and reflection by the tissues, which vary with different wavelengths. (Adapted from Ref. [13]. Copyright 2011, John Wiley & Sons.)

effect. As they are scattered in the few topmost layers of the skin and also largely absorbed by bioavailable fluorophores in the skin, the reachability to the target site is poor. It is clearly shown that the absorption wavelength of PS is expected to be above 650 nm (far-red) and near-IR (~1100 nm) to have maximum depth penetration. This is the most important criteria in the selection of PS systems [13]. Despite brilliant blue and green light emission property, many of such PS probes are excluded in clinical trials due to the above reason. However, in practical PDT applications PS having higher wavelength in NIR regime (>850 nm) relatively suffers with fast nonradiative transition leading to thermal loss [14, 15]. Moreover, the higher wavelength light source ranging between 650 and 850 nm can penetrate upto 3 mm of depth into the tissue, which largely affects the wide applicability of PDT treatment [16]. To avoid these problems, recent studies lay emphasis on bioluminescence and self-luminescent systems, which bring illumination closer to the target site. Another strategy is to develop FRET pair systems of visible light absorbing donor and near-IR emitting acceptor so as to have large absorption cross-section with deeper penetrating abilities.

ii) The fast proliferation in solid tumors with an imperfect vascular system creates a hypoxic microenvironment, which is deprived of oxygen supply. Low oxygen level in the tumor tissue is the main problem for ineffective response toward chemotherapy and photodynamic therapy. In a hypoxic microenvironment, excited PS transfers its energy to organic substrates instead of tissue oxygen. Thermal ablation of cells is one of the alternative ways to kill hypoxic tumors. Recently, photothermal therapy (PTT) using

CP has been initiated for conversion of light energy to thermal energy for causing tumor ablation.

iii) Currently, organic dyes based PDT treatment that is progressing in clinical practice show poor target selectivity and they tend to accumulate largely in the skin. Such dyes are to be replaced by CPs with specific functional groups in future PDT. This allows site-specific accumulation of PS with negligible toxicity and prolonged circulation time in body fluids. The chemical stability, water solubility, and injectable formulations are also additional features expected in an ideal PS to promote renal clearance.

10.2 Conjugated Polymers as Photosensitizers

Generally, a CP can serve as a better PS over other dyes in PDT because of its many advantages as already discussed in Section 10.1.3. The foremost advantage is that a CP can retain its electronic features upon functionalization with various pendant groups. In most of organic dye based PS, peripheral functionalization of targeting groups decreases PDT efficiency due to structural changes. This evokes fatal consequences to normal cells lasting for months after the treatment. Secondly, a CP exhibits tunable absorption wavelength characteristics spanning above 700 nm or ~NIR region with changes incorporated in the polymer design. CP- based PSs are classified into three types based upon their structural design and mode of sensitization in PDT.

10.2.1 Far-Red/Near-IR Emitting CP as Photosensitizers

Far-red and near-IR emitting conjugated polymers act as direct PSs without the mediation of any other chromophores. In recent years, the development of NIR emissive CP is steadily growing with more numbers of reports growing. The chemical structures of far-red and near-IR-emitting polymers are shown in Scheme 10.1. It is noted that benzathiadiazole, diketopyrrole, and bodipy are the monomers bringing extensive conjugation in CPs for excellent absorption in the far-red/near-IR regime ranging between 650 and 1100 nm.

10.2.2 CP as Energy Transfer Systems to Photosensitizing Dyes

CPs act as energy transfer systems to photosensitizing dyes (generally porphyrin) to improve the production of singlet oxygen generation. The photosensitizing dyes are attached to CPs via either covalent conjugation or encapsulation in a CP matrix to exhibit two-photon absorption properties. CP behaves as light-harvesting antennas for porphyrin that amplify the production of singlet oxygen to several fold. The two-photon excitation photodynamic therapy (2P-PDT) techniques are advantageous over the traditional one-photon counterparts because they offer deeper penetration into body tissues, more confined treatment areas, and three-dimensional spatial selectivity to reduce adverse effects to nearby normal tissues [17]. Scheme 10.2 shows structures of such PS systems in which CPs are either covalently or noncovalently conjugated with dyes.

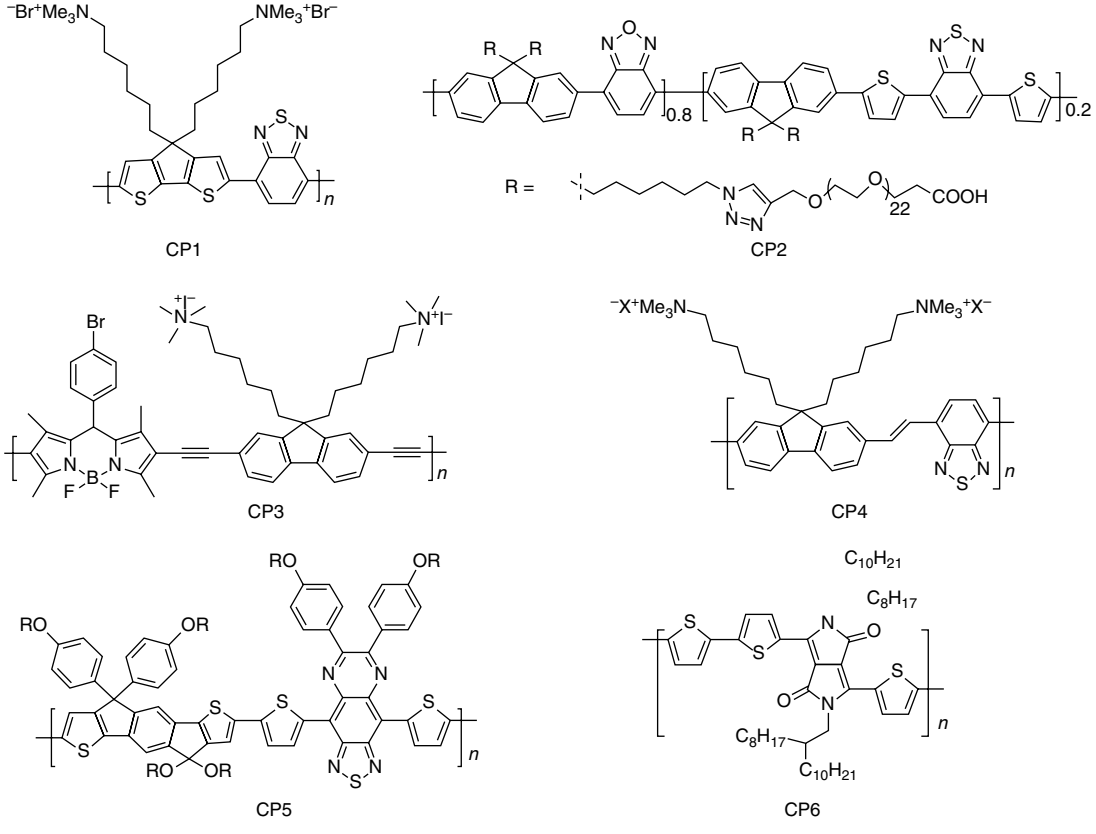

Scheme 10.1 Far-red- and near-IR-emitting conjugated polymers used in PDT.

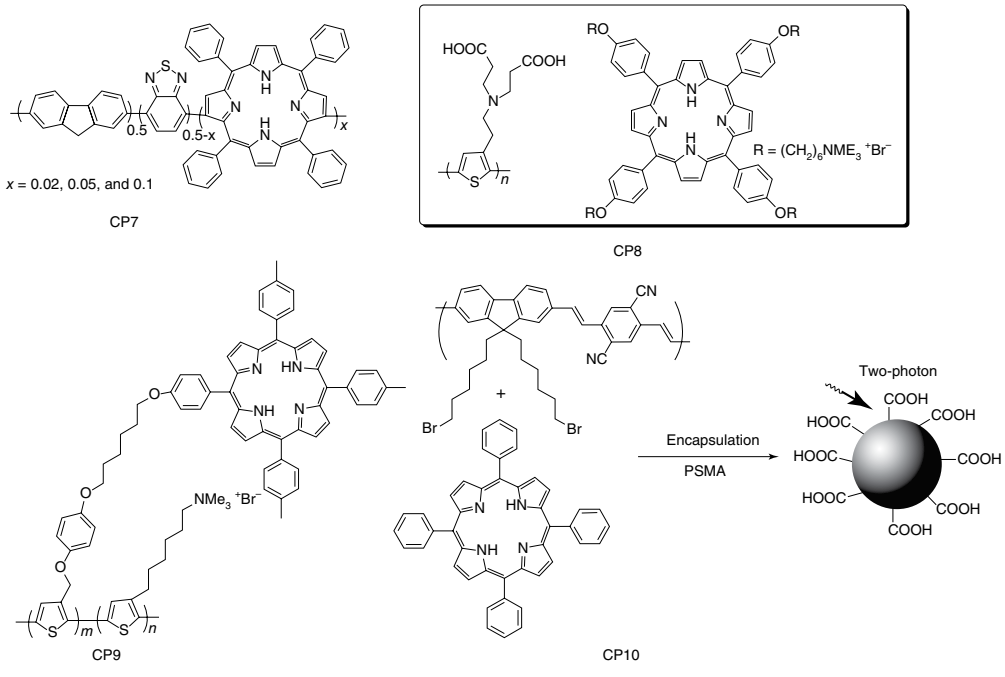

Scheme 10.2 Conjugated polymers as energy transfer systems to Porphyrin dyes for PDT.

10.2.3 Hybrid Photosensitizers based on CP

To meet the purpose of noninvasive light activation, CPs are combined with other light-harvesting chemical families. This approach gains keen attention in recent studies and many demonstrations have started to explore new hybrid designs. Some of the notable hybrid designs are described as follows. CPs are attached to metal complexes that display absorption in the near-IR regions and a CP mediates the energy transfer. The commonly used metal complexes are iridium (Ir) Zinc, Platinum and upconversion nanoparticles (NPs)-based metal complexes as shown in Scheme 10.3. Noble metal plasmonic nanostructures such as Au NPs are made composites with CP.

Bioluminescence is the best alternative for replacing external light illumination to overcome nonspecific targeting and depth penetration problems. Bioluminescence is the phenomenon of light emission induced from enzymatic chemical reactions in a biological environment bringing noninvasive PDT. The key advantage of bioluminescence is site-specific light activation for generation of $^1O_2$ in its vicinity.

10.3 Applications of CP-Based Photodynamic Therapy

10.3.1 Antimicroorganism Activity

CP-based PDT was first demonstrated successfully for antimicrobial treatment by Whitten group in 2005 [18]. Cationic conjugate polymers can strongly bind with negatively charged surfaces of microorganisms through electrostatic interactions. Under light irradiation, adhered polymers generate reactive species that effectively kill the microorganism. The structure of the cationic polymer CP15 (Figure 10.6a) and biocidal activity over *E. Coli* bacteria under ambient conditions are shown in Figure 10.6b. When PPE polymer is incubated with *E.coli* bacteria at different times, it clearly shows killing of bacteria whereas control experiment without PPE were not able to show any toxicity toward bacteria.

Further, series of cationic PPE polymers functionalized with quaternary ammonium moieties were further developed to enhance the biocidal activity against bacterial families namely *Cobetia marina* and *Pseudomonas aeruginosa* under visible light as shown in Figure 10.7 [19]. The multiple cationic charges of quaternary ammonium salts assist in tight binding with the surface of bacteria. PPE derivatives (CP16-18) are covalently grafted onto the surface of silica colloidal particles (5 and 30 μm diameter) to form colloidal polymer beads. This enables entrapping of bacteria in the interface of beads in close proximity to PPE polymers. The mechanism of the biocidal activity of grafted PPE was schematically represented in Figure 10.8. Silica colloidal particles play the role in uniform beads formation and also in bringing CP and bacteria into close proximity.

Whitten and coworkers compared antibacterial activities of cationic PPEs (CP16-19) between light and dark conditions [20]. The structure of CP19 is slightly different from that of CP16-18 wherein phenyl moiety is replaced with

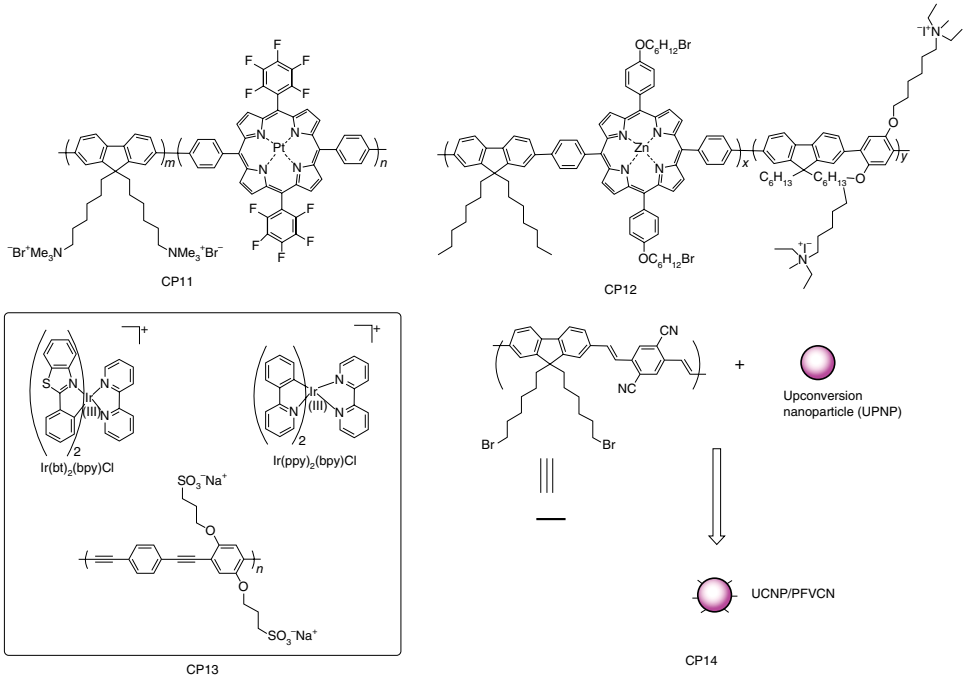

Scheme 10.3 Hybrid photosensitizers based on conjugated polymers for PDT.

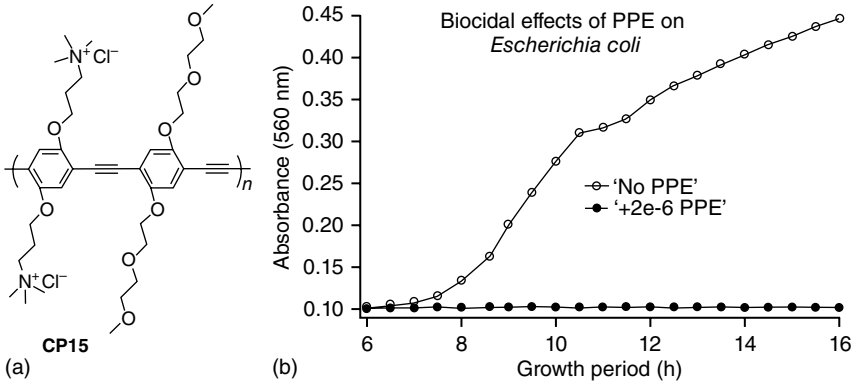

Figure 10.6 (a) Structure of cationic polymer PPE and (b) growth curves of *E. Coli* bacteria with and without the presence of CP15 for 16 h under light irradiation at 560 nm. (Adapted from Ref. [18]. Copyright 2005, American Chemical Society.)

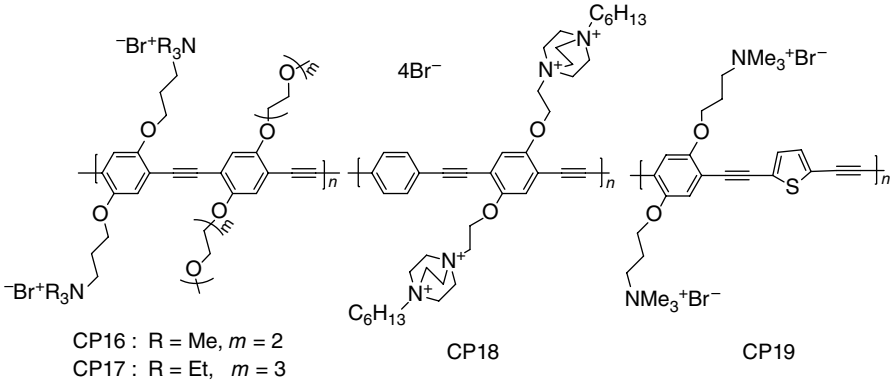

Figure 10.7 Structure multiple QA groups functionalized CPEs.

thiophene moiety. The biocidal activity of CP19 against *Pseudomonas aeruginosa* in the dark is remarkably higher than that in the presence of light. On the other hand, CP16-18 polymers do not show any antibacterial activity even after prolonged incubation and light exposure. The increment in hydrophobicity due to thiophene ring accompanied with QA groups help to easily penetrate hydrophobic lipid membranes of bacterial wall. Upon light irradiation, CP19 tends to aggregate in solution within silica microspheres leading to poor production of singlet oxygen. Aggregate formation is absent in dark conditions and therefore, the activity was significant with 95% killing efficiency.

The idea of colloidal beads for trapping bacteria was put into practice in the development of microcapsules and Whitten and coworkers who synthesized CP 18 through layer-by-layer deposition on a $MnCO_3$ template [21]. Incubation of CP18 capsules with *Pseudomonas aeruginosa* exhibits very strong antimicrobial activity >95% efficiency under white-light irradiation. Figure 10.9 represents the confocal microscopy images of microcapsules incubated with CP18 irradiated under white light exposure for 10 min (a) and 1 h (b).

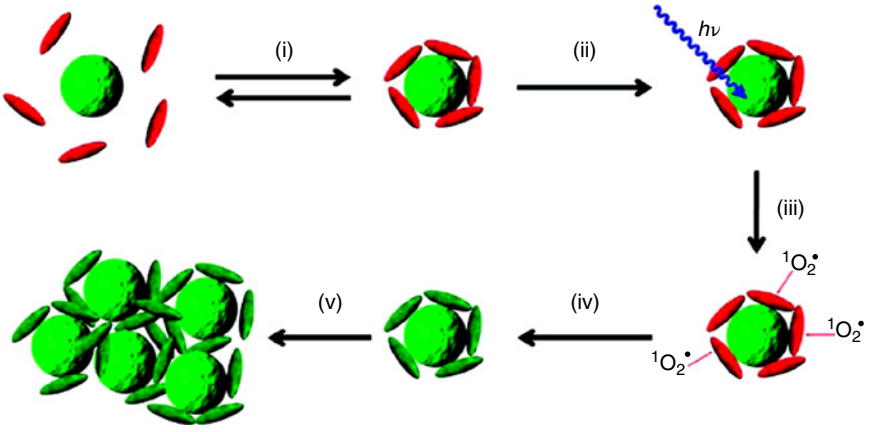

Figure 10.8 Mechanism of biocidal activity of PPE grafted on silica colloidal particles. (Adapted from Ref. [19]. Copyright 2008, American Chemical Society.) (i) The first step is either reversible physisorption or covalent grafting of CP onto the surface of silica colloidal particles to form polymer beads and they entrap bacteria inside the beads under dark conditions. In second step (ii) illumination of light leads to production of ROS from polymer beads to kill of bacteria in step (iii) and to degrade bacterial membranes (iv). Finally, (v) large aggregated assemblies of dead bacterial cells associated with the polymer beads collected as debris.

Moggio and coworkers combined CP with noble metal NP such as gold [22] and silver [23] NPs to form antifungal composites. PPE polymer CP20 (see Figure 10.10) is functionalized with bromobenzene thiol moiety to coordinate with gold surfaces via Au—S coordination and π–π interactions. The antimicrobial activity of the composite was very low with 1.84% for *E. coli* and no activity

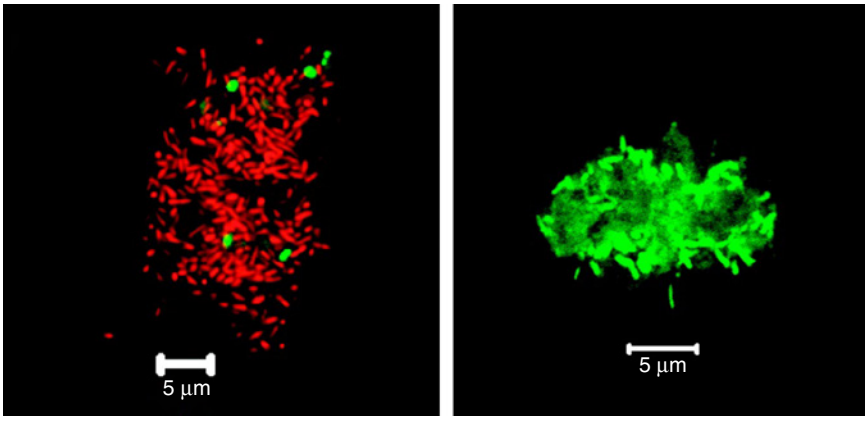

Figure 10.9 CLSM image of a microcapsule cluster 10 min after introduction into a solution of *P. aeruginosa* kept in the dark. (b) Interior image of microcapsule cluster, showing bacteria entrapped within the cluster and killed after 1 h of exposure to white light. (Red – alive bacteria; green – dead bacteria). (Adapted from Ref. [21]. Copyright 2009, American Chemical Society.)

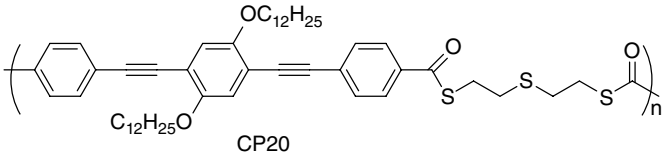

Figure 10.10 Chemical structure of CP20 polymer.

was observed toward *P. variotii* fungus. The main reason for low antimicrobial activity was the masking effect of gold NP over CP20 hindering contact with the fungus. To realize the biocidal activity, they designed CP20/silver NP nanocomposite. Silver NP did not quench the fluorescence of CP20 and exhibited a very strong fluorescence. The composite film was incubated with *P. variotii* fungi resulting in deposition of fungi on the surface of the composite film and fluorescence quenching. There is good contact between CP20 and fungi resulting in breakage of mycelium of *P. variotii* fungi.

Whitten and other workers focused antibacterial PDT systems with known bacteria but this protocol cannot be applied in mixed biological systems. To provide a rational solution to this problem, Wang *et al*. demonstrated the detection, cellular imaging, and killing of bacteria over mammalian cells using cationic PPV polymer [24]. CP21 was added to a mixture of bacteria and mammalian cells but CP21 selectively binds with bacteria over mammalian cells because bacterial surface possesses high negative charge (see Figure 10.11). Selective binding of CP21 to bacterial cells helps us to kill the bacteria via ROS generation without affecting the mammalian cells present in the same solution. Further, the antimicrobial activity of CP21 has been studied simultaneously in dark and light conditions. With selective fluorescence imaging of CP21 over bacterial cells such as Gram-positive *B. Subtilis* and Gram-negative ampicillin-resistant *E. coli*, Jurkat T mammalian cells was observed (see Figure 10.12) in confocal microscopy.

QA pendants are involved in disrupting cell membranes in the dark and, in light, PPV backbone generates ROS to kill the cells effectively. This report was the first to demonstrate integrated selective recognition with the help of

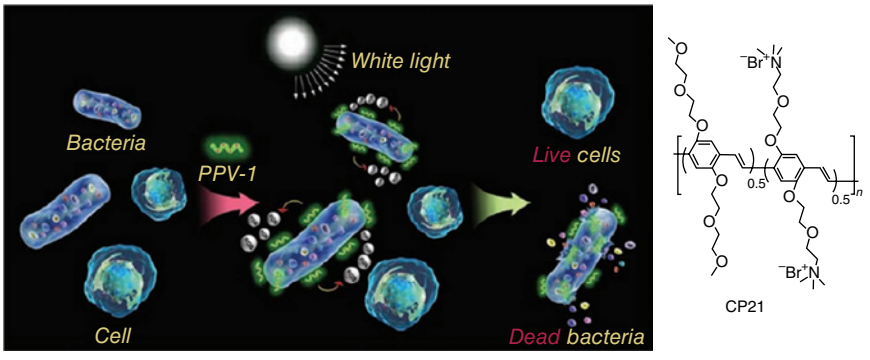

Figure 10.11 Structure and antimicrobial activity of PPV polymer. (Adapted from Ref. [24]. Copyright 2011, John Wiley & Sons.)

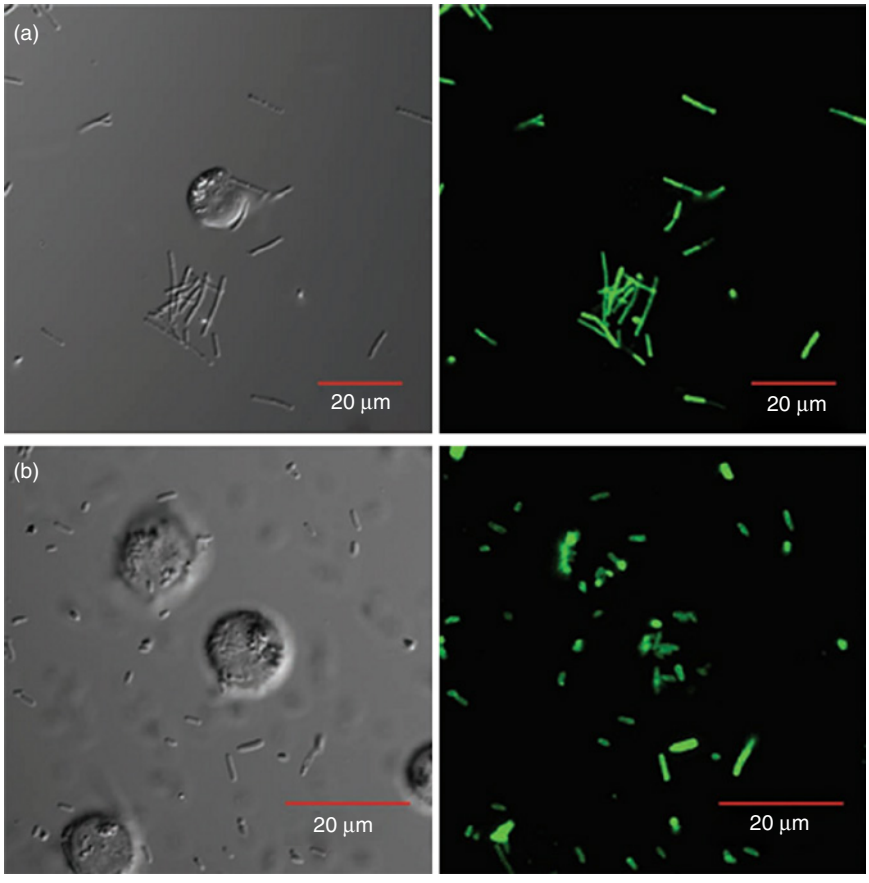

Figure 10.12 CLSM images of Jurkat T cells and Gram-positive *B. Subtilis* incubated with CP21 (a) and Jurkat T cells and Gram-negative ampicillin-resistant *E. coli* incubated with CP21 (b). Left: bright field images, right: fluorescent images. (Adapted from Ref. [24]. Copyright 2011, John Wiley & Sons.)

fluorescence imaging and bacteria killing in a complex system under white light irradiation using CP-based PDT. Generally, PSs that possesses biological cues can have negligible dark toxicity to normal cells during circulation in body fluids. Naturally occurring hematoporphyrin (HP) has been majorly employed as PS in PDT treatment for the same purpose in the past decades. To impart biocompatibility to CPs, Wu *et al.*, coupled CP with porphyrin for synergistic operation. When cationic PFP is self-assembled with anionic HP, researchers observed >9-fold enhancement in HP emission 1P excitation (380 nm) and 30-fold enhancement under 2P excitation conditions (800 nm) [25]. CP mediates energy transfer to porphyrin effectively which is a factor that has significant increment in HP emission. Later, Wu and coworkers synthesized tetraphenylporphyrin (TPP)-doped conjugated polymer nanoparticles (CPN)-based PS with the size of 50 nm [26]. There is 21-fold enhancement in the emission of TPP by two-photon excitation indicating better energy transfer from CP to TPP as compared with

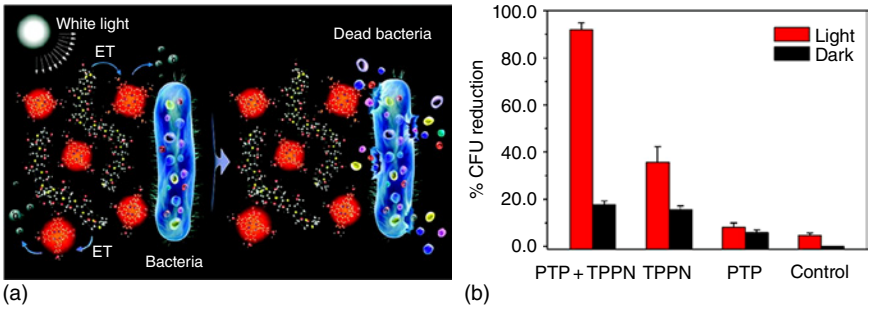

Figure 10.13 (a) Binding and biocidal activity of PT/TPPN complex and (b) % killing efficiency CP8 compared with PTP and TPPN controls under dark and light irradiation. (Adapted from Ref. [27]. Copyright 2009, American Chemical Society.)

HP system. The enhancement in porphyrin emission ultimately improves ROS production. Another important advantage in coupling CP with porphyrin is that site-specific targeting can be realized.

For the first time, Wang and coworkers demonstrated polythiophene (PTP)-porphyrin-based PDT systems (CP8) for antibacterial activity [27]. Polythiophene as donor was functionalized with carboxylic acid to make anionic PTP and porphyrin (TPPN) as acceptor was functionalized with QA to make cationic porphyrin (CP8). Addition of TPPN to PTP made a strong electrostatic complex with a net positive charge. This electrostatic complex was illuminated with white light to check the generation of singlet oxygen compared with TPPN alone. The results highlight the superiority of electrostatic complex with high biocidal activity over TPPN because of additional energy transfer from PTP to TPPN (see Figure 10.13a). The positively charged complex had strong binding and subsequently killed Gram-negative *E. coli* and Gram-positive *B subtilis* with 70% and >90% efficiency, respectively. Figure 10.13b enumerates the biocidal activity of the PTP–TPPN (CP8) complex both in the presence and absence of light along with controlled experiments using PTP and TPPN alone.

Wang and coworkers developed light-activated polythiophene (PT), TPN and CP9-based CP for antifungal activity [28]. CP9 polymer was used already to demonstrate higher singlet oxygen generation that was effective inkilling cancer cells. The porphyrin content was reduced to less than 1% to remove the dark biocidal activity of CP9 polymer. *Aspergillus niger* was chosen as the model fungi which is the most common fungus to impart strong resistance against antifungal chemical agents. Bodipy-based conjugated polymer (CP3) was developed by Wang and coworkers to demonstrate antibacterial properties against *Escherichia coli* bacteria along with imaging applications [29].

Wang and coworkers developed CP-based antibacterial switch using the PDT approach [30]. Antibacterial switch consists of PPV-based cationic conjugated polymer, oxygen, and white light irradiation. This antibacterial switch works via simple addition of cucurbit[7]uril (CB[7]) and adamantane (AD) to PPV leading to a reversible supramolecular assembly (PPV/CB[7]) and disassembly (PPV + CB[7]/AD) process without complicated synthesis or without modifying the active site of the CP (see Figure 10.14). Cationic PPV polymer has the ability

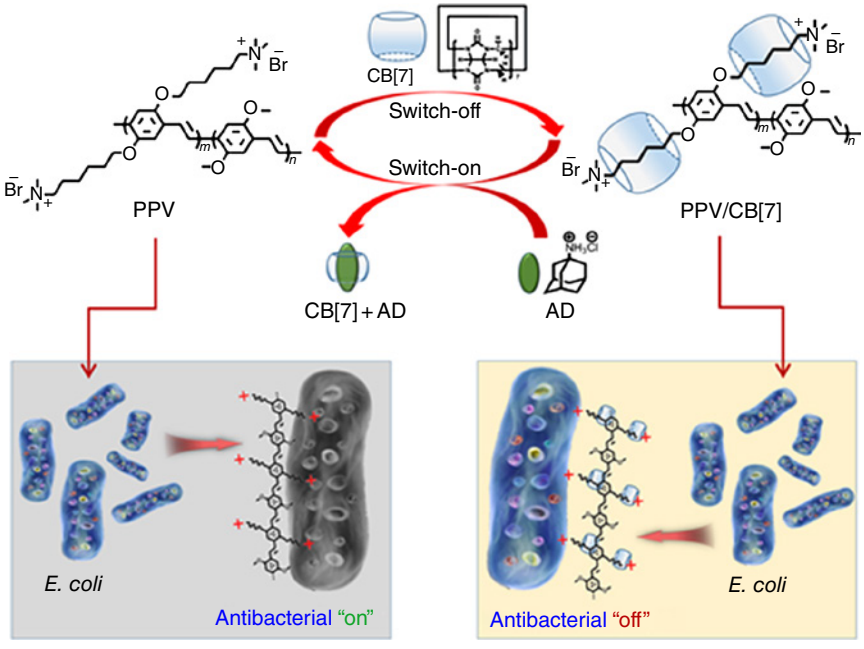

Figure 10.14 Supramolecular antibiotic reversible switch. (Adapted from Ref. [30]. Copyright 2015, John Wiley & Sons.)

to bind and permeate through Gram-negative *E. coli* bacterial cell membrane through electrostatic and hydrophobic interactions, respectively, using cationic QA as the backbone. Irradiation of white light produces ROS and ultimately kills the bacteria (see Figure 10.14). Addition of CB[7] forms a supramolecular host–guest pair between CB[7] and QA groups because CB[7] possesses hydrophilic exterior with hydrophobic cavity facilitating cation–dipole interactions toward QA ions. Addition of (CB[7]) forms a supramolecular complex with QA groups leading to poor contact between oxygen and encapsulated polymers generate negligible ROS.

Encapsulated polymers cannot enter bacteria via electrostatic interactions mechanism, which was confirmed from zeta potential measurements. The polymer does not impart cytotoxicity in switch off mode (see Figure 10.14). Switch "off" mode can be reversed to switch "on" mode by adding cationic (AD) group, which forms more stronger supramolecular complex with CB[7] and retrieves 95% of its antibacterial activity. This method offers a very simple addition of molecules to polymer allowing switch turn-on into turn-off mode reversibly.

To improve the detection strategy of pathogens, a similar supramolecular switch consisting of cationic PFP and PFP-CB[7] was made. This pair was able to reversibly assemble and dissemble in the presence of AD. This reversible supramolecular complex interacts with pathogens such as bacteria and fungi through different degrees of interactions before and after disassembly of the supramolecular complex. [31] This differential interaction with pathogens provides detectable fluorescence and different signal read out to identify the pathogens via simple

addition. Inspired by the work on PFP- based supramolecular switches, very recently Wang and coworkers introduced the pretreatment strategy to the switch using Triton X which is a well-known non-ionic surfactant and also disaggregates CP for amplification of bioactivity [32]. The antibacterial activity of PFP and PFP/CB[7] supramolecular complex without pretreatment with Triton X-100 was ineffective because of the strong aggregating behavior of PFP and PFP/CB[7] in aqueous medium. Pretreatment of PFP and PFP/CB[7] with Triton X-100 (0.06%) could change aggregation behavior of PFP, which is confirmed by the fluorescence and zeta potential measurements leading to effective biocidal activity. The antibacterial ability of PFP can be turned off by adding CB[7] and turned on again with the addition of AD. Moreover, the regulation of the antibacterial ability of PFP/Triton X both in the dark and under white light irradiation was realized.

10.3.2 Antitumor Therapy

The success of CP-based PDT strategy for antimicrobial activities has attracted researchers to extend this to antitumor activities. As there is alarming rise in the number of cancer patients all over the world, tumor treatment emerges as a hot topic in research to date. There are tremendous efforts taken by the scientific community in developing novel strategies and material design for targeted killing of cancer cells. Wang and coworkers pioneered in CP-based PDT for tumor treatment and also initiated CP-based PTT. In 2010, a novel cationic polythiophene (PMNT) (Scheme 10.4) polymer was designed to penetrate renal cell carcinoma (A498) cancer cells and to induce apoptosis in cancer cells under light irradiation within 6 min [33]. Light irradiation (at $\lambda = 455/470$) over incubated CP22 with A498 cells results in caspase-3 expression confirming the entry of PMNT into cytoplasm and induced cell apoptosis.

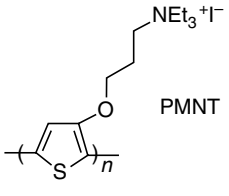

CP22

Scheme 10.4 Chemical structure of PMNT.

Tumor killing efficiency of PDT depends on major factors, namely, irradiating wavelength, absorption cross-section and quantum yield (QY) of CP, and ROS generation efficiency. The important works dealing with strategies and designs to meet these factors will be discussed in this section. Near-IR wavelength irradiation is suggested for deeper penetration and therefore, PS-like porphyrin moieties having strong far-red/near-IR absorption are adopted in the design. The strategy of FRET between visible light-absorbing donors (D) and NIR-emitting acceptors (A) is also employed in some of the designs. The strong energy

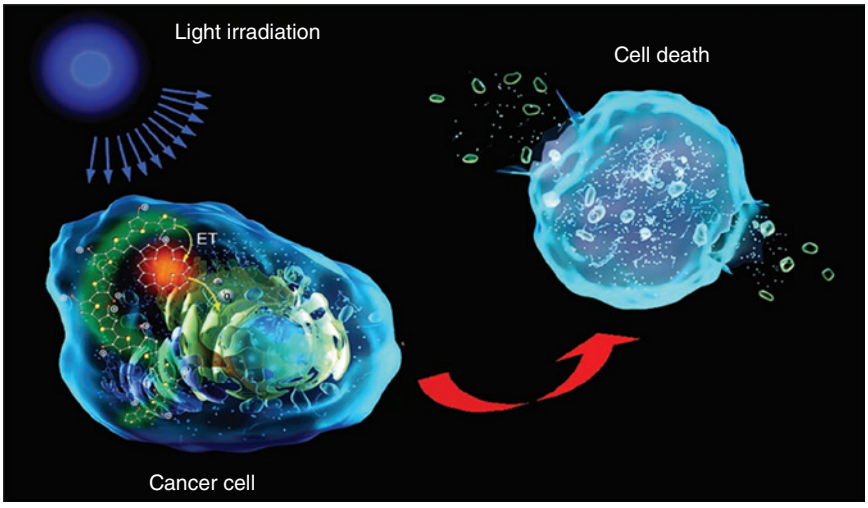

Figure 10.15 Schematic representation of cancer cell death induced by ROS generation in PDT.

transfer from D to A intensifies the NIR emission with high QY. Wang and coworkers designed a copolymer using polythiophene and porphyrin. Covalent incorporation of porphyrin moieties in the CP backbone improves ROS generation due to FRET and the killing efficiency of A498 and A549 cancer cells increases multifold [34] which is schematically represented in Figure 10.15.

Generally, PSs pose leaching problems imparting negative dark toxicity. CP-based quantum dots, P-dots are enriched with photostability to overcome leaching problems. P-dots of PFBT-TPP polymer are synthesized and utilized for PDT [35]. P-dots with short emission lifetimes face interference from background fluorescence and autofluorescence of cells and other biosubstrates. Hence, conjugated backbone is covalently attached with phosphorescent metal complexes having long emission lifetime. A ratiometric sensor is developed by conjugating blue-light-emitting polyfluorene (PF) with red-phosphorescence-emitting Ir metal complexes (see Figure 10.16). It is noted that the triplet energy state of Ir complexes is feasible for triplet–triplet annihilation with triplet oxygen that leads to singlet oxygen generation and quenching of phosphorescence as oxygen sensing signal. When there is complete quenching of phosphorescence with ROS generation, blue emission from PF visibly appears. The intensity of blue light is slightly lower than that of the parent PF due to marginal FRET from PF to Ir complexes [36].

The delivery of PSs is mostly accomplished through encapsulation in amphiphilic polymer micelles/vesicles. When PS is taken as encapsulated form, aggregation quenching effects with poor QY of ROS will be imposed. Liu and coworkers developed a new conjugated copolymer consisting of tetraphenylethylene (TPE), an iconic aggregation-induced emission (AIE) active group as the electron donor, and anthraquinone (AQ) as the acceptor. The polymer inherits the characteristics of both the monomers and thus it exhibits AIE after encapsulated in PEG-matrices.

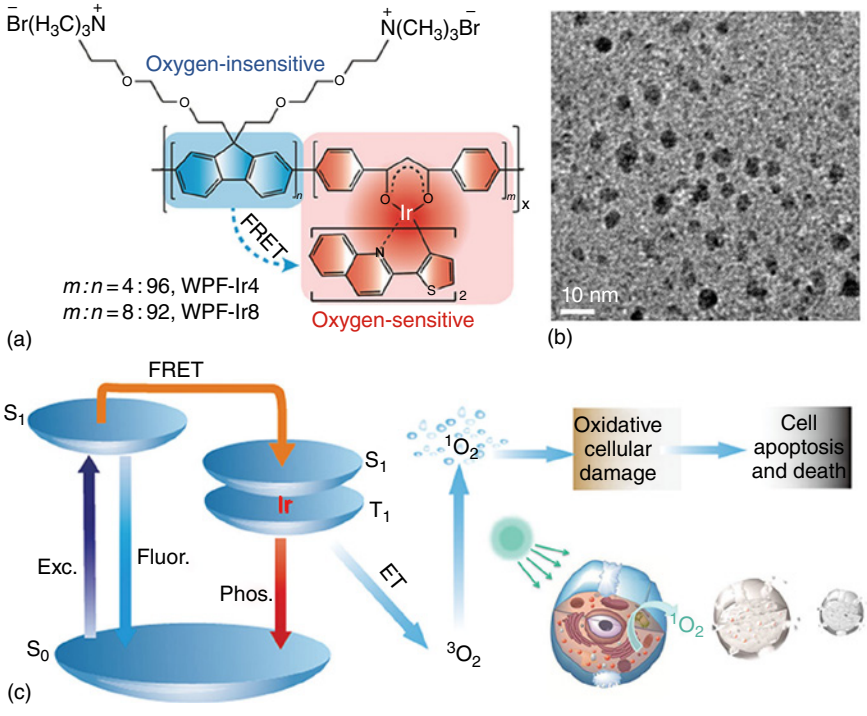

Figure 10.16 (a) Chemical structures of phosphorescent CPs with the Ir(III) complexes; (b) HR-TEM of WPF-Ir4 in aqueous solution; and (c) mechanisms illustrating oxygen sensing and PDT. (Adapted from Ref. [36]. Copyright 2014, John Wiley & Sons.)

There is strong FRET from TPE to AQ making it an NIR emissive polymer for efficient singlet oxygen generation under white light irradiation [37].

The periphery of the CPN is functionalized for specific location of cancer cells and further penetration into cytoplasm. When CPN is functionalized with —COOH groups, it is not easy to stain the cells because of repulsive forces from the negative charge on the cells. It is necessary for cofunctionalization with an antibody (**a**nti-epCAM) and a (protein) transcriptional activator protein [38]. Drug resistance in cancer cells poses big challenges to chemotherapy. Wang and coworkers introduced a new therapy modality through light manipulation to combat drug resistance (see Figure 10.17). They used OPV as PS that is anchored in the cell membrane through electrostatic interactions. During the time of polymer penetration (time window – 0–45 min) into the membrane, light irradiation is manipulated. This creates defects in the cell membrane and influxes the drugs into cells. It is also noted that interaction between drug and OPV is also an additional factor for drug influx. Among the drugs tested, doxorubicin influx is the highest because of pi–pi interactions between the backbone of OPV and doxorubicin [39].

Bioluminescence is indispensable for site-specific light activation in place of an external source. The generation of reactive oxygen species can be controlled in the vicinity of bioluminescence (see Figure 10.18). Wang group collaborated on

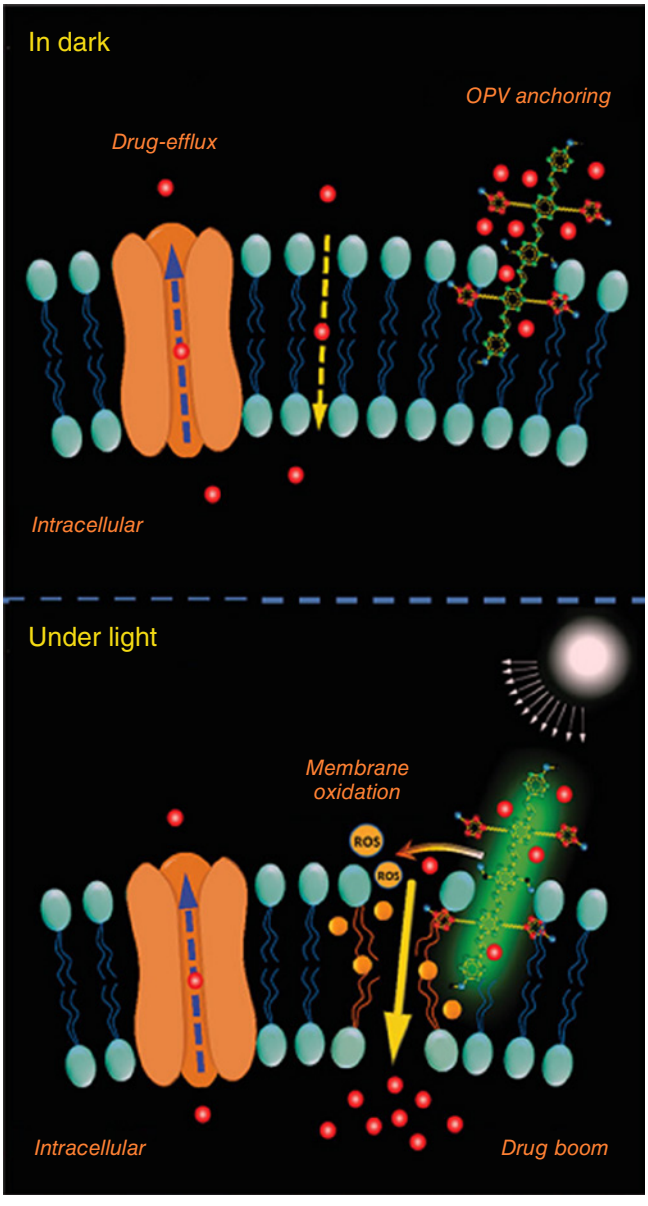

Figure 10.17 Schematic representation of mechanism of light manipulated drug-uptake approach to combat drug resistance in cancer cells. (Adapted from Ref. [39]. Copyright 2014, John Wiley & Sons.)

implementing this concept of bioluminescence as a light source in PDT [40]. They used a mixture of luminol, hydrogen peroxide, and horseradish peroxidase (HRP) for chemically induced light activation by CP. Oxidized luminol in the presence of hydrogen peroxide and HRP emits brilliant blue light and the energy is transferred to CP (BRET). Cationic OPV, which can penetrate the cell, was

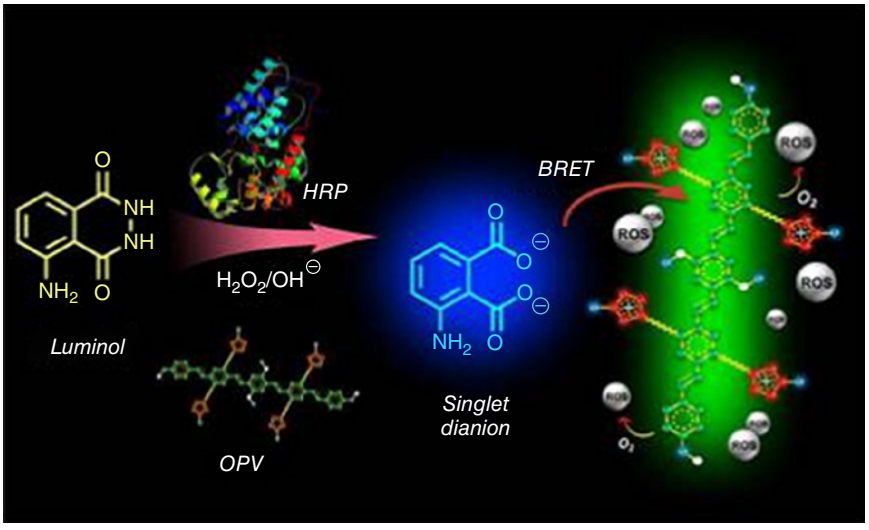

Figure 10.18 Lumol-induced BRET transfer to PPV for effective PDT. (Adapted from Ref. [40]. Copyright 2012, American Chemical Society.)

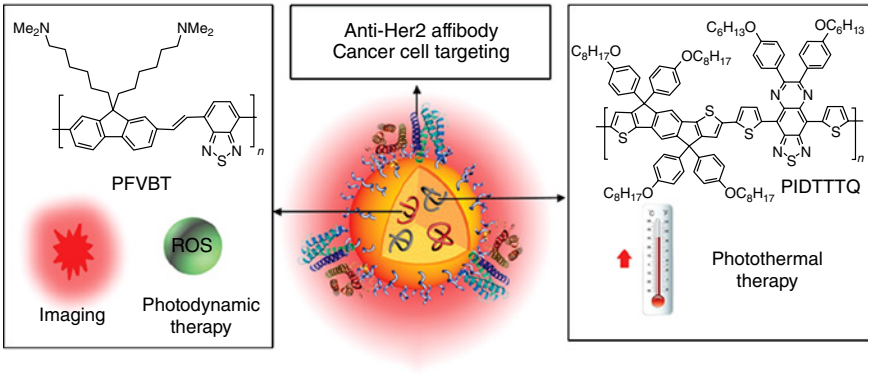

Figure 10.19 Schematic illustration of the combined functions of PDT and PTT in single system. (Adapted from Ref. [41]. Copyright 2017, John Wiley & Sons.)

chosen as PS and upon BRET, PS involved in ROS generation was used for killing of tumors *in vivo* even in the deeper tissue.

PTT is an indispensable strategy to treat hypoxic tumors that are cancer tissue deprived of oxygen levels. Near-IR/FIR probes are advantageous in PTT to convert light energy into thermal energy. The local rise in temperature due to thermal energy dissipation causes cell ablation and ultimately cell death [34]. Wang and coworkers synthesized the first example of CP-based PTT and demonstrated along with designing guidelines. In the design, a FRET pair is adopted to have visible light absorption and NIR emission for achieving greater absorption cross-section and deeper penetration. The choice of porphyrin as an NIR emissive unit adds another benefit of ROS generation. Bin Liu and coworkers, developed

conjugated polymer nanoparticles with porphyrin as the donor and BT as the acceptor that shows large absorption at a long wavelength Q band (see Figure 10.19). The aggregation of encapsulated CPN increases the exciton energy dissipation of porphyrin. The high nonradiative decay rate increases the conversion efficiency of light energy into thermal energy. PFBT is also coencapsulated for image guiding cellular apoptosis. The same group designed single system for combining PDT and PTT via encapsulation of PFVBT and PFDTTTQ for ROS generation and light into thermal energy conversion, respectively, in PEG-matrices functionalized with targeting antibodies [41].

Wang and coworkers designed series of P-dots using different thiophene-based units as donor and diketopyrrolopyrrole as acceptor. All of the P-dots in that series display strong NIR absorbance and high photothermal conversion efficiency resulting in ablation of cancer cells both *in vitro* and *in vivo* with 100% tumor elimination [42]. Zhu and coworkers combined two-photon activated 2PA energy transfer with photothermal effect for enhanced efficiency in PDT. In this contribution, the idea is to use the photothermal effect occurring by NIR light irradiation to switch on FRET. A core shell unimolecular micelle architecture is formed by taking 2PA hyper branched CP in the core and thermoresponsive hyper branched polyether as shell (HCP@HPE). The shell is functionalized with chlorine e6 (Ce6) as acceptor to HCP for feasible FRET in FIR emission. When the NIR is irradiated, the shell collapses triggering FRET between donor and acceptor. The switch-on IR emission involves in efficient ROS generation for killing tumors (see Figure 10.20) [43].

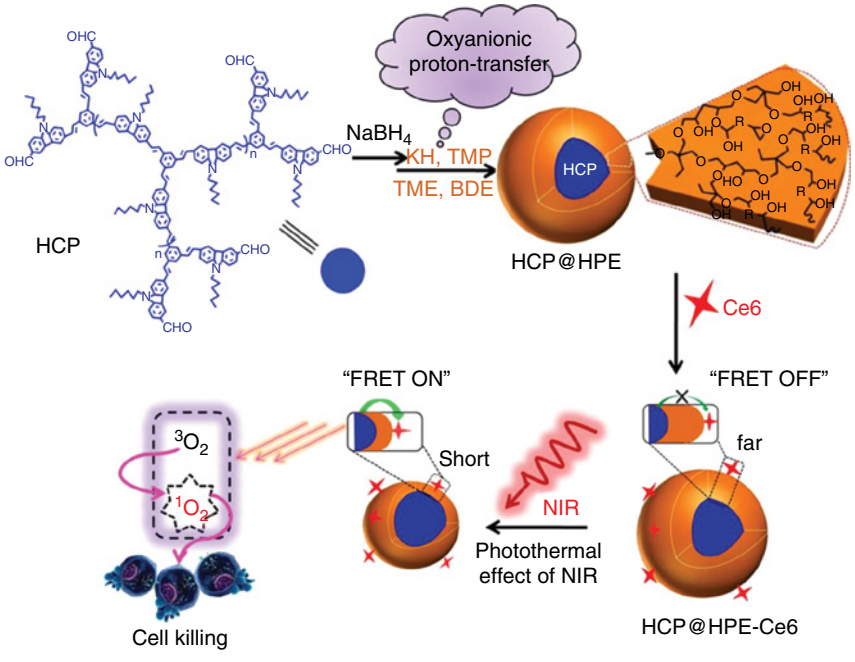

Figure 10.20 Illustration of thermoresponsive HCP@HPE unimolecular micelles and illustration of the combination of 2P-FRET and photothermal effect of NIR for photodynamic therapy. (Adapted from Ref. [43]. Copyright 2016, John Wiley & Sons.)

10.4 Conclusions and Future Perspectives

PDT has been an ever-growing technique offering diverse treatments for various ailments such as tumor, microbial infections, ophthalmology, and acne. The role of major components and photochemical mechanistic insights are described with schematic representations. Light-activated PS generates singlet oxygen as a key cytotoxic agent for killing diseased tissues. The limited diffusion of $^1O_2$ to single cell length is advantageous for selective killing but the challenge is site-specific generation of $^1O_2$ species. The penetration depth of external light sources is another serious concern. The visible light is limited to a <2 mm depth penetration thereby restricting wide applicability. NIR probes show deeper tissue penetrating abilities (>3 mm) and therefore, developing such probes attains great research interest at present. Research has also been focused on adopting bioluminescence in place of external light source. Future research has to explore more number of designs in selective bioluminescent probes.

The design of PS plays a pivotal role in target-oriented accumulation and efficient reactive species generation. Conjugated polymers attract researchers for broad absorption, solubility, and easy functionalization that have led to the use of CP as PS in PDT. Donor acceptor pair of CP with porphyrin, two-photon absorption CPs and P-dots are designed for enhancing ROS generation.

CP-based PDT finds applications for antimicrobial and antitumor treatments so far and further research activities are ongoing extensively. The strategy is to exploit electrostatic interactions for cell penetration and ROS generation and subsequent killing of bacterial cell/tumors under light irradiation. Whitten and coworkers pioneered in developing series of cationic CPs, polymer beads, and microcapsules but these were limited in scope for complex systems. Wang group were successful in selective killing of bacteria in complicated environments and also integrated recognition, imaging, and killing in single PDT systems. Further, the same group developed supramolecular switches using cucurbituril hosts with germicide action. Composites of CP with metal NPs have been reported for antifungal activity. In, 2010 Wang and coworkers pioneered in developing anticancer PDT systems. PDT is also applied to increase drug efflux in drug-resistance cells. To treat hypoxic tumors with low oxygen content, photothermal therapy was introduced. Liu *et al.* developed novel designs of NIR emissive CP for combining PTT and PDT in single systems. NIR light-triggered thermoresponsive polymers are of great interest for causing cancer cell ablation.

In the future, CP-based PDT systems can be explored for treating other diseases such as acne, HIV, and vascular targeting. Water-soluble CP can be developed into hydrogels having ability for noninvasive penetration into skin layers in acne treatment. The scope of research on CP-based PDT is expanding day-by-day with full-fledged potential for achieving noninvasive and nontoxic PDT in clinical treatments.

References

1 Fitzpatrick, T.B. and Pathak, M.A. (1959) Historical aspects of methoxsalen and other furocoumarins. *J. Invest. Dermatol.*, **32**, 229–231.

2 Bloomfield, M. (1897) *Sacred Books of the East; Hymns of Atharva-Veda*, vol. **XLII**, Clarendon Press, Oxford.

3 Jonathan, P.C., Bryan, Q.S., Imran, R., Conor, L.E., Kimberly, S.S., Sarika, V., Brian, W.P., and Tayyaba, H. (2010) Imaging and photodynamic therapy: mechanisms, monitoring and optimization. *Chem. Rev.*, **110**, 2795–2838.

4 Zhu, C., Liu, L., Yang, Q., Lv, F., and Wang, S. (2012) Water-soluble conjugated polymers for imaging, diagnosis, and therapy. *Chem. Rev.*, **112**, 4687–4735.

5 Liu, P., Poon, Y.F., Li, W., Zhu, H.-Y., Yeap, S.H., Cao, Y., Qi, X., Zhou, C., Lamrani, M., Beuerman, R.W., Kang, E.-T., Mu, Y., Li, C.M., Chang, M.W., Jan Leong, S.S., and Chan-Park, M.B. (2011) A polycationic antimicrobial and biocompatible hydrogel with microbe membrane suctioning ability. *Nat. Mater.*, **10**, 149–156.

6 Liu, J. and Liu, B. (2017) Red and near infrared fluorescent conjugated polyelectrolytes for biomedical applications. *J. Polym. Sci., Part A: Polym. Chem.*, **55**, 519–532.

7 Lv, F., Qiu, T., Liu, L., Ying, J., and Wang, S. (2016) Recent advances in conjugated polymer materials for disease diagnosis. *Small*, **12**, 696–705.

8 Ethirajan, M., Chen, Y., Joshi, P., and Pandey, R.K. (2011) The role of porphyrin chemistry in tumor imaging and photodynamic therapy. *Chem. Soc. Rev.*, **40**, 340–362.

9 Lucky, S.S., Soo, K.C., and Zhang, Y. (2015) Nanoparticles in photodynamic therapy. *Chem. Rev.*, **115**, 1990–2042.

10 Zhou, Z., Song, J., Nie, L., and Chen, X. (2016) Reactive oxygen species generating systems meeting challenges of photodynamic cancer therapy. *Chem. Soc. Rev.*, **45**, 6597–6626.

11 Oleinick, N.L., Morris, R.L., and Belichenko, I. (2002) The role of apoptosis in response to photodynamic therapy: what, where, why, and how. *Photochem. Photobiol. Sci.*, **1**, 1–21.

12 Sharman, W.M., Allen, C.M., and Van Lier, J.E. (2000) Role of activated oxygen species in photodynamic therapy. *Methods Enzymol.*, **319**, 376–400.

13 Agostinis, P., Berg, K., Cengel, K.A., Foster, T.H., Girotti, A.W., Gollnick, S.O., Hahn, S.M., Hamblin, M.R., Juzeniene, A., Kessel, D., Korbelik, M., Moan, J., Mroz, P., Nowis, D., Piette, J., Wilson, B.C., and Golab, J. (2011) Photodynamic therapy of cancer: an update. *CA-Cancer J. Clin.*, **61**, 250–281.

14 Wilson, B. (2002) Photodynamic therapy for cancer: principles. *Can. J. Gastroenterol. Hepatol.*, **16**, 393–396.

15 Luo, S., Zhang, E., Su, Y., Cheng, T., and Shi, C. (2011) A review of NIR dyes in cancer targeting and imaging. *Biomaterials*, **32**, 7127–7138.

16 Hong, G., Diao, S., Chang, J., Antaris, A.L., Chen, C., Zhang, B., Zhao, S., Atochin, D.N., Huang, P.L., Andreasson, K.I., Kuo, C.J., and Dai, H. (2014) Through-skull fluorescence imaging of the brain in a new near-infrared window. *Nat. Photonics*, **8**, 723–730.

17 Grimland, J.L., Wu, C., Ramoutar, R.R., Brumaghim, J.L., and McNeill, J. (2011) Photosensitizer-doped conjugated polymer nanoparticles with high cross-sections for one- and two-photon excitation. *Nanoscale*, **3**, 1451–1455.

18 Lu, L., Rininsland, F.H., Wittenburg, S.K., Achyuthan, K.E., McBranch, D.C., and Whitten, D.G. (2005) Biocidal activity of a light-absorbing fluorescent conjugated polyelectrolyte. *Langmuir*, **21**, 10154–10159.

19 Chemburu, S., Corbitt, T.S., Ista, L.K., Ji, E., Fulghum, J., Lopez, G.P., Ogawa, K., Schanze, K.S., and Whitten, D.G. (2008) Light-induced biocidal action of conjugated polyelectrolytes supported on colloids. *Langmuir*, **24**, 11053–11062.

20 Corbitt, T.S., Ding, L., Ji, E., Ista, L.K., Ogawa, K., Lopez, G.P., Schanze, K.S., and Whitten, D.G. (2009) Light and dark biocidal activity of cationic poly(arylene ethynylene) conjugated polyelectrolytes. *Photochem. Photobiol. Sci.*, **8**, 998–1005.

21 Corbitt, T.S., Sommer, J.R., Chemburu, S., Ogawa, K., Ista, L.K., Lopez, G.P., Whitten, D.G., and Schanze, K.S. (2009) Conjugated polyelectrolyte capsules: light-activated antimicrobial micro "roach motels". *ACS Appl. Mater. Interfaces*, **1**, 48–52.

22 Ramos, J.C., Ledezma, A., Moggio, I., Arias, E., Vazquez, R.A., Martinez, C.A., Torres, J.R., Ziolo, R.F., Garcia, P., Sepulveda, S., Yacaman, M.J., and Olivas, A. (2009) Composites of bromobenzenethiol functionalized gold nanoparticles and the fluorescent poly(phenylene ethynylene) pPET3OC12-sqS for optical biosensors. *J. Nano Res.*, **5**, 37–46.

23 Ramos, J.C., Ledezma, A., Arias, E., Moggio, I., Martinez, C.A., and Castillon, F. (2010) Optical and morphological characterisation of a silver nanoparticle/fluorescent poly(phenylenethynylene) composite for optical biosensors. *Vacuum*, **84**, 1244–1249.

24 Zhu, C.L., Yang, Q., Liu, L., Lv, F., Li, S., Yang, G., and Wang, S. (2011) Multifunctional cationic poly(*p*-phenylene vinylene) polyelectrolytes for selective recognition, imaging, and killing of bacteria over mammalian cells. *Adv. Mater.*, **23**, 4805–4810.

25 Wu, C.L. and Xu, Q.H. (2009) Enhanced one- and two-photon excitation emission of a porphyrin photosensitizer by FRET from a conjugated polyelectrolyte. *Macromol. Rapid Commun.*, **30**, 504–508.

26 Shen, X.Q., He, F., Wu, J.H., Xu, G.Q., Yao, S.Q., and Xu, Q.H. (2011) Enhanced two-photon singlet oxygen generation by photosensitizer-doped conjugated polymer nanoparticles. *Langmuir*, **27**, 1739–1744.

27 Xing, C.F., Xu, Q.L., Tang, H.W., Liu, L.B., and Wang, S. (2009) Conjugated polymer/porphyrin complexes for efficient energy transfer and improving light-activated antibacterial activity. *J. Am. Chem. Soc.*, **131**, 13117–13124.

28 Xing, C., Yang, G., Liu, L., Yang, Q., Lv, F., and Wang, S. (2012) Conjugated polymers for light-activated antifungal activity. *Small*, **8**, 525–529.

29 Chong, H., Nie, C., Zhu, C., Yang, Q., Liu, L., Lv, F., and Wang, S. (2012) Conjugated polymer nanoparticles for light-activated anticancer and antibacterial activity with imaging capability. *Langmuir*, **28**, 2091–2098.

30 Bai, H., Yuan, H., Nie, C., Wang, B., Lv, F., Liu, L., and Wang, S. (2015) A supramolecular antibiotic switch for antibacterial regulation. *Angew. Chem. Int. Ed.*, **54**, 13208–13213.

31 Bai, H., Chen, H., Hu, R., Li, M., Lv, F., Liu, L., and Wang, S. (2016) Supramolecular conjugated polymer materials for in situ pathogen detection. *ACS Appl. Mater. Interfaces*, **8**, 31550–31557.

32 Bai, H., Zhang, H., Hu, R., Chen, H., Lv, F., Liu, L., and Wang, S. (2017) Supramolecular conjugated polymer systems with controlled antibacterial activity. *Langmuir*, **33**, 1116–1120.

33 Liu, L., Yu, M., Duan, X., and Wang, S. (2010) Conjugated polymers as multifunctional biomedical platforms: anticancer activity and apoptosis imaging. *J. Mater. Chem.*, **20**, 6942–6947.

34 Xing, C., Liu, L., Tang, H., Feng, X., Yang, Q., Wang, S., and Bazan, G.C. (2011) Design guidelines for conjugated polymers with light activated anticancer activity. *Adv. Funct. Mater.*, **21**, 4058–4067.

35 Chang, K., Tang, Y., Fang, X., Yin, S., Xu, H., and Wu, C. (2016) Incorporation of porphyrin to π-conjugated backbone for polymer-dot-sensitized photodynamic therapy. *Biomacromolecules*, **17**, 2128–2136.

36 Shi, H., Ma, X., Zhao, Q., Liu, B., Qu, Q., An, Z., Zhao, Y., and Huang, W. (2014) Ultra small phosphorescent polymer dots for ratiometric oxygen sensing and photodynamic cancer therapy. *Adv. Funct. Mater.*, **24**, 4823–4830.

37 Wu, W.W., Feng, G., Xu, S., and Liu, B. (2016) A photostable far-red/near-infrared conjugated polymer photosensitizer with aggregation-induced emission for image guided cancer cell ablation. *Macromolecules*, **49**, 5017–5025.

38 Feng, L., Zhu, J., and Wang, Z. (2016) Biological functionalization of conjugated polymer nanoparticles for targeted imaging and photodynamic killing of tumor cells. *ACS Appl. Mater. Interfaces*, **8**, 19364–19370.

39 Wang, B., Yuan, H., Liu, Z., Nie, C., Liu, L., Lv, F., Wang, Y., and Wang, S. (2014) Cationic oligo (*p*-phenylene vinylene) materials for combating drug resistance of cancer cells by light manipulation. *Adv. Mater.*, **26**, 5986–5990.

40 Yuan, H., Chong, H., Wang, B., Zhu, C., Liu, L., Yang, Q., Lv, F., and Wang, S. (2012) Chemical molecule-induced light-activated system for anticancer and antifungal activities. *J. Am. Chem. Soc.*, **134**, 13184–13187.

41 Feng, G., Fang, Y., Liu, J., Geng, J., Ding, D., and Liu, B. (2017) Multifunctional conjugated polymer nanoparticles for image-guided photodynamic and photothermal therapy. *Small*, **13**, 1602807.

42 Li, S., Wang, X., Hu, R., Chen, H., Li, M., Wang, J., Wang, Y., Liu, L., Lv, F., Liang, X.J., and Wang, S. (2016) Near-infrared (NIR)-absorbing conjugated polymer dots as highly effective photothermal materials for in vivo cancer therapy. *Chem. Mater.*, **28**, 8669–8675.

43 Huang, Y., Qiu, F., Shen, L., Chen, D., Su, Y., Yang, C., Li, B., Yan, D., and Zhu, X. (2016) Combining two-photon-activated fluorescence resonance energy transfer and near-infrared photothermal effect of unimolecular micelles for enhanced photodynamic therapy. *ACS Nano*, **10**, 10489–10499.

11

Conjugated Polymers for Near-Infrared Photothermal Therapy of Cancer

Ligeng Xu, Xuejiao Song, and Zhuang Liu

Soochow University, Institute of Functional Nano & Soft Materials (FUNSOM), 199 Ren-ai Road, Suzhou Industrial Park, Suzhou, 215123, China

11.1 Introduction

As discussed in other chapters, the unique physiochemical properties such as high conductivity, good stability, and biocompatibility make organic conjugated polymers promising candidates in biomedical applications [1, 2]. In addition, some kinds of conjugated polymers also show unique absorption in the near-infrared (NIR) region with ideal photostability [3]. Furthermore, the heat energy can be generated from the absorbed optical energy with high efficiency [4]. Recently, as an emerging treatment modality, photothermal therapy (PTT), which employs heat generated from the absorbed optical energy by light-absorbing agents, can selectively heat cancers with minimal invasiveness and low toxicity to normal tissues [5]. Meanwhile, besides directly ablating tumors, this therapeutic strategy can also induce antitumor immune responses for combination cancer immunotherapy through inducing the release of tumor-associated antigens from treated tumor tissues [6–11]. All these abovementioned unique advantages of conjugated polymers make it a promising photothermal agent for cancer treatment. Recently, we and other groups have discovered the potential applications of those organic conjugated polymers as photothermal agents for cancer treatment. Moreover, the conjugated polymers-based multifunctional nanoplatforms have been also developed for precision cancer treatment or combination therapy. Undoubtedly, there are still perspectives and challenges for the conjugated polymers-based cancer treatment in future. All these abovementioned progresses and issues will be discussed in this chapter.

11.2 Conjugated Polymers for Cancer Photothermal Therapy

Until now, several kinds of conjugated polymers with high NIR absorbance including polyaniline (PANI), polypyrrole (PPy), poly-(3,4-ethylenedioxythiophene):poly

Conjugated Polymers for Biological and Biomedical Applications, First Edition. Edited by Bin Liu

(4-styrenesulfonate) (PEDOT: PSS), poly[9,9-bis(4-(2-ethylhexyl)phenyl)-fluorene-*alt*-*co*-6,7-bis(4-(hexyloxy)phenyl)-4,9-di(thiophen-2-yl)-thiadiazoloquinoxaline] (PFTTQ), and donor–acceptor ones have shown great potential as photothermal agents for cancer treatment.

11.2.1 Polyaniline (PANI) Nanoparticles

PANI is the first conjugated polymer reported as a photothermal agent for treatment of cancer [12–14]. Generally speaking, PANI nanoparticles will transit from the emeraldine base (EB) state to the emeraldine salt (ES) state in the presence of dopants such as strong acids, Lewis acids, transition metals, and alkali ions [15]. Subsequently, the absorption peak shows a significant red-shift toward the NIR region. Yang *et al.* [12] took full advantage of the unique properties of the intracellular microenvironment of cancer cells, that is, potential biodopants such as protons, alkali ions, and oxidative species, to realize the transition of polyaniline nanoparticles (PANPs) from the EB state (EB-PANPs) to the ES state (ES-PANPs) (Figure 11.1a). It was shown that the NIR-absorbing ES-PANPs

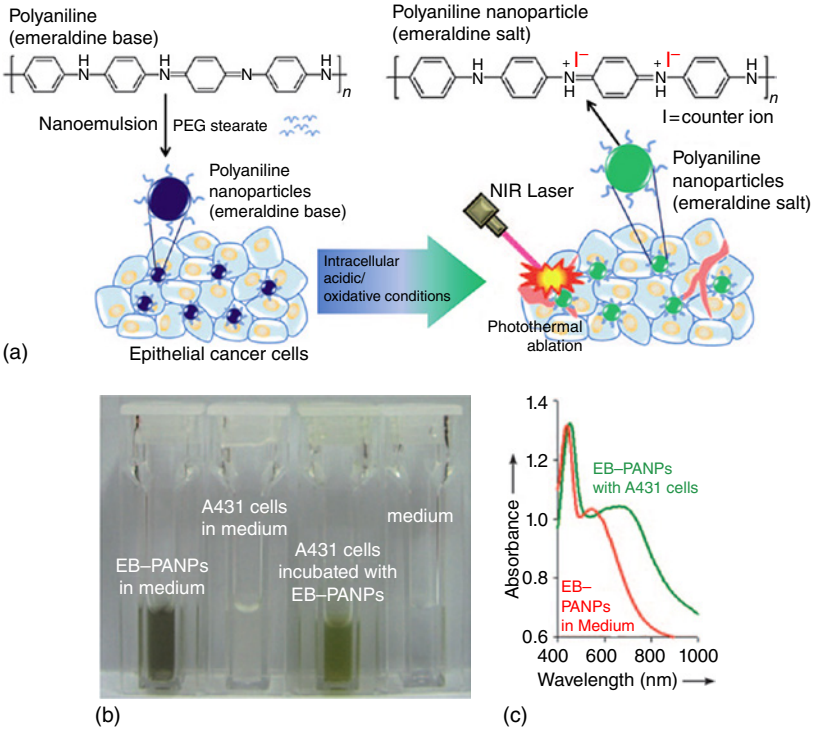

Figure 11.1 Polyaniline nanoparticles (PANP) serve as NIR-absorbing photothermal agents within a tumor. (a) The scheme of the preparation of PANP. (b) Photographs of EB-PANPs in culture medium, A431 cells in culture medium, A431 cells incubated with EB-PANPs (transition to ES-PANPs), and the free medium. (c) Absorption spectra of A431 cells treated with EB-PANPs (transition to ES-PANPs) and free EB-PANPs in culture medium. (Reproduced with permission from Ref. [12]. Copyright 2011, WILEY-VCH Verlag GmbH & Co. KGaA, Weinheim.)

formed when EB-PANPs were incubated with live epithelial cancer cells (A431) but not with the A431 cell lysate (Figure 11.1b, c). Furthermore, both *in vitro* and *in vivo* experiments showed that A431 cancer cells and A431 tumors could be effectively ablated when treated with ES-PANPs followed by exposure to 808 nm NIR laser at a power density of 2.45 W cm^{-2} for 5 min. Another study by Zhou *et al.* [14] also demonstrated the high photothermal conversion efficiency and excellent *in vivo* therapeutic efficacy of the functionalized PANPs using intratumoral injection.

11.2.2 Polypyrrole (PPy) Nanoparticles

Among different kinds of conjugated polymers explored for PTT applications, polypyrrole (PPy) is the most extensively studied [3, 16, 17]. Owing to its strong NIR absorbance, PPy nanoparticles have shown great potential as contrast agents for optical coherence tomography (OCT) in cancer diagnosis [18]. Moreover, the nanoparticles have also shown promising applications in biosensor [19], drug delivery [20], and nerve regeneration [21]. However, their potential application in cancer photothermal therapy was just discovered in the past few years. In 2012, our group systematically investigated its therapeutic potential at *in vitro* and *in vivo* levels for cancer PTT [3]. In this study, PPy nanoparticles were synthesized via aqueous phase polymerization using poly(vinyl alcohol) (PVA) as a stabilizing agent. Importantly, this kind of PPy nanoparticles showed excellent stability in physiological solutions and ideal photostability without any significant decrease even after laser exposure for a long time (1 h), which is greatly useful for photothermal therapy. Meanwhile, PPy nanoparticles exhibited no obvious toxicity to various types of cells (4T1, U937, and 293T cells) even at the highest concentration (100 μg ml^{-1}). Besides demonstrating high efficacy for photothermal cancer cells ablation *in vitro*, it was found that PVA-coated PPy nanoparticles used in photothermal therapy could completely eliminate mouse breast tumor (4T1 tumor model) at a dosage of 2 mg kg^{-1} using 808 nm NIR laser irradiation with an ultralow power density of 0.25 W cm^{-2} for 5 min. Furthermore, the *in vivo* toxicity assays indicated that PVA-coated PPy nanoparticles did not show any apparent toxicity to organs including heart, liver, spleen, lung, and kidney.

Nearly at the same time, Chen *et al.* developed the poly(vinylpyrrolidone) (PVP)-coated PPy nanoparticles using the same preparation method [16]. In this study, PVP-coated PPy nanoparticles were intravenously injected into 4T1 tumor-bearing mice at a dosage of 10 mg kg^{-1} and high therapeutic efficacy was demonstrated using a 808nm-NIR laser with the power density of 1 W cm^{-2} for 5 min. Moreover, no tumor relapse was observed even at a long time (60 days) post irradiation. Besides therapeutic efficacy evaluations, the biodistribution and toxicity profile of the nanoparticles in important organs such as liver, spleen, and kidney were also investigated by selecting SiO_2@PPy nanoparticles to simulate the *in vivo* behavior of PVP-coated PPy nanoparticles using inductively coupled plasma-atomic emission spectrometry (ICP-AES) and HE staining assay. The nanoparticles showed high accumulation in tumor (5% ID g^{-1}) although mainly locating in liver and spleen. However, it did not show any damage to liver, spleen, and kidney.

11.2.3 PEDOT:PSS–PEG Nanoparticles

As another organic conjugated polymer, poly(3,4-ethylenedioxythiophene):poly(4-styrenesulfonate) (PEDOT:PSS) with strong absorbance in NIR region has shown broad applications in organic electronics [22–24]. It is known that the reticuloendothelial system (RES) is the major barrier for nanomaterials before they arrive at target tissues including tumors. Therefore, in our previous study [25], PEDOT:PSS polymer was modified with polyethylene glycol (PEG) to improve its physiological stability and the blood circulation half-life, which would be greatly helpful for

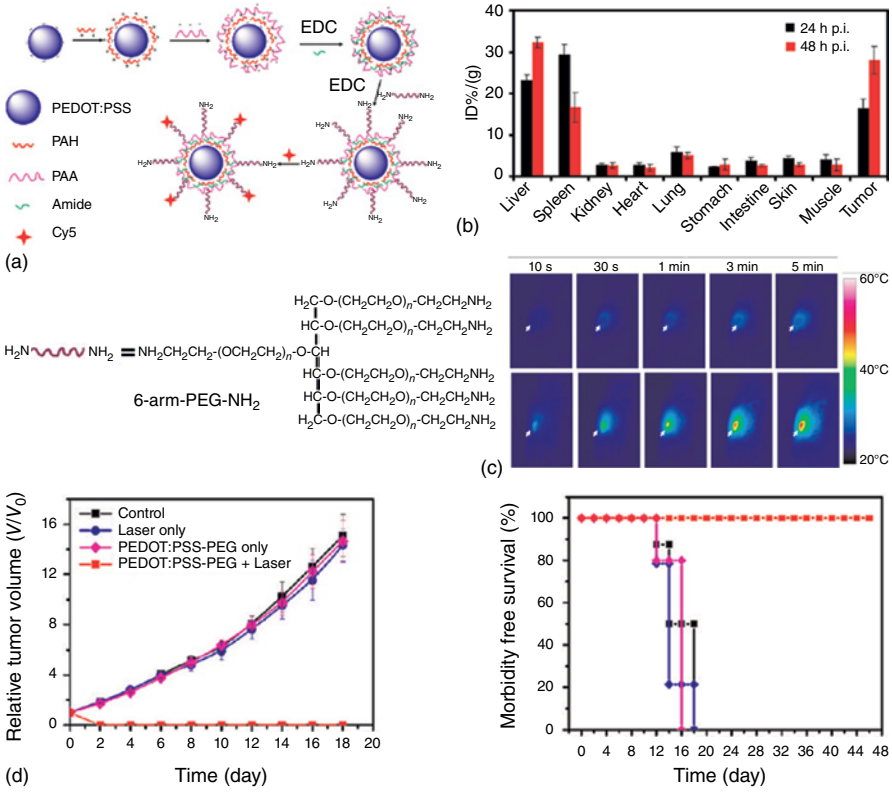

Figure 11.2 PEDOT:PSS–PEG nanoparticles showed ideal therapeutic efficacy under NIR laser irradiation. The preparation scheme (a) and biodistribution (b) of the stealth PEDOT:PSS nanoparticles. (c) Infrared thermal images of 4T1 tumor-bearing mice without (upper row) or with (lower row) intravenous injection of PEDOT:PSS–PEG (10 mg kg^{-1}, 48 h pi) under 808 nm laser irradiation taken at different time intervals. The laser power density was 0.5 W cm^{-2}. Arrows point to the tumors. (d) Growth of 4T1 tumors in different groups of mice after treatment and survival curves of mice after various treatments. PEDOT:PSS–PEG-injected mice after PTT treatment showed 100% survival ratio over 45 days. The relative tumor volumes were normalized to their initial sizes. For the treatment group, 10 mice injected with PEDOT:PSS–PEG at 48 h pi were exposed to the 808 nm laser (0.5 W cm^{-2}, 5 min). The other three groups of mice were used as controls: untreated (control, $n = 8$); laser only without PEDOT:PSS–PEG injection (laser only, $n = 14$); injected with PEDOT:PSS–PEG but without laser irradiation (PEDOT:PSS–PEG only, $n = 10$). Error bars were based on standard deviations. (Reproduced with permission from Ref. [25]. Copyright 2012, American Chemical Society.)

tumor accumulation via the enhanced permeability and retention (EPR) effect (Figure 11.2a). As expected, the biodistribution analysis using fluorescence imaging indicated that this stealth PEGylated PEDOT:PSS polymeric nanoparticles could effectively accumulate in tumor at 48 h post intravenous injection at a dosage of 10 mg kg^{-1} (Figure 11.2b). Meanwhile, PEG molecules did not influence the NIR absorbance of PEDOT:PSS and the temperature increased rapidly when the nanoparticle containing solution was exposed to NIR laser at the power density of 1 W cm^{-2} (Figure 11.2c). Moreover, *in vivo* experiments demonstrated that such stealth nanoparticles-based photothermal therapy could completely eliminate mouse breast tumors at day 2 post irradiation (Figure 11.2d).

11.2.4 Donor–Acceptor (D–A) Conjugated Polymers

Undoubtedly, high heat conversion efficiency is greatly desired for effective photothermal therapy. However, the heat generation efficacy of the abovementioned conjugated polymers still needs improvement because of their broad absorption band and because part of the absorbed energy will decay through radiative pathways. Actually, the absorption property can be tuned using the donor–acceptor (D–A) approach and the band gap of D–A conjugated polymers can be tailored by attaching certain electron donor and electron acceptor monomers. Recently, D–A conjugated polymers have shown broad applications in organic photovoltaics and field-effect transistors. However, D–A conjugated polymers usually exhibit poor solubility in aqueous solvents, limiting their potential application in biomedical fields. Although multiple methods such as nanoprecipitation, amphiphilic polymer encapsulation, and mini-emulsion procedures have been adopted for improving the solubility, cytotoxic surfactants such as sodium dodecylsulfate (SDS) have been used for dispersing the nanoparticles. To address these critical issues, MacNeill and coworkers [26] synthesized two kinds of low band gap D–A conjugated polymers (PCPDTBT, PCPDTBSe) using solvent evaporation and sonication method, in which no additional dispersion reagents were required. Furthermore, it was indicated that those polymeric nanoparticles were nontoxic to RKO and HCT116 colorectal cancer cells without NIR laser irradiation. When exposed to a 808-nm-NIR laser at the power density of 0.6 W cm^{-2} for 5 min, 75–80% of cancer cells were eliminated at nano-PCPDTBSe concentrations above 125 μg ml^{-1}, while 90–95% of cells were killed at nano-PCPDTBT concentrations above 62 μg ml^{-1}. However, this study did not evaluate the therapeutic efficacy of those D–A conjugated polymers used in *in vivo* tumor models.

In addition, Geng *et al.* [27] prepared D–A conjugated polymer nanoparticles based on poly[9,9-bis(4-(2-ethylhexyl)phenyl)fluorene-*alt*-*co*-6,7-bis(4-(hexyloxy)phenyl)-4,9-di(thiophen-2-yl)thiadiazolo-quinoxaline] (PFTTQ) using Suzuki polymerization. PFTTQ polymeric nanoparticles were modified with 1,2-distearoyl-*sn*-glycero-3-phosphoethanolamine-*N*-[methoxy (polyethylene glycol)-2000] (DSPE–PEG 2000) and the size of the obtained PEGylated nanoparticles could be finely tuned by controlling the initial PFTTQ and PEG concentrations (Figure 11.3). More importantly, the high electron deficiency of thiadiazoloquinoxaline sections in PFTTQ endowed the nanoparticles with

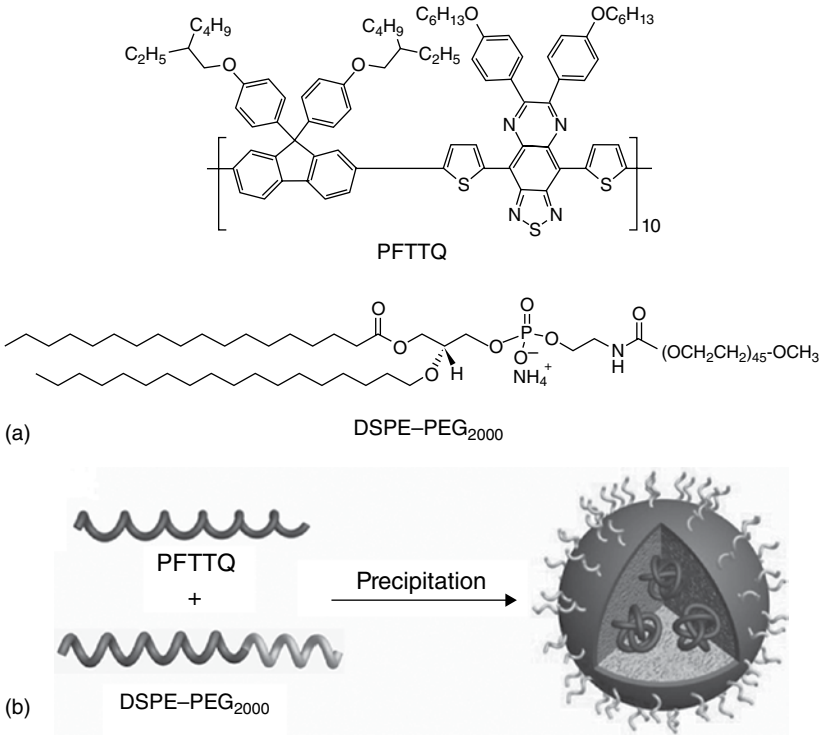

Figure 11.3 The structure (a) and preparation scheme (b) of PFTTQ conjugated polymeric nanoparticles. (Reproduced with permission from Ref. [27]. Copyright 2015, Wiley-VCH Verlag GmbH & Co. KGaA, Weinheim.)

high nonradiative decay rates, which was greatly useful for the high heat conversion efficiency. It was found that the temperature of PFTTQ nanoparticles suspension (0.5 mg ml^{-1}) could rapidly increase to more than 50 °C upon 808 nm laser irradiation (0.75 W cm^{-2}) for 5 min, comparable to that of gold nanorods (Au NRs) with the same absorbance (805 nm). Noteworthy is that the absorbance of PFTTQ NPs only slightly decreased by less than 5% after 1 h continuous NIR laser irradiation at a power density of 1 W cm^{-2}, indicating the good photostability of PFTTQ NPs. Furthermore, the nanoparticles exhibited highly efficient therapeutic efficacy for HeLa tumor mouse model.

Although several strategies have been developed for enhancing high heat conversion efficiency, extensive efforts are still required to maximize the photothermal therapeutic efficacy. Porphyrin derivatives with large extinction coefficients have been extensively applied for fluorescence imaging, PTT, as well as photodynamic therapy (PDT) via tuning exciton dissipation pathways. Inspired by the unique physicochemical properties of porphyrin, Guo *et al.* [28] developed a kind of porphyrin-based conjugated polymer (PorCP) nanoparticle with highest photothermal conversion efficacy (PCE, 63.8%) among existing conjugated polymers by constructing a D–A structure. Porphyrin as donor was linked to the acceptor-benzothiadiazole (BT) through an ethynylene bridge. Such a D–A

structure could efficiently introduce intramolecular charge transfer (ICT) to red-shift and enhance the Q band absorption in the NIR range. Moreover, when porphyrin was introduced into the conjugated polymer backbone, the elongated conjugation could further lead to higher molar absorbance on average based on each porphyrin unit. In this study, the PorCP nanoparticles were also coated with cell penetrating peptide (Tat) for efficient uptake into cancer cells.

11.3 Imaging Guided Photothermal Therapy

The abovementioned studies have demonstrated that organic conjugated polymers could be promising photothermal agents for effective cancer treatment. For further development of cancer photothermal therapy, imaging can be a very useful modality for improving the therapeutic efficacy of cancer treatment. Firstly, tumor imaging can provide information about the tumor location, size, and shape, which are greatly helpful for cancer treatment that demand high efficiency and specificity. Secondly, the real-time tracking of photothermal agents after systemic administration by imaging is greatly important to achieve the optimized therapeutic outcome. Thirdly, advanced imaging techniques are required to monitor the therapeutic response after treatment in clinic. Therefore, in our previous study [29], we developed the PEGylated ultrasmall iron oxide doped polypyrrole nanoparticles (IONP@PPy–PEG NP) for multimodal imaging guided photothermal therapy. The ultrasmall iron oxide nanoparticles (6 nm) modified with DMSA served as multiple cores and were coated with PPy using $FeCl_3 \cdot 6H_2O$ as the polymerization inducer, dodecylbenzenesulfonate (SDBS) as the emulsifier, and polyvinyl alcohol (PVA) as the stabilizer. Then, IONP@PPy–PEG nanoparticles were prepared utilizing the layer-by-layer (LBL) coating method (Figure 11.4a, b). It was shown that PEG modifiers did not affect the super paramagnetic property of the IONP@PPy nanoparticles and that the nanoparticles exhibited T_2-weighted MR signal in a concentration-dependent manner (Figure 11.4c, d). Meanwhile, *in vivo* MR imaging indicated that the nanoparticles could effectively accumulate into the tumor as early as at 1 h post intravenous injection (Figure 11.5a). Furthermore, strong photoacoustic signal of PPy with NIR absorption could be observed at 24 h post injection (Figure 11.5b), providing another evidence for the strong accumulation of IONP@PPy–PEG nanoparticles. Additionally, in comparison with an untreated group, IONP@PPy–PEG nanoparticles-based photothermal therapy could completely eliminate the tumor when tumor-bearing mice were exposed to NIR irradiation at the power density of 1.5 W cm^{-2} for 5 min at 24 h post injection. All these evidences indicate that IONP@PPy–PEG nanoparticles-based photothermal therapy can effectively and accurately eliminate tumors under the guidance of bimodal tumor imaging.

It is well known that targeted delivery is one of the most used strategies in cancer treatment. As for particulate delivery system, the surface will be generally modified with targeting moieties such as small molecules, peptides, or antibodies [30, 31]. However, the surface functionalization may complicate the particle surfaces and change surface charges and morphologies, leading to protein corona

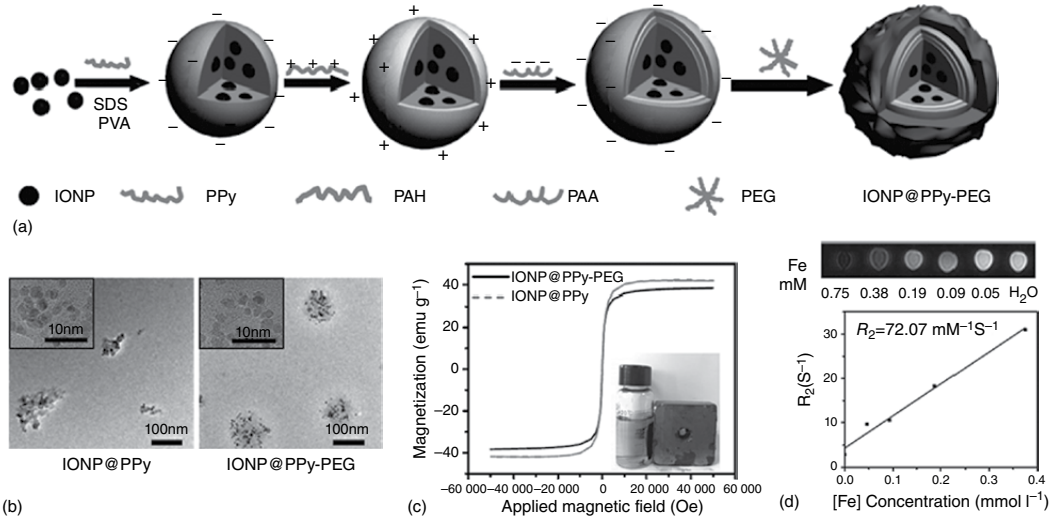

Figure 11.4 The synthesis and characterizations of IONP@PPy–PEG nanocomposite (a) a schematic showing the fabrication process of IONP@PPy–PEG nanocomposite (b) TEM images of IONP@PPy nanocomposite before and after PEGylation. Insets are higher resolution images. (c) Magnetization loops of IONP@PPy and IONP@PPy–PEG. Inset is a photo of an IONP@PPy–PEG solution placed nearby a magnet. (d) T_2-weighted MR images (up) and the T2 relaxation rates (R_2) plot (bottom) of IONP@PPy–PEG solutions at different iron concentrations. (Reproduced with permission from Ref. [29]. Copyright 2013, Wiley-VCH Verlag GmbH & Co. KGaA, Weinheim.)

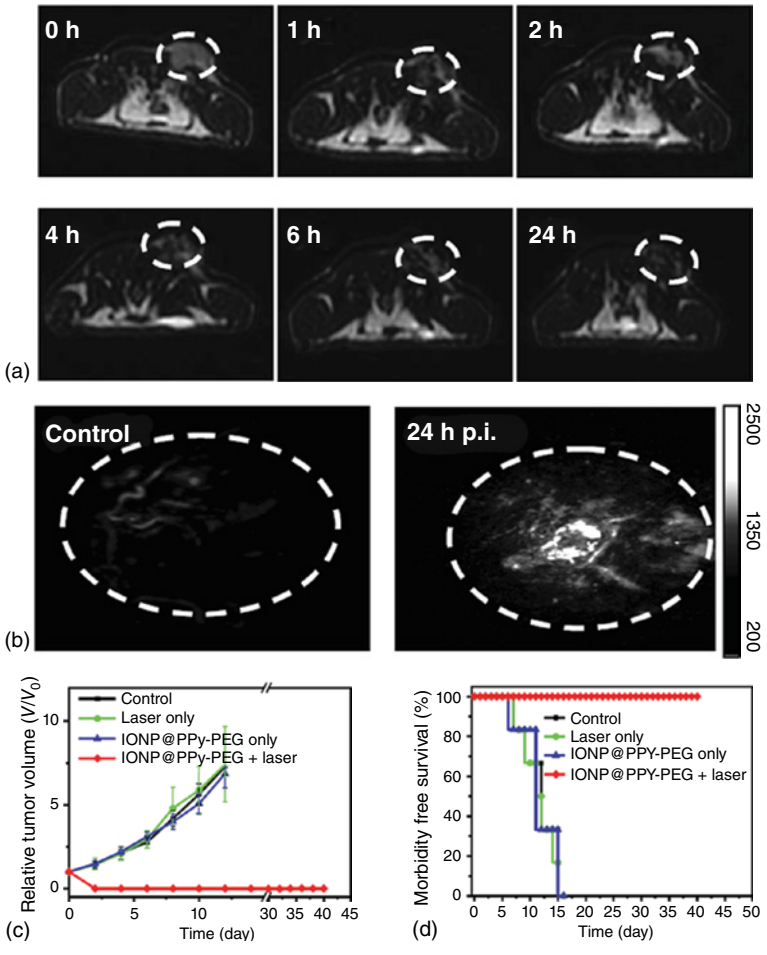

Figure 11.5 The *in vivo* bimodal imaging and photothermal therapy using IONP@PPy–PEG nanoparticles. (a) T_2-weighted MR images of 4T1 tumor-bearing mice i.v. injected with IONP@PPy–PEG (0.8 mg ml^{-1}, 0.2 ml) taken at different time post injection. White circles highlight the tumor site. (b) Photoacoustic images of mice before injection and at 24 h post injection with IONP@PPy–PEG (0.8 mg ml^{-1}, 0.2 ml). (c) Growth of 4T1 tumors in different groups of mice after various treatments indicated. The relative tumor volumes were normalized to their initial sizes. For the treatment group, six mice injected with IONP@PPy–PEG at 24 h post injection were exposed to the 808-nm laser (1.5 W cm^{-2}, 5 min). The other three groups of mice with six mice per group were used as controls: untreated; laser only; injected with IONP@PPy–PEG but without laser irradiation. (d) Survival curves of mice after various treatments indicated. IONP@PPy–PEG injected mice after PTT treatment showed 100% survival ratio over 40 days. (Reproduced with permission from Ref. [29]. Copyright 2014, Wiley-VCH Verlag GmbH & Co. KGaA, Weinheim.)

or large variations in cellular uptake [32]. Actually, besides surface chemistry engineering, tuning the size of particles may be another useful approach for selective delivery since different cell types have different cut-off values for the size of particles [33]. Extensive evidences [33, 34] have indicated that particles

with micrometer sizes could be selectively internalized into cancer cells other than normal cells compared to nanoparticles. Meanwhile, the increase in size not only effectively increases the drug loading capacity but also controls their sustained release in large particles over a longer time span, which makes drug administration less frequent but more effective to offer more convenience and better patient compliance [34]. Utilizing this unique advantage of microparticles, Feng *et al.* [35] developed poly(lactide-*co*-glycolide) (PLGA)-based theranostic microparticles which simultaneously co-encapsulating two kinds of conjugated polymers for fluorescence imaging-guided photothermal therapy of cancer cells. In this study, PFTTQ and PFBT mainly located in the core and shell of the PLGA microparticles, respectively. PFTTQ conjugated polymer exhibiting broad NIR absorption served as photothermal agent, while poly(9,9-dihexylfluorene-*alt*-2,1,3-benzothiadiazole) (PFBT) conjugated polymer as imaging modality showed strong green fluorescence (Figure 11.6a, b). Interestingly, it was observed

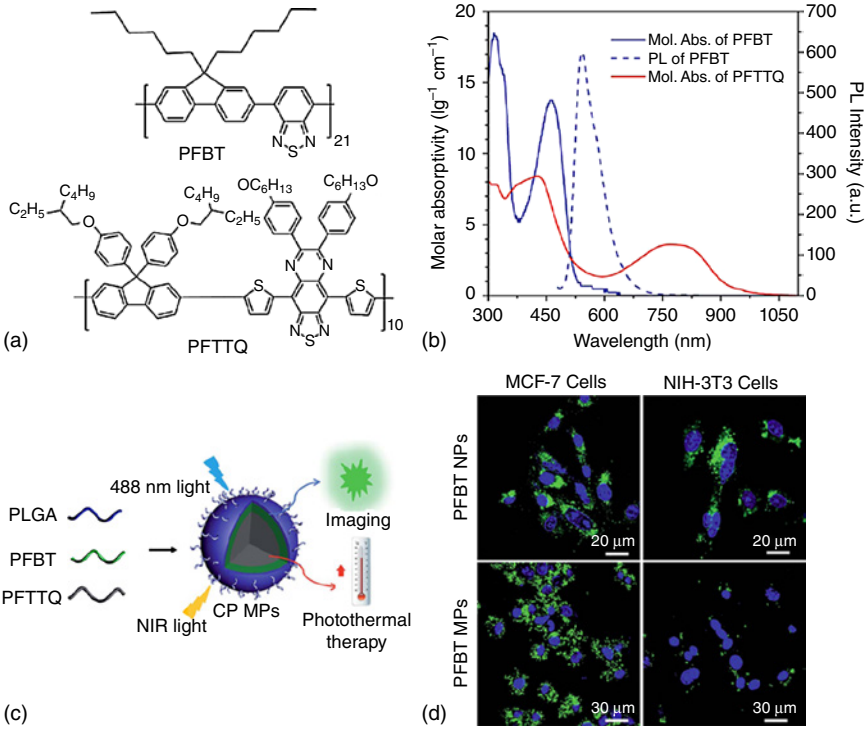

Figure 11.6 Conjugated polymer microparticles for selective cancer cell image-guided photothermal therapy. Chemical structures of PFBT and PFTTQ (a), UV–vis (solid line) spectra of PFBT (blue, 0.01 mg ml^{-1}) and PFTTQ (red, 0.01 mg ml^{-1}), and PL spectrum of PFBT (dashed blue line) in DCM upon excitation at 460 nm (b). (c) Schematic illustration of CP MPs formation. (d) CLSM images of PFBT NP treated MCF-7 and NIH-3T3 cells, PFBT MP treated MCF-7 and NIH-3T3 cells. Both the cells were incubated with these particles at PFBT concentration of 30 μg ml^{-1} for 6 h. The PFBT signal is collected above 505 nm upon excitation at 488 nm. The nucleus signal from DAPI is collected between 430 and 470 nm upon excitation at 405 nm. (Reproduced with permission from Ref. [35]. Copyright 2015, Royal Society of Chemistry.)

that PLGA microparticles could only be efficiently internalized into breast cancer cells (MCF-7) but not normal fibroblast cells (NIH3T3) while PFBT nanoparticles could effectively enter into both kinds of cells (Figure 11.6c). The *in vitro* study demonstrated that PFTTQ/PFBT-co-loaded PLGA microparticles could selectively kill MCF-7 other than NIH3T3 cells.

Generally speaking, tumor metastasis is the major contributor for the death of cancer patients. Before metastasis to distant sites, cancer cells usually spread to sentinel lymph nodes (SLNs). Therefore, SLNs biopsy (SLNB) is an important useful tool for diagnosis and prognosis of tumor metastasis in clinic. Currently, the most common SLNB clinical approaches include methylene blue staining and radioactive colloid labeling [36]. However, there are some critical issues to be addressed for these two approaches. For instance, the location and depth of SLNs need to be determined by preoperative data, or by exposing the SLN through surgical operation for the methylene blue approach, which will lead to severe allergic reactions for patients [37]. As for radioactive labeling, besides requiring special facilities for detection, its poor spatial resolution lead to the unsatisfactory precision for the localization and resection of SLNs [38]. Moreover, the safety issue is another obstacle for radioactive labeling detection. Therefore, imaging techniques for noninvasive, nonionizing, and high-resolution mapping of SLNs are greatly desired for cancer metastasis at the early stage. Photoacoustic (PA) imaging with high-resolution and deep tissue penetration capabilities have been used in SLNB [39]. In this technique, non-ionizing laser pulses are delivered into biological tissues. Some of the delivered energy will be absorbed and converted into heat, leading to transient thermoelastic expansion and thus wideband (i.e., MHz) ultrasonic emission, which can be detected by ultrasonic transducer. However, most endogenous optical contrast agents absorb in the visible region of the spectrum, resulting in light scattering in biological tissues and lead to the limited imaging sensitivity and resolution.

Recently, conjugated polymers with strong NIR absorption have demonstrated great potentials in PA vascular imaging [40]. Therefore, conjugated polymers can serve as an ideal dual-functional agent for PA imaging-guided photothermal therapy. In contrast to their polymeric analogs and conventional NIR-absorbing conjugated polymers such as PPy and PEDOT, conjugated oligomers with better-defined molecular structures can be purified to greater extent, while offering the potential of molecular design to achieve absorbance in the NIR range with better repeatability and reproducibility. Utilizing these unique advantages, Cai *et al.* [41] developed conjugated oligomer N4-encapsulated nanoparticles using precipitation method, which exhibiting strong PA signal (Figure 11.7a, b). It was shown that N4 nanoparticles exhibited ideal stability even within several months at 4 °C and nontoxic to multiple cancer cells without irradiation. *In vivo* experiment demonstrated that the intrinsic optical absorption of SLN provides negligible PA contrast, while the PA signal intensity of SLN reached the maximum at 10 min post N4 NP injection, showing clearly visible PA images of the SLN. Meanwhile, the intensity began to slowly decrease at 20 min but persisted 90 min post injection (Figure 11.7c). All these above evidences indicate that N4 nanoparticles with PA imaging capability can be an ideal PTT agent for precisely ablating metastasized SLN.

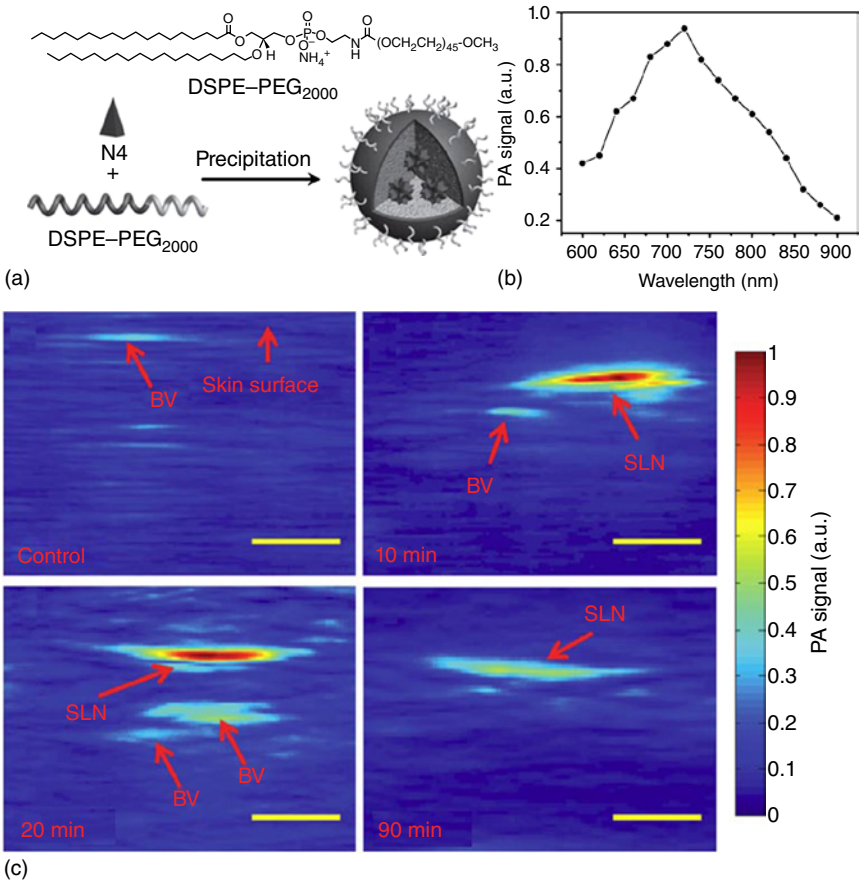

Figure 11.7 Encapsulated conjugated oligomer nanoparticles for real-time photoacoustic sentinel lymph node imaging. (a) Schematic illustration for the preparation of N4 NPs. (b) The PA intensity of N4 NPs upon laser excitation at different wavelength from 600 to 900 nm. The N4 NP concentration is 0.5 mg ml^{-1}. (c) Real-time PA imaging of SLN before and after N4 NPs injection. Excitation wavelength is 800 nm. BV stands for blood vessels. Scale bars: 1 mm. (Reproduced with permission from Ref. [41]. Copyright 2016, Wiley-VCH Verlag GmbH & Co. KGaA, Weinheim.)

11.4 Conjugated Polymers for Combination Cancer Treatment

Because of the extreme complexity of tumor initiation and progression, there are many barriers to be addressed for effective cancer treatment. Therefore, combining multiple therapeutic strategies are greatly required to improve the final outcome of cancer treatment, as evidenced by extensive previous studies [42–44]. Recently, we [45–47] and other groups have done series studies on combining conjugated polymer-based photothermal therapy with other strategies such as chemotherapy and photodynamic therapy.

11.4.1 Combined Photodynamic and Photothermal Therapy

Following our previous imaging-guided PPy-based photothermal therapy, we also explored the synergistic effects of imaging-guided photothermal and photodynamic therapy. There have been many evidences [3, 12, 17, 25] indicated that surface modification was greatly important for the application of conjugated polymers because of their hydrophobicity. Actually, few functional groups on the surface of conjugated polymers could be available for the modification. That is to say, it is difficult to directly conjugate modifiers to those organic polymers. Inspired by the stabilizer properties of albumin to various kinds of nanoparticles for improving their biocompatibility [48], we developed a one-step method for integrating photodynamic therapy to PPy-based photothermal therapy by preconjugating bovine serum albumin with the photosensitizer-chlorin e6 (Ce6) which serving as the stabilizer during the polymerization of PPy (Figure 11.8a) [46]. The rapid increase of the temperature and high production of singlet oxygen upon laser irradiations provided solid evidence for the feasibility of our rational design (Figure 11.8b). Another unique advantage of our designed nanoparticles is that, besides the fluorescence imaging of Ce6, Gd^{3+}-based magnetic resonance imaging (MRI) also could be adopted through its chelating with Ce6 (Figure 11.8c–e). Both the strong fluorescence and MR signals at 6 h post injection indicated that PPy@BSA–Ce6 (Gd) nanoparticles could effectively accumulate into tumors and provide important information for the subsequent phototherapies with high accuracy. Finally, the *in vivo* evidences demonstrated that those imaging-guided photodynamic and photothermal combination therapy could more efficiently eliminate tumors compared to the single therapeutic modality.

Generally speaking, multifunctional nanoplatform for imaging-guided combination cancer treatment is usually composed of multiple agents such as imaging modality, photodynamic/chemo/photothermal agents. There is no doubt that it is difficult to control the balance among these functional molecules for maximizing the synergistic effects and minimizing side effects of different kinds of treatment modalities. Owing to their delocalized π-conjugated backbones and excellent light-harvesting properties, conjugated polymers can exhibit different functions when their backbone structure are precisely engineered and have shown promising applications in sensing, imaging, and biomedical applications [1, 49]. Inspired by the unique properties of conjugated polymers, Feng *et al.* [50] synthesized lipid-polyethylene glycol (PEG) nanoparticles coencapsulating two kinds of conjugated polymers including poly[9,9-bis(2-(2-(2-methoxyethoxy) ethoxy)-ethyl) fluorenyldivinylene]-*alt*-4,7-(2,1,3-benzothiadiazole) (PFVBT) and poly[(4,4,9,9-tetrakis(4-(octyloxy)phenyl)-4,9-dihydros-indacenol-dithiophene-2,7-diyl)-*alt*-*co*-4,9-bis(thioph en-2-yl)-6,7-bis(4-(hexyloxy)phenyl)-thiadiazolo-quinoxaline] (PIDTTTQ). In this study, PFVBT with bright red fluorescence served as both imaging modality and photosensitizer, while PIDTTTQ with high NIR absorption was the PTT agent. It was found that coloading of these unique nanoparticles offered high brightness, good colloidal and photostability, efficient ROS production, and high light-to-heat conversion efficiency. Furthermore, anti-HER2 antibody was coated onto the surface of nanoparticles for enhancing the therapeutic

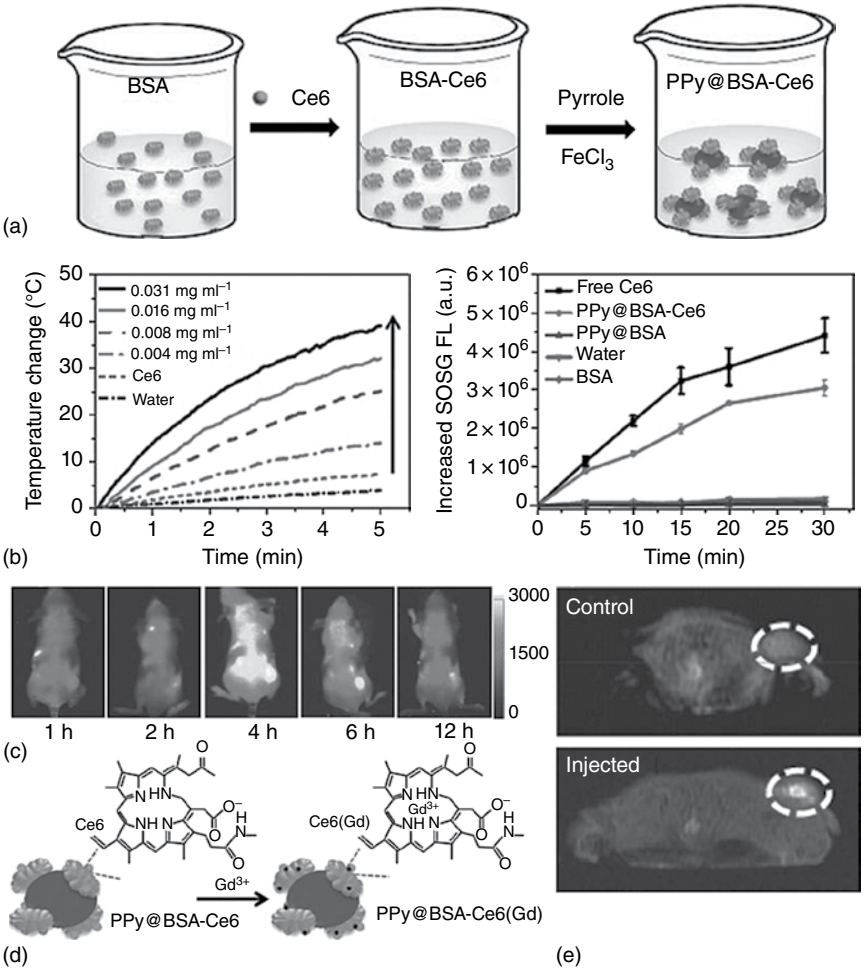

Figure 11.8 The scheme and characterizations of PPy@BSA–Ce6(Gd) nanoparticles and the bimodal imaging *in vivo*. (a) A scheme showing the fabrication of PPy@BSA–Ce6 nanoparticles. (b) Temperature elevation of water and PPy@BSA–Ce6 solutions of different concentrations over a period of 5 min under exposure of the NIR light (808 nm,0.8 W cm^{-2}). Detection of singlet oxygen by the SOSG test for different samples including free Ce6, PPy@BSA–Ce6, PPy@BSA, and BSA under the 660 nm light exposure (5 mW cm^{-2}) for different periods of time. PPy@BSA–Ce6 showed largely retained light-triggered SO generation ability compared with free Ce6 at the same Ce6 concentration (1×10^{-6} M). (c) *In vivo* fluorescence images of 4T1 tumor-bearing mice taken at different time points post injection of PPy@BSA–Ce6. The autofluorescence of the mouse was removed by spectral unmixing. (d) A scheme showing the fabrication PPy@BSA–Ce6 (Gd). (e) T1-weighted MR images of 4T1 tumor-bearing mice before injection and 6 h after i.v. injection with PPy@BSA–Ce6(Gd). White circles highlight the tumor site. (Reproduced with permission from Ref. [46]. Copyright 2015, Wiley-VCH Verlag GmbH & Co. KGaA, Weinheim.)

efficacy of fluorescence imaging-guided PDT–PTT combination cancer treatment. Both *in vitro* and *in vivo* evidences demonstrated that this imaging-guided combination of PDT–PTT treatment exhibited better therapeutic efficacy than that of PDT or PTT alone.

11.4.2 Combined Photothermal Chemotherapy

It is known that chemotherapy, as one of the first-line treatment modalities, has been used in clinics for years. But its limited efficacy and severe side effects are always great concerns. Therefore, various types of strategies involving enhancing the targeting efficacy of drug carriers and increasing the cellular uptake of drugs have been explored to address these problems [51, 52]. Recently, among those strategies, external stimulus-responsive nanoplatforms for remotely controllable cancer treatments have attracted great attention due to their advantages such as increasing drug accumulation in targeted lesions and decreasing systemic toxicities. As mentioned [29, 46], imaging-guided PPy-based photothermal therapy and its combination modality have demonstrated encouraging therapeutic efficacy in eliminating cancers. Actually, previous studies by the authors [53] and others [54] have demonstrated that mild photothermal heating could increase the permeability of cell membranes without damaging the cells and thereby promote the intracellular delivery of drugs and genes. Therefore, considering the aromatic ring of the chemotherapeutic drug-doxorubicin (DOX) and the hydrophobicity of conjugated polymers, we developed a chemotherapeutic drug-loaded multifunctional nanocomposites based on PEGylated Fe_3O_4@PPy (Fe_3O_4@PPy–PEG) core–shell nanoparticles [47], obtaining Fe_3O_4@PPy–PEG–DOX through hydrophobic interaction and π–π stacking (Figure 11.9a). In our design, the Fe_3O_4 core was used for magnetic field (MF) controlled drug delivery as well as for MR imaging. As for the PPy shell, it could be utilized for enhancing the cellular uptake and drug release of DOX besides serving as a photothermal agent. As expected, it was shown that both the external magnetic field and mild photothermal treatment (808 nm laser at the power density of 0.35 W cm^{-2}) could promote the intracellular uptake of DOX when loaded onto the Fe_3O_4@PPy–PEG nanoparticles (Figure 11.9b). Furthermore, mild photothermal treatment could lead to the effective DOX release to kill cancer cells (Figure 11.9b), which was greatly helpful for the synergistic effects of chemotherapy and photothermal ablation modality (Figure 11.9d). Meanwhile, those nanoparticles with Fe_3O_4 cores could serve as T2 contrast agents in MR imaging for post-treatment tumor prognosis (Figure 11.9c). Our study provides evidence for the feasibility of imaging-guided, remotely controlled cancer therapy with an excellent synergistic antitumor effect, and promises further development of NIR-absorbing organic nanoparticles and organic–inorganic nanocomposites for photothermal therapy and combination cancer treatment.

Encouraged by the good synergistic effects of photothermal therapy with chemo- [47] or photodynamic therapy [53] in our previous studies, we [45] also explored the synergistic effects of photothermal-, chemo-, and photodynamic therapies utilizing PEDOT:PSS–PEG nanoparticles as the versatile drug carriers for DOX and Ce6 through hydrophobic interaction and π–π stacking. It was

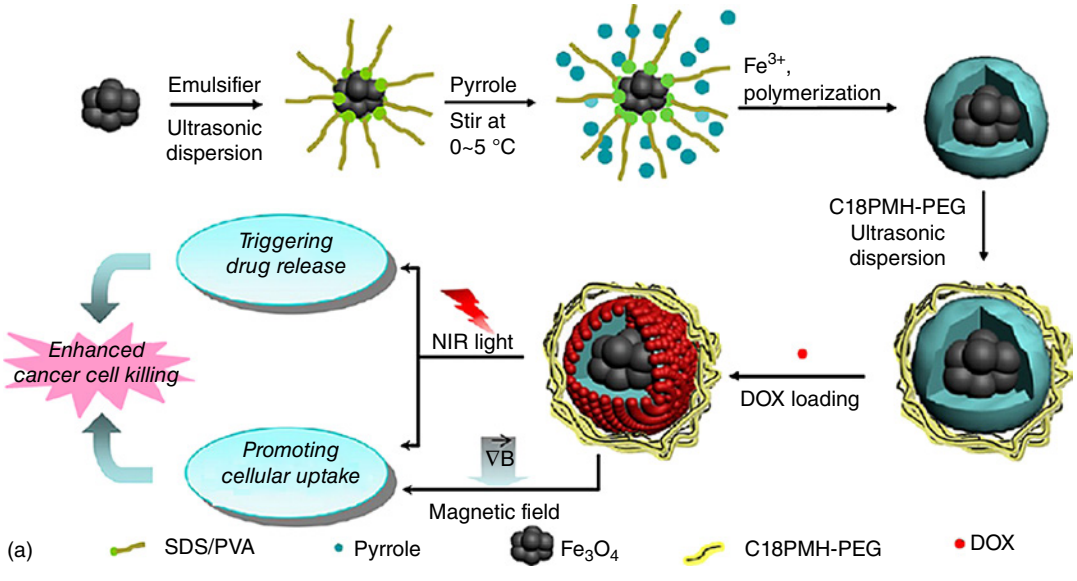

Figure 11.9 The scheme of Fe_3O_4@PPy–PEG–DOX multifunctional nanoplatform (a) and the *in vitro* (b) and *in vivo* evaluations on the effects of the external stimuli on the cellular uptake of DOX, MR imaging (c) and the synergistic therapeutic efficacy (d). (Reproduced with permission from Ref. [47]. Copyright 2013, American Chemical Society.)

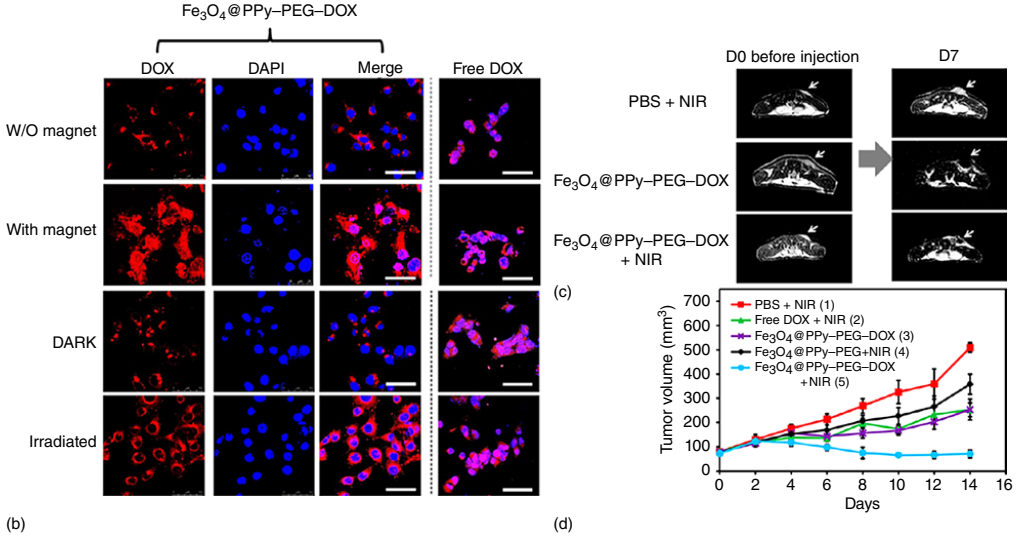

Figure 11.9 (*Continued*)

found that PEDOT:PSS–PEG could dramatically enhance the solubility of SN38 while maintaining its cytotoxicity to cancer cells. For the delivery of photodynamic therapy, owing to the remarkably enhanced intracellular delivery of Ce6 once it was loaded onto PEDOT:PSS–PEG nanoparticles, PEDOT:PSSPEG-Ce6 offered significantly stronger photodynamic therapeutic efficacy compared to free Ce6. Moreover, utilizing DOX loaded PEDOT:PSS–PEG as the model system, we further demonstrated combined photothermal and chemotherapy, realizing a strong synergistic effect in cancer cell destruction. Our study highlights the great potential of NIR-absorbing polymeric nanoparticles as multifunctional drug carriers for potential combination cancer therapy with high efficacy.

Besides thermo- and magnetic-responsive controlled drug release, light-responsive therapeutic platforms also can be utilized to modulate the drug release for maximizing the synergistic effect of chemotherapy and photothermal therapy. Actually, most of the light-responsive systems are activated by UV/vis light [55], while the photothermal agents are activated by a NIR laser. Therefore, two light sources with different wavelengths are typically required to modulate drug release and simultaneously realize the combination of PTT and chemotherapy. However, it is difficult to focus two light beams at the same position. In addition, the limited tissue penetration of UV/vis light also leads to the unsatisfactory drug release behavior for synergistic effects of combination photothermal chemotherapies. Recently, the development of two-photon regulated drug delivery systems may be useful to address the abovementioned challenge [56, 57]. Considering the unique hydrophobic photo-responsive property of 2-diazo-1,2-naphthoquinone (DNQ), which can undergo one or two-photon-induced Wolff rearrangement and drastically change into a hydrophilic molecule [58], Yuan *et al.* [59] constructed poly(L-lysine)-*graft*-poly(ethylene glycol) (PLL-*g*-PEG) nanoparticles containing DNQ moiety (PLL-*g*-PEG/DNQ) by conjugating the residual primary amine groups of PLL with 2-diazo-1-naphthol-5-sulfonyl chloride (sc-DNQ) (Figure 11.10a). Then, they coencapsulated the photothermal agent-PFTTQ and the chemotherapeutic drug DOX into this kind of nanoparticles. Meanwhile, dual drugs-loaded nanoparticles were coated with cyclic arginine-glycine-aspartic acid (cRGD) for targeting integrin overexpression cancer cells. It was shown that the nanoparticles would disassemble after exposed to NIR laser (800 nm) due to the Wolff rearrangement of DNQ moiety (Figure 11.10b–d), which could be used for controlling the drug released from the nanoparticles. Drug release profile indicated that 24.5 ± 2.1% of DOX could be released from the nanoparticles within 40 min after NIR laser irradiation. Moreover, this two-photon-regulated combination therapeutic nanoplatform exhibited lower half-maximal inhibitory concentration (IC50) than that of chemo- or photothermal therapy alone.

11.5 Outlook and Perspectives

In the past few years, organic NIR-absorbing conjugated polymeric nanoparticles have shown promising applications as a new generation of photothermal agents for cancer therapy because of their high photostability, photothermal

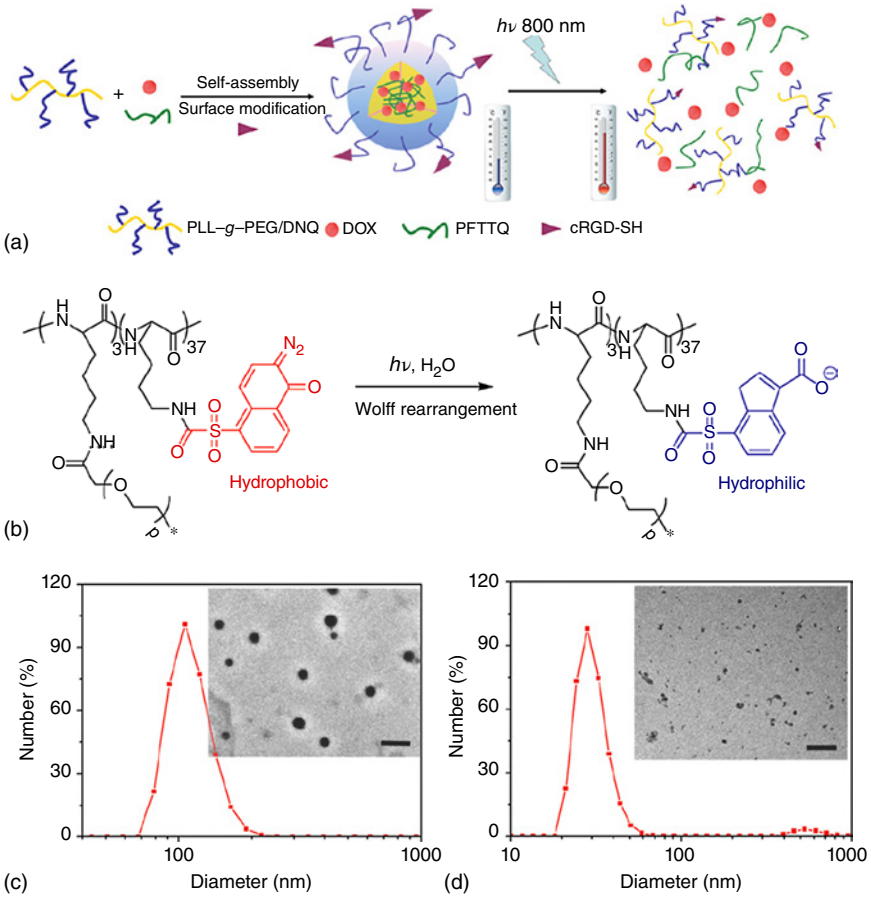

Figure 11.10 Schematic illustration of the two-photon laser-regulated combination photothermal and chemotherapy with fast drug release (a); chemical structure of PLL-*g*-PEG/DNQ and its hydrophilic counterpart after Wolff rearrangement in aqueous media upon two-photon laser irradiation (b); size distribution and TEM image (inset) of PFTTQ/DOX NPs in aqueous media before and after NIR laser irradiation. (Reproduced with permission from Ref. [59]. Copyright 2015, Royal Society of Chemistry.)

conversion efficiency, and good biocompatibility after functionalization. Moreover, their hydrophobic properties endow them with versatile drug-carrier capacities, which enable combination cancer therapy with high efficacy. As summarized in Table 11.1, a variety of organic conjugated polymer nanoparticles have demonstrated high photothermal therapeutic efficiencies under NIR laser irradiation with different power densities. However, it is difficult to conclude which kind of conjugated polymer-based photothermal therapy is the best one for cancer treatment because of the variations in experimental details including different particle sizes, surface chemistry, injection routes, and animal models used in different research groups. Nevertheless, an ideal photothermal agent should satisfy the following requirement: (i) low toxicity; (ii) high photothermal

Table 11.1 A summary of various conjugated polymeric nanoparticles explored in photothermal therapy.

Organic polymeric nanoparticle	Surface chemistry	Size (nm)	Irradiation	Experimental details	References
Polyaniline	Polyoxyethylene-sterate-coated	115.6 ± 16.3 nm	808 nm, 2.45 W cm^{-2}, 5 min	*In vivo* treatment with intratumoral injection. Dose = 5 mg kg^{-1}.	[12]
	F127-coated	48.5 ± 1.5 nm	808 nm, 0.5 W cm^{-2}, 3 min	*In vivo* treatment with intratumoral injection. Dose = 2.5 mg kg^{-1}.	[14]
PPy	PVA-coated	~60 nm	808 nm, 0.1, 0.25, 0.5 W cm^{-2}, 5 min	*In vivo* treatment with intratumoral injection. Dose = 2 mg kg^{-1}.	[3]
	PVP-coated	50 ± 5 nm	808 nm, 1 W cm^{-2}, 5 min	*In vivo* treatment with intravenous injection. Dose = 10 mg kg^{-1}.	[16]
	IONP@PPy–PEG	~100 nm	808 nm, 1.5 W cm^{-2}, 5 min	*In vivo* imaging-guided treatment with intravenous injection. Dose = 8 mg kg^{-1}	[29]
	Fe_3O_4@PPy–PEG–DOX	150 nm	808 nm, 0.35 W cm^{-2}, 25 min	*In vivo imaging-guided* treatment with intratumoral injection. Dose of DOX = 1 mg kg^{-1}, Fe_3O_4@PPy–PEG = 8 mg kg^{-1}.	[47]
	PPy@BSA–Ce6 (Gd)	35 nm	808 nm, 0.5 W cm^{-2},5 min; 660 nm, 5 mW cm^{-2}, 1 h	*In vivo* treatment with intravenous injection. Dose of PPy = 8 mg kg^{-1}, Ce6 = 1.2 mg kg^{-1}.	[46]

PEDOT	PEDOT:PSS–PEG	80–90 nm	808 nm, 0.5 W cm^{-2}, 5 min	*In vivo* treatment with intravenous injection. Dose = 10 mg kg^{-1}.	[25]
	PEDOT:PSS–PEG–DOX–SN38–Ce6	155.3 ± 12.5 nm	808 nm, 0.25 W cm^{-2}, 20 min; 660 nm, 0.1 W cm^{-2}, 10 min	*In vitro* ablation of cancer cells. Effective concentration = mg ml^{-1}.	[45]
Nano-PCPDTBT, Nano-PCPDTBSe	No modification	298.4 nm or 154.3 nm	808 nm,0.6 W cm^{-2}, 5 min	*In vitro* ablation of cancer cells. Effective concentration = 62 μg ml^{-1} or 125 μg ml^{-1}	[26]
PFTTQ	DSPE–PEG	35 ± 10 nm	808 nm, 0.75 W cm^{-2}, 10 min	*In vivo* treatment with intratumoral injection. Dose = 2 mg kg^{-1}.	[27]
PFVBT–PIDTTTQ	DSPE–PEG	34 ± 0.9 nm	808 nm, 0.5 W cm^{-2}, 6 min	*In vivo* treatment with intravenous injection.	[28]
PFTTQ/DOX–PLL-*g*-PEG/DNQ	cRGD-coated	78.5 ± 6.4 nm	808 nm, 1 W cm^{-2}, 10 min	*In vitro* ablation of cancer cells. Effective concentration =13.7 μg ml^{-1}.	[50]
Porphrin-BT	DSPE-PEG, Tat coated	42 ± 3.4 nm	808 nm, 0.75 W cm^{-2},10 min	*In vitro* ablation of cancer cells. Effective concentration = 5 μg ml^{-1}	[59]

conversion efficiency; (iii) efficient accumulation in tumors; (iv) easy synthesis in a reliable and highly reproducible manner.

Although increasing evidences indicate the great potential of photothermal therapy based on conjugated polymers and the related combination cancer treatment strategies, there are still a number of important issues that need to be addressed. (i) Although existing studies have demonstrated the low toxicity profiles of different kinds of conjugated polymeric nanoparticles with well-controlled surface coating (e.g., PEGylated PEDOT:PSS, PVA, or PEG-coated PPy) in *in vitro* and *in vivo* levels, their biodegradability, metabolism, and long-term toxicology profiles are still largely unknown. This is likely the most challenging question in this field [60]. (ii) Some kinds of conjugated polymeric nanoparticles (e.g., PEDOT:PSS–PEG) have exhibited efficient tumor homing capacity via the passive EPR effect. Actually, there could still be more room for improvement, that is, further enhancing the tumor targeting ability and specificity of these polymeric nanoparticles by taking advantage of active tumor targeting (e.g., conjugation of targeting ligands on nanoparticles) or physical tumor targeting (e.g., MF-induced tumor accumulation). (iii) Until now, the combination of conjugated polymers-based photothermal therapy with other modalities such as chemo- and photodynamic therapies has shown good synergistic effects. However, how to rationally design the combination cancer treatments is still not very clear. Meanwhile, given the extreme complexity of tumor progression such as the tumor microenvironments (TME), smart responsive/tuning TME photothermal nanoplatforms may be greatly desired for combating tumor progression, metastasis and relapse.

Nevertheless, there are also some other unique advantages besides the photothermal ablation itself with minimal invasiveness, low side effects and high specificity. For instance, our latest study showed that photothermal therapy could effectively induce tumor-associated antigen-specific immune responses for combination cancer immunotherapy via destroying tumor cells [6]. Furthermore, our previous study [61] also indicated that PEGylated PEDOT:PSS nanoparticles could serve as potential vaccine adjuvants for improving the immunogenicity of model antigen-ovalbumin (OVA). All these evidences shed light for the future developments of biodegradable, multifunctional, organic conjugated polymers-based photothermal nanoplatforms in combination cancer treatment, which may provide the next generation first-line treatment modality in clinical cancer therapy.

References

1 Zhu, C., Liu, L., Yang, Q., Lv, F., and Wang, S. (2012) Water-soluble conjugated polymers for imaging, diagnosis, and therapy. *Chem. Rev.*, **112**, 4687–4735.

2 Smela, E. (2003) Conjugated polymer actuators for biomedical applications. *Adv. Mater.*, **15**, 481–494.

3 Yang, K., Xu, H., Cheng, L., Sun, C.Y., Wang, J., and Liu, Z. (2012) In vitro and in vivo near-infrared photothermal therapy of cancer using polypyrrole organic nanoparticles. *Adv. Mater.*, **24**, 5586–5592.

4 Xu, L.G., Cheng, L., Wang, C., Peng, R., and Liu, Z. (2014) Conjugated polymers for photothermal therapy of cancer. *Polym. Chem. (UK)*, **5**, 1573–1580.
5 Cheng, L., Wang, C., Feng, L.Z., Yang, K., and Liu, Z. (2014) Functional nanomaterials for phototherapies of cancer. *Chem. Rev.*, **114**, 10869–10939.
6 Chen, Q., Xu, L.G., Liang, C., Wang, C., Peng, R., and Liu, Z. (2016) Photothermal therapy with immune-adjuvant nanoparticles together with checkpoint blockade for effective cancer immunotherapy. *Nat. Commun.*, 7.
7 Wang, C., Xu, L.G., Liang, C., Xiang, J., Peng, R., and Liu, Z. (2014) Immunological responses triggered by photothermal therapy with carbon nanotubes in combination with anti-CTLA-4 therapy to inhibit cancer metastasis. *Adv. Mater.*, **26**, 8154–8162.
8 Tao, Y., Ju, E.G., Ren, J.S., and Qu, X.G. (2014) Immunostimulatory oligonucleotides-loaded cationic graphene oxide with photothermally enhanced immunogenicity for photothermal/immune cancer therapy. *Biomaterials*, **35**, 9963–9971.
9 Guo, L.R., Yan, D.D., Yang, D.F., Li, Y.J., Wang, X.D., Zalewski, O. *et al.* (2014) Combinatorial photothermal and immuno cancer therapy using chitosan-coated hollow copper sulfide nanoparticles. *ACS Nano*, **8**, 5670–5681.
10 Li, X., Naylor, M.F., Le, H., Nordquist, R.E., Teague, T.K., Howard, C.A. *et al.* (2010) Clinical effects of in situ photoimmunotherapy on late-stage melanoma patients a preliminary study. *Cancer Biol. Ther.*, **10**, 1081–1087.
11 Zhou, F., Wu, S., Song, S., Chen, W.R., Resasco, D.E., and Xing, D. (2012) Antitumor immunologically modified carbon nanotubes for photothermal therapy. *Biomaterials*, **33**, 3235–3242.
12 Yang, J., Choi, J., Bang, D., Kim, E., Lim, E.-K., Park, H. *et al.* (2011) Convertible organic nanoparticles for near-infrared photothermal ablation of cancer cells. *Angew. Chem. Int. Ed.*, **50**, 441–444.
13 Ibarra, L.E., Yslas, E.I., Molina, M.A., Rivarola, C.R., Romanini, S., Barbero, C.A. *et al.* (2013) Near-infrared mediated tumor destruction by photothermal effect of PANI-Np in vivo. *Laser Phys.*, **23**, 066004.
14 Zhou, J., Lu, Z.G., Zhu, X.J., Wang, X.J., Liao, Y., Ma, Z.F. *et al.* (2013) NIR photothermal therapy using polyaniline nanoparticles. *Biomaterials*, **34**, 9584–9592.
15 Dimitriev, O.P. (2004) Doping of polyaniline by transition-metal salts. *Macromolecules*, **37**, 3388–3395.
16 Chen, M., Fang, X., Tang, S., and Zheng, N. (2012) Polypyrrole nanoparticles for high-performance in vivo near-infrared photothermal cancer therapy. *Chem. Commun.*, **48**, 8934–8936.
17 Zha, Z., Yue, X., Ren, Q., and Dai, Z. (2013) Uniform polypyrrole nanoparticles with high photothermal conversion efficiency for photothermal ablation of cancer cells. *Adv. Mater.*, **25**, 777–782.
18 Au, K.M., Lu, Z.H., Matcher, S.J., and Armes, S.P. (2011) Polypyrrole nanoparticles: a potential optical coherence tomography contrast agent for cancer imaging. *Adv. Mater.*, **23**, 5792–5795.
19 Yoon, H., Lee, S.H., Kwon, O.S., Song, H.S., Oh, E.H., Park, T.H. *et al.* (2009) Polypyrrole nanotubes conjugated with human olfactory receptors: high-performance transducers for FET-type bioelectronic noses. *Angew. Chem. Int. Ed.*, **48**, 2755–2758.

20 Oh, W.K., Yoon, H., and Jang, J. (2010) Size control of magnetic carbon nanoparticles for drug delivery. *Biomaterials*, **31**, 1342–1348.

21 Abidian, M.R., Corey, J.M., Kipke, D.R., and Martin, D.C. (2010) Conducting-polymer nanotubes improve electrical properties, mechanical adhesion, neural attachment, and neurite outgrowth of neural electrodes. *Small*, **6**, 421–429.

22 Khodagholy, D., Doublet, T., Gurfinkel, M., Quilichini, P., Ismailova, E., Leleux, P. *et al.* (2011) Highly conformable conducting polymer electrodes for in vivo recordings. *Adv. Mater.*, **23**, 268–272.

23 Yun, J.M., Yeo, J.S., Kim, J., Jeong, H.G., Kim, D.Y., Noh, Y.J. *et al.* (2011) Solution-processable reduced graphene oxide as a novel alternative to PEDOT:PSS hole transport layers for highly efficient and stable polymer solar cells. *Adv. Mater.*, **23**, 4923–4928.

24 Vosgueritchian, M., Lipomi, D.J., and Bao, Z. (2011) Highly conductive and transparent PEDOT:PSS films with a fluorosurfactant for stretchable and flexible transparent electrodes. *Adv. Mater.*, **22**, 421–428.

25 Cheng, L., Yang, K., Chen, Q., and Liu, Z. (2012) Organic stealth nanoparticles for highly effective in vivo near-infrared photothermal therapy of cancer. *ACS Nano*, **6**, 5605–5613.

26 MacNeill, C.M., Coffin, R.C., Carroll, D.L., and Levi-Polyachenko, N.H. (2013) Low band gap donor-acceptor conjugated polymer nanoparticles and their NIR-mediated thermal ablation of cancer cells. *Macromol. Biosci.*, **13**, 28–34.

27 Geng, J.L., Sun, C.Y., Liu, J., Liao, L.D., Yuan, Y.Y., Thakor, N. *et al.* (2015) Biocompatible conjugated polymer nanoparticles for efficient photothermal tumor therapy. *Small*, **11**, 1603–1610.

28 Guo, B., Feng, G.X., Manghnani, P.N., Cai, X.L., Liu, J., Wu, W.B. *et al.* (2016) A porphyrin-based conjugated polymer for highly efficient in vitro and in vivo photothermal therapy. *Small*, **12**, 6243–6254.

29 Song, X.J., Gong, H., Yin, S.N., Cheng, L., Wang, C., Li, Z.W. *et al.* (2014) Ultra- small iron oxide doped polypyrrole nanoparticles for in vivo multimodal imaging guided photothermal therapy. *Adv. Funct. Mater.*, **24**, 1194–1201.

30 Lal, S., Clare, S.E., and Halas, N.J. (2008) Nanoshell-enabled photothermal cancer therapy: impending clinical impact. *Acc. Chem. Res.*, **41**, 1842–1851.

31 Huang, X.H., El-Sayed, I.H., Qian, W., and El-Sayed, M.A. (2006) Cancer cell imaging and photothermal therapy in the near-infrared region by using gold nanorods. *J. Am. Chem. Soc.*, **128**, 2115–2120.

32 Lesniak, A., Salvati, A., Santos-Martinez, M.J., Radomski, M.W., Dawson, K.A., and Aberg, C. (2013) Nanoparticle adhesion to the cell membrane and its effect on nanoparticle uptake efficiency. *J. Am. Chem. Soc.*, **135**, 1438–1444.

33 Zauner, W., Farrow, N.A., and Haines, A.M.R. (2001) In vitro uptake of polystyrene microspheres: effect of particle size, cell line and cell density. *J. Controlled Release*, **71**, 39–51.

34 Win, K.Y., Ye, E.Y., Teng, C.P., Jiang, S., and Han, M.Y. (2013) Engineering polymeric microparticles as theranostic carriers for selective delivery and cancer therapy. *Adv. Healthc. Mater.*, **2**, 1571–1575.

35 Feng, G.X., Liu, J., Geng, J.L., and Liu, B. (2015) Conjugated polymer microparticles for selective cancer cell image-guided photothermal therapy. *J. Mater. Chem. B*, **3**, 1135–1141.

36 Pan, D.P.J., Cai, X., Kim, B., Stacy, A.J., Wang, L.H.V., and Lanza, G.M. (2012) Rapid synthesis of near infrared polymeric micelles for real-time sentinel lymph node imaging. *Adv. Healthc. Mater.*, **1**, 582–589.

37 Krag, D.N., Anderson, S.J., Julian, T.B., Brown, A.M., Harlow, S.P., Costantino, J.P. *et al.* (2010) Sentinel-lymph-node resection compared with conventional axillary-lymph-node dissection in clinically node-negative patients with breast cancer: overall survival findings from the NSABP B-32 randomised phase 3 trial. *Lancet Oncol.*, **11**, 927–933.

38 Nakajima, M., Takeda, M., Kobayashi, M., Suzuki, S., and Ohuchi, N. (2005) Nano-sized fluorescent particles as new tracers for sentinel node detection: experimental model for decision of appropriate size and wavelength. *Cancer Sci.*, **96**, 353–356.

39 Ntziachristos, V. and Razansky, D. (2010) Molecular imaging by means of multispectral optoacoustic tomography (MSOT). *Chem. Rev.*, **110**, 2783–2794.

40 Liu, J., Geng, J.L., Liao, L.D., Thakor, N., Gao, X.H., and Liu, B. (2014) Conjugated polymer nanoparticles for photoacoustic vascular imaging. *Polym. Chem. (UK)*, **5**, 2854–2862.

41 Cai, X.L., Liu, X.F., Liao, L.D., Bandla, A., Ling, J.M., Liu, Y.H. *et al.* (2016) Encapsulated conjugated oligomer nanoparticles for real-time photoacoustic sentinel lymph node imaging and targeted photothermal therapy. *Small*, **12**, 4873–4880.

42 Hughes, P.E., Caenepeel, S., and Wu, L.C. (2016) Targeted therapy and checkpoint immunotherapy combinations for the treatment of cancer. *Trends Immunol.*, **37**, 462–476.

43 Khalil, D.N., Smith, E.L., Brentjens, R.J., and Wolchok, J.D. (2016) The future of cancer treatment: immunomodulation, CARs and combination immunotherapy. *Nat. Rev. Clin. Oncol.*, **13**, 273–290.

44 Nunez, C., Capelo, J.L., Igrejas, G., Alfonso, A., Botana, L.M., and Lodeiro, C. (2016) An overview of the effective combination therapies for the treatment of breast cancer. *Biomaterials*, **97**, 34–50.

45 Gong, H., Cheng, L., Xiang, J., Xu, H., Feng, L.Z., Shi, X.Z. *et al.* (2013) Near-infrared absorbing polymeric nanoparticles as a versatile drug carrier for cancer combination therapy. *Adv. Funct. Mater.*, **23**, 6059–6067.

46 Song, X.J., Liang, C., Gong, H., Chen, Q., Wang, C., and Liu, Z. (2015) Photosensitizer-conjugated albumin-polypyrrole nanoparticles for imaging-guided in vivo photodynamic/photothermal therapy. *Small*, **11**, 3932–3941.

47 Wang, C., Xu, H., Liang, C., Liu, Y.M., Li, Z.W., Yang, G.B. *et al.* (2013) Iron oxide @ polypyrrole nanoparticles as a multifunctional drug carrier for remotely controlled cancer therapy with synergistic antitumor effect. *ACS Nano*, **7**, 6782–6795.

48 Chen, Q., Wang, C., Cheng, L., He, W., Cheng, Z., and Liu, Z. (2014) Protein modified upconversion nanoparticles for imaging-guided combined photothermal and photodynamic therapy. *Biomaterials*, **35**, 2915–2923.

49 Thomas, S.W., Joly, G.D., and Swager, T.M. (2007) Chemical sensors based on amplifying fluorescent conjugated polymers. *Chem. Rev.*, **107**, 1339–1386.

50 Feng, G., Fang, Y., Liu, J., Geng, J., Ding, D., and Liu, B. (2017) Multifunctional conjugated polymer nanoparticles for image-guided photodynamic and photothermal therapy. *Small*, **13**, DOI: 10.1002/smll.201770014

51 Farokhzad, O.C., Cheng, J., Teply, B.A., Sherifi, I., Jon, S., Kantoff, P.W. *et al.* (2006) Targeted nanoparticle-aptamer bioconjugates for cancer chemotherapy in vivo. *Proc. Natl. Acad. Sci. USA*, **103**, 6315–6320.

52 Goren, D., Horowitz, A.T., Tzemach, D., Tarshish, M., Zalipsky, S., and Gabizon, A. (2000) Nuclear delivery of doxorubicin via folate-targeted liposomes with bypass of multidrug-resistance efflux pump. *Clin. Cancer Res.*, **6**, 1949–1957.

53 Tian, B., Wang, C., Zhang, S., Feng, L., and Liu, Z. (2011) Photothermally enhanced photodynamic therapy delivered by nano-graphene oxide. *ACS Nano*, **5**, 7000–7009.

54 Sherlock, S.P., Tabakman, S.M., Xie, L., and Dai, H. (2011) Photothermally enhanced drug delivery by ultrasmall multifunctional FeCo/graphitic shell nanocrystals. *ACS Nano*, **5**, 1505–1512.

55 Gohy, J.F. and Zhao, Y. (2013) Photo-responsive block copolymer micelles: design and behavior. *Chem. Soc. Rev.*, **42**, 7117–7129.

56 Lin, Q.N., Huang, Q., Li, C.Y., Bao, C.Y., Liu, Z.Z., Li, F.Y. *et al.* (2010) Anticancer drug release from a mesoporous silica based nanophotocage regulated by either a one- or two-photon process. *J. Am. Chem. Soc.*, **132**, 10645–10647.

57 Brown, S. (2008) Photodynamic therapy – two photons are better than one. *Nat. Photonics*, **2**, 394–395.

58 Urdabayev, N.K. and Popik, V.V. (2004) Wolff rearrangement of 2-diazo-1(2*H*)-naphthalenone induced by nonresonant two-photon absorptionof NIR radiation. *J. Am. Chem. Soc.*, **126**, 4058–4059.

59 Yuan, Y., Wang, Z., Cai, P., Liu, J., Liao, L.D., Hong, M. *et al.* (2015) Conjugated polymer and drug co-encapsulated nanoparticles for chemo- and photo-thermal combination therapy with two-photon regulated fast drug release. *Nanoscale*, **7**, 3067–3076.

60 Song, X., Chen, Q., and Liu, Z. (2015) Recent advances in the development of organic photothermal nano-agents. *Nano Res.*, **8**, 340–354.

61 Gong, H., Xiang, J., Xu, L.G., Song, X.J., Dong, Z.L., Peng, R. *et al.* (2015) Stimulation of immune systems by conjugated polymers and their potential as an alternative vaccine adjuvant. *Nanoscale*, **7**, 19282–19292.

12

Conjugated Polymers for Disease Diagnosis and Theranostics Medicine

Akhtar Hussain Malik[1], *Sameer Hussain*[1], *Sayan Roy Chowdhury*[1], *and Parameswar Krishnan Iyer*[1,2]

[1] *Indian Institute of Technology Guwahati, Department of Chemistry, Near Doul Gobinda Road, Guwahati, 781039, India*
[2] *Indian Institute of Technology Guwahati, Centre for Nanotechnology, Near Doul Gobinda Road, Guwahati, 781039, India*

12.1 Introduction

Conjugated polymers (CPs) and oligomers are made up of repeating units (Figure 12.1) that could be distinguished by analyzing the changes in their properties upon addition or removal of one or more repeating units [1]. The focus on CPs since the 1970s has been on utilizing these fascinating classes of materials in optoelectronic devices such as solar cells, OLEDs, and displays. Subsequently, the Nobel Prize was awarded to three eminent scientists Alan J. Heeger, Alan G. MacDiarmid, and Hideki Shirakawa in 2000 "for the discovery and development of conductive polymers." The general characteristic of a conjugated molecule can be described as the sequence of altering double (or triple) and single bonds. These alternating double and single bonds generally stabilize a molecule thermodynamically, and additionally give the molecule certain characteristics, such as the ability to absorb and emit light or transport electrical charges. Such unique features of these materials endorse their widespread applications in multidisciplinary areas of chemical, biological, and material science [2].

Early and accurate diagnosis is essential for the effective cure of any disease/health disorder and thus play a vital role in clinical medicine and therapeutics.

From chemistry to biology or physics to medicine and biomedical devices the development of rapid, advanced, and noninvasive methods for theranostic applications remains utmost challenging and a priority for research for investigators due to the ever increasing human health problems as well as for public safety. To overcome these existing problems and to address the urgent need of diagnosis, imaging, and therapy, CPs and their corresponding nanoparticles (CPNs) have recently emerged as excellent theranostic tools in the treatment of cancer, cardiovascular diseases, neurodegenerative disorders, kidney diseases, infectious diseases, and so on [2–5].

Conjugated Polymers for Biological and Biomedical Applications, First Edition. Edited by Bin Liu

12.2 Disease Diagnostics via Conjugated Polymers

12.2.1 Detection of Pathogens (*E. coli*, *C. albicans*, *B. subtilis*)

Infections caused by microbial pathogens in humans have become a global health problem. Disease diagnostics via detection of such disease-causing agents such as *Escherichia coli* (*E. coli*), *Candida albicans* (*C. albicans*), influenza virus, hepatitis B virus, using CPs has emerged as one of the most encouraging methods in clinical research [2].

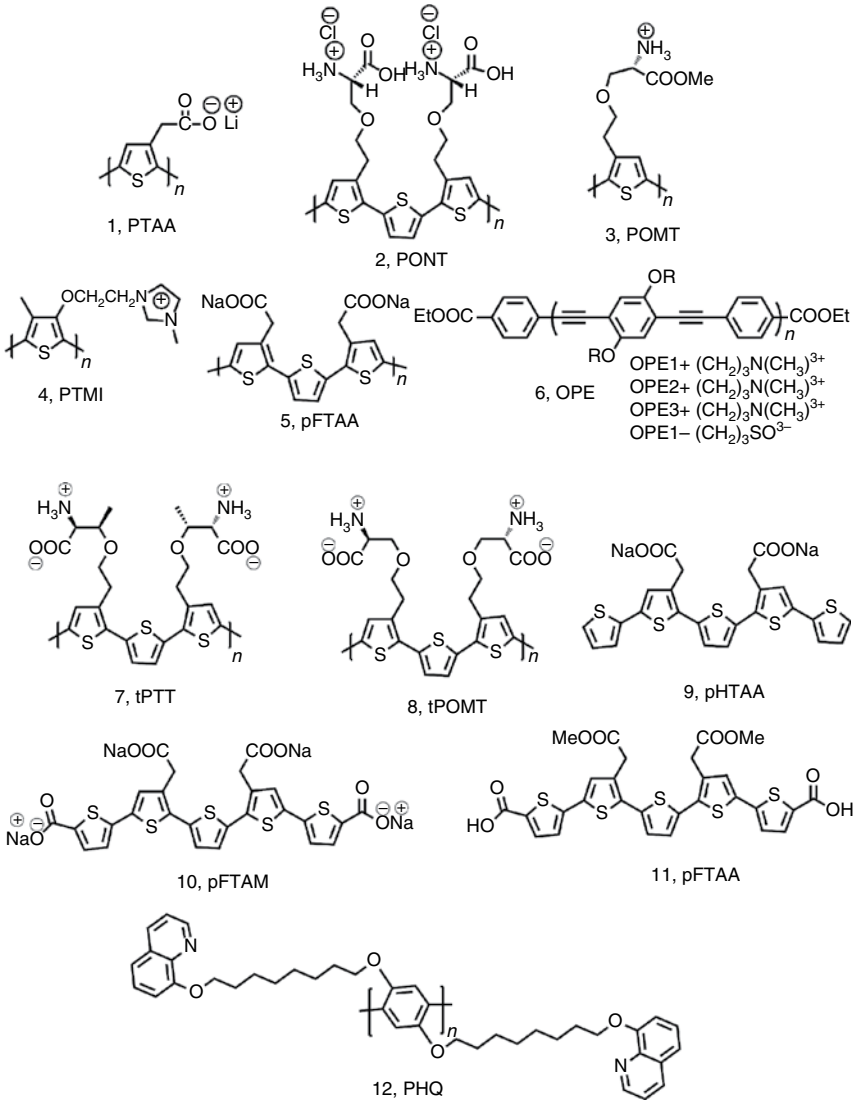

Figure 12.1 Chemical structures of some reported CPs and oligomers.

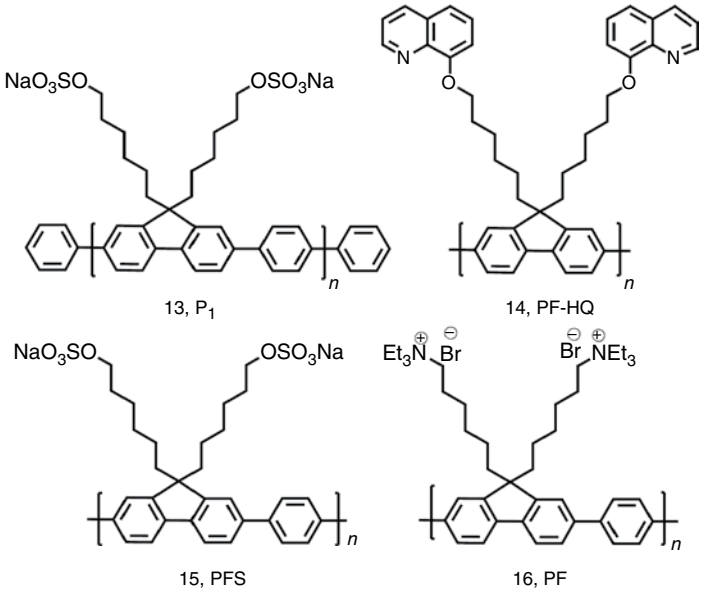

Figure 12.1 (*Continued*)

Among all pathogens, *E. coli* is the most hazardous microbial agent responsible for several food-borne diseases, thus requiring rapid and precise detection techniques [6]. The colorimetric detection of *E. coli* and influenza virus via visible absorption spectrometry was first demonstrated by Baek and coworkers using sialic acid/mannose ligands incorporated glycopolythiophenes [7]. Later, Swager and coworkers reported α-mannose appended poly (*p*-phenylene ethynylene) (PPE) comprising several carbohydrate units on a single polymer chain for multivalent detection of pathogens [8]. The polymer displayed bright green fluorescence with bacteria *E. coli* stain as a result of aggregation. Furthermore, the pathogen detection can be achieved within 10–15 min unlike previously reported slow systems that needed several days for detection due to selective growth of bacteria in liquid media and/or plates. Later, Bunz group reported two α-mannose-functionalized PPE derivatives P1 and P2 (Figure 12.2a) for the detection of lectins and *E. coli* [9]. They increased the spacer length between sugar and polymer backbone to improve the flexibility in side chains and incorporated more complex trimannose to enhance the sensitivity. CPs P1 and P2 displayed significant fluorescence quenching with lectin concanavalin A (ConA) with a Stern–Volmer constant (K_{sv}) value of 1.6×10^8 and $1.1 \times 10^{10}\,M^{-1}$, respectively. Such high K_{sv} values represent strong binding of PPEs with ConA as a result of analyte-induced aggregation. The polymers were then used to investigate their binding affinities with mannose-binding *E. coli* stain (ORN178) and mannose nonbinding *E. coli* stain (ORN 208), respectively. Although, both the strains led to staining, no bacterial agglutination was detected for ORN 208. The bacterial agglutination on exposure to P1 or P2 is believed to be facilitated by the presence of favorable mannose-binding sites in ORN 178. Moreover, P2 induces

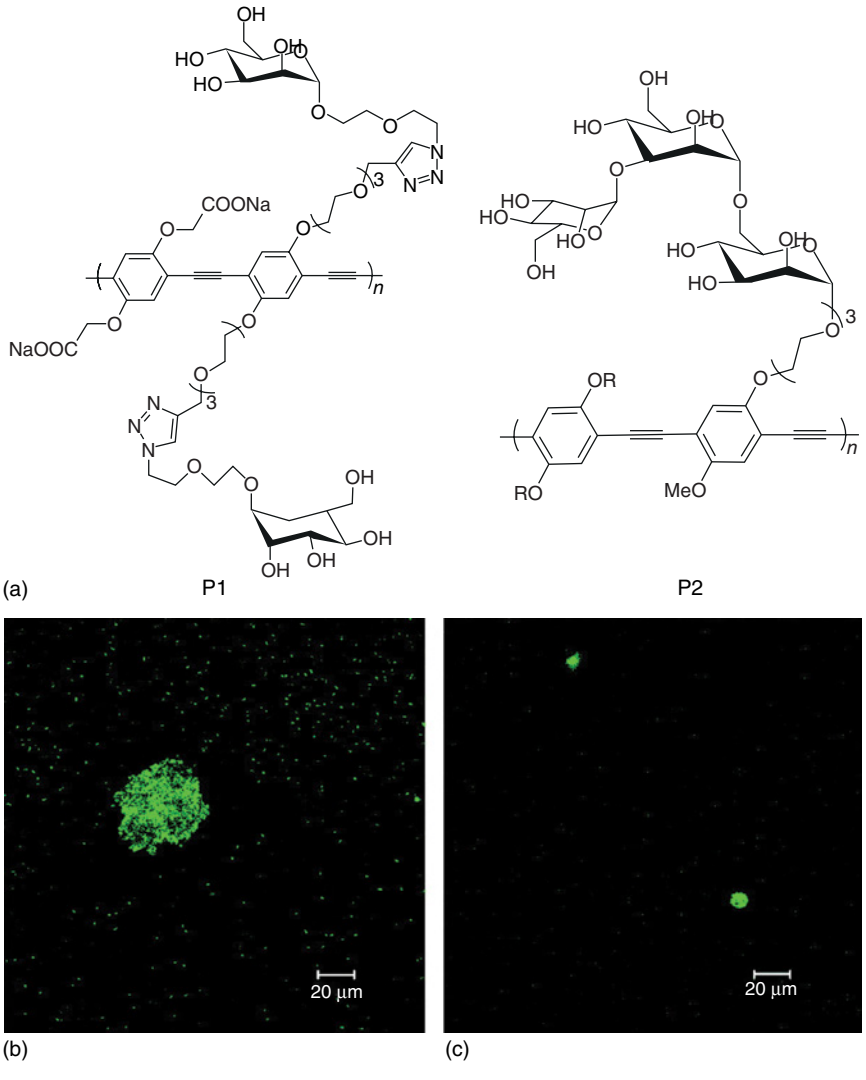

Figure 12.2 (a) Structure of newly developed PPE derivatives P1 and P2. Confocal laser scanning microscopy (CLSM) images of (b) P1 and (c) P2 with mannose-binding *E. coli* strain ORN 178. (Reproduced with permission from Ref. [9]. Copyright 2008, American Chemical Society.)

the formation of denser fluorescent clusters compared to P1 that showed interspersed loose aggregates (Figure 12.2b,c), confirming the superiority of the former in detecting *E. coli*.

During subsequent years, Liu and coworkers also synthesized three neutral sugar (β-glucose and α-mannose) incorporated polyfluorene derivatives via post-polymerization functionalization for the detection of *E. coli* [10]. To enhance the degree of freedom, the polymers were tuned with variable lengths of ethylene glycol linker. The polymers with long poly (ethylene glycol) (PEG) linker dis-

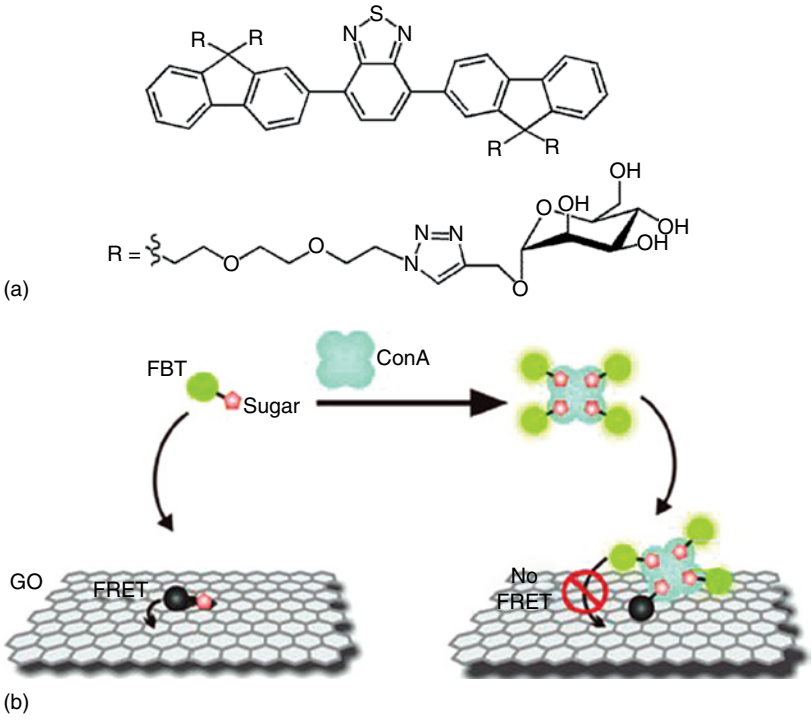

Figure 12.3 Structure of (a) oligomer FBT and (b) its application in the detection of ConA using GO/FBT hybrid probe. (Reproduced with permission from Ref. [11]. Copyright 2011, John Wiley & Sons.)

played good water solubility and better flexibility to the attached sugar components viz. β-glucose and α-mannose. As expected, the polymers displayed remarkable fluorescent aggregates exclusively with mannose-binding *E. coli* stain ORN 178 as confirmed via red shifted UV–vis absorption and emission spectra. Since, most of the previously reported sugar-appended CPs exhibited poor water solubility and undesirable background fluorescence, Liu and coworkers developed another water-soluble fluorene derivative FBT (Figure 12.3a) with four pendant α-mannose on the side chains[11]. This neutral oligomer FBT was employed as an excellent light-up probe for monitoring ConA and *E. coli* with the advantage of eliminating background signals. The emission of oligomer FBT was almost quenched in the presence of graphene oxide (GO) through FRET mechanism (Figure 12.3b). However, in the presence of ConA, the fluorescence of FBT was significantly recovered due to more favorable binding of FBT with ConA through protein–carbohydrate interaction. This indicates the applicability of the FBT-GO hybrid system for light-up sensing of ConA with high selectivity and a very low detection limit of ~0.5 nM. Furthermore, the light-up response of GO/FBT probe due to unique protein–carbohydrate interaction also helps in discriminating different strains of *E. coli* without any background emission.

Wang and coworkers for the first time demonstrated optical detection/discrimination of microbial pathogens fungi and bacteria using a blend of two

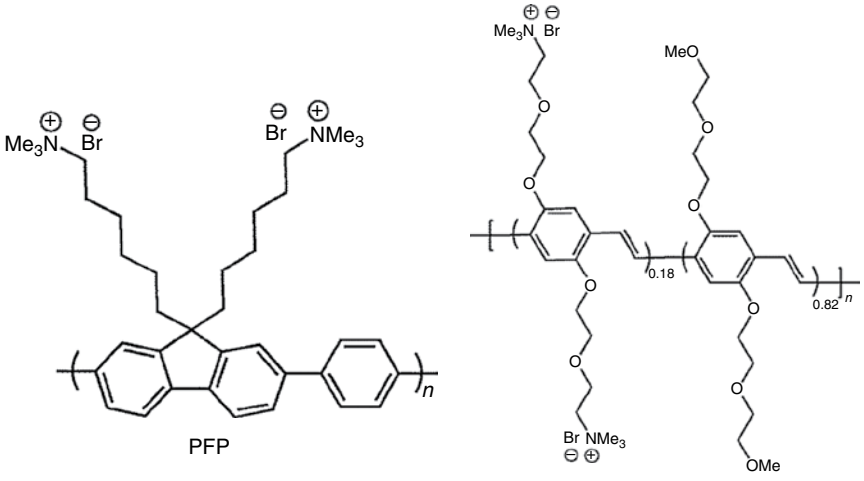

Figure 12.4 Structures of (a) two cationic polymer PFP and PPV used (b) for the detection of pathogens based on FRET. ((a) Reproduced with permission from Ref. [2]. Copyright 2012, American Chemical Society and (b) Reproduced with permission from Ref. [12]. Copyright 2011, Royal Society of Chemistry.)

water-soluble conjugated polymers (WSCPs) (Figure 12.4a) [12]. In this study, the versatile cationic WSCP PFP acts as the energy donor, a novel cationic CP PPV employed as the energy acceptor, while *C. albicans* fungus and *E. coli* bacterium were chosen as the representative microorganisms. To facilitate the process of FRET, the two cationic CPs were brought into close proximity via favorable Columbic binding with negatively charged surfaces of the microbial membrane (Figure 12.4b). Owing to the distinct surface structures and chemical composition in their cell walls, the polymers displayed variable binding situations with these pathogens. Both *C. albicans* and *E. coli* exhibited net negative charges on the surface and, therefore, both the polymers could easily bind at the surface via electrostatic attractions to assist FRET mechanism. However, the cell wall of *C. albicans* consists largely of β-glucans, chitin, and mannoprotiens unlike peptidoglycan as in the case of *E coli*. Such variations in the surface structures enable

different binding affinities to the blend of cationic polymers. *C. albicans* captured more PFP and less PPV due to the absence of PEG groups along the side chain that resist nonspecific adsorption to protein and cell surfaces. Hence, *C. albicans* mediated the weak FRET between the polymers compared to *E. coli* that expedited strong FRET. Such variable FRET responses assist in visual and optical detection/discrimination of these microbial pathogens. In contrast to the previously reported sophisticated procedures, this method is simple and low cost, and provides rapid and most efficient visualization and discrimination of bacteria and fungi which possibly has long-term impact on clinical diagnosis.

Later on, another similar cationic WSCP PPVE (Figure 12.5a) consisting of a simple alkyl chain as linker instead of ethylene glycol was reported by the same group [13]. The polymer PPVE itself has the capability to discriminate Gram-positive bacteria (*Bacillus subtilis*), Gram-negative bacteria (*E. coli*), and fungi (*C. albicans*) under a fluorescence microscope by simply changing the ionic strengths of the phosphate buffer saline (PBS) solution used (Figure 12.5b). All the three species were stained with 5 μM PPVE in variable concentrations of PBS ranging from 5 to 40 mM. Stained *E. coli* showed sharp decrement in fluorescence intensity with increase in the buffer concentration and the intensity was negligible at 40 mM concentration. Similar change was observed for fungi *C. albicans*. However, stained *B. subtilis* showed slow decrement in the emission intensity on increasing the buffer concentration from 20 to 40 mM with negligible change in the range of 5–20 mM. Such anomalous behavior is attributed to (a) different cell wall composition of these species, (b) electrostatic interactions of polymer with *C. albicans* and *E. coli,* and (c) hydrophobic interactions of polymer PPVE with *B. subtilis* as evident from thermodynamical and zeta potential studies. Thus, the detection and discrimination of these three vital microbial species can be realized rapidly using single polymer PPVE in just few hours unlike previous methods that require polymer blend that usually took several days.

12.2.2 Detection of Cancer Biomarkers (DNA Methylation, miRNAs, Hyaluronidase, Spermine)

Cancer is an abnormal and unregulated growth of cells, in which these cells have the potential to metastasize to other body parts through blood and lymph systems. It is a major health crisis and a vicious disease across the globe and the second leading cause of deaths in the United States and other developed countries. The hallmarks [14] of cancer that constitute a principle for rationalizing the complexities of neoplastic diseases are shown in Figure 12.6, which includes sustaining proliferative signaling, evading growth suppressors, resisting cell death, enabling replicative immortality, inducing angiogenesis, and activating invasion and metastasis. Complete elimination of cancerous tissues remains a challenging task for researchers around the globe, because cancer cells can attack normal adjacent tissues and can spread to distant body parts. For the effective treatment of cancer, diagnosis is an essential part of clinical medicine, and accurate diagnosis is a critical criterion. Biomarkers hold great potential in the field of diagnostic technology to detect a change in the physiological state of a patient, which

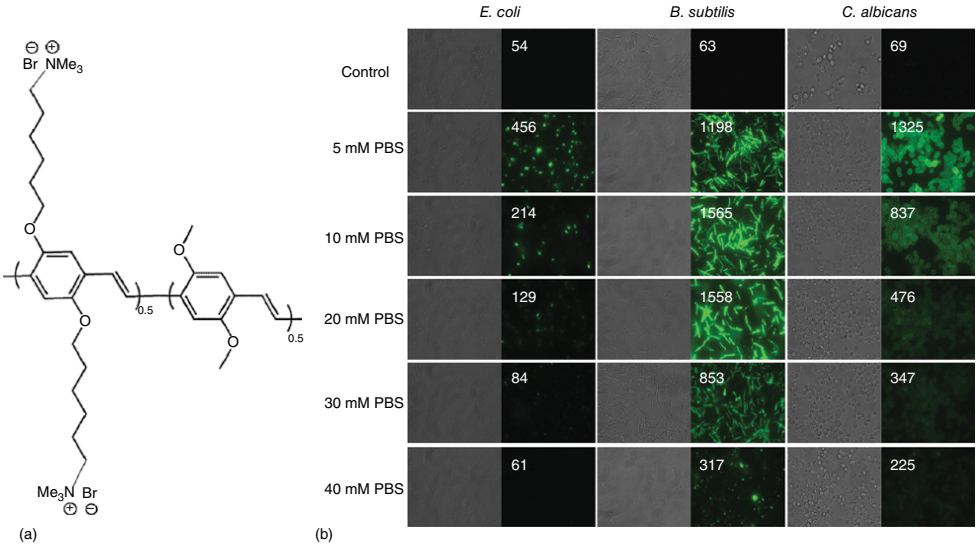

Figure 12.5 (a) Structure of cationic polymer PPVE and (b) its adsorption [PPVE = 5 μM] on the surfaces of *E. coli*, *B. subtilis*, and *C. albicans* in different concentrations of PBS. The corresponding numbers on the images depict the emission intensity values as determined by DVC View and Microsoft Excel softwares. (Reproduced with permission from Ref. [13]. Copyright 2014, John Wiley & Sons.)

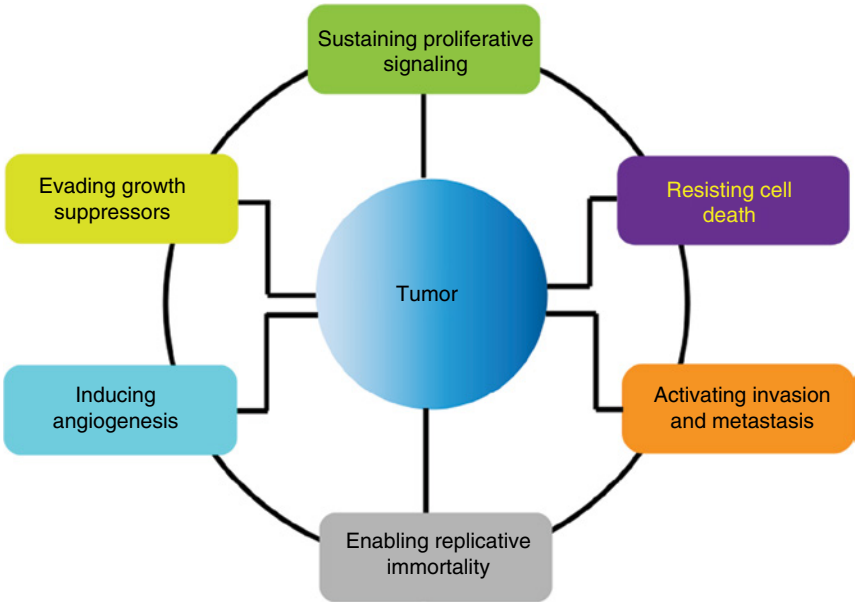

Figure 12.6 Hallmarks of cancer-distinctive and complementary capabilities that enable tumor growth and metastatic dissemination.

correlates with the risk or progression of a disease or to assess the effectiveness of a particular therapy. Here, we discuss current advances in the diagnosis as well as treatment of cancer using CPs as an important tool.

12.2.2.1 DNA Methylation

Incorporation of a methyl group to the 5-position of cytosine (pyrimidine ring) resulting in 5-methylcytosine is known as DNA methylation, which almost exclusively occurs within a CpG dinucleotide thereby altering the function of genes. Changes in DNA methylation are linked to the pathogenesis of human malignancies. During the past two decades research in DNA methylation and chromatin fields have motivated great interest in the epigenetics of cancer [15]. It is assumed that DNA methylation is associated with almost all types of cancers. As a result, identification of abnormal DNA methylation is very useful to develop distinctive therapeutic and diagnostic strategies. Aberrations of DNA methylation in the case of cancer can be a significant therapeutic target from a clinical perspective. There is a very low methylation level at CpG islands in normal tissues, and the stability of DNA is high, which convey that detection of DNA methylation has a promising future in the area of early detection of cancer and molecular diagnostics. Wang and coworkers developed convenient and efficient cationic CP-based FRET system to determine the methylation levels of specific CpG sites of plasmid and human colon cancer cell [16]. This protocol combined the highly selective single base extension (SBE) reaction with significant optical amplification of CPs. After the treatment of DNA specific methylation agents DNA methylation levels can convert into a C/T polymorphism,

bisulfite, alters non-methylated C base to U base, but the methylated C base remains unchanged. Methylation-specific probe is treated by bisulfite in case of methylated DNA and the SBE reaction starts with DNA Taq polymerase in the presence of fluorescein-labeled G base (dGTP-Fl), hence dGTP-Fl is successfully involved in the extension products. However, for a nonmethylated DNA sample, there is no dGTP-Fl incorporated. Upon addition of CCP to the systems, strong electrostatic interactions between CCP and DNA extension products reduce the distance between the fluorescein unit and CCP, hence efficient FRET takes place from CCP to fluorescein (Figure 12.7) for the methylated DNA sample, but no FRET signal was observed for nonmethylated samples. Picomolar levels of DNA could be easily detected by utilizing the enhanced fluorescein emission offered by the optical amplification of CCP. On the basis of this detection methodology, the methylation status of three CpG sites in the p16 promoter region has been identified for human colon cancer cell line (HT29) and the prominent FRET signal verified the hyper-methylation in the p16 promoter region of HT29 cells.

Owing to the complicated processes and alterations of multiple pathways involved in tumor cells, single methylation biomarker detection is insufficient. Therefore, development of cumulative detection of multiple methylation markers will definitely advance the detection efficiently. Based on the above mentioned method, CCP-based FRET protocol was further extended to identify multiple epigenetic methylation markers simultaneously, and to detect and diagnose colon cancer by a cumulative study of the DNA methylation in promoter regions [17].

In this study, seven genes were chosen as candidate genes, and their methylation status were analyzed. A statistic method, namely, Wilks' λ-test was carried out to check whether there were differences between the means of identified groups of subjects on a combination of dependent variables in multivariate analysis of variance. After this analysis, three genes, adenomatosis polyposis coli (APC), vimentin (VIM), and cyclin dependent kinase inhibitor 2A (CDKN2A/P16) were selected for the final detection equation to detect colon cancer. The methylation levels were calculated for 110 samples with high accuracy of 86.3% and the cumulative detection reached a sensitivity of 86.7%, which is much higher than that obtained by the single methylation detection method (41.7–65%). Moreover, the relationship between the CpG island methylator phenotype and important clinical parameters for colon cancer was analyzed and the results indicate that cumulative methylation detection of genes related to colon cancer with CCP-based FRET method holds the potential for early detection and differential diagnosis of cancer in a simple, noninvasive, and economical manner. Since, the diagnostic result depends on a statistical analysis of a large number of samples, this method is difficult to be used for point-of-care diagnostics. To overcome the problem of the aforementioned statistics and cumulative analysis method associated with point-of-care diagnostics, Wang and coworkers established an associated analysis method of DNA methylation level by the CCP-based FRET method for the detection of ovarian cancer [18]. In this study, methylation levels of three promoter genes including RASSF1A, OPCML, and HOXA9 of 35 samples from ovarian cancer patients and 11 normal samples were evaluated via improved associated analysis. The calculated methylation level of

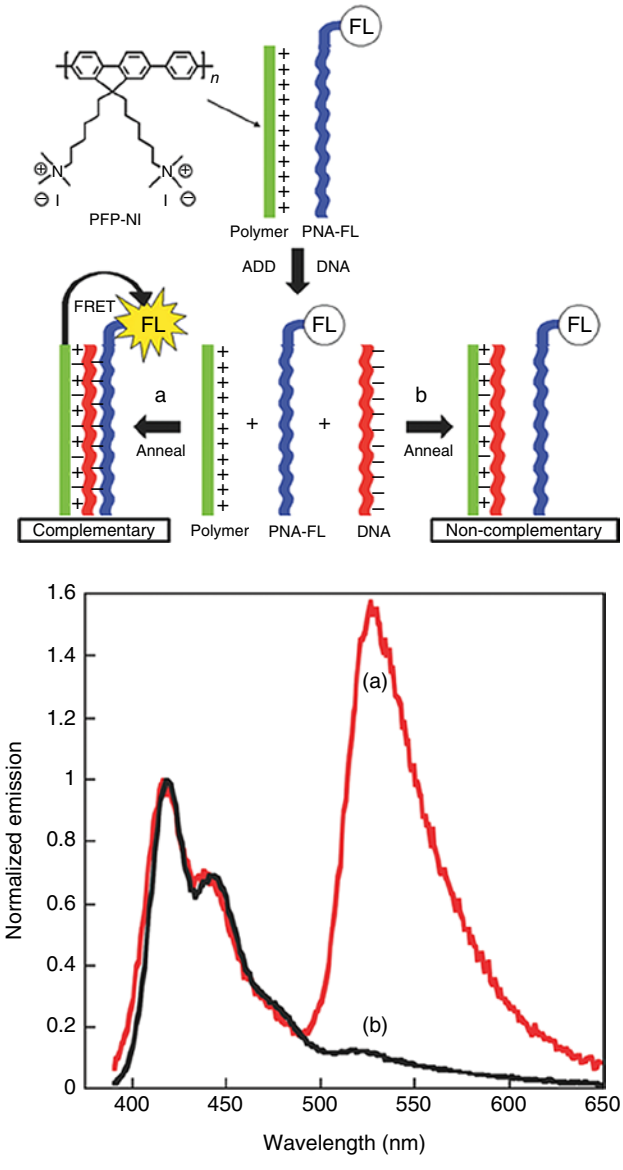

Figure 12.7 Schematic demonstration of CCP-based ssDNA sequence detection with a specific PNA-FI optical reporter probe, and the corresponding emission spectra for complementary (a) and noncomplementary (b) DNA by the excitation of conjugated polymers. (Reproduced with permission from Ref. [16]. Copyright 2008, American Chemical Society.)

the promoter genes were distributed to three sections and three values were given for these three sections. As shown in Figure 12.8, the output value is 1, when E is smaller than 0.3; the output value is 2 when E is between 0.3 and 0.7; and the output value is 3 when E is higher than 0.7. To get the "SUM" the output

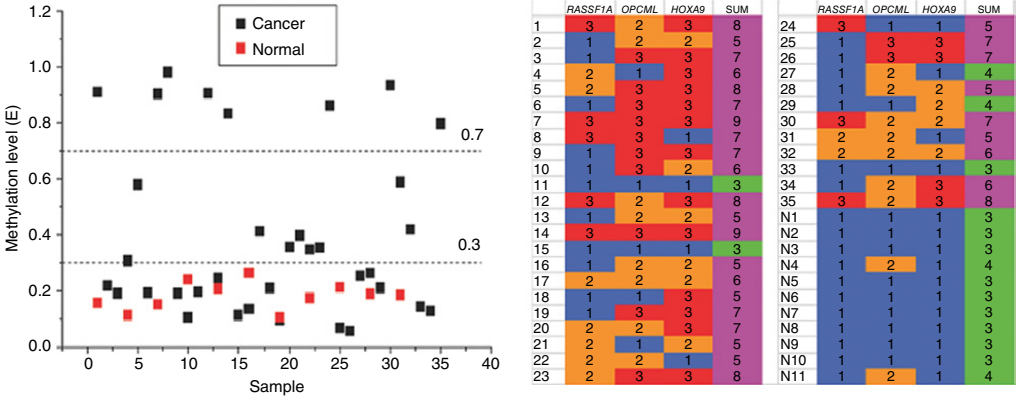

	RASSF1A	OPCML	HOXA9	SUM
1	3	2	3	8
2	1	2	2	5
3	1	3	3	7
4	2	1	3	6
5	2	3	3	8
6	1	3	3	7
7	3	3	3	9
8	3	3	1	7
9	1	3	3	7
10	1	3	2	6
11	1	1	1	3
12	3	2	3	8
13	1	2	2	5
14	3	3	3	9
15	1	1	1	3
16	1	2	2	5
17	2	2	2	6
18	1	1	3	5
19	1	3	3	7
20	2	2	3	7
21	2	1	2	5
22	2	2	1	5
23	2	3	3	8

	RASSF1A	OPCML	HOXA9	SUM
24	3	1	1	5
25	1	3	3	7
26	1	3	3	7
27	1	2	1	4
28	1	2	2	5
29	1	1	2	4
30	3	2	2	7
31	2	2	1	5
32	2	2	2	6
33	1	1	1	3
34	1	2	3	6
35	3	2	3	8
N1	1	1	1	3
N2	1	1	1	3
N3	1	1	1	3
N4	1	2	1	4
N5	1	1	1	3
N6	1	1	1	3
N7	1	1	1	3
N8	1	1	1	3
N9	1	1	1	3
N10	1	1	1	3
N11	1	2	1	4

Figure 12.8 The distribution of *E* for RASSF1A promoter of 46 samples measured by the CCP-based FRET technique, and the corresponding values and sum of the values for RASSF1A, OPCML, and HOXA9 genes. (Reproduced with permission from Ref. [18]. Copyright 2014, American Chemical Society.)

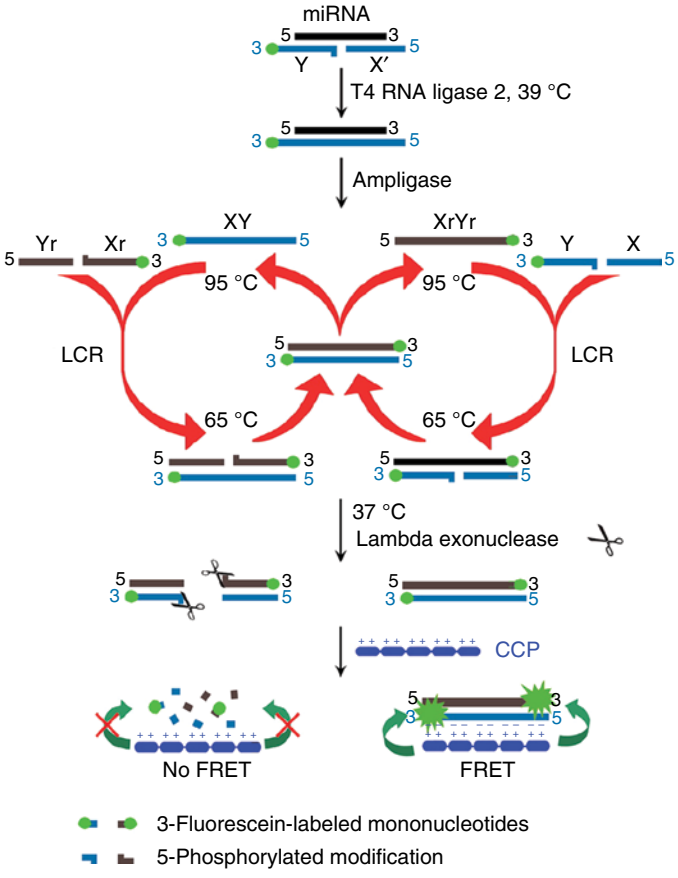

Figure 12.9 Principle of LCR and lambda exonuclease-assisted CCP biosensing for miRNA detection. (Reproduced with permission from Ref. [19]. Copyright 2014, American Chemical Society.)

values of the three candidate genes RASSF1A, OPCML, and HOXA9 were summed and a threshold was assigned to discriminate cancer samples by comparing the "SUM" of the three genes of cancer to normal samples. A sensitivity of 85.7% and a specificity of 100% for ovarian cancer detection were achieved through the associated analysis of methylation levels of three promising genes (Figure 12.9).

12.2.2.2 MicroRNAs (miRNA) Detection

MicroRNAs are a class of single-stranded, small non-coding ribonucleic acid molecules with about 22 nucleotides that control a group of cellular functions through directly interacting with target mRNAs [20, 21]. It is known from previous studies that certain miRNAs can perform a vital role in various cellular processes, including cell growth, proliferation, differentiation and apoptosis [22]. The expression levels of miRNAs are directly associated with human cancers, where miRNAs can act as either oncogenes or tumor suppressors. Therefore,

miRNA detection is crucial for cancer diagnosis [23, 24] and therapy as well as drug screening.

Li and coworkers designed an approach for homogeneous detection of miRNA that made full use of ligase chain reaction (LCR) and lambda exonuclease-assisted CCP biosensing technique [19]. In LCR, for carrying out ligation-based exponential amplification, two pairs of oligonucleotide probes were designed and each pair consisted of two probes that were adjacent and perfectly complementary to target miRNA or the ligated DNA strand. Lambda exonuclease, a processive exodeoxyribonuclease that acts on 5′-3′ direction of double stranded DNA (dsDNA) and degrades specifically the 5′-phosphorylated strand of double stranded DNA. On single-stranded DNA (ssDNA) and nonphosphorylated DNA [25, 26] the enzyme displayed low activity. In order to carry out homogeneous miRNA detection, lambda exonuclease is introduced to degrade the excess fluorescence-labeled 5′-phosphorylated probes after LCR to eliminate the background signal. At the same time, fluorescein-labeled LCR products could not be degraded because the LCR products without 5′-phosphorylated modification were not the preferred substrates of lambda exonuclease. Finally, the LCR products were bound to CCPs through electrostatic interactions to initiate FRET (Figure 12.9). In this protocol, only one lambda exonuclease was employed, and only fluorescein-labeled probe was required in each pair of probes in LCR thereby, reducing the complex probe modifications and cost. The simple and sensitive method paves a new way for homogeneous miRNA detection and molecular diagnosis.

Cheng and coworkers developed a novel strategy for the detection of miRNAs by combining DSN-assisted amplification with homogeneous multiplex biosensing of CCPs [27]. Duplex-specific nuclease (DSN) was applied in detection of miRNA with its distinctive feature that it degrades both dsDNA and also the DNA in the DNA–RNA hybrid [28, 29]. Furthermore, for ssDNA and RNA, DSN showed no activity. Hence, DSN is appropriate for detection of miRNA based on its characteristic ability of DNA cleavage in the DNA-miRNA heteroduplex. In this protocol, a complementary sequence of fluorescence-probe-labeled dye containing fluorescein and Cy3 corresponding to target miRNAs were designed. On introducing CCPs, efficient FRETs from CCPs to fluorescence probes takes place because of the strong electrostatic interaction between CCPs and probes. Furthermore, the fluorescence probes complementary to the target miRNAs break down to small oligonucleotide fragments in the presence of DNS, whereas the target miRNAs were released and later hybridized with the new fluorescence probes, resulting in the cycled digestion of the fluorescence probes. After the probes were digested, the electrostatic interactions between fluorophore-labeled oligonucleotide fragments and CCPs become weak so that no efficient FRET takes place from CCPs to fluorophores (Figure 12.10). Compared to the previously reported methods of miRNA detection and CCP-based sensing strategy, the present method has numerous advantages. Firstly, the strategy integrates isothermal DSN-induced DNA amplification with CCP biosensing, which confirms miRNAs detection with high sensitivity and specificity in a homogeneous fashion. Secondly, multiplex detection of miRNAs can be attained efficaciously, resulting from the CCP-based multiple FRET and outstanding signal amplification ability of CCP.

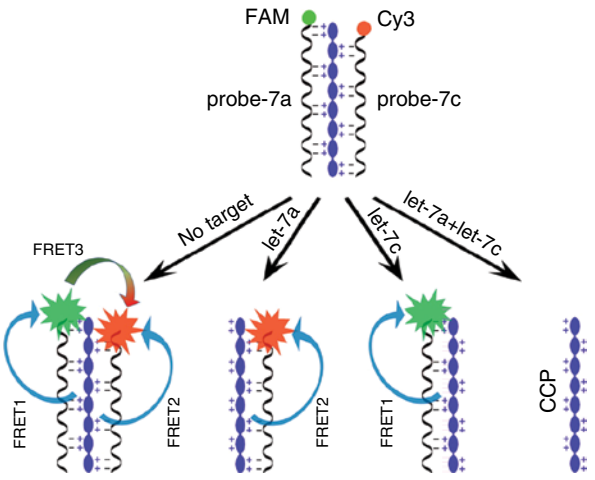

Figure 12.10 Principle of multiplex detection of miRNAs by the mixed probes. (Reproduced with permission from Ref. [27]. Copyright 2016, American Chemical Society.)

12.2.2.3 Hyaluronidase (HAase) Detection

Besides DNA and miRNAs, there are various other cancer-related biomarkers such as spermine, glutathione, hyaluronidase, pyrophosphate, and so on, which are equally important in the diagnosis of various types of tumors. HAase is secreted by tumor cells and is closely associated with the presence of tumors. Unambiguously, the levels of HAase increases in many tumor cells, such as bladder carcimoma [30, 31], prostate [32, 33], malignant melanoma [34], and brain and neck cancer. Thus, HAase has become a new type of tumor marker since it has been recognized to be overexpressed in various kinds of cancer cells.

Huang *et al.* designed a simple and sensitive method for HAase detection using a probe based on a fluorescent CCP/hyaluronan–doxorubicin (HADox) complex [35]. In this method, CCP was used which formed a complex with anionic HA conjugated with the model anticancer drug Dox (Figure 12.11). Efficient electron transfer (ET) from CCP to Dox (the quencher) occurred in the complex and triggered a "turn off" signal of CCP. When HAase was present, HA was degraded into small fragments and Dox was released, resulting in the obvious fluorescence recovery of CCP.

12.2.2.4 Spermine Detection

Iyer and coworkers developed a CCP-surfactant- based assembly that was successfully used for the trace detection of biogenic amine spermine (Figure 12.12) in urine specimens with high selectivity and sensitivity [36]. Spermine, a biogenic polyamine usually found in eukaryotic cells and body fluids, plays a vital role in the regulation of several cellular processes like cell growth and proliferation [37, 38]. These polyamines are among the most abundant organic polycations found in the human body and are known to be involved in numerous stages of protein synthesis, stabilization of nucleic acid conformations, and cytoskeleton structures. It has been observed that enhanced levels of spermine in urine

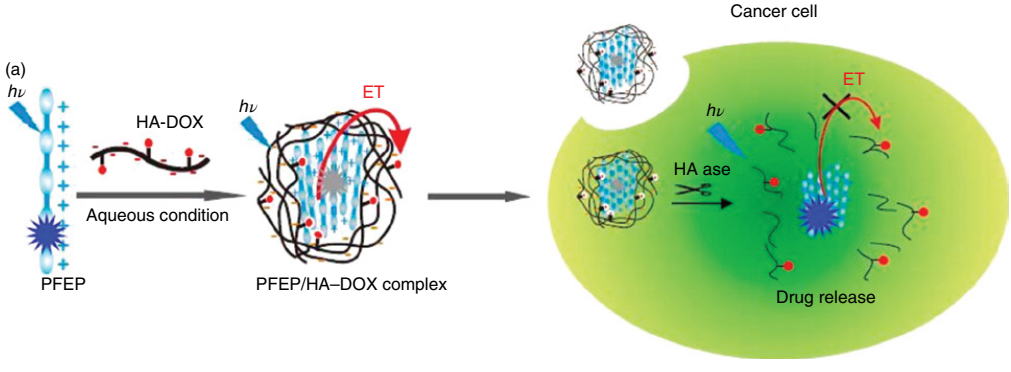

Figure 12.11 Schematic illustration of the overall strategy for HAase detection. (Reproduced with permission from Ref. [35]. Copyright 2015, American Chemical Society.)

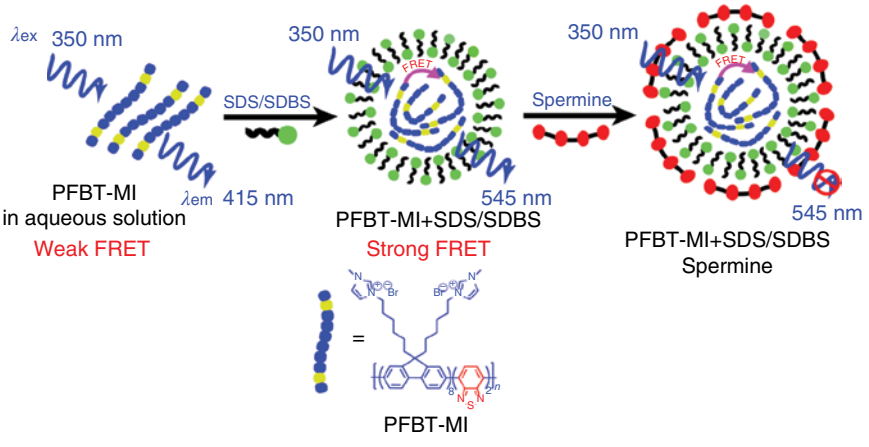

Figure 12.12 Schematic representation of proposed sensing mechanism for the detection of surfactants SDS/SDBS and spermine. (Reproduced with permission from Ref. [36]. Copyright 2016, American Chemical Society.)

and blood are liable to cause many types of cancers such as prostatic and colon cancer. Thus, it is regarded as an excellent biomarker for early cancer detection and an indicator for assessing the efficiency of cancer chemotherapy during the long-term treatment of patients [37–39].

12.2.3 Detection of Other Important Biomarkers (Acid Phosphatase, Bilirubin)

The use of CPs in molecular diagnosis of diseases has recently emerged as one of the most promising areas due to its incredible impact on human health issues. In recent years, various CP-based materials have been successfully utilized for the detection of disease-related biomarkers (single nucleotide polymorphisms (SNPs) and mutation, bilirubin, trypsin, acid phosphatase, pyrophosphate, dopamine, etc.) [2, 5]. Many such biomarkers assist in the early diagnosis of diseases and thus their detection is vital in minimizing the hazardous and cruel aftermath of the diseases in humans.

12.2.3.1 Acid Phosphatase (ACP) Detection

Acid phosphatase (ACP) is an abundant hydrolase enzyme that plays a crucial role in phosphatase scavenging inside the human body. Its abnormal elevated level in body fluids instigates various diseases such as prostate cancer, Gaucher disease, and some other disorders related to bones, kidneys, and veins [40, 41]. Hence, ACP recently emerged as an excellent serum biomarker for prostate cancer and could also be diagnostically employed in the clinical evaluation of associated diseases. Iyer and Dwivedi developed an assay (Figure 12.13) comprising Fe^{3+} bounded anionic CP (P1) nonfluorescent assembly for the continuous and real-time detection of ACP enzyme under acidic conditions at very low nanomolar levels [42]. Extensively used ACP substrate *p*-nitrophenyl phosphate (p-NPP) was found to be ineffective toward the quenched emission of P1-Fe^{3+} assembly

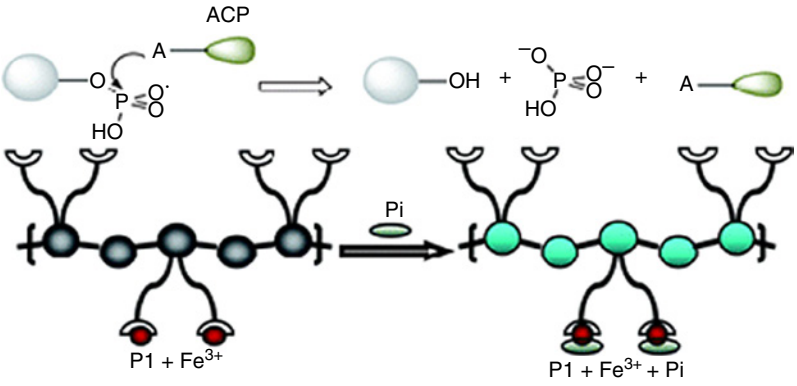

Figure 12.13 As assay for the detection of ACP in human blood serum using assembly of WSCP P1 and Fe^{3+} (Reproduced with permission from Ref. [42]. Copyright 2013, Royal Society of Chemistry.)

even after incubation of 8 h. The assembly was then utilized for the hydrolysis of *p*-NPP substrate using ACP enzyme at pH 6.0 in a 15 mM Tris–HCl buffer. The results indicated that a minor quantity of ACP enzyme was adequate to generate significant fluorometric changes during the enzymatic hydrolysis. Control experiment in the absence of *p*-NPP confirms that ACP enzyme itself could not the affect the fluorescence of assembly. Enzymatic hydrolysis of *p*-NPP with the function of time and different concentration of ACP further confirmed the feasibility of the system in continuous, real-time detection of ACP at very low nanomolar regime and potential in the diagnosis of acid phosphatase diseases.

12.2.3.2 Bilirubin Detection

Bilirubin is a yellow-colored pigment generated during the catabolic pathway of red blood cells. It is considered as an important biomarker in serum to diagnose liver disorders [43]. Bilirubin concentration can rise upto >50 μmol l^{-1} (>2.5 mg) from its normal level of <25 μmol (<1.2 mg dl^{-1}) in the blood of patients suffering from jaundice [44]. Excess bilirubin levels could also lead to acute health effects on human (e.g., brain hemorrhage) by crossing the blood–brain barrier. Asha and Senthilkumar developed a new protocol (Figure 12.14) based on neutral water-soluble conjugated polyfluorene PF–Ph–GlcA for the selective and sensitive detection of free bilirubin in human blood serum [45]. D-Glucuronic acid groups were attached onto the side chain of polymers that act as specific recognition site for bilirubin and also improve solubility of the polymer in aqueous media. On introducing bilirubin to the solution of polymer PF–Ph–GlcA, the emission peak of the polymer was quenched with the appearance of a new bilirubin emission peak due to efficient energy transfer (as evident by strong spectral overlap between the absorption spectrum of bilirubin and the emission spectrum of polymer) and favorable noncovalent interactions between the polymer and bilirubin. The change in the color of the solution from blue to light green was clearly visible under UV light (lamp excited at 325 nm). The sensitive detection of bilirubin at nanomolar regime was successfully achieved even at high alkaline

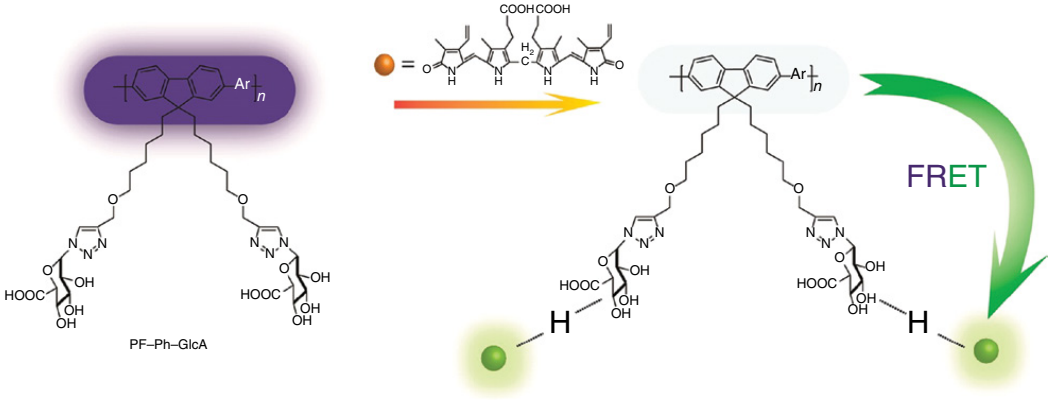

Figure 12.14 FRET-assisted selective detection of bilirubin in human blood serum using water-soluble conjugated polyfluorene PF–Ph–GlcA. (Reproduced with permission from Ref. [45]. Copyright 2015, American Chemical Society.)

conditions and in human serum samples without the interference of most common interfering agents, namely, proteins, hemoglobin, biliverdin, glucose, cholesterol and so on confirming the applicability of probe in real-time diagnosis of liver-related diseases.

12.3 Conjugated Polymers for Cancer Theranostics

12.3.1 Photodynamic Therapy (PDT)

Photodynamic therapy (PDT) involves two individually nontoxic components that are united to induce cellular and tissue effects in an oxygen-dependent manner (Figure 12.15). The first component of PDT is a photosensitive molecule known as a photosensitizer that restricts to a target cell and/or tissue. The second component involves the activation of the sensitizer by administration of light of specific wavelength to generate singlet oxygen ($^1O_2$) and other reactive oxygen species (ROS) from molecular oxygen. The detailed mechanism of $^1O_2$ generation via WSCPs is presented in Figure 12.16. On irradiation, WSCPs lead to the generation of singlet excited state (S1), which is then transformed into a long-lived triple excited state (T1) via intersystem crossing. The production of $^1O_2$ is sensitized by energy transfer from T1 to ground-state molecular oxygen ($^3O_2$).

It is known that PDT mediates tumor destruction via three main mechanisms [46, 47]. In the first case, the ROS generated by PDT can kill tumor cells directly. PDT also damages the tumor-associated vasculature, leading to tumor infarction. Finally, PDT can trigger an immune response against tumor cells. These three mechanisms can also impact each other and the combination of all these components is required for long-term tumor control. PDT has specific advantages over other conventional therapies, in terms of its minimally invasive nature, tolerance of repeated doses, and fast healing process [48]. However, the limited tumor selectivity and water solubility of most photosensitizers affect PDT efficiency and may induce the phototoxicity to neighboring normal tissues.

To further improve PDT's effectiveness, polymer-photosensitizer conjugates or photosensitizer-loaded nanoparticles, such as polyplex micelles, gold nanoparticles,

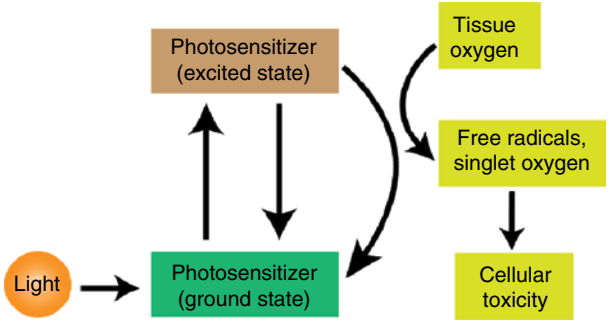

Figure 12.15 Basic mechanism of action of photodynamic therapy.

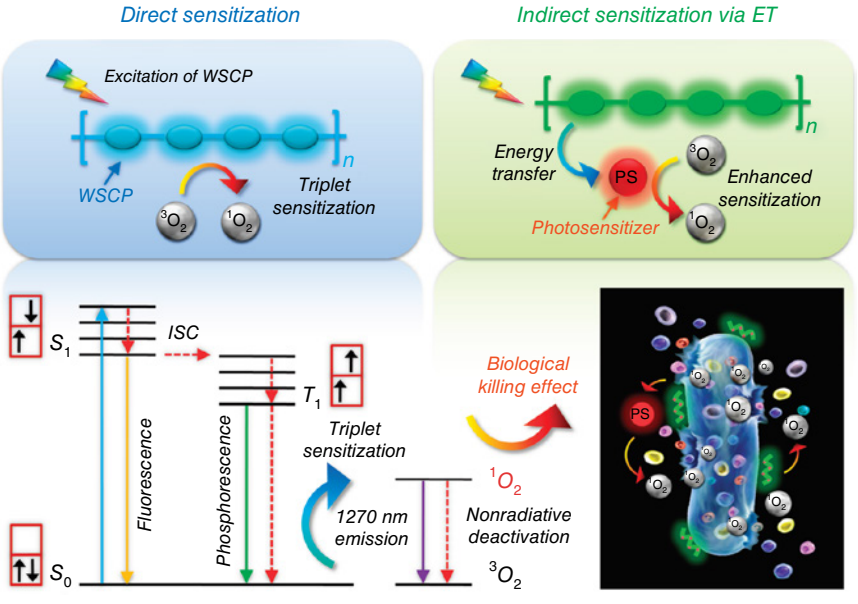

Figure 12.16 Mechanistic route of $^1O_2$ generation by WSCPs by different pathways. (Reproduced with permission from Ref. [2]. Copyright 2012, American Chemical Society.)

upconverting nanoparticles, carbon dots, and mesoporous silica nanoparticles are utilized to optimize the tumor accumulation of therapeutics [49–55]. However, cancer therapy depending upon a single therapeutic scheme usually remains suboptimal. Combination of photothermal therapy (PTT) and chemotherapy could offer higher therapeutic efficiency than monotherapies [56–58] and thus has the potential for inducing antitumor immunity [59].

Liu and coworkers developed a nanoplatform-centered method that offers targeted cell imaging and therapy, triggered drug release and PDT upon single NIR laser irradiation [56]. In this protocol, doxorubicin (DOX), a chemotherapeutic drug, was covalently linked to a PEGylated CPE photosensitizer via a UV-cleavable linker, the CPE–DOX thus obtained was used to encapsulate hydrophobic upconversion nanoparticles (UCNPs) in aqueous media (Figure 12.17). The upconverted UV light acted as a switch to activate the drug release for cancer chemotherapy upon shining NIR laser irradiation. In the meantime, the converted visible light could trigger the photosensitizer to produce ROS for photodynamic therapy. More importantly, to enhance the receptor-facilitated endocytosis, the CPE–DOX coated NP surface was modified with the targeting moiety. This synergistic effect of targeted delivery and light-regulated photodynamic and chemotherapy upon single NIR laser irradiation are extremely helpful for optimization of therapeutic efficacy in cancer treatment.

Gu and coworkers reported [57] an innovative strategy of CP-based nanocarrier proficient with light-triggered ROS generation and subsequent hypoxia-responsive anticancer drug release (Figure 12.18). The protocol (designated DOX/CP-NI NPs) consists of three elements: CP (CP-NI) which is capable of generating ROS and has been grafted with 2-nitroimidazole on the side chain as

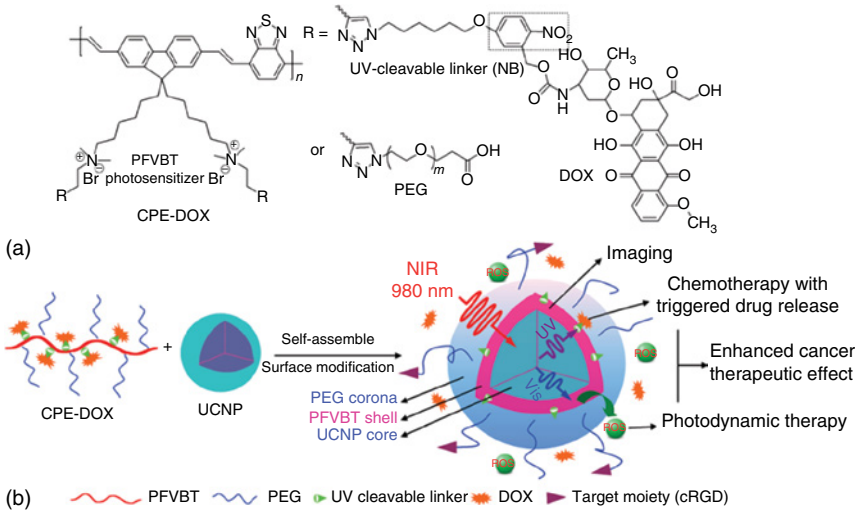

Figure 12.17 (a) Chemical structure of the PEGylated CPE covalently linked with anticancer drug doxorubicin (DOX) via a UV-cleavable linker CPE–DOX and (b) schematic illustration of the near-infrared (NIR) laser regulated initiation of the photosensitizer to generate ROS for photodynamic therapy and on-demand drug release for chemotherapy (Reproduced with permission from Ref. [56]. Copyright 2014, Royal Society of Chemistry.)

a hypoxia agent, polyvinyl alcohol (PVA)-based surface coatings, and encapsulated drug doxorubicin hydrochloride (DOX) (Figure 12.18a). CPs were designed to have a dithiophene–benzotriazole moiety that can be exploited as a visible/near-infrared (vis/NIR) light-activated ROS generation source, and the dithiophene–thienopyrazine moiety as an NIR imaging agent. In order to attain hypoxia-responsive transduction, CP was further grafted with 2-nitroimidazole (NI), a hydrophobic component. NI can be converted to hydrophilic 2-amino-imidazoles under a hypoxic environment via a single-electron reduction catalyzed by a series of nitroreductases coupled to bioreducing agents, such as NADPH, a plentiful coenzyme in tissues. The present strategy provided a new way for stimuli-responsive drug-delivery systems, which can go through a series of programed multiple triggers for achieving cumulative treatment efficiency.

12.3.2 Photothermal Therapy (PTT)

PTT is one of the phototherapy methods based on the principle of conversion of light energy into thermal energy via the irradiation of photothermal agents (PTAs) [58, 59]. PTAs used in PTT have strict requirements and high standards that include the absorbance of NIR light, high photothermal conversion efficiency, high photostability, good biocompatibility, and low cytotoxicity. PTAs can be mainly divided into two categories, namely, inorganic and organic PTAs.

Metal-based nanomaterials (gold nanomaterials), layered transition metal dichalcogenides (e.g., MoS_2, WS_2, and WSe_2), carbon nanomaterials (carbon nanotubes, graphene, and their derivatives), quantum dots, upconversion

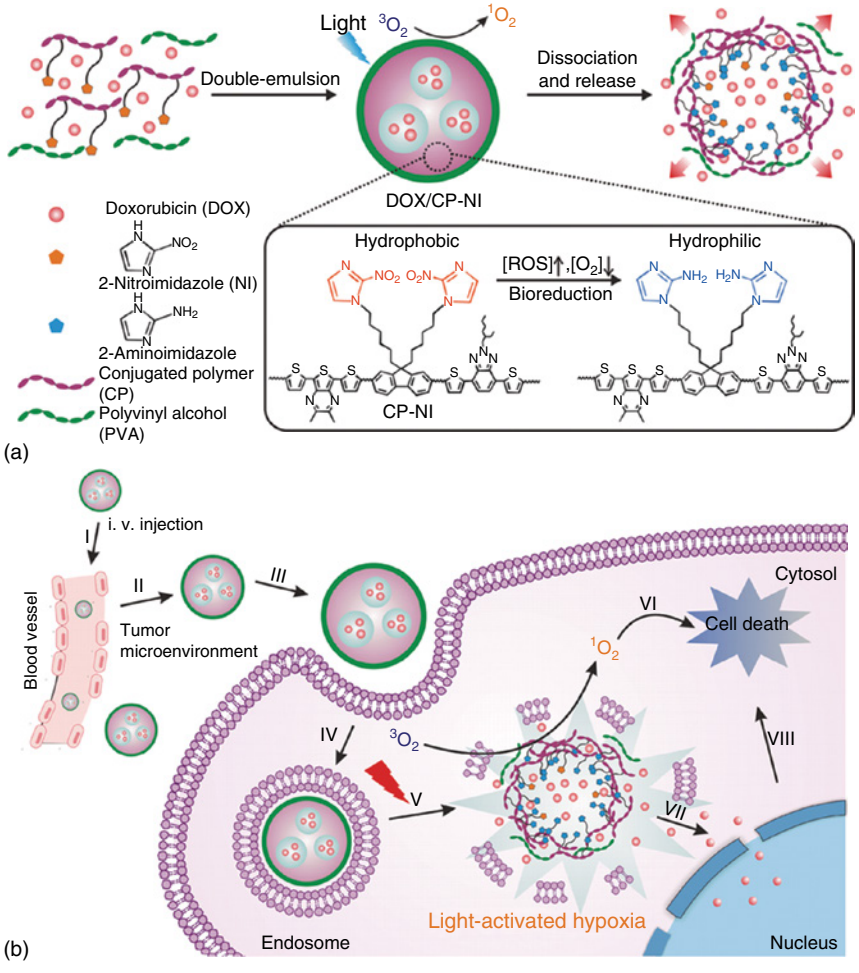

Figure 12.18 Schematic of the light-activated hypoxia-responsive drug-delivery system. (a) Formation and mechanism of DOX/CP-NI NPs. (b) Schematic of DOX/CP-NI NPs for ROS generation and inducing a local hypoxic environment capable of hypoxia-responsive release DOX into cell nuclei for enhanced synergistic anticancer efficacy (Reproduced with permission from Ref. [57]. Copyright 2016, John Wiley & Sons.)

nanocomposites and black phosphorus quantum dots are some of the outstanding representatives of inorganic PTAs. PTAs centered on polymers have evinced much more research interest for PTT [60, 61] because polymeric PTAs possess a desirable photothermal conversion efficiency, high photostability, exhibit good biodegradability, and low toxicity as compared to the inorganic PTAs.

Liu and coworkers reported the design and synthesis of a porphyrin-based CP (PorCP) with strong NIR absorbance near 800 nm and high photothermal conversion efficiency (PCE) for efficient PTT [62]. PorCP contains alternating porphyrin moiety, which acts as donor (D) connected to benzothiadiazole (BT) acting as acceptor (A) by means of an ethynylene bridge (Figure 12.19). Presence

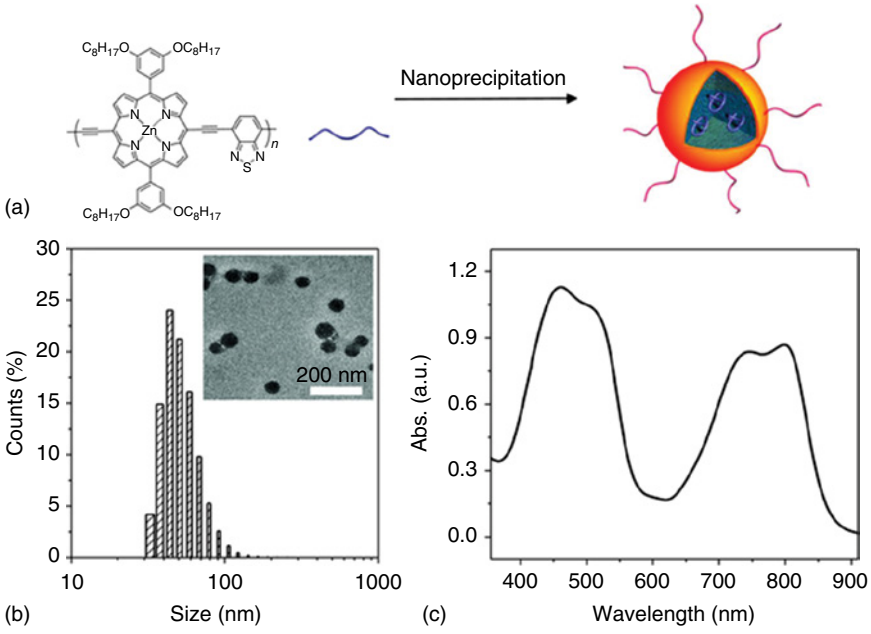

Figure 12.19 (a) Schematic illustration of PorCP NP formation; (b) DLS result of PorCP NPs in aqueous solution (the inset is the TEM image of PorCP NPs); and (c) UV–vis spectrum of PorCP NPs in aqueous medium. (Reproduced with permission from Ref. [62]. Copyright 2016, John Wiley & Sons.)

of such a D–A structure was capable of efficiently introducing intramolecular charge transfer (ICT) to redshift and improving the Q band absorption in the NIR range. Moreover, when porphyrin is introduced into the CP backbone, the increase in conjugation length can further lead to higher molar absorbance on average based on each porphyrin unit. Furthermore, encapsulation of PorCP was performed in polymeric shells to form PorCP NPs so as to increase the effective drug delivery into cancer cells, and the cell surface was altered with cell penetrating peptide (Tat) forming PorCP-Tat NPs to increase the cellular uptake. The encapsulation also induces π–π stacking of porphyrin moieties along the polymer chains, which resulted in aggregation-caused quenching and nonradiative decay of excitons. As a result, PorCP NPs exhibits a high PCE of 63.8%, neglectable fluorescence or ROS generation, and good photostability. To clearly visualize the cellular uptake process, a fluorescent CP poly (9,9-dihexylfluorene-*alt*-2,1,3-benzothiadiazole (PFBT) was coencapsulated with PorCP into NPs to form PorCP–PFBT–Tat NPs. Upon NIR irradiation, PorCP–Tat NPs tainted cancer cells showed fast and efficient ablation because of high photothermal efficacy of the PorCP NPs as revealed by cell viability and live/death staining assays. It was also demonstrated that PorCP–Tat NPs were effective in *in vivo* ablation of liver tumors using a zebrafish model.

The amalgamation of other therapies such as chemotherapy, photodynamic therapy, gene therapy, and radiotherapy models, with PTT might provide enhanced therapeutic performances in comparison with therapies with

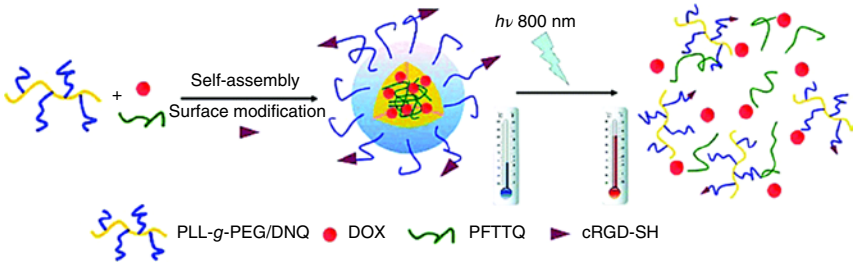

Figure 12.20 Schematic illustration of PLL-*g*-PEG/DNQ (PFTTQ/DOX NPs) formation and the combination of photothermal therapy and chemotherapy regulated by a two-photon laser (Reproduced with permission from Ref. [66]. Copyright 2015, Royal Society of Chemistry.)

PTT alone. Some examples of these multifunctional PTAs based on combined therapy strategies have recently attracted increasing research interest [63–65].

Liu and coworkers assimilated PFTTQ with DOX and cyclic arginine–glycine–aspartic acid (cRGD) tripeptide, and fabricated NPs for simultaneous chemotherapy and PTT (Figure 12.20) [66]. Poly-L-lysine-*g*-PEG, having 2-diazo-1,2-naphthoquinone (DNQ) moieties act as the encapsulation matrix, upon NIR two-photon laser irradiation can change from hydrophobic to hydrophilic, thus controlling the release of DOX. PTT of PFTTQ in association with the chemotherapy of DOX can be simultaneously activated by two-photon laser irradiation. Moreover, the cRGD tripeptide was introduced on the surface of the NPs, which helps in targeting cancer cells. In an MTT assay, the half-maximal inhibitory concentration (IC_{50}) of the NPs to MDA-MB-231 cells for combination therapy was 13.7 mg ml^{-1} in comparison with 147.8 mg ml^{-1} for sole chemotherapy and 36.2 mg ml^{-1} for PTT. Evidently, the synergistic cell inhibition of the NPs was a considerable advantage.

12.4 Studying Neurodegenerative Disorders

12.4.1 Diagnostics via Conjugated Polymers

Extracellular protein aggregates are considered one of the most important of pathological indications of various neurodegenerative diseases, such as prion [e.g., Bovine spongiform encephalopathies (BSE or mad cow disease), sheep scrapie (SC), Creutzfeldt Jacob disease (CJD), and Kuru], Parkinson's, Huntington's, and Alzheimer's disease (AD), amyotrophic lateral sclerosis (ALS), dementia with Lewy bodies (DLB), progressive supranuclear palsy (PSP), multiple system atrophy (MSA), corticobasal degeneration (CBD), frontotemporal dementia (FTD), spinocerebellar ataxia (SCA) disorders and spinal muscular atrophy, among others. Loss of neuronal populations in the brain and/or spinal cord as seen in these disorders leads to many different symptoms, including cognitive impairment, speech difficulties, and motor dysfunction. Two parallel worlds exist that believe that targeting or modulating either intracellular neurofibrillary tangles or extracellular amyloid plaques would provide success against

neurodegeneration [67]. CPs are well known for their optical stability, high quantum yields, and the alternating double and single bonds generally stabilizes a molecule thermodynamically; also, they give the molecule certain characteristics, such as the ability to absorb and emit light or transport electrical charges. Their optical properties and amplified signals are widely used for imaging purposes and to record biological processes. This chapter details the development of CP-based staining protocol and their advantages over the recently used amyloidotropic dyes. These fibrillar protein aggregates share a similar core structure independent of the amino acid sequence of the peptides building up the final fibrillar form but their cascade of folding is still far from understood. The plaques found in a diseased brain do not provide a direct correlation to disease progression. Therefore, numerous efforts have been made to dissolve, break, modulate, or prevent the production of aggregates. To distinguish preclinical disease for early diagnosis and modulation may bring a delay in disease progression so that we can make our plans and ideas work at least toward care giving. CPs are promising candidates as they can cross the blood–brain barrier and stain the heterogenic aggregates that give rise to a hue of colors as well as modulate the protein aggregates. In this section, we review the progress that has been made so far in this area using CPs and explain their selectivity toward protein aggregates resulting in a distinct backbone aggregation and a change in color when viewed by an optical spectrometer as well as by the naked eye. We also described the structural prototype that is mandatory either to stain or to modulate the toxic aggregates. But still CP-based therapies are confined to the laboratory, and approaches based on decreasing production, increasing clearance, decreasing aggregation, and removing aggregates of both Aβ and tau are under development for future clinical trials.

In 2005, Konradsson [68] and Inganäs [68, 69] with coworkers described how two different LCPs, one anionic, PTAA (1, Figure 12.1) [69], and regioregular, zwitterionic, conjugated oligoelectrolyte, tPOWT [68], could be used for the detection of fibrillated bovine insulin and chicken lysozyme *in vitro*. Although it is rare to observe iatrogenic (i.e., treatment-induced) protein aggregates due to administration of peptide pharmaceuticals, the therapeutic effect of the peptide drug becomes limited if the peptide has been converted into amyloid fibrils. These first studies [68, 69] showed that CPs could be utilized for distinguishing native and fibrillated proteins *in vitro*. Clearly, the CPs demonstrated a distinct spectral signature when bound to amyloid fibrils and by plotting the ratio of the intensity of the emitted light at a specific wavelength, the kinetics of amyloid fibrillation could be followed. The conjugated polyelectrolyte (CPE) binds to the native form of proteins and to the amyloid fibrillar form of proteins. These forms can easily be distinguished, due to the conformational changes of the CPE backbone upon binding to different forms of the proteins, as minor perturbations of the geometry of the CPE backbone are reflected as alterations of the electronic structure of the conjugated backbone. Thus, binding of the CPE to different forms of proteins gave rise to different optical features for the CPE.

Later, Hammarström and coworkers [70] developed a staining protocol based on the binding properties of CPs to amyloid fibril deposits present in different human tissues. A staining protocol was made by varying pH to elucidate selective

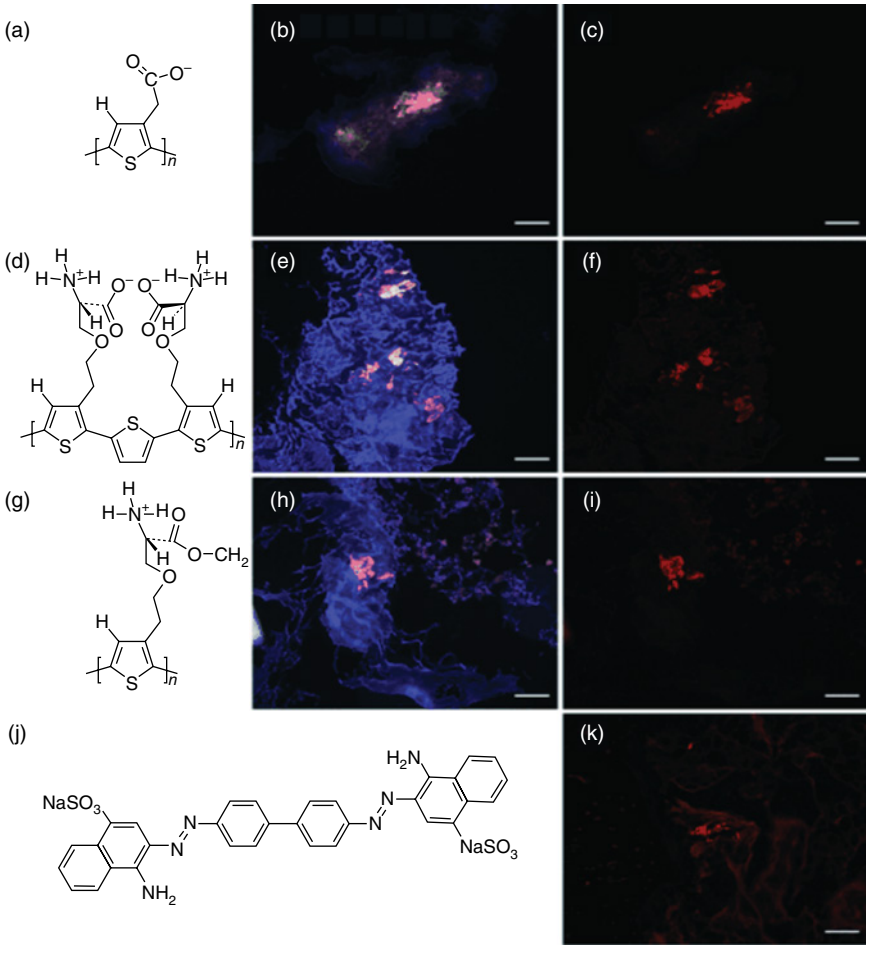

Figure 12.21 Chemical structures of different conjugated polyelectrolytes and fluorescence images of islet amyloid in human pancreas. (b) and (c) Tissue stained with PTAA (a; 2.5 μg ml^{-1}) in Na carbonate (100 mM, pH 10) for 2 h. (e) and (f) Tissue stained with PONT (d; 2.5 μg ml^{-1}) in glycine·HCl (100 mM, pH 2.5) for 2 h. (h) and (i) Tissue stained with POMT (g; 2.5 μg ml^{-1}) in Na carbonate (100 mM, pH 10) for 2 h. (k) Tissue stained by Congo red (j). Scale bars (white lines) represent 150 μm. (Reproduced with permission from Ref. [70]. Copyright 2006, American Chemical Society.)

staining conditions for PTAA (100 mm Na carbonate, pH 10), PONT (2, Figure 12.1) in an acidic buffer solution (pH 2.5) and POMT (3, Figure 12.1) in Na carbonate (pH 10). At alkaline pH, interactions between PTAA and other molecules, such as proteins and nucleic acids, in the tissue samples were unfavorable due to electrostatic repulsion, as most of the biomolecules and polythiophenes are negatively charged at pH 10. The characteristic orange-red fluorescence of PTAA pH 10; (Figure 12.21) appeared due to planar CPE chains bound to ordered amyloid fibrils [69].

Later, the same group [71] demonstrated how LCPs can be valuable to monitor the aggregate structure of *in vivo* formed amyloid deposits, which includes

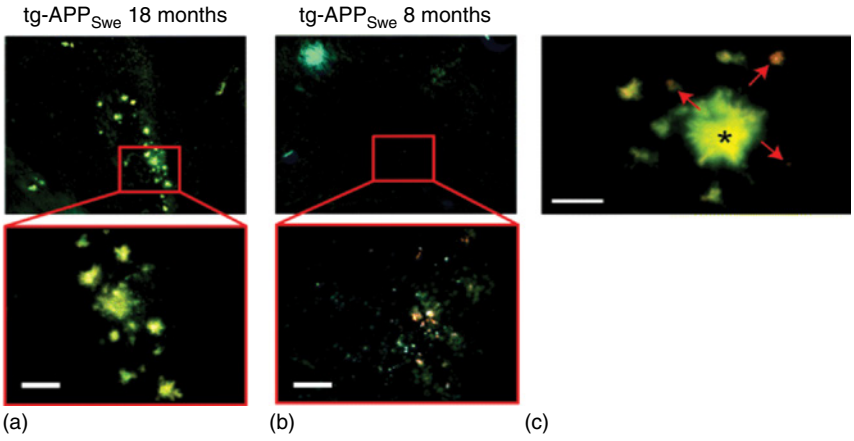

Figure 12.22 LCP staining of sectioned brains from tg-APP Swe mice at different ages. (a) Histological staining of hippocampus of an 18 mo tg-APP Swe mouse with tPTT (405 nm filter). (b) Histological staining of hippocampus of a 8 mo tg-APP Swe mouse with tPTT (405 nm filter) (c) Histological staining of a core plaque in the cerebral cortex of a 18 mo tg-APP Swe mouse by PTAA (470/546 nm filters). The scale bars indicate 50 μm. (Reproduced with permission from Ref. [71]. Copyright 2007, American Chemical Society.)

architecture, maturity, and origin. Using LCPs it was possible to distinguish amyloid-β 1–42 peptide (Aβ1-42) fibril conformations, by analyzing *in vitro* generated amyloid fibrils of Aβ1-42 formed under quiescent and agitated conditions (Figure 12.22). LCPs were then shown to resolve such conformational heterogeneity of amyloid deposits in frozen *ex vivo* brain sections from a transgenic mouse model (tg-APPswe) with Alzheimer's disease (AD).

Comparative LCP fluorescence showed that compact-core plaques of amyloid precursor protein (APP) transgenic mice were composed of rigid dense amyloid. A more abundant form of amyloid plaque displayed a morphology of a compact center with a protruding diffuse exterior. In contrast to sterically rigid amyloidotropic dyes such as thioflavin T (ThT) [72] and Congo red [73], LCPs have a flexible thiophene backbone, which provide a correlation between the conformation of the probe and the spectral characteristic of that particular conformation.

Sigurdson *et al.* [74] used LCPs that emitted conformation-dependent fluorescence spectra, for characterizing prion strains. LCP fluorescence yielded stronger signals than ThT and Congo red birefringence, resulting in higher sensitivity and detection of deposits that would have otherwise gone undetected with other amyloidotropic methods. LCP reactivity and emission spectra of brain sections discriminated among four immunohistochemically indistinguishable serially mouse-passaged prion strains derived from sheep scrapie, chronic wasting disease (CWD), bovine spongiform encephalopathy (BSE), and mouse-adapted Rocky Mountain Laboratory scrapie prions. Furthermore, using LCPs they differentiated field isolates of BSE and bovine amyloidotic spongiform encephalopathy, and identified noncongophilic deposits in prion-infected deer and sheep. Fibrils with distinct morphologies generated from chemically identical recombinant PrP yielded unique LCP spectra, suggesting that spectral

characteristic differences resulted from distinct supramolecular PrP structures. Thus, LCPs could detect structural differences among discrete protein aggregates and to link protein conformational features with disease phenotypes.

This discovery was an eye opener for the scientific community and these techniques are supposed to aid the fundamental understanding of strain conformational protein variants in a wide range of protein misfolding disorders. However, all of these happenings are not detrimental when inside the brain parenchyma. Crossing the blood–brain barrier remains a big challenge till now for these types of conjugate polymeric materials. To remedy this shortcoming, Aslund *et al.* developed [75] pentameric thiophene scaffold (p-FTAA, pHTAA, pFTAM) with molecular weights ranging from 530 to 650 Da, absorption and emission maxima in the ranges of 380–400 and 515–540 nm, which are used for real-time visualization of cerebral protein aggregates in transgenic mouse models of neurodegenerative diseases by multiphoton microscopy. One of the LCOs, p-FTAA (11, Figure 12.1), was utilized for *ex vivo* spectral assignment of distinct prion deposits from two mouse-adapted prion strains. p-FTAA (11, Figure 12.1) also revealed staining of transient soluble pre-fibrillar nonthioflavinophilic Aβ-assemblies during *in vitro* fibrillation of Aβ peptides. In brain tissue samples, Aβ deposits and neurofibrillary tangles (NFTs) were readily identified (Figure 12.23) by a

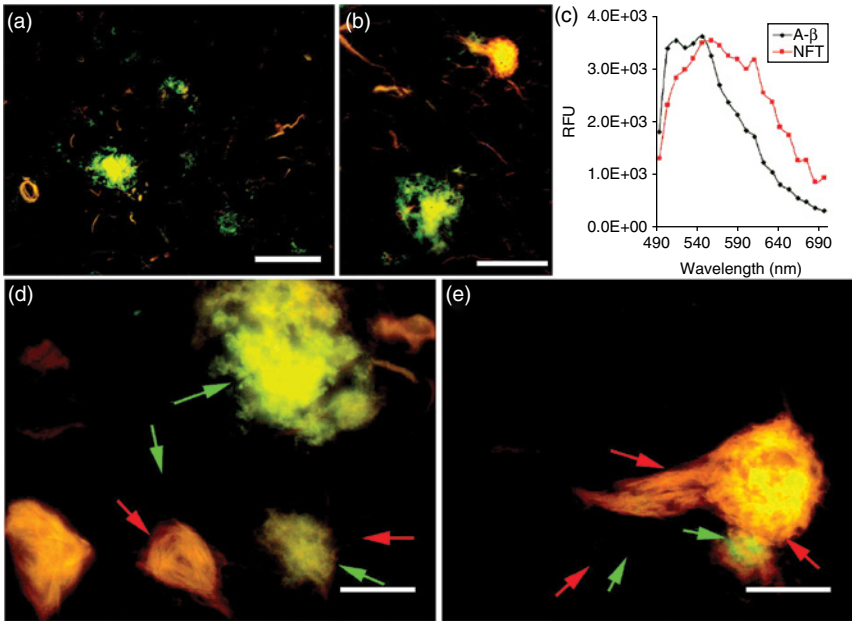

Figure 12.23 (a,b) High resolution fluorescence images showing an overview of the interplay between Aβ deposits (green), NFTs, and dystrophic neurites (yellow red). (c) Emission spectra of p-FTAA bond to Aβ aggregates (green spectrum) or NFTs (red spectrum). (d,e) High resolution fluorescence images showing the details of the interplay between Aβ deposits (green), NFTs, and dystrophic neurites (yellow red). Selected Aβ deposits and NFTs are highlighted (green and red arrows, respectively) to indicate striking spacial co-localization. Scale bar = 50 μm (image a), 20 μm (image b), and 10 μm (images d and e). (Reproduced with permission from Ref. [75]. Copyright 2009, American Chemical Society.)

strong fluorescence from p-FTAA and the LCO staining that showed complete colocalization with conventional antibodies (6E10 and AT8). In addition, a patchy islet-like staining of individual Aβ plaque was unveiled by the anti-oligomer A11 antibody during costaining with p-FTAA.

Previous findings have offered practical research tools for studying protein aggregation diseases, which have facilitated the study of amyloid origin and pathogenesis *in vitro* and in animal models. Amyloidoses are diseases of disparate etiologies characterized by extracellular amyloids. A much more precise readout from LCP fluorescence from three anionic polythiophenes (earlier PTAA, trimeric tPTAA, pentameric p-FTAA) were obtained by Nilsson *et al.* compared to common polarized absorbance of Congo red toward human systemic amyloidoses [76]. Blinded cluster assignments of spectral profiles of tissue samples from 108 tissue samples derived from 96 patients identified three nonoverlapping classes, which were found to match AA (derived from serum amyloid A (AA) protein associated with chronic immune activation, as in chronic infections, autoimmune or hereditary inflammatory diseases, or cancer), AL (that consists of Ig light chains, or fragments thereof, and is associated with various B cell lymphoproliferative disorders including multiple myeloma), and ATTR (that consists of transthyretin deposits and occurs sporadically or in association with transthyretin mutations that enhance protein misfolding and fibril formation) immunotyping. Amyloid deposits stained with PTAA or tPTAA emitted yellow-red fluorescence, whereas p-FTAA emitted extremely intense green-yellow fluorescence. While full visible-light emission spectra (450–700 nm) on excitation through a 405/30 long-pass filter (LP 450) from LCP-stained amyloid deposits with a Spectramax camera at intervals of 8–10 nm, had its absolute emission maximum located at a wavelength of λ550 nm for p-FTAA, the emission maxima for PTAA and tPTAA were located at longer wavelengths (560–600 nm). Owing to its very high quantum yield, p-FTAA proved to be the most sensitive dye and unlike Congo red, collagen did not score positive with any of the LCP stains. The emission profiles of PTAA appear to reliably distinguish between amyloids of distinct biochemical subtypes but less dramatic spectral changes were observed for tPTAA, whereas the p-FTAA spectrum did not appreciably change on binding to the various amyloids. Nonplanar, disperse PTAA chains emit light λ530–540 nm, whereas planar transition of the backbones shifts their emission maximum toward longer wavelengths. This transition is often accompanied by stacking of the LCP chains, leading to intermolecular fluorescence resonance energy transfer and to a relative increase in emission intensity at λ640–650 nm. Thioflavins and Congo red are chemically nondiscriminatory and therefore unsuitable for molecular subtyping. The main pitfall of Congo red staining is that it is not very sensitive and that it requires experience to reliably differentiate amyloids from a plethora of physiologically birefringent tissue constituents. The fluorescent dyes, thioflavin T, and S, are more sensitive than Congo red, but their emission maxima in the blue range can overlap with the autofluorescence of tissue components [77, 78]. What sets LCPs apart from Congo red and thioflavins, however, is their capacity to undergo characteristic spectral emission shifts when associated with amyloids. This property allows for separating amyloid-associated signals from autofluorescent tissue constituents,

thus preventing the detection of false positives. The spectral signatures of LCPs (distinct PTAA spectroscopic signatures when bound to different amyloid subtypes) can be used as surrogates for the molecular structure of the respective protein aggregates. PTAA spectra stands tall in presence of amyloid fibrils of different morphologies generated in recombinant, chemically defined systems lacking all ancillary constituents such as serum amyloid P component, heparan sulfate proteoglycan, and complement constituents. Since antibodies identify specific chemical entities while LCP spectroscopy yields information on the conformational state of protein aggregates, an optimal typing may be reached by combining both. In rare instances, if more than one subtype of amyloid coexists in the same individual, the LCP spectral assignment is particularly useful in such instances. The spectral signature of PTAA, and therefore the molecular subtyping, is more easily affected by excessive fixation than its overall fluorescence – perhaps because cross-linking fixatives distort the structure of protein aggregates, or renders them impermeable to LCPs. Therefore, mildly fixed cryosections of tissue samples would give better spectroscopic interpretations for the differentiation of amyloid subtypes.

Recently, a series of fluorescent, soluble oligo (*p*-phenylene ethynylene)s (OPEs) were developed by Donabedian *et al.* [79] to detect amyloids *in vitro* by binding-activated superluminescence, with low micromolar affinity and high selectivity for the amyloid conformer. The OPEs (6, Figure 12.1) track the kinetics of amyloid fibril formation from native hen egg white lysozyme (HEWL) similarly to ThT, and the dependence of binding affinity on OPE length supports the theory of a linear binding groove. OPEs exhibit drastic fluorescence enhancement and useful absorbance red shift when introduced to the HEWL amyloid conformer. The fluorescence properties and optical activity of the bound OPEs are highly dependent on OPE chain length and charge. The longer cationic OPEs are the most promising ligands for imaging purposes. OPE2+ and OPE3+ (Figure 12.1), in particular, have sufficiently low binding constants and optical band gap to be used for *ex vivo* staining. On a molecular level, several effects are probably at work, including restriction of internal rotation, planarization, reduction of quenching by water, and J-type aggregation. For all four OPEs, reduction of quenching by water when bound to hydrophobic sites on HEWL is responsible for some of the drastic fluorescence enhancement.

12.4.2 Therapeutic Strategies to Prevent Neurodegenerative Disorders

In previous studies, conjugated poly- and oligoelectrolytes were generally used as optical probes to monitor amyloid fibril formation *in vitro* and the interaction was observed to result in conformation changes in polymer backbone that affected their optical responses correlating the state of amyloid. For the first time, Herland, Inganäs, and coworkers [80] showed that molecular combing of the PTAA/insulin fibril can be achieved on hydrophobic surfaces formed by PDMS printing in a way so that individual fibrils can be coated with PTAA by forming a complex between PTAA and amyloid-like fibrils of bovine insulin. Furthermore, the aligned fibrils can be positioned on surfaces through transfer

printing (TP). The PTAA-coated fibrils have been studied with single-molecule spectroscopy (SMS) to analyze the fluorescence from single objects. The alignment of the fibrils on surfaces makes measurements of the anisotropy of the emitted light from the fibrillar complexes possible. PTAA is highly oriented on the fibrils and it can also be determined that the polymer chains are aligned along the fibril axis. The change in surface energy due to the PDMS compared to hydrophilic substrates gives an interaction with the PTAA/insulin fibril complex of the right order of magnitude to make molecular combing possible. The organization of PTAA on the fibrils is with the polymer chain along the fibrillar axis leading to a clear correlation between the intensity of the emitted light from the fibrillar complexes and the maximum peak value unlike other fibrillar networks.

In earlier sections we have seen that LCPs having thiophene backbones are highly specific to amyloid conformations and may represent potential antiprion compounds. Margalith *et al*. showed that these LCPs can be used to reduce the infectivity of prion-containing brain homogenates and of prion-infected cerebellar organotypic cultured slices (COCS) by stabilizing the conformation of PrPC or of a transition intermediate [81]. A broad range of LCPs including cationic POMT, PTMI, anionic PTAA, pHTAA, pFTAA zwitterionic POWT, and PBAT were used (1% brain homogenate obtained from mice infected with RML6 prions (Rocky Mountain Laboratory strain) with each LCP (1–900 $\mu g\,ml^{-1}$)), which was found to increase the proteinase K (PK) resistance of PrPSc in a concentration-dependent manner augmenting the formation of oligomeric SDS-stable PrPSc aggregates. At low concentrations, the LCPs appear to render PrPSc more stable to PK digestion, and at submicellar concentrations may prevent prion replication by hyperstabilization of the PrPSc conformation, resulting in reduced fiber frangibility. ELISA measurements on COCS showed reduced levels of PrPC, indicating that PTAA might deplete PrPC from the cell surface or modulate PrPC levels in prion trafficking and thus prevent efficient transition of PrPC into PrPSc by either stabilizing the spatial conformation of PrPC or by protecting the binding site for the template PrPSc molecule.

In the case of amyloids, targeting the robust amyloid fibril and crossing the blood–brain barrier is key to combat these diseases. Hence, biomolecules were the initial choice for the scientific community. CPs are best known to screen metal ions due to their amplified optical responses compared to small molecules and selectivity can also be achieved by tailoring their side chains. Aβ is also found to have a high affinity for neurotoxic metals such as iron and copper; the accumulation and localization of these metals in the brain is indirectly related to the generation of neurotoxic hydrogen peroxide, oxidative stress, and free-radical formation and thus contribute to disease progression. The altered metabolism of heme and nonheme iron proteins and their accumulation in brain has a significant role in the pathogenesis of AD. Iyer and coworkers designed CPs [82, 83] selective to neurotoxic metal ions and examined clearance of metal-mediated amyloid deposits. Both P1 (13, Figure 12.1, polyfluorene based) and PHQ (12, Figure 12.1, polyparaphenylene based) were found to bind with iron-containing heme and nonheme proteins at the nanomolar level. P1 and PHQ showed anti-AD activity and were shown to inhibit Aβ fibrillation, which was confirmed by *in*

vitro control studies by doping CSF of healthy individuals (HCSF) with Aβ (1–40) with and without iron using a ThT-binding assay test and electron microscopy analysis. Both these polymers helped to regulate redox-active metals present in the brain thereby helping indirectly in controlling the neurotoxicity and preventing damage to the brain. PHQ and P1 can trap iron including ferritin and thus diminish amyloid aggregates in Aβ1-40 and CSF samples, significantly reducing the formation of neurotoxic chemicals and radicals in the brain and disrupting the toxic polypeptides and preventing them from aggregating again.

Similar polyfluorene derivatives were further explored by another research group (one cationic, 15, Figure 12.1, PF and one anionic, 16, Figure 12.1, PFS), and showed an increase in the fibrillization kinetics of α-synuclein (AS) due to complexation of these charged polymers with the various AS-aggregated species including amyloid fibrils and oligomers [84]. Irrespective of their charges on the side chains, they were shown to accelerate the fibrillization but ultimately were found to be very distinct than their pristine fibrillar form. Both polymers were bound to fibrils more efficiently than the oligomers and to the lowest extent to monomers. Hydrophobicity of the polymer backbone seems to be the key to interact with such robust fibrils but they were unable to alter the major secondary structure of oligomers and fibrils. An optical response with higher emission intensity was achieved upon incorporation of polymers into higher order fibrils. This opens up a new possibility that these structures can be modified to modulate the toxic amyloid more selectivity.

Iyer and coworkers [85] also developed a polyfluorene derivative with hydroxyquinoline substituted on its side chain, PF-HQ (14, Figure 12.1) which itself formed amyloid-like fibrillar and protofibrillar self-aggregates (Figure 12.24a) thus providing a similar surface motif to interact with Aβ1–40 via hydrophobic interaction and finally inhibit protein aggregation. Formation of polymer–protein coaggregates guided the blocking of central hydrophobic protein core which is responsible for fibril formation. At low concentration, PF-HQ redirects the aggregation process to a disordered coaggregate that finally transforms into well-ordered nanocoaggregates with time (Figure 12.24b). Low intrinsic toxicity of PF-HQ even at higher concentration, negatively charged surface, amyloid-like surface motif, and abundant binding sites make this CP template a unique platform with excellent inhibitory modulation ability of Aβ1–40 aggregation and may likely find application as a potential therapeutic material for amyloid-related diseases. This CP shows a dual effect of inhibiting Aβ1–40 self-aggregation as well as β-sheet breaking by first providing sufficient amyloid-like surface so that the protein gets adsorbed and then the appended hydroxyquinolines binding sites available in abundance along with the hydrophobic polymeric core trap the toxic intermediates, leading to the formation of nontoxic coaggregates. The disadvantage associated with PF-HQ was that they precipitate out at higher concentration and blood–brain barrier permeability remains a challenge. Most likely, a short polymer or an oligomeric unit having a core of $n = 3–5$ may overcome the above limitations and have additional therapeutic value.

CPs with a backbone of thiophene, fluorene, and benzene are chosen by the community to explore their action against neurodegenerative diseases. When it

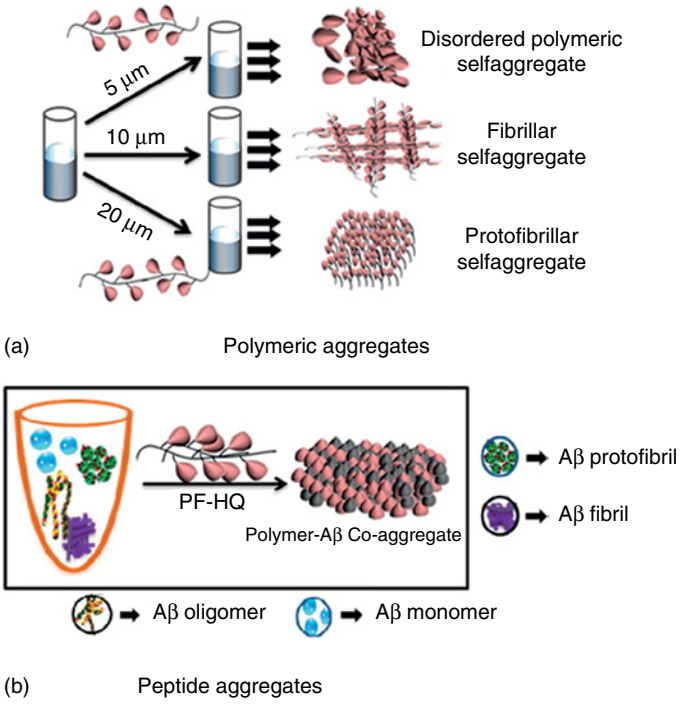

Figure 12.24 (a) PF-HQ self-aggregates in aqueous medium (b) modulation of amyloid aggregates in the presence of PF-HQ and formation of polymer–protein coaggregates. (Reproduced with permission from Ref. [85]. Copyright 2016, American Chemical Society.)

comes to addressing the urgent stimulating need of diagnosis and imaging, LCPs have proved to be much better than the already existing amyloidotropic dyes. An understanding of the modes of interaction between LCPs and the amyloid-like fibril is of great importance for further development of the LCPs that can interact and modulate with amyloid selectively leaving other fibrillar proteins intact. Crossing the blood–brain barrier and related human health problems and safety still remain issues to be addressed. Polythiophenes with anchored anionic and amino acid functionalized side groups are proved to be useful for staining purposes as change in pH results in a change in overall charge on the appended side groups of the polymeric backbone, which indirectly controls their aggregation and is reflected in their optical spectrum. In the presence of distinct amyloid, their subtype and even collagen, they interact electrostatically leading to different aggregation of thiophene backbone and hence a hue in optical response is achieved. To alter these robust structures, hydrophobic interactions seem to be key as aromatic amino acid residues align themselves parallel to the fibril axis and form a ladder motif. Aggregation of polyfluorenes can be controlled when they are substituted with hydrophobic side groups, and so often they end up forming nano-objects in water. They show a tremendous optical stability over pH, which indirectly confirms the formation of stable polymeric aggregates. These aggregates can be controlled to give a particular shape

and size to target-specific amyloid subtype designed to be a therapeutic agent. But whether they can cross the blood–brain barrier efficiently remains to be seen. As these polymeric nanoparticles are too hydrophobic to handle, they start precipitating out at higher concentration. Recently, these issues are being taken care of by making composites with FDA approved polymers or biomolecules that can be used to provide these hydrophobic polymeric nanoparticles a hydrophilic surface and help them to cross the blood–brain barrier. CPs may not be the best choice as a potential drug, but they are of high theranostic value as they can stain as well as modulate the early aggregates. The oligomers and intermediate prefibrillar amyloid aggregates are considered as more neurotoxic than their final form as found in the diseased brain. The fate of these aggregates still remains unclear and brain plasticity may play a bigger positive role to adapt them with time. Disease progression can be controlled by this development and perhaps most importantly the conjugate polymeric template offers a novel and powerful route to modify its surface properties to define the intermolecular forces that hinder protein aggregation and, thus, open a new window to fight against this devastating disease.

References

1 Jenkins, A.D., Kratochvil, P., Stepto, R.F.T., and Suter, U.W. (1996) *Pure Appl. Chem.*, **68**, 2287–2311.
2 Zhu, C., Liu, L., Yang, Q., Lv, F., and Wang, S. (2012) *Chem. Rev.*, **112**, 4687–4735.
3 Elsabahy, M., Heo, G.S., Lim, S.–.M., Sun, G., and Wooley, K.L. (2015) *Chem. Rev.*, **115**, 10967–11011.
4 Wang, Y., Schanze, K.S., Chi, E.Y., and Whitten, D.G. (2013) *Langmuir*, **29**, 10635–10647.
5 Lia, K. and Liu, B. (2014) *Chem. Soc. Rev.*, **43**, 6570–6597.
6 Vogt, R.L. and Dippold, L. (2005) *Public Health Rep.*, **120**, 174–178.
7 Baek, M.G., Stevens, R.C., and Charych, D.H. (2000) *Bioconjugate Chem.*, **11**, 777–788.
8 Disney, M.D., Zheng, J., Swager, T.M., and Seeberger, P.H. (2004) *J. Am. Chem. Soc.*, **126**, 13343–13346.
9 Phillips, R.L., Kim, I.B., Carson, B.E., Tidbeck, B., Bai, Y., Lowary, T.L., Tollbert, L.M., and Bunz, U.H.F. (2008) *Macromolecules*, **41**, 7316–7320.
10 Xue, C.H., Velayudham, S., Johnson, S., Saha, R., Smith, A., Brewer, W., Murthy, P., Bagley, S.T., and Liu, H.Y. (2009) *Chem. Eur. J.*, **15**, 2289–2295.
11 Wang, L.H., Pu, K.Y., Li, J., Qi, X.Y., Li, H., Zhang, H., Fan, C.H., and Liu, B. (2011) *Adv. Mater.*, **23**, 4386–4391.
12 Zhu, C.L., Yang, Q., Liu, L.B., and Wang, S. (2011) *J. Mater. Chem.*, **21**, 7905–7912.
13 Yuan, H., Liu, Z., Liu, L., Lv, F., Wang, Y., and Wang, S. (2014) *Adv. Mater.*, **26**, 4333–4338.
14 Hanahan, D. and Weinberg, R.A. (2011) *Cell*, **144**, 646–674.

15 Laird, P.W. (2003) *Nat. Rev. Cancer*, **3**, 253–266.
16 Feng, F., Wang, H., Han, L., and Wang, S. (2008) *J. Am. Chem. Soc.*, **130**, 11338–11343.
17 Yang, Q., Dong, Y., Wu, W., Zhu, C., Chong, H., Lu, J., Yu, D., Liu, L., Lv, F., and Wang, S. (2012) *Nat. Commun.*, **3**, 1206–1214.
18 Zhang, J., Xing, B., Song, J., Zhang, F., Nie, C., Jiao, L., Liu, L., Lv, F., and Wang, S. (2014) *Anal. Chem.*, **86**, 346–350.
19 Yuan, Z., Zhou, Y., Gao, S., Cheng, Y., and Li, Z. (2014) *ACS Appl. Mater. Interfaces*, **6**, 6181–6185.
20 Bushati, N. and Cohen, S.M. (2007) *Annu. Rev. Cell Dev. Biol.*, **23**, 175–205.
21 Pritchard, C.C., Cheng, H.H., and Tewari, M. (2012) *Nat. Rev. Genet.*, **13**, 358–369.
22 Lujambio, A. and Lowe, S.W. (2012) *Nature*, **482**, 347–355.
23 Fabian, M.R., Sonenberg, N., and Filipowicz, W. (2010) *Annu. Rev. Biochem.*, **79**, 351–379.
24 Calin, G.A. and Croce, C.M. (2006) *Nat. Rev. Cancer*, **6**, 857–866.
25 Mitsis, P.G. and Kwagh, J.G. (1999) *Nucleic Acids Res.*, **27**, 3057–3063.
26 Perkins, T.T., Dalal, R.V., and Mitsis, P.G. (2003) *Science*, **301**, 1914–1918.
27 Zhou, Y., Zhang, J., Zhao, L., Li, Y., Chen, H., Li, S., and Cheng, Y. (2016) *ACS Appl. Mater. Interfaces*, **8**, 1520–1526.
28 Shcheglov, M., Zhulidov, A.S., Bogdanova, P.A., Staroverov, E.A., Rasskazov, D.B., and Lukyanov, V.A. (2002) *Genome Res.*, **12**, 1935–1942.
29 Nilsen, I.W., Øverbø, K., Havdalen, L.J., Elde, M., Gjellesvik, D.R., and Lanes, O. (2010) *PLoS One*, **5**, 10295.
30 Whatcott, C.J., Han, H., Posner, R.G., Hostetter, G., and Von Hoff, D.D. (2011) *Cancer Discovery*, **1**, 291–296.
31 Tan, J.-X., Wang, X.Y., Li, H.Y., Su, X.L., Wang, L., Ran, L., Zheng, K., and Ren, G.S. (2011) *Int. J. Cancer*, **128**, 1303–1315.
32 Lokeshwar, V.B., Rubinowicz, D., Schroeder, G.L., Forgacs, E., Minna, J.D., Block, N.L., Nadji, M., and Lokeshwar, B.L. (2001) *J. Biol. Chem.*, **276**, 11922–11932.
33 Benitez, A., Yates, T.J., Lopez, L.E., Cerwinka, W.H., Bakkar, A., and Lokeshwar, V.B. (2011) *Cancer Res.*, **71**, 4085–4095.
34 Liu, D.C., Pearlman, E., Diaconu, E., Guo, K., Mori, H., Haqqi, T., Markowitz, S., Willson, J., and Sy, M.S. (1996) *Proc. Natl. Acad. Sci. USA*, **93**, 7832–7837.
35 Huang, Y., Song, C., Li, H., Zhang, R., Jiang, R., Liu, X., Zhang, G., Fan, Q., Wang, L., and Huang, W. (2015) *ACS Appl. Mater. Interfaces*, **7**, 21529–21537.
36 Malik, A.H., Hussain, S., and Iyer, P.K. (2016) *Anal. Chem.*, **88**, 7358–7364.
37 Russell, D.H. and Durie, B.G.M. (1978) *Polyamines as Biochemical Markers of Normal and Malignant Growth*, Raven Press, New York.
38 Seiler, N., Delcros, J.G., and Moulinoux, J.P. (1996) *Int. J. Biochem. Cell Biol.*, **28**, 843–861.
39 Tanima, D., Imamura, Y., Kawabata, T., and Tsubaki, K. (2009) *Org. Biomol. Chem.*, **7**, 4689–4694.
40 Bull, H., Murray, P.G., Thomas, D., Fraser, A.M., and Nelson, P.N. (2002) *Mol. Pathol.*, **55**, 65–72.

41 Makarov, D.V., Loeb, S., Getzenberg, R.H., and Partin, A.W. (2009) *Annu. Rev. Med.*, **60**, 139–151.
42 Dwivedi, A.K. and Iyer, P.K. (2013) *Anal. Methods*, **5**, 2374–2378.
43 Boyer, T.D., Manns, P.P., and Sanyal, A.J. (eds) (2011) Hepatology: A Textbook of Liver Disease, Saunders, London.
44 Silbernagl, S. and Despopoulos, A. (eds) (2009) *Color Atlas of Physiology*, Thieme, Stuttgart.
45 Senthilkumar, T. and Asha, S.K. (2015) *Macromolecules*, **48**, 3449–3461.
46 Dougherty, T. *et al.* (1998) *JNCI Cancer Spectr.*, **90** (889), 905.
47 Hasan, T., Ortel, B., Moor, A., and Pogue, B. (2003) Photodynamic therapy of cancer, in *Holland–Frei Cancer Medicine* (eds D. Kufe *et al.*), BC Decker, Inc., Hamilton, ON.
48 Lovell, J.F., Liu, T.W., Chen, J., and Zheng, G. (2010) *Chem. Rev.*, **110**, 2839–2857.
49 Cheng, L., Wang, C., Feng, L., Yang, K., and Liu, Z. (2014) *Chem. Rev.*, **114**, 10869–10939.
50 Nomoto, T., Fukushima, S., Kumagai, M., Machitani, K., Arnida, Matsumoto, Y., Oba, M., Miyata, K., Osada, K., Nishiyama, N., and Kataoka, K. (2014) *Nat. Commun.*, **5**, 3545(1–10).
51 Cheng, Y., Meyers, J.D., Broome, A.-M., Kenney, M.E., Basilion, J.P., and Burda, C. (2011) *J. Am. Chem. Soc.*, **133**, 2583–2591.
52 Wang, C., Cheng, L., Liu, Y., Wang, X., Ma, X., Deng, Z., Li, Y., and Liu, Z. (2013) *Adv. Funct. Mater.*, **23**, 3077–3086.
53 Wang, Y., Wang, K., Zhao, J., Liu, X., Bu, J., Yan, X., and Huang, R. (2013) *J. Am. Chem. Soc.*, **135**, 4799–4804.
54 Dong, K., Liu, Z., Li, Z., Ren, J., and Qu, X. (2013) *Adv. Mater.*, **25**, 4452–4458.
55 Castano, A.P., Mroz, P., Wu, M.X., and Hamblin, M.R. (2008) *Proc. Natl. Acad. Sci. USA*, **105**, 5495–5500.
56 Yuan, Y., Min, Y., Hu, Q., Xing, B., and Liu, B. (2014) *Nanoscale*, **6**, 11259–11272.
57 Qian, C., Yu, J., Chen, Y., Hu, Q., Xiao, X., Sun, W., Wang, C., Feng, P., Shen, Q.D., and Gu, Z. (2016) *Adv. Mater.*, **28**, 3313–3320.
58 Yang, K., Hu, L., Ma, X., Ye, S., Cheng, L., Shi, X., Li, C., Li, Y., and Liu, Z. (2012) *Adv. Mater.*, **24**, 1868–1872.
59 Huang, X., El-Sayed, I.H., Qian, W., and El-Sayed, M.A. (2006) *J. Am. Chem. Soc.*, **128**, 2115–2120.
60 Chen, Q., Liang, C., Wang, X., He, J., Li, Y., and Liu, Z. (2014) *Biomaterials*, **35**, 9355–9362.
61 Song, X., Zhang, R., Liang, C., Chen, Q., Gong, H., and Liu, Z. (2014) *Biomaterials*, **57**, 84–92.
62 Guo, B., Feng, G., Manghnani, P.N., Cai, X., Liu, J., Wu, W., Xu, S., Cheng, X., Teh, C., and Liu, B. (2016) *Small*, **12**, 6243–6254.
63 Feng, L., Yang, X., Shi, X., Tan, X., Peng, R., Wang, J., and Liu, Z. (2013) *Small*, **9**, 1989–1997.
64 Yi, X., Yang, K., Liang, C., Zhong, X., Ning, P., Song, G., Wang, D., Ge, C., Chen, C., Chai, Z., and Liu, Z. (2015) *Adv. Funct. Mater.*, **25**, 4689–4699.
65 Zhou, M., Chen, Y., Adachi, M., Wen, X., Erwin, B., Mawlawi, O., Lai, S.Y., and Li, C. (2015) *Biomaterials*, **57**, 41–49.

66 Yuan, Y., Wang, Z., Cai, P., Liu, J., Liao, L.-D., Hong, M., Chen, X., Thakor, N., and Liu, B. (2015) *Nanoscale*, **7**, 3067–3076.

67 Braak, H. and Braak, E. (1998) *J. Neural. Transm. Suppl.*, **53**, 127–140.

68 Herland, A., Nilsson, K.P.R., Olsson, J.D.M., Hammarström, P., Konradsson, P., and Inganäs, O. (2005) *J. Am. Chem. Soc.*, **127**, 2317–2323.

69 Nilsson, K.P.R., Herland, A., Hammarström, P., and Inganäs, O. (2005) *Biochemistry*, **44**, 3718–3724.

70 Nilsson, K.P.R., Hammarström, P., Ahlgren, F., Herland, A., Schnell, E.A., Lindgren, M., Westermark, G.T., and Inganäs, O. (2006) *ChemBioChem*, **7**, 1096–1104.

71 Nilsson, K.P.R., Åslund, A., Berg, I., Nyström, S., Konradsson, P., Herland, A., Inganäs, O., Stabo-Eeg, F., Lindgren, M., Westermark, G.T., Lannfelt, L., Nilsson, L.N.G., and Hammarström, P. (2007) *ACS Chem. Biol.*, **2**, 553–560.

72 Naiki, H., Higuchi, K., Hosokawa, M., and Takeda, T. (1989) *Anal. Biochem.*, **177**, 244–249.

73 Klunk, W.E., Pettegrew, J.W., and Abraham, D.J. (1989) *J. Histochem. Cytochem.*, **37**, 1273–1281.

74 Sigurdson, C.J., Nilsson, K.P.R., Hornemann, S., Manco, G., Polymenidou, M., Schwarz, P., Leclerc, M., Hammarström, P., Wüthrich, K., and Aguzzi, A. (2007) *Nat. Methods*, **4**, 1023–1030.

75 Aslund, A., Sigurdson, C.J., Klingstedt, T., Grathwohl, S., Bolmont, T., Dickstein, D.L., Glimsdal, E., Prokop, S., Lindgren, M., Konradsson, P., Holtzman, D.M., Hof, P.R., Heppner, F.L., Gandy, S., Jucker, M., Aguzzi, A., Hammarstrom, P., and Nilsson, K.P. (2009) *ACS Chem. Biol.*, **4**, 673–684.

76 Nilsson, K.P.R., Ikenberg, K., Åslund, A., Fransson, S., Konradsson, P., Röcken, C., Moch, H., and Aguzzi, A. (2010) *Am. J. Pathol.*, **176**, 563–574.

77 Klein, M.A., Kaeser, P.S., Schwarz, P., Weyd, H., Xenarios, I., Zinkernagel, R.M., Carroll, M.C., Verbeek, J.S., Botto, M., Walport, M.J., Molina, H., Kalinke, U., Acha Orbea, H., and Aguzzi, A. (2001) *Nat. Med.*, **7**, 488–492.

78 Picken, M.M. (2007) *Curr. Opin. Nephrol. Hypertens.*, **16**, 196–203.

79 Donabedian, P.L., Pham, T.K., Whitten, D.G., and Chi, E.Y. (2015) *ACS Chem. Neurosci.*, **6**, 1526–1535.

80 Herland, A., Björk, P., Hania, P.R., Scheblykin, I.G., and Inganäs, O. (2007) *Small*, **3**, 318–325.

81 Margalith, I., Suter, C., Ballmer, B., Schwarz, P., Tiberi, C., Sonati, T., Falsig, J., Nyström, S., Hammarström, P., Aslund, A., Nilsson, K.P., Yam, A., Whitters, E., Hornemann, S., and Aguzzi, A. (2012) *J. Biol. Chem.*, **287**, 18872–18887.

82 Dwivedi, A.K. and Iyer, P.K. (2014) *Macromol. Biosci.*, **14**, 508–514.

83 Muthuraj, B., Hussain, S., and Iyer, P.K. (2013) *Polym. Chem.*, **4**, 5096–5107.

84 Ghosh, D., Dutta, P., Chakraborty, C., Singh, P.K., Anoop, A., Jha, N.N., Jacob, R.S., Mondal, M., Mankar, S., Das, S., Malik, S., and Maji, S.K. (2014) *Langmuir*, **30**, 3775–3786.

85 Chowdhury, S.R., Agarwal, M., Meher, N., Muthuraj, B., and Iyer, P.K. (2016) *ACS Appl. Mater. Interfaces*, **8**, 13309–13319.

13

Polymer-Grafted Conjugated Polymers as Functional Biointerfaces

Alissa J. Hackett[1,2], Lisa T. Strover[2,3], Paul Baek[1,2], Jenny Malmström[2,4], and Jadranka Travas-Sejdic[1,2]

[1] *The University of Auckland, Polymer Electronics Research Centre, School of Chemical Sciences, 23 Symonds St, Auckland, 1010, New Zealand*
[2] *MacDiarmid Institute for Advanced Materials and Nanotechnology, Kelburn Parade, Wellington, 6012, New Zealand*
[3] *Ben-Gurion University of the Negev, Jacob Blaustein Institutes for Desert Research, Department of Solar Energy and Environmental Physics, Midreshet-Ben Gurion, 84990, Israel*
[4] *The University of Auckland, Department of Chemical and Materials Engineering, 2-6 Park Avenue, Auckland, 1023, New Zealand*

13.1 Introduction

Conjugated polymers (CPs) are conductive in their doped state (>1 S cm^{-1}) and display unique optoelectronic behavior. This, combined with the possibility of large-scale synthesis, makes them excellent alternatives to traditional metal conductors and semiconductors for use as organic electronics [1–3]. Despite the many attractive properties of CPs, the low solubility of traditional unfunctionalized CPs makes them difficult to process and has limited their use. This can be attributed to the intrinsic rigidity of the conjugated backbone and strong interchain interactions. In the organic electronics field, these drawbacks can be overcome by functionalization of CPs with the addition of side chains. A prevalent example of this is the functionalization of polythiophenes with linear or branched alkyl side chains to yield poly(3-alkylthiophenes) (P3ATs) for photovoltaics, light-emitting diodes, and field-effect transistor applications [4, 5]. The presence of alkyl side chains on P3AT plays a crucial role in molecular packing, as well as in the polymer's solubility in a range of organic solvents [6, 7]. Therefore, careful design of such side chains for CPs can result in improved performance of CP-based devices. To further improve CP material properties, polymeric side chains can be grafted onto the CP backbone. This enables modification of a broad range of the CPs' material properties, including molecular packing and optoelectronic, chemical, and mechanical properties [8].

Many of these improved material properties are particularly important when considering interfacing CPs with biological materials. The interface between biological and man-made materials is central in biomedical applications such as biosensing, tissue engineering, and implantable devices. Ideally, material in

Conjugated Polymers for Biological and Biomedical Applications, First Edition. Edited by Bin Liu

contact with tissue should be designed with appropriate bulk properties, and also engineered to elicit specific surface interactions with spatiotemporal control. The specific interactions (or lack thereof) of proteins with the material play a central role in mediating the biological response. While various materials, including metals and ceramics, have been utilized as functional biointerfaces, organic polymers are particularly well suited to these applications due to their mechanical properties, which can be designed to be compatible with those of soft biological materials, and allow for good interfacial contact [9]. Organic polymers are also amenable to functionalization or copolymerization, which allows for facile modification of material properties. CPs, many of which are biocompatible, offer further advantages over conventional organic polymers due to their unique optical and electrical properties [10–16]. For example, CPs are promising as stimuli-responsive materials, as they can be reversibly oxidized and reduced – a process leading to reversible changes in charged state, conductivity, morphology, and dopant levels. Changes in such molecular-level properties can also affect macroscale properties such as biomolecular adhesiveness and wettability [8]. Stimuli-responsive properties have been explored for materials displaying controlled drug delivery properties [17–19] and for reversible cell/biomolecule adhesion for cell culture and tissue engineering applications [20–23]. A unique feature of CPs is that they are both electron and ion conductors. This gives them an advantage in exchanging signals with cells, transducing ionic to electrical signals and vice versa. This is particularly important for interfacing with the neural system [12, 24–31]. Material characteristics of particular importance for biointerfaces include mechanical properties [32, 33], degradation rate, porosity [34, 35], surface chemistry and topography, the display of signals to cells (through proteins or peptides), and spatial distribution of surface properties and signals [36–39]. Functionalization of surfaces with polymer brushes provides a facile route for modifying these properties, with excellent control over physical properties and chemical functionality [40–44]. CP-based polymer brushes may be synthesized either at the surface or in solution for subsequent deposition as thin films. If the grafting density at the surface is sufficiently high, the CP-based graft copolymers adopt a stretched "polymer brush" conformation. The behavior, synthesis, and applications of polymer brushes have been extensively studied in literature [45–51], which means that there is a wealth of knowledge to draw from when designing CP-*g*-brush hybrid materials.

This chapter focuses on the emerging field of modification of CPs with polymer brushes for biointerface applications. The chapter starts with briefly outlining well-known and commonly employed approaches to introduce biorelevant functionality in CPs (Section 13.2), followed by the rest of the chapter discussing CPs with grafted polymer chains. First, the potential applications of polymer grafted CPs as biointerfaces are introduced, focusing on the unique properties that make these materials suited for the discussed applications (Section 13.3). We then discuss the synthetic approaches to CP-containing graft copolymers, with particular reference to copolymer chemistries of interest for biointerfaces applications (Section 13.4). Finally, we conclude the chapter and offer some suggestions on how this exciting and expanding research field may progress (Section 13.5).

13.2 Methods of Functionalizing CPs

13.2.1 Biodopants

A very simple route to impart new functionality and properties to CPs is to use different dopant ions. The type of molecular dopant used is known to affect the biocompatibility of CPs, which is a key factor in biointerfaces. Aside from the toxic or nontoxic nature of the dopant itself, the choice of dopant also affects the mechanical properties and surface topography of the CP biointerface, which in turn affect cellular behavior [24, 52, 53]. Further effects can be seen by using dopants with a direct impact on cellular interactions – such as biologically derived dopant molecules [24, 54–58]. More specific effects can be seen when doping the CP with peptide sequences or proteins. This approach has been previously demonstrated through the inclusion of peptide sequences and/or neurotrophic growth factors in PPy films [59–63].

13.2.2 Biomolecule Attachment

Using the doping mechanism of CPs to incorporate bioactive material into polymer films is rather straightforward, but is limited to highly charged molecules. By covalently binding (bio)molecules to the CP, a wider range of (bio)molecules can be targeted. Direct attachment to a CP film also ensures that the bioactive molecules are displayed at the interface. A notable example of this approach is that of Sanghvi *et al.*, who developed a generic peptide functionalization approach based on a peptide sequence that was identified through phage-display to bind strongly to the PPy interface [64]. The well-known fibronectin-derived cell adhesion peptide "RGD" has also been directly covalently attached to PPy via an activated cysteine residue in the flanking peptide sequence [65, 66]. Specific protein components can also simply be physisorbed to CP interfaces prior to cell culture to improve cell adhesion to the material [67, 68]. Physisorption has the advantage of being very simple to carry out, but in order to increase the stability of the protein coating a covalent coupling may be desired [69, 70].

13.2.3 Copolymers and Polymer Blends

The conjugated nature of CPs significantly reduces the polymer chain flexibility, in turn affecting their bulk properties. Thus, the added benefits in functionality of CPs come at the cost of not being as soft, flexible, and processable as conventional polymers. To address this, "hybrid" materials have been developed, which incorporate the desirable attributes of the two polymer types. Such hybrid materials can be produced through blending [71–76]. However, such an approach is limited to using chemically similar components in the blends to avoid phase separation, which in this case leads to conductive domains isolated by insulating domains [77, 78]. To ensure a homogenous material, and to truly alter the properties of the CP (such as solubility), copolymers can be produced. Various architectures may be produced by copolymerization, such as dendrimers [79], "rod-coil" block copolymers [80], and graft copolymers [8].

The remaining part of this chapter will focus on graft copolymers incorporating a CP backbone, including densely grafted copolymers that form bottle brushes in solution, and brushes tethered to CP-coated surfaces.

13.3 CP-Based Polymer Brushes as Biointerfaces: Rationale and Applications

The versatility in functionality and architecture of grafted polymers holds great promise for the design and engineering of a new generation of CP-based materials, particularly for biomedical applications.

The discovery that commonly studied CPs (including PEDOT, PAni, and PPy) are biocompatible [24, 81–86] makes these polymers interesting candidates for both *in vitro* and *in vivo* biomedical applications, as alternatives to metallic biomaterials [87, 88]. Compared to standard conductive materials, CPs are softer, more flexible and offer versatile routes to introduce the desired chemical and physical properties, as discussed later in this chapter. With suitable functionalization, CPs are well suited to applications including biocompatible electrodes, biosensors, implantable devices, and tissue engineering substrates. Grafting of polymer brushes at the CP interface offers a route to incorporate desirable functionalities, such as targeted binding sites or nonfouling properties. Interactions between brush chains and the CP backbone in its various charged/uncharged states may also be exploited in order to obtain stimuli-responsive "smart" conductive surfaces [44].

In addition to introducing added functionality, grafting of polymeric side chains can also enhance the utility of the CP itself: for example, by extending the range of accessible optoelectronic properties [1, 89], or by modifying the solubility/processability and mechanical properties of the copolymer [90, 91]. The prospect of modifying local mechanical properties is particularly attractive as cells respond strongly to the mechanical properties of their surrounding extracellular matrix or artificial scaffold (2D or 3D) *in vivo* and *in vitro* [32, 92, 93]. The biologically relevant mechanical properties span a wide range depending on the cell/tissue type; thus, the versatility offered by CP-based brushes in this regard makes them ideal candidates for use as biointerfaces. To date, although limited work has been done on using CP-based graft copolymers in biomedical applications, the potential of such materials in this field has been demonstrated.

13.3.1 Antifouling

One of the greatest challenges in the development of biomedical devices is the problem of surface fouling through the adsorption of proteins and other biomolecules. Fouling can significantly reduce the sensitivity and efficacy of biosensors and biomonitoring devices, and can lead to implant rejection if not adequately addressed. As described in Section 13.2.2, proteins can be readily physisorbed to CP surfaces in an uncontrolled manner and, therefore, it is desirable to develop new CP-based materials that can resist surface fouling.

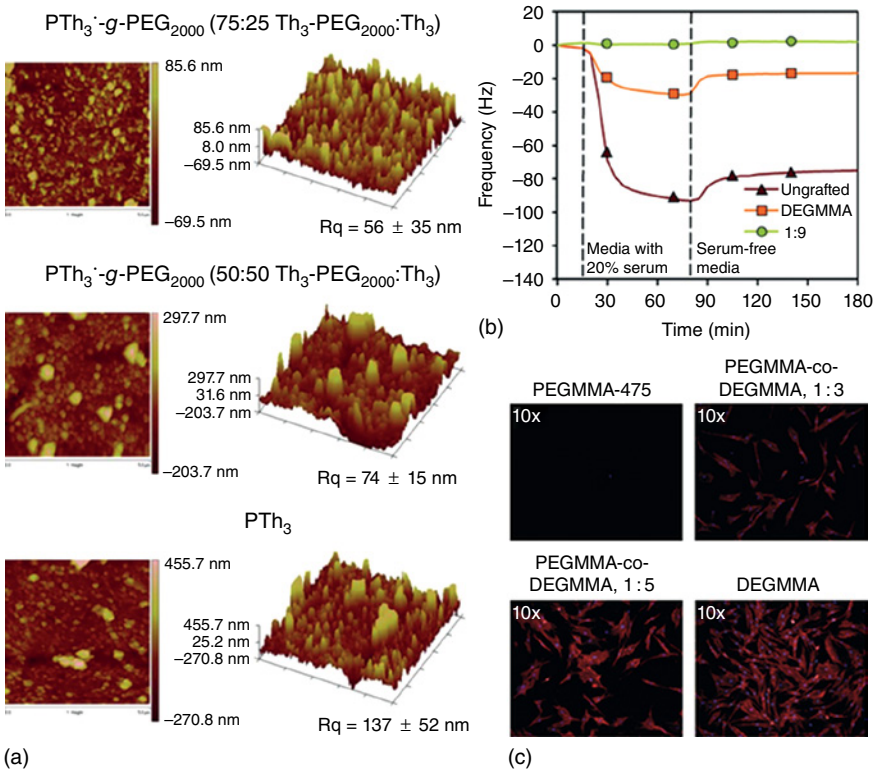

Figure 13.1 (a) Typical AFM height images of PEG-grafted CPs as well as unfunctionalized CP surfaces. (Reproduced with permission from Ref. [94]. Copyright 2015, John Wiley & Sons.) (b) Frequency response demonstrating the relative protein resistance of ungrafted PBrEDOT, and PBrEDOT grafted with PDEGMMA and P(PEGMMA-*co*-DEGMMA, monomer ratio 1:9 brushes in serum-free media and 20% serum, measured using Quartz Crystal Microbalance with Dissipation. (Reproduced with permission from Ref. [95]. Copyright 2015, Royal Society of Chemistry.) (c) Fibroblast adhesion on PBrEDOT grafted with P(PEGMMA-*co*-DEGMMA) brushes of different compositions, showing variable cell adhesion based on brush composition. Blue = DAPI (nucleus), red = phalloidin (actin). (Reproduced with permission from Ref. [67]. Copyright 2017, Inderscience Publishing.)

Several research groups have explored the possibility of grafting poly(ethylene glycol) (PEG) derivatives and other antifouling polymer brushes from CPs in order to curb nonspecific protein adsorption, capitalizing on the widely recognized protein-repelling properties of PEGs (Figure 13.1a) [94, 96, 97]. Some concerns have been raised regarding the stability and biocompatibility of PEG and, therefore, significant efforts to find alternatives to PEGs are ongoing [98]. However, PEG remains a powerful and widely used antifouling compound. PPy-*g*-PEG surfaces investigated by Molino *et al.* for example showed complete rejection of mouse myoblast adhesion [99]. Meanwhile, Chen *et al.* investigated PAni-*g*-PPEGMA as a protein-resistant surface for use in electroactive biomaterials such as biosensors or devices for biological implants [100]. Recently, PEG-based methacrylate monomers were grafted from PEDOT substrates functionalized with

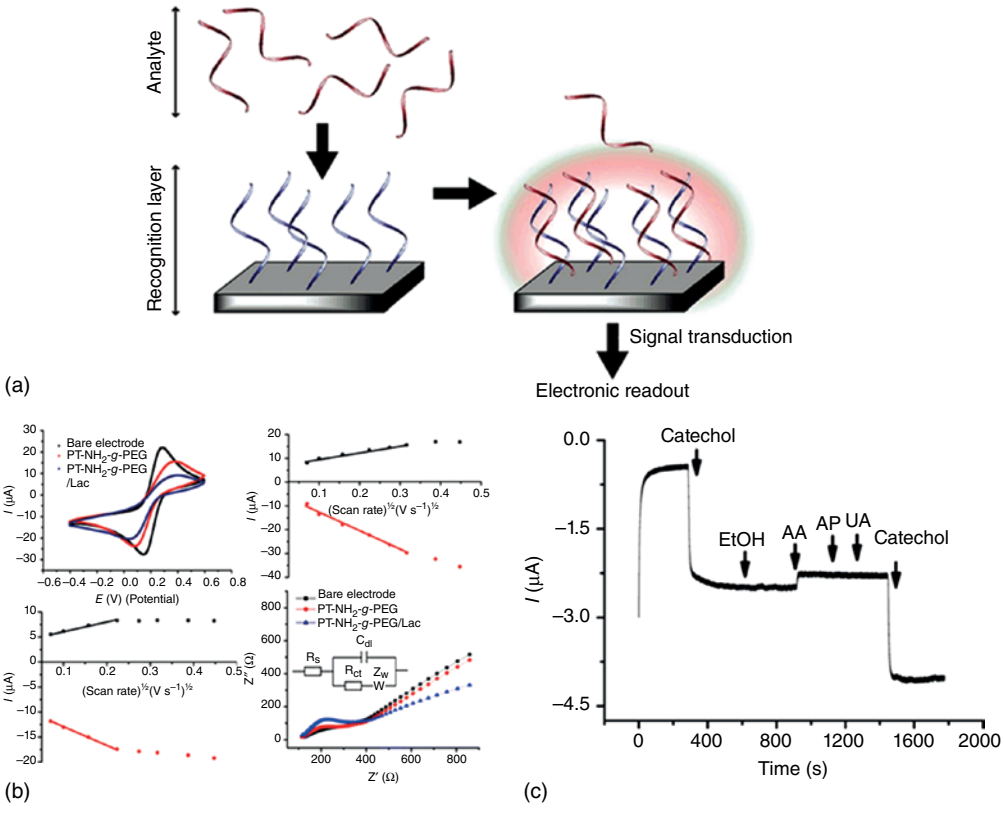

Figure 13.2 (a) General biosensor design, where the interaction between the target analyte and the sensing element (recognition layer), such as CP-based graft copolymer, is readout as an electronic signal. (Reproduced with permission from Ref. [102]. Copyright 2003, Nature Publishing Group.) (b) Various electrochemical techniques involved in characterizing the surface of graft copolymer modified electrodes. (Zig zag direction from top left: cyclic voltammetry, scan rate dependence of peak currents, and Nyquist diagrams obtained by electrochemical impedance spectroscopy) [103]. (c) Electrochemical detection of various analytes at the graft copolymer modified electrode surface. (Reproduced with permission from Ref. [103]. Copyright 2015, American Chemical Society.)

ATRP initiators, with an interest in tuning the surface properties by copolymerizing two different poly(ethylene glycol) methyl ether methacrylate (PEGMMA) macromonomers with differing molecular weights: di(ethylene glycol) methyl ether methacrylate (DEGMMA, MW = 188.22) and PEGMMA-500 (MW = 500) [95]. As expected, the swollen brushes were demonstrated to be protein rejecting with effectiveness increasing when the more hydrophilic PEGMMA-500 monomer was incorporated into the brush. The polymer with a 9 : 1 monomer ratio of DEGMMA:PEGMMA-500 displayed complete protein rejection after an hour of exposure to 20% serum, while the PDEGMMA homopolymer brushes demonstrated almost 80% reduction in bound protein compared to the ungrafted PEDOT control (as determined by quartz crystal microbalance with dissipation measurements, Figure 13.1b). Further studies revealed that the swollen brushes were also cell repelling, with the extent of cell rejection dependent on the composition of the copolymer brushes (Figure 13.1c) [67]. Such tailored protein and cell adhesion is an important step in preparing CP biointerfaces with desired properties for particular applications or cell types. Zhao *et al*. produced a similar functionalized PEDOT film, from which brushes of poly(oligo(ethylene glycol) methacrylate) (POEGMA) and zwitterionic poly([2-(methacryloyloxy)ethyl] dimethyl-(3-sulfopropyl)ammonium hydroxide) (PSBMA) were grafted [101]. Both brushes caused complete rejection of bovine serum albumin (BSA) and fibrinogen (Fn) binding. The brushes also prevented adhesion of NIH3T3 fibroblast cells after incubation for 24 h, while the fibroblasts readily adhered to the ungrafted PEDOT film.

13.3.2 Biosensing

Biosensors are devices that enable detection of biomolecules by combining a biological recognition event with a physiochemical detection mechanism. Biosensing plays an increasingly important role in a wide range of fields, including health care, environmental monitoring, food quality monitoring, and biosecurity, where biosensors are used to detect genetic abnormalities, pathogens, viruses, toxins, and biological markers of diseases [102]. In general terms, biosensing relies on a highly specific and selective interaction between a probe – commonly attached to a surface – and its target analyte (Figure 13.2a). A good biosensor should enable the formation of a highly specific probe–target complex in a way that the complex formation triggers a usable readout signal [104]. This readout signal is generally either electrical or optical in the case of CP-based biosensors [105–108].

Grafting of CPs with functionalized polymeric side chains offers interesting opportunities to explore in the development of CP-based biosensors. Grafted brushes allow us to investigate the effects of variations in parameters, such as surface charge density, hydrophilicity/hydrophobicity, and the degree of film swelling, on the electrochemical/optoelectrical sensor response. For example, grafting can reduce the aggregation of soluble CP chains, which can lead to quenching of photoluminescence in optical sensing systems [109, 110]. Grafting also provides a route toward improving biocompatibility of the sensing materials and reducing nonspecific surface interactions, as well as a new method of attaching the probe molecule or other biomolecules [111, 112]. Importantly, as the

majority of biosensors operate in aqueous environments such as biological media, it is critical that the CP remains electroactive under these conditions.

There are limited examples in the literature of CP-based brushes utilized for biosensing applications. However, some examples illustrate the potential of these materials. In a study by Kang *et al.*, the authors synthesized hydrophilic PAni-*g*-PAAc (poly(acrylic acid)) and PAni-*g*-PNaSS (poly(sodium 4-styrenesulfonate)) substrates with side chains suited to the immobilization of proteins or enzymes, thus providing a template for biocompatible electrodes and sensors [113]. In order to improve the electroactivity of polythiophene (PTh) in aqueous solutions, and thereby its efficiency as a biosensor, Akbulut *et al.* synthesized polythiophene films grafted with amine- or PEG-functionalized units alternating with unfunctionalized "spacer" thiophene units [103]. The amine groups were used to immobilize laccase (Lac) enzyme, and the system was tested as an electrochemical catechol biosensor (Figure 13.2b, c). The system demonstrated improved sensitivity compared to previously reported Lac biosensors [114, 115], with a linear range from 2.5 to 500 μM. This was attributed to the PEG chains, which improved the electroactivity of the PTh backbone in the aqueous solutions; this was particularly important, as the addition of Lac enzyme appeared to hinder electron transfer between the electrode and solution. The authors have also used similar methodologies to produce poly(*p*-phenylene)s (PPPs) grafted with PEG and covalently bound poly-L-lysine [116], demonstrating that these techniques can be extended to other CPs and brush types.

13.3.3 Tissue Engineering

CPs are interesting materials for tissue engineering – in particular, where the tissue in question is known to respond to electrical stimuli (such as nerve or muscle tissue where electrical impulses are part of the biological function) [52, 54, 117]. CPs may also be used to entrap drugs and deliver them when electrically stimulated, which has broader implications for *in vivo* tissue engineering as well as for other targeted drug delivery applications [17, 19, 118]. Cells and tissues are highly sensitive to the mechanical properties of their surroundings. While being more flexible than metals, CPs are much stiffer than most biological tissues and commodity polymers normally used in tissue engineering scaffolds. Therefore, grafting of side chains to CPs to modify the mechanical properties can have significant implications on their implementation in tissue engineering. Additionally, the introduction of functional groups in grafted side chains can be used to specifically tailor biomolecular interactions. The most prevalent example of this is the addition of specific peptides to mediate cell binding [70, 119]. In this case, the CP should also be rendered antifouling by appropriate functionalization to prevent nonspecific interactions with the substrate. Such an approach was utilized to achieve tunable protein and cell interactions with PEDOT-*g*-P(HOEGMA-*co*-OEGMA) surfaces [67]. The PEG-derivative brushes imparted protein and cell-rejecting properties, and further functionalization with an integrin ligand, namely, cyclic RGD, rendered the surface specifically cell adhesive.

In a study by Zhao *et al.*, the authors reported the use of dibromothiophenes modified with short oligo(ethylene glycol) chains (OEG) (2 or 4 repeating units)

capped with either methyl or benzyl groups [120]. As dropcast films, the OEG-modified PTh demonstrated good electrochemical stability in water. Although PEG is typically used to prevent protein and cell adhesion, the short chains in this study did not hinder cell adhesion; spincoated films were able to support the growth and proliferation of NIH3T3 fibroblast cells to confluence within 84 h (Figure 13.3a-f). In general, PEG must either be very densely packed (self-assembled monolayers), or presented as long, densely grafted brushes to be protein and cell repelling [121]. The ability to graft long side chains from a CP backbone is highly dependent on the synthetic approach – a topic that will be discussed in the following section of this chapter. Often, the incorporation of bulky side chains, such as long PEG chains, on a CP brush precursor monomer would prevent efficient polymerization of that monomer. In order to incorporate bulky side chains on CP backbones, several groups have investigated the use of CP precursor oligomers containing a single functionalized unit and several unfunctionalized "spacer" units. This approach is intended to reduce steric hindrance and improve polymerization efficiency for the synthesis of side-chain-functionalized CPs. Bendrea *et al*. electrochemically polymerized PTh-*g*-PEG from pentathiophene oligomers with methyl-capped PEG chains attached to the central thiophene [122]. With the added spacing between the attached polymer, longer PEG chains (22 or 44 repeat units) could be incorporated, although the resulting films were still not protein rejecting. The pentamonomers readily yielded smooth films, which were used to culture epithelial Vero cells. After seven days, the PTh-*g*-PEG films displayed greater cell viability than both steel and culture plate controls.[123] Extending on this study, Maione *et al*. investigated the effect of graft density on PTh-*g*-PEG films with 42 repeat units, using PEG-grafted terthiophenes instead of the previous pentathiophenes [94]. These were copolymerized with ungrafted terthiophenes in different ratios to modify grafting density, and investigated for potential cytotoxicity using Cos-7 fibroblast-like cells. After 24 h, ungrafted PTh_3 showed about 50% reduction in cell viability compared to steel and culture plate controls, while grafted PTh_3-*g*-PEG films demonstrated similar cell viability compared to the control substrates. Likewise, the grafted films also showed significantly greater cell attachment and proliferation compared to the steel control.

13.3.4 Stimuli-Responsive Materials

For certain applications, it may be desirable to have materials with properties that can be switched "on" or "off" in response to stimuli. For example, tissue culture requires scaffolds that promote cell adhesion and growth on the substrate. However, conventional cell harvesting techniques frequently use enzymes to degrade cell adhesion proteins and disrupt cell-substrate binding, which can also damage cell–cell binding and lead to cell sheet degradation. A gentler approach would be to switch the properties of the scaffold from cell-binding to cell-repelling, allowing the tissue or cell sheet to easily lift off the surface in one piece [124]. Thermoresponsive poly(*N*-isopropylacrylamide) (PNIPAM) has been used commercially for this purpose, with cell-binding characteristics readily modulated through temperature [125]. Incorporation of CPs into similar

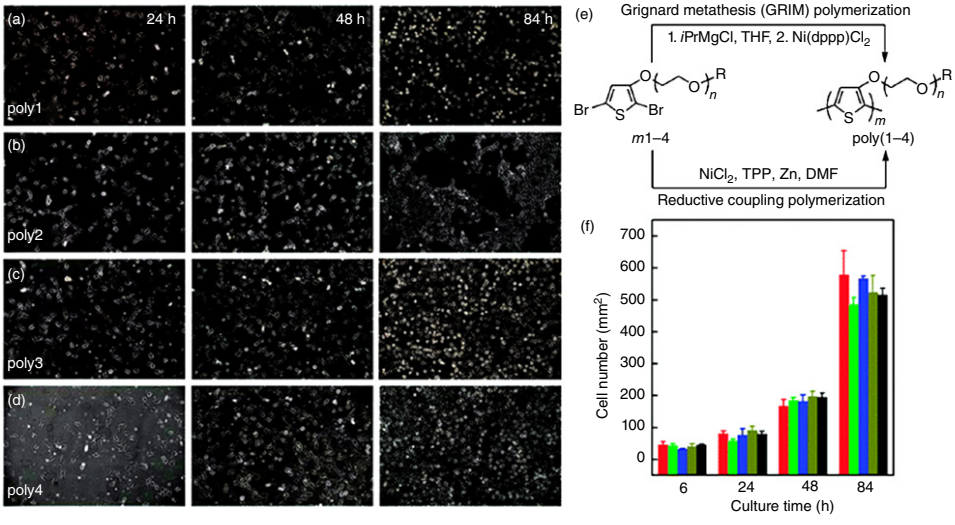

Figure 13.3 (a–d) Optical microscope images of NIH3T3 fibroblast cells on oligoethylene glycol-containing polythiophene surfaces at different culture times, demonstrating its use as biointerface for tissue engineering scaffolds. (e) Synthesis of polythiophene with oligoethylene glycol side chains. (f) Comparison of cell density of NIH3T3 fibroblast cells cultured on standard tissue culture plate (red) and on functional oligoethylene glycol-containing polythiophene surfaces (rest of the color). (Reproduced with permission from Ref. [120]. Copyright 2012, American Chemical Society.)

stimuli-responsive materials can thus potentially provide a mechanism for electrical switching, through oxidation and reduction of the CP backbone. Alternatively, the combination of CPs with other stimuli-responsive polymers can produce electroactive surfaces with properties that can be modulated by other means, such as temperature, pH, or salt.

CP-based graft copolymer brushes are particularly well suited for applications as stimuli-responsive materials, with multiple mechanisms available for exploitation. CP backbones can be chemically or electrochemically oxidized and reduced to reversibly cycle between oxidized (conductive) and neutral (insulating) states. This process is accompanied by reversible chemical and morphological changes, due to the accompanying influx or efflux of dopant ions (along with solvent) to balance charge. These processes lead to inherent stimuli-responsive behavior of CPs, derived from a combination of transitions of chemical, physical, and mechanical properties that accompany redox processes [126]. For example, distinctive electrochronic switching between the oxidized and reduced structures of many CPs is well documented [127], which could potentially be exploited in a biological setting as redox probes. Changes in hydrophilicity/hydrophobicity also commonly accompany doping/dedoping of CPs, and have been exploited for the design of surfaces with reversibly switchable wettability [128, 129].

By grafting side chains, the scope of switchable properties and mechanisms is greatly expanded. Changes in environmental conditions such as temperature, pH, or salt concentration can all induce changes in the conformation of grafted side chains, which in turn can affect macroscopic surface properties [22, 47]. Another possible mechanism for conformational switching of side chains is to exploit interactions between charges on grafted polymers and those of dopant ions and/or on the CP backbone. Owing to the changes in the CP's charged state and doping, which accompany redox processes, CP-based graft copolymer brushes may also be responsive to an electrochemical trigger [44, 130]. On a macroscopic scale, changes in side chain conformation may manifest in changes in material or surface properties including wettability, interaction with biomolecules, cells and analytes, or in absorption/emission profiles [131–134].

As mentioned above, of the most well-studied biocompatible and temperature- responsive polymers is PNIPAM, which is already widely used for biointerface applications. PNIPAM is water soluble, adopting an extended conformation below its lower critical solution temperature (LCST), but contracting due to favorable interchain interactions above the LCST. This transition occurs at 32 °C, making PNIPAM highly useful for biological applications [135]. These features have been exploited in tissue engineering to lift off entire cell sheets without disturbing the deposited extracellular matrix through standard enzyme treatments [125, 136]. Combining the temperature-responsive behavior of PNIPAM with the optoelectronic properties of CPs, water-soluble PTh-*g*-PNIPAM polymers can be induced to exhibit thermochromic responses due to conformational switching of PNIPAM side chains, which in turn modulates the effective conjugation length of the PTh backbone (Figure 13.4a) [137, 139]. While these studies are of limited use for biological applications, similar approaches may be applied to more biologically relevant CP backbones. Sun *et al.* polymerized Py-capped PNIPAM macromonomers in the presence of $AgNO_3$ as an oxidizing agent,

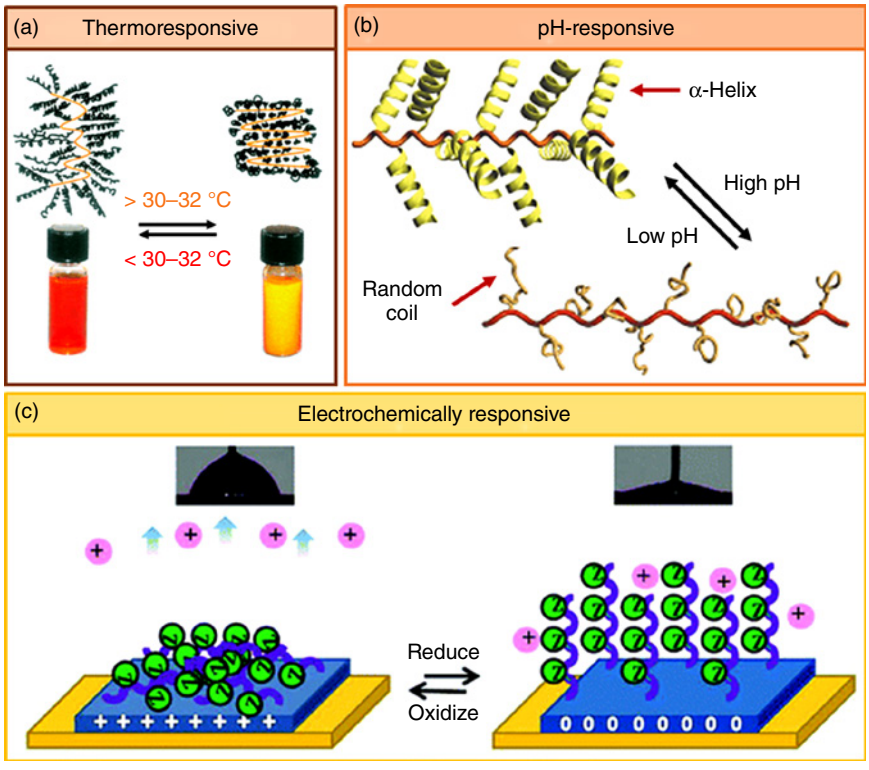

Figure 13.4 (a) Thermoresponsive behavior of PNIPAAm-grafted polythiophene, showing the change in conformation with temperature below or above its LCST. (Reproduced with permission from Ref. [137]. Copyright 2005, John Wiley & Sons.) (b) Graphical illustration showing the reversible helix-coil transition of the grafted peptide side chains of a poly(phenylacetylene)-based graft copolymer with the change in pH. (Reproduced with permission from Ref. [138]. Copyright 2004, John Wiley & Sons.) (c) Electrochemically responsive wettability and conformational switch of zwitterionic polymer brushes grafted from a polypyrrole-based backbone. (Reproduced with permission from Ref. [44]. Copyright 2012, American Chemical Society.)

thereby producing PPy-*g*-PNIPAM/silver nanocomposites *in situ* [140]. The brushes were water soluble only when the PPy content was low. The nanocomposite formation was attributed to the strong interaction between PNIPAM and metal atoms. Thermoresponsive behavior was observed by UV–vis and fluorescence spectroscopy and an increasing PPy content resulted in a lower LCST, attributable to the relative hydrophobicity of PPy. The addition of silver nanoparticles is interesting from a biointerface perspective, as silver is well known to have an antibacterial effect while being well tolerated *in vivo* [141, 142].

PEG-derivatives are also known to exhibit thermoresponsive behavior similar to PNIPAM, with the advantage of tunable LCST behavior based on the number of ethylene glycol units present [143, 144]. Das *et al.* demonstrated that this tunability extended to PEG-based grafted CPs by preparing water-soluble, thermosensitive PTh-*g*-poly(poly(ethylene glycol) methyl ether methacrylate) (PPEGMMA) graft copolymers, using PEGMMA macromonomers of

different molecular weights [89]. Changes in polymer morphology and photoluminescence intensity were observed around the cloud point temperature, as the PPEGMMA chains collapsed. The ability to tailor protein and cell adhesion has also been demonstrated, using thermoresponsive PEDOT substrates that had been grafted with PPEGMMA brushes [95]. As with Das *et al.*'s work [89], this was achieved through copolymerizing two different PEGMMA monomers with differing molecular weights, with a resultant dual control over the brush conformation (temperature and salt type and concentration). In turn, the electrochemical properties of the surfaces were altered; this provides a route to modulate electrochemical interactions between the surface and tissues by environmental stimuli.

While temperature-responsiveness is a generally mild and biologically relevant stimulus, other environmental triggers can also be explored for stimuli-responsive CP-based brushes. For example, a study by Wang *et al*. investigated pH-responsive poly(thiophene)-*g*-poly(*N*,*N*-dimethylaminoethyl methacrylate) PTh-*g*-PDMA that showed reversible conformational transitions, correlated to changes in the UV–vis absorbance and fluorescence emission spectra [145]. In another study, Maeda *et al*. prepared switchable optically active helical polymeric material based on poly(phenylacetylene) with polypeptide side chains where conformational changes in the polypeptide, induced by stimuli including solvent or pH, were capable of inducing changes in the pitch of the helix in the CP backbone (Figure 13.4b) [138]. These types of responsive systems may be of interest in applications such as targeted drug delivery systems, where a loaded drug molecule can be released by conformational changes of a polymeric carrier. For instance, certain cancer cells are known to increase the pH of their local environment when compared to healthy cells, which attribute could act as an appropriate trigger [146–148].

Perhaps, the mildest and most interesting stimuli from a biological perspective, are electrochemically induced responsiveness. CP-based brushes are very promising as a means for preparing electrochemically responsive electrodes [149]. Electrochemically triggered conformational switching of zwitterionic brushes grafted from thin films of electropolymerized PPy derivatives has recently been reported, with accompanying changes in surface wettability (Figure 13.4c) [44]. Homopolymer and block copolymer brushes of poly(3-(methacryloylamido) propyl)-*N,N′*-dimethyl(3-sulfopropyl) ammonium hydroxide) (PMPDSAH) and poly(methyl methacrylate)-*b*-PMPDSAH were grafted by SI-ATRP from a poly(pyrrole-*co*-pyrrolyl butyric acid) film. The same macroinitiator was later used to grow ABC random polyampholyte brushes, comprising methyl methacrylate (MMA), methacryloxyethyltrimethylammonium chloride (METAC), and 3-sulfopropyl methacrylate potassium salt (SPMA). The brushes were found to exhibit a salt-dependent change in conformation, as studied by electrochemical impedance spectroscopy [130]. In another study, pH-responsive electrochemical behavior of PEDOT-*g*-PAA modified electrodes was demonstrated. Interestingly, the grafted side chains enhanced redox processes of the PEDOT when the brushes were charged (high pH), while redox reactions were partially inhibited when the brushes were neutral at low pH [150]. Similar stimuli-responsive behavior in CP-based graft copolymers may ultimately be

exploited for smart surfaces, particularly in the biomedical field, where characteristics such as surface wettability, or the adhesive/repulsive nature of the surface toward cells or biomolecules, may be dynamically controlled. However, it should be noted that generally neither cells nor proteins have a wide tolerance for changes in pH.

13.3.5 Emerging Bioelectronics Materials Based on Grafted CPs

CP-based graft copolymers demonstrate great potential in the rapidly growing discipline of stretchable electronics [151–154]. For such applications, the active material needs to possess sufficient conductivity that can be retained at large strains. Self-healing of the mechanical and electrical properties is another strongly desired trait, which could improve the device's lifetime. Clearly, these characteristics would be also highly desirable in some biomedical applications of CPs, including development of electronic skin [152]. Such desired mechanical and self-healing properties required for stretchable bioelectronics can be achieved by incorporating appropriately designed side chains. While stretchable and self-healing polymers are widely discussed [155–157], studies on the design and engineering of polymer-grafted CPs for stretchable and self-healing organic bioelectronics are very limited.

The methodology of grafting onto CPs enables one to finetune the viscoelastic and mechanical properties of the resulting polymer by selectively designing the side-chain polymers, while optimize the electrical and optoelectronic performances by varying the graft density or graft length [109, 110]. There is a wide range of biological signals from electrocardiograms as well as from physiological information that could be collected continuously from the human body with suitable implants [154]. However, overcoming the current challenges lies in our ability to integrate devices with the human body and to specifically access the target organs to measure and monitor the vital signals [158]. The use of these intrinsically conductive, yet deformable and soft, graft copolymers in bioelectronics holds great promise for such electronic devices.

13.4 Synthesis of CP-Based Graft Copolymer Brushes

The vast range of attainable structures and chemistries of CP-based graft copolymers makes them highly suitable for a diverse array of applications. A number of synthetic routes for the design of CP-based graft copolymers are available, and the synthetic approach used plays a vital role in determining the resulting polymer structures and surface properties. The literature on graft copolymers generally categorizes three approaches for the synthesis of graft copolymers, all of which are applicable to the grafting of polymer brushes from a CP backbone. These comprise "grafting to," "grafting from" and "grafting through" approaches, which have been reviewed in detail elsewhere [159, 160]. With regard to CP-based graft copolymers, the "grafting through" method involves the synthesis of macromonomers, which consists of conventional polymer chains end-functionalized with a monomer of the desired conjugated backbone. These macromonomers can then

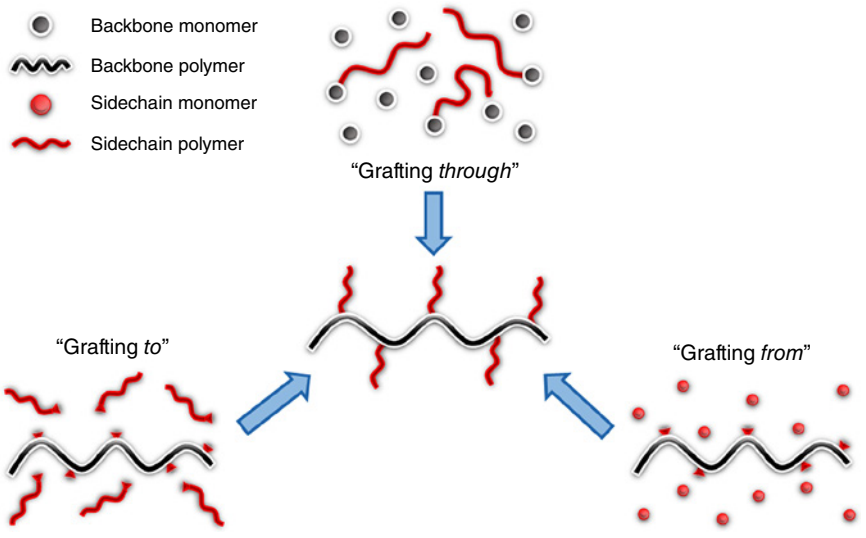

Figure 13.5 Generalized categories of graft copolymer synthesis: grafting through (macromonomer approach), grafting to, and grafting from (macroinitiator approach).

be (co)polymerized at the monomeric end-groups to yield a CP-backbone functionalized with side chains in a comb-like architecture [161]. Alternatively, "grafting from" requires macroinitiators that are basically CP backbones functionalized with initiating sites, from which polymer chains are subsequently grown [162]. Finally, the "grafting to" (Figure 13.5) method comprises the chemical attachment of preformed polymer chains to the conductive backbone [163]. All of these approaches have advantages and disadvantages, as will be discussed briefly in the following paragraphs.

The synthetic approach must consider which methodologies will give access to desired chemistries, achievable grafting densities, control over polymer architecture and regioregularity, and monomer/polymer solubility. The first decision to be taken should be whether the polymerization should be performed directly on a substrate or in solution. Approaches may be readily adapted to grafting using a surface-immobilized film. For solution polymerization, the "grafting through" approach requires the macromonomers to be soluble, while the "grafting from" approach requires a soluble CP backbone; however, both backbone and polymer chains must be soluble for "grafting to."

The next question is with regard to which types of polymerization reactions should be used for the CP backbone and for the grafted side chains. To start with, polymeric side chains are frequently polymerized by controlled radical polymerization (CRP) techniques, which allow for excellent control over copolymer architecture and compatibility with a range of functional groups. The control over the polymerization is due to an equilibrium between active and dormant states of polymer chain growth, giving first-order polymerization kinetics with low termination and predeterminable molecular weight [164]. A wide range of vinyl-functionalized monomers have been polymerized using CRP methods, which include techniques such as nitroxide-mediated polymerization (NMP)

[165], reversible addition–fragmentation chain-transfer (RAFT) polymerization [166–168], and atom transfer radical polymerization (ATRP) [169, 170]. Within the family of ATRP reactions, various techniques have been developed specifically to allow for the reduction of (toxic) catalysts and improve control over polymerization in the presence of water and/or air. These ATRP techniques include A(R)GET (activators (re)generated by electron transfer), electrochemically mediated eATRP, and ICAR (initiators for continuous activator regeneration), and have been reviewed in depth elsewhere [170, 171]. All of the aforementioned CRP techniques are applicable to a range of monomers, are able to produce polymers with low polydispersity and predictable molecular weight, and retain end-functionality whereby polymerization can be reinitiated.

Meanwhile, CRP methods are generally not compatible with polymerization of CP backbones due to the structure of the precursor monomers. Instead, the CP backbones may be synthesized either directly on to a surface, using electrochemical [172] or chemical vapor deposition methods [173], or alternatively in solution, for example, by oxidative chemical polymerization [174] or by a number of transition metal-catalyzed cross-coupling (polycondensation) reactions [1]. Electropolymerization is frequently utilized to produce CPs, as the resulting film properties can be controlled through modifying the parameters such as monomer concentration, solvent, electrolyte salt, potential, and polymerization time [172]. However, this method is challenging to be scaled up. As many biomedical applications require large- scale polymer production, chemical polymerization of the CP backbone may be preferential for industrial purposes [175].

Although grafted side chains can optimize optoelectronic properties in an application-specific manner, the incorporation of insulating polymeric side chains may compromise the CP's electronic properties [176]. In order to balance processability and the desired physical properties with device performance, the degree of side chain length or the grafting density should be considered, as these aspects of CP-based graft copolymers would determine their conformation both in solution and in solid state.

In the following sections, we will briefly describe some approaches to CP-based graft copolymer synthesis, categorized into "grafting through," "grafting to," and "grafting from" methodologies, with a focus on synthetic methods applicable to copolymer chemistries and architectures of interest for biointerfaces.

13.4.1 Grafted CPs: Synthesis by "Grafting Through" Approach

The versatility of the "grafting through" method depends on the ease with which the macromonomers (i.e., polymers incorporating a polymerizable end-functionality) can be (co)polymerized via chemical polymerization in solution, or by (electro)chemical polymerization directly onto a substrate. The "grafting through" approach can, therefore, be used to make a variety of materials once the macromonomers have been synthesized.

Several initial studies on CP-based graft copolymers produced films directly on a substrate by copolymerization of macromonomers. In these studies, commodity polymers such as poly(dimethylsiloxane) (PDMS), poly(styrene) (PS) or poly(tetrahydrofuran) (PTHF), were side- or end-functionalized with pyrrole or

thiophene moieties to yield macromonomers. The macromonomers were then co(electro)polymerized with conventional CP precursor monomers such as pyrrole and thiophene to yield cross-linked and graft copolymer architectures. [41, 177–180] These early studies demonstrated the successful incorporation of some of the most commonly studied CPs (namely PTh and PPy) into graft copolymers as a route to prepare CP films with improved mechanical properties. While these works were not specifically targeted at producing biointerfaces, they have paved the way for synthesis of electroactive materials with tailored functionalities.

More recently, electrochemical polymerization of end-functionalized macromonomers has been used to produce CP-based graft copolymers including PTh-*g*-PEO [181] and poly(triphenylamine)-*g*-poly(ε-caprolactone) [182]. The main limitation with this method pertains to the electropolymerization process. It is probable that long polymer chains on the macromonomers sterically hinder electropolymerization, and thus the electropolymerized films produced by these methods are unlikely to be obtained with dense brush-like grafting. It has been shown that macromonomers that do not electropolymerize on their own will often copolymerize well with nonfunctionalized CP monomers, likely due to the reduced steric hindrance [181].

The macromonomers can also be polymerized in solution and deposited as thin films for use as biointerfaces. This approach is particularly attractive for the synthesis of processable graft copolymers. Macromonomers based on hydrophilic polymers have been (co)polymerized in solution to yield water-soluble CP-based graft copolymers, thus reinforcing the possibility of depositing conductive films under benign conditions [183–185]. Dendrimers have also been used as solubilizing groups for CPs. Malenfant and Fréchet copolymerized dibrominated dendrimer-oligothiophene macromonomers with 2,5-bis(trimethylstannyl)thiophene [186]. In addition to their potential as solubilizers, dendrimers are of interest due to their ability to induce the formation of highly organized structures. Polymers with diverse architectures can also be solution (co)polymerized from macromonomers with mid-chain functionalities, generally using transition metal catalyzed reactions such as Suzuki coupling (Figure 13.6) [187–189]. These versatile synthetic techniques may be utilized to incorporate moieties of interest for biointerface applications.

An alternative approach to "grafting through" on a surface has been reported by Grande *et al*. who electropolymerized a CP film onto a surface, where the CP film itself presented methacrylate moieties [190]. These surface-presented methacrylate groups were then incorporated into polymer chains (PS, poly(methyl methacrylate) (PMMA), P*t*BA) growing in solution, thus tethering the polymer chains to the surface. Unlike other approaches discussed in this section, in this case it was the commodity polymer, not the CP, which was "grafted through."

CRP methods (primarily ATRP) have also been used to synthesize a range of macromonomers as precursors for CP-based graft copolymers. The polymerizable CP-backbone precursor is commonly incorporated as end-groups in the macromonomers, by using a CP-precursor with an ATRP initiating site to grow the commodity polymer from. In this way, post-polymerization functionalization can be avoided, which simplifies the process [96, 138]. While CRP can yield a range of interesting end-functionalized structures, not all macromonomers of

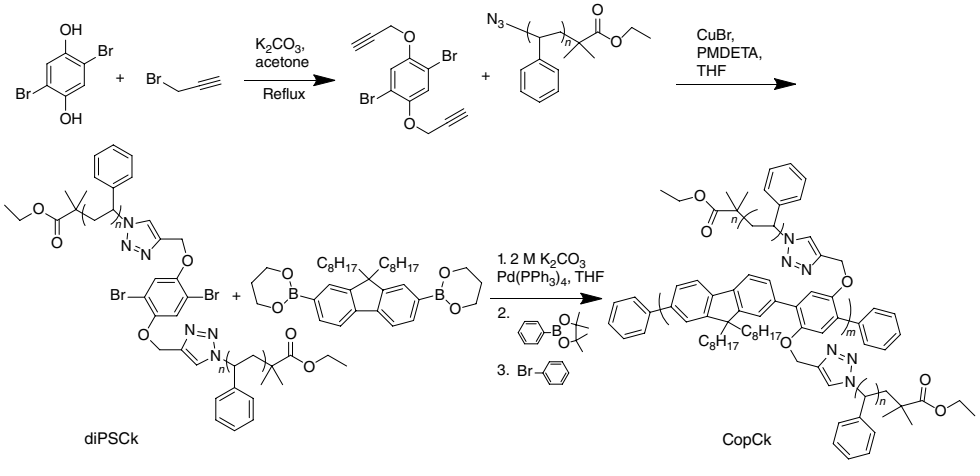

Figure 13.6 Synthesis of poly(fluorene–phenylene)-*g*-(polystyrene) from a mid-chain functionalized macromonomer. (Reproduced with permission from Ref. [187]. Copyright 2010, John Wiley & Sons.)

interest can be accessed by this route. Other techniques such as ring opening polymerization (ROP) have been useful for grafting of polymers such as poly(ε-caprolactone) (PCL) and poly(L-lactide) (PLLA) [191], which have been used in many studies of CP-based graft copolymer brushes for biomedical applications as they are biodegradable, biocompatible, and readily synthesized. Several PCL macromonomers synthesized by ROP have been described in the literature as precursors for CP-based graft copolymers, such as PPy-*g*-PCL [182, 192, 193]. In some cases, where a commercially available functional commodity polymer is available, post-functionalization of the macromonomer with a CP-precursor may be a more viable approach. An example of this is hydroxyl-terminated PDMS which was used in the synthesis of poly(phenylacetate)-*g*-PDMS [194]. Depending on their solubility and chemistry, macromonomers produced by the above methods may be compatible with "grafting through" either in solution, or directly onto a substrate by electropolymerization or oxidative chemical polymerization.

By selecting appropriate side chain functionalities, CP-based graft copolymers have been engineered from macromonomers to yield materials suitable for biointerface applications. Maione *et al.* synthesized PTh-*g*-PEG via a macromonomer approach using either a pentathiophene-PEG macromonomer or a terthiophene-PEG macromonomer copolymerized with terthiophene (via electropolymerization using constant potential) [94]. PEG and its derivatives are important in the biomaterial field as they are commonly used to prevent non-specific adsorption of proteins and biomolecules [98].

13.4.2 Grafted CPs: Synthesis by "Grafting To" Approach

The "grafting to" method for CP functionalization provides a good control over brush characteristics such as molecular weight and composition, as the polymer brushes are synthesized prior to attachment to the CP backbone. As both the backbone and side chains are synthesized separately prior to grafting, the "grafting to" approach is compatible with any number of polymerization techniques and conditions. This method allows for excellent control over the structure and polydispersity of both graft copolymer components and permits accurate characterization of their properties, which may not be easily determined using "grafting through" or "grafting from" approaches, especially when working with surface-tethered brushes. It can also facilitate the production of patterned or mixed brushes on surfaces, by selective functionalization of the CP backbone with appropriate attachment sites [163]. The main drawback however, is the difficulty of achieving high grafting density [195]. To address this issue, cloud-point grafting techniques have been used for "grafting to" of PEG-derivatives, where dense grafting is achieved by exploiting the limited solubility of the polymers in an aqueous solution with a high salt concentration [194, 196]. However, to the best of our knowledge, this technique has not yet been applied in the production of CP-based grafted polymers.

With these points in mind, the "grafting to" method is a feasible approach for CP-based grafted polymers that have either low molecular weight side chains, or lack high grafting density (i.e., "brush regime"). "Grafting to" of relatively dense PAni-*g*-PEO brushes via chlorosulfonation of PAni provides an example of the

viability of this technique using low molecular weight side chains, producing an electroactive, biocompatible, and protein- and platelet-resistant material for use in biomedical applications – specifically for sensing applications in this case [197]. The "grafting to" approach has experienced a resurgence in recent years, aided by the development of "click chemistry" performed under mild conditions [97]. The azide–alkyne click coupling is the most reported method, but thiol–ene coupling has also been demonstrated as a viable approach for "grafting to" synthesis of polymer brushes [198]. Click chemistry may not overcome the drawback of limited grafting density discussed earlier, but the technique is still favored due to its ease and versatility, and has successfully been applied to the synthesis of a range of functional CP-based graft copolymers [99, 198–200]. Azide–alkyne click coupling has been used to modify a conjugated polyelectrolyte (CPE) with an amino-PEG in order to enhance fluorescence quantum yields for probes for biological analytes (Figure 13.7). The amino groups in this case also offer sites for further functionalization with folic acid to convert the brushes into cellular probe [200]. This post-functionalization was considered when choosing the "grafting to" method, as it allowed the retention of the amino groups.

13.4.3 Grafted CPs: Synthesis by "Grafting From" Approach

A method that completely circumvents the issue of low grafting density seen with the "grafting to" and "grafting through" methods is the "grafting from" method. Thus, if densely grafted copolymer brushes are desired, the "grafting from" method is the most straightforward and applicable approach, in part due to the commercial availability of functionalized monomers that can be readily derivatized with relevant initiating sites [201]. As the CP backbone is polymerized prior to grafting, this ensures that CP polymerization is not sterically hindered by the polymer brushes. Thus, this method allows for longer and denser brushes compared to "grafting through" approaches, with a greater likelihood of achieving a true dense bottle brush conformation [202]. Grafting from a functional backbone (macroinitiator) can be initiated by a range of chain-growth polymerization mechanisms, including near-UV-light-induced polymerization, ATRP, and RAFT [164, 170]. "Grafting from" a surface is readily achievable, with surface-initiated CRP methods being well-established [47], and provided that the backbone is soluble, similar approaches can be used to produce molecular brushes in solution by grafting from a polymeric macroinitiator. It is worth noting however, that the solubility of CPs is a well-known challenge, which somewhat hampers the solution "grafting from" technique.

Early examples of "grafting from" CPs utilized thermal and/or near-UV-light-induced grafting. While these approaches provide less control than CRP techniques, they have the advantage of not requiring specially functionalized macroinitiators when grafting from CPs. Acrylamide (AAm), 4-styrenesulfonic acid sodium salt (NaSS), and acrylic acid (AAc) were grafted from PAni in the form of emeraldine base (EM) films by near-UV-light-induced graft copolymerization [113]. This work provided proof-of-concept for the synthesis of materials that may be useful as electrodes or sensors, as the hydrophilic grafted polymers potentially allowed subsequent immobilization of proteins or enzymes. However,

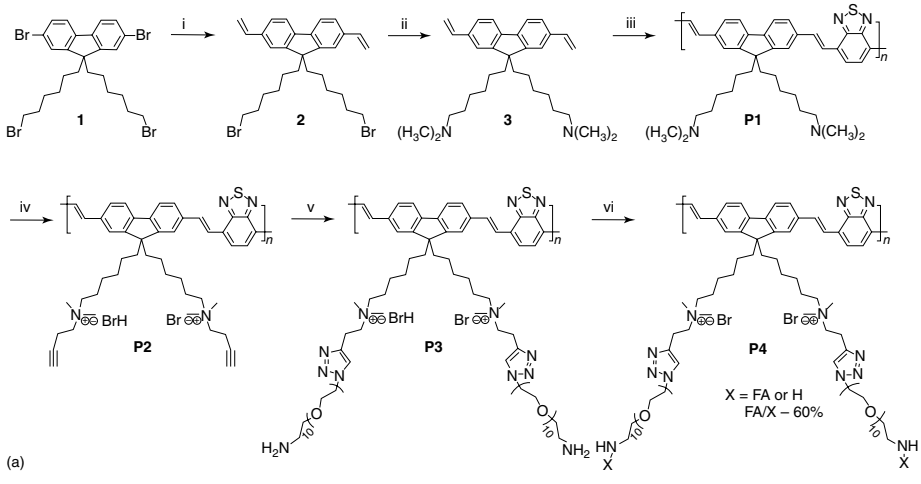

Figure 13.7 (a) Synthesis of densely grafted PEG from a conjugated polymer through click chemistry. The graft copolymer was further modified with folic acid to fabricate molecular brush based cellular probe (b, d). Fluorescence and (e, g) fluorescence/transmission overlapped images of MCF-7 cells stained by graft copolymers with and without folic acid modification. (c) Fluorescence and (f) fluorescence/transmission overlapped images of unstained MCF-7 cells. Strong fluorescence is shown for folic acid modified graft copolymer stained MCF-7 cells (d, g). (Reproduced with permission from Ref. [200]. Copyright 2010, John Wiley & Sons.)

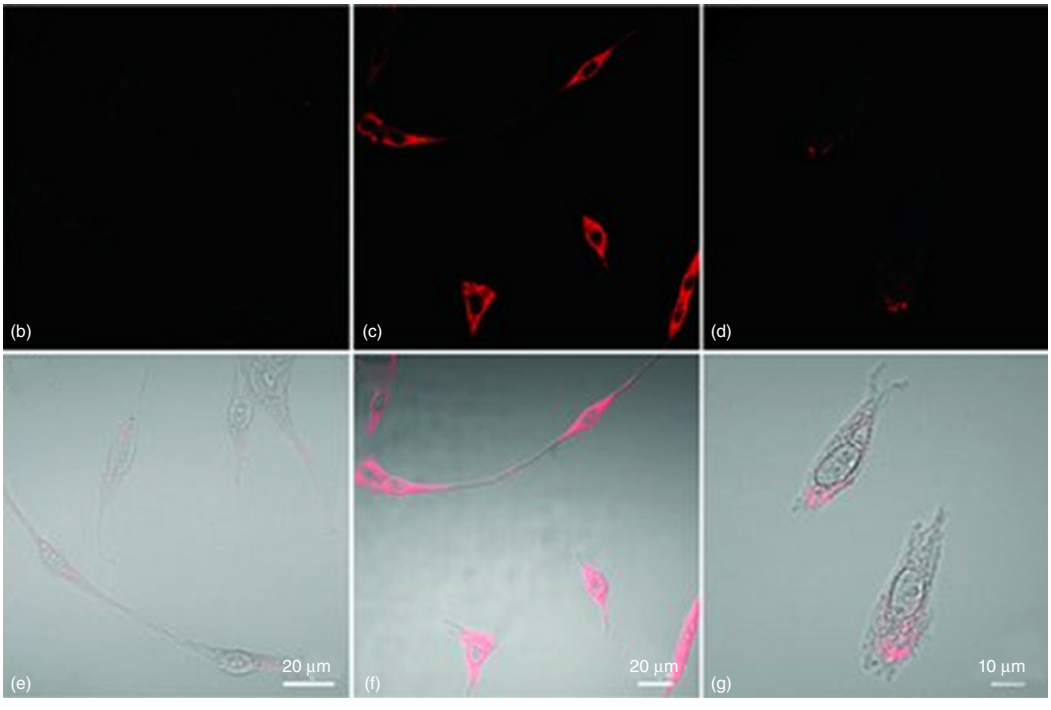

Figure 13.7 (*Continued*)

this polymerization approach yielded ungrafted homopolymer in solution as well as grafted brushes, due to the uncontrolled radical mechanism. The versatility of both thermal and near-UV-light-induced polymerization for surface-initiated grafting has also been demonstrated [203, 204]. PAni-*g*-PAAc is one example produced in this way, which is of particular importance to the field of biointerface as it can be used for immobilization of biomolecules; Kang *et al*. demonstrated covalent immobilization of collagen and of the enzyme glucose oxidase on this material [205]. Roux *et al*. extended this work and performed surface-initiated radical polymerization (SIRP) from an electropolymerized carboxylic acid-functionalized PPy film on a gold electrode [206]. A radical initiator (azo compound) was covalently immobilized at the carboxylic acid moieties, and grafting of PS was successfully performed. In this case, use of the azo-functionalized CP macroinitiator was motivated by the desire to avoid the thermal instability of thiol SAMs (which are often used as initiators for surface-initiated radical polymerization), but this work can be seen as a precursor to later work using surface-initiated controlled radical polymerization (SI-CRP) from appropriately functionalized macroinitiators.

Costanzo and Stokes were among the first to report the synthesis of a conjugated polymer with an attached ATRP initiator for subsequent grafting [90]. In their study, hydroxyl-functionalized PTh was modified with an ATRP initiator. They estimated that this procedure led to functionalization of 86% of the backbone, from which they were able to graft short poly(methyl acrylate) brushes with low polydispersities and predictable molecular weights (MWs). In a similar study, Massoumi *et al*. attached initiating groups to polyaniline (PAani) post-polymerization, which were used to graft PMMA brushes [207]. The grafted brushes improved solubility in polar solvents, and the grafted polymer showed defined electroactivity in aqueous H_2SO_4 – both of which are important, as many bioapplications require aqueous conditions. Several other examples demonstrate ATRP from both PTh and PPy films [40, 145, 208]. Grafted brushes can also control biodegradation in physiological conditions; for example, Domagala *et al*. reported that grafting short biocompatible oligo(3-hydroxybutryate) chains increased the rate of degradation of solubilized PPy backbones in phosphate buffered saline (PBS) [209].

To perform the "grafting from" ATRP described above, a CP-based ATRP macroinitiator is needed. CP-based macroinitiators functionalized with bromoester initiating sites are readily obtained by the facile esterification of commercially available hydroxyl-functionalized precursors, using dibromoesters such as 2-bromopropionyl bromide or 2-bromoisobutyryl bromide. Other halogen functionalities can also be used as macroinitiators, but it is important to note that the efficiency of the initiator in ATRP is highly dependent on its structure [210, 211]. Much of the work on this approach has focused on the design and synthesis of CP-based (SI-)ATRP macroinitiators [43, 44, 95, 130, 150, 208]. For example, Chams *et al*. successfully grafted poly(dimethylaminoethyl methacrylate) brushes via SI-ARTP from a CP film. This was done by first synthesizing a dithienylpyrrole-based ATRP initiator, which was electropolymerized at a low oxidation potential to yield a thin film macroinitiatior [212]. In another example, we prepared PTh-*g*PS and PTh-*g*-(PS-*b*-PAA) graft copolymers by

ATRP both in solution and by surface-initiated grafting. The precursor in these cases was a terthiophene monomer functionalized with a bromoester initiating site (BrTTh); the purpose of the termonomer was to provide spacing between initiating sites, and allow better control over brush density. The monomer was either polymerized in solution by oxidative chemical polymerization, or electropolymerized on to a conductive substrate, followed by grafting of homopolymer or diblock polymer brushes [208]. In this case, copolymers synthesized in solution could be deposited as thin films, and both solution-polymerized and surface-grafted brushes were electroactive provided that grafting times were short (~1 h or less). If CPs are to be used as electroactive materials in a biological environment, it is a prerequisite they are electroactive in aqueous environments; however, PTh generally displays poor electroactivity in aqueous conditions, in contrast to poly(pyrrole) [213]. Thus, in order to combine the ease of functionalization of thiophenes with the aqueous electroactivity of pyrrole, we synthesized a new bromoester-functionalized termonomer, 2-(2,5-di(pyrrol-2-yl) thiophen-3-yl)ethyl 2-bromopropanoate) (PyThon). This termonomer was readily electropolymerized onto gold electrodes, and polystyrene (PS), poly(2,3,4,5,6-pentafluorostryene (PPFS), and poly(ethylene glycol) methyl ether acrylate (PEGMA) brushes were all grafted from the film via SI-ATRP [43].

To explore a more readily available CP-precursor for ATRP, we also reported the simple one-step synthesis of (3,4-ethylenedioxythiophene)methyl 2-bromopropanoate (BrEDOT) monomer [150]. After electropolymerization, *t*BA brushes were grafted by ATRP, followed by acid hydrolysis to give charged PAA brushes. Surface plasmon resonance and cyclic voltammetry measurements demonstrated the pH-responsiveness of the PAA brushes, which in turn led to changes in electrochemical behavior when switching between acidic and basic solutions. The improved electrochemistry in this case was attributed both to an improved solubility in the charged state and to a self-doping effect. However, an inherent issue of using the pH responsive brushes in biointerfaces is the sensitivity of biological systems to pH variations. Thus, we used the same PBrEDOT substrates as a backbone to graft brushes using thermoresponsive PEGMMA macromonomers, with the motivation that these brushes would be stimuli-responsive within conditions compatible with biological systems [95]. The swollen brushes were demonstrated to be protein-rejecting and also cell-repelling, with the extent of protein/cell rejection dependent on the length of the PEG chains in the macromonomer.

One drawback of the surface-initiated "grafting from" synthesis of CP-based brushes/graft copolymers is the inherent difficulty in confirming controlled grafting. For surface-confined polymer brushes, increased brush thickness as grafting progresses is often used as a proxy [185, 215, 216]. Unfortunately, brush thickness is generally measured either by ellipsometry or by profilometry, which tend to give unreliable results for CP-based brushes due to their light absorptive properties and roughness respectively. One alternative is to use neutron or X-ray reflectivity to identify brush thickness, provided there is significant scattering contrast between the brush layer and the CP backbone [217, 218]. However, these techniques obviously may not be feasible for routine

sample analysis. Another option is to add a dissolved sacrificial initiator with a similar structure to that of the macroinitiator during the grafting reaction. GPC of the dissolved polymer then provides a proxy for the analysis of the grafted polymer. However, it must be noted that the presence of a sacrificial initiator will affect the kinetics of the reaction to the point where sacrificial initiator is sometimes used with the explicit purpose of improving control over polymerization in SI-ATRP [219].

Aside from ATRP, surface-initiated reversible addition–fragmentation chain-transfer (SI-RAFT) polymerization has also been used to prepare a range of CP-based graft copolymer brushes. RAFT works in a similar manner to ATRP, in that it is a controlled radical polymerization technique. However, in the case of SI-RAFT, grafting occurs not from an initiator on the CP backbone, but a "chain transfer agent" (CTA), which facilitates chain transfer between active and dormant states of polymer growth. Grande *et al*. developed a new electropolymerizable RAFT chain transfer agent containing thiophene, 2-(thiophen-3-yl)ethyl 4-cyano-4-(phenylcarbonothioylthio) pentanoate (Cbz-CTA), which could be electrocopolymerized with 9*H*-carbazole [220]. The resulting film was used to graft PS-*b*-PtBA block copolymer side chains. The same research group also designed a thiobenzoate-functionalized terthiophene macro-CTA, 2-(thiophen-3-yl)ethyl 4-cyano-4-(phenylcarbonothioylthio)pentanoate 2-(2,5-di(thiophen-2-yl)thiophen-3-yl)ethanol [42]. After electropolymerization, these films were used to graft a range of homopolymers (PMMA, P*t*BA, and poly(carbazole ethyl methacrylate) (PCzEMA)) and diblock copolymers (PMMA-*b*-PPFS and PMMA-*b*-PS). This study demonstrated that a range of macromolecular architectures and surface chemistries could be achieved using this technique. The electrodeposited macro-CTA approach has also been extended to graft patterned binary polymer brushes. First, the macro-CTA was electropolymerized onto a patterned conducting substrate, followed by PS grafting. The nonelectropatterned segments of the surface were then backfilled with an ATRP initiator tethered to the substrate via silanization, and PNIPAM was grafted via SI-ATRP [221]. This dual functionalization approach can be used to pattern biomolecules, cells, or tissues on the substrate – for instance, backfilling with a protein-repellent polymer brush can guide cells to grow solely in the electrically active regions (Figure 13.8).

For the abovementioned SI-RAFT approaches, the CTA is immobilized on the CP backbone via the CTA's "R-group," and therefore the CTA necessarily detaches and reattaches to the surface-immobilized CP/propagating graft copolymer during grafting (Figure 13.9). This may lead to bimolecular termination at an unusually high rate. It will also result in unbound polymer being synthesized in solution during the grafting process [47]. It is also possible to conduct SI-RAFT with the CTA attached to the surface by the Z-group, resulting in a "grafting to" mechanism, or else with a surface-tethered conventional free radical initiator with the CTA in solution [47]. However, to our knowledge, neither of these approaches has yet been used to graft from CPs. These methods also produce ungrafted polymer, which can be advantageous for characterizing the grafted polymer by proxy, but may be undesirably wasteful for large-scale applications.

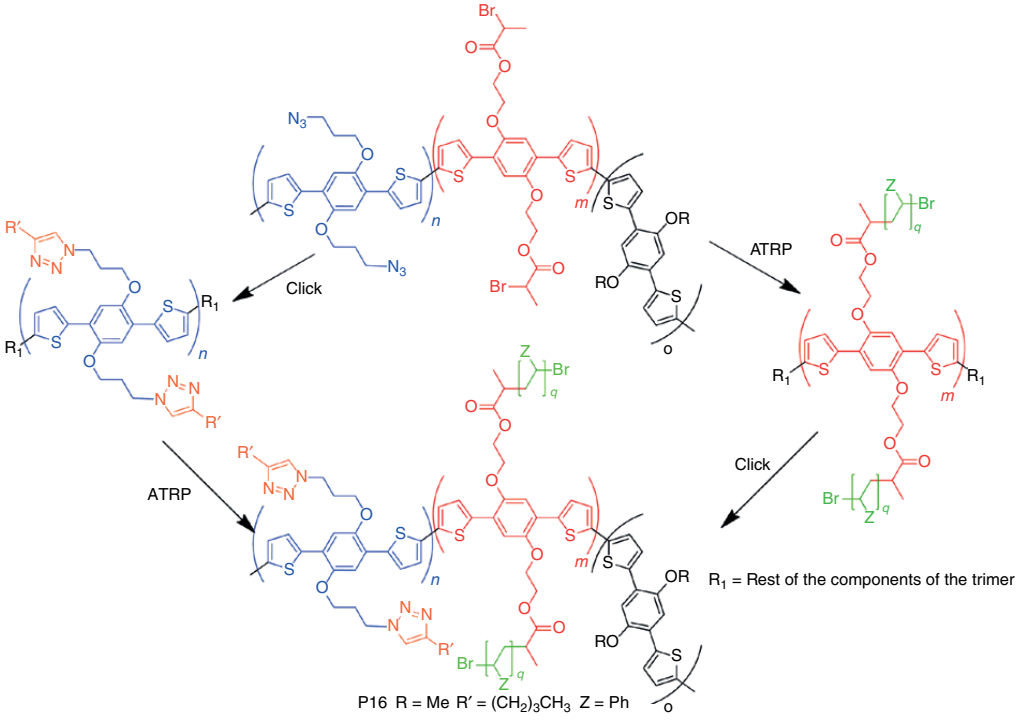

Figure 13.8 Reaction scheme showing the interchangeable functionalization of CPs through "grafting from" ATRP as well as "grafting to" "click" reactions. (Reproduced with permission from Ref. [214]. Copyright 2015, Royal Society of Chemistry.)

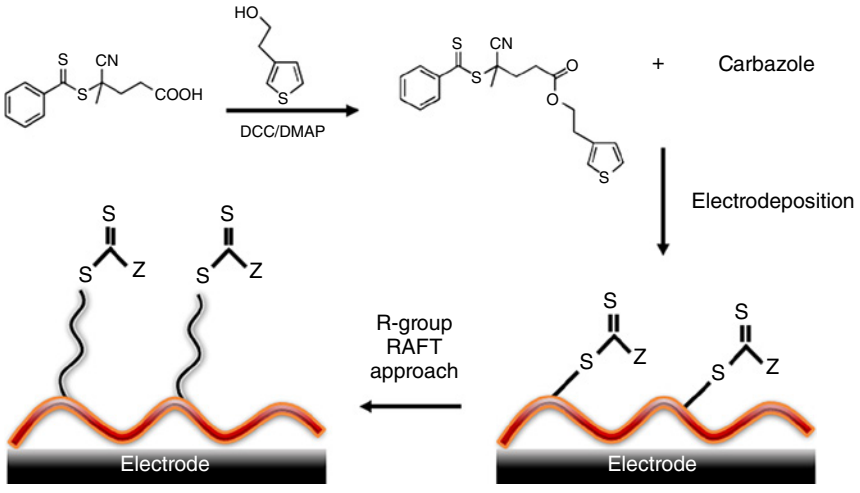

Figure 13.9 General scheme showing the electrodeposition of CTA-containing thiophene monomer and carbazole, where polymer brushes can be grown through R-group RAFT approach.

13.5 Conclusions and Outlook

Since the early days of polymer electronics, functionalization of conjugated polymers has been important to improve the chemical, physical, and optoelectrical properties to tailor the CPs for applications in polymer electronics thin film devices. Suitable functionalization also extends the utility of CP-based materials to other applications, particularly in bioelectronics, with notable examples being biocompatible electrodes and neural probes, biosensors, implantable devices, and tissue engineering.

An interesting and versatile extension of traditional chemical functionalization of CPs is grafting of the conjugated polymers with "conventional" polymeric side chains, opening routes to new "hybrid" materials with dual (or multiple) designed characteristics. Using this method, graft copolymers that are stimuli-responsive and conductive (that may be utilized in both solutions and in thin films) or surfaces that are conductive and antifouling can be easily prepared. The grafted polymeric side chains can be chosen to offer functionalities for adding further functional moieties; for example, adding a specific cell binding motif to a conductive and antifouling surface for tissue engineering applications. Therefore, the design and synthesis of polymer-grafted CPs present a versatile route to advanced multifunctional materials for uses in bioelectronics. However, to date, limited work has been done in this research field, leaving this class of materials wide open for exploration.

An important consequence of grafting of polymeric side chains onto CPs is to make CPs, soluble and therefore solution processable. Another significant consequence is that the mechanical properties of CPs are changed – an attractive prospect in designing biointerfaces based on CPs, as cells can respond to mechanical changes in their environment.

As discussed throughout this chapter, a wide range of approaches and techniques are available for the synthesis of polymer-grafted CPs. Which of these approaches and methodologies to choose will depend on the desired properties of the final material, and is directed by limitations of the synthesis parameters. For example, diverse structures and chemistries may be obtained by applying the "grafting through" approach. The synthesis and end-functionalization of macromonomers in that approach relies on a range of polymerization techniques already well developed in the context of conventional polymerizations. Using CRP techniques, well-defined side chains can be obtained; however, complex chemistry may be required to synthesize appropriately functionalized macromonomers. A possible obstacle here in achieving a good control over the macromolecular architecture is that dense grafting may be sterically hindered by bulky side chains, particularly if the polymerization is conducted from a surface. Thus, while "grafting through" methodology may have some disadvantages in preparing CP-based graft copolymers, it offers a valuable approach for engineering complex chemistries that may not be accessible by other routes. The "grafting to" technique suffers similar difficulties in obtaining densely grafted chains; however, the relative simplicity of click chemistry available lends itself to "grafting to" synthesis, making this an attractive approach. If densely grafted copolymer brushes are desired, the "grafting from" method may provide the most straightforward and easily applicable approach of the three approaches discussed.

With regard to the practical applications of the polymer-grafted CP-based copolymer, the presence of brushes seems to be particularly well suited in stimuli-responsive materials, with multiple mechanisms available for exploitation. In addition, CP backbones can be chemically or electrochemically oxidized/reduced, providing stimuli-responsive materials attractive for smart biointerfaces, where surface wettability, the fouling nature of the surface, and electrical conductivity may be dynamically controlled. As discussed earlier, polymer-grafted CPs offer interesting opportunities in the development of CP-based biosensors. It is expected that the number of studies that exploit grafting of polymers onto CPs for biosensing will increase in the near future as the methodology is explored more widely, the materials obtained are more fully characterized, and the effect of grafting on the optoelectronic properties of CPs are better understood. The utilization of CP sensors *in vivo*, where fouling/encapsulation is a significant issue, would particularly benefit from CPs that have been functionalized with both probes and antifouling chains. This need is expected to facilitate such developments. However, from all of the possible bioelectronics applications of the grafted CPs, tissue engineering appears to be the most exciting as cell tissue substrates can be made functional, specific, and electrically conducting.

It is, however, important to recognize that the electrical conductivity of such grafted CPs may be compromised and complicated by the addition of the polymeric grafts. Interestingly, some of the recent studies suggest some good synergetic properties of the grafted chains and CP electroactivity, where the chains improve solvation of the CPs. This is particularly important for more hydrophobic CPs when used in aqueous media – as is the case in biomedical applications.

References

1 Jaymand, M., Hatamzadeh, M., and Omidi, Y. (2015) Modification of polythiophene by the incorporation of processable polymeric chains: recent progress in synthesis and applications. *Prog. Polym. Sci.*, **47**, 26–69.
2 Olsen, B.D. and Segalman, R.A. (2008) Self-assembly of rod-coil block copolymers. *Mater. Sci. Eng., R*, **62**, 37–66.
3 Günes, S., Neugebauer, H., and Sariciftci, N.S. (2007) Conjugated polymer-based organic solar cells. *Chem. Rev.*, **107**, 1324–1338.
4 Savagatrup, S., Printz, A.D., Rodriquez, D., and Lipomi, D.J. (2014) Best of both worlds: conjugated polymers exhibiting good photovoltaic behavior and high tensile elasticity. *Macromolecules*, **47**, 1981–1992.
5 Takagi, K., Nagase, T., Kobayashi, T., and Naito, H. (2014) High performance top-gate field-effect transistors based on poly(3-alkylthiophenes) with different alkyl chain lengths. *Org. Electron.*, **15**, 372–377.
6 Brown, P.J., Thomas, D.S., Köhler, A., Wilson, J.S., Kim, J.-S., Ramsdale, C.M., Sirringhaus, H., and Friend, R.H. (2003) Effect of interchain interactions on the absorption and emission of poly(3-hexylthiophene). *Phys. Rev. B*, **67**, 064203.
7 Ho, V., Boudouris, B.W., and Segalman, R.A. (2010) Tuning polythiophene crystallization through systematic side chain functionalization. *Macromolecules*, **43**, 7895–7899.
8 Strover, L.T., Malmström, J., and Travas-Sejdic, J. (2016) Graft copolymers with conducting polymer backbones: a versatile route to functional materials. *Chem. Rec.*, **16**, 393–418.
9 Rohman, G. (2014) *Materials Used in Biomaterial Applications*, John Wiley & Sons, Inc., Biomaterials, pp. 27–81.
10 Luo, S.C. (2013) Conducting polymers as biointerfaces and biomaterials: a perspective for a special issue of polymer reviews. *Polym. Rev.*, **53**, 303–310.
11 Lee, J.Y. (2013) Electrically conducting polymer-based nanofibrous scaffolds for tissue engineering applications. *Polym. Rev.*, **53**, 443–459.
12 Lin, P., Yan, F., Yu, J., Chan, H.L.W., and Yang, M. (2010) The application of organic electrochemical transistors in cell-based biosensors. *Adv. Mater.*, **22**, 3655–3660.
13 Molino, P.J. and Wallace, G.G. (2015) Next generation bioelectronics: advances in fabrication coupled with clever chemistries enable the effective integration of biomaterials and organic conductors. *APL Mater.*, **3**, 014913.
14 Oh, W.-K., Kwon, O.S., and Jang, J. (2013) Conducting polymer nanomaterials for biomedical applications: cellular interfacing and biosensing. *Polym. Rev.*, **53**, 407–442.
15 Strakosas, X., Bongo, M., and Owens, R.M. (2015) The organic electrochemical transistor for biological applications. *J. Appl. Polym. Sci.*, **132**.
16 Wallace, G. and Spinks, G. (2007) Conducting polymers – bridging the bionic interface. *Soft Matter*, **3**, 665–671.
17 George, P.M., LaVan, D.A., Burdick, J.A., Chen, C.Y., Liang, E., and Langer, R. (2006) Electrically controlled drug delivery from biotin-doped conductive polypyrrole. *Adv. Mater.*, **18**, 577–581.

18 Simon, D.T., Kurup, S., Larsson, K.C., Hori, R., Tybrandt, K., Goiny, M., Jager, E.W.H., Berggren, M., Canlon, B., and Richter-Dahlfors, A. (2009) Organic electronics for precise delivery of neurotransmitters to modulate mammalian sensory function. *Nat. Mater.*, **8**, 742–746.

19 Svirskis, D., Travas-Sejdic, J., Rodgers, A., and Garg, S. (2010) Electrochemically controlled drug delivery based on intrinsically conducting polymers. *J. Controlled Release*, **146**, 6–15.

20 Cole, M.A., Voelcker, N.H., Thissen, H., and Griesser, H.J. (2009) Stimuli-responsive interfaces and systems for the control of protein–surface and cell–surface interactions. *Biomaterials*, **30**, 1827–1850.

21 Mendes, P.M. (2008) Stimuli-responsive surfaces for bio-applications. *Chem. Soc. Rev.*, **37**, 2512–2529.

22 Stuart, M.A.C., Huck, W.T.S., Genzer, J., Muller, M., Ober, C., Stamm, M., Sukhorukov, G.B., Szleifer, I., Tsukruk, V.V., Urban, M., Winnik, F., Zauscher, S., Luzinov, I., and Minko, S. (2010) Emerging applications of stimuli-responsive polymer materials. *Nat. Mater.*, **9**, 101–113.

23 Wei, M., Gao, Y., Li, X., and Serpe, M.J. (2017) Stimuli-responsive polymers and their applications. *Polym. Chem.*, **8**, 127–143.

24 Asplund, M., Thaning, E., Lundberg, J., Sandberg-Nordqvist, A.C., Kostyszyn, B., Inganas, O., and von Holst, H. (2009) Toxicity evaluation of PEDOT/biomolecular composites intended for neural communication electrodes. *Biomed. Mater.*, **4**, 12.

25 Asplund, M., von Holst, H., and Inganäs, O. (2008) Composite biomolecule/PEDOT materials for neural electrodes. *Biointerphases*, **3**, 83–93.

26 Isaksson, J., Kjäll, P., Nilsson, D., Robinson, N., Berggren, M., and Richter-Dahlfors, A. (2007) Electronic control of Ca^{2+} signalling in neuronal cells using an organic electronic ion pump. *Nat. Mater.*, **6**, 673–679.

27 Kim, S.Y., Kim, K.-M., Hoffman-Kim, D., Song, H.-K., and Palmore, G.T.R. (2011) Quantitative control of neuron adhesion at a neural interface using a conducting polymer composite with low electrical impedance. *ACS Appl. Mater. Interfaces*, **3**, 16–21.

28 Lee, J.Y., Bashur, C.A., Goldstein, A.S., and Schmidt, C.E. (2009) Polypyrrole-coated electrospun PLGA nanofibers for neural tissue applications. *Biomaterials*, **30**, 4325–4335.

29 Moulton, S.E., Higgins, M.J., Kapsa, R.M.I., and Wallace, G.G. (2012) Organic bionics: a new dimension in neural communications. *Adv. Funct. Mater.*, **22**, 2003–2014.

30 Yang, S.Y., Kim, B.N., Zakhidov, A.A., Taylor, P.G., Lee, J.K., Ober, C.K., Lindau, M., and Malliaras, G.G. (2011) Detection of transmitter release from single living cells using conducting polymer microelectrodes. *Adv. Mater.*, **23**, H184–H188.

31 Yoshida Kozai, T.D., Langhals, N.B., Patel, P.R., Deng, X., Zhang, H., Smith, K.L., Lahann, J., Kotov, N.A., and Kipke, D.R. (2012) Ultrasmall implantable composite microelectrodes with bioactive surfaces for chronic neural interfaces. *Nat. Mater.*, **11**, 1065–1073.

32 Discher, D.E., Janmey, P., and Wang, Y.-L. (2005) Tissue cells feel and respond to the stiffness of their substrate. *Science*, **310**, 1139–1143.

33 Gautrot, J.E., Malmström, J., Sundh, M., Margadant, C., Sonnenberg, A., and Sutherland, D.S. (2014) The nanoscale geometrical maturation of focal adhesions controls stem cell differentiation and mechanotransduction. *Nano Lett.*, **14**, 3945–3952.

34 Drury, J.L. and Mooney, D.J. (2003) Hydrogels for tissue engineering: scaffold design variables and applications. *Biomaterials*, **24**, 4337–4351.

35 Hollister, S.J. (2005) Porous scaffold design for tissue engineering. *Nat. Mater.*, **4**, 518–524.

36 Malmström, J., Lovmand, J., Kristensen, S., Sundh, M., Duch, M., and Sutherland, D.S. (2011) Focal complex maturation and bridging on 200 nm vitronectin but Not fibronectin patches reveal different mechanisms of focal adhesion formation. *Nano Lett.*, **11**, 2264–2271.

37 Arnold, M., Cavalcanti-Adam, E.A., Glass, R., Blümmel, J., Eck, W., Kantlehner, M., Kessler, H., and Spatz, J.P. (2004) Activation of integrin function by nanopatterned adhesive interfaces. *ChemPhysChem*, **5**, 383–388.

38 Missirlis, D. and Spatz, J.P. (2014) Combined effects of PEG hydrogel elasticity and cell-adhesive coating on fibroblast adhesion and persistent migration. *Biomacromolecules*, **15**, 195–205.

39 Chen, C.S., Mrksich, M., Huang, S., Whitesides, G.M., and Ingber, D.E. (1997) Geometric control of cell life and death. *Science*, **276**, 1425–1428.

40 Lin, C.-H., Chou, W.-J., and Lee, J.-T. (2012) Three-dimensionally ordered macroporous nitroxide polymer brush electrodes prepared by surface-initiated atom transfer polymerization for organic radical batteries. *Macromol. Rapid Commun.*, **33**, 107–113.

41 Yagci, Y. and Toppare, L. (2003) Electroactive macromonomers based on pyrrole and thiophene: a versatile route to conducting block and graft polymers. *Polym. Int.*, **52**, 1573–1578.

42 Grande, C.D., Tria, M.C., Jiang, G., Ponnapati, R., and Advincula, R. (2011) Surface-grafted polymers from electropolymerized polythiophene RAFT agent. *Macromolecules*, **44**, 966–975.

43 Strover, L.T., Malmström, J., Laita, O., Reynisson, J., Aydemir, N., Nieuwoudt, M.K., Williams, D.E., Dunbar, P.R., Brimble, M.A., and Travas-Sejdic, J. (2013) A new precursor for conducting polymer-based brush interfaces with electroactivity in aqueous solution. *Polymer*, **54**, 1305–1317.

44 Pei, Y., Travas-Sejdic, J., and Williams, D.E. (2012) Reversible electrochemical switching of polymer brushes grafted onto conducting polymer films. *Langmuir*, **28**, 8072–8083.

45 Zhao, B. and Brittain, W.J. (2000) Polymer brushes: surface-immobilized macromolecules. *Prog. Polym. Sci.*, **25**, 677–710.

46 Halperin, A., Tirrell, M., and Lodge, T.P. (1992) Tethered chains in polymer microstructures, in *Macromolecules: Synthesis, Order and Advanced Properties*, Springer Berlin Heidelberg, Berlin, Heidelberg, pp. 31–71.

47 Barbey, R., Lavanant, L., Paripovic, D., Schüwer, N., Sugnaux, C., Tugulu, S., and Klok, H.-A. (2009) Polymer brushes via surface-initiated controlled radical polymerization: synthesis, characterization, properties, and applications. *Chem. Rev.*, **109**, 5437–5527.

48 Edmondson, S., Osborne, V.L., and Huck, W.T.S. (2004) Polymer brushes via surface-initiated polymerizations. *Chem. Soc. Rev.*, **33**, 14–22.

49 Bhattacharya, A. and Misra, B.N. (2004) Grafting: a versatile means to modify polymers: techniques, factors and applications. *Prog. Polym. Sci.*, **29**, 767–814.

50 Boyes, S.G., Granville, A.M., Baum, M., Akgun, B., Mirous, B.K., and Brittain, W.J. (2004) Polymer brushes – surface immobilized polymers. *Surf. Sci.*, **570**, 1–12.

51 Kato, K., Uchida, E., Kang, E.-T., Uyama, Y., and Ikada, Y. (2003) Polymer surface with graft chains. *Prog. Polym. Sci.*, **28**, 209–259.

52 Liu, X., Gilmore, K.J., Moulton, S.E., and Wallace, G.G. (2009) Electrical stimulation promotes nerve cell differentiation on polypyrrole/poly (2-methoxy-5 aniline sulfonic acid) composites. *J. Neural Eng.*, **6**, 065002.

53 Gelmi, A., Higgins, M.J., and Wallace, G.G. (2010) Physical surface and electromechanical properties of doped polypyrrole biomaterials. *Biomaterials*, **31**, 1974–1983.

54 Gilmore, K.J., Kita, M., Han, Y., Gelmi, A., Higgins, M.J., Moulton, S.E., Clark, G.M., Kapsa, R., and Wallace, G.G. (2009) Skeletal muscle cell proliferation and differentiation on polypyrrole substrates doped with extracellular matrix components. *Biomaterials*, **30**, 5292–5304.

55 Harman, D.G., Gorkin, R., Stevens, L., Thompson, B., Wagner, K., Weng, B., Chung, J.H.Y., In Het Panhuis, M., and Wallace, G.G. (2015) Poly(3,4-ethylenedioxythiophene):dextran sulfate (PEDOT:DS) – a highly processable conductive organic biopolymer. *Acta Biomater.*, **14**, 33–42.

56 Collier, J.H., Camp, J.P., Hudson, T.W., and Schmidt, C.E. (2000) Synthesis and characterization of polypyrrole–hyaluronic acid composite biomaterials for tissue engineering applications. *J. Biomed. Mater. Res.*, **50**, 574–584.

57 Stewart, E.M., Liu, X., Clark, G.M., Kapsa, R.M.I., and Wallace, G.G. (2012) Inhibition of smooth muscle cell adhesion and proliferation on heparin-doped polypyrrole. *Acta Biomater.*, **8**, 194–200.

58 Yuan, G.L. and Kuramoto, N. (2003) Synthesis and chiroptical properties of optically active poly(*N*-alkylanilines) doped and intertwined with dextran sulfate in aqueous solution. *Macromolecules*, **36**, 7939–7945.

59 Green, R.A., Lovell, N.H., and Poole-Warren, L.A. (2010) Impact of co-incorporating laminin peptide dopants and neurotrophic growth factors on conducting polymer properties. *Acta Biomater.*, **6**, 63–71.

60 Thompson, B.C., Moulton, S.E., Ding, J., Richardson, R., Cameron, A., O'Leary, S., Wallace, G.G., and Clark, G.M. (2006) Optimising the incorporation and release of a neurotrophic factor using conducting polypyrrole. *J. Controlled Release*, **116**, 285–294.

61 Richardson, R.T., Thompson, B., Moulton, S., Newbold, C., Lum, M.G., Cameron, A., Wallace, G., Kapsa, R., Clark, G., and O'Leary, S. (2007) The effect of polypyrrole with incorporated neurotrophin-3 on the promotion of neurite outgrowth from auditory neurons. *Biomaterials*, **28**, 513–523.

62 Stauffer, W.R. and Cui, X.T. (2006) Polypyrrole doped with 2 peptide sequences from laminin. *Biomaterials*, **27**, 2405–2413.

63 Zhang, L., Stauffer, W.R., Jane, E.P., Sammak, P.J., and Cui, X.T. (2010) Enhanced differentiation of embryonic and neural stem cells to neuronal fates on laminin peptides doped polypyrrole. *Macromol. Biosci.*, **10**, 1456–1464.

64 Sanghvi, A.B., Miller, K.P.H., Belcher, A.M., and Schmidt, C.E. (2005) Biomaterials functionalization using a novel peptide that selectively binds to a conducting polymer. *Nat. Mater.*, **4**, 496–502.

65 De Giglio, E., Sabbatini, L., Colucci, S., and Zambonin, G. (2000) Synthesis, analytical characterization, and osteoblast adhesion properties on RGD-grafted polypyrrole coatings on titanium substrates. *J. Biomater. Sci., Polym. Ed.*, **11**, 1073–1083.

66 De Giglio, E., Sabbatini, L., and Zambonin, P.G. (1999) Development and analytical characterization of cysteine-grafted polypyrrole films electrosynthesized on Pt- and Ti-substrates as precursors of bioactive interfaces. *J. Biomater. Sci., Polym. Ed.*, **10**, 845–858.

67 Malmström, J., Hackett, A.J., Feisst, V., and Travas-Sejdic, J. (2017) Modulation of cell adhesion to conductive polymers. *Int. J. Nanotechnol.*, **14**, 235–250.

68 Molino, P.J., Higgins, M.J., Innis, P.C., Kapsa, R.M.I., and Wallace, G.G. (2012) Fibronectin and bovine serum albumin adsorption and conformational dynamics on inherently conducting polymers: a QCM-D study. *Langmuir*, **28**, 8433–8445.

69 Liu, X., Yue, Z., Higgins, M.J., and Wallace, G.G. (2011) Conducting polymers with immobilised fibrillar collagen for enhanced neural interfacing. *Biomaterials*, **32**, 7309–7317.

70 Maione, S., Gil, A.M., Fabregat, G., Del Valle, L.J., Triguero, J., Laurent, A., Jacquemin, D., Estrany, F., Jiménez, A.I., Zanuy, D., Cativiela, C., and Alemán, C. (2015) Electroactive polymer-peptide conjugates for adhesive biointerfaces. *Biomater. Sci.*, **3**, 1395–1405.

71 Kaur, G., Adhikari, R., Cass, P., Bown, M., and Gunatillake, P. (2015) Electrically conductive polymers and composites for biomedical applications. *RSC Adv.*, **5**, 37553–37567.

72 Khan, S. and Narula, A.K. (2016) Bio-hybrid blended transparent and conductive films PEDOT:PSS:Chitosan exhibiting electro-active and antibacterial properties. *Eur. Polym. J.*, **81**, 161–172.

73 Baek, P., Aydemir, N., Chaudhary, O.J., Wai Chi Chan, E., Malmstrom, J., Giffney, T., Khadka, R., Barker, D., and Travas-Sejdic, J. (2016) Polymer electronic composites that heal by solvent vapour. *RSC Adv.*, **6**, 98466–98474.

74 Hansen, T.S., West, K., Hassager, O., and Larsen, N.B. (2007) Highly stretchable and conductive polymer material made from poly(3,4-ethylenedioxythiophene) and polyurethane elastomers. *Adv. Funct. Mater.*, **17**, 3069–3073.

75 Noh, J.-S. (2014) Highly conductive and stretchable poly(dimethylsiloxane):poly(3,4-ethylenedioxythiophene):poly(styrene sulfonic acid) blends for organic interconnects. *RSC Adv.*, **4**, 1857–1863.

76 Lee, S., Jeon, H., Jang, M., Baek, K.-Y., and Yang, H. (2015) Tunable solubility parameter of poly(3-hexyl thiophene) with hydrophobic side-chains to achieve rubbery conjugated films. *ACS Appl. Mater. Interfaces*, **7**, 1290–1297.

77 Su, G.M., Lim, E., Jacobs, A.R., Kramer, E.J., and Chabinyc, M.L. (2014) Polymer side chain modification alters phase separation in ferroelectric-semiconductor polymer blends for organic memory. *ACS Macro Lett.*, **3**, 1244–1248.

78 Zhang, G., Yang, H., He, L., Hu, L., Lan, S., Li, F., Chen, H., and Guo, T. (2016) Importance of domain purity in semi-conducting polymer/insulating polymer blends transistors. *J. Polym. Sci., Part B: Polym. Phys.*, **54**, 1760–1766.

79 Mangione, M.I., Spanevello, R.A., Rumbero, A., Heredia, D., Marzari, G., Fernandez, L., Otero, L., and Fungo, F. (2013) Electrogenerated conductive polymers from triphenylamine end-capped dendrimers. *Macromolecules*, **46**,4754–4763.

80 Lohwasser, R.H. and Thelakkat, M. (2012) Synthesis of amphiphilic rod-coil P3HT-b-P4VP carrying a long conjugated block using NMRP and click chemistry. *Macromolecules*, **45**, 3070–3077.

81 Bidez, P.R., Li, S., MacDiarmid, A.G., Venancio, E.C., Wei, Y., and Lelkes, P.I. (2006) Polyaniline, an electroactive polymer, supports adhesion and proliferation of cardiac myoblasts. *J. Biomater. Sci., Polym. Ed.*, **17**, 199–212.

82 Ghasemi-Mobarakeh, L., Prabhakaran, M.P., Morshed, M., Nasr-Esfahani, M.H., Baharvand, H., Kiani, S., Al-Deyab, S.S., and Ramakrishna, S. (2011) Application of conductive polymers, scaffolds and electrical stimulation for nerve tissue engineering. *J. Tissue Eng. Regener. Med.*, **5**, e17–e35.

83 Balint, R., Cassidy, N.J., and Cartmell, S.H. (2014) Conductive polymers: towards a smart biomaterial for tissue engineering. *Acta Biomater.*, **10**, 2341–2353.

84 Ateh, D.D., Navsaria, H.A., and Vadgama, P. (2006) Polypyrrole-based conducting polymers and interactions with biological tissues. *J. Royal Soc. Interface*, **3**, 741–752.

85 Wong, J.Y., Langer, R., and Ingber, D.E. (1994) Electrically conducting polymers can noninvasively control the shape and growth of mammalian cells. *Proc. Natl. Acad. Sci. USA*, **91**, 3201–3204.

86 Humpolicek, P., Kasparkova, V., Saha, P., and Stejskal, J. (2012) Biocompatibility of polyaniline. *Synth. Met.*, **162**, 722–727.

87 Higgins, M.J. and Wallace, G.G. (2013) Surface and biomolecular forces of conducting polymers. *Polym. Rev.*, **53**, 506–526.

88 Green, R.A., Lovell, N.H., Wallace, G.G., and Poole-Warren, L.A. (2008) Conducting polymers for neural interfaces: challenges in developing an effective long-term implant. *Biomaterials*, **29**, 3393–3399.

89 Das, S., Samanta, S., Chatterjee, D.P., and Nandi, A.K. (2013) Thermosensitive water-soluble poly(ethylene glycol)-based polythiophene graft copolymers. *J. Polym. Sci., Part A: Polym. Chem.*, **51**, 1417–1427.

90 Costanzo, P.J. and Stokes, K.K. (2002) Synthesis and characterization of poly(methyl acrylate) grafted from poly(thiophene) to form solid-state fluorescent materials. *Macromolecules*, **35**, 6804–6810.

91 Mecerreyes, D., Pomposo, J.A., Bengoetxea, M., and Grande, H. (2000) Novel pyrrole end-functional macromonomers prepared by ring-opening and atom-transfer radical polymerizations. *Macromolecules*, **33**, 5846–5849.

92 Das, R.K., Gocheva, V., Hammink, R., Zouani, O.F., and Rowan, A.E. (2016) Stress-stiffening-mediated stem-cell commitment switch in soft responsive hydrogels. *Nat. Mater.*, **15**, 318–325.

93 Di Cio, S. and Gautrot, J.E. (2016) Cell sensing of physical properties at the nanoscale: mechanisms and control of cell adhesion and phenotype. *Acta Biomater.*, **30**, 26–48.

94 Maione, S., Fabregat, G., del Valle, L.J., Bendrea, A.-D., Cianga, L., Cianga, I., Estrany, F., and Alemán, C. (2015) Effect of the graft ratio on the properties of polythiophene-*g*-poly(ethylene glycol). *J. Polym. Sci., Part B: Polym. Phys.*, **53**, 239–252.

95 Hackett, A.J., Malmstrom, J., Molino, P.J., Gautrot, J.E., Zhang, H., Higgins, M.J., Wallace, G.G., Williams, D.E., and Travas-Sejdic, J. (2015) Conductive surfaces with dynamic switching in response to temperature and salt. *J. Mater. Chem. B*, **3**, 9285–9294.

96 Qin, Z., Chen, Y., Zhou, W., He, X., Bai, F., and Wan, M. (2008) Synthesis and properties of polymer brushes composed of poly(diphenylacetylene) main chain and poly(ethylene glycol) side chains. *Eur. Polym. J.*, **44**, 3732–3740.

97 Evans, R.A. (2007) The rise of AzideAlkyne 1,3-dipolar click cycloaddition and its application to polymer science and surface modification. *Aust. J. Chem.*, **60**, 384–395.

98 Banerjee, I., Pangule, R.C., and Kane, R.S. (2011) Antifouling coatings: recent developments in the design of surfaces that prevent fouling by proteins, bacteria, and marine organisms. *Adv. Mater.*, **23**, 690–718.

99 Molino, P.J., Zhang, B., Wallace, G.G., and Hanks, T.W. (2013) Surface modification of polypyrrole/biopolymer composites for controlled protein and cellular adhesion. *Biofouling*, **29**, 1155–1167.

100 Chen, Y., Kang, E.T., Neoh, K.G., Wang, P., and Tan, K.L. (2000) Surface modification of polyaniline film by grafting of poly(ethylene glycol) for reduction in protein adsorption and platelet adhesion. *Synth. Met.*, **110**, 47–55.

101 Zhao, H., Zhu, B., Luo, S.C., Lin, H.A., Nakao, A., Yamashita, Y., and Yu, H.H. (2013) Controlled protein absorption and cell adhesion on polymer-brush-grafted poly(3,4-ethylenedioxythiophene) films. *ACS Appl. Mater. Interfaces*, **5**, 4536–4543.

102 Drummond, T.G., Hill, M.G., and Barton, J.K. (2003) Electrochemical DNA sensors. *Nat. Biotech.*, **21**, 1192–1199.

103 Akbulut, H., Bozokalfa, G., Asker, D.N., Demir, B., Guler, E., Odaci Demirkol, D., Timur, S., and Yagci, Y. (2015) Polythiophene-g-poly(ethylene glycol) with lateral amino groups as a novel matrix for biosensor construction. *ACS Appl. Mater. Interfaces*, **7**, 20612–20622.

104 Turner, A., Karube, I., and Wilson, G.S. (1987) *Biosensors: Fundamentals and Applications*, Oxford University Press.

105 Aydemir, N., Malmstrom, J., and Travas-Sejdic, J. (2016) Conducting polymer based electrochemical biosensors. *Phys. Chem. Chem. Phys.*, **18**, 8264–8277.

106 Zhu, B., Hackett, A.J., and Travas-Sejdic, J. (2016) Biosensing applications based on conducting polymers, in *Encyclopedia of Polymer Science and Technology*, John Wiley & Sons, Inc..

107 Peng, H., Zhang, L., Soeller, C., and Travas-Sejdic, J. (2009) Conducting polymers for electrochemical DNA sensing. *Biomaterials*, **30**, 2132–2148.

108 Travas-Sejdic, J. and Srinivas, A. (2014) Optical gene detection using conjugated polymers, in *Optical Properties of Functional Polymers and Nano Engineering Applications*, CRC Press, pp. 61–86.

109 Damavandi, M., Baek, P., Pilkington, L.I., Javed Chaudhary, O., Burn, P., Travas-Sejdic, J., and Barker, D. (2017) Synthesis of grafted

poly(*p*-phenyleneethynylene) via ARGET ATRP: towards nonaggregating and photoluminescence materials. *Eur. Polym. J.*, **89**, 263–271.

110 Baek, P., Kerr-Phillips, T., Damavandi, M., Chaudhary, O.J., Malmstrom, J., Chan, E.W.C., Shaw, P., Burn, P., Barker, D., and Travas-Sejdic, J. (2016) Highly processable, rubbery poly(*n*-butyl acrylate) grafted poly(phenylene vinylene)s. *Eur. Polym. J.*, **84**, 355–365.

111 Akkahat, P. and Hoven, V.P. (2011) Introducing surface-tethered poly(acrylic acid) brushes as 3D functional thin film for biosensing applications. *Colloids Surf., B*, **86**, 198–205.

112 Akkahat, P., Kiatkamjornwong, S., Yusa, S.-i., Hoven, V.P., and Iwasaki, Y. (2012) Development of a novel antifouling platform for biosensing probe immobilization from methacryloyloxyethyl phosphorylcholine-containing copolymer brushes. *Langmuir*, **28**, 5872–5881.

113 Kang, E.T., Neoh, K.G., Tan, K.L., Uyama, Y., Morikawa, N., and Ikada, Y. (1992) Surface modifications of polyaniline films by graft copolymerization. *Macromolecules*, **25**, 1959–1965.

114 Santhiago, M. and Vieira, I.C. (2007) l-Cysteine determination in pharmaceutical formulations using a biosensor based on laccase from *Aspergillus oryzae*. *Sens. Actuators, B*, **128**, 279–285.

115 Gomes, S. and Rebelo, M. (2003) A new laccase biosensor for polyphenols determination. *Sensors*, **3**, 166.

116 Akbulut, H., Endo, T., Yamada, S., and Yagci, Y. (2015) Synthesis and characterization of polyphenylenes with polypeptide and poly(ethylene glycol) side chains. *J. Polym. Sci., Part A: Polym. Chem.*, **53**, 1785–1793.

117 Hardy, J.G., Sukhavasi, R.C., Aguilar, D., Villancio-Wolter, M.K., Mouser, D.J., Geissler, S.A., Nguy, L., Chow, J.K., Kaplan, D.L., and Schmidt, C.E. (2015) Electrical stimulation of human mesenchymal stem cells on biomineralized conducting polymers enhances their differentiation towards osteogenic outcomes. *J. Mater. Chem. B.*, **3**, 8059–8064.

118 Hardy, J.G., Amend, M.N., Geissler, S., Lynch, V.M., and Schmidt, C.E. (2015) Peptide-directed assembly of functional supramolecular polymers for biomedical applications: electroactive molecular tongue-twisters (oligoalanine–oligoaniline–oligoalanine) for electrochemically enhanced drug delivery. *J. Mater. Chem. B.*, **3**, 5005–5009.

119 Oyman, G., Geyik, C., Ayranci, R., AK, M., Odaci Demirkol, D., Timur, S., and Coskunol, H. (2014) Peptide-modified conducting polymer as a biofunctional surface: monitoring of cell adhesion and proliferation. *RSC Adv.*, **4**, 53411–53418.

120 Zhao, H., Zhu, B., Sekine, J., Luo, S.C., and Yu, H.H. (2012) Oligoethylene–glycol-functionalized polyoxythiophenes for cell engineering: syntheses, characterizations, and cell compatibilities. *ACS Appl. Mater. Interfaces*, **4**, 680–686.

121 Lowe, S., O'Brien-Simpson, N.M., and Connal, L.A. (2015) Antibiofouling polymer interfaces: poly(ethylene glycol) and other promising candidates. *Polym. Chem.*, **6**, 198–212.

122 Bendrea, A.-D., Fabregat, G., Cianga, L., Estrany, F., del Valle, L.J., Cianga, I., and Aleman, C. (2013) Hybrid materials consisting of an all-conjugated

polythiophene backbone and grafted hydrophilic poly(ethylene glycol) chains. *Polym. Chem.*, **4**, 2709–2723.

123 Bendrea, A.-D., Fabregat, G., Torras, J., Maione, S., Cianga, L., del Valle, L.J., Cianga, I., and Aleman, C. (2013) Polythiophene-*g*-poly(ethylene glycol) graft copolymers for electroactive scaffolds. *J. Mater. Chem. B*, **1**, 4135–4145.

124 Tang, Z., Akiyama, Y., and Okano, T. (2012) Temperature-responsive polymer modified surface for cell sheet engineering. *Polymers*, **4**, 1478.

125 Nash, M.E., Healy, D., Carroll, W.M., Elvira, C., and Rochev, Y.A. (2012) Cell and cell sheet recovery from pNIPAm coatings; motivation and history to present day approaches. *J. Mater. Chem.*, **22**, 19376–19389.

126 Chen, T., Ferris, R., Zhang, J., Ducker, R., and Zauscher, S. (2010) Stimulus-responsive polymer brushes on surfaces: transduction mechanisms and applications. *Prog. Polym. Sci.*, **35**, 94–112.

127 Chandrasekhar, P. (1999) *Conducting Polymers, Fundamentals and Applications: A Practical Approach*, Kluwer Academic, Boston.

128 Xu, L., Chen, W., Mulchandani, A., and Yan, Y. (2005) Reversible conversion of conducting polymer films from superhydrophobic to superhydrophilic. *Angew. Chem. Int. Ed.*, **44**, 6009–6012.

129 Isaksson, J., Robinson, N.D., and Berggren, M. (2006) Electronic modulation of an electrochemically induced wettability gradient to control water movement on a polyaniline surface. *Thin Solid Films*, **515**, 2003–2008.

130 Pei, Y., Travas-Sejdic, J., and Williams, D.E. (2012) Electrochemical switching of conformation of random polyampholyte brushes grafted onto polypyrrole. *Langmuir*, **28**, 13241–13248.

131 Peng, S. and Bhushan, B. (2012) Smart polymer brushes and their emerging applications. *RSC Adv.*, **2**, 8557–8578.

132 Liu, X., Ye, Q., Song, X., Zhu, Y., Cao, X., Liang, Y., and Zhou, F. (2011) Responsive wetting transition on superhydrophobic surfaces with sparsely grafted polymer brushes. *Soft Matter*, **7**, 515–523.

133 Shivapooja, P., Ista, L., Canavan, H., and Lopez, G. (2012) ARGET-ATRP synthesis and characterization of PNIPAAm brushes for quantitative cell detachment studies. *Biointerphases*, **7**, 1–9.

134 Li, C., Jin, J., Liu, J., Xu, X., and Yin, J. (2014) Stimuli-responsive polypropylene for the sustained delivery of TPGS and interaction with erythrocytes. *ACS Appl. Mater. Interfaces*, **6**, 13956–13967.

135 Krishnamoorthy, M., Hakobyan, S., Ramstedt, M., and Gautrot, J.E. (2014) Surface-initiated polymer brushes in the biomedical field: applications in membrane science, biosensing, cell culture, regenerative medicine and antibacterial coatings. *Chem. Rev.*, **114**, 10976–11026.

136 Kwon, O.H., Kikuchi, A., Yamato, M., Sakurai, Y., and Okano, T. (2000) Rapid cell sheet detachment from poly(*N*-isopropylacrylamide)-grafted porous cell culture membranes. *J. Biomed. Mater. Res.*, **50**, 82–89.

137 Balamurugan, S.S., Bantchev, G.B., Yang, Y., and McCarley, R.L. (2005) Highly water-soluble thermally responsive poly(thiophene)-based brushes. *Angew. Chem. Int. Ed.*, **44**, 4873–4876.

138 Maeda, K., Kamiya, N., and Yashima, E. (2004) Poly(phenylacetylene)s bearing a peptide pendant: helical conformational changes of the polymer backbone

stimulated by the pendant conformational change. *Chem. Eur. J.*, **10**, 4000–4010.

139 Choi, J., Ruiz, C.R., and Nesterov, E.E. (2010) Temperature-induced control of conformation and conjugation length in water-soluble fluorescent polythiophenes. *Macromolecules*, **43**, 1964–1974.

140 Sun, X.-L., He, W.-D., Li, J., He, N., Han, S.-C., and Li, L.-Y. (2008) Preparation of polypyrrole-*graft*-poly(*N*-isopropylacrylamide)/silver nanocomposites from pyrrolyl-capped macromonomer by $AgNO_3$ and their stimuli responsibility of light emission. *J. Polym. Sci., Part A: Polym. Chem.*, **46**, 6950–6960.

141 Nam, G., Purushothaman, B., Rangasamy, S., and Song, J.M. (2016) Investigating the versatility of multifunctional silver nanoparticles: preparation and inspection of their potential as wound treatment agents. *Int. Nano Lett.*, **6**, 51–63.

142 Lopez-Heras, M., Theodorou, I.G., Leo, B.F., Ryan, M.P., and Porter, A.E. (2015) Towards understanding the antibacterial activity of Ag nanoparticles: electron microscopy in the analysis of the materials-biology interface in the lung. *Environ. Sci.*, **2**, 312–326.

143 Becer, C.R., Hahn, S., Fijten, M.W.M., Thijs, H.M.L., Hoogenboom, R., and Schubert, U.S. (2008) Libraries of methacrylic acid and oligo(ethylene glycol) methacrylate copolymers with LCST behavior. *J. Polym. Sci., Part A: Polym. Chem.*, **46**, 7138–7147.

144 Luzon, M., Boyer, C., Peinado, C., Corrales, T., Whittaker, M., Tao, L., and Davis, T.P. (2010) Water-soluble, thermoresponsive, hyperbranched copolymers based on PEG-methacrylates: Synthesis, characterization, and LCST behavior. *J. Polym. Sci., Part A: Polym. Chem.*, **48**, 2783–2792.

145 Wang, M., Zou, S., Guerin, G., Shen, L., Deng, K., Jones, M., Walker, G.C., Scholes, G.D., and Winnik, M.A. (2008) A water-soluble pH-responsive molecular brush of poly(*N*,*N*-dimethylaminoethyl methacrylate) grafted polythiophene. *Macromolecules*, **41**, 6993–7002.

146 Saxena, S. and Jayakannan, M. (2016) Enzyme and pH dual responsive l-amino acid based biodegradable polymer nanocarrier for multidrug delivery to cancer cells. *J. Polym. Sci., Part A: Polym. Chem.*, **54**, 3279–3293.

147 Tian, K., Jia, X., Zhao, X., and Liu, P. (2016) pH/reductant dual-responsive core-cross-linked micelles via facile in situ ATRP for tumor-targeted delivery of anticancer drug with enhanced anticancer efficiency. *Mol. Pharmaceutics*, **13**, 2683–2690.

148 Kato, Y., Ozawa, S., Miyamoto, C., Maehata, Y., Suzuki, A., Maeda, T., and Baba, Y. (2013) Acidic extracellular microenvironment and cancer. *Cancer Cell Int.*, **13**, 89.

149 Plamper, F.A. (2015) Changing polymer solvation by electrochemical means: basics and applications, in *Porous Carbons – Hyperbranched Polymers–Polymer Solvation* (eds T.E. Long, B. Voit, and O. Okay), Springer International Publishing, Cham, pp. 125–212.

150 Malmström, J., Nieuwoudt, M.K., Strover, L.T., Hackett, A., Laita, O., Brimble, M.A., Williams, D.E., and Travas-Sejdic, J. (2013) Grafting from poly(3,4-ethylenedioxythiophene): a simple route to versatile electrically addressable surfaces. *Macromolecules*, **46**, 4955–4965.

151 Hammock, M.L., Chortos, A., Tee, B.C.K., Tok, J.B.H., and Bao, Z. (2013) 25th anniversary article: the evolution of electronic skin (E-skin): a brief history, design considerations, and recent progress. *Adv. Mater.*, **25**, 5997–6038.

152 Benight, S.J., Wang, C., Tok, J.B.H., and Bao, Z. (2013) Stretchable and self-healing polymers and devices for electronic skin. *Prog. Polym. Sci.*, **38**, 1961–1977.

153 Onorato, J., Pakhnyuk, V., and Luscombe, C.K. (2017) Structure and design of polymers for durable, stretchable organic electronics. *Polym. J.*, **49**, 41–60.

154 Rogers, J.A., Ghaffari, R., and Kim, D.-H. (2016) *Stretchable bioelectronics for medical devices and systems*, Springer.

155 Wu, D.Y., Meure, S., and Solomon, D. (2008) Self-healing polymeric materials: a review of recent developments. *Prog. Polym. Sci.*, **33**, 479–522.

156 Yang, Y. and Urban, M.W. (2013) Self-healing polymeric materials. *Chem. Soc. Rev.*, **42**, 7446–7467.

157 Li, C.-H., Wang, C., Keplinger, C., Zuo, J.-L., Jin, L., Sun, Y., Zheng, P., Cao, Y., Lissel, F., Linder, C., You, X.-Z., and Bao, Z. (2016) A highly stretchable autonomous self-healing elastomer. *Nat. Chem.*, **8**, 618–624.

158 Choi, S., Lee, H., Ghaffari, R., Hyeon, T., and Kim, D.-H. (2016) Recent advances in flexible and stretchable bio-electronic devices integrated with nanomaterials. *Adv. Mater.*, **28**, 4203–4218.

159 Hadasha, W. and Klumperman, B. (2014) Atom transfer radical polymerization as a powerful tool in the synthesis of molecular brushes. *Polym. Int.*, **63**, 824–834.

160 Khabibullin, A., Mastan, E., Matyjaszewski, K., and Zhu, S. (2016) Surface-initiated atom transfer radical polymerization, in *Controlled Radical Polymerization at and from Solid Surfaces* (ed. P. Vana), Springer International Publishing, Cham, pp. 29–76.

161 Cho, H.Y., Krys, P., Szcześniak, K., Schroeder, H., Park, S., Jurga, S., Buback, M., and Matyjaszewski, K. (2015) Synthesis of poly(OEOMA) using macromonomers via "grafting-through" ATRP. *Macromolecules*, **48**, 6385–6395.

162 Matyjaszewski, K., Dong, H., Jakubowski, W., Pietrasik, J., and Kusumo, A. (2007) Grafting from surfaces for "everyone": ARGET ATRP in the presence of air. *Langmuir*, **23**, 4528–4531.

163 Zdyrko, B. and Luzinov, I. (2011) Polymer brushes by the "grafting to" method. *Macromol. Rapid Commun.*, **32**, 859–869.

164 Braunecker, W.A. and Matyjaszewski, K. (2007) Controlled/living radical polymerization: features, developments, and perspectives. *Prog. Polym. Sci.*, **32**, 93–146.

165 Grubbs, R.B. (2011) Nitroxide-mediated radical polymerization: limitations and versatility. *Polym. Rev.*, **51**, 104–137.

166 Moad, G., Rizzardo, E., and Thang, S.H. (2005) Living radical polymerization by the RAFT process. *Aust. J. Chem.*, **58**, 379–410.

167 Moad, G., Rizzardo, E., and Thang, S.H. (2009) Living radical polymerization by the RAFT process a second update. *Aust. J. Chem.*, **62**, 1402–1472.

168 Moad, G., Rizzardo, E., and Thang, S.H. (2012) Living radical polymerization by the RAFT process – a third update. *Aust. J. Chem.*, **65**, 985–1076.

169 Matyjaszewski, K. (2012) Atom transfer radical polymerization: from mechanisms to applications. *Isr. J. Chem.*, **52**, 206–220.

170 Matyjaszewski, K. (2012) Atom transfer radical polymerization (ATRP): current status and future perspectives. *Macromolecules*, **45**, 4015–4039.

171 Matyjaszewski, K. and Tsarevsky, N.V. (2014) Macromolecular engineering by atom transfer radical polymerization. *J. Am. Chem. Soc.*, **136**, 6513–6533.

172 Bidan, s. (2010) Electropolymerized films of π-conjugated polymers: a tool for surface functionalization: a brief historical evolution and recent trends, in *Electropolymerization*, Wiley-VCH Verlag GmbH & Co. KGaA, pp. 1–26.

173 Bhattacharyya, D., Howden, R.M., Borrelli, D.C., and Gleason, K.K. (2012) Vapor phase oxidative synthesis of conjugated polymers and applications. *J. Polym. Sci., Part B: Polym. Phys.*, **50**, 1329–1351.

174 Omastová, M. and Mičušík, M. (2012) Polypyrrole coating of inorganic and organic materials by chemical oxidative polymerisation. *Chem. Pap.*, 392.

175 Inzelt, G., Pineri, M., Schultze, J.W., and Vorotyntsev, M.A. (2000) Electron and proton conducting polymers: recent developments and prospects. *Electrochim. Acta*, **45**, 2403–2421.

176 Fang, L., Zhou, Y., Yao, Y.-X., Diao, Y., Lee, W.-Y., Appleton, A.L., Allen, R., Reinspach, J., Mannsfeld, S.C.B., and Bao, Z. (2013) Side-chain engineering of isoindigo-containing conjugated polymers using polystyrene for high-performance bulk heterojunction solar cells. *Chem. Mater.*, **25**, 4874–4880.

177 Nazzal, A.I. and Street, G.B. (1985) Pyrrole–styrene graft copolymers. *J. Chem. Soc., Chem. Commun.*, 375–376.

178 Stanke, D., Hallensleben, M.L., and Toppare, L. (1995) Graft copolymers and composites of poly(methyl methacrylate) and polypyrrole Part I. *Synth. Met.*, **72**, 89–94.

179 Stanke, D., Hallensleben, M.L., and Toppare, L. (1995) Graft copolymers and composites of poly(methyl methacrylate) and polypyrrole Part II. *Synth. Met.*, **73**, 261–266.

180 Alkan, S., Toppare, L., Hepuzer, Y., and Yagci, Y. (1999) Block copolymers of thiophene-capped poly(methyl methacrylate) with pyrrole. *J. Polym. Sci., Part A: Polym. Chem.*, **37**, 4218–4225.

181 Qi, L., Sun, M., and Dong, S. (2006) Synthesis and characterization of novel polythiophenes containing poly(ethylene oxide) side chains. *J. Appl. Polym. Sci.*, **102**, 1803–1808.

182 Bendrea, A.-D., Vacareanu, L., and Grigoras, M. (2010) Synthesis, characterization and (electro)chemical polymerization of triphenylamine-end-functionalized poly(ε-caprolactone). *Polym. Int.*, **59**, 624–629.

183 Yin, W. and Ruckenstein, E. (2000) Water-soluble self-doped conducting polyaniline copolymer. *Macromolecules*, **33**, 1129–1131.

184 Bae, W.J., Kim, K.H., Jo, W.H., and Park, Y.H. (2005) A water-soluble and self-doped conducting polypyrrole graft copolymer. *Macromolecules*, **38**, 1044–1047.

185 Edmondson, S., Vo, C.-D., Armes, S.P., and Unali, G.-F. (2007) Surface polymerization from planar surfaces by atom transfer radical polymerization using polyelectrolytic macroinitiators. *Macromolecules*, **40**, 5271–5278.

186 Malenfant, P.R.L. and Fréchet, J.M.J. (2000) Dendrimers as solubilizing groups for conducting polymers: preparation and characterization of polythiophene functionalized exclusively with aliphatic ether convergent dendrons. *Macromolecules*, **33**, 3634–3640.

187 Bolognesi, A., Galeotti, F., Mróz, W., Gancheva, V., and Terlemezyan, L. (2010) Towards semiconducting graft copolymers: switching from ATRP to "click" approach. *Macromol. Chem. Phys.*, **211**, 1488–1495.

188 Cianga, I. and Yagci, Y. (2001) Polystyrene macromonomer with boronic acid propanediol diester functionality prepared by ATRP for synthesis of comb-like polyphenylenes. *Polym. Bull.*, **47**, 17–24.

189 Cianga, I., Hepuzer, Y., and Yagci, Y. (2002) Poly(*p*-phenylene) graft copolymers with polytetrahydrofuran/polystyrene side chains. *Polymer*, **43**, 2141–2149.

190 Grande, C.D., Tria, M.C., Felipe, M.J., Zuluaga, F., and Advincula, R. (2011) RAFT "grafting-through" approach to surface-anchored polymers: electrodeposition of an electroactive methacrylate monomer. *Eur. Phys. J. E*, **34**, 15.

191 Zhang, C., Wang, H., Su, G., Li, R., Shen, X., Zhang, S., Geng, Q., Liu, F., Otsuka, I., Satoh, T., and Kakuchi, T. (2012) Synthesis and conformation effects of poly(phenylacetylene)s having chiral and racemic polylactide pendants. *Polym. Int.*, **61**, 1158–1162.

192 Mecerreyes, D., Stevens, R., Nguyen, C., Pomposo, J.A., Bengoetxea, M., and Grande, H. (2002) Synthesis and characterization of polypyrrole-*graft*-poly(ε-caprolactone) copolymers: new electrically conductive nanocomposites. *Synth. Met.*, **126**, 173–178.

193 Cianga, I., Mercore, V.M., Grigoras, M., and Yagci, Y. (2007) Poly(thienyl-phenylene)s with macromolecular side chains by oxidative polymerization of well-defined macromonomers. *J. Polym. Sci., Part A: Polym. Chem.*, **45**, 848–865.

194 Emilsson, G., Schoch, R.L., Feuz, L., Höök, F., Lim, R.Y.H., and Dahlin, A.B. (2015) Strongly stretched protein resistant poly(ethylene glycol) brushes prepared by grafting-to. *ACS Appl. Mater. Interfaces*, **7**, 7505–7515.

195 Tria, M.C.R., Grande, C.D.T., Ponnapati, R.R., and Advincula, R.C. (2010) Electrochemical deposition and surface-initiated RAFT polymerization: protein and cell-resistant PPEGMEMA polymer brushes. *Biomacromolecules*, **11**, 3422–3431.

196 Kingshott, P., Thissen, H., and Griesser, H.J. (2002) Effects of cloud-point grafting, chain length, and density of PEG layers on competitive adsorption of ocular proteins. *Biomaterials*, **23**, 2043–2056.

197 Li, Z.F. and Ruckenstein, E. (2004) Grafting of poly(ethylene oxide) to the surface of polyaniline films through a chlorosulfonation method and the biocompatibility of the modified films. *J. Colloid Interface Sci.*, **269**, 62–71.

198 Wei, B., Ouyang, L., Liu, J., and Martin, D.C. (2015) Post-polymerization functionalization of poly(3,4-propylenedioxythiophene) (PProDOT) via thiol-ene "click" chemistry. *J. Mater. Chem. B*, **3**, 5028–5034.

199 Rugen-Penkalla, N., Klapper, M., and Müllen, K. (2012) Highly charged conjugated polymers with polyphenylene backbones and poly(acrylic acid) side chains. *Macromolecules*, **45**, 2301–2311.

200 Pu, K.-Y., Li, K., and Liu, B. (2010) A molecular brush approach to enhance quantum yield and suppress nonspecific interactions of conjugated polyelectrolyte for targeted far-red/near-infrared fluorescence cell imaging. *Adv. Funct. Mater.*, **20**, 2770–2777.

201 Saha, S. and Baker, G.L. (2015) Surface-tethered conjugated polymers created via the grafting-from approach. *J. Appl. Polym. Sci.*, **132**.

202 Feng, C., Li, Y., Yang, D., Hu, J., Zhang, X., and Huang, X. (2011) Well-defined graft copolymers: from controlled synthesis to multipurpose applications. *Chem. Soc. Rev.*, **40**, 1282–1295.

203 Shen, J., Tsuchiya, K., and Ogino, K. (2008) Synthesis and characterization of highly fluorescent polythiophene derivatives containing polystyrene sidearms. *J. Polym. Sci., Part A: Polym. Chem.*, **46**, 1003–1013.

204 Wang, M., Kumar, S., Coombs, N., Scholes, G.D., and Winnik, M.A. (2010) Structure and excited-state interactions in composites of CdSe nanorods and interface-compatible polythiophene-*graft*-poly(*N*,*N*-dimethylaminoethyl methacrylates). *Macromol. Chem. Phys.*, **211**, 393–403.

205 Kang, E.T., Neoh, K.G., Huang, S.W., Lim, S.L., and Tan, K.L. (1997) Surface-functionalized polyaniline films. *J. Mater. Chem. B*, **101**, 10744–10750.

206 Roux, S., Duwez, A.-S., and Demoustier-Champagne, S. (2003) Surface initiated polymerization of styrene from a carboxylic acid functionalized polypyrrole coated electrode. *Langmuir*, **19**, 306–313.

207 Massoumi, B., Mozaffari, Z., and Mohammadi, R. (2014) Synthesis and properties of electroactive polyaniline-*graft* polymethyl methacrylate copolymer by atom transfer radical polymerization. *Int. J. Polym. Mater. Polym. Biomater.*, **63**, 800–807.

208 Strover, L., Roux, C., Malmström, J., Pei, Y., Williams, D.E., and Travas-Sejdic, J. (2012) Switchable surfaces of electroactive polymer brushes grafted from polythiophene ATRP-macroinitiator. *Synth. Met.*, **162**, 381–390.

209 Domagala, A., Domagala, W., Ledwon, P., Musiol, M., Janeczek, H., Stolarczyk, A., Kurcok, P., Adamus, G., and Lapkowski, M. (2016) *N*-Oligo(3-hydroxybutyrate)-functionalized polypyrroles: towards bio-erodible conducting copolymers. *Polym. Int.*, **65**, 1395–1404.

210 Rodda, A.E., Ercole, F., Nisbet, D.R., Forsythe, J.S., and Meagher, L. (2015) Optimization of aqueous SI-ATRP grafting of poly(oligo(ethylene glycol) methacrylate) brushes from benzyl chloride macroinitiator surfaces. *Macromol. Biosci.*, **15**, 799–811.

211 Tang, W. and Matyjaszewski, K. (2007) Effects of initiator structure on activation rate constants in ATRP. *Macromolecules*, **40**, 1858–1863.

212 Chams, A., Dupeyre, G., Jouini, M., Yassar, A., and Perruchot, C. (2013) Direct growth of polymer brushes from an electrodeposited conducting poly(dithienylpyrrole) layer functionalized with ATRP initiating moieties. *J. Electroanal. Chem.*, **708**, 20–30.

213 Spires, J.B., Peng, H., Williams, D.E., Soeller, C., and Travas-Sejdic, J. (2010) Solvent-induced microstructure changes and consequences for electrochemical activity of redox-active conducting polymers. *Electrochim. Acta*, **55**, 3061–3067.

214 Chan, E.W.C., Baek, P., Barker, D., and Travas-Sejdic, J. (2015) Highly functionalisable polythiophene phenylenes. *Polym. Chem.*, **6**, 7618–7629.
215 Jones, D.M., Brown, A.A., and Huck, W.T.S. (2002) Surface-initiated polymerizations in aqueous media: effect of initiator density. *Langmuir*, **18**, 1265–1269.
216 Doubina, N., Jenkins, J.L., Paniagua, S.A., Mazzio, K.A., MacDonald, G.A., Jen, A.K.Y., Armstrong, N.R., Marder, S.R., and Luscombe, C.K. (2011) Surface-initiated synthesis of poly(3-methylthiophene) from indium tin oxide and its electrochemical properties. *Langmuir*, **28**, 1900–1908.
217 Karim, A., Satija, S.K., Douglas, J.F., Ankner, J.F., and Fetters, L.J. (1994) Neutron reflectivity study of the density profile of a model end-grafted polymer brush: influence of solvent quality. *Phys. Rev. Lett.*, **73**, 3407–3410.
218 Hamilton, W.A., Smith, G.S., Alcantar, N.A., Majewski, J., Toomey, R.G., and Kuhl, T.L. (2004) Determining the density profile of confined polymer brushes with neutron reflectivity. *J. Polym. Sci., Part B: Polym. Phys.*, **42**, 3290–3301.
219 Audouin, F., Larragy, R., Fox, M., O'Connor, B., and Heise, A. (2012) Protein immobilization onto poly(acrylic acid) functional macroporous polyHIPE obtained by surface-initiated ARGET ATRP. *Biomacromolecules*, **13**, 3787–3794.
220 Grande, C.D., Tria, M.C., Jiang, G., Ponnapati, R., Park, Y., Zuluaga, F., and Advincula, R. (2011) Grafting of polymers from electrodeposited macro-RAFT initiators on conducting surfaces. *React. Funct. Polym.*, **71**, 938–942.
221 Tria, M.C.R. and Advincula, R.C. (2011) Electropatterning of binary polymer brushes by surface-initiated RAFT and ATRP. *Macromol. Rapid Commun.*, **32**, 966–971.

Index

Conjugated Polymers for Biological and Biomedical Applications, First Edition. Edited by Bin Liu

h

i

k

l